

Special Issue Reprint

---

# Mathematical Modeling of Engineering and Socio-Economic Processes and Systems

---

Edited by  
Sergei Viktorovich Aliukov, Anatoliy Alekseevich Alabugin  
and Konstantin Vladimirovich Osintsev

[mdpi.com/journal/mathematics](https://mdpi.com/journal/mathematics)

# **Mathematical Modeling of Engineering and Socio-Economic Processes and Systems**

# Mathematical Modeling of Engineering and Socio-Economic Processes and Systems

Editors

**Sergei Viktorovich Aliukov**

**Anatoliy Alekseevich Alabugin**

**Konstantin Vladimirovich Osintsev**



Basel • Beijing • Wuhan • Barcelona • Belgrade • Novi Sad • Cluj • Manchester

*Editors*

Sergei Viktorovich Aliukov  
Department of  
Automotive Engineering  
South Ural State University  
Chelyabinsk  
Russia

Anatoliy Alekseevich  
Alabugin  
Department of Digital  
Economics and  
Information Technologies  
South Ural State University  
Chelyabinsk  
Russia

Konstantin Vladimirovich  
Osintsev  
Department of Industrial  
Heat Power Engineering  
South Ural State University  
Chelyabinsk  
Russia

*Editorial Office*

MDPI  
St. Alban-Anlage 66  
4052 Basel, Switzerland

This is a reprint of articles from the Special Issue published online in the open access journal *Mathematics* (ISSN 2227-7390) (available at: [https://www.mdpi.com/si/mathematics/mathematical\\_modeling\\_engineering\\_socio-economic\\_processes\\_systems](https://www.mdpi.com/si/mathematics/mathematical_modeling_engineering_socio-economic_processes_systems)).

For citation purposes, cite each article independently as indicated on the article page online and as indicated below:

Lastname, A.A.; Lastname, B.B. Article Title. <i>Journal Name</i> <b>Year</b> , <i>Volume Number</i> , Page Range.
--

**ISBN 978-3-7258-1195-3 (Hbk)**

**ISBN 978-3-7258-1196-0 (PDF)**

**[doi.org/10.3390/books978-3-7258-1196-0](https://doi.org/10.3390/books978-3-7258-1196-0)**

© 2024 by the authors. Articles in this book are Open Access and distributed under the Creative Commons Attribution (CC BY) license. The book as a whole is distributed by MDPI under the terms and conditions of the Creative Commons Attribution-NonCommercial-NoDerivs (CC BY-NC-ND) license.

# Contents

<b>About the Editors</b> . . . . .	<b>vii</b>
<b>Preface</b> . . . . .	<b>ix</b>
<b>Vladimir Kodkin, Ekaterina Kuznetsova, Alexander Anikin and Alexander A. Baldenkov</b> Frequency Criterion for the Existence of Sliding Processes in Control Systems with an Arbitrary Variable Structure Reprinted from: <i>Mathematics</i> <b>2024</b> , <i>12</i> , 856, doi:10.3390/math12060856 . . . . .	<b>1</b>
<b>Sergei Aliukov</b> Modeling of Rapidly Changing Macroeconomic Processes Based on the Analysis of Jump and Generalized Functions Reprinted from: <i>Mathematics</i> <b>2024</b> , <i>12</i> , 138, doi:10.3390/math12010138 . . . . .	<b>20</b>
<b>Elena Lyaskovskaya, Gulnaz Khalilova and Kristina Grigorieva</b> Dynamic Analysis of the EU Countries Sustainability: Methods, Models, and Case Study Reprinted from: <i>Mathematics</i> <b>2023</b> , <i>11</i> , 4807, doi:10.3390/math11234807 . . . . .	<b>45</b>
<b>Konstantin Kostromitin, Konstantin Melnikov and Dar'ya Nikonova</b> Analytical and Numerical Study of Information Retrieval Method Based on Single-Layer Neural Network with Optimization of Computing Algorithm Performance Reprinted from: <i>Mathematics</i> <b>2023</b> , <i>11</i> , 3648, doi:10.3390/math11173648 . . . . .	<b>85</b>
<b>Sergey Surovtcev, Elena Zadorozhnaya, Nadezhda Khozenyuk and Oleg Mashkov</b> Building of a Mathematical Model for Solving the Elastic–Gas–Dynamic Task of the Gas Lubrication Theory for Petal Bearings Reprinted from: <i>Mathematics</i> <b>2023</b> , <i>11</i> , 2901, doi:10.3390/math11132901 . . . . .	<b>105</b>
<b>Konstantin Gavrilov, Yuriy Rozhdestvenskii and Ildar Umurzakov</b> A Method for Mathematical Modeling of Hydrodynamic Friction of Plunger Pairs with Consideration of Microgeometry Reprinted from: <i>Mathematics</i> <b>2023</b> , <i>11</i> , 2637, doi:10.3390/math11122637 . . . . .	<b>124</b>
<b>Evgeny V. Solomin and Gleb N. Ryavkin</b> Horizontal Axis Wind Turbine Weather Vane Aerodynamic Characteristics: Delayed Detached Eddy Simulation and Experimental Approach Reprinted from: <i>Mathematics</i> <b>2023</b> , <i>11</i> , 1834, doi:10.3390/math11081834 . . . . .	<b>135</b>
<b>Vladimir Shepelev, Aleksandr Glushkov, Ivan Slobodin and Yuri Cherkassov</b> Measuring and Modelling the Concentration of Vehicle-Related PM2.5 and PM10 Emissions Based on Neural Networks Reprinted from: <i>Mathematics</i> <b>2023</b> , <i>11</i> , 1144, doi:10.3390/math11051144 . . . . .	<b>151</b>
<b>Elena Zadorozhnaya, Igor Levanov, Igor Mukhortov and Vlad Huduyakov</b> Investigation of the Convergence of a Multi-Grid Algorithm for Solving the Task of Pressure in the Thin Lubricating Film of the Non-Newtonian Fluid Reprinted from: <i>Mathematics</i> <b>2023</b> , <i>11</i> , 54, doi:10.3390/math11010054 . . . . .	<b>174</b>
<b>Viacheslav Morozov, Vladimir Shepelev and Viktor Kostyrchenko</b> Modeling the Operation of Signal-Controlled Intersections with Different Lane Occupancy Reprinted from: <i>Mathematics</i> <b>2022</b> , <i>10</i> , 4829, doi:10.3390/math10244829 . . . . .	<b>192</b>

<b>Konstantin Gavrilov, Yuriy Rozhdestvenskii and Ildar Umurzakov</b> The Construction of Models of Rough Surfaces' Interaction: Markov's Approach Reprinted from: <i>Mathematics</i> <b>2022</b> , <i>10</i> , 3607, doi:10.3390/math10193607 . . . . .	<b>216</b>
<b>Veniamin Mokhov, Sergei Aliukov, Anatoliy Alabugin and Konstantin Osintsev</b> A Review of Mathematical Models of Macroeconomics, Microeconomics, and Government Regulation of the Economy Reprinted from: <i>Mathematics</i> <b>2023</b> , <i>11</i> , 3246, doi:10.3390/math11143246 . . . . .	<b>229</b>
<b>Inna Elyukhina</b> Mathematical Models in High-Temperature Viscometry: A Review Reprinted from: <i>Mathematics</i> <b>2023</b> , <i>11</i> , 2300, doi:10.3390/math11102300 . . . . .	<b>266</b>
<b>Konstantin Osintsev, Sergei Aliukov and Anatoliy Alabugin</b> A Review of Methods, and Analytical and Experimental Studies on the Use of Coal–Water Suspensions Reprinted from: <i>Mathematics</i> <b>2022</b> , <i>10</i> , 3915, doi:10.3390/math10203915 . . . . .	<b>286</b>

# About the Editors

## **Sergei Viktorovich Aliukov**

Sergei Viktorovich Aliukov was born in Chelyabinsk, Russia, in 1957. He received his M.S. degree in Mechanical Engineering from South Ural State University, Chelyabinsk, in 1978, his M.S. degree in Mathematics from the Ural State University, Yekaterinburg, Russia, in 1984, and his Ph.D. in Mechanical Engineering and doctorate in the field of Mechanical Engineering from South Ural State University in 1983 and 2005, respectively. He is currently a professor at South Ural State University. He works in the Department of Automotive Engineering and the Department of Digital Economics and Information Technologies. He is the author of three books, more than 150 articles, and ten inventions. His research interests include mathematical modeling processes and applications, mathematical problems, and non-linear dynamic systems. Some of his scientific research achievements have been applied in engineering.

## **Anatoliy Alekseevich Alabugin**

Anatoliy Alekseevich Alabugin, Doctor of Economics, Professor at the Department of Digital Economics and Information Technologies and the Industrial Heat Power Engineering Department of South Ural State University, author of over 150 scientific papers in domestic and foreign publications, including monographs, teaching aids, and registered intellectual property. Member of two dissertation councils in economic sciences. Graduated from the Faculty of Power Engineering of the Chelyabinsk Polytechnic Institute in 1971 and graduated in 1981 with a targeted postgraduate degree from the Moscow Power Engineering Institute in the Department of Energy Economics. In 1981, he defended his thesis for the degree of Candidate of Economic Sciences, and in 2007, he did the same for his Doctorate of Economic Sciences. The main direction of his scientific research is the management of innovative and high-tech development of socio-economic systems in the context of an imbalance in the goals of their objects and techno-humanitarian conflicts.

## **Konstantin Vladimirovich Osintsev**

Konstantin Vladimirovich Osintsev was born in Chelyabinsk, Russia, in 1986. He received his M.S. degree in Engineering and Ph.D. in Industrial Heat Engineering from South Ural State University (SUSU), Chelyabinsk, in 2008 and 2009, respectively. Since 2013, he has been the Head of the Industrial Heat Department, SUSU. He has published more than 150 high-quality journal articles and conference papers and holds more than ten patent rights. His numerous scientific research achievements have been applied in industrial heat engineering. His research interests include the steam turbines of thermal power plants and thermodynamics and heat transfer.

# Preface

Topics covered in this reprint include, but are not limited to, the following:

The mathematical modeling of scientific and engineering problems;

Optimization and control in engineering applications;

Analytical and numerical methods for solving engineering and socio-economic problems;

The integration of economic and mathematical models and approaches;

Improving the mathematical description of modern evolutionary, spasmodic, and impulsive processes and phenomena.

**Sergei Viktorovich Aliukov, Anatoliy Alekseevich Alabugin, and Konstantin Vladimirovich  
Osintsev**  
*Editors*



Article

# Frequency Criterion for the Existence of Sliding Processes in Control Systems with an Arbitrary Variable Structure

Vladimir Kodkin \*, Ekaterina Kuznetsova, Alexander Anikin and Alexander A. Baldenkov

Department of Electric Drive, Mechatronics and Electromechanics, South Ural State University, 454080 Chelyabinsk, Russia; ket\_ke@mail.ru (E.K.); anikinas@susu.ru (A.A.); baloo@mail.ru (A.A.B.)

\* Correspondence: kodkinvl@susu.ru

**Abstract:** The article proposes a criterion for the existence of sliding processes according to the frequency characteristics of the control device and the control object. It is shown that the conditions for the existence of slip are equivalent to the conditions for the absolute stability of equivalent circuits of the original systems with a variable structure. This approach is proposed by the authors as an alternative to the method of phase trajectories and state space equations used by other researchers. Frequency criteria make it possible to formulate several practical engineering provisions that are very important for the implementation of this control method in real electric drives. The main conclusions are confirmed by simulation of both processes in systems with a variable structure and in equivalent circuits.

**Keywords:** control systems with variable structure (VSS); sliding modes (SM); slow and fast movements; perfect glide; phase trajectories; control object

**MSC:** 93D15

## 1. Introduction

Variable structure systems (VSS) with sliding modes (SM) are a striking example of the effectiveness of the use of new mathematical methods in technical automation systems.

In these systems, the theory of which is exhaustively described in the books of Emelyanov S.V. and Utkin V.I. [1–4], transient processes are formed by switching the feedback sign in the vicinity of the sliding space (or trajectory).

The essence of this control is that in a certain region of the phase space around the switching surface, conditions for counter movements are created. The phase trajectory is “decomposed” into two movements: fast and slow. These movements have the necessary rigidity to external disturbances and changes in system parameters. When the sign of the feedback changes, the control forms a switching line (surface), on which the phase trajectory of the automatic control system (ACS) remains until the end of the transient process. In this case, the switching surface is a “slow” movement and movements around the surface are “fast”.

Most often, the creation of discontinuous controls in real automatic control systems creates undesirable oscillatory processes. Therefore, when creating sliding processes, it is important to take into account the specific parameters of “fast” movements, i.e., their frequency and amplitude. An ideal glide is considered to be one in which the frequency of “fast” movements is very high and the amplitude is very small. But in reality, it is very difficult to obtain such processes. They are influenced by small inertia and delays in the ACS, nonlinearities, etc. It is very difficult to take their influence into account in differential equations. In traditional ACS, their influence is effectively taken into account by the frequency characteristics of the ACS units. Therefore, the task of assessing sliding processes using frequency methods is very relevant.

**Citation:** Kodkin, V.; Kuznetsova, E.; Anikin, A.; Baldenkov, A.A. Frequency Criterion for the Existence of Sliding Processes in Control Systems with an Arbitrary Variable Structure. *Mathematics* **2024**, *12*, 856. <https://doi.org/10.3390/math12060856>

Academic Editor: Asier Ibeas

Received: 31 January 2024

Revised: 5 March 2024

Accepted: 13 March 2024

Published: 14 March 2024



**Copyright:** © 2024 by the authors. Licensee MDPI, Basel, Switzerland. This article is an open access article distributed under the terms and conditions of the Creative Commons Attribution (CC BY) license (<https://creativecommons.org/licenses/by/4.0/>).

Conditions for Ideal Sliding of Second-Order VSS

Figure 1 shows an ACS of the second order, in which the control object (CO) is a double integrator, as the link most prone to instability among the elementary dynamic links; the controller (C) is an amplifier with coefficient  $K$ ; and the switching trajectory shaper (TG) is a forcing link with time constant  $T_1$ .

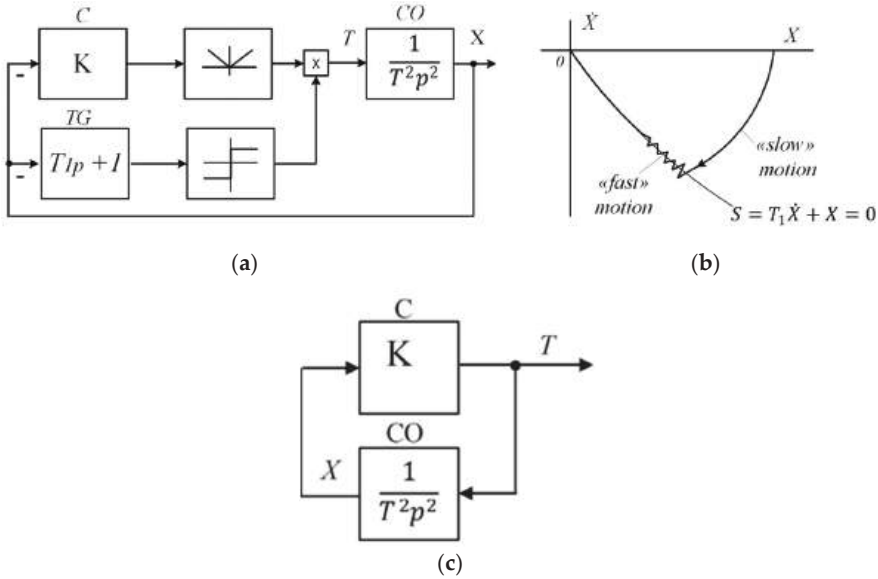


**Figure 1.** (a) Block diagram of second-order VSS, (b) phase trajectory of the process, and (c) diagram of the circuit formed by the amplifier (C) and the control object (CO).

Initial System of Differential Equations VSS:

$$\begin{cases} T^2 \ddot{x} + K|x| \text{sign} S = 0 \\ S = T_1 \dot{x} + x \end{cases} \quad (1)$$

In the works of Emelyanov and Utkin [1–4], a method of equivalent control was developed and conditions for the existence of sliding processes were obtained for systems with control objects described by differential equations of order  $n$  and sliding trajectory equations of order  $(n-1)$ . In work [3], ideal SM conditions for electric drives were obtained, which are close to the systems presented in Figure 1, using the equivalent control method for systems described by Equation (1).

The equivalent control method is close to the second Lyapunov method and evaluates the existence of a phase space in which, due to ACS Equation (1), the condition  $S \times \dot{S} < 0$  is satisfied in the vicinity of  $S = 0$ .

For systems described by Equation (1), these conditions are reduced to the following inequality:

$$T_1 > \sqrt{\frac{T^2}{K}} \quad (2)$$

$T_{1\text{boundary}} = \sqrt{\frac{T^2}{K}}$ , called the boundary time constant of the sliding trajectory, determines the boundary speed of sliding processes. The condition connects the time constant  $T_1$  of the sliding trajectory, the parameters of the control object ( $T^2$ ), and the parameters of the controller ( $K$ ). The order of the control object and the order of the switching trajectory correspond to the conditions derived by S.V. Emelyanov and V.P. Utkin; therefore, the fulfillment of the conditions of slow movement simultaneously determines the absence

of “fast” movements around the sliding trajectory with a finite frequency and amplitude. With ideal sliding, their frequency tends to  $\infty$  and their amplitude tends to 0.

This principle of forming transient processes in automatic control systems, which requires high speed, seems very promising for electromechanical systems, in which fast and slow variables are always present. Fast movements are the armature current and the voltage at the motor armature; slow movements are the speed and angular movements of the output shaft.

## 2. Problem Statement: State of the Issue

However, studies of such systems very quickly confirmed that special, more accurate criteria for the existence of sliding processes for real automatic control systems are required. Moreover, some factors that were little taken into account in linear systems, for example, small delays of dynamic links, static external disturbances, limitations of mechanical moments, etc. in sliding mode systems can lead to qualitative changes in transient processes. Taking these features into account significantly complicated the criteria and conditions obtained for the main slow movement.

The work [5] shows how sliding processes are influenced by discrete elements, but it is also very important to determine how small inertia of the control object affects them. To solve this problem, the method of analyzing the frequency characteristics of control systems with a variable structure (ACS with a variable structure) is very effective.

In recent years, many works have been published on sliding processes in automatic control systems [6–14]. These works use methods similar to the equivalent control method [5–7] or the second Lyapunov method [8,9]. The results of these calculations are most often quite difficult to apply in real control systems, particularly in electromechanical control systems.

According to the authors of this article, the widespread use of VSS in real automatic control systems will be facilitated by sliding criteria that work “universally” in technical systems containing known features—nonlinearity, delays, and high-order links. Also, how stability criteria “work” in linear and nonlinear automatic control systems has been investigated by Nyquist and V.M. Popov [1–5], whose studies were very close to each other in final formulations and mathematical content.

In a previously published work [5], “engineering” criteria for sliding according to the frequency characteristics of an automatic control system with a variable structure were formulated. Further, with the help of simulation, it was shown how sliding is carried out in systems with discretization of various regulator channels. This article presents the results of simulation ACS, in which, in addition to double integrators that describe the main inertia of electromechanical ACS, links with lower inertia are introduced. Most electromechanical automatic control systems can be reduced to such structures. Attempts to construct sliding processes in such systems in accordance with the above methods (using differential equations with the order of the switching trajectory one below the order of the equation) lead to a significant complication of the ACS. It becomes necessary to build observers and supplement the ACS with models for indirectly measuring the coordinates that are necessary to form the switching trajectory. Moreover, this coordinate cannot be measured in reality. The frequency method proposed in [5] can largely solve these problems. Frequency criteria make it possible to solve the problems of synthesizing “real slip”, i.e., having finite parameters of “fast” movements—their amplitude and frequency.

Let us return to the sliding condition obtained for second-order control systems. Let us take into account that the time constant  $\sqrt{\frac{T^2}{K}}$  is a parameter determined by the circuit formed by the control object CO and the controller C.

Condition (2) can be formulated as follows: **the time constant of the sliding trajectory must be greater than the time constant of the circuit formed by the control object link and the regulator link.**

2.1. On the Connection between Electromechanical Automatic Control Systems and Second-Order Automatic Control Systems

Most real electromechanical automatic control systems can be represented with sufficient accuracy by a combination of a double integrator and a high-order link or nonlinear structures. This approach is widespread both in works on sliding processes and in works on the stability of nonlinear automatic control systems.

In almost all electromechanical systems, connections in mechanical links are described by integrators with time constants of 0.1–10 s, electrical connections are described by inertia with time constants of 0.001–0.1 s, and the non-rigidity of the gearbox is described by oscillatory structures with time constants of 0.1–1 s. Thus, the presence of a double integrator with large time constants and other features for the analysis of sliding processes should be considered acceptable. Verification of the proposed criteria by mathematical simulation in this example can be considered sufficient. In all of these works, the provisions are also confirmed by theoretical calculations or simulation.

The condition for electromechanical systems can be interpreted by the logarithmic frequency characteristics (LFC) of the ACS elements presented in Figure 1.

Figure 2 shows the LFC structure and transient diagrams for various options for fulfilling condition (2).

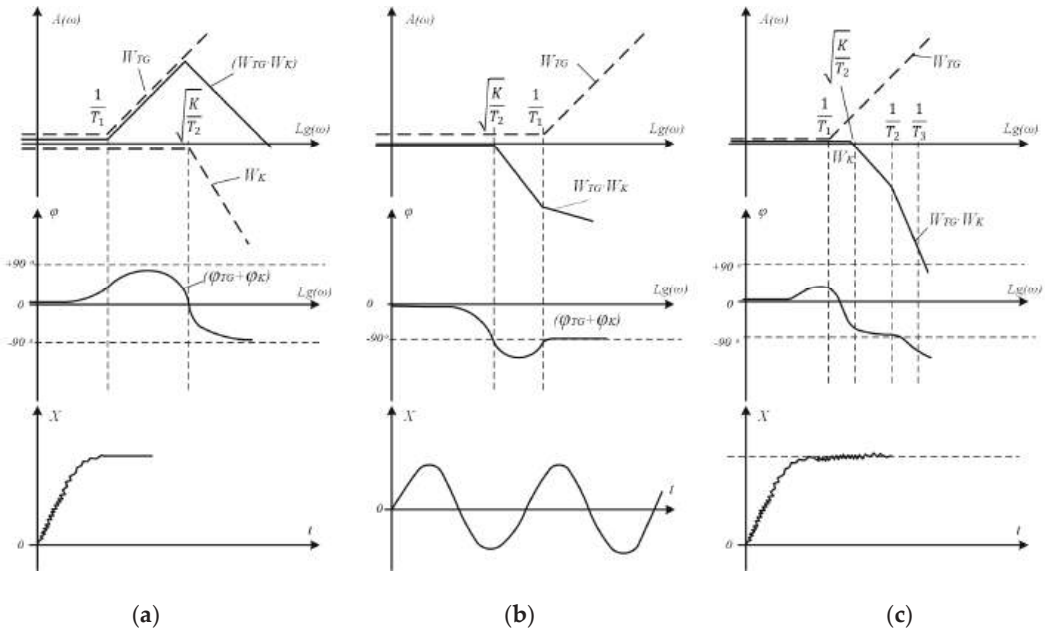


Figure 2. LAFC, LPFC, and transient processes in systems with ideal (a), critical (b), and real (c) slip.

Figure 2a–c show the frequency characteristics of the link that forms the sliding trajectory  $W_{TG}$  (forcing link) and the circuit formed by the amplifier link C and the control object CO—A double integrator (Figure 1c).

The transfer function of this circuit is as follows:

$$W_K = \frac{W_{AM} \cdot W_{CO}}{1 + W_{AM} \cdot W_{CO}}$$

The process in Figure 2a corresponds to ideal sliding. The sliding condition (2) is satisfied. In this case, condition (2) is equivalent to two conditions connecting the frequency characteristics of ACS blocks:

- The condition for ideal sliding of the VSS is satisfied if two links—the slip former and the circuit, including the regulator and the control object—form a series connection, the equivalent phase characteristic of which does not pass the value  $(-90^\circ)$  and  $(-90^\circ)$  is achieved at  $\omega \rightarrow \infty$ .

$$\varphi[W_K \cdot W_{TG}] > -90^\circ \tag{3}$$

here,

$$W_K = \frac{W_{AM} \cdot W_{CO}}{1 + W_{AM} \cdot W_{CO}} \tag{4}$$

The fulfillment of this condition is very clearly verified by the amplitude-phase characteristics of the control system, including the logarithmic characteristics (LFC in Figure 2).

The same condition can be formulated as follows:

- Sliding processes will exist if the real part of the complex frequency transfers function of the serial connection of the circuit path shaper link formed by the control object and the controller is positive over the entire frequency range:

$$Re[W_K \cdot W_{TG}] > 0 \tag{5}$$

$$W_K = \frac{W_C \cdot W_{CO}}{1 + W_C \cdot W_{CO}} \tag{6}$$

This condition, in turn, is the condition for the absolute stability [2] of an equivalent circuit containing the same links in a slightly different configuration, shown in Figure 3.

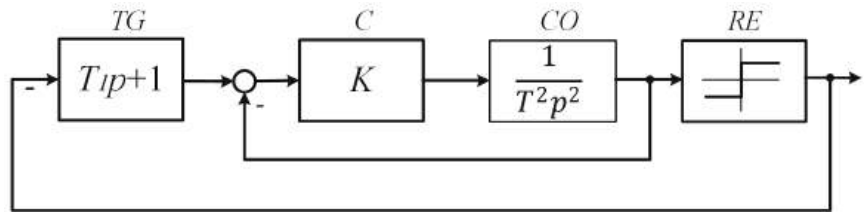


Figure 3. Equivalent circuit of a system with a second-order variable structure.

VSS replacement scheme:

Specifically, the stability of this system according to V.M. Popov [15,16] coincides with the existence of ideal sliding processes in the original scheme, and instability with violation of these conditions is shown in Figure 2b.

Figure 2b shows the characteristics and processes when conditions (2) are not met.

If condition (2) is not met, then the process is self-oscillatory, as in Figure 2b. In this case, at a frequency less than the cutoff frequency of the sliding trajectory shaper,  $\frac{1}{T_1}$ , the phase shift of the series connection of the TG links and the circuit reaches values less than  $(-90^\circ)$ . There are no stable, slow slips in the VSS. The equivalent circuit is unstable in this case since condition (4) is violated.

Let us propose a hypothesis that the stability condition (5), corresponding to the ideal sliding condition (2), will be preserved for any systems whose frequency characteristics satisfy condition (5). Then, applying the criterion of V.M. Popov, one can obtain a very convenient interpretation of various variants of sliding modes, which is extremely important for the practical application of SM in VSS.

Condition for the existence of sliding processes in systems of arbitrary order.

In a control system with a variable structure, with a control object of a general type (Figure 4), a sliding mode will exist if the condition of absolute stability is satisfied for its equivalent circuit (Figure 5):

$$Re[W_K \cdot W_{TG}] > 0 \tag{7}$$

or

$$\varphi[W_K \cdot W_{TG}] > -90^\circ \tag{8}$$

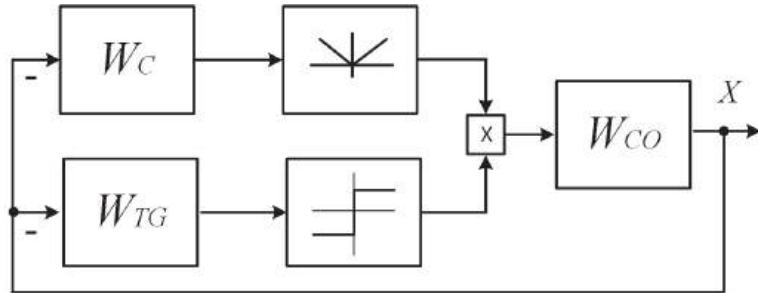


Figure 4. VSS with dynamic links of arbitrary order.

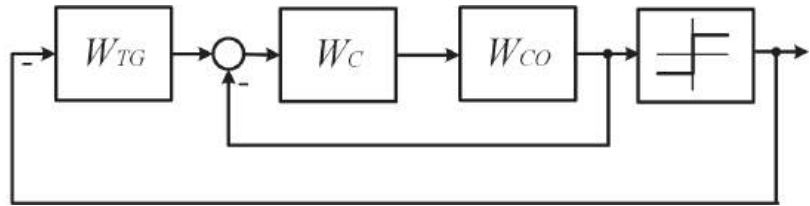


Figure 5. Equivalent circuit of a control system with a variable structure and a control object of arbitrary order.

This sliding condition can be applied to automatic control systems with nonlinear links in the control object and high-order links, and be the basis of engineering criteria for sliding processes.

The stability criterion in the equivalent circuit (4) can be used to assess the presence of slippage in the original system (1) when analyzing transient processes in a system with almost any nonlinear object, i.e., any object to which the theory of absolute stability is applicable, which excludes a detailed analysis of each specific case, as is performed in the theory of sliding processes in VSS [1–3].

Particular attention should be paid to the fact that the proposed criterion (4) is very close to the stability criteria of linear and nonlinear automatic control systems that are familiar to engineers—the Nyquist and V.M. Popov criteria.

### 2.2. Real Sliding

Let us consider the case of an automatic control system with additional inertial links.

If condition (2) is satisfied for the values of the time constants of the control object, but the VSS contains delay or hysteresis links that change the transfer functions of the control object (CO) and their frequency characteristics in the high-frequency region, the real sliding mode begins in the VSS—fast movements have a finite frequency and amplitude. This is shown in Figure 2c and is clearly shown by the frequency conditions (2)–(5). In the high-frequency zone, there is a region of space in which sliding movements do not exist—that is, fast movements have finite parameters.

Due to the characteristics of the object, the phase shift reaches a critical value ( $-90^\circ$ ) at a finite frequency and amplitude, which determines the parameters of fast movements (Figure 2c).

This condition is very important for real automatic control systems. In the substitution diagram, this circumstance will be clearly “embodied”.

The frequency at which equality is satisfied is the frequency of self-oscillations in the equivalent circuit and the frequency of rapid movements in the existing sliding process. In this case, self-oscillations with a finite frequency and amplitude will exist in the equivalent circuit.

That is, the proposed frequency criteria for the existence of slip in an automatic control system of arbitrary order in terms of the stability of equivalent circuits make it possible to determine the parameters of real slip, i.e., their amplitude and frequency, which is very important for real electric drives. In this way, a frequency condition is obtained that is convenient for engineering calculations and does not connect the order of the control object and the order of the sliding trajectory—that is, the main problems have been overcome. We need to check this on models.

**3. Theoretical «Origin» of the Problems**

Variable structure systems are systems in which the control experiences discontinuities at the switching surface. The conditions for hyperstability of a nonlinear automatic control system imply the existence of a positive Lyapunov function [5,6], including an equilibrium state that has a negative sign derivative with respect to time due to the equation of the system. For a sliding process, the domain of existence of this function may exclude part of the space. For ideal sliding, only the switching surface itself can be excluded; for real, the part of the space around this surface can be excluded (Figure 1b).

The area of this space will determine the conditions of oscillation of fast movements—their frequency and amplitude. Moreover, the frequency method will determine them very clearly and accurately: the frequency of violation of the sliding conditions will determine these parameters, first the frequency and then the amplitude of oscillations of the output coordinate in the equivalent circuit.

These real parameters are very important for real, automatic control systems. Therefore, let us check these provisions on the model. Frequency conditions show very well how high-order links influence the conditions for the existence of SM and the parameters of fast movements.

The frequency condition simultaneously analyzes processes both in the low-frequency zone—slow, and in the high-frequency zone—fast, i.e., an engineering criterion can be created that describes all the parameters of sliding processes [7–9].

All these conditions are clearly illustrated by simulation.

**4. Simulation of VSS with a High (Fourth)-Order Object**

Figure 6 shows a diagram of the model in the MatLab (ver R2017b) software environment.

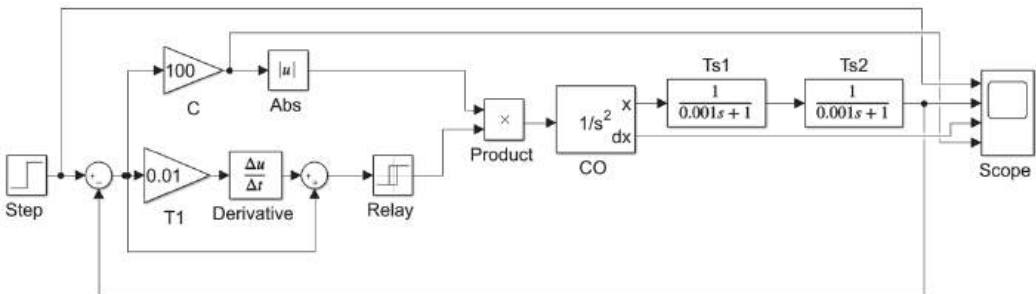


**Figure 6.** Diagram of a variable structure system with a 4th-order control object—a double integrator and two links with low inertia.

Control object  $T_2 = 1s^2$  and two inertial links with small time constants ( $T_{s1} = T_{s2}$ )—0.001s.

Controller with  $K = 100$ .

The forcing link with a time constant  $T_1$  forms the sliding trajectory. In Figures 7–9, the processes in the VSS model are shown:

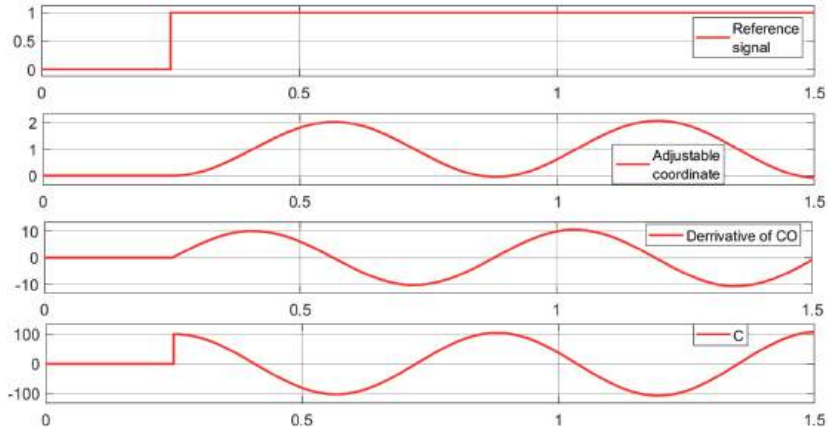


Figure 7. Processes of VSS shown in Figure 6 when condition (2) is violated.

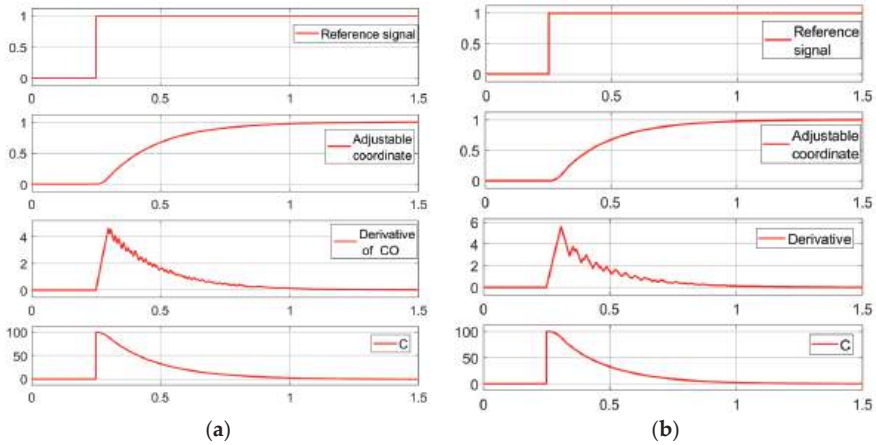


Figure 8. Sliding processes in VSS (Figure 6) with a high-order control object: (a) quasi-ideal sliding; (b) real sliding.

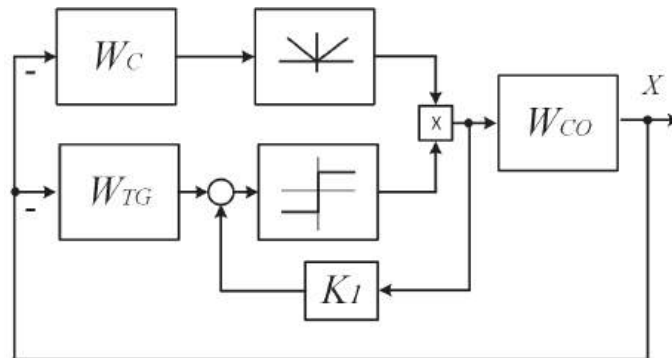


Figure 9. VSS diagram with additional cross-link to form a sliding trajectory.

- Diagram 1—reference signal;
- Diagram 2—adjustable coordinate;
- Diagram 3—derivative of the adjustable coordinate;
- Diagram 4—increased mismatch between the setting signal and the controlled coordinate.

In the first experiment (Figure 7), the parameters of the slip former are the time constant  $T_1 = 0.01s$  and  $T_{1boundary} = 0.1s$ .

Condition (2) is not satisfied. The process of changing the output coordinate is self-oscillation of all coordinates, there is no sliding, and the LFCs are similar to those shown in Figure 2b.

In the second model, the parameters of the link forming the slip are changed— $T_1 = 0.2s$ . Condition (2) is satisfied.

$$T_{1boundary} = 0.1s \quad T_1 = 0.2s.$$

The process shown in Figure 8a is close to ideal sliding (“quasi-ideal” sliding).

Figure 8b shows processes in the same model with small time constants in the control object increased to 0.01 s. The amplitude increased and the frequency of oscillations of the derivative of the controlled variable decreased (diagram 3). The diagram of the controlled variable (diagram 2) remained virtually unchanged. The LFCs are similar to those shown in Figure 2c. The phase shift of the equivalent link reaches a value of  $-90$  at a large but finite frequency  $\omega = \frac{1}{T_2}$ .

Simulation confirmed the validity of the condition for the existence of slip in the system constructed according to the scheme in Figure 1, in which the sliding trajectory has an order lower than the control object by 2 or more orders of magnitude. In this case, the condition for the existence of slow sliding processes and real, fast oscillations around the sliding trajectory with finite amplitude and frequency is satisfied.

For most electric drives, fast movements with the parameters presented in Figure 8 will be acceptable. But for drives with high precision requirements, it is necessary to obtain a mechanism for reducing the amplitude and increasing the frequency of fast movements. One of the effective methods is the use of cross-links.

#### 4.1. Cross Connections and Quasi-Ideal SM

In control systems for real electric drives, the sliding path former link is most often a first-order forcing link, the time constant of which is determined by the requirements for the speed of the drive. The control object simultaneously contains several inertial links with small time constants, except for the second-order integrating link. In this case, it is quite difficult to accurately determine the sliding trajectory equation using an equivalent control method [1–4,7–9]. Experiments have shown that for such a system, cross-coupling based on the control signal of the electric drive—the control signal or the voltage at the motor armature—will be effective.

This relationship is shown in the VSS diagram (Figure 9) and in the substitution diagram (Figure 10).

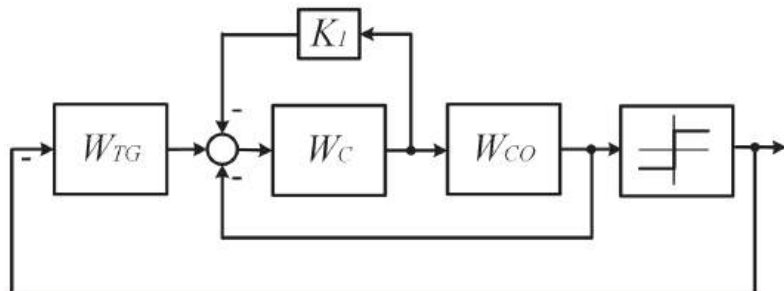


Figure 10. Equivalent circuit of VSS with cross-coupling (Figure 9).

This signal, in relation to the output signal  $X$ , will be a forced signal with the required parameters that ensure the fulfillment of the sliding conditions (4) or the stability of the equivalent circuit.

Taking into account the connection, the condition will take the form (5).

$$W_{TG}^* = W_{TG} + K_1 U = W_{TG} + \frac{K_1}{W_{CO}}$$

$$\varphi \left[ \frac{W_{CO} \cdot W_K}{W_{CO} \cdot W_K + 1} \cdot \left( W_{TG} + \frac{K_1}{W_{CO}} \right) \right] > -90^\circ$$

$$Re \left[ \left( W_{TG} + \frac{K_1}{W_{CO}} \right) \cdot \frac{W_{CO} \cdot W_K}{1 + W_{CO} \cdot W_K} \right] > 0 \tag{9}$$

$$\varphi[W_K \cdot W_{TG}] > -90^\circ \tag{10}$$

Since condition (2) will be met, the sliding will be very close to ideal along the slow coordinate; the fast ones will have a minimum amplitude (Figure 11) close to 0.

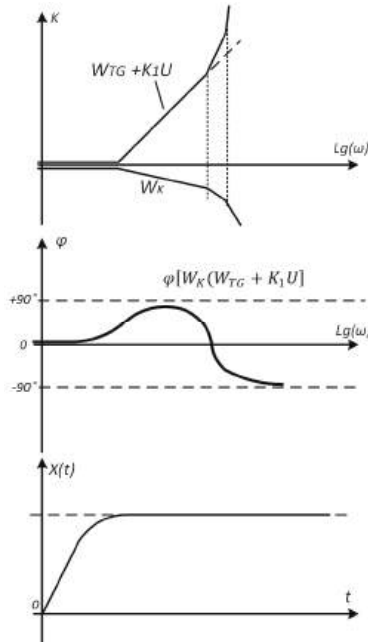


Figure 11. LFCs of the equivalent link forming the sliding trajectory in the cross-coupled VSS.

Cross-coupling defines the feedback LFC as the sum of the output signal of the high-order link and cross-coupling—that is, it excludes small delays and delays from the formative switching signal, which appear at high frequencies, as follows from the LFC (Figure 11).

Specifically, the sliding trajectory will have a more complex structure and frequency characteristic.

The conditions for sliding and stability of the equivalent circuit will take the form

$$Re \left[ \left( W_{TG} + \frac{K_1}{W_{CO}} \right) \cdot \frac{W_{CO} \cdot W_K}{1 + W_{CO} \cdot W_K} \right] > 0 \tag{11}$$

$$\varphi[W_K \cdot W_{TG}] > -90^\circ \tag{12}$$

For a system with significant elasticity and nonlinearities in the high-frequency zone—that is, the frequency of elastic vibrations—rapid movements will form around a surface formed by other coordinates, which are more reliable, and in the zone of slow movements around adjustable coordinates—speed and movement.

$$W_{TG}^* = W_{TG} + K_1 U = W_{TG} + \frac{K_1}{W_{CO}}$$

4.2. Simulations Confirming the Effectiveness of Cross-Coupling

Figure 12a shows a cross-coupled VSS model and transient processes with a real sliding process with a coupling coefficient  $K_1$  equal to 0 (Figure 12b). Figure 12c shows processes with a coefficient  $K_1$  equal to 0.01, which makes the process quasi-ideal—without oscillations around the slip line in the presence of high-order links in the control object. It was not possible to obtain a similar result in an arbitrary-order VSS without cross-coupling [17,18].

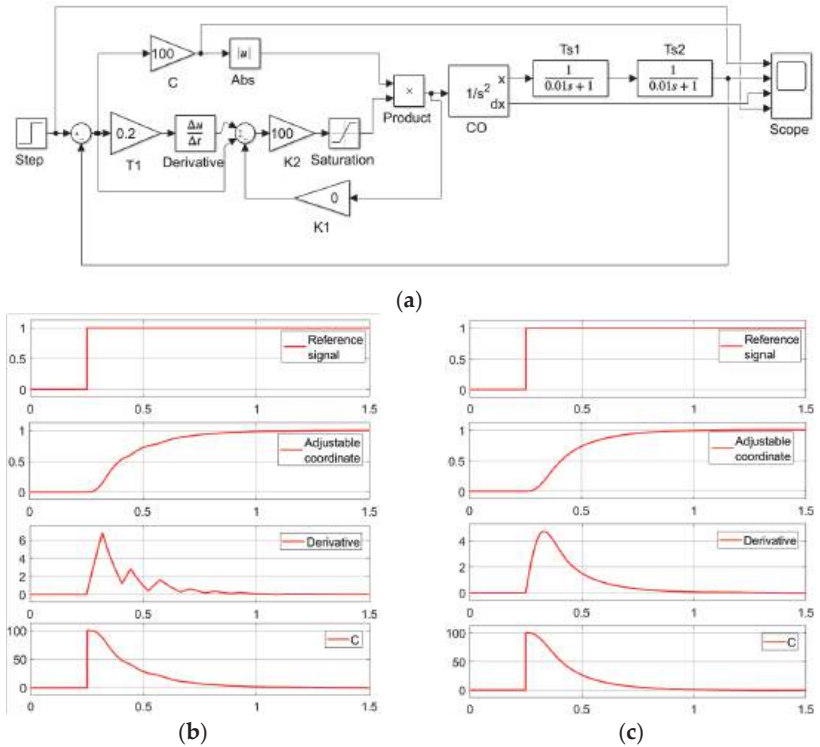


Figure 12. Model diagram (a), processes without cross-coupling ( $K_1 = 0$ ) (b), and processes in ACS with initial cross-coupling ( $K_1 = 0.01$ ) (c).

Figure 13 shows the processes in the system with increased “small” inertia. We increase the time constant of the inertial link to 0.02 s.

The process has remained almost unchanged, with the exception of slowing down the approach to the sliding path.

In Figure 14, the same time constant ( $T_{s1}$ ) increases to 0.05 s.

Low-frequency oscillations with a large amplitude appear, and sliding conditions are violated in the low-frequency zone (analogous to the state shown in Figure 2b).

To fulfill the conditions for the existence of sliding processes, the time constant of the sliding trajectory ( $T_1$ ) was increased to 0.5 s.

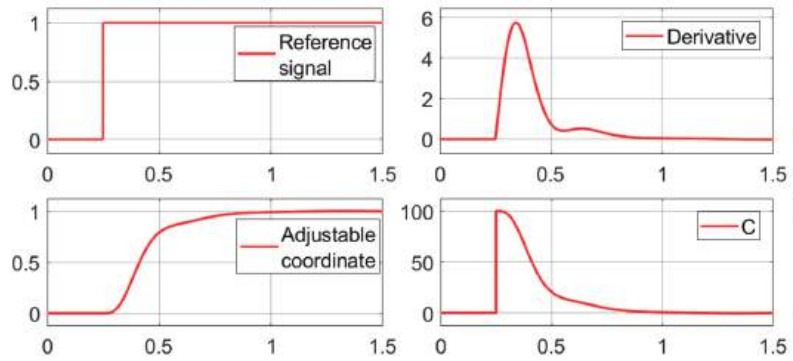


Figure 13. Processes with increased low inertia ( $T_{s1}$ ) up to 0.02 s.

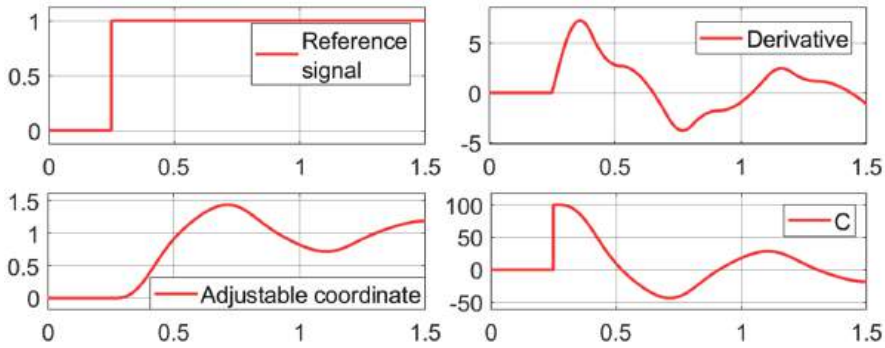


Figure 14. Processes with increased low inertia ( $T_{s1}$ ) up to 0.05 s.

By increasing the time constant of the sliding trajectory, we increase the performance margin of the VSS, which was defined earlier as the ratio of the real  $T_1$  to the boundary one  $T_{1boundary}$ .

Low-frequency conditions are met, the frequency of oscillations around the trajectory increases, and the amplitude decreases (Figure 15).

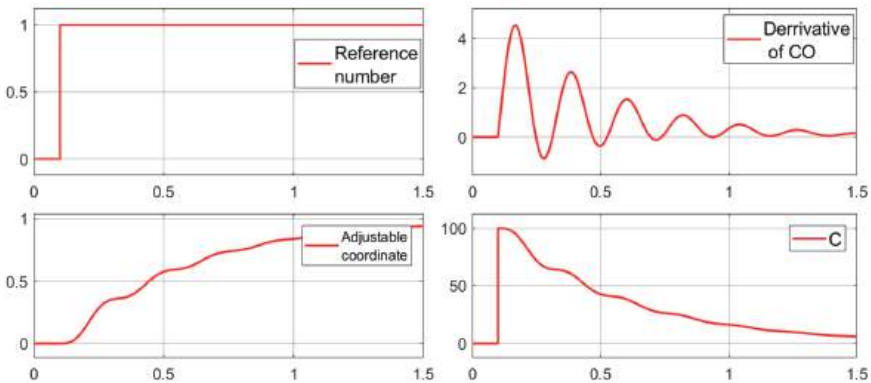


Figure 15. Processes with an increased sliding trajectory time constant ( $T_1$ ) of 0.5 s.

When we increase the cross-coupling coefficient, the oscillation amplitude decreases and the frequency increases (Figure 16).

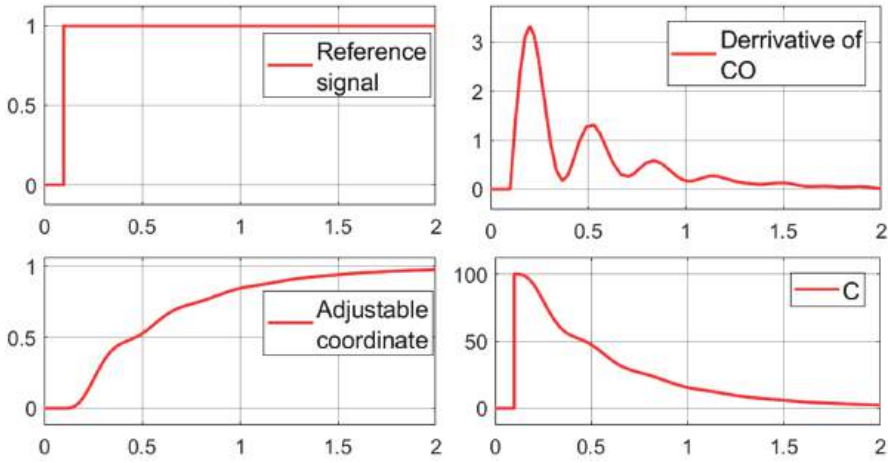


Figure 16. Processes with increased cross-coupling coefficient  $K_1 = 0.02$ .

In Figure 17, showing the processes with an increase in the cross-coupling coefficient to 0.05 s, the time of the transition process does not change and the amplitude of the oscillations decreases to almost 0. Such processes in real ACS with plant parameters corresponding to the model in Figure 6 are close to ideal and are unattainable for ACS with linear controllers, for example, PID controllers [19,20].

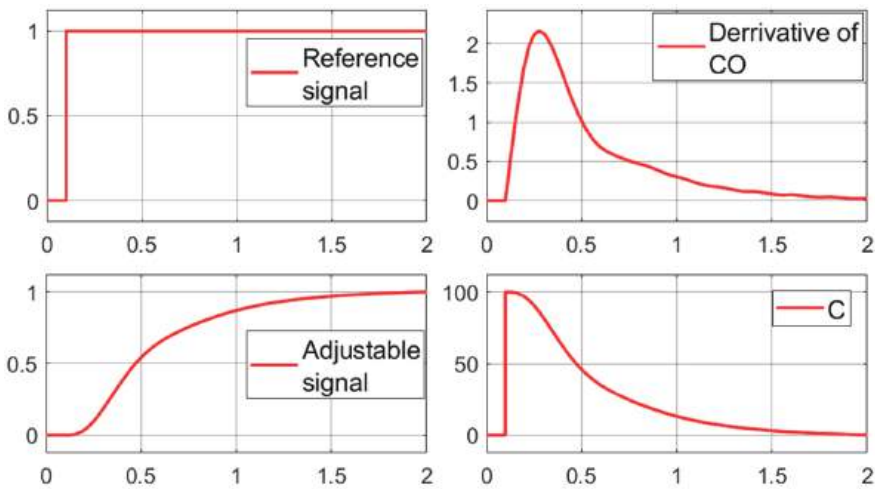


Figure 17. Processes with increased cross-coupling ( $K_1$ ) up to 0.05.

Thus, the possibility of synthesizing SMs close to ideal has been confirmed. With increased high-order inertia without increasing the order of the sliding trajectory, the cross-coupling is responsible for oscillations around the sliding trajectory because it contains high-order components. The low-frequency trajectory does not change. Thus, by increasing the cross-coupling coefficient  $K_1$ , we improve the parameters of fast movements without increasing the order of the sliding trajectory.

4.3. Simulation in Equivalent Circuit

The stability of the equivalent circuit is also improved, since the high-frequency zone of the link is excluded from the operation of the circuit. This improvement is reflected by a decrease in the range of rapid movements.

Figure 18 shows a model of the equivalent circuit of a system with sliding, and Figure 19 shows stable processes with changing parameters of self-oscillations in full accordance with the provisions of the article—self-oscillations reduce the amplitude and increase the frequency with the introduction of cross-coupling ( $K_1 = 0.01$ ), which reduces the sliding amplitude to the parameters of quasi-ideal sliding.

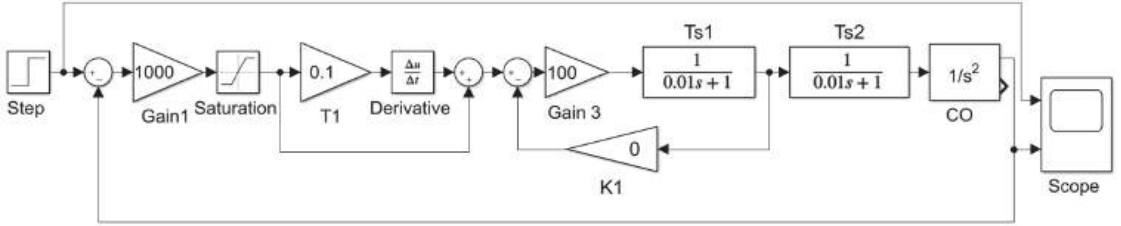


Figure 18. Fourth-order VSS with cross-coupling.

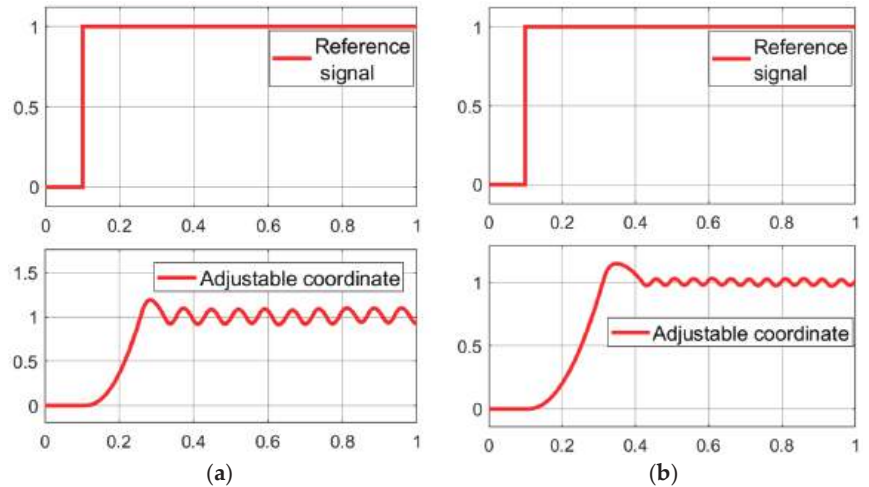
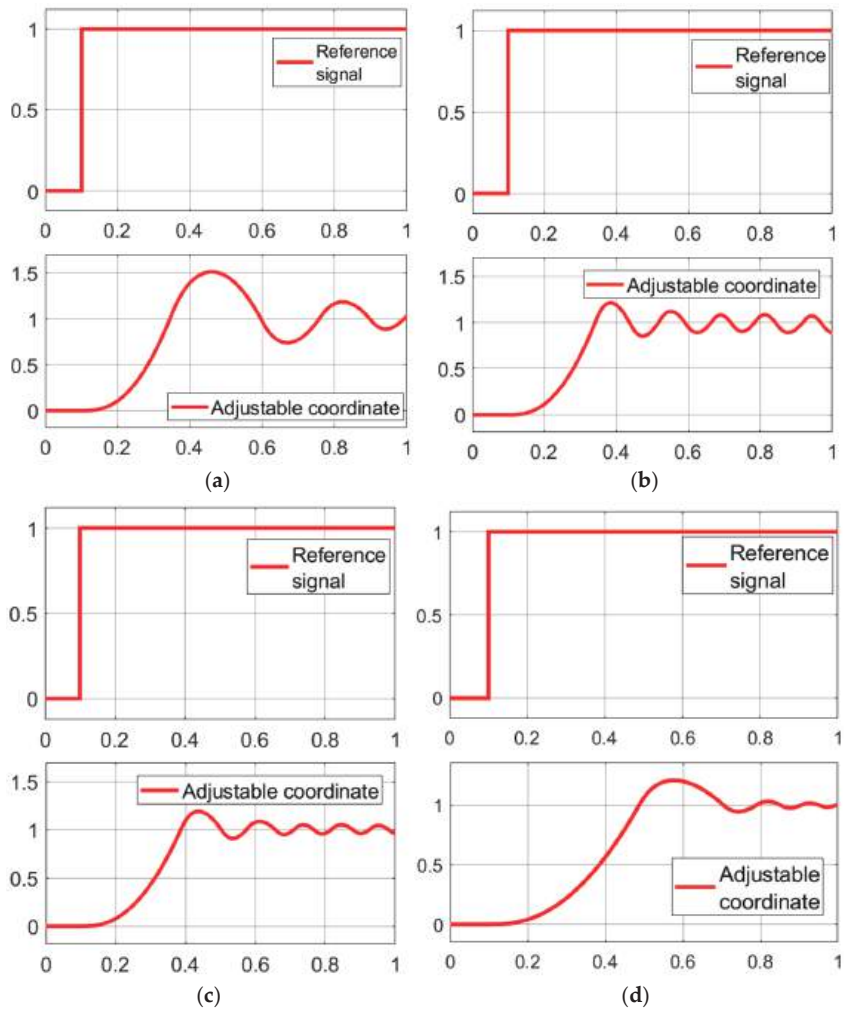


Figure 19. Processes in the equivalent circuit model: (a) without cross-coupling ( $K_1 = 0$ ); (b) with cross-coupling ( $K_1 = 0.01$ ).

Figure 20 shows the processes in the equivalent circuit with an increased time constant of the control object  $T_{s2}$  in Figure 20a, an increased time constant of the slip former  $T_1$  in Figure 20b, and with increased cross-coupling coefficients  $K_1$  in Figure 20c,d.

The diagrams show that the cross-coupling coefficient  $K_1$  affects only the parameters of high-frequency oscillations of fast movements without affecting the parameters of slow movements.

The simulation confirms the frequency criteria for the existence of slip in systems with control objects of a higher order than the sliding trajectory equation. Simulation also confirms the possibility of creating quasi-ideal sliding in electromechanical systems in which high-order links are taken into account by links with low inertia. The simulation results in the original VSS are shown in Table 1, and the processes in the equivalent circuit are shown in Table 2.



**Figure 20.** Processes in the equivalent circuit model: (a) with increased small time constant  $T_{s2} = 0.05$  s; (b) with increased sliding trajectory time constant  $T_1 = 0.2$  s; (c) with increased cross-coupling  $K_1 = 0.02$ ; (d) with more increased cross-coupling  $K_1 = 0.05$ .

**Table 1.** Simulation results in the original VSS.

Figure No./Model Characteristic	$t_{t.p.}$ —Time of Transient Process of Slow Movements	$\omega_o$ —Frequency of Oscillation of Fast Movements	$A_o$ —Amplitude of Oscillation of Fast Movements
Figure 12b, Original model. Small time constant, without cross-coupling. $T_1 = 0.2$ s., $K_1 = 0$ , $T_{s1} = 0.01$ s.	$\approx 1$ s.	$\approx 3.33$ Hz.	$\approx 0.01$
Figure 12c. With cross-coupling. $T_1 = 0.2$ s., $K_1 = 0.01$ , $T_{s1} = 0.01$ s.	$\approx 1$ s.	without oscillation	without oscillation

Table 1. Cont.

Figure No./Model Characteristic	$t_{t.p.}$ —Time of Transient Process of Slow Movements	$\omega_o$ —Frequency of Oscillation of Fast Movements	$A_o$ —Amplitude of Oscillation of Fast Movements
Figure 13. Increased small time constant $T_{s1}$ . $T_1 = 0.2$ s., $K_1 = 0.01$ , $T_{s1} = 0.02$ s	$\approx 1$ s	$\approx 1.33$ Hz.	$\approx 0.01$
Figure 14. More increased small time constant $T_{s1}$ . $T_1 = 0.2$ s., $K_1 = 0.01$ , $T_{s1} = 0.05$ s	$> 1.5$ s.	$\approx 0.5$ Hz.	$\approx 0.5$
Figure 15. Increased sliding trajectory time constant. $T_1 = 0.5$ s., $K_1 = 0.01$ , $T_{s1} = 0.05$ s	$> 1.5$ s.	$\approx 1$ Hz.	$\approx 0.1$
Figure 16. Increased cross-coupling. $T_1 = 0.5$ s., $K_1 = 0.02$ , $T_{s1} = 0.05$ s	4 s.	$\approx 5$ Hz.	$\approx 0.1$
Figure 17. More increased cross-coupling. $T_1 = 0.5$ s., $K_1 = 0.05$ , $T_{s1} = 0.05$ s	$\approx 2$ s.	without oscillation	without oscillation

Table 2. Simulation results in the equivalent circuit.

Figure No.	$\omega_o$ —Frequency of Oscillation	$A_o$ —Amplitude of Oscillation
Figure 19a. Original diagram without cross-coupling. $T_1 = 0.1$ s., $K_1 = 0$ , $T_{s2} = 0.01$ s.	$\approx 15$ Hz	$\approx 0.1$
Figure 19b. With cross-coupling. $T_1 = 0.1$ s., $K_1 = 0.01$ , $T_{s2} = 0.01$ s.	$\approx 20$ Hz	$\approx 0.1$
Figure 20a. Increased small time constant. $T_1 = 0.1$ s., $K_1 = 0.01$ , $T_{s2} = 0.05$ s.	$\approx 5$ Hz	$\approx 0.3$
Figure 20b. Increased sliding trajectory time constant. $T_1 = 0.2$ s., $K_1 = 0.01$ , $T_{s2} = 0.05$ s.	$\approx 10$ Hz	$\approx 0.15$
Figure 20c. Increased cross-coupling. $T_1 = 0.2$ s., $K_1 = 0.02$ , $T_{s2} = 0.05$ s.	$\approx 10$ Hz.	$\approx 0.1$
Figure 20d. More increased cross-coupling. $T_1 = 0.2$ s., $K_1 = 0.05$ , $T_{s2} = 0.05$ s.	$\approx 10$ Hz.	$\approx 0.01$

Simulation allows us to study detailed changes in the parameters of control systems, change individual parameters in the required range, and track their impact. It is very difficult to change all the parameters of the control object in detail, as is performed in the proposed article. For this reason, such studies attach special importance to simulation.

#### 4.4. Experiments

An example of correction of discontinuous processes in the control of electromechanical automatic control systems is a complex of asynchronous electric drives with frequency control of transport mechanisms, as discussed in articles [21,22]. When transporting sheet materials, the moment of “double” sheet gripping occurred, when two drives simultaneously acted on the sheet. The drive of the pulling roll experienced oscillatory influences associated with the final rigidity of the transported material. These influences disrupted the drive control, which, in the absence of a “double” grip, was extremely smooth and monotonous.

Double sheet gripping was always accompanied by an oscillatory transient process, which can be interpreted as discontinuous control with a large amplitude of damped “fast movements”. It should be noted that according to the technology performed by the mecha-

nisms on this line, such processes were unacceptable since they led to uneven processing of the transported material. Diagram of a complex of electric drives interconnected through transportable non-rigid material is shown in Figure 21. Figure 22 shows diagrams of the processes of the moment developed by the pulling drive with a double grip. None of the traditional management methods gave the desired result. Transient oscillatory processes were preserved under scalar (a), vector sensorless (b), and vector closed (c) controls. Only the introduction of a dynamic positive connection for the developed torque made it possible to significantly reduce this oscillation, as follows from Figure 22d. In this case, the dynamic coupling reduces the amplitude of rapid movements in the same way as cross-coupling in sliding systems. These studies are described in detail in [22].

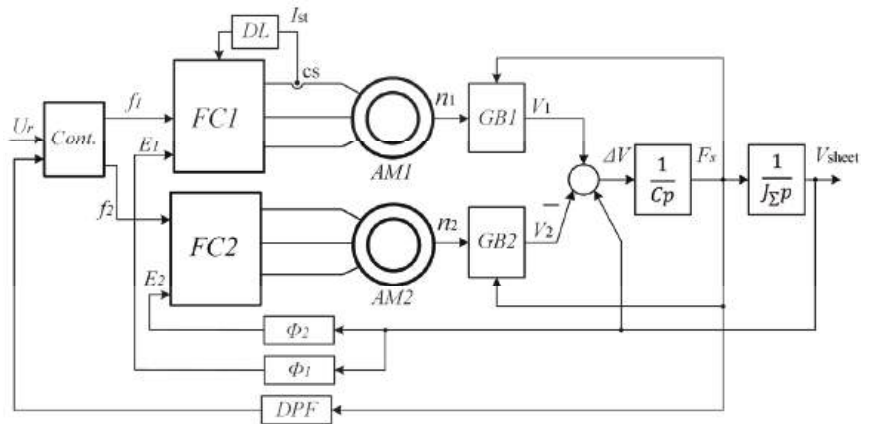


**Figure 21.** Diagram of a complex of electric drives interconnected through transportable non-rigid material. FC1, FC2—frequency converters; AM1, AM2—asynchronous motors;  $\frac{1}{Cp}$ ,  $\frac{1}{J\Sigma p}$ —transfer functions identifying the connection through a non-rigid material; Cont.—controller; DPF—dynamic block of positive feedback of the developed force.

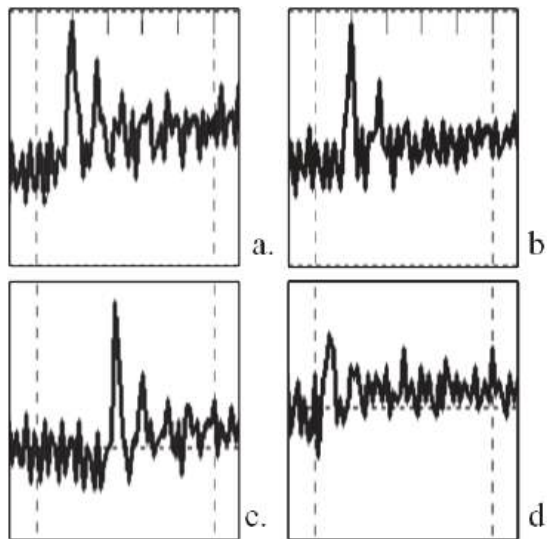


**Figure 22.** Transient processes of the developed force during double material gripping (a) with scalar drive control, (b) with vector sensorless control, (c) with vector control with speed feedback, and (d) with the introduction of positive force feedback.

## 5. Results Discussion

In recent years, there has been significant interest in systems with a variable structure with sliding processes [7–10] due to the fact that these systems are capable of providing high-precision dynamic transient processes in control systems with variable parameters—that is, with uncertainties. However, the main approaches remain the same: the entire analysis is based on a description of the behavior of control systems in the state space. This requires a detailed description of the object controlled by differential equations. In real technical systems, it is not always possible to obtain such equations. This is a significant limiting factor for the widespread implementation of systems with variable structure in real engineering systems.

In a number of works, the authors of this article proposed frequency methods for analyzing the conditions for the existence of slip in systems with a variable structure.

This article also shows the connection between the sliding conditions in systems with nonlinearities and the stability condition in the nonlinear equivalent circuit of the original system. The simulation showed both the effectiveness of systems with sliding and the effectiveness of the proposed criteria for the existence of sliding processes.

## 6. Conclusions

The paper presents the frequency conditions for the existence of sliding modes in control systems of arbitrary order with a sliding trajectory described by a first-order forcing link. Process simulation was carried out, which confirmed the frequency criteria.

It is shown that the sliding condition in systems with a variable structure (VSS) corresponds to the conditions of absolute stability proposed in the work of the nonlinear equivalent circuit of the VSS.

It is shown that cross connections for the formation of a switching trajectory (trajectory of a sliding process) will allow the formation of a sliding process close to ideal (with an infinitely small amplitude and an infinitely large frequency of fast movements) in a system with a high-order control object and first-order switching trajectory.

The presented results of simulation in VSS with a fourth-order object confirm the main results and provisions of the article.

These provisions can become the basis for engineering criteria for the existence of sliding processes in real electromechanical systems.

**Author Contributions:** Methodology, V.K., E.K., A.A. and A.A.B. All authors have read and agreed to the published version of the manuscript.

**Funding:** This research received no external funding.

**Data Availability Statement:** Data are contained within the article.

**Conflicts of Interest:** The authors declare no conflict of interest.

## References

1. Emelyanov, S.V. *Automatic Control Systems with Variable Structure*; Nauka: Moscow, Russia, 1892; p. 336.
2. Emelyanov, S.V. *Theory of Systems with Variable Structure*; Nauka: Moscow, Russia, 1981; p. 368.
3. Utkin, V.A. *Sliding Modes in Optimization and Control Problems*; Nauka: Moscow, Russia, 1981; p. 368.
4. Emelyanov, S.V.; Korovin, S.K. *New Types of Feedback: Management in Conditions of Uncertainty*; Nauka; Fizmatlit: Moscow, Russia, 1997; p. 35.
5. Kodkin, V.L. Discreteness in time and evaluation of the effectiveness of automatic control systems: Examples of the influence of discreteness on mathematical regularity. In *Control Theory in Engineering*; IntechOpen: London, UK, 2020. [CrossRef]
6. Edwards, C.; Fossas Colet, E.; Fridman, L. *Advances in Variable Structure and Sliding Mode Control*; Springer: Berlin, Germany, 2006; ISBN 978-3-540-32800-1.
7. Bartolini, G.; Fridman, L.; Pisano, A.; Usai, E. *Modern Sliding Mode Control Theory—New Perspectives and Applications*; Springer: Berlin, Germany, 2008; ISBN 978-3-540-79016-7.
8. Nateghi, S.; Shtessel, Y.; Edwards, C.; Barbot, J.P. Secure State Estimation and Attack Reconstruction in Cyber-Physical Systems: Sliding Mode Observer Approach. In *Control Theory in Engineering*; IntechOpen: London, UK, 2019. [CrossRef]

9. Samantaray, J.; Chakrabarty, S. Discrete Time Sliding Mode Control. In *Control Theory in Engineering*; IntechOpen: London, UK, 2020. [CrossRef]
10. Tran, A.-T.; Minh, B.L.N.; Huynh, V.V.; Tran, P.T.; Amaefule, E.N.; Phan, V.-D.; Nguyen, T.M. Load Frequency Regulator in Interconnected Power System Using Second-Order Sliding Mode Control Combined with State Estimator. *Energies* **2021**, *14*, 863. [CrossRef]
11. Jiang, T.; Yan, Y.; Yu, S.-H. Adaptive Sliding Mode Control for Unmanned Surface Vehicles with Predefined-Time Tracking Performances. *J. Mar. Sci. Eng.* **2023**, *11*, 1244. [CrossRef]
12. Yao, G.; Cheng, Y.; Wang, Z.; Xiao, Y. Study on a Second-Order Adaptive Sliding-Mode Observer Control Algorithm for the Sensorless Permanent Magnet Synchronous Motor. *Processes* **2023**, *11*, 1636. [CrossRef]
13. Gao, B.; Zhang, W.; Zheng, L.; Zhao, H. Research on High-Precision Position Control of Valve-Controlled Cylinders Based on Variable Structure Control. *Machines* **2023**, *11*, 623. [CrossRef]
14. Aschauer, G.; Schirrer, A.; Kozek, M. Co-Simulation of Matlab and FlightGear for Identification and Control of Aircraft. *IFAC-Papers* **2015**, *48*, 67–72. [CrossRef]
15. Rush, N.; Abets, P.; Lalua, M. *Lyapunov's Direct Method in the Theory of Stability*; Mir: Moscow, Russia, 1980; p. 300.
16. Popov, V.M. *Hyperstability of Automatic Systems*; Nauka: Moscow, Russia, 1970; p. 456.
17. Li, S.; Yu, X.; Fridman, L.; Man, Z.; Wang, X. Advances in Variable Structure Systems and Sliding Mode Control—Theory and Applications. In *Studies in Systems, Decision and Control*; Springer: London, UK, 2017; Volume 24, ISBN 978-3-319-62895-0.
18. Ferrara, A.; Incremona, G.P.; Cucuzzella, M. *Advanced and Optimization Based Sliding Mode Control*; SIAM: Pavia, Italy, 2019; ISBN 978-1611975833. [CrossRef]
19. Meerov, M.V.; Yu, N.; Mikhailov, V.G. *Fridman Fundamentals of Automatic Control*; Nedra Publishing House: Moscow, Russia, 1972; 752p.
20. Tsyypkin, I.Z. *Foundations of the Theory of Automatic Systems: Textbook; Manual for Universities*; Nauka Publishing House: Moscow, Russia, 1977; 559p.
21. Kodkin, V.L.; Anikin, A.; Baldenkov, A. *Nonlinear Dynamics of Asynchronous Drive: Engineering Interpretation and Correction Techniques*; IntechOpen: London, UK, 2020.
22. Kodkin, V.L.; Anikin, A. On the physical nature of frequency control problems of induction motor drives. *Energies* **2021**, *14*, 4246.

**Disclaimer/Publisher's Note:** The statements, opinions and data contained in all publications are solely those of the individual author(s) and contributor(s) and not of MDPI and/or the editor(s). MDPI and/or the editor(s) disclaim responsibility for any injury to people or property resulting from any ideas, methods, instructions or products referred to in the content.



Article

# Modeling of Rapidly Changing Macroeconomic Processes Based on the Analysis of Jump and Generalized Functions

Sergei Aliukov

School of Economics and Management, Department of Digital Economy and Information Technology, South Ural State University, 454080 Chelyabinsk, Russia; aliukovsv@susu.ru

**Abstract:** In recent years, the economies of many countries around the world have been in a situation of intense, rapidly changing, abrupt processes. The current situation urgently requires a change in the economic paradigm in the near future, which leads to the need to develop new conceptual models. The purpose of the article is to develop basic theoretical principles and practical approaches to modeling macroeconomic processes based on the analysis of jump and generalized functions. The objectives of the study are the following: (1) describe the main types of impulse and jump functions using examples from economic theory and practice; (2) perform an analytical representation of impulse and jump functions; (3) select macroeconomic characteristics to analyze rapidly changing processes in the economy; and (4) create models and mechanisms for forecasting impulsive and abrupt changes in the macroeconomy. The approaches to the development of macroeconomic theory and its methods proposed in the article are not associated with the use of evolutionary continuous functions; for example, power functions, which is typical for many canonical macroeconomic models. These approaches do not include management decisions to achieve optimal values of given target functions, which is typical for recursive macroeconomic models of dynamic programming. This article is about formulating the main provisions of macroeconomic theory and its methods, which, with varying degrees of accuracy, could give a forecast about the upcoming possibility of sudden changes (impulse, shock, spasmodic, and others) in the macroeconomic situation. The research methodology is statistical analysis, special methods developed by the author for studying impulse, and jump processes. As a result of this study, the basic principles of modeling macroeconomic theory based on rapid impulse and abrupt changes were formulated, approaches to constructing the tools of this theory were outlined, and problems and tasks for further research were identified.

**Citation:** Aliukov, S. Modeling of Rapidly Changing Macroeconomic Processes Based on the Analysis of Jump and Generalized Functions. *Mathematics* **2024**, *12*, 138. <https://doi.org/10.3390/math12010138>

Academic Editor: Maria C. Mariani

Received: 13 December 2023

Revised: 27 December 2023

Accepted: 29 December 2023

Published: 31 December 2023



**Copyright:** © 2023 by the author. Licensee MDPI, Basel, Switzerland. This article is an open access article distributed under the terms and conditions of the Creative Commons Attribution (CC BY) license (<https://creativecommons.org/licenses/by/4.0/>).

**Keywords:** macroeconomics; theoretical foundations; impulse and jump characteristics

**MSC:** 37N40

## 1. Introduction

There are a lot of problems in the area of macroeconomics. Two main questions are the following: “Why are some countries rich and others poor?”, and “Why does the economy in some countries grow fast and in others slowly?” [1]. To answer these questions, we need to analyze data relating to the economic performance of various countries.

Currently, there are different models of economic growth. Let us look at the most famous of them.

The foundations of modern growth theory were laid by Nobel Prize winner R. Solow, who developed the neoclassical theory of economic growth [2], in which the main role was played by the accumulation of physical capital. Solow also showed for the first time that the key factor of economic growth is technical progress, which he set exogenously [3]. The main focus of the Solow model, along with traditional issues of capital accumulation, is on the relationship between the two main factors of production, labor and capital, as well as their relationship with the exogenous source of changes in productivity—technical progress.

Solow's growth theory, like all classical growth theories, is based on the law of diminishing returns of factors, which is the main condition for achieving an equilibrium state and sustainable development. According to this law, under constant technical conditions, a consistent increase in any of the production factors by an additional unit, with the others remaining unchanged, leads to a decreasing increase in production. This occurs under conditions of perfect competition. The production function in the economic growth model is the Cobb–Douglas function, which includes a power function, the basis of which is physical capital, and the exponent varies from zero to one. The mathematical basis of Solow's economic growth model is the first-order Bernoulli differential equation.

From the point of view of this article, the disadvantage of the Solow model is that it is based on continuous functions and does not take into account impulse, shock, step, spasmodic, and other types of rapidly changing processes characteristic of modern macroeconomics. In addition, this model includes a multiplier that expresses a measure of productivity. To this day, economists have been unable to quantify this multiplier with a high enough degree of realism. Solow himself called this measure "a measure of our ignorance" [4]. This drawback sharply reduces the possibility of practical use of the model for solving real problems and predicting economic events.

In the Mankiw–Romer–Weil model [5], human capital is introduced into the basic neoclassical Solow model of economic growth, which improves the theoretical provisions of the model and is more consistent with empirical data than the similar result of the Solow model without human capital. However, the main results of the basic neoclassical model remain unchanged; sustainable economic growth depends on external technological progress, while the savings rate and institutional and behavioral parameters do not affect it. Therefore, sustainable economic growth remains exogenous in nature.

The shortcomings of this model are similar to those of the Solow macroeconomic model. Just like the Solow model, the Mankiw–Romer–Weil model is based on continuous power functions, which does not allow it to be used to describe abrupt macroeconomic processes.

The recursive macroeconomic Stokey–Lucas–Prescott models [6] are based on dynamic programming methods developed by R. Bellman [7]. Dynamic programming is associated with the ability to represent the management process in the form of a chain of sequential actions or steps, unfolded over time and leading to a goal. The control process can be divided into parts represented as a dynamic sequence and interpreted as a step-by-step program. The dynamic programming problem is formulated as follows: it is required to determine a control that transfers the system from the initial state to the final state, in which the objective function takes an extreme value.

In 1970, the outstanding American scientist Paul Samuelson received the Nobel Prize in Economics for his scientific work that developed static and dynamic economic theory [8–10]. In his works with extensive use of mathematical methods, Samuelson sought to show that the entire economic theory is based on two main economic hypotheses: the concept of an economic optimum (maximum/minimum) and the determination of the conditions of economic equilibrium. The development of such a theory requires the introduction of an objective function, a production function, and the application of the method of comparative statics. This method consists, strictly speaking, of studying how the variables of an equilibrium system react to changes in its parameters.

An American economist Gary Stanley Becker received the 1992 Nobel Memorial Prize in Economic Sciences "for having extended the domain of microeconomic analysis to a wide range of human behaviour and interaction, including nonmarket behaviour". In his analysis [11–13], Becker proceeded from the idea of human behavior as rational and expedient, applying concepts such as scarcity, price, opportunity costs, etc., to a wide variety of aspects of human life.

From modern models that address economic volatility, using empirical data, we can note, for example, neoclassical macroeconomics, developed in [14]. These models filter macroeconomic time series by business cycles and long-term components. Empirical values of macroeconomic indicators are considered within the framework of neoclassical models

with long-term changes in technology and public policy. But, this approach neutralizes the influence of shocks and abrupt, rapidly changing processes in the macroeconomy.

The approach to the categories of shock theory presented in [15] brings us closer to understanding shocks in the context of the cyclical development of national economies and at the global level. The study develops Slutsky's hypothesis about the cyclical model of the economic system's response to random impacts of impulses (shocks) in combination with the impulse transmission approach to Ragnar Frisch's macroeconomic business cycle model. However, the article does not include approaches to the mathematical description of rapidly changing macroeconomic processes and the possibility of their prediction.

The goals and methods of the approaches to macroeconomic theory proposed in this article are completely different. It is not about a dynamic management process with a specifically defined goal and an assigned target function. This article outlines some possible approaches to creating the foundations of macroeconomic theory and its methods, which, with varying degrees of accuracy, could give a forecast about the upcoming possibility of sharp changes (impulse, shock, spasmodic, and others) of the macroeconomic situation, both in a negative and positive direction. The development of the theory itself undoubtedly requires a large amount of additional macroeconomic research and support from the macroeconomic community. What management decisions will be made to correct the situation based on the forecasts made remains outside the scope of the proposed approach to the analysis of fast-moving processes in macroeconomics.

The economies of many countries are strongly influenced by rapidly changing processes and phenomena, crisis events, epidemics, military operations, and so on. This is especially evident in recent years [16–21]. Examples include the global pandemic, events in Ukraine, Russia, Israel, Palestine, and Europe, fuel and food crises, and others. The new paradigm requires the development of new economic theories and economic and mathematical models that take into account impulse, step, and spasmodic changes in economic indicators. The article describes new mathematical methods that make it possible to analyze macroeconomic processes with impulse, generalized, and piecewise linear functions. Methods for approximating these functions by means of analytical expressions are considered. The possibilities of forecasting macroeconomic processes with impulse and jump characteristics are presented.

To determine the preliminary framework of macroeconomic theory, taking into account rapidly changing processes, it is necessary to include in the analysis the behavior of individuals and social groups and their reaction to the emergence of crisis situations. This task is complex since social models are difficult to formalize. Solving such a problem requires extensive research based on accumulated statistical information, which is beyond the scope of this article. The author plans to carry out such work in the context of his further research on this topic.

Let us note some publications in which shock situations are studied in various aspects of macroeconomic theory [22–33]. Note that these works represent only a small part of the publications on the selected topic. This, once again, indicates the relevance of developing a macroeconomic theory with rapidly changing characteristics.

## 2. Main Types of Impulse and Step Characteristics

In the scientific literature, there are discrepancies in the definitions of impulse and step characteristics depending on the areas of their use (signal transmission, electrical engineering, automatic control theory, dynamic systems, catastrophe theory, and others) [34–37]. For definiteness, in this paper, by jump characteristics, we mean functions with a sharp change in values with subsequent stabilization of values at a new level (shifts). By impulse responses, we mean functions with a sharp short-term change in values (shocks). The words "sharp" and "short-term" have a subjective meaning; however, their definitions can be clarified using the terms "outliers", "standard deviation", and other statistical concepts.

Next, we present idealized models of these characteristics and their applications in the field of economic analysis. Naturally, in practice, fluctuations caused by many random causes are superimposed on trend lines.

1. Single jump function (single step function, Heaviside function, “step”).

One way to write this function is:

$$f(x) = \begin{cases} 0, & x < 0; \\ 1, & x \geq 0. \end{cases}$$

A graph of the function is shown in Figure 1a.

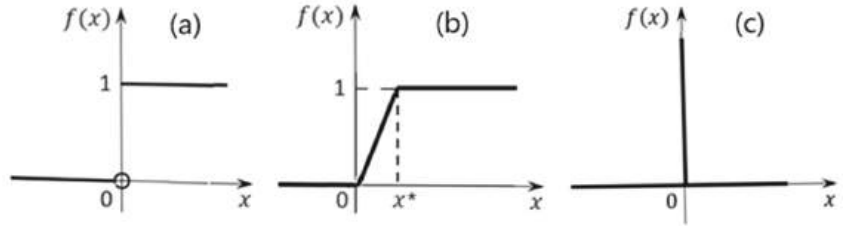


**Figure 1.** Graphs of the unit jump function: (a) idealized; (b) with a transition period; and (c) delta functions ( $x^*$  is value of  $x$ ).

In practice, a sharp change in the values of the function does not occur instantly but over a certain transitional time period  $x^*$  (Figure 1b). For example, an abrupt change in the exchange rate of the national currency tenge in Kazakhstan in February 2014 against the US dollar and the euro took place over several days (Table 1). The official website of the National Bank of the Republic of Kazakhstan is [www.nationalbank.kz](http://www.nationalbank.kz) (accessed on 15 October 2023).

**Table 1.** Exchange rates in Kazakhstan.

Date	Dollar Exchange Rate	Euro Exchange Rate
10 February 2014	155.5	210.89
11 February 2014	155.56	212.25
12 February 2014	163.9	224.07
13 February 2014	184.5	251.57

The unit jump function is the antiderivative function for the delta function (Dirac function) [36]. The delta function graph is shown in Figure 1c.

Examples of the manifestation of the unit jump function in the economy are shown in Figure 2.

In September 2020, the incidence of COVID-19 began to increase in most countries. In June 2020, the National Bureau of Economic Research (USA) announced a recession or recession in the economy since February. In absolute terms, the number of unemployed increased from 5787 people. (February) to 23,078 people. (April). In August, it amounted to 13,550 people.

In order to highlight the trend in more detail, it is possible to use a statistical procedure for smoothing the average value (Figure 3).

2. A unit pulse (rectangular function, normalized rectangular window) is given by the following expression:

$$f(x) = \begin{cases} 0, & |x| > 0.5; \\ 0.5, & |x| = 0.5; \\ 1, & |x| < 0.5. \end{cases}$$

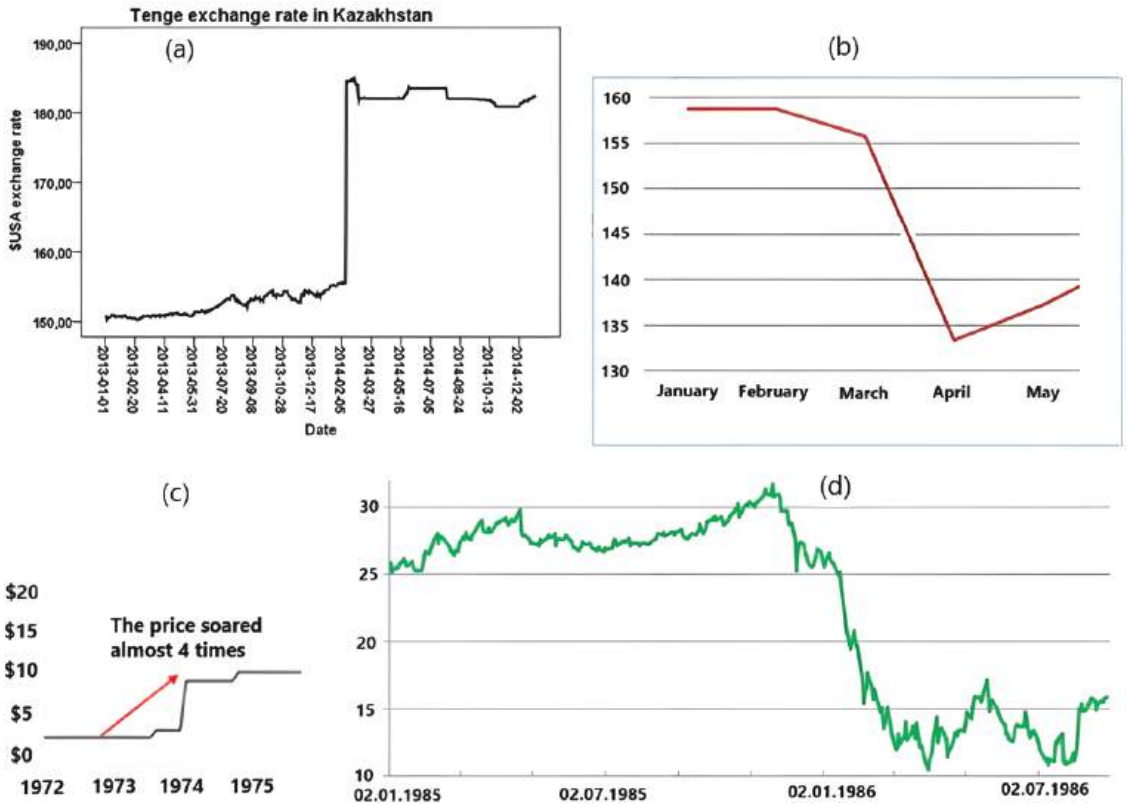


Figure 2. Examples of abrupt changes in the economy: (a) change in the tenge exchange rate in Kazakhstan [38]; (b) the number of people employed in the USA, million people, January–May 2020 [39]; (c) WTI oil price dynamics [40]; (d) oil price from January 1985 to July 1986 [41].

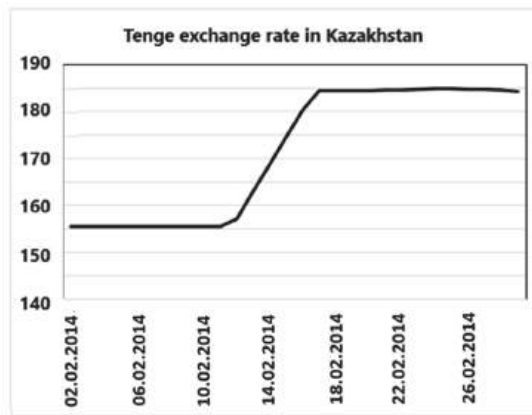


Figure 3. Graph of the smoothed average for the change in the tenge exchange rate.

The graph of the function is shown in Figure 4a.

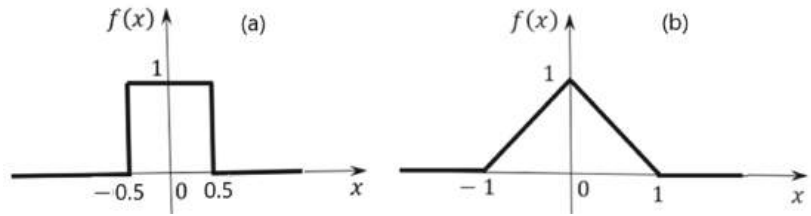


Figure 4. Graphs of impulse functions.

3. Triangular impulse (triangular function) is a piecewise linear function given by:

$$f(x) = \begin{cases} 1 - |x|, & |x| < 1; \\ 0, & |x| \geq 1. \end{cases}$$

The graph of the function is shown in Figure 4b.

Examples of impulse functions in the economy are shown in Figure 5.

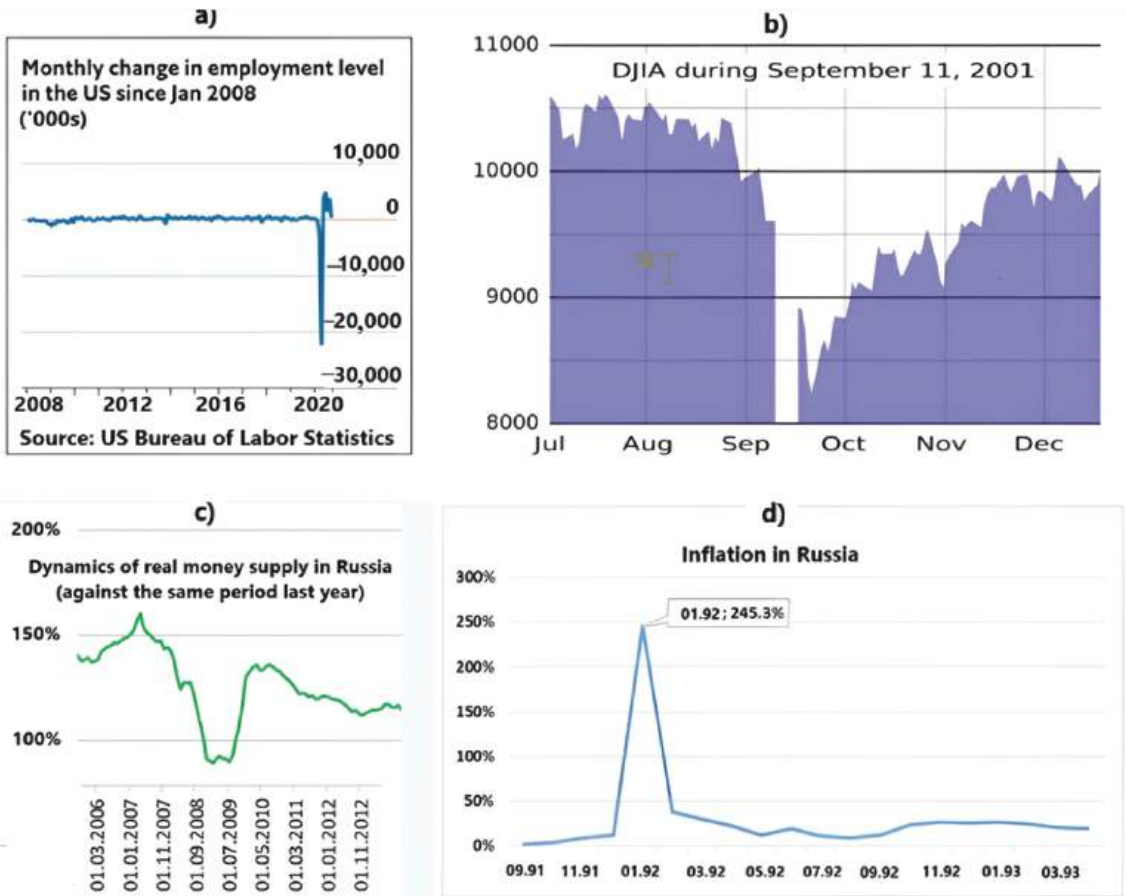


Figure 5. Examples of impulse changes in the economy: (a) monthly change in employment level in the USA [42]; (b) Dow Jones industrial index [43]; (c) dynamics of real money supply in Russia [44]; (d) inflation in Russia [44].

The graph in Figure 5a largely corresponds to the delta function.

Figure 5b shows the macroeconomic shock caused by the 11 September 2001 terrorist attacks and is reflected in the Dow Jones Industrial Average. After the initial panic, the DJIA rose rapidly, falling only marginally from its pre-attack levels.

4. To describe rapidly changing macroeconomic processes, various combinations of impulse and jump models are possible. For example, Figure 6 shows the stepwise transformation of the Russian ruble exchange rate from one stable state to another through an impulse transition process. This shows the effect of the interaction of the step and impulse functions. The trend line is highlighted in red. Figure 7 shows the dynamics of the world cycle: industrial production, 2019–2022, and seasonally adjusted quarterly growth rates. In the figure, we see a combination of two oppositely directed impulses. It is also possible to display various variants of piecewise linear functions.

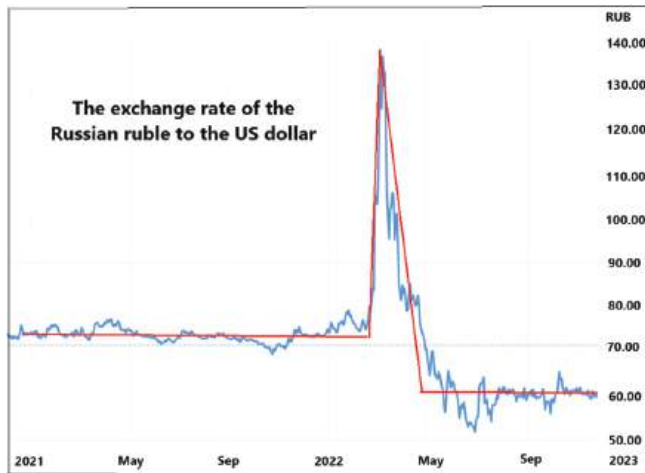


Figure 6. The exchange rate of the Russian ruble against the US dollar (blue line—initial data; red line—approximation).

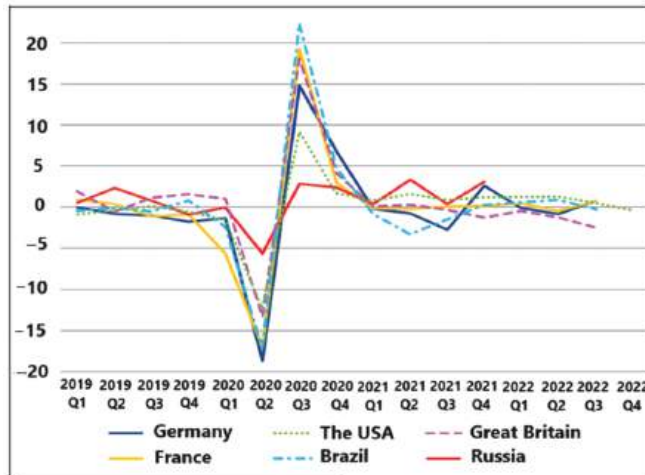


Figure 7. Dynamics of the world cycle: industrial production, 2019–2022, and seasonally adjusted quarterly growth rates [44].

### 3. Approximations of Step, Impulse, and Generalized Functions

#### 3.1. Description of the Methods

Note the logical function by which a national economy (E), in general, is described, respectively:

$$E = F(N_i, s, \sigma, r),$$

where:

- $N_i$ —the firms that make up the economy;
- $s$ —the relationships that are constituted between firms;
- $\sigma$ —the synergy factor in the functioning of a system;
- $r$ —the residual factor.

Note that the variable values  $s$ ,  $\sigma$ , and  $r$  in crisis states of the economy can have a spasmodic character.

It should also be noted that most economic processes are characterized by cyclical development over a fairly long period of time. The stages of cyclical development may differ (sometimes significantly) from each other, including under the influence of crisis phenomena. However, the evolution of economic processes in many cases follows a certain pattern, repeating itself after a certain period of time.

The methods developed in this article are based on the use of trigonometric functions, which, by their definition, are periodic. Consequently, these methods can be used for mathematical modeling of cyclical macroeconomic processes over a long time period. At the same time, these methods also make it possible to describe short-term, rapidly changing macroeconomic processes if these methods are used for short periods of time. In this sense, the proposed methods are universal.

Approximations of step, impulse, and generalized functions make it possible to more accurately identify trends in rapidly changing processes and describe existing processes in macroeconomics. These functional forms may become useful as predictive tools.

Currently, there are many methods for approximating piecewise linear functions using analytic expressions. This article describes only the methods proposed by the author that have a number of advantages over known approximations. These methods, like the Fourier series, are based on the use of trigonometric expressions. The difference lies in the fact that trigonometric expressions in the developed methods have the form of nested, recursive functions [45–48]. The methods were further developed in [49,50] and many other scientific papers.

Let us recall the definition of the function  $sign(x)$  :

$$sign(x) = \begin{cases} -1, & x < 0; \\ 0, & x = 0; \\ 1, & x > 0. \end{cases}$$

For example, let us take a step function, which will explain the main idea of the approximation:

$$f_0(x) = sign(\sin x). \tag{1}$$

The step function is often used to describe the Fourier series. Therefore, the choice of a step function is convenient for comparing and identifying the advantages and disadvantages of expansion into the Fourier series and the methods developed by the author.

It is known that the Fourier expansion of the proposed function (1) is characterized by certain disadvantages [51,52]. The Gibbs effect can be noted. In the developed methods, the initial step function is approximated by a recursive sequence of periodic trigonometric functions, which eliminates the shortcomings of the Fourier series expansion:

$$\{f_n(x) \mid f_n(x) = \sin((\pi/2) \cdot f_{n-1}(x)), f_1(x) = \sin x; n - 1 \in N\} \subset C^\infty[-\pi, \pi]. \tag{2}$$

The approximation sequences of function (2) are based on the interval  $[-\pi, \pi]$ , and they are “stationary points”.

In Figure 8, the thickened line marks the initial step function. The thin lines show the graphs of five successive approximations by the proposed method. The functions are periodic; therefore, it is enough to consider them within one period. The results of studying these functions using simple mathematical transformations can be generalized to periodic functions with an arbitrary period.

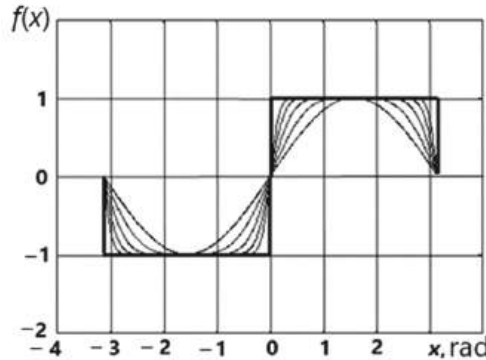


**Figure 8.** Graphs of the step function (the thick line) and five successive approximations of this function (the thin lines).

Figure 8 shows that even the first approximations of the proposed iterative sequence quickly converge to the step function (1). At the same time, the shortcomings of the expansion into the Fourier series, in particular, the Gibbs effect [51], are completely leveled.

The developed methods of trigonometric approximation using an iterative recursive procedure differ in some of their properties. Let us note some of them.

Periodic functions  $f_n(x)$  and  $f_0(x)$  with period  $2\pi$  are odd. Periodic functions  $f_n(x + \pi/2)$  and  $f_0(x + \pi/2)$  are even. It follows from this fact that one can only study the approximating sequence of function (2) on the interval  $[0, \pi/2]$ ; it would be enough.

Let  $\{f_n(x)\} \subset L_2[0, \pi/2]$  and  $f_0(x) \in L_2[0, \pi/2]$ , because  $\sup_{n \in \mathbb{N}} \sup_{x \in [0, \pi/2]} |f_n(x)| = 1 < \infty$

(because the function is limited)  $f_n(x)$  and  $\sup_{n \in \mathbb{N}} \int_0^{\pi/2} f_n = 1 < \infty$  (since the function  $f_n(x)$  is monotonic on the segment  $[0, \pi/2]$ ); then, using Helly’s theorem, we can extract a subsequence from the given sequence  $\{f_n(x)\}$ . This subsequence converges to some function  $f$  at each point from  $[0, \pi/2]$ , and, additionally,  $\int_0^{\pi/2} f \leq \overline{\lim}_{n \rightarrow \infty} \int_0^{\pi/2} f_n$ . The original function  $f$  may be such a function  $f_0(x)$ . Let us prove this statement.

**Theorem 1.** *The sequence  $f_n(x)$  converges pointwise to the function  $f_0(x)$ , but not uniformly.*

**Proof.** In  $x = 0$  and  $x = \pi/2$ , there is  $f_n(x) - f_0(x) = 0, \forall n \in \mathbb{N}$ . Therefore,  $f_n(x) \xrightarrow{n \rightarrow \infty} f_0(x)$  since  $\forall \varepsilon > 0 \exists n^* \in \mathbb{N} \forall n : n > n^* \Rightarrow |f_n(x) - f_0(x)| = 0 < \varepsilon$ . For instance,  $n^* = 1$ .

$f_n(x) = \sin((\pi/2) \cdot f_{n-1}(x)) > f_{n-1}(x) > \dots > f_1(x) > 0$  for any  $x \in (0, \pi/2)$  since  $\sin x > (2/\pi) \cdot x, \forall x \in (0, \pi/2)$ .  $f_n(x), \forall x \in (0, \pi/2)$  has a finite limit  $\lim_{n \rightarrow \infty} f_n(x) = A \in \mathbb{R}$ .  $A = \lim_{n \rightarrow \infty} \sin((\pi/2) \cdot f_{n-1}(x)) = \sin((\pi/2) \cdot \lim_{n \rightarrow \infty} f_{n-1}(x)) = \sin((\pi/2) \cdot A)$ ,  $A = 0$  or  $A = 1$ .  $A = 1 = f_0(x)$  since  $f_n(x)$  is increasing and positive. For  $x \in (0, \pi/2)$ ,  $f_n(x) \xrightarrow{n \rightarrow \infty} f_0(x)$ .  $f_n(x)$  converges at  $x = 0$  and  $x = \pi/2$ . Therefore,  $f_n(x) \xrightarrow{n \rightarrow \infty} f_0(x), \forall x \in [0, \pi/2]$ .  $f_0(x)$  is not continuous on  $[0, \pi/2]$ . Therefore, the convergence is pointwise, but not uniform.  $\square$

**Theorem 2.**  *$f_n(x)$  converges in the norm to  $f_0(x)$  in the spaces  $L_1[0, \pi/2]$  and  $L_2[0, \pi/2]$ .*

**Proof.** We take a sequence of minorant functions for  $f_n(x)$ :

$$\{\eta_n(x) \mid \eta_n(x) = (2/\pi) \cdot \arctg(n\pi); n \in \mathbf{N}\} \subset C^\infty[0, \pi/2].$$

$f_n(x) \geq \eta_n(x), \forall n \in \mathbf{N}, \forall x \in [0, \pi/2]$ . The measure for the set of discontinuity points of  $f_0(x)$  is zero.  $f_n(x)$  and  $\eta_n(x)$  are non-negative and limited on the segment  $[0, \pi/2]$  in  $L_1[0, \pi/2]$ :

$$\|f_0(x) - f_n(x)\| = \int_0^{\pi/2} (1 - f_n(x))dx \leq \int_0^{\pi/2} (1 - \eta_n(x))dx = \frac{\pi}{2} - \arctg\frac{\pi n}{2} + \frac{1}{\pi n} \cdot \ln\left(1 + (\pi n)^2/4\right).$$

$$\lim_{n \rightarrow \infty} \left(\frac{\pi}{2} - \arctg\frac{\pi n}{2} + \frac{1}{\pi n} \cdot \ln\left(1 + (\pi n)^2/4\right)\right) = 0; \text{ therefore, } \|f_0(x) - f_n(x)\| \xrightarrow{n \rightarrow \infty} 0.$$

The same is true for  $f_n(x)$  in  $L_2[0, \pi/2]$ .  $\square$

$f_n(x)$  is fundamental in  $L_1[-\pi, \pi]$  and  $L_2[-\pi, \pi]$  but not in  $C[-\pi, \pi]$ .

The angular function  $f_1(x)$  may not necessarily be the sine, but another one, including non-periodic ones. For  $|f_1(x)| < 2, \lim_{n \rightarrow \infty} f_n(x) = \text{sign}(f_1(x))$ . With (2), it is possible to approximate an arbitrary step function. For example, consider:

$$f(x) = \begin{cases} h, & x \in (x_1, x_2), \\ 0, & x \notin (x_1, x_2) \end{cases} \tag{3}$$

and take the function  $f_1(x) = \exp(1 - (ax + b)^2) - 1$  as the angular one.  $f_1(x_1) = f_1(x_2) = 0, a = 2/(x_1 - x_2); b = (x_1 + x_2)/(x_2 - x_1), \text{ so}$

$\{f_n(x) \mid f_n(x) = (h/2) \cdot (1 + \sin \varphi_n(x)), \varphi_n(x) = (\pi/2) \cdot \sin \varphi_{n-1}, \varphi_1(x) = (\pi/2) \cdot f_1(x), n-1 \in \mathbf{N}\}$  converges to  $f(x)$ , as shown in Figure 9.

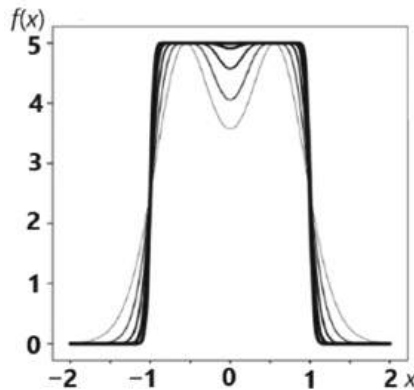


**Figure 9.** Graphs of successive approximations of the bar function.

This approximating procedure makes it possible to create a mathematical analytical description of macroeconomic processes in a columnar form with arbitrary finite values of the width and height of the column. Note that the developed methods are universal and can be used to describe not only macroeconomic processes but also processes in other branches of science and technology. For example, the developed approximations of bar-shaped functions were widely used to create a new theory of semiconductors [53], and were also used in other areas.

Any step function with  $h_i$  on  $(x_{1i}, x_{2i})$  can be approximated by the sum:  $\sum_{i=1}^k \{f_n(x)\}_i$ .

$f(x) = \sum_{i=1}^k h_i \cdot f_{0i}(x)$ ,  $h_i \in R$ , where  $f_{0i}(x) = \text{sign}(\sin(l_i x - x_i))$ ,  $l_i, x_i \in R$ , can approximate any periodic step function. The convergence of  $f_n(x) = \sum_{i=1}^k h_i \cdot f_{ni}(x)$  to  $f(x)$  in the norm is ensured by the proved theorem since  $\|f_{0i}(x) - f_{ni}(x)\| \xrightarrow{n \rightarrow \infty} 0$  in  $L_1[-\pi, \pi]$  and  $L_2[-\pi, \pi]$ , and:

$$\|f(x) - f_n(x)\| = \left\| \sum_{i=1}^k h_i \cdot f_{0i}(x) - \sum_{i=1}^k h_i \cdot f_{ni}(x) \right\| \leq \sum_{i=1}^k |h_i| \cdot \|f_{0i}(x) - f_{ni}(x)\| \xrightarrow{n \rightarrow \infty} 0.$$

### 3.2. Generalized Functions and Approximation

Generalized functions [54] began to be used in the 20th century to solve problems in the field of quantum physics. The solution to such tasks required supplementing the generally recognized mathematical concept of a function. This concept suggests that with a function, we understand a certain statement; accordingly, for each value of an independent variable belonging to a certain set, one value of the dependent variable is indicated. To solve the problems of quantum physics, it was necessary to introduce functions that go beyond the usual definitions. At present, generalized functions are used not only for solving problems of quantum physics but also for solving other problems in various fields of science and engineering.

Let us consider the concept of a generalized function in more detail.

Let us take a linear space  $Y$ . Functions in the traditional mathematical sense are points in this space. A function is given on  $Y$ , and for each point  $y \in Y$  from the space under consideration, we can specify a certain number. The defined function will be written  $I : Y \rightarrow R$ , or  $I(y)$ .

The function is linear under the assumption  $I(\alpha y_1 + \beta y_2) = \alpha I(y_1) + \beta I(y_2)$ ,  $\forall y_1, y_2 \in Y$ ,  $\forall \alpha, \beta \in R$ , and continuous when  $y_n \Rightarrow y^*$  follows  $I(y_n) \rightarrow I(y^*)$ ,  $\forall y_n, y^* \in Y$ . We consider our functions on the set of real numbers  $R$ .

A function  $\varphi(x)$  is finite if it is equal to zero outside  $[a, b]$ , and the boundaries of this segment are determined by  $\varphi(x)$ . Any continuous function with compact support is basic.  $C_0$  is a set of basic functions.

Next, consider a continuous function  $f(x)$ , which can have a finite number of discontinuity points. The function is bounded on any finite interval.

A function is defined by the integral  $I(\varphi) = \int_{-\infty}^{+\infty} f(x)\varphi(x)dx$ . Any basic function  $\varphi(x)$  will be finite. In this case, we have a regular function.

According to the definition in [39], any linear continuous function  $I(\varphi)$  on  $C_0$  is called a generalized function if:

1.  $I(\alpha\varphi_1 + \beta\varphi_2) = \alpha I(\varphi_1) + \beta I(\varphi_2)$ ,  $\forall \varphi_1, \varphi_2 \in C_0, \forall \alpha, \beta \in R$ ;
2.  $I(\varphi_n) \rightarrow I(\varphi)$ , if  $\varphi_n \Rightarrow \varphi$  in  $C_0$ .

A generalized function that cannot be represented by the integral  $I(\varphi) = \int_{-\infty}^{+\infty} f(x)\varphi(x)dx$  is called singular. For example, the  $\delta$ -function or the Dirac function is a singular generalized function  $I(\varphi) = \varphi(0)$ .

The basic idea of singular generalized functions can be visualized if we consider a generalized function from the point of view of the limit of a sequence of approximating functions with traditional definitions. In this case, generalized functions are perceived through the prism of their approximating procedures. For example, suppose:

$$\delta_n(x) = \begin{cases} n/2, & \forall x \in [-1/n, 1/n], \\ 0, & \forall x \notin [-1/n, 1/n]. \end{cases}$$

The functions of this sequence have graphs corresponding to the graph of the step function shown in Figure 10.



with an increase in the number of nested functions in the proposed expression. Using the integral condition written in the definition of the  $\delta$ -function, one can find the amplitude of the approximation dependence.

Let us show how to find the height of the approximation peak. We know that the  $\delta$ -function is the derivative of the unit jump function:

$$H(x) = \begin{cases} 1, & \forall x > 0; \\ 0, & \forall x < 0. \end{cases}$$

We can approximate the unit jump function (Heaviside function) by a sequence of analytic functions  $H_n(x) = 0.5(1 + f_n(x))$ . The sequence  $f_n(x)$  is defined by (2) on  $[-\pi/2, \pi/2]$ .

For instance, we have (Figure 12):

$$H_9(x) = 0.5(1 + \sin(A(A(A(A(A(A(A(A(x)))))))))),$$

$$H_{10}(x) = 0.5(1 + \sin(A(A(A(A(A(A(A(A(A(x)))))))))),$$

$$H_{11}(x) = 0.5(1 + \sin(A(A(A(A(A(A(A(A(A(A(x)))))))))),$$

where  $A(x) = \frac{\pi}{2} \sin x$ .

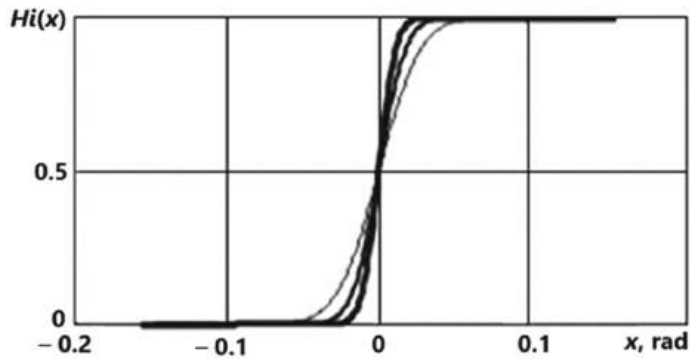


Figure 12. Graphs of approximations of the Heaviside function.

The larger the approximation number, the greater the graph thickness (Figure 12).

Graphs of the first derivatives of successive functions  $H_9(x)$ ,  $H_{10}(x)$ , and  $H_{11}(x)$  are shown in Figure 13. They characterize successive approximations of the delta function.

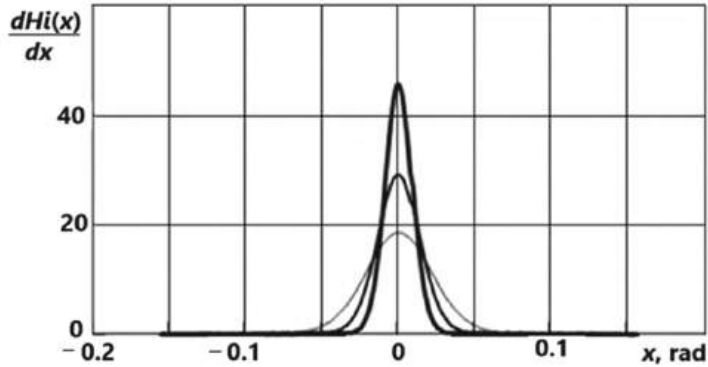


Figure 13. Graphs of approximations for the  $\delta$ -function.

For the sequence  $H_n(x) = 0.5(1 + f_n(x))$ , we obtain:

$$\frac{dH_n(x)}{dx} = \frac{\pi^{n-1}}{2^n} \prod_{k=1}^{n-1} \cos\left(\frac{\pi}{2} f_k(x)\right) \cdot \cos x.$$

Therefore, we have:

$$A_n = \frac{\pi^{n-1}}{2^n}.$$

The performed analytical approximations of step, impulse, and generalized functions make it possible to use the methods of mathematical analysis in the analysis and forecasting of rapid changes in the macroeconomic situation.

The developed methods are universal and have found application in various fields of scientific research and practical applications [53,55–59].

#### 4. Choice of Macroeconomic Indicators for the Analysis of Impulse and Spasmodic Processes

The totality of macroeconomic parameters is controversial. Nevertheless, it is possible to single out macroeconomic parameters, the importance of which the overwhelming majority of macroeconomists agree. We will divide the parameters into two groups (Table 2) [8]. Note that macroeconomic indicators are largely interconnected.

**Table 2.** The macroeconomic parameters.

Main Indicators	Additional Indicators
1. GDP per capita PPP, USD	1. GDP, USD billion
2. GDP annual growth rate, last, %	2. Population, million
3. GDP annual growth Rate, previous, %	3. Male retirement age, years
4. Unemployment rate, %	4. Female retirement age, years
5. Consumer price index	5. Male life expectancy at birth, years
6. Trade balance, % of GDP	6. Female life expectancy at birth, years
7. Corporate tax rate, %	7. Current account to GDP, %
8. Personal income tax rate, %	
9. Sales tax rate, %	
10. Exchange rate	
11. Net external debt, % of GDP	
12. Interest rate, %	
13. Inflation rate, %	
14. Government debt to GDP, %	
15. Saving rate (national savings/GNDI), %	

As a rule, macroeconomic indicators have annual values, in some cases, quarterly and monthly. This is the difficulty of applying macroeconomic indicators for the analysis of fast-moving (impulsive and spasmodic) economic processes. As practice shows, in some cases, the macroeconomic situation can change dramatically in a matter of days. Examples of macroeconomic indicators with daily values are the exchange rate, energy prices (and even hours and minutes) on stock exchanges, and others. Table 3, for example, shows prices for Brent crude oil.

**Table 3.** Brent oil price.

Date	7 July 2023	6 July 2023	5 July 2023	4 July 2023	3 July 2023
Price, USD per barrel	78.47	76.52	76.65	76.25	74.65

The daily change in the situation on some macroeconomic indicators can be estimated indirectly. For example, the daily unemployment rate can be estimated by the number of welfare claims filed in a country during the day. Modern computer technology makes it quite easy to perform this.

To improve the accuracy of forecasting crisis situations, economic analysis should be carried out on a set of macroeconomic indicators, which provides a more holistic view of pre-crisis realities. First of all, macroeconomic indicators with greater inertia to changes are of interest. Note that macroeconomic shifts can also occur in a positive direction, which can be determined, for example, by investments and a high level of innovative development.

**5. Approaches to Methods for Forecasting Macroeconomic Events**

*5.1. Control Rules*

In quality control systems [60–62], control rules have been developed (Table 4), which should be paid attention to if violations of specified standards are suspected in the near future. The probability of manifestation of each of these rules within the framework of a random process is small; therefore, each of these manifestations indicates a probable violation of the course of a normal process. Therefore, with some probability, a loss of quality should be expected.

**Table 4.** Control rules.

Values above + 3 sigma	Values below are 3 sigma
2 of the last 3 above + 2 sigma	2 of the last 3 below are 2 sigma
4 of the last 5 above + 1 sigma	4 of the last 5 below are 1 sigma
8 points in a row above the center line	8 points in a row below the center line
6 points in a row ascending	6 points in a row descending
14 points in a row alternately	

The problem of applying similar rules in the analysis of macroeconomic processes lies in the fact that in practice, changes in macroeconomic processes can occur not only for random reasons but also as a result of purposeful managerial actions. Such mathematical models do not include human behavior in the analysis, and their implications can only be intuited by macroeconomic decision-makers [11]. Therefore, for application in macroeconomic theory with impulsive and abrupt changes, these rules must be formulated with some “margin”; for example, not one value above +3 sigma but two, and not one value above + 3 sigma but one value above + 4 sigma, etc. At the same time, the probability of an error of the first kind decreases (false prediction of an impulse or abrupt development of an event series), but the probability of an error of the second kind increases (ignoring such a development). For example, Figure 14 shows graphs of the same data set in the  $\mp 3\sigma$  range (Figure 14a) and in the  $\mp 4\sigma$  range (Figure 14b). The range boundaries are marked with dotted lines. Some points that are critical in the range  $\mp 3\sigma$  are not critical in the range  $\mp 4\sigma$ . Therefore, the standard quality control rules for predicting possible crisis phenomena in the framework of the new macroeconomic theory need to be reformulated.

Some of the rules can be left unchanged; for example, six points in a row in ascending (descending) order. This rule indicates the existence of a trend, which can lead to abrupt changes in the macroeconomic process.

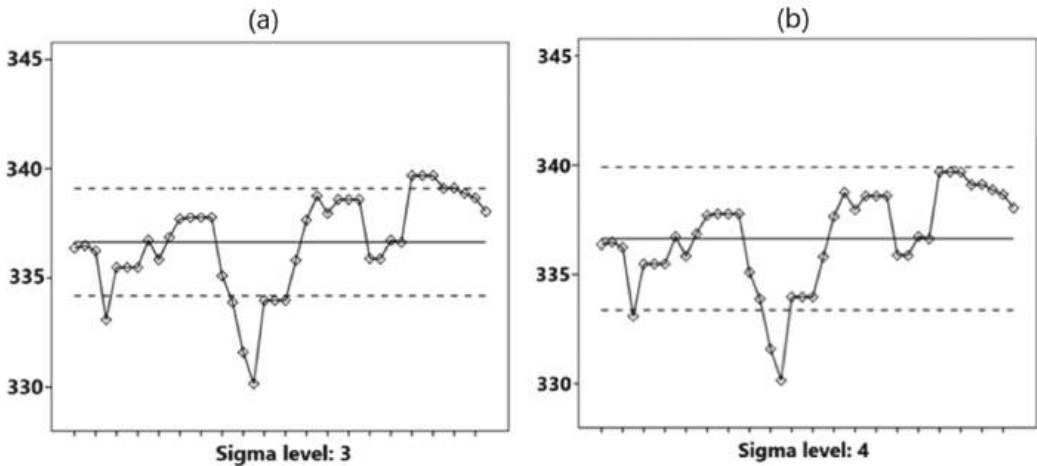


**Figure 14.** Graphs of the data set in the ranges (a)  $\pm 3\sigma$  and (b)  $\pm 4\sigma$ .

The creation of a new system of rules for predicting rapid changes in macroeconomic indicators is possible on the basis of statistical processing of information and heuristic methods. Pay attention to weak signals. Note that predictions made on the basis of a system of attention-grabbing criteria can only be realized with a certain probability, which is common when using statistical methods.

In the context of the frequent lack of daily data, we will give examples of forecasts for a rapid change in macroeconomic indicators by month.

Figure 15a shows a graph of the Brent oil price (USD per barrel) for several consecutive months in 2007-08. Source of information: 1. <https://investfunds.ru> (accessed on 15 October 2023); 2. <https://ru.investing.com> (accessed on 15 October 2023). It follows in the graph that three points break the rules. Of particular interest is point number 3, since at this point three rules are violated at once (Table 5).

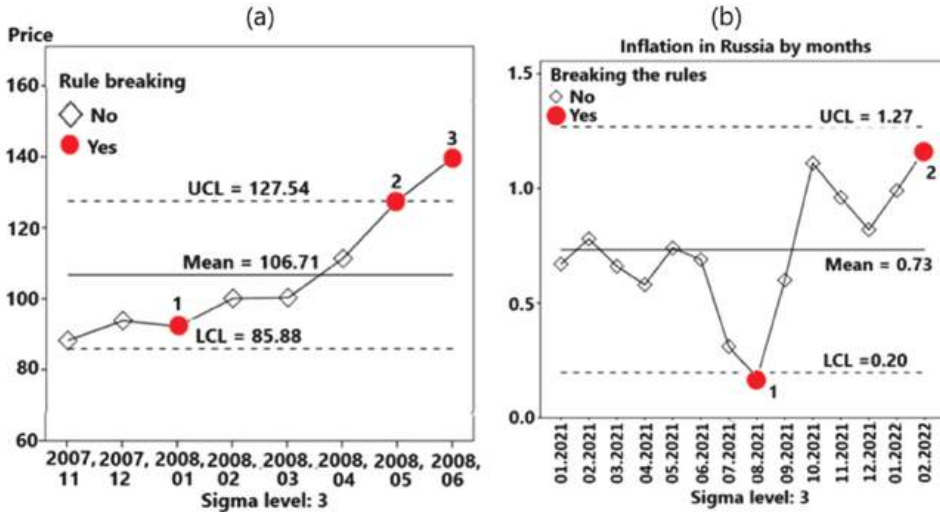


Figure 15. Examples of completed forecasts: (a) Brent oil price (USD per barrel); (b) inflation in Russia by months as a percentage of the previous period.

Table 5. Dynamics of oil prices.

Date	Violations for Points
January 2008	2 points from the last 3 below – 2 sigma
May 2008	Greater than + 3 sigma
June 2008	Greater than + 3 sigma
June 2008	2 points from the last 3 above + 2 sigma
June 2008	6 points in a row ascending

Figure 15b shows the graph of inflation in Russia by months as a percentage of the previous period. Source of information: Rosstat data, <https://rosstat.gov.ru/folder/10705> (accessed on 12 November 2023). Regarding points 1 and 2, point 2 is of particular interest since in the subsequent period (in March 2022), the inflation rate jumped sharply to a value of 7.61.

Let us take another example. Table 6 contains the values of the average monthly nominal accrued wages in rubles of employees in the whole economy of the Russian Federation. Source: Rosstat, <https://rosstat.gov.ru> (accessed on 12 January 2023). The December 2019 salary figure is omitted as the annual bonus is usually paid in the month of December, which greatly distorts the overall picture.

Table 6. Average monthly salary in rubles.

01.	02.	03.	04.	05.	06.	07.	08.	09.	10.	11.	01.	02.	03.
2019	2019	2019	2019	2019	2019	2019	2019	2019	2019	2019	2020	2020	2020
42,263	43,062	46,324	48,030	47,926	49,348	46,509	44,961	45,541	46,549	46,285	46,674	47,257	50,948

A graph of the average monthly salary of points 1, 2, and 3 is shown in Figure 16.

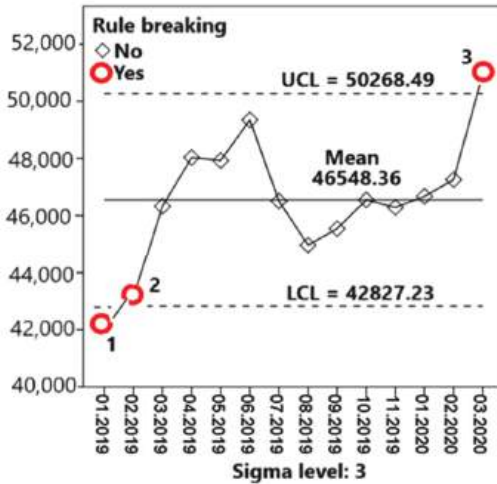


Figure 16. Schedule of the average monthly salary.

Violation of control rules at critical points is explained in Table 7.

Table 7. Violation of control rules.

Date	Violations for Points
01.2019	Less than - 3 sigma
02.2019	2 points from the last 3 below - 2 sigma
03.2020	Greater than + 3 sigma

It should be noted that in the considered examples (Figures 15 and 16), the control rules of the theory of quality were applied. Within the framework of the new macroeconomic paradigm, it is necessary to revise and adjust the system of control rules based on the accumulated statistics and heuristic considerations.

We note the main issues that require further development within the framework of the new macroeconomic theory:

1. Creation of a system of macroeconomic indicators with fixed daily values;
2. Detailing a set of statistical rules for predicting crises and fast-moving, impulsive, and spasmodic changes in macroeconomic processes.

5.2. Theoretical Foundations of the Technique

For each macroeconomic indicator  $X$ , we define:

$n$ —number of consecutive days with daily observations  $X_1, X_2, \dots, X_n$ ;

$\bar{X}$ —sample mean,  $\bar{X} = \frac{1}{n} \sum_{i=1}^n X_i$ ;

$\sigma$ —sample standard (mean square) deviation,  $\sigma = \sqrt{\frac{\sum_{i=1}^n (X_i - \bar{X})^2}{n-1}}$ .

We construct the central line mean corresponding to the sample mean  $\bar{X}$ , and the lines  $\pm\sigma$ ,  $\pm2\sigma$ ,  $\pm3\sigma$ , and  $\pm4\sigma$ :

UCL—upper control limit;

LCL—lower control limit.

The upper UCL and lower LCL reference lines can correspond to values of  $\pm3\sigma$  or  $\pm4\sigma$  depending on our choice, as explained in Section 5.1. Next, to forecast possible abrupt changes in the macroeconomic situation, we use the control rules from Section 5.1.

As noted earlier, in order to improve the accuracy of forecasts based on the provisions of the new macroeconomic theory, macroeconomic indicators should be considered not separately, but in their totality. In this case, it is required to apply methods of multivariate analysis, such as multivariate scaling, factor analysis, cluster analysis, and others.

The new macroeconomic theory requires the accumulation of statistical data on the daily values of macroeconomic indicators due to their possible rapid change. This work is only at the beginning of the journey and requires additional effort. However, the development of computer technology does not raise doubts about the possibility of successfully solving this problem. At present, however, the overwhelming majority of macroeconomic indicators are measured by years, and only at best by quarters and months. Therefore, it is still difficult to give specific examples of forecasts based on the daily values of a set of macroeconomic indicators. It is only possible to outline some analogies of such approaches based on the annual values of macroeconomic indicators. Regarding these analogies, let us consider the dynamics of a certain set of macroeconomic indicators of the Russian Federation for the period 2012–2022 (Table 8). Source: compiled by the author based on data from the Federal State Statistics Service: <https://rosstat.gov.ru/folder/10705> (accessed on 9 October 2023).

**Table 8.** Dynamics of macroeconomic indicators in Russia for the period 2012–2022.

Year	GDP Growth at Current Prices, %	Unemployment Rate, %	Industrial Production Index in % of the Previous Year	Consumer Price Indices for Services at the End of the Period in % to December of the Previous Year	Labor Productivity Index in the Economy in % of the Previous Year
2012	13.3	5.5	103.4	107.28	103.8
2013	7.2	5.5	100.4	108.01	102.1
2014	8.3	5.2	101.7	110.45	100.8
2015	5.1	5.6	100.2	110.20	98.7
2016	3.0	5.5	101.8	104.89	100.1
2017	7.3	5.2	103.7	104.35	102.1
2018	13.1	4.8	103.5	103.94	103.1
2019	5.5	4.6	103.4	103.75	102.4
2020	−1.8	5.8	97.9	102.70	99.6
2021	25.7	4.8	105.3	104.98	103.7
2022	13.4	3.9	99.4	113.19	102.8

Using the ALSICAL multidimensional scaling procedure, you can obtain a visual representation of multidimensional tabular information (Figure 17a). The figure shows that 2020, 2021, and 2022 stand out sharply in terms of the totality of their indicators. Further analysis shows the economic crisis in 2020 and a sharp improvement in the situation in 2021 and 2022.

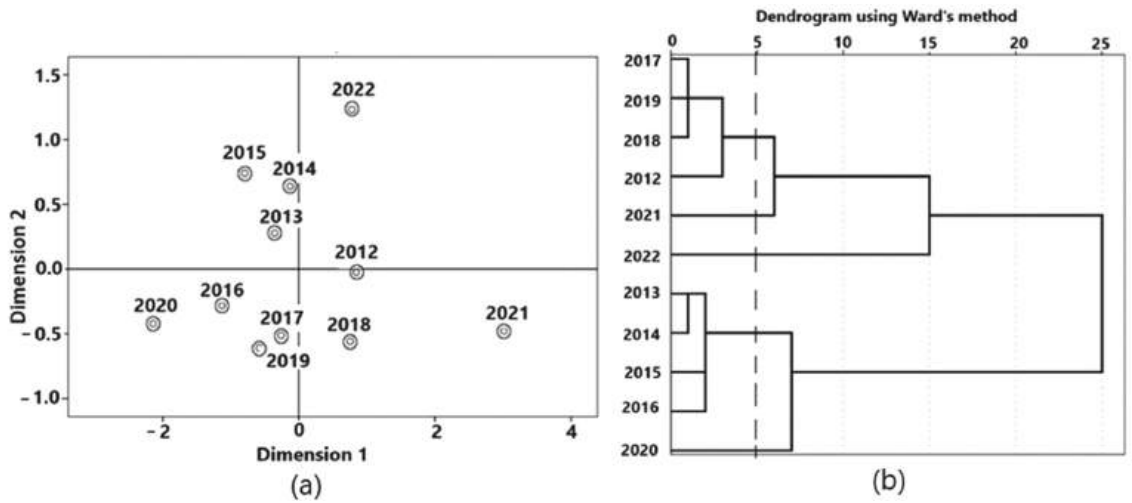


Figure 17. Visual representation of multidimensional information: (a) multidimensional scaling; (b) cluster analysis dendrogram.

The conclusions made are confirmed by cluster analysis. Figure 17b is a dendrogram showing the possibility of splitting the variable “Year” into five clusters (section along the dotted line).

Clustering is presented in Table 9. The average values of variables by clusters are presented in Table 10.

Table 9. Clustering.

Year	2012	2013	2014	2015	2016	2017	2018	2019	2020	2021	2022
Cluster	1	2	2	2	2	1	1	1	3	4	5

Table 10. Mean values of variables by clusters.

Ward Method		GDP Growth at Current Prices, %	Unemployment Rate, %	Industrial Production Index in % of the Previous Year	Consumer Price Indices for Services at the End of the Period in % to December of the Previous Year	Labor Productivity Index in the Economy in % of the Previous Year
1	Mean	9.8000	5.0250	103.5000	104.8300	102.8500
	N	4	4	4	4	4
2	Mean	5.9000	5.4500	101.0250	108.3875	100.4250
	N	4	4	4	4	4
3	Mean	−1.8000	5.8000	97.9000	102.7000	99.6000
	N	1	1	1	1	1
4	Mean	25.7000	4.8000	105.3000	104.9800	103.7000
	N	1	1	1	1	1
5	Mean	13.4000	3.9000	99.4000	113.1900	102.8000
	N	1	1	1	1	1
Total	Mean	9.1000	5.1273	101.8818	106.7036	101.7455
	N	11	11	11	11	11

Multidimensional scaling methods have a great advantage, as they allow you to process multidimensional information and present the results of processing visually. This allows the use of macroeconomic variables in their totality to identify possible pre-crisis

and forecast other rapidly changing macroeconomic situations. In addition to the previous examples, let us consider a more complete set of Russia’s macroeconomic indicators in the dynamics of their changes over the period 2004–2011 (Table 11).

**Table 11.** Dynamics of the main macroeconomic indicators of Russia in 2004–2011 (growth rate, %). Source: Rosstat and the Bank of Russia.

Years	2004	2005	2006	2007	2008	2009	2010	2011
Unemployment	7.9	7.6	6.9	6.1	6.4	8.6	7.6	7.3
Inflation, December to December	11.7	10.9	9.0	9.3	13.0	8.8	7.4	6.3
Gross domestic product	7.2	6.4	6.7	8.1	5.6	−7.9	4.0	4.1
Industrial products	8.3	4.0	4.9	6.1	2.1	−10.8	8.3	4.1
Agricultural products	3.0	2.4	3.6	3.3	1.8	−5.5	−2.3	7.4
Real disposable income of the population	10.4	11.1	10.0	10.7	2.9	1.1	3.5	4.2
Retail turnover	13.3	12.8	13.0	15.9	13.2	−5.0	4.5	4.8
Gold and foreign exchange reserves of the Central Bank (billion US dollars)	130.0	175.0	300.0	479.4	426.3	439.0	500.2	585.8
Volume of the stabilization fund (billion rubles)	489.0	522.3	2180.0	3859.0	4027.6	1830.5	1279.9	1300.0
Investments in fixed assets	11.7	10.5	13.5	20.3	9.8	−11.0	5.9	9.0
World oil price (Urals)	34.4	50.6	61.1	69.3	94.4	61.1	78.2	90.0
Export of goods, billion US dollars	183.2	243.6	304.5	355.5	471.6	304.0	400.4	380.4
Import of goods, billion US dollars	97.4	125.3	163.9	223.4	291.9	192.0	248.7	250.1

A visual representation of the results of applying multidimensional scaling is given in Figure 18.

It can be seen in the figure that the years 2005 and 2005, 2007 and 2008, and 2010 and 2011 are pairwise close in terms of the totality of initial macroeconomic indicators. The years 2006 and 2009 occupy rather isolated positions and, therefore, differ from the rest and each other.

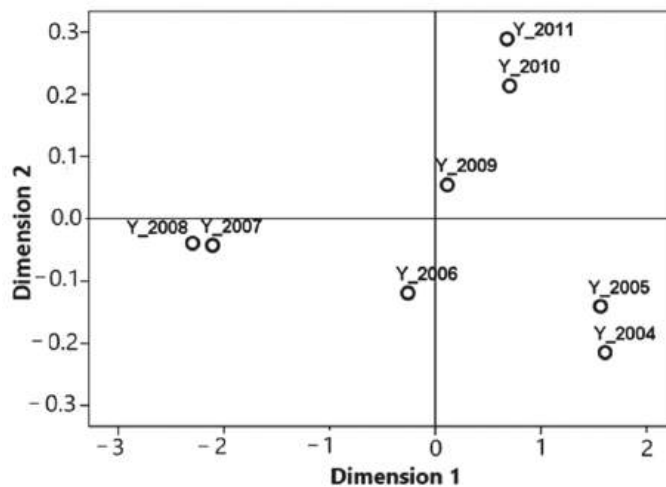


**Figure 18.** Graphical representation of the results of multivariate scaling.

A similar processing of information for predicting rapid macroeconomic changes is assumed in the framework of the new macroeconomic theory in the presence of a set of variables with daily values and daily monitoring.

Currently, work is also underway to improve the mechanism of foresight control [63–65].

## 6. Discussion

1. Modern macroeconomic processes are significantly influenced by social, political, economic, and other types of crises, which are highly relevant in today's fast-paced economic environment. The new economic paradigm urgently requires the creation of a macroeconomic theory based on new principles. Undoubtedly, such a task is complex, and its solution can only be obtained through more theoretical and empirical research. Nevertheless, it is possible and necessary to outline some approaches to creating such a theory.

To provide a practical substantiation of these statements, this article provides numerous real examples in the field of macroeconomics, illustrating rapid changes (shock, impulse, step, shift, and others) in the values of macroeconomic indicators. Mathematical descriptions of such variables are usually performed using piecewise linear functions, the types of which are presented in the article. These functions often have discontinuities, making it difficult to analyze such functions. It is necessary to consider these functions by section, and the problem arises of coordinating the obtained solutions by sections to obtain a solution for the entire process as a whole. This article describes new methods of analytical approximations of piecewise linear functions that allow us to solve this problem for mathematical modeling of rapidly changing macroeconomic processes.

In addition, this article describes, in detail, with examples, statistical approaches for the analysis of rapidly changing macroeconomic processes and their forecasting. A methodology for the practical use of these statistical approaches is presented, and recommendations are given for further improvement of the proposed approaches and methods.

2. From a theoretical point of view, the value of this article lies in the description of new approaches to macroeconomic theory, taking into account the reflection of modern conditions, characterized by crisis and rapidly changing processes. The creation of such a theory will make it possible with some probability to predict rapid changes in macroeconomic indicators and make proactive management decisions to reduce the possible negative consequences of such changes. Potential beneficiaries of the research and further development of the new macroeconomic theory may include, for example, government experts from major countries in the world, large companies, banks, investment funds, software companies, etc.

To improve the theory and methods of its practical use, it would be advisable to take into account the behavior of people and social groups and their response to rapidly changing modern macroeconomic processes. In addition, we note that the developed models can be used as the basis for artificial intelligence methods. In this sense, the developed approaches and methods of artificial intelligence do not contradict but help each other.

## 7. Conclusions

1. This article describes only the basic approaches to mathematical modeling of macroeconomic processes with rapidly changing characteristics of the impulse and spasmodic type and formulates the main provisions of the developed model. These provisions need further development and improvement based on statistical analysis.
2. The modern macroeconomic paradigm is characterized by rapid impulsive and abrupt changes, in some cases within a few days, so the analysis of macroeconomic processes should be based on the analysis of macroeconomic characteristics with daily values.
3. For daily monitoring of the macroeconomic situation within the framework of the developed model, it is necessary to create a system for daily collection and processing

- of macroeconomic information, which can be performed on the basis of automated systems with the widespread use of computer technology.
4. Daily values of macroeconomic indicators are best expressed in relative values, in the form of the dynamics of their changes for comparative analysis and identification of critical points.
  5. It is necessary to clarify the system of criteria for predicting possible rapid changes in the macroeconomy and identifying critical points. This may require expanded ranges of acceptable changes compared to traditional statistical methods and control rules; for example, a point falling outside the  $\mp 4\sigma$  range, with not one but several points falling outside the  $\mp 3\sigma$  range. The system of criteria may include rules, such as several (6 or 8) points in a row in ascending (or descending) order, to identify an emerging trend, and other control rules. Improvement of the system should be carried out using accumulated statistics of rapidly changing macroeconomic processes and heuristic methods and rules.
  6. To increase the accuracy of forecasts using the developed methods, macroeconomic indicators should be considered not separately but in their totality. At the same time, to identify pre-crisis conditions and possible rapid positive changes, methods of multidimensional information processing, for example, multidimensional scaling, cluster analysis, factor analysis, and others, can be useful.
  7. This article describes the methods developed by the author for the analytical approximation of step and generalized functions, which make it possible to describe impulse and jump functions using traditional methods of mathematical analysis. This reveals the successive connection between the developed and existing methods of macroeconomic analysis.

**Funding:** This research received no external funding.

**Institutional Review Board Statement:** Not applicable.

**Informed Consent Statement:** Not applicable.

**Data Availability Statement:** Data are available upon request.

**Acknowledgments:** The author thanks South Ural State University (SUSU) for its support.

**Conflicts of Interest:** The author declares no conflicts of interest.

## References

1. Weil, D.N. *Economic Growth*, 2nd ed.; Addison Wesley Press: New York, NY, USA, 2009; 565p.
2. Solow, R.A. Contribution to the Theory of Economic Growth. *Q. J. Econ.* **1956**, *70*, 65–94. [CrossRef]
3. Akaev, A.A. Models of AN-type innovative endogenous growth and their substantiation. *Modernization. Innovation. Res.* **2015**, *6*, 70–79. [CrossRef]
4. LeClair, D. Technological Change, Economic Growth, and Business Education. Available online: <https://gbsn.org/technological-change-economic-growth-and-business-education> (accessed on 25 November 2023).
5. Mankiw, N.E.; Romer, D.; Weil, D.N. A contribution to the empirics of economic growth. *Q. J. Econ.* **1992**, *107*, 407–437. [CrossRef]
6. Stokey, N.; Lucas, R.; Prescott, E. *Recursive Methods in Economic Dynamics*; Harvard University Press: Cambridge, MA, USA, 1989.
7. Bellman, R. *Dynamic Programming*; Princeton University Press: Princeton, NJ, USA, 1957.
8. Samuelson, P.A.; Nordhaus, W.D. *Economics: An Introductory Analysis*, 19th ed.; McGraw–Hill: New York, NY, USA, 2009.
9. Samuelson, P.A. Economic Theory and Mathematics—An Appraisal. *Am. Econ. Rev.* **1952**, *42*, 56–66.
10. Samuelson, P.A. *Foundations of Economic Analysis, Enlarged ed.*; Harvard University Press: Cambridge, MA, USA, 1983; 604p.
11. Becker, G.S. *The Economic Approach to Human Behavior*; University of Chicago Press: Chicago, IL, USA, 1976; 314p.
12. Becker, G.S. *Economic Theory*; distributed by Random House; Knopf: New York, NY, USA, 1971; 222p.
13. Becker, G.S. *Human Capital: A Theoretical and Empirical Analysis, with Special Reference to Education*, 2nd ed.; National Bureau of Economic Research, Inc.: Cambridge, MA, USA, 1975; 268p.
14. Hansen, G.D.; Ohanian, L.E. Chapter 26—Neoclassical Models in Macroeconomics, *Handbook of Macroeconomics*; Elsevier: Amsterdam, The Netherlands, 2016; Volume 2, pp. 2043–2130.
15. Pilipenko, Z.A.; Savenkova, E.V.; Pilipenko, A.I.; Morosova, E.A.; Pilipenko, O.I. Impulse Transmission Model of Macroeconomic Cycle Within the Framework of the Theory of Shocks: Aspect of Economic Security. In *Dependability Engineering and Complex*

- Systems: Proceedings of the Eleventh International Conference on Dependability and Complex Systems DepCoS-RELCOMEX, Brunów, Poland, 27 June–1 July 2016*; Springer: Cham, Switzerland, 2016; Volume 470. [CrossRef]
16. Basu, S.; Bundick, B. *Uncertainty Shocks in a Model of Effective Demand*; Working Papers, no. 12–15; Federal Reserve Bank of Boston: Boston, MA, USA, 2012.
  17. Barsky, R.B.; Basu, S.; Lee, K. Whither News Shocks? *NBER Macroecon. Annu.* **2014**, *29*, 225–264. [CrossRef]
  18. Gueron, P.; Fernandez-Villaverde, J.; Rubio-Ramirez, J. Estimating Dynamic Equilibrium Models with Stochastic Volatility. *Forthcom. J. Econom.* **2015**, *185*, 216–229.
  19. Sergeevich, S.O. Economic growth of a rapidly changing economy: Theoretical formulation. *Econ. Reg.* **2016**, *2*, 359.
  20. Heimberger, P. This time truly is different: The cyclical behavior of fiscal policy during the Covid-19 crisis. *J. Macroecon.* **2023**, *76*, 103522. [CrossRef]
  21. Acevedo, S.; Mrkaic, M.; Novta, N.; Pugacheva, E.; Topalova, P. The Effects of Weather Shocks on Economic Activity: What are the Channels of Impact? *J. Macroecon.* **2020**, *65*, 103207. [CrossRef]
  22. Aliukov, S.; Buleca, J. Comparative Multidimensional Analysis of the Current State of European Economies Based on the Complex of Macroeconomic Indicators. *Mathematics* **2022**, *10*, 847. [CrossRef]
  23. Hill, E.; St Clair, T.; Wial, H.; Wolman, H.; Atkins, P.; Blumenthal, P.; Ficenec, S.; Friedhoff, A. *Economic Shocks and Regional Economic Resilience. In Urban and Regional Policy and Its Effects: Building Resilient Regions*; Brookings Institution Press: Washington, DC, USA, 2012; Volume 9780815722854, pp. 193–274.
  24. Ramey, V.A. *Macroeconomic Shocks and Their Propagation*. University of California: San Diego, CA, USA. NBER, Cambridge, MA. *Handbook of Macroeconomics* **2016**, *2*, 71–162. [CrossRef]
  25. Bruneckiene, J.; Pekarskiene, I.; Palekiene, O.; Simanaviciene, Z. An Assessment of Socio-Economic Systems' Resilience to Economic Shocks: The Case of Lithuanian Regions. *Sustainability* **2019**, *11*, 566. [CrossRef]
  26. Adelson, M. The Deeper Causes of the Financial Crisis: Mortgages Alone Cannot Explain It. 2013. Available online: [http://www.bfjlaward.com/pdf/25892/16-31\\_Adelson\\_JPM\\_0412.pdf](http://www.bfjlaward.com/pdf/25892/16-31_Adelson_JPM_0412.pdf) (accessed on 12 September 2023).
  27. Ginevicius, R.; Gedvilaite, D.; Stasiukynas, A.; Sliogeriene, J. Quantitative Assessment of the Dynamics of the Economic Development of Socioeconomic Systems Based on the MDD Method. *Inz. Ekon.-Eng. Eco.* **2018**, *29*, 264–271. [CrossRef]
  28. Bazzi, S.; Blattman, C. Economic Shocks and Conflict: Evidence from Commodity Prices. *Am. Econ. J. Macroecon.* **2014**, *6*, 1–38. [CrossRef]
  29. Ciccone, A. Economic Shocks and Civil Conflict: A Comment. *Am. Econ. J. Appl. Econ.* **2011**, *3*, 215–227. [CrossRef]
  30. Wardley-Kershaw, J.; Schenk-Hoppé, K.R. Economic Growth in the UK: Growth's Battle with Crisis. *Histories* **2022**, *2*, 28. [CrossRef]
  31. Iuga, I.C.; Mihalciuc, A. Major Crises of the XX1st Century and Impact on Economic Growth. *Sustainability* **2020**, *12*, 9373. [CrossRef]
  32. Novo-Corti, I.; Țircă, D.-M.; Ziolo, M.; Picatoste, X. Social Effects of Economic Crisis: Risk of Exclusion. An Overview of the European Context. *Sustainability* **2019**, *11*, 336. [CrossRef]
  33. Murphy, R. Explaining Inflation in the Aftermath of the Great Recession. *J. Macroecon.* **2014**, *40*, 228–244. [CrossRef]
  34. Zagashvili, Y.V.; Rudenko, V.G. "Dynamic Characteristics of Piezogenerators" News of higher educational institutions. *Instrumentation* **2021**, *64*, 626–637.
  35. Plotnikov, V.A.; Makarov, S.V.; Kolubaev, E.A. Spasmodic Deformation and Pulsed Acoustic Emission under Loading of Aluminum-Magnesium Alloys. *News Altai State Univ.* **2014**, *N 1–2*, 207–210.
  36. Koldunov, E.D.; Filonova, E.S. Econometric Modeling of Impulse Response of Macroeconomic Indicators. *Fundam. Res.* **2022**, *6*, 5–10. Available online: <https://fundamental-research.ru/ru/article/view?id=43264> (accessed on 19 July 2023).
  37. Brylina, O.G. Static and dynamic spectral characteristics of a multi-zone converter with frequency-width-pulse modulation. *Bull. South Ural. State Univ. Ser. Power Eng.* **2013**, *13*, 70–79.
  38. Available online: [www.nationalbank.kz](http://www.nationalbank.kz) (accessed on 24 November 2023).
  39. Available online: <https://www.bls.gov> (accessed on 21 September 2020).
  40. Available online: <https://fred.stlouisfed.org/> (accessed on 17 October 2023).
  41. Available online: <http://geoinform.ru/sem-s-polovinoj-tysyach-slancevyx-skvazhin-zhdut-svoego-chasa> (accessed on 12 September 2023).
  42. Available online: <https://catalog.archives.gov/id/584> (accessed on 12 October 2023).
  43. Available online: <https://www.economicportal.ru/ponyatiya-all/makroekonomicheskiy-shok.html> (accessed on 12 September 2023).
  44. Available online: <https://rosstat.gov.ru/> (accessed on 12 September 2023).
  45. Alyukov, S.V. Approximation of step functions in problems of mathematical modeling. *Math. Model Comput. Simul.* **2011**, *3*, 661–669. [CrossRef]
  46. Alyukov, S.V. Modeling of dynamic processes with piecewise linear characteristics, *Izvestiya Vysshikh Uchebnykh Zavedenii. Appl. Nonlinear Dyn.* **2011**, *19*, 27–34.
  47. Alyukov, S.V. *Dynamics of Inertial Stepless Automatic Transmissions*; INFRA-M: Moscow, Russia, 2013; 251p.
  48. Alyukov, S.V. Approximation of generalized functions and their derivatives. Questions of atomic science and technology. Series: Mathematical modeling of physical processes. Sarov: Russian Federal Nuclear Center—VNIIEF. *Ser. Math. Model. Phys. Process* **2013**, *2*, 57–62.

49. Alyukov, S.V. A new method for the analytical approximation of the Heaviside function. *Mod. Sci. Bull.* **2013**, *12*, 7–10.
50. Aliukov, S.; Alabugin, A.; Osintsev, K. Review of Methods, Applications and Publications on the Approximation of Piecewise Linear and Generalized Functions. *Mathematics* **2022**, *10*, 3023. [CrossRef]
51. Helmsberg, G. The Gibbs phenomenon for Fourier interpolation. *J. Approx. Theory* **1994**, *78*, 41–63. [CrossRef]
52. Zhuk, V.V.; Natanson, G.I. *Trigonometric Fourier Series and Elements of Approximation Theory*; L.: Publishing House Leningrad University: Saint Petersburg, Russia, 1983; 188p.
53. Seregina, E.V.; Stepovich, M.A.; Makarenkov, A.M. On the modification of a model of minority charge-carrier diffusion in semiconductor materials based on the use of recursive trigonometric functions and the estimation of the stability of solutions for the modified model. *J. Synch. Investig.* **2014**, *8*, 922–925. [CrossRef]
54. Arfken, G.B.; Weber, H.J. *Mathematical Methods for Physicists*, 5th ed.; Academic Press: Boston, MA, USA, 2000; ISBN 978-0-12-059825-0.
55. Osintsev, K.V.; Aliukov, S.V. Experimental Investigation into the Exergy Loss of a Ground Heat Pump and its Optimization Based on Approximation of Piecewise Linear Functions. *J. Eng. Phys. Thermophy* **2022**, *95*, 9–19. [CrossRef]
56. Osintsev, K.V.; Aliukov, S.V. Mathematical modeling of discontinuous gas-dynamic flows using a new approximation method, Materials Science. *Energy* **2020**, *26*, 41–55. [CrossRef]
57. Cai, W. Implementation of Mathematical Modeling Teaching Based on Intelligent Algorithm. In Proceedings of the ICISCAE'21, Dalian, China, 24–26 September 2021; pp. 622–626.
58. Aliukov, S. Approximation of Electrocardiograms with Help of New Mathematical Methods. *Comput. Math. Model.* **2018**, *29*, 59–70. [CrossRef]
59. Ubaru, S.; Saad, Y. Fast Methods for Estimating the Numerical Rank of Large Matrices. Department of Computer Science and Engineering, University of Minnesota, Twin Cities, MN USA. In Proceedings of the 33rd International Conference on Machine Learning, New York, NY, USA, 19–24 June 2016; Volume 48.
60. Putri BA, D.; Handayani, D. Analysis of Product Quality Control using Six Sigma Method. In *IOP Conference Series: Materials Science and Engineering*; IOP Publishing: New York, NY, USA, 2019; Volume 697, p. 012005. [CrossRef]
61. Thakur, V.; Akerele, O.A.; Brake, N.; Wiscombe, M.; Broderick, S.; Campbell, E.; Randell, E. Use of a Lean Six Sigma approach to investigate excessive quality control (QC) material use and resulting costs. *Clin. Biochem.* **2023**, *112*, 53–60. [CrossRef] [PubMed]
62. Krotov, M.; Mathrani, S.K. A Six Sigma Approach Towards Improving Quality Management in Manufacturing of Nutritional Products. *J. Ind. Eng. Manag. Sci.* **2017**, *1*, 225–240. [CrossRef]
63. Alabugin, A.; Aliukov, S.; Khudyakova, T. Models and Methods of Formation of the Foresight-Controlling Mechanism. *Sustainability* **2022**, *14*, 9899. [CrossRef]
64. Alabugin, A.; Aliukov, S. Modeling Regulation of Economic Sustainability in Energy Systems with Diversified Resources. *Science* **2020**, *3*, 15. [CrossRef]
65. Alabugin, A.; Aliukov, S.; Khudyakova, T. Review of Models for Socioeconomic Approaches to the Formation of Foresight Control Mechanisms: Genesis. *Sustainability* **2022**, *14*, 11932. [CrossRef]

**Disclaimer/Publisher’s Note:** The statements, opinions and data contained in all publications are solely those of the individual author(s) and contributor(s) and not of MDPI and/or the editor(s). MDPI and/or the editor(s) disclaim responsibility for any injury to people or property resulting from any ideas, methods, instructions or products referred to in the content.



Article

# Dynamic Analysis of the EU Countries Sustainability: Methods, Models, and Case Study

Elena Lyaskovskaya \*, Gulnaz Khalilova and Kristina Grigorieva

Department of Digital Economics and Information Technologies, South Ural State University, 76 Lenin Prospekt, 454080 Chelyabinsk, Russia

\* Correspondence: liaskovskaiaa@susu.ru

**Abstract:** The agenda for sustainable development actualizes sustainability analysis of countries' social, ecological, and economic conditions, as well as the necessity of designing practical recommendations to realize the sustainable development goals (SDGs). Sustainability analysis is a part of decision making and policy development in a broad environmental, economic, and social context. That is why this analysis goes beyond simple technical assessment. In order to make sustainability a target variable in development strategies, it is necessary to use special methods combining mathematical tools and managerial content. The paper systematizes modern mathematical methods for assessing economic sustainability and proposes a methodology for the integrated assessment of the social, economic, and environmental sustainability of countries, which were tested on data from 24 EU countries over 12 periods. The case study results derived from spatial and temporal samples are consistent with the currently observed processes in the EU. The content basis is the UN concept of sustainable development, the instrumental basis is multivariate comparisons, the Mahalanobis distances method, the correlation and regression analysis, analysis of variance, time series analysis, and trends analysis. Composite indices of social, economic, and environmental sustainability of the EU countries, each of them including five indicators, were developed in this study; the levels of social, economic, and environmental sustainability of EU countries were determined, as well as individual instability indicators. Mahalanobis distances and relative and absolute sustainability indicators were calculated and determined. Cluster analysis of the EU countries by levels of social, economic, and environmental instability and Mahalanobis distances, the diagnosis of the current situation and dominant trends were carried out for testing the hypothesis that there are positive relations between the instability of development and Mahalanobis distances. Hypotheses about the relationship between instability and the level of country development, reflected in the values of socio-economic and environmental indicators, and whether countries with good values of social, environmental, and economic indicators are the most sustainable, were investigated.

**Keywords:** resilience; sustainable development; instability; multivariate comparisons; Mahalanobis distance; time series; trends analysis; correlation and regression analysis; cluster analysis; analysis of variance

MSC: 37M10

**Citation:** Lyaskovskaya, E.; Khalilova, G.; Grigorieva, K. Dynamic Analysis of the EU Countries Sustainability: Methods, Models, and Case Study. *Mathematics* **2023**, *11*, 4807. <https://doi.org/10.3390/math11234807>

Academic Editor: Chuangyin Dang

Received: 24 October 2023

Revised: 21 November 2023

Accepted: 24 November 2023

Published: 28 November 2023



**Copyright:** © 2023 by the authors. Licensee MDPI, Basel, Switzerland. This article is an open access article distributed under the terms and conditions of the Creative Commons Attribution (CC BY) license (<https://creativecommons.org/licenses/by/4.0/>).

## 1. Introduction

The concept of resilience as a system's ability to exist despite the unfavorable effects of factors of various geneses is used in different sciences in which objects are complex systems—in technology, biology, economics, and others. For economic systems, the concept of resilience as the ability to recover from a shock or disturbance has become widespread in the last decade. Hence, resilience is defined as the ability to anticipate, react to, and recover from disorder [1]. The term “sustainability”, used in macroeconomics, has been understood as a long-term equilibrium between the exploitation of resources and the development of human

society. The currently used term “sustainable development” implies balanced development from the position of three components—economic, environmental, and social. In recent years, the concept of sustainable development has not only attracted much attention from scientists, practitioners, and international organizations, but has also been firmly embedded in politics. The focus is on the problems of resource scarcity, environmental degradation, climate change, natural disasters, pandemics, social disproportions, digital inequality, supply chain instability, rural development problems, the impact of disruptive innovations and new digital business models, and urban sustainability problems [2–12].

The current sustainable development agenda necessitates the creation of methods for analyzing the sustainability of territorial entities; social, ecological, and economic conditions; and the development of practical recommendations for achieving sustainable development goals. Sustainability assessment is conducted as a stage of decision making and policy development in broad environmental, economic, and social contexts, and it goes beyond technical assessment. Meanwhile, there is currently no universal methodology to quantify the sustainability of a socio-economic system. This is due to the diversity of conceptual and methodological approaches. Thus, the authors understand sustainability as resilience or resistance to the impact of internal and external shocks, the ability to recover from them, and taking a new trajectory of development; as well as sustainability or the development of nonantagonistic orientation, characterized by the achievement of social, environmental, and economic objectives, taking into account the interests of all participants, and present and future generations.

**2. Literature Review/Background**

There is no single approach to the definition of sustainability, as the methods of assessing sustainable development are diverse. We conducted systematization of existing approaches to analyze the sustainability of countries and regions and the economic-mathematical models used in them, is based on research of contemporary authors and international organizations’ documents [3–9,13–42].

The systematization of approaches to the analysis of sustainability of territorial entities is presented in the Table 1.

**Table 1.** Approaches to analyzing the sustainability of territorial entities.

Sustainability Measurement	Approach	Authors
Qualitative analysis of sustainability	Impact of the pandemic situation on progress towards the SDGs	[9]
	Identification of sustainable development targets with a focus on justifying their relevance	[14]
	The need to link social, environmental, and economic indicators to the public vision of sustainable development and the UN SDGs	[3,15]
	The need for sustainable transformation of markets and society	[16]
	The need to identify positive contributions to sustainable development that facilitate stakeholder decision making	[17]
	Linking digital transformation and sustainability	[18]
	Understanding the political and governance dimensions of sustainability	[19]
	Examining resilience and vulnerability through the lenses of evolutionary dynamics and exposure to shocks	[4]
	Using the concept of hysteresis to examine the possible responses of the economic system to crisis shocks	[5]
	Impact of global shocks on regional resilience	[6]
	A theoretical framework for incorporating sustainability indicators into the decision-making process is proposed	[26]
	Developing urban resilience indicators: adaptive capacity, absorptive capacity, and transformative capacity	[31]

Table 1. Cont.

Sustainability Measurement	Approach	Authors
Quantitative analysis of sustainability	Developing statistical indices: regional resilience to economic shocks and postcrisis recovery	[7]
	Using three types of measurements: arithmetic mean, geometric mean, and entropy index	[21]
	Vector autoregressive modeling and impulse response function (IRF)	[22]
	Bayesian Model Averaging (BMA)	[23]
	Simple Additive Weighting (SAW)	[8]
	Method of residuals of vector autoregression (VAR)	[24]
	Econometric panel data methods	[25]
	Chi-Square Test of Homogeneity $X^2$ )	[27]
	Autoregression method with smooth transition (STAR)	[28]
	Multi-level logistic regression model	[29]
	Fixed-effects model	[30]
	the Technique for Order of Preference by Similarity to Ideal Solution (TOPSIS) methods	[32]
	Multidimensional approach with support for building information modeling (BIM)	[34]
	TOPSIS method with application of the structural differences indicator—V.M. Ryabtsev index	[40]
	Methods of comparative, abstract-logical and statistical analysis, calculation, and graphic method “radar (polygon) of competitiveness”	[41]
Resistance index and recovery index	[42]	

A report by the Leadership Council of the Sustainable Development Solutions Network [13] examines 100 global monitoring indicators covering all Sustainable Development Goals and targets. A discussion paper on Principles of Using Quantification to Operationalize the SDGs and Criteria for Indicator Selection, prepared by the United Nations Statistics Division, focuses on principles of using quantification to operationalize the SDGs and criteria for indicator selection. It includes criteria for selecting SDG indicators, including Relevant, Methodologically sound, Measurable, Easy to communicate and access, limited in number, and Outcome focused at the global level [13].

The interaction of multiple extreme events with the coronavirus pandemic and the impact on progress towards the SDGs is the subject of a study [9]. Studies on the identification of sustainable development targets with a focus on justifying their relevance are of interest [14]. In [13,15], the authors emphasize the need to link social, environmental, and economic indicators with the public vision of sustainable development and with the UN SDGs. Sustainable transformation of markets and society is necessary to assess sustainable development [16]. Current measurements and approaches to sustainability assessment focus on reducing negative environmental impacts [17]: while measuring sustainability it is necessary to identify positive contributions to sustainable development that facilitate stakeholder decision making. The relationship between digital transformation and sustainability is addressed by [18]. Digital transformation enhances corporate sustainability through mechanisms that improve human capital, strengthen innovation capabilities, ease financial constraints, and strengthen internal controls. To understand the political and governance aspects of resilience, in [19], the authors showed that national policies largely explain both the resilience of regions to previous crises and their vulnerability to the current economic crisis.

Analyzing the sustainability of economic development implies identifying the factors determining it and testing the relevant hypotheses based on the construction of econometric relationships [20]. Spatial economy models based on panel samples of countries and regions prove the influence of intersectoral interactions and spatial effects on sustainability [14]. For example, in [15], it is shown that the level of sustainability of regional development

depends on both the sectoral diversification of the economy and the sustainability of the economies of neighboring regions.

Using the concept of spatial economic resilience, researchers [4] consider resilience and vulnerability through the prism of evolutionary dynamics and exposure to shocks. In [5], it is substantiated that the regional economic system is able to adapt its structure (firms, industries, technologies, and institutions) to an acceptable trajectory of production and employment growth; using the concept of “hysteresis” (movement from one equilibrium area to another), and possible reactions of the system to crisis shocks are considered. The central issue of [6] is the impact of global shocks on regional resilience.

Two statistical indices are used to measure resilience based on the dynamics of economic processes [7]: the first one characterizes the resilience of the region to economic shocks:

$$\beta_{res}^{EU} = \left[ \left( E_t^R - E_{t-1}^R \right) / E_{t-1}^R - \left( E_t^{EU} - E_{t-1}^{EU} \right) / E_{t-1}^{EU} \right] / \left| \left( E_t^{EU} - E_{t-1}^{EU} \right) / E_{t-1}^{EU} \right|,$$

where  $E^R$  is the employment at regional level (persons)  $E^{EU}$  is the employment at the EU-27 level (persons);  $t - 1$  is the starting year of the crisis period (2008); and  $t$  is the end year of the economic recovery period (2015);

The second demonstrates recovery from the crisis:

$$\beta_{res}^N = \left[ \left( E_t^R - E_{t-1}^R \right) / E_{t-1}^R - \left( E_t^N - E_{t-1}^N \right) / E_{t-1}^N \right] / \left| \left( E_t^N - E_{t-1}^N \right) / E_{t-1}^N \right|,$$

where  $E^N$  is the employment at country level (persons).

A positive index  $\beta_{res}^{EU}$  implies that the region experienced smaller relative employment losses (or higher relative employment gains) and/or recovered faster than national employment changes. The assessment of sustainability indicators is categorized into four groups:

Group I: Low resistance and slow recovery ( $\beta_{ress}^{EU} < 0$  and  $\beta_{rec}^{EU} < 0$ ).

Group II: Low resistance and fast recovery ( $\beta_{ress}^{EU} < 0$  and  $\beta_{rec}^{EU} > 0$ ).

Group III: High resistance and slow recovery ( $\beta_{ress}^{EU} > 0$  and  $\beta_{rec}^{EU} < 0$ ).

Group IV: High resistance and fast recovery ( $\beta_{ress}^{EU} > 0$  and  $\beta_{rec}^{EU} > 0$ ).

The first group, i.e., the group with the worst performance (low resistance/slow recovery), is the reference category for which all parameters and random errors are set to zero. A three-level random intercept logistic regression model ( $y_{ijk}$ ) is applied to capture the interactions between resistance and recovery phases:

$$y_{ijk} = a_0 + a_1 x_{ijk} + u_{jk} + v_k + e_{ijk},$$

where  $i = 1, \dots, I_{jk}$  ( $I_{jk}$  denotes the number of NUTS-3 regions in NUTS-2 region  $j$  within country  $k$ );  $j = 1, \dots, J_k$  ( $J_k$  denotes the number of NUTS-2 regions in country  $k$ );  $k = 1, \dots, K$  ( $K$  denotes the number of countries);  $u_{jk}$  is the NUTS-2 regional random intercept;  $v_k$  is the country random intercept; and  $e_{ijk}$  is the NUTS-3 regional error term.

To build a regional index of sustainable development [21], three types of measurements were used:

- (1) Arithmetic mean index—the average of six regional development performance indicators: economic growth rate (EGR), open unemployment rate (IUNP), poverty rate (POV), human development index (HDI), Gini index (GI), and environmental quality index (IKLH);
- (2) Geometric mean index ( $RSDI_g$ ):

$$RSDI_g = \sqrt[6]{IEG \times HDI \times EQI \times (1 - IPOV) \times (1 - GI) \times (1 - IUNP)}.$$

Using the geometric mean eliminates the disadvantage of linear measuring.

(3) Entropic index ( $E_j$ ):

$$E_j = -k \sum_{i=1}^m p_{ij} \ln p_{ij}$$

A number of works investigate the sensitivity of sustainable development of regions to their sectoral and institutional structure. Thus, in [22], the authors applied vector autoregressive modeling (VAR) (used to study linear interdependencies between several time series) and impulse response function (IRF) (the response of the national economy to a unit shock in each sector, thus revealing the endogenous mechanism of national economic turbulence). As a result, the key sectors of the economy with the greatest potential for its imbalance were identified: construction, real estate, and financial services, while the industrial sector has the greatest potential for “stabilization”.

$$gdpR_t = v + A_1 gdpR_{t-1} + A_2 gdpR_{t-2} + \dots + A_p gdpR_{t-p} + \mu_t, \quad (t = 1, \dots, T),$$

where  $gdpR_t = (gdpR_{Nt}, gdpR_{Agrt}, \dots, gdpR_{REt})'$  denote a  $(n \times 1)$  vector of the cyclical component of GDP growth rate of the nation and each sector.  $A_i$  are  $(n \times n)$  coefficient matrices and  $v = (v_1, \dots, v_n)'$  is a fixed  $(n \times 1)$  vector of intercept terms.  $\mu_t = (\mu_{1t}, \dots, \mu_{nt})'$  is a  $(n \times 1)$  white noise vector process satisfying the conditions of  $E(\mu_t) = 0$ ,  $E(\mu_t \mu_s') = \Sigma \mu$  and  $E(\mu_t \mu_s') = 0$  for  $s \neq t$ .

In [6], the relationship between sustainable development and the effectiveness of public administration in regions was investigated using Bayesian Model Averaging (BMA) by calculating the posterior probability of the model (Posterior Model Probability  $p(M_k|y, X)$ ):

$$p(M_k|y, X) = \frac{p(y, X|M_k)p(M_k)}{\sum_{k=1}^{2^K} p(y, X|M_k)p(M_k)}$$

where  $p(y, X|M_k)$  is the marginal likelihood and  $p(M_k)$  is the prior model probability.

In [8] a weighted sum of indices characterizing the performance of basic economic functions by sectors of the economy is used to measure sustainability at the industry level, using the multicriteria decision-making method Simple Additive Weighting (SAW). This approach is highly operational and is based on an additive function:

$$S_j = \sum_{k=\{F,V,E\}} q_k S_{Kj}$$

where  $q_k$  are the weights of resilience functions and  $\sum_{k=\{F,V,E\}} q_k = 1$ .

Using an empirical approach, applying the residuals vector autoregression (VAR) method, in [24] estimated resilience through the correlation between the change in output and the total shock due to institutional characteristics and the level of industrialization:

$$X_t = A(L)X_{t-i} + e_t,$$

where

$$X_t = \begin{bmatrix} y_t \\ p_t \\ r_t \\ m_t \end{bmatrix} \text{ and } e_t = \begin{bmatrix} e_{yt} \\ e_{pt} \\ e_{rt} \\ e_{mt} \end{bmatrix}.$$

In [25], the authors, using econometric methods of panel data, showed that sustainable economic development is determined by the relationship between embeddedness ( $Emb_j$ )

and resilience. Embeddedness has a positive effect on resilience up to a certain point, after which increasing embeddedness has a negative effect on resilience:

$$Emb_j = \frac{\sum_{i=1}^n Z_{ij}^d}{\sum_{i=1}^n Z_{ij}^d + Z_{ij}^m}$$

where  $Z$  is the intermediate flows between sectors  $i$  and  $j$  ( $n$  being the total number of sectors),  $d$  stands for domestic flows (e.g., transactions between sectors within the same region), and  $m$  represents imported inputs from outside the region.

In [26], a theoretical framework for incorporating sustainability indicators into the decision-making process for transportation projects at the conceptual planning level is proposed, according to which economic sustainability planning requires consideration of regional characteristics, including industrial diversity and human capital, in addition to transportation accessibility.

The approach [27] to achieving sustainability, includes equilibrium and econometric analysis, the use of the Chi-Square Test of Homogeneity (Chi-Square Test of Homogeneity  $X^2$ ) to identify endogenous and exogenous factors of the regional economy, including industrialization:

$$X^2 = \sum \left( \frac{(O_{a,b} - E_{a,b})^2}{E_{a,b}} \right),$$

where  $O_{a,b}$  is the observed value in population  $a$  for level  $b$  of the categorical variable, and  $E_{a,b}$  is the expected frequency count in population  $a$  for level  $b$  of the categorical variable.

In [28], the authors, using the smooth transition autoregressive (STAR) method, evaluated the economic sustainability of Italian regions. The identified regional characteristics are related to the presence of spatial interactions and factors such as economic diversity, export performance, financial constraints, and human and social capital. For a univariate time series  $y_t$ , the STAR model is as follows:

$$y_t = \phi_1' y_t^{(p)} (1 - G(s_t; \gamma, c)) + \phi_2' y_t^{(p)} G(s_t; \gamma, c) + \varepsilon_t,$$

where  $y_t^{(p)} = (1, y_t^{(p)})'$ ,  $y_t^{(p)} = (y_{t-1}, \dots, y_{t-p})'$ ,  $\phi_i = (\phi_{i0}, \phi_{i1}, \dots, \phi_{ip})'$  are parameters to be estimated,  $i = 1, 2$  and  $\varepsilon_t$  is a white-noise error process with mean zero and variance  $\sigma^2$ .

In [29] the factors determining crisis resilience in European regions were studied. Using a multilevel logistic regression model  $y_{ij}^*$  the authors studied regional employment in crisis periods and substantiated the need to reduce regional differences by developing differentiated regional development policies:

$$y_{ij}^* = \beta_0 + \beta_1 x_{ij} + u_j + e_{ij}^*$$

where  $e_{ij}^*$  is the regional (level 1) residual and  $u_j$  is the country (level 2) residual.

The relationship between the diversity of industries and economic stability of the territory was investigated in [30] by assessing the impact of industrial diversity and concentration on the stability of the unemployment rate. For this purpose, the authors used a fixed effects model  $Y_{it}$ .

$$Y_{it} = \beta_0 + X_{it}\beta + \delta\gamma_t + \Theta\gamma_{t-1} + \alpha Z_{it} + \Omega I_{it} + \Omega V_{it} + \varepsilon_{it},$$

where  $Y_{it}$  is the county  $i$  unemployment rate in year  $t$ ;  $X_{it}$  is a row vector of regressors;  $\beta$  is the corresponding vector of coefficients;  $\gamma_t$  is the relevant national or local shock indicator;  $\gamma_{t-1}$  is the lag of the national or local shock indicator and  $\Theta$  is the corresponding coefficient;  $Z_{it}$  and the corresponding coefficients represents the interaction between population density and diversity capturing urbanization;  $I_{it}$  with  $\Omega$  as the corresponding coefficient is the interaction of the diversity term with the shock variable, with  $\Omega$  as the corresponding

coefficient; and  $V_{it}$  represents the interaction of the diversity term with the lag of the local shock variable, with  $\bar{U}$  as the corresponding coefficient.

The authors proved that although unemployment was lower in more concentrated counties, employment was higher in counties with more diverse industry structures in the face of national or local shocks [30].

In the context of rapidly developing urbanization, the concepts of resilience and urban sustainability, are interrelated paradigms, acting as elements of preventive protection. The key indicators of urban resilience in the authors' model [31] were three components: adaptive capacity (education, health, food and water), absorptive capacity (community support, urban green spaces, protective infrastructure, and access to transportation), and transformative capacity (communication technologies, multi-stakeholder collaboration, emergency services for public, and community-oriented urban planning).

The study [32] is devoted to measuring the economic sustainability of cities. The authors used six indicators: economic growth, openness, social development, environmental protection, natural conditions, and technological innovation. The Technique for Order of Preference by Similarity to Ideal Solution (TOPSIS) methods and the Technique for Order of Preference by Similarity to Ideal Solution (TOPSIS) methods were used to identify spatial and temporal trends. A four-step approach was used to create the TOPSIS model.

Step 1: Construct a standardized matrix:  $X = \{x_{ij}\}_{m \times n}$ , to standardize all indicators:

$$\begin{aligned}
 & \left\{ \begin{array}{l} \frac{(x_{ij} - x_{min})}{(x_{max} - x_{min})} \\ \frac{(x_{max} - x_{ij})}{(x_{max} - x_{min})} \end{array} \right. \\
 & x_{ij}(\text{benefit index}) \\
 & x_{ij}(\text{cost index}) \\
 & (I = 1, 2, 3 \dots m; j = 1, 2, 3 \dots n)
 \end{aligned}$$

where  $x_{ij}$  is the normalized value of the  $j$ th indicator of the  $i$ th city.

Step 2: Determine the "optimal plan"  $X^+$  and "worst plan"  $X^-$ :

$$\begin{aligned}
 X^+ &= \{x_1^+, x_2^+, x_3^+, \dots, x_n^+\}, x_j^+ = \max_j \{x_{ij}\} (i = 1, 2, 3, \dots, m) \\
 X^- &= \{x_1^-, x_2^-, x_3^-, \dots, x_n^-\}, x_j^- = \min_j \{x_{ij}\} (i = 1, 2, 3, \dots, m)
 \end{aligned}$$

where  $x_i^+$  is the optimal value of the indicator and  $x_i^-$  is the worst value of the indicator.

Step 3: Calculate the sum distance between the individual samples  $X^+$  and  $X^-$ :

$$\begin{aligned}
 D_i^+ &= \sqrt{\sum_{j=1}^n \omega_j (x_{ij} - x_j^+)^2} (i = 1, 2, 3, \dots, m) \\
 D_i^- &= \sqrt{\sum_{j=1}^n \omega_j (x_{ij} - x_j^-)^2} (i = 1, 2, 3, \dots, m)
 \end{aligned}$$

where  $D_i$  is the weight coefficient between the indicator data.

Step 4: Calculate the relative closeness of each sample to the "ideal" sample:

$$C_i = \frac{D_i^-}{D_i^+ + D_i^-} (i = 1, 2, 3, \dots, m)$$

where,  $C_i$  is the closeness of the  $i$ th sample and the "optimal plan";  $0 \leq C_i \leq 1$ .

In [33], a social sustainability assessment framework for residential buildings is developed using a weighted aggregation approach to improve their operational value. A multidimensional approach supported by building information modeling (BIM) has been proposed to ensure the sustainability of building materials supply [34].

Despite the availability of a variety of assessment methods and tools, the most commonly used approach is the use of a system of indicators [35]. According to [36], sustainable development assessment models should (have to be) balanced, include reasonable indicators, and take into account both the existing interrelationships between indicators and the subjectivity of the used qualitative criteria of sustainable development. For a comprehensive assessment of sustainable development [37], the economic sustainability index is used, which assesses the results in four areas—macroeconomic stability, microeconomic efficiency of the market, good governance, and social development.

The article [40] proposes a cluster approach as the most effective tool for managing sustainable development of territories based on the TOPSIS method (Technique for Ordered Preference through Similarity to Ideal Solution (TOPSIS) methods). To analyze quantitative changes in individual sustainability criteria and to assess structural shifts of the region territorial-production system, the index of structural differences—V.M. Ryabtsev’s index—has been used:

$$R_i = \sqrt{\frac{\sum_{j=1}^n (P_{ij}^1 - P_{ij}^0)^2}{\sum_{j=1}^n (P_{ij}^1 + P_{ij}^0)^2}},$$

where  $R_i$  is the index of structural differences of the  $i$ -th territory sustainability component;  $P_{ij}^1$  is estimated values of  $j$ -th stability criterion of  $i$ -th territory, achieved under the influence of changes in economic relations, market processes, interregional, and intersectoral relations;  $P_{ij}^0$  is assessed values of the  $j$ -th stability criterion of  $i$ -th territory, determined at the initial stage of study (before assessing the impact of territories interaction within a cluster).

The assessment of the sustainability of regional socio-economic systems in [41] is carried out using a systematic approach and a combination of methods of comparative, abstract-logical and statistical analysis, as well as the calculation and graphic method “radar (polygon) of competitiveness”. The determination of the integral assessment of the parameters of each region is based on the determination of the areas of their polygons according to the formula:

$$S_i = 1/2\sin(360^\circ/8) \times (K_{1i} \times K_{2i} + K_{2i} \times K_{3i} + K_{3i} \times K_{4i} + K_{4i} \times K_{5i} + K_{5i} \times K_{6i} + K_{6i} \times K_{7i} + K_{7i} \times K_{8i} + K_{8i} \times K_{1i}),$$

where  $K_{ij}$ —coordinates of the polygon (radar) vertices in the coordinate axes with the origin in the center of the circle for the region;  $k = 8$ —number of individual evaluated criteria.

Using the resistance index and recovery index in [42] the authors study the resistance of regions to recessionary shocks in times of economic crises. The resistance index is calculated by the formula:

$$\beta_{res} = [(\Delta E_r/E_r)/(\Delta E_N/E_N)]/|\Delta E_N/E_N|,$$

where  $(\Delta E_r/E_r)$  and  $(\Delta E_N/E_N)$ —percentage changes in employment at the regional and national levels, respectively.

The recovery index is calculated:

$$\beta_{res} = (\Delta E_r/E_r)/(\Delta E_N/E_N)$$

Higher values of the resistance and recovery indices indicate a more stable position of the region relative to the national economy.

Based on the analysis results, a number of conclusions can be drawn. There are numerous studies analyzing the achievement of the Sustainable Development Goal in individual countries. As a rule, the methods used in them are based on the comparison of normative values, UN SDGs, and actual data for individual countries. Separately, there are studies on how national economies can recover from shocks. In our research we are guided by the idea that the methodology of resilience assessment should combine both

the UN ideology of sustainable development, i.e., simultaneous consideration of social, environmental, and economic components, and resilience, which implies maintaining the trajectory of social, environmental and economic development, i.e., achieving and maintaining the specified levels of indicators that form social, environmental, and economic sustainability. At the same time, the development trajectory should be assessed not only within a single country (internal comparison), but should be comparative in nature, taking into account the approximation or removal of country indicators to the average values of the sample (external comparison).

There is no single methodological approach for sustainability assessment of countries and territorial entities. This is caused by the shortcomings of the rating approach, different units of measurement of used indicators, as well as the problem of indicators justification. The barrier is also the complexity of managerial use of composite indicators, in which it is difficult to determine the contribution of individual sustainability factors. In addition, new types of sustainability are appearing now, making sustainable development a complex and multifaceted concept encompassing various dimensions. The problem of comparative analysis of sustainability is the lack of harmonized statistical data, due to the heterogeneity of countries development.

Each of presented in Table 1 methods and described above can be characterized by its merits and are aimed at solving certain problems. However, currently there is a research gap consisting in the need to combine in one methodology the diagnostic potential, or assessment of the social, economic, and environmental development sustainability level, and the management potential, or revealing the countries features by comparison indicators of each country with the average ones. Remarkably, in the challenges of overcoming development imbalances, macroeconomic and microeconomic inequalities remain relevant. This study aims to address this research gap (Section 3)

The core of modern approaches in measuring sustainability is the principle of balancing social, environmental, and economic aspects that form the policy of sustainable development management. In order to make sustainability a target variable in development strategies, it is necessary to use special methods combining mathematical tools and managerial content.

### 3. Materials and Methods

The dynamic approach has been used to analyze the sustainability of the EU countries as open social, economic, and ecological systems [38]. The dynamic stability of a socio-economic system is understood as its movement near a certain stable trend and weak reaction to the impact of internal and external shocks.

The distinctive feature of the developed method is its universality, i.e., the possibility of using it for different sets of indicators that form composite indices of social economic and environmental sustainability. The main limitation for the choice of private indicators is the availability of statistical information in the context of individual countries throughout the period under consideration.

The developed methodological approach for analyzing the dynamic sustainability of countries as open systems includes 7 stages, presented in the Table 2. The framework presented in the table consists of 3 blocks, developed in accordance with the existing research gap in the field of dynamic analysis of countries sustainable development.

**Table 2.** Methodology for analyzing the dynamic sustainability of countries as open socio-economic systems.

Stage Name	Stage Content
1. Informative	Selection of countries to be analyzed
2. Staged	Development and substantiation of composite indices reflecting social, economic and environmental components of sustainability in accordance with the UN concept of sustainable development and the European Union statistical reporting system
3. Statistic	<p>3.1 Collection of statistical information on indicators included in the social, economic and environmental composite indices</p> <p>3.2 Testing for the presence of a unit root in panel data using the Dickey–Fuller test:  <math>\Delta y_t = \alpha + \beta t + \gamma y_{t-1} + \delta_1 \Delta y_{t-1} + \dots + \delta_p - 1 \Delta y_{t-p} + 1 + \epsilon_t</math>                      where <math>\Delta y_t</math> is the first difference of the variable of interest at time <math>t</math>, <math>\alpha</math> is a constant term, <math>\beta t</math> represents a time trend, <math>\gamma y_{t-1}</math> captures the lagged dependent variable, <math>\delta_1 \Delta y_{t-1} + \dots + \delta_p - 1 \Delta y_{t-p} + 1</math> includes lagged differences of the variable up to order <math>p - 1</math>, <math>\epsilon_t</math> is the error term.</p> <p>4. Aggregation of composite indices and determination of instability levels for each of them as well as for individual indicators via Mahalanobis distances</p>
4. Methodical	<p>4.1 Construction of <math>x</math>—multidimensional vectors of indicators for each <math>i</math>-th country (<math>i = 1 \dots 24</math>) for each <math>j</math>-th (<math>j = 1 \dots 5</math>) indicator included in the economic, social, and environmental composite indices, where  <math>x = (x_1, x_2, x_3, \dots, x_K)^T</math></p> <p>4.2 Construction of a vector of mean values for each indicator included in the economic, social, and environmental composite index—<math>\mu</math>.  <math>\mu = (\mu_1, \mu_2, \mu_3, \dots, \mu_K)</math></p> <p>4.3 Calculation the inverse covariance matrix of indices <math>S^{-1}</math></p> <p>4.4 Aggregation of indicators included in composite indices. Determination of the Mahalanobis distance—<math>D_{Mit}(x)</math> for each <math>i</math>-th country (<math>i = 1, m</math>) in each <math>t</math>-th year (<math>t = 1, n</math>) for composite indices—economic, social, and environmental  <math>D_M(x) = \sqrt{(x - \mu)^T S^{-1} (x - \mu)}</math></p> <p>4.5 Calculation of <math>D_{Mit}</math>—linear time regressions of Mahalanobis distances for each country over the study period (for each aggregate index) and their estimation by the least squares method.</p> <p>4.6 Separating of the trend and cyclical component of linear time regressions of Mahalanobis distances for each country over the study period (for each aggregate index) by the least squares method.  <math>D_{Mit} = \alpha_{0i} + \alpha_{1i} \times t + e_{it}</math>                      where <math>\alpha_{0i}</math> и <math>\alpha_{1i}</math>—regression coefficients, <math>e_{it}</math>—regression residuals</p> <p>4.7 Calculation of the absolute level of instability of social, economic, and environmental development of countries through  <math>\sigma_{ei}</math>—calculation of the mean square deviation of the residuals of the Mahalanobis distance regression for each country for the period under study. The higher the level of instability, the greater the fluctuations of economic, social, and environmental development of the country relative to its own stable trend.  <math>\sigma_{ei} = \sqrt{\text{Var}(e_{it})} = \sqrt{\sum_{t=1}^n e_{it}^2}</math></p> <p>4.8 Calculation of the relative level of instability of social, economic, and environmental development of countries  <math>V_{ei} = \frac{\sigma_{ei}}{D_{mi}}</math>                      where <math>D_{mit}</math>—mean of predicted value of Mahalanobis distance (using time series regression).</p>
5. Analytic	Visualization and analysis of the obtained results on the levels of economic, environmental, and social instability of the EU countries.
6. Verifying	Assessment of the reliability of the obtained results and testing of the hypothesis about the relationship between the instability of countries and the indicators included in the composite indices.
7. Predictive	Using the results of the analysis for decision making.

First, the economic, social, and environmental space under study is multidimensional. Therefore, for the analysis, it is necessary to use complex composite indices that include a

set of indicators for each development direction and reflect the current content of the UN Sustainable Development Goals. The development of indices is of a variable nature. Their number is determined by the objectives of the analysis, and the indicators forming them are determined by the availability and quality of statistical data. In the study we used three composite indices of economic, environmental, and social sustainability. The indicators selected in their composition reflect the nine existing pillars of sustainable development. The problem of comparative analysis of sustainability is the lack of harmonized statistical data due to the heterogeneity of countries' development, so the statistical stage includes testing for the presence of a unit root in panel data using the Dickey–Fuller test.

Secondly, the assessment of sustainability of development should have the character of external evaluation, i.e., it is necessary to study not just the dynamics of change in the indicators forming composite indices, but the trajectory of social, economic, and environmental development of countries in relation to the average values in the sample. Therefore, the Mahalanobis distance method is chosen as the basis. The use of the Mahalanobis method distances to assess the sustainability of multidimensional and scale-invariant development is characterized by a number of merits. First, it solves the problem of multidimensional indicators, and invariant to their scale due to the normalization of private indicators. Second, it allows us to solve the problem of collinearity of private indicators due to through the inclusion of the covariance matrix. Third, the average distance of countries from the center for a number of indicators is used as a basis for comparison (benchmark). Fourth, the analysis of Mahalanobis distances over a certain time interval allows us to reveal how the place of a particular country relative to the central tendency changes in dynamics and how smooth this change is [38].

Third, in order to make sustainability a target variable in development strategies, it is necessary to use special methods that combine mathematical tools and managerial content. Based on the analysis, it is necessary to identify the unevenness of social economic and environmental development of countries. To identify the indicators that have the greatest impact on sustainable development, a correlation and regression analysis between Mean indicator values included in composite indices and absolute instability level was conducted. Thus, microeconomic aspects of instability were considered. In order to identify macroeconomic aspects, a cluster analysis using k-means clustering has been carried out. Clusters were developed according to the parameters of actual annual mean of Mahalanobis distance and Absolute level of instability. At the same time, to ensure completeness, accuracy, and visualization of the results, logarithms of indicators were used.

Adhering to the principles of the UN concept of sustainable development [13], 3 composite indices reflecting social, economic, and environmental components were developed to study the dynamic sustainability of the EU countries. The Mahalanobis distance method was used to assess the sustainability of development. To identify fluctuations of composite indices and their constituent indicators from a stable trend, time regressions were used.

The use of the Mahalanobis method distances to assess the sustainability of multidimensional and scale-invariant development is characterized by a number of merits. First, it solves the problem of multidimensional indicators, and invariant to their scale due to the normalization of private indicators. Second, it allows us to solve the problem of collinearity of private indicators due to through the inclusion of the covariance matrix. Third, the average distance of countries from the center for a number of indicators is used as a basis for comparison (benchmark). Fourth, the analysis of Mahalanobis distances over a certain time interval allows us to reveal how the place of a particular country relative to the central tendency changes in dynamics and how smooth this change is [38].

The study is based on the data of Eurostat [39]. The sample consists of 24 EU countries: Belgium, Bulgaria, Czechia, Denmark, Germany, Estonia, Spain, France, Italy, Cyprus, Latvia, Lithuania, Luxembourg, Hungary, Malta, Netherlands, Austria, Poland, Portugal, Romania, Slovenia, Slovakia, Finland, and Sweden. Data for a 9-year time period from 2012 to 2020 has been used. Fifteen indicators were selected to construct composite indices of economic, environmental, and social sustainability (Table 3). Economic indicators

determine the level of economic development of countries. Environmental indicators characterize the state and trends in their environment. Social indicators are indicators of the standard of living of the population of the countries.

**Table 3.** Composition of composite sustainability indices of the EU countries.

Index	Indicators and Unit of Measure
Economic sustainability	Real GDP per capita, euros per capita House price index, annual average Harmonized Index of Consumer Prices, average annual index Compensation of employees, million euros Gross fixed capital formation, million euros
Environmental sustainability	Primary energy consumption, million tons of oil equivalent Average CO2 emissions per kilometer from new passenger cars Emissions intensity from industry, grams per euro Net greenhouse gas emissions Recycling rate of municipal waste, %
Social sustainability	Unemployment rate, % Working poverty rate, % Average and median income by age and sex, euros Fertility rates by age group Gini coefficient of equivalent disposable income, scale from 0 to 100

While developing the composite indices, we drew from the nine pillars of sustainable development highlighted today—social equity, environmental protection, economic value added, eco-innovation, resource efficiency, circular (cyclical economy), low carbon, equity (equality), and good governance and partnership.

It should be emphasized that such indicators as return on investment, local economy, and market capacity characterize the economic sustainability of the national economy most fully. However, the possibilities of their use in the study are limited by the following factors. The return on investment is determined by sectoral affiliation and can vary significantly within the economy of one country. In the conditions of globalization and internationalization of business, integration of individual countries’ economies into the world supply chains, it is quite difficult to assess the capacity of local markets in relation to the national economy. The existing statistical observation in Eurostat does not allow providing reliable data on all countries and ensuring the convergence of results. It is also logical that the assessment of the vulnerability of the local economy determined by the level of its diversification has a great predictive potential. However, in the proposed study the local economy was assessed using universal macroeconomic indicators.

Aggregation of indicators into composite indices of economic, environmental, and social sustainability was carried out by calculating Mahalanobis distances—mean normalized distances of each country to the center. The level of instability is measured using the mean square deviation of the Mahalanobis distances regression residuals: the greater the deviation, the greater the instability, as it indicates the large discrepancies between the observed and predicted values.

**4. Main Part/Results**

As a result of using developed methodology, an economic, social, and environmental sustainability of 24 EU countries was analyzed. Regressions of three composite resilience indices for each of the five indicators in the three indices that contribute to the integral level of sustainability was determined. Absolute and relative levels of economic, social, and environmental instability for each country were calculated.

Currently, there is a limited amount of research on the application of stationary and nonstationary time series in calculating the Mahalanobis distance. This aspect requires

additional attention and indepth investigation to fully assess the impact of stationarity and nonstationarity of time series on the process of calculating the Mahalanobis distance.

The Mahalanobis distance, utilized to measure the extent of data points’ remoteness in a multidimensional space of variables, does not seek to confine the analysis to the stationarity or nonstationarity of time series. However, its efficacy is accentuated when dealing with multidimensional data, where variables are measured in a coordinated manner, and the assumption of normal distribution of data is maintained. The application of this method is particularly advantageous in the context of outlier detection or identification of structural features in the data.

In order to analyze the presence of a unit root in panel data and to confirm the suitability of the chosen method of analysis in this study, we applied the Dickey–Fuller test (Table 4).

**Table 4.** Results of the Dickey–Fuller test for various indicators and countries.

Country	Indicators and Unit of Measure	ADF Stat	p-Value
Italy	Real GDP per capita, euros per capita	−1.8	0.12
Hungary	House price index, annual average	−3.2	0.01
Latvia	Average CO2 emissions per kilometer from new passenger cars	−2.5	0.003
Cyprus	Working poverty rate	−2.7	0.02
Malta	Net greenhouse gas emissions	−0.5	0.78
Finland	Gini coefficient of equivalent disposable income, scale from 0 to 100	−3.5	0.005
Romania	Unemployment rate	−1.2	0.25

The study involved the Dickey–Fuller test, which assesses the presence of a unit root in panel data and serves as a crucial tool in time series analysis. This test helps determine whether a time series is stationary or contains a unit root, indicating nonstationarity. For each time series, the Dickey–Fuller test is applied to assess the presence of a unit root. The test results typically include the ADF (Augmented Dickey–Fuller) statistic and p-value. If the p-value is less than the significance level (e.g., 0.05), we can reject the null hypothesis of a unit root.

In practice, the Dickey–Fuller test exhibited both a p-value lower than the significance level and confirmation of the null hypothesis regarding the presence of a unit root. However, our perspective is based on the notion that when calculating the Mahalanobis distance, the hypothesis of a unit root lacks statistical significance. This is explained by the unique characteristics of the multidimensional space of variables in which the Mahalanobis distance operates, which may not fully align with the assumptions of the Dickey–Fuller test.

It is also noteworthy that the Mahalanobis distance, utilized in a multidimensional space, considers correlations and variability between variables, making it more sensitive to structural changes in the data.

Furthermore, in the context of analyzing multidimensional data, especially in the case of time series, the application of the Dickey–Fuller test may be limited by the assumption of independence and homogeneity in the structure of time series, which does not always correspond to the real conditions of the data. These factors can influence the statistical significance of the Dickey–Fuller test in assessing the presence of a unit root.

Therefore, our opinion is that in this context, the hypothesis of a unit root, confirmed by the Dickey–Fuller test, does not necessarily translate into statistically significant associations in the multidimensional space of variables used for calculating the Mahalanobis distance.

The conducted research results and the case studies—the findings in terms of individual indicators included in the composite indices of economic, environmental, and social sustainability—are presented in Table 5, which shows the annual mean values, maximum and minimum values of Mahalanobis distance by country, as well as the levels of instability for each indicator and composite indices.

Table 5. Sustainability assessment of the EU countries.

Indicator	Unit of Measure	Mahalanobis Distance and Instability Level for Economic Indicators										
		Predicted Value of Mahalanobis Distance (Time Series Regression)		Absolute Level of Instability ( $\sigma_{ei}$ )		Relative Level of Instability ( $V_{ei}$ )		Countries Mean		Min/Country		
		Max/Country	Min/Country	Countries Mean	Max/Country	Min/Country	Countries Mean	Max/Country	Min/Country	Countries Mean	Max/Country	Min/Country
Real GDP per capita	EUR million per capita	83,187.5	5867.5	287,9473	938,9834	91,1463	0.0131	0.0418	Cyprus	0.0045	Belgium	0.0045
Housing Price Index	annual average	114,5863	100,1538	4.8424	11,741	0.5243	0.0432	0.0939	Finland	0.0051	Finland	0.0051
The Harmonized Index of Consumer Prices	Average annual index	102,755	100,4375	1.2522	Romania	0.4567	0.0122	0.0227	Hungary	0.0045	Hungary	0.0045
Compensation of employees	EUR million	1,606,478,625	4483,8625	3822,4075	14,869,9583	188,1354	0.0301	0.0841	Romania	0.007	Denmark	0.007
Gross fixed capital formation	EUR million	633,044,125	2076,375	3742,0951	15,979,3963	233,7455	0.0575	0.1541	Cyprus	0.0195	France	0.0195
<i>Economic development instability level (V<sub>ei</sub>)</i>				0.6851	France	0.4064	0.3982	0.8446	Slovenia		Germany	0.1064
<i>Mahalanobis distance D<sub>M</sub>(x) : economic component</i>		<i>Max/country</i>	<i>Min/country</i>			Lithuania						
		4.1842	1.003									
		Germany	Slovakia									
		2.0149										
Mahalanobis Distance and Instability Level for Environmental Indicators												
Indicator	Unit of Measure	Predicted Value of Mahalanobis Distance (Time Series Regression)		Absolute Level of Instability ( $\sigma_{ei}$ )		Relative Level of Instability ( $V_{ei}$ )						
		Max/Country	Min/Country	Countries Mean	Max/Country	Min/Country	Countries Mean	Max/Country	Min/Country			
Primary energy consumption	mln tons of oil equivalent	296,475	0.85	1.1283	4.361	0.08	0.0297	0.0941	Malta	0.0104	France	0.0104
Average CO2 emissions per km from new passenger cars	-	138,075	106,7875	3.397	4,6989	1.2655	0.0274	0.0379	Malta	0.0111	Malta	0.0111
Emissions intensity from industry	grams per euro	0.915	0.0163	0.0183	0.1923	0	0.0912	0.2876	Netherlands	0	Germany	0
Net GHG emissions	-	153,05	30,4875	4.6846	20,0661	0.9886	0.0582	0.1788	Estonia	0.0147	Germany	0.0147
Recycling rate of municipal waste	%	66,175	11,675	1.8661	5,3435	0.3097	0.0628	0.1958	Slovenia	0.0059	Belgium	0.0059
<i>Environmental development instability level (V<sub>ei</sub>)</i>				0.1195	Slovenia	Netherlands		0.26	Latvia		Netherlands	
<i>Mahalanobis distance D<sub>M</sub>(x) : environmental component</i>		<i>Max/country</i>	<i>Min/country</i>									
		3.3119	0.5551									
		Denmark	Finland									
		1.554										

Table 5. Cont.

Indicator	Unit of Measure	Mahalanobis Distance and Instability Level for Social Indicators														
		Predicted Value of Mahalanobis Distance (Time Series Regression)				Absolute Level of Instability ( $\sigma_{it}$ )				Relative Level of Instability ( $V_{it}$ )						
		$D_{mit}$		Countries Mean		Max/Country		Min/Country		Countries Mean		Max/Country		Min/Country		
Unemployment rate	%	20.4625	Spain	4.1125	Germany	0.6285	Cyprus	2.1656	Germany	0.098	Cyprus	0.1759	Cyprus	0.021	Denmark	
Working poverty rate	%	17.675	Romania	3.325	Finland	0.5412	Bulgaria	1.2152	Belgium	0.1653	Hungary	0.1382	Hungary	0.0229	Italy	
Average and median income by age and sex	euro	34,456.5	Luxembourg	2607.5	Romania	339,8443	Cyprus	1111.6099	France	28,7586	Romania	0.0931	Romania	0.0013	France	
Fertility rates by age group	-	1.9388	France	1.2986	Spain	0.0277	Latvia	0.0846	Belgium	0.0073	Latvia	0.0523	Latvia	0.0043	Belgium	
Gini coefficient of equivalent disposable income	0 to 100 scale	37.4625	Bulgaria	23.8125	Slovakia	0.6447	Cyprus	1.557	Italy	0.2913	Cyprus	0.0489	Cyprus	0.0089	Italy	
<i>Social development instability level (V<sub>it</sub>)</i>	-	3.6308	Romania	1.1953	Netherlands	0.1285	Cyprus	0.323	Belgium	0.0457	Estonia	0.1866	Estonia	0.0224	France	
Mahalanobis distance $D_M(x)$ : social component	-	3.6308	Romania	1.1953	Netherlands	2.0846	Countries mean	3.6308	Romania	2.0846	Countries mean	2.0846	Countries mean	2.0846	Countries mean	2.0846

Based on the results of the economic, environmental, and social instability development study of the EU countries, the following conclusions can be drawn.

For the period under review from 2012 to 2020, Germany is characterized by the lowest level of economic instability and Slovenia by the highest one. France is characterized by the lowest level of social instability and Estonia by the highest one. France is characterized by the lowest level of environmental instability and Finland by the highest one. These results obtained are consistent with the ongoing political, economic, and social developments in the EU countries. Thus, the social sustainability of France is also supported by the ongoing unrest in the country due to the pension reform.

Maps of economic, social, and environmental instability of the countries has been developed and presented in Figures 1–3.

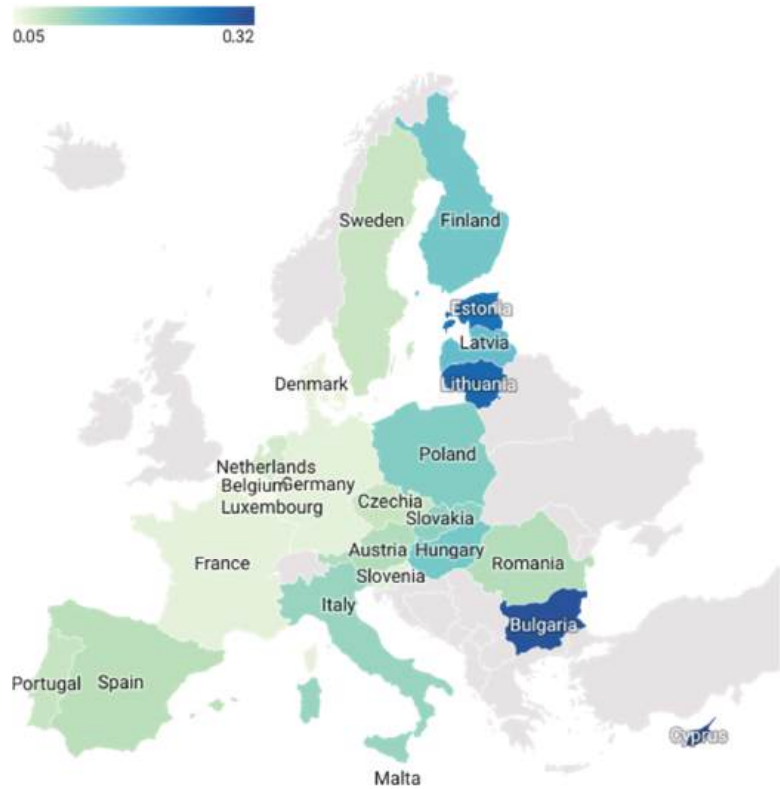
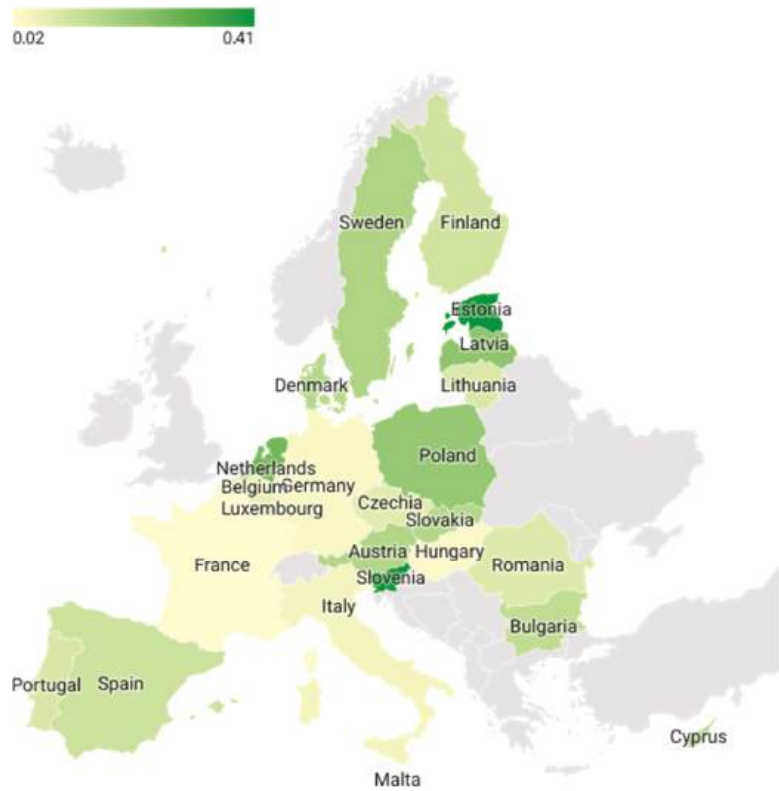


Figure 1. Absolute level of social instability in EU countries.



**Figure 2.** Absolute level of environmental instability in EU countries.

Germany and France stand out from other countries on economic, social, and environmental instability maps, having good values of indicators and positive trends. This indicates a more effective approach to addressing challenges.

**Economic stability:** Both countries have large economies that are well developed and diversified. This allows them to sustainably cope with economic crises and maintain a high standard of living for their citizens.

**Environmental stability:** Germany and France are actively investing in environmental technologies and innovations such as renewable energy, electric vehicles, and waste management. This allows them to reduce emissions of carbon dioxide and other harmful substances and protect the environment.

**Social stability:** Both countries have developed social protection systems that provide their citizens with access to healthcare, education, and other social services. This helps reduce inequality and poverty in society.

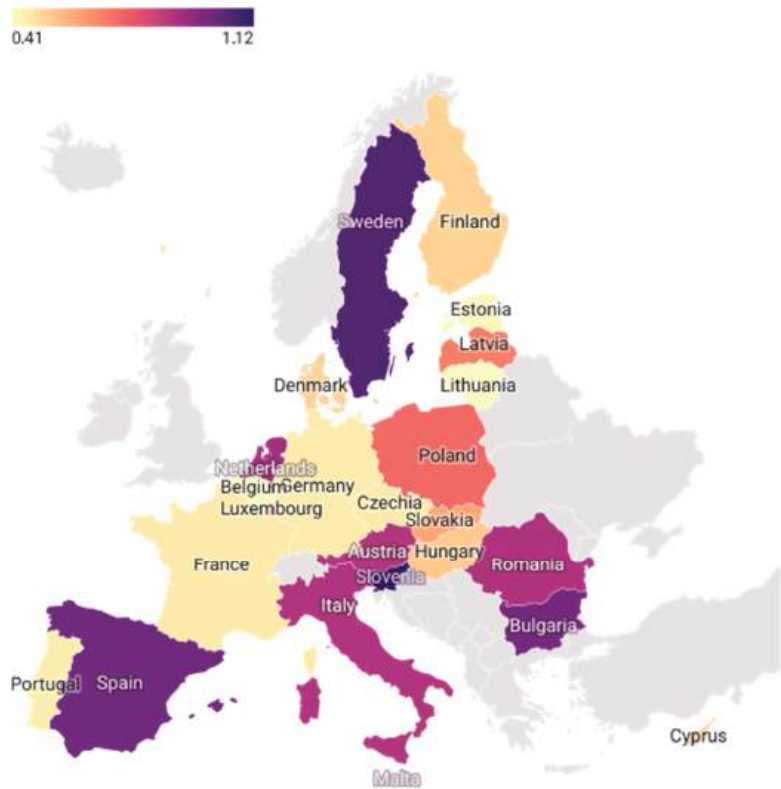


**Figure 3.** Absolute level of economic instability in EU countries.

Maps of Mahalanobis distance for economic, social, and composite indices were developed and presented in Figures 4–6.

It should be emphasized that countries with the lowest values of social, environmental, and economic instability can be characterized by both high and low Mahalanobis distances. Analyzing the sustainability of countries as dynamic systems, two hypotheses are of interest. The first is whether the positive relationship between instability and the level of country development, reflected in the values of socio-economic and environmental indicators. For this purpose, a correlation and regression analysis between the level of absolute instability and the mean value for each indicator included in the composite sustainability indices was carried out, presented in Section 4.1.

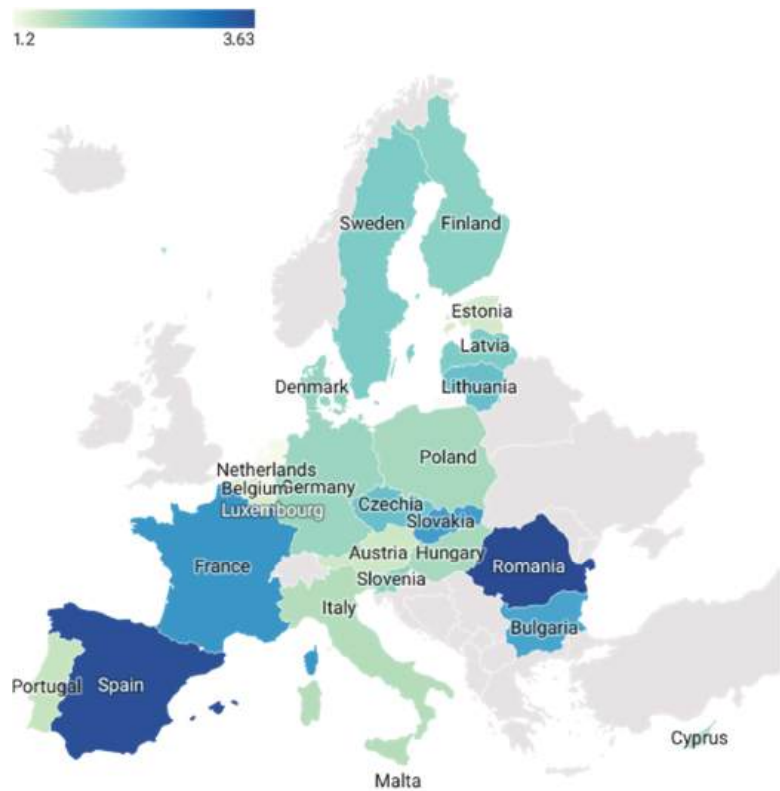


**Figure 4.** Mahalanobis distance: social composite index.

The second is whether countries with good values of social, environmental, and economic indicators are the most sustainable. Or, vice versa, sustainability is characterized by countries with worse values of social, environmental, and economic indicators. Does the value of a country's distance from the center in terms of each component (social, economic, and environmental Mahalanobis distance) affect the countries level of instability? To identify regularities in this process, a cluster analysis of countries by these characteristics has been carried out, presented in Section 4.2

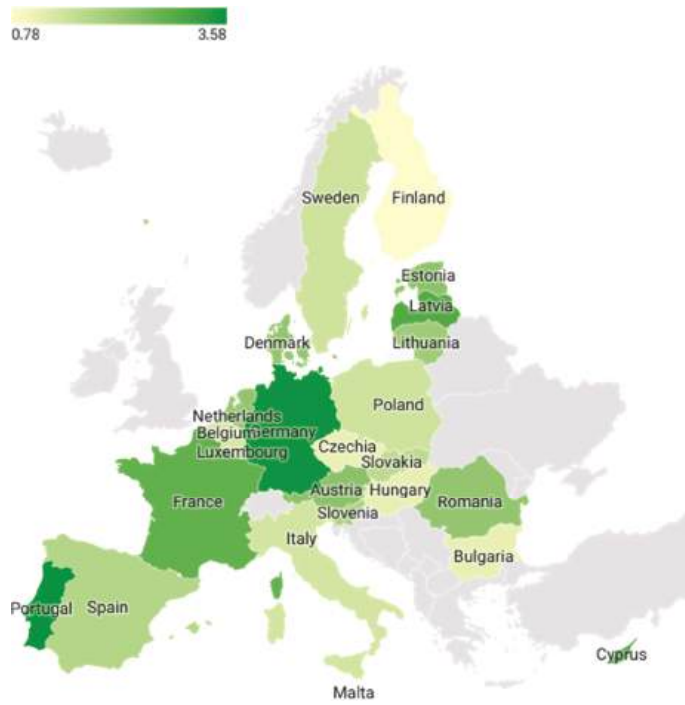


Figure 5. Mahalanobis distance: environmental composite index.

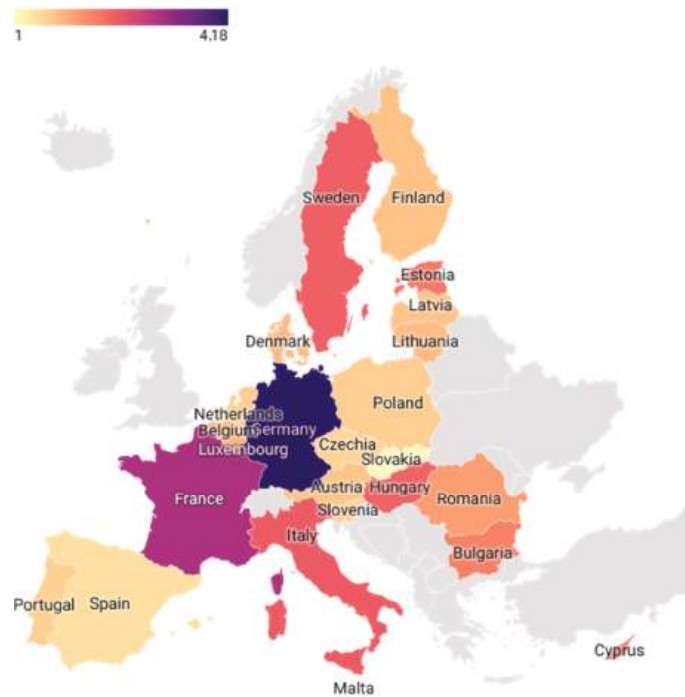


Figure 6. Mahalanobis distance: economic composite index.

#### 4.1. A Visual Representation of the Level of Absolute Instability of Development of the EU Countries in the Context of Individual Indicators

In order to analyze the impact of individual indicators on country dynamics relative to sustainable development goals, the calculation of the indicators mean for the observed period has been performed for each of the countries under consideration. This stage of the analysis provided insights into impact of countries mean levels for them sustainable development. The calculation of the mean values of the indicators for the observed period has been provided a systematic way to analyze the dynamics of the countries' development based on the selected indicators. This allowed us to draw more informed conclusions about the relationship between the variables under study and their impact on the sustainable development.

To further analyze the impact of the selected indicators on the level of countries' instability, a regression model was constructed. The mean values of 15 indicators for each country were calculated and supplemented by data on levels of absolute instability of indicators. The construction of the regression model made it possible to assess the link between the level of instability and sustainable development indicators. This methodological approach facilitates a more indepth examination of the relationships between the variables analyzed, which in turn allows for the identification of key factors that influence the degree of instability in development.

The regression model, built on the basis of the mean values of indicators for each country, provides a tool for a deeper understanding of the relationships between selected variables and the level of instability in development. Using linear regression, we can assess how changes in instability are associated with changes in levels of sustainable development indicators.

The use of time series in the analysis provides an opportunity to account for the dynamics of variable changes over time. Linear regression allows us to model these dynamics and determine the impact of each indicator on the overall degree of instability. Such analysis is applicable to identify key factors determining sustainable development in countries.

Thus, the methodology chosen for the study offers a systematic approach to the analysis and interrelation of different variables, enabling more well-founded conclusions about the factors influencing the degree of instability in the development of countries.

##### 4.1.1. Absolute Instability of the EU Countries Social Development: Individual Indicators Analysis

The unemployment rate is one of the key indicators of economic and social development. The indicator reflects the number of people who are unemployed and looking for work as a percentage of the total working-age population. As can be seen in Figure 7, there is a weak positive correlation between the mean unemployment rate and the absolute level of indicator instability. A high unemployment rate can have a negative effect on the economy and social development of the country, as it leads to a decrease in consumer demand, deterioration in the quality of life of the population and a possible increase in social tensions. In turn, this may lead to a decrease in investment and economic activity, which further aggravates the situation.

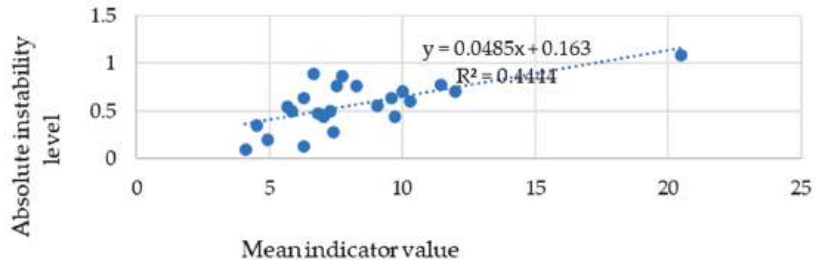


Figure 7. Unemployment rate.

The Figures 7–21 show the results of the analysis for the indicators determining social, economic, and environmental sustainability, the relationships between its means and instability level.

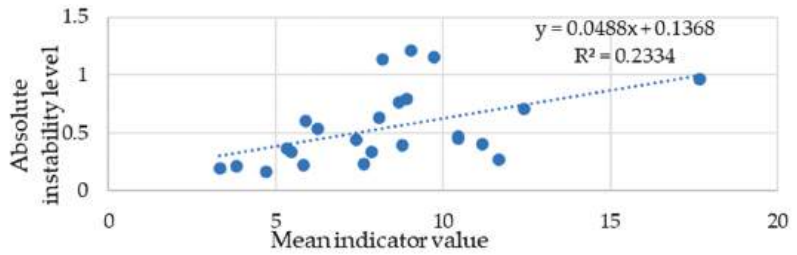


Figure 8. Working poverty rate.

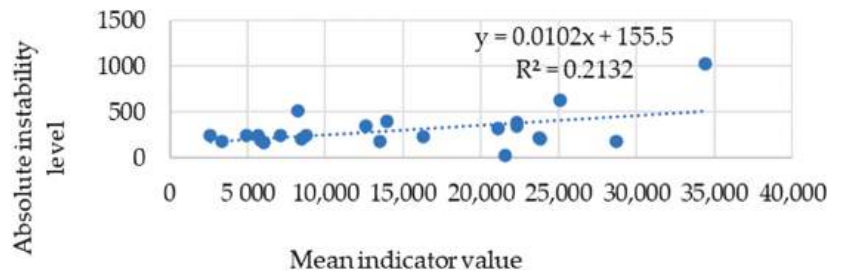


Figure 9. Average and median income by age and sex.

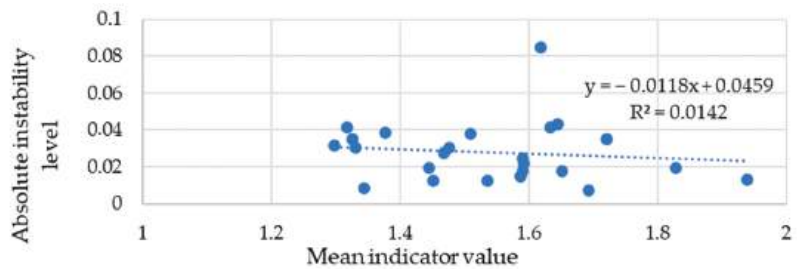


Figure 10. Fertility rates by age group.

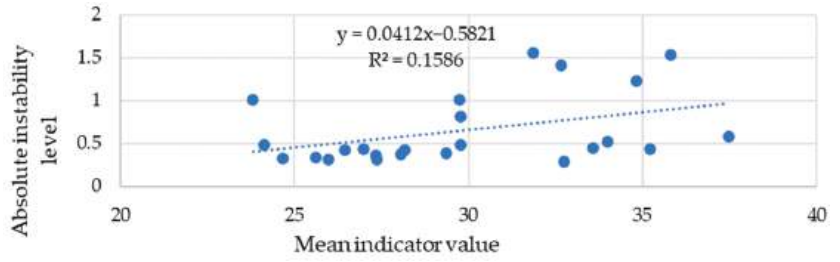


Figure 11. Gini coefficient of equivalent disposable income.

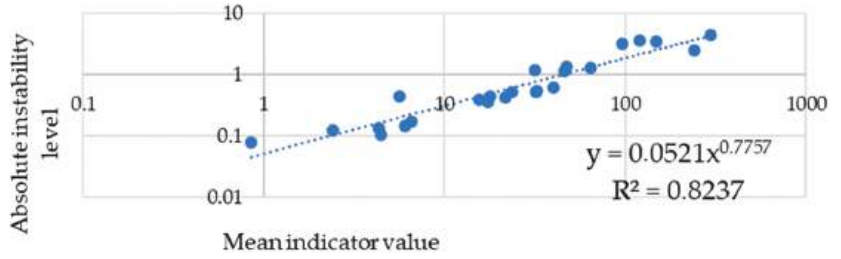


Figure 12. Primary energy consumption.

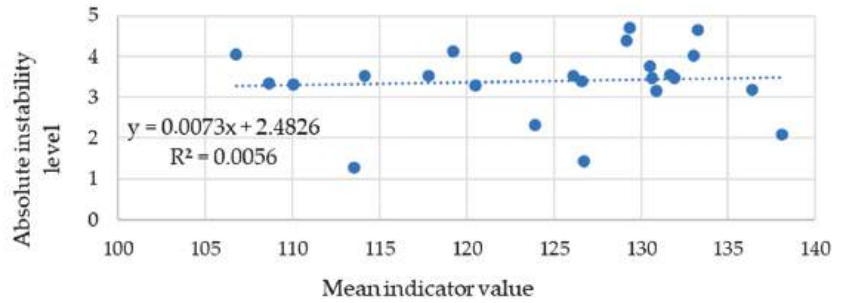


Figure 13. Average CO2 emissions per kilometer from new passenger cars.

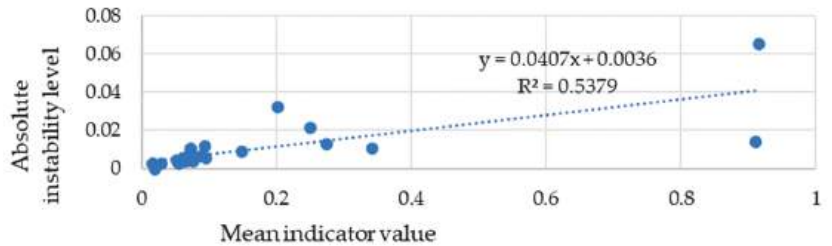


Figure 14. Emissions intensity from industry.

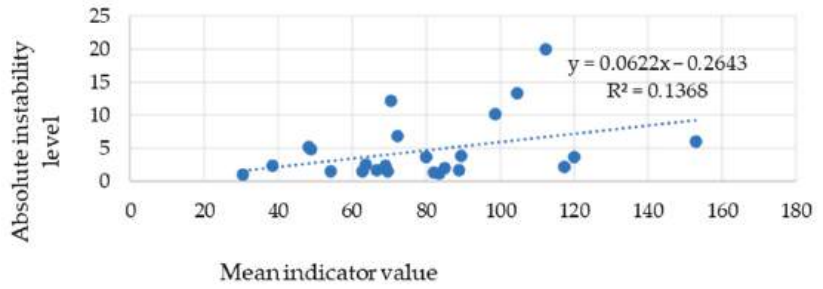


Figure 15. Greenhouse gas emissions.

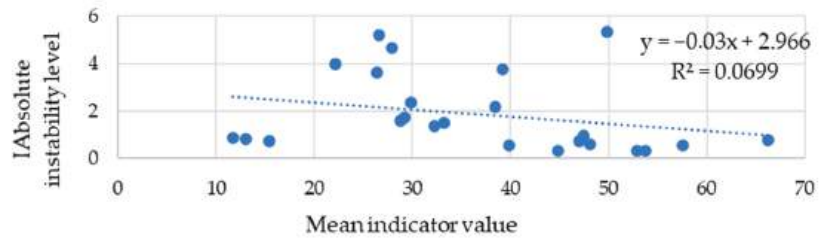


Figure 16. Recycling rate of municipal waste.

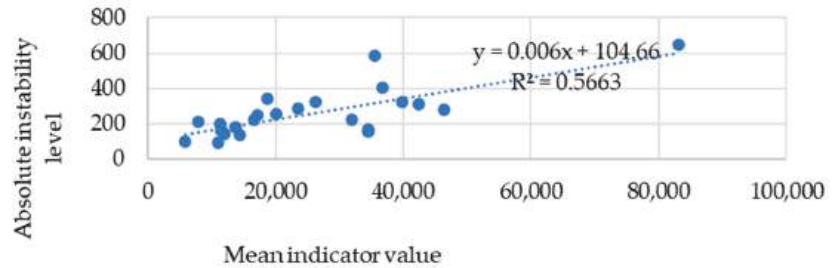


Figure 17. Real GDP per capita.

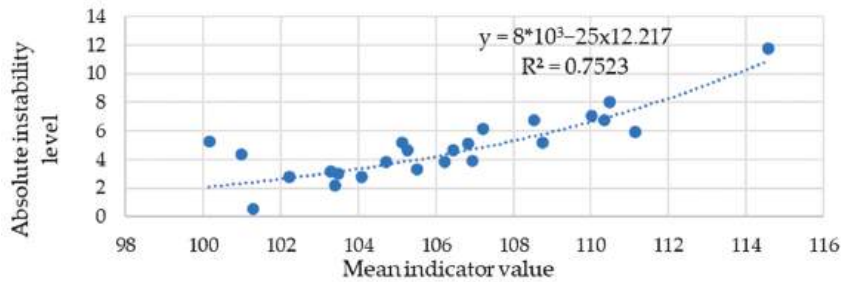


Figure 18. Housing Price Index.

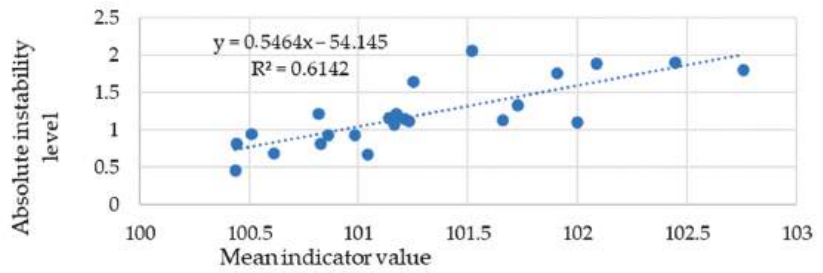


Figure 19. The Harmonized Index of Consumer Prices.

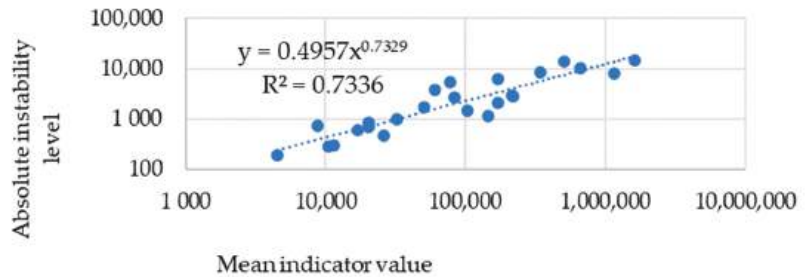


Figure 20. Compensation of employees.

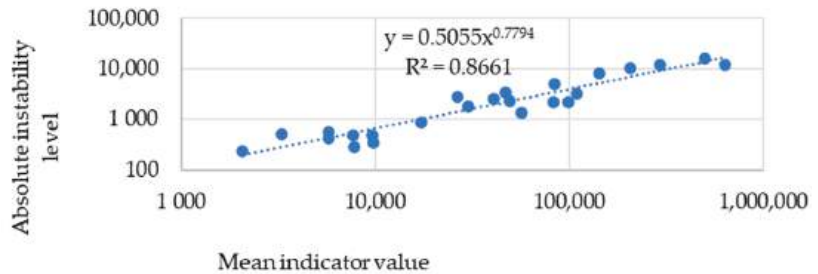


Figure 21. Gross fixed capital formation.

There is no link between the mean working poverty rate unemployment rate and the absolute level of indicator instability (Figure 8). One of the main goals of sustainable development is the fight against inequality and poverty. The Working Poverty Rate relates to the economic and social well-being of people working in different sectors of the economy. The indicator measures how large a percentage of workers are at risk of poverty, i.e., earning below the poverty threshold. Poverty risk indicators depend on many factors, including economic growth, employment, social protection, education, and health care systems, and government antipoverty policies. Different countries may have their own characteristics and reasons that explain the high poverty risk rate among working people.

There is no link between the mean of average and median income by age and sex and the absolute level of indicator instability (Figure 9). Average and median per capita income are indicators that reflect the average and median level of income in a country divided by the number of inhabitants. In general, average and median per capita income are important indicators for assessing the economic well-being of a country and its population. In the framework of sustainable development, this indicator shows how the population's income is distributed across age groups and gender. This indicator can help identify population groups that have particular difficulty in generating sufficient income to meet

their needs and improve their economic situation. It can also help the government and other stakeholders to develop programs and support measures for those who are more vulnerable.

There is no link between the mean of fertility rates by age group and the absolute level of indicator instability (Figure 10). Fertility rates by age group are an important component of sustainable development because they allow us to assess the demographic situation in a country and to predict its future changes. For example, if fertility rates among young women are low, this may lead to a decline in the population in the long-term and cause problems with the pension system and the economy as a whole. On the other hand, if fertility rates are high among young women, this can create problems with overpopulation and environmental problems. Therefore, it is important to analyze and monitor age-disaggregated fertility rates and take appropriate measures to support the sustainable development of the country.

There is no link between the mean of Gini coefficient of equivalent disposable income and the absolute level of indicator instability (Figure 11). The Gini coefficient of equivalent disposable income is a measure of income inequality in a society. It shows how income is distributed in a society, and the higher the Gini coefficient, the greater the inequality in income distribution. To achieve sustainable development, it is necessary to reduce the level of inequality in income distribution. This can be achieved by creating fairer and more efficient taxation systems, raising wages, creating new jobs, and increasing access to education and health care. Reducing inequalities in income distribution can also lead to more balanced economic development and sustainable use of resources, which contributes to the achievement of sustainable development as a whole.

#### 4.1.2. Absolute Instability of the EU Countries Environmental Development: Individual Indicators Analysis

There is a strong link between the mean of primary energy consumption and the absolute level of indicator instability (Figure 12). Reducing energy consumption is one of the keys to reducing pollution and combating climate change. Studying primary energy demand can determine how much energy is used in different sectors of the economy and what measures can be taken to reduce consumption. Studying primary energy demand indicators allows countries to participate in the global dialog on climate and sustainable development. By comparing data between different countries and regions, best practices can be identified and strategies can be developed to reduce energy consumption and combat climate change.

There is no link between the mean of average CO<sub>2</sub> emissions per kilometer from new passenger cars and the absolute level of indicator instability (Figure 13). The indicator of average CO<sub>2</sub> emissions per kilometer from new passenger cars is used to evaluate the environmental performance of cars and to compare their environmental performance. This indicator allows consumers to compare different car models and choose more environmentally friendly options. CO<sub>2</sub> emissions are a major source of greenhouse gases that contribute to global warming and climate change. Passenger cars are a major source of CO<sub>2</sub> emissions, so reducing emissions from new cars can have a significant impact on reducing air emissions and slowing global warming. Average CO<sub>2</sub> emissions per kilometer from new passenger cars is also an important tool for government regulators, who can use it to set emission standards and implement legislative measures to reduce CO<sub>2</sub> emissions. Some countries have already set strict standards for CO<sub>2</sub> emissions from new cars to encourage car manufacturers to develop and produce more environmentally friendly models.

There is a link between the mean of emissions intensity from industry and the absolute level of indicator instability (Figure 14). Emissions intensity from industry is an important tool for achieving sustainable development. It reflects the amount of pollution emitted by an industry per unit of output or unit of service, which allows measuring resource efficiency and identifying opportunities to improve the environmental performance of industrial processes. Emission intensity can be used to compare different industries and

companies and to assess the effectiveness of measures aimed at reducing emissions. An increase in emission intensity may be associated with increased production, but a lack of attention to reducing emissions can lead to environmental degradation and adversely affect human and ecosystem health.

There is no link between the mean of greenhouse gas emissions and the absolute level of indicator instability (Figure 15). Net greenhouse gas emissions reflect the level of atmospheric pollution and the impact of human activity on climate change. Net greenhouse gas emissions are the amount of gases that would be emitted into the atmosphere in the absence of any emission reduction measures. Greenhouse gases such as carbon dioxide (CO<sub>2</sub>), methane, and nitrogen dioxide cause the greenhouse gas effect, which leads to climate change and global changes such as increases in the Earth's surface temperature, sea level rise, and extreme weather events. Estimating the net greenhouse gas emissions indicator is an important step in assessing the environmental sustainability of businesses, industries, and countries as a whole. This indicator helps to develop a clearer understanding of how changes in economic activity affect climate change and the extent to which these changes are aligned with sustainable development goals.

There is no link between the mean of recycling rate of municipal waste and the absolute level of indicator instability (Figure 16). The recycling rate of municipal waste—reflects the ability of a society to use resources efficiently and reduce the negative impact on the environment. Utility waste management reduces the amount of waste that ends up in landfills and interacts with the environment, including causing soil and water pollution, methane, and other greenhouse gas emissions. In addition, proper waste management can provide additional opportunities for energy and material production. For example, recycling technologies can produce biogas that can be used to generate electricity and heat, as well as produce secondary raw materials that can be used in the production of new goods.

#### 4.1.3. Absolute Instability of the EU Countries Economic Development: Individual Indicators Analysis

There is a link between the mean of real GDP per capita and the absolute level of indicator instability (Figure 17). Real GDP per capita is a measure of economic development that reflects the average income earned by each person in a country. It is one of the key indicators used to assess the standard of living in a country. In the context of sustainable development, real GDP per capita can serve as an indicator, but not as the main criterion. It can be used to measure the level of economic development in combination with other indicators such as the happiness index, human development index, and equity index. These indicators can complement real GDP per capita and provide a broader understanding of sustainable development, taking into account its social and environmental aspects.

There is a strong link between the mean of Housing Price Index and the absolute level of indicator instability (Figure 18). The house price index is an important indicator in the economy that reflects changes in the cost of housing in the market. Determining housing affordability: The house price index measures the level of affordability of housing for the population. If housing prices are rising too fast, it may mean that many people cannot afford to buy a home, which can lead to social problems. On the other hand, if housing prices are too low, it may indicate that investment in the sector is limited, which could lead to a housing shortage in the future. Impact on Economic Growth: The house price index can have a significant impact on a country's economic growth. If housing prices rise too fast, it can lead to an economic bubble that can eventually burst, causing an economic crisis. On the other hand, if housing prices are too low, it could mean that investment in the sector is limited, which could slow economic growth. Determining the stability of the financial system: The house price index can also be used to determine the stability of a country's financial system. If house prices fluctuate widely, it may indicate that the country's financial system is unstable. On the other hand, if house prices are rising steadily and predictably, it may indicate that the country's financial system is stable and

sound. Sustainable urban development: The house price index can also be used to assess the sustainable development of cities. If housing prices in cities are rising too fast, this can lead to housing becoming unaffordable for many people, as well as urban infrastructures such as the transportation system and utilities.

There is a link between the mean of Harmonized Index of Consumer Prices and the absolute level of indicator instability (Figure 19). The Harmonized Index of Consumer Prices is a measure of inflation in the Eurozone and the European Union and key indicator of price stability limiting economic growth and sustainable development in case of high meanings.

There is a strong link between the mean of compensation of employees and the absolute level of indicator instability (Figure 20). The employee compensation has an important role in sustainable development, as it is a key factor in ensuring a decent standard of living for working people, reducing social inequality, and increasing economic stability. A high level of employee compensation helps improve the quality of life of the population, which in turn contributes to higher levels of life satisfaction, better health, and better educated people. Higher wages can also lead to lower crime rates and higher levels of social stability. In addition, high levels of pay can stimulate economic growth as it can lead to increased consumer demand, investment, and production of goods and services. Overall, employee compensation plays an important role in the sustainable development of the economy and society as a whole.

There is a strong link between the mean of gross fixed capital formation and the absolute level of indicator instability (Figure 21). The gross fixed capital formation is an important indicator in sustainable development, as it reflects the amount of investment aimed at creating new and modernizing existing production facilities and infrastructure. This makes it possible to improve production efficiency, reduce resource consumption and environmental emissions, and create new jobs. High indicators of gross fixed capital formation indicate that the state and private companies invest significant resources in the economy aimed at the development of production and infrastructure. This increases the level of productivity and competitiveness of the economy, which contributes to sustainable development.

#### 4.1.4. The Results of the Analysis of the EU Countries Composite Sustainability Indexes Are Summarized in Table 6

Based on conducted study, the conclusion about more significant influence of economic indicators on sustainable development can be made. According to the analysis results positive relationships between the absolute instability and the mean values of indicators were revealed for all five economic development indicators (Real GDP per capita  $R^2 = 0.5663$ , Housing Price Index  $R^2 = 0.7523$ , The Harmonized Index of Consumer Prices  $R^2 = 0.6142$ , Compensation of employees  $R^2 = 0.7336$ , Gross fixed capital formation  $R^2 = 0.8661$ ). For environmental development, significant positive relationships were found only for two indicators (Primary energy consumption  $R^2 = 0.8237$  and Emissions intensity from industry  $R^2 = 0.5379$ ). There were no significant positive relationships found for social indicators.

Thus, the hypothesis about the positive relationship between absolute instability and the level of economic development were confirmed.

**Table 6.** Results of the composite indices analysis of EU countries sustainability (Instability level by Mean indicator value).

Indicator	Description	R <sup>2</sup> Coefficients of Determination
<b>Social development</b>		
Unemployment rate, %	The absolute minimum instability was recorded in Germany and the maximum in Cyprus.	R <sup>2</sup> = 0.4444
Working poverty rate, %	The maximum level of instability is reached in Bulgaria, while the most stable countries are Belgium.	R <sup>2</sup> = 0.2334
Average and median income by age and sex, euros	France is the most stable country in terms of average and median income, while Cyprus is the most instable.	R <sup>2</sup> = 0.2132
Fertility rates by age group	The highest instability is in Latvia and the lowest in Belgium.	R <sup>2</sup> = 0.0142
Gini coefficient of equivalent disposable income, scale from 0 to 100	The most unstable country is Cyprus and the most stable is Italy.	R <sup>2</sup> = 0.1586
<b>Environmental development</b>		
Primary energy consumption, million tons of oil equivalent	The absolute minimum instability was recorded in Germany and the maximum in Malta.	R <sup>2</sup> = 0.8237
Average CO2 emissions per kilometer from new passenger cars	The highest instability is in Cyprus and the lowest in Malta.	R <sup>2</sup> = 0.0056
Emissions intensity from industry, grams per euro	Germany is the most stable in terms of emission intensity, while Estonia has the highest level of instability.	R <sup>2</sup> = 0.5379
Net greenhouse gas emissions	The highest instability is in Slovenia, the lowest in Lithuania.	R <sup>2</sup> = 0.1368
Recycling rate of municipal waste, %	Slovenia has the maximum level of instability, and the Netherlands is the most stable.	R <sup>2</sup> = 0.0699
<b>Economic development</b>		
Real GDP per capita, euros per capita	Cyprus has the highest instability of this indicator, while Latvia has the lowest one. Relative volatility is high in Cyprus, Romania, and Slovenia. A significant positive correlation between real GDP per capita and its absolute instability was found.	R <sup>2</sup> = 0.5663
House price index, annual average	The lowest instability is found in Sweden and Finland, explained by high living standards and social infrastructure, government programs, and relatively low population density. The highest instability is observed in Hungary.	R <sup>2</sup> = 0.7523
Harmonized Index of Consumer Prices, average annual index	The most sustainable economy by this criterion is Denmark, the least sustainable is Romania.	R <sup>2</sup> = 0.6142
Compensation of employees, million euros	France has the lowest level of instability; Malta has the biggest one.	R <sup>2</sup> = 0.7336
Gross fixed capital formation, million euros	Lithuania has the lowest level of instability; Slovenia has the biggest one.	R <sup>2</sup> = 0.8661

#### 4.2. Countries Clustering by Instability Level and Mahalanobis Distance

To comprehend the differences in the level of absolute instability of countries in relation with their location relative to the center, clustering has been conducted, and the results are presented in Tables 4–6. Additionally, with the aim of reducing the variability of

values and approaching the distribution of data to normal, logarithmic transformation of variables was applied. This transformation is particularly valuable when dealing with data that exhibit pronounced differences in scale. Logarithmic transformation contributes to stabilizing the variance, which is especially beneficial in the analysis of data with significant disparities in measurement scales. Remarkably, against the backdrop of this logarithmic transformation of variables, distinct data clusters became apparent on the graphs, providing additional rationale for conducting cluster analysis. This analytical approach, coupled with logarithmic transformation, yields a deeper understanding of the data structure and reveals potential groupings, thereby complementing our study. The study employed cluster analysis, taking into account the trendline and coordinate axes, to analyze the grouping of data in a multidimensional space of variables. As a result of this analysis, clusters were formed, encompassing data points close to the trendline or sharing similar values along the coordinate axes. Such an approach allows for the identification of not only general trends in the data but also the delineation of groups that exhibit similar behavior regarding specific parameters.

This analytical approach provides additional insight into the structure of the data, highlighting groups that behave similarly in the context of the examined parameters. The obtained results contribute to a more in-depth analysis of relationships and groupings within the data, enriching the study from both practical and theoretical perspectives.

The chosen method for cluster analysis in this study was implemented using the k-means method. The process commenced with determining the optimal number of clusters through hierarchical analysis on a randomly selected sample of observations. This stage precisely identified the required number of clusters for further analysis.

Subsequently, cluster centers were computed, and all objects were grouped within a specified threshold value relative to these centers. This method effectively classifies objects and highlights groups based on similarities in characteristics.

Three groups of countries characterized by a certain combination of the Mahalanobis distance and the level of absolute instability were identified for each component of sustainable development.

#### 4.2.1. Economic Instability and Mahalanobis Distance

The results of clustering by economic component are presented in Table 7 and Figure 22.

Countries in the first group (Belgium, Czech Republic, Denmark, etc., blue dots) are characterized by low levels of both economic instability and Mahalanobis distance.

This indicates a stable economic situation, the proximity of countries to typical economic conditions and structures, it is “stability of averages”.

The second group of countries (Bulgaria, Spain, Italy, etc., yellow dots) with high levels of economic instability, have a variety of Mahalanobis distance. This shows the different factors and reasons behind the instability and dynamics. For some countries, instability is associated with an improving economic situation, while for others it is associated with a deteriorating economic situation. It can also mean an uneven distribution of risks and opportunities within the group.

The countries of the third group (Germany, France, and Luxembourg, green dots) are characterized by a low level of economic instability with high values of Mahalanobis distance. This is the stability of the strong, indicating their higher degree of structural and institutional development.

**Table 7.** Countries clustering by instability level and Mahalanobis distance: economic component.

Country	Actual Annual Mean of Mahalanobis Distance $D_M(x)$ : Economic Component	The Logarithmized Indicator of the Actual Annual Mean Mahalanobis Distance $D_M(x)$ : Economic Component	Absolute Level of Economic Instability ( $\sigma_{ei}$ )	The Logarithmized Indicator of Absolute Level of Economic Instability ( $\sigma_{ei}$ )
Group 1				
Belgium	1.722725	0.543907	0.409835	−0.892
Czechia	1.43804	0.363281	0.453816	−0.79006
Denmark	1.662579	0.50837	0.513459	−0.66659
Estonia	2.261746	0.816137	0.426228	−0.85278
Cyprus	2.470512	0.904425	0.522356	−0.64941
Latvia	1.576571	0.455252	0.679275	−0.38673
Lithuania	1.645522	0.498058	0.406427	−0.90035
Hungary	2.46509	0.902228	0.524834	−0.64467
Poland	1.500569	0.405844	0.722617	−0.32488
Portugal	1.476101	0.389404	0.445552	−0.80844
Slovakia	1.00303	0.003025	0.599783	−0.51119
Finland	1.595168	0.466979	0.507716	−0.67783
Group 2				
Bulgaria	2.17622	0.77759	0.98911	−0.010949
Spain	1.316341	0.274856	0.998452	−0.00155
Italy	2.532318	0.929135	0.885382	−0.121737
Malta	1.513124	0.414176	0.998652	−0.001349
Netherlands	1.490197	0.398909	0.908555	−0.0959
Austria	1.574231	0.453767	0.88101	−0.126687
Romania	1.908763	0.646455	0.888924	−0.117743
Slovenia	1.459393	0.378021	1.123585	0.1165247
Sweden	2.490111	0.912327	1.055267	0.053794
Group 3				
Germany	4.184196	1.431314	0.45107	−0.796133
France	3.165009	1.152156	0.454696	−0.788126
Luxembourg	3.730695	1.316594	0.595061	−0.519091

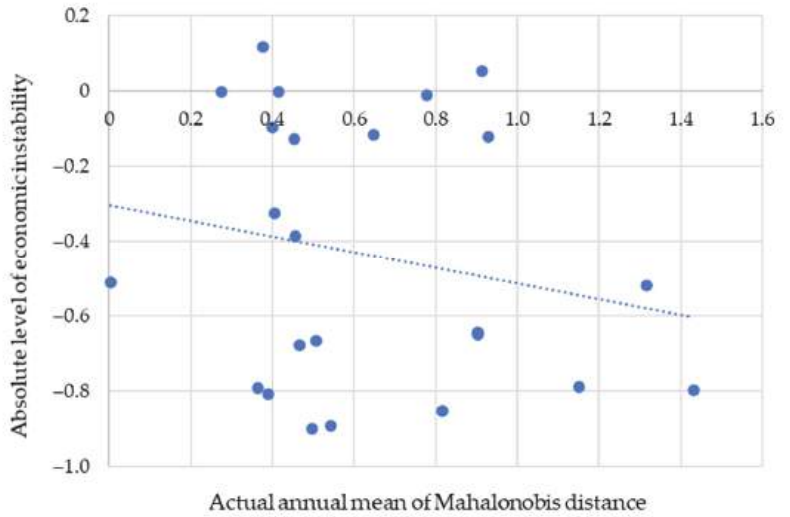
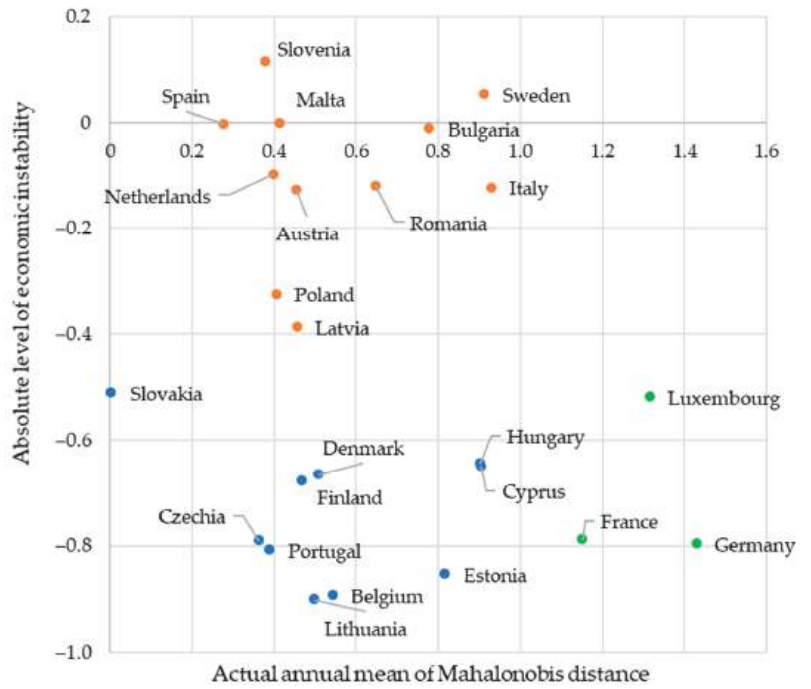


Figure 22. Countries clustering by instability level and Mahalanobis distance: economic component.

#### 4.2.2. Environmental Instability Mahalanobis Distance

The results of clustering by environmental component are presented in Table 8 and Figure 23.

**Table 8.** Countries clustering by instability level and Mahalanobis distance: environmental component.

Country	Actual Average Annual of Mahalanobis Distance $D_M(x)$ : Environmental Component	The Logarithmized Indicator of the Actual Annual Mean Mahalanobis Distance $D_M(x)$ : Environmental Component	Absolute Level of Environmental Instability ( $\sigma_{ei}$ )	The Logarithmized Indicator of Absolute Level of Environmental Instability ( $\sigma_{ei}$ )
<b>Group 1</b>				
Belgium	1.350153	0.300218	0.06021	−2.80992
Bulgaria	1.032936	0.032405	0.108699	−2.21918
Czechia	0.663746	−0.40986	0.139035	−1.97303
Denmark	1.942485	0.663968	0.107747	−2.22797
Spain	1.218586	0.197691	0.107822	−2.22728
Italy	1.376201	0.319327	0.048043	−3.03565
Cyprus	1.46999	0.385255	0.057645	−2.85345
Latvia	1.449912	0.371503	0.126555	−2.06708
Lithuania	1.248839	0.222214	0.117151	−2.14429
Luxembourg	1.545372	0.435265	0.067826	−2.69081
Hungary	0.770962	−0.26012	0.057639	−2.85356
Malta	2.257614	0.814308	0.100339	−2.2992
Austria	1.735137	0.551086	0.068845	−2.6759
Portugal	1.986742	0.686496	0.135539	−1.9985
Romania	1.635023	0.491657	0.059712	−2.81823
Finland	0.555094	−0.58862	0.14431	−1.93579
Sweden	0.960564	−0.04023	0.141604	−1.95472
<b>Group 2</b>				
Estonia	1.594864	0.466789	0.203053	−1.594287
Netherlands	2.181423	0.779977	0.281171	−1.268794
Poland	1.358841	0.306632	0.226757	−1.483876
Slovenia	1.467398	0.383491	0.238761	−1.432294
Slovakia	1.231558	0.20828	0.204782	−1.585809
<b>Group 3</b>				
Germany	3.511935	1.256167	0.041093	−3.191921
France	2.753832	1.012993	0.022838	−3.779326

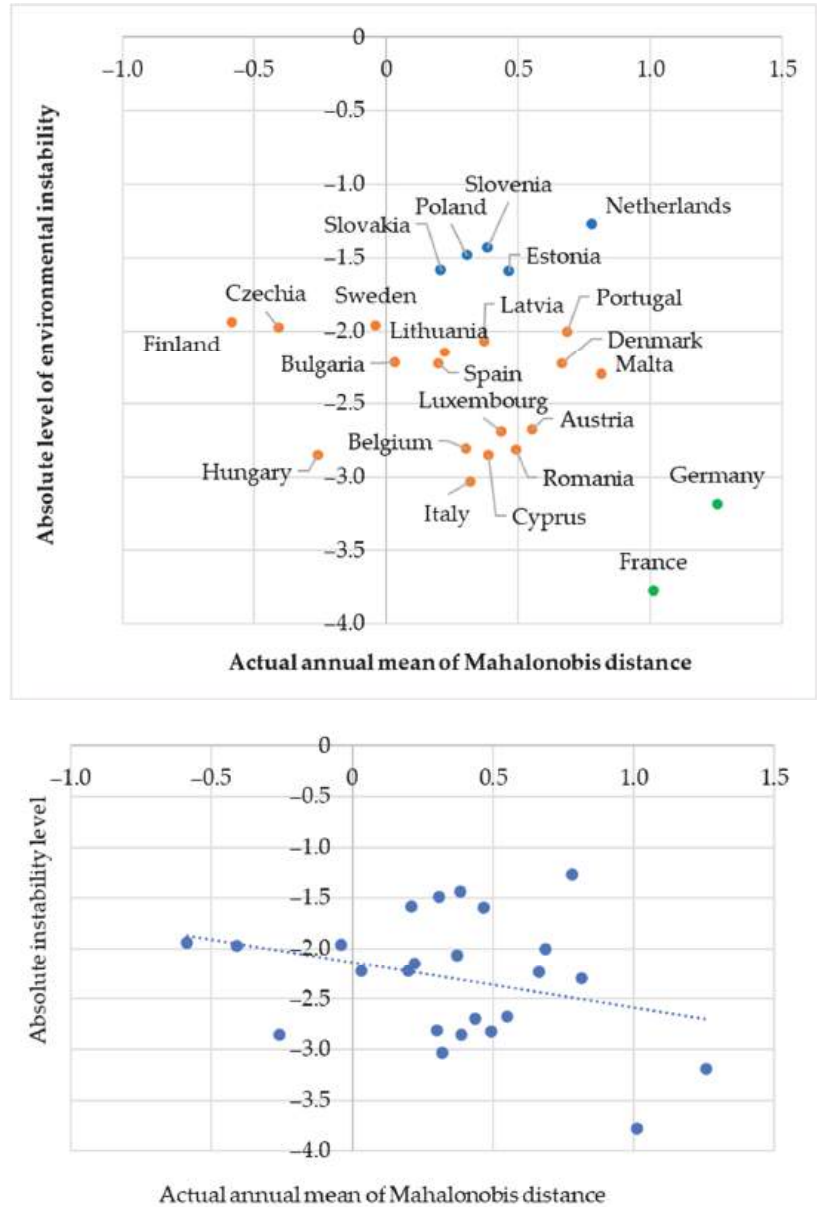


**Figure 23.** Countries clustering by instability level and Mahalanobis distance: environmental component.

Group 1 combines countries (Belgium, Finland, Sweden, etc., yellow dots) with a low level of environmental instability and average values of Mahalanobis distance, this is explained by balanced indicators of environmental development.

Group 2 (blue dots) combines countries with high values of ecological instability at different values of Mahalanobis distance, indicating the need for additional efforts to improve the ecological situation.

Group 3 (green dots) combines countries with low levels of environmental instability with high values of Mahalanobis distance. These countries can be titled environmentally

sustainable: they are distinguished with high environmental indicators, which indicates an effective approach to solving environmental challenges by the government.

4.2.3. Social Instability and Mahalanobis Distance

The results of clustering by social component are presented in Table 9 and Figure 24.

**Table 9.** Countries clustering by instability level and Mahalanobis distance: social component.

Country	Actual Average Annual of Mahalanobis Distance $D_M(x)$ : Social Component	The Logarithmized Indicator of the Actual Annual Mean Mahalanobis Distance $D_M(x)$ : Social Component	Absolute Level of Social Instability ( $\sigma_{ei}$ )	The Logarithmized Indicator of Absolute Level of Social Instability ( $\sigma_{ei}$ )
Group 1				
Belgium	1.405775	0.340589	0.045743	-3.08471
Czechia	1.157742	0.769062	0.082497	-2.49499
Denmark	1.858317	0.619671	0.057589	-2.85442
Germany	1.814493	0.595806	0.061115	-2.795
Italy	1.665848	0.510334	0.117942	-2.13756
Latvia	1.976631	0.681394	0.160174	-1.83149
Hungary	1.748698	0.558872	0.141873	-1.95283
Malta	2.204657	0.790572	0.100075	-2.30183
Netherlands	1.195286	0.178385	0.075661	-2.5815
Austria	1.49891	0.404738	0.101067	-2.29198
Poland	1.748501	0.558759	0.13115	-2.03141
Portugal	1.537017	0.429844	0.084972	-2.46543
Slovenia	1.885746	0.634324	0.063522	-2.75636
Slovakia	2.579947	0.947769	0.125195	-2.07789
Finland	1.906261	0.645144	0.144791	-1.93247
Sweden	1.988097	0.687178	0.08333	-2.48495
Group 2				
Bulgaria	2.505123	0.918338	0.31004	-1.171055
Estonia	1.442053	0.366068	0.269071	-1.312779
Cyprus	1.80721	0.591784	0.322967	-1.130205
Lithuania	2.167123	0.7734	0.281446	-1.267814
Group 3				
Spain	3.555128	1.268391	0.093193	-2.373087
France	2.680796	0.986114	0.059926	-2.81465
Luxembourg	3.070261	1.121762	0.073073	-2.616296
Romania	3.63081	1.289456	0.098707	-2.315602

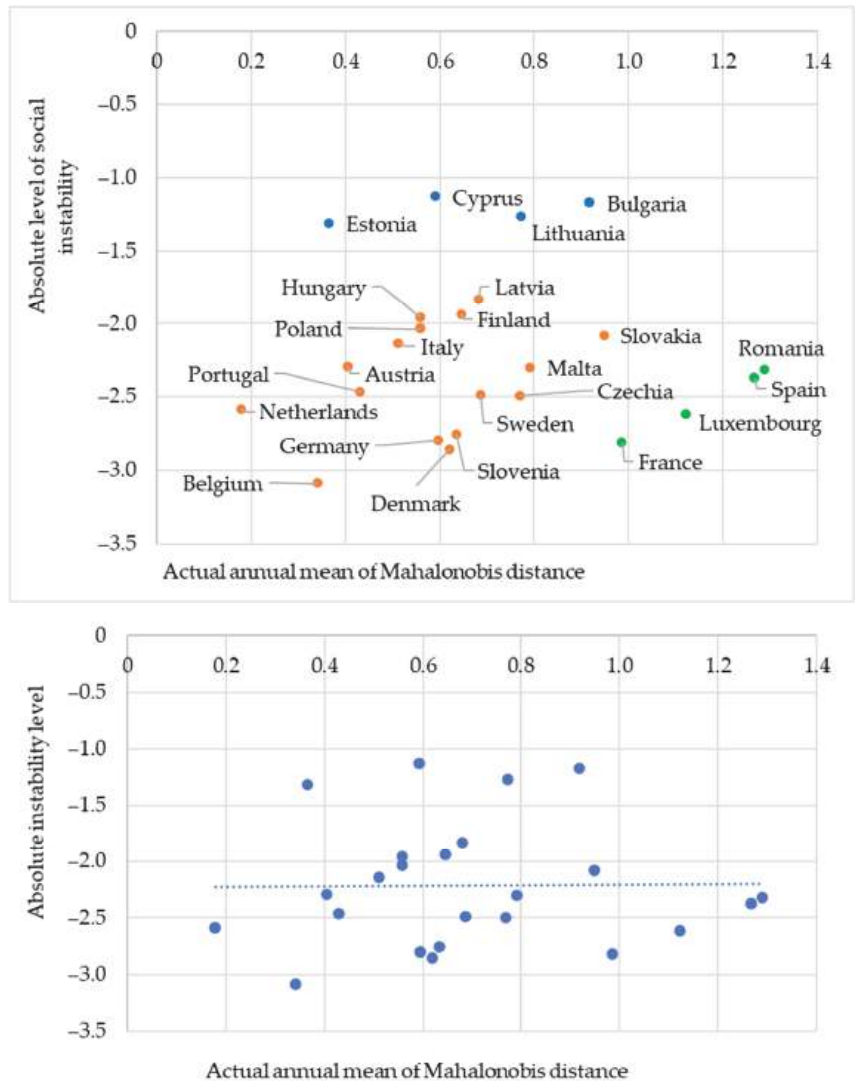


**Figure 24.** Countries clustering by instability level and Mahalanobis distance: social component.

Group 1 (yellow dots) includes countries with low indicators of social instability and moderate Mahalanobis distance, which is associated with stable social indicators, relative equilibrium in social variables. This may be the result of a combination of different factors such as social programs, social safety nets, education, and health care.

Group 2 (blue dots) includes countries with high social instability with moderate Mahalanobis distance. The social challenges evidenced by the values of social indicators may be the result of complex social and economic dynamics that require careful consideration and appropriate measures to improve the situation. Social instability related to average values cause Mahalanobis distance to be small, which can be explained by the insufficient availability of quality social services, limited access to education and health care, and insufficient social support for vulnerable populations.

Group 3 (green dots) includes countries with low levels of social instability with high Mahalanobis distance. It includes countries with high social indicators, with a high level

of social infrastructure development, including high-quality education and health care systems, extensive social programs, and support for the population. High social indicators with high Mahalonobis distance are also a consequence of the general economic situation, which is conducive to social well-being.

Characterized by higher socio-economic indicators, developed countries demonstrate sustained dynamic economic development and high levels of environmental sustainability, with attention to environmental conservation. While countries with lower levels of socio-economic development, facing challenges in economic sustainability and achieving certain living standards, also require support in ensuring environmental performance, environmental sustainability, and reducing negative impacts on the environment.

Summarizing the results of the analysis of economic, environmental, and social sustainability, we can conclude that Germany and France are the leaders of sustainable development among the EU countries (Figure 25).

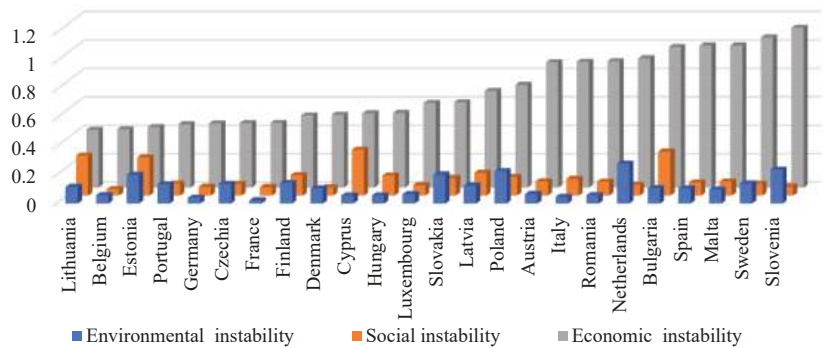


Figure 25. Economic, social, and environmental instability of EU countries.

The absolute leader is France, which social sustainability indicators is provided by protest potential of the society, as shown by the events of recent months. Instability of development can both be an indication of crisis phenomena in a country and a negative by-product of it.

### 5. Conclusions

1. Currently, there is no single methodological math approach for sustainability assessment of countries and territorial entities. This is caused predominantly by the different in existing concepts, the applied mathematics indicators and them conceptual content, and variety of unit measurement. In addition, new types of sustainability are appearing now, making sustainable development a complex and multifaceted concept encompassing various dimensions.
2. The barrier to practical usage of mathematical models to countries resilience and sustainability assessing is the complexity of the managerial usage of composite indicators, when determining the contribution of individual sustainability factors represents an ambiguity task. The problem of comparative analysis of sustainability is the lack of harmonized statistical data, due to the heterogeneity of countries development.
3. To form the policy of sustainable development management, the core of approaches to assessing countries sustainability should be the principles of simultaneous consideration of social, environmental, and economic aspects, as well as possibility to identify meaningful variables in composite indices. In order to make sustainability a target variable in development strategies, it is necessary to use special methods combining mathematical tools and reasonable managerial content.
4. A methodological approach consisting of seven successive stages to integrated assessment of social, economic, and environmental sustainability of countries has been

- created. It allows us to define position of European countries in sustainable development content relative to each other. An approach considers the requirements dictated by the multidimensionality of the studied economic, social, and environmental space and allows us to present the results of the comparative analysis visually, as well as to determine the direction of sustainability management for each country. The instrumental basis of methodological approach consists of multivariate comparisons, the Mahalanobis distances method, the correlation and regression analysis, analysis of variance, time series analysis and trends analysis.
5. Composite indices of social, economic, and environmental sustainability of the EU countries, each of them including five indicators, were developed in this study. Developed indices considering multidimensionality features of used data allows us to identify countries dynamics in achieving sustainable development goals. For assessing economic sustainability, Real GDP per capita, House price index, Harmonized Index of Consumer Prices, Compensation of employees, and Gross fixed capital formation were chosen to create a composite index. For assessing environmental sustainability, primary energy consumption, average CO<sub>2</sub> emissions per kilometer from new passenger cars, emissions intensity from industry, net greenhouse gas emissions, and recycling rate of municipal waste were chosen to create a composite index. For assessing social sustainability, unemployment rate, working poverty rate, average and median income by age and sex, fertility rates by age group, and Gini coefficient of equivalent disposable income were chosen to create a composite index.
  6. The sustainability of each indicator in each group (environmental, social, and economic) has been divided into two components: growth rate and fluctuations. The growth rate is a constant component and reflects a stable trend of the indicator change. Fluctuation, on the other hand, is a nonconstant component and reflects the variability of the indicator around the trend. This variability can be measured by volatility, i.e., fluctuations of the indicator around its average value. Thus, analyzing the stability of indicators allows us to divide the dynamics into a stable trend and the risk associated with fluctuations of the indicator around this trend.
  7. To create a common composite index for each group (environmental, social, and economic), Mahalanobis distances were calculated based on chosen indicators. The methodology is the finding of the average distance between the multivariate vector containing the values of all private indicators and the center of the multivariate distribution. This made it possible to assess how much each private indicator contributes to the overall sustainability score and to determine which indicators are most important.
  8. A linear time regression analysis has been conducted to identify four main parameters (deviation of the country from the countries' mean, sustainable rate of development of the country, absolute level of the countries' instability, and relative level of instability). This analysis assessed the relationship between various indicators such as the deviation of the country from the countries mean, the sustainable rate of development of the country, the absolute level, and the relative level of country's instability.
  9. Based on the Eurostat's 12-year period data, the levels of social, economic, and environmental sustainability of 24 EU countries were determined. Individual instability indicators of 15 chosen indicators were determined and analyzed. Mahalanobis distances, relative, and absolute instability levels of each composite indexes were calculated (social, economic, and environmental). The most and least sustainable countries for each component of sustainable development were identified. The case study results derived from spatial and temporal samples are consistent with the currently observed processes in the EU. Developed visual representation of the case study results were made.
  10. Hypotheses that there are positive relationships between instability and the level of country development, reflected in the values of socio-economic and environmental indicators, were proposed and tested. According to the analysis result of positive relationships were revealed for all five economic development indicators, for two

environmental indicators. There were no significant positive relationships found for social indicators. As a result of the analysis, the role of economic factors as having more significant impact on the stability of a situation were confirmed.

11. The study used several methods, including Mahalanobis distances analysis, time series, trends analysis, correlation and regression analysis, cluster analysis, and analysis of variance. The conducted cluster analysis made it possible to identify three groups of countries depending on Mahalanobis distance and the level of socio-ecological and economic instability. It has been revealed that there are countries with a high Mahalanobis distance and a low level of environmental, social, and economic instability.

**Author Contributions:** Conceptualization, E.L. and K.G.; methodology, E.L.; validation, G.K. and E.L. formal analysis, E.L., G.K., and K.G.; investigation, E.L., G.K., and K.G.; resources, E.L., G.K. and K.G.; data collection, G.K. and K.G.; writing—original draft preparation, E.L.; writing—review and editing, E.L.; visualization, G.K.; supervision, E.L.; project administration, E.L.; funding acquisition, G.K. and E.L. All of the authors contributed significantly to the completion of this manuscript, conceiving and designing the research, writing and improving the paper. All authors have read and agreed to the published version of the manuscript.

**Funding:** This research received no external funding.

**Data Availability Statement:** Data is available on demand.

**Conflicts of Interest:** The authors declare no conflict of interest.

## References

1. Foster, K.A. *A Case Study Approach to Understanding Regional Resilience*; Working Paper 2007-08; Institute of Urban and Regional Development, University of California: Berkeley, CA, USA, 2007.
2. Olawumi, T.O.; Chan, D.W.M. Identifying and prioritizing the benefits of integrating BIM and sustainability practices in construction projects: A Delphi survey of international experts. *Sustain. Cities Soc.* **2018**, *40*, 16–27. [CrossRef]
3. Da Pimentel Silva, G.D.; Sherren, K.; Parkins, J.R. Using news coverage and community-based impact assessments to understand and track social effects using the perspectives of affected people and decision makers. *J. Environ. Manag.* **2021**, *298*, 113467. [CrossRef]
4. Modica, M.; Reggiani, A. Spatial Economic Resilience: Overview and Perspectives. *Netw. Spat. Econ.* **2014**, *15*, 211–233. [CrossRef]
5. Martin, R. Regional economic resilience, hysteresis and recessionary shocks. *J. Econ. Geogr.* **2012**, *12*, 1–32. [CrossRef]
6. Van Bergeijk, P.A.G.; Brakman, S.; Van Marrewijk, C. Heterogeneous economic resilience and the great recession's world trade collapse. *Pap. Reg. Sci.* **2017**, *96*, 3–12. [CrossRef]
7. Giannakis, E.; Bruggeman, A. Regional disparities in economic resilience in the European Union across the urban-rural divide. *Reg. Stud.* **2019**, *54*, 1200–1213. [CrossRef]
8. Volkov, A.; Žičkienė, A.; Morkunas, M.; Baležentis, T.; Ribašauskiene, E.; Streimikiene, D.A. Multi-Criteria Approach for Assessing the Economic Resilience of Agriculture: The Case of Lithuania. *Sustainability* **2021**, *13*, 2370. [CrossRef]
9. Donkor, F.K.; Mitoulis, S.-A.; Argyroudis, S.; Aboelkhair, H.; Canovas, J.A.B.; Bashir, A.; Cuaton, G.P.; Diatta, S.; Habibi, M.; Hölbling, D.; et al. SDG Final Decade of Action: Resilient Pathways to Build Back Better from High-Impact Low-Probability (HILP) Events. *Sustainability* **2022**, *14*, 15401. [CrossRef]
10. Lyaskovskaya, E.A. Digitalization of the Russian Federation: A Study of Regional Aspects of Digital Inclusion. *Bull. S. Ural. State Univ. Ser. Econ. Manag.* **2021**, *15*, 45–56, In Russian. [CrossRef]
11. Lyaskovskaya, E.A. Economic sustainability of an enterprise in the context of digital economy. *Bull. S. Ural. State Univ. Ser. Econ. Manag.* **2022**, *16*, 87–99, In Russian. [CrossRef]
12. Lyaskovskaya, E.A. Digitalization, labor market and economic development. *Bull. South Ural. State Univ. Ser. Econ. Manag.* **2022**, *16*, 192–196, In Russian. [CrossRef]
13. United Nations Statistical Division. *Discussion Paper on Principles of Using Quantification to Operationalize the SDGs and Criteria for Indicator Selection*; EGM on the Indicator Framework: New York, NY, USA, 2015.
14. Hák, T.; Janoušková, S.; Moldan, B. Sustainable Development Goals: A Need for Relevant Indicators. *Ecol. Indic.* **2016**, *60*, 565–573. [CrossRef]
15. Nishitani, K.; Nguyen, T.B.H.; Trinh, T.Q.; Wu, Q.; Kokubu, K. Are corporate environmental activities to meet sustainable development goals (SDGs) simply greenwashing? An empirical study of environmental management control systems in Vietnamese companies from the stakeholder management perspective. *J. Environ. Manag.* **2021**, *296*, 113364. [CrossRef]
16. Panchal, R.; Singh, A.; Diwan, H. Does circular economy performance lead to sustainable development?—A systematic literature review. *J. Environ. Manag.* **2021**, *293*, 112811. [CrossRef]

17. Dijkstra-Silva, S.; Schaltegger, S.; Beske-Janssen, P. Understanding positive contributions to sustainability. A systematic review. *J. Environ. Manag.* **2022**, *320*, 115802. [CrossRef]
18. Wang, D.; Chen, S. Digital Transformation and Enterprise Resilience: Evidence from China. *Sustainability* **2022**, *14*, 14218. [CrossRef]
19. Kakderi, C.; Tasopoulou, A. Regional economic resilience: The role of national and regional policies. *Eur. Plan. Stud.* **2017**, *25*, 1435–1453. [CrossRef]
20. Duran, H.E.; Fratesi, U. Employment volatility in lagging and advanced regions: The Italian case. *Growth Change J. Urban Reg. Policy.* **2020**, *51*, 207–233. [CrossRef]
21. Rahma, H.; Fauzi, A.; Juanda, B.; Widjojanto, B. Development of a Composite Measure of Regional Sustainable Development in Indonesia. *Sustainability* **2019**, *11*, 5861. [CrossRef]
22. Mai, X.; Chan, R.C.K.; Zhan, C. Which Sectors Really Matter for a Resilient Chinese Economy? A Structural Decomposition Analysis. *Sustainability* **2019**, *11*, 6333. [CrossRef]
23. Rios, V.; Gianmoena, L. The link between quality of government and regional resilience in Europe. *J. Policy Model.* **2020**, *42*, 1064–1084. [CrossRef]
24. Sondermann, D. Towards more resilient economies: The role of well-functioning economic structures. *J. Policy Model.* **2018**, *40*, 97–117. [CrossRef]
25. Kitsos, A.; Carrascal-Incera, A.; Ortega-Argilés, R. The Role of Embeddedness on Regional Economic Resilience: Evidence from the UK. *Sustainability* **2019**, *11*, 3800. [CrossRef]
26. Chacon-Hurtado, D.; Losada-Rojas, L.L.; Yu, D.; Gkritza, K.; Fricker, J.D. A Proposed Framework for the Incorporation of Economic Resilience into Transportation Decision Making. *J. Manag. Eng.* **2020**, *36*, 04020084. [CrossRef]
27. Pretorius, O.; Drewes, E.; van Aswegen, M.; Malan, G. A Policy Approach towards Achieving Regional Economic Resilience in Developing Countries: Evidence from the SADC. *Sustainability* **2021**, *13*, 2674. [CrossRef]
28. Di Caro, P. Testing and explaining economic resilience with an application to Italian regions. *Pap. Reg. Sci.* **2015**, *96*, 93–113. [CrossRef]
29. Giannakis, E.; Bruggeman, A. Determinants of regional resilience to economic crisis: A European perspective. *Eur. Plan. Stud.* **2017**, *25*, 1394–1415. [CrossRef]
30. Brown, L.; Greenbaum, R.T. The role of industrial diversity in economic resilience: An empirical examination across 35 years. *Urban Stud.* **2016**, *54*, 1347–1366. [CrossRef]
31. Zeng, X.; Yu, Y.; Yang, S.; Lv, Y.; Sarker, M.N.I. Urban Resilience for Urban Sustainability: Concepts, Dimensions, and Perspectives. *Sustainability* **2022**, *14*, 2481. [CrossRef]
32. Yu, H.; Liu, Y.; Liu, C.; Fan, F. Spatiotemporal Variation and Inequality in China's Economic Resilience across Cities and Urban Agglomerations. *Sustainability* **2018**, *10*, 4754. [CrossRef]
33. Ahmad, T.; Thaheem, M.J. Developing a residential building-related social sustainability assessment framework and its implications for BIM. *Sustain. Cities Soc.* **2017**, *28*, 1–15. [CrossRef]
34. Ahmadian, F.F.A.; Rashidi, T.H.; Akbarnezhad, A.; Waller, S.T. BIM-enabled sustainability assessment of material supply decisions. *Eng. Constr. Arch. Manag.* **2017**, *24*, 668–695. [CrossRef]
35. Ramos, T.; Pires, S.M. Sustainability Assessment: The Role of Indicators. In *Sustainability Assessment Tools in Higher Education Institutions: Mapping Trends and Good Practices Around the World*; Caeiro, S., Filho, W., Jabbour, C., Azeiteiro, U., Eds.; Springer International Publishing: Cham, Switzerland, 2013; pp. 81–99. ISBN 978-331902375-5.
36. Büyükoçkan, G.; Karabulut, Y. Sustainability performance evaluation: Literature review and future directions. *J. Environ. Manag.* **2018**, *217*, 253–267. [CrossRef] [PubMed]
37. Briguglio, L.; Cordina, G.; Farrugia, N.; Vella, S. Economic vulnerability and resilience: Concepts and measurements. *Oxf. Dev. Stud.* **2009**, *37*, 229–247. [CrossRef]
38. Malkina, M.Y. Sustainability of regional economies and its factors. *Nauchnye Tr. Volnogo Ekon. Obs. Ross.* **2021**, *230*, 397–403.
39. Eurostat. 2022. Available online: <https://ec.europa.eu/eurostat/web/main/data/database> (accessed on 30 December 2022).
40. Ferova, I.S.; Lobkova, E.V.; Tanenkova, E.N.; Kozlova, S.A. Tools for Assessing Sustainable Development of Territories Taking into Account Cluster Effects. *J. Sib. Fed. Univ.* **2019**, *12*, 600–626. [CrossRef]
41. Podol'naya, N.N.; Ryabova, S.G. Sustainability of regional socio-economic systems: Evaluation toolkit and the nature of development. *Natl. Interests Priorities Secur.* **2017**, *13*, 827–842. [CrossRef]
42. Yakovina, M.Y.; Korableva, A.A. Recessionary shocks and regional economic sustainability. *Bull. Sib. Inst. Bus. Inf. Technol.* **2020**, *3*, 117–123. [CrossRef]

**Disclaimer/Publisher's Note:** The statements, opinions and data contained in all publications are solely those of the individual author(s) and contributor(s) and not of MDPI and/or the editor(s). MDPI and/or the editor(s) disclaim responsibility for any injury to people or property resulting from any ideas, methods, instructions or products referred to in the content.

Article

# Analytical and Numerical Study of Information Retrieval Method Based on Single-Layer Neural Network with Optimization of Computing Algorithm Performance

Konstantin Kostromitin \*, Konstantin Melnikov and Dar'ya Nikonova

Department of Information Security, South Ural State University, Chelyabinsk 454080, Russia; kostya.melnikov.01@inbox.ru (K.M.); d.nikonova@inbox.ru (D.N.)

\* Correspondence: kostromitinki@susu.ru

**Abstract:** This work presents a mathematical model of a fast-acting single-layer artificial neural network applied to the task of image reconstruction after noise. For research purposes, this algorithm was implemented in the Python and C++ programming languages. The numerical simulation of the recovery efficiency of the described neural network was performed for different values of the noise factor, the number of samples required to train elements in the sample and the dimensionality of the coupling coefficients,  $w$ . The study of the mathematical model of this neural network is presented; as a result, it is possible to identify its essence, to reduce the number of operations required to recover a single element and to increase recovery accuracy by changing the order of calculation of coupling coefficients,  $w$ .

**Keywords:** single-layer neural network model; data recovery; noise; numerical simulation; coupling coefficients

**MSC:** 68T05; 68T07; 68T10

**Citation:** Kostromitin, K.; Melnikov, K.; Nikonova, D. Analytical and Numerical Study of Information Retrieval Method Based on Single-Layer Neural Network with Optimization of Computing Algorithm Performance. *Mathematics* **2023**, *11*, 3648. <https://doi.org/10.3390/math11173648>

Academic Editors: Sergei Viktorovich Aliukov, Anatoliy Alekseevich Alabugin and Konstantin Vladimirovich Osintsev

Received: 26 June 2023  
Revised: 12 August 2023  
Accepted: 15 August 2023  
Published: 23 August 2023



**Copyright:** © 2023 by the authors. Licensee MDPI, Basel, Switzerland. This article is an open access article distributed under the terms and conditions of the Creative Commons Attribution (CC BY) license (<https://creativecommons.org/licenses/by/4.0/>).

## 1. Introduction

Currently, mathematical models of artificial neural networks are actively used to solve a large number of different problems.

Neural networks have revolutionized the field of machine learning and artificial intelligence. Over the past few decades, significant advancements have been made in the development and application of neural networks, leading to remarkable achievements in various domains. This introduction will provide an overview of the accomplishments in neural networks and their implications for the field.

Neural networks, due to the structure and function of the human brain, consist of connected nodes (neurons) for the control and transmission of information. These networks are capable of learning complex patterns and relationships from vast amounts of data, enabling them to perform tasks that were previously challenging or impossible for traditional machine learning algorithms [1].

One of the major achievements in neural networks is their success in image and speech recognition tasks. Convolutional neural networks (CNNs) have demonstrated exceptional performance in image classification, object detection, and segmentation. Recurrent neural networks (RNNs) have made significant contributions to speech recognition and natural language processing [2].

Neural networks have also shown remarkable progress in other domains, including natural language processing, machine translation, recommender systems, and medical diagnosis. These advancements have been fueled by the availability of large-scale datasets, improved network architectures, and advancements in computational power [3,4].

The world of neural networks is constantly evolving, with the number of publications and research growing every day. Let us talk about the most interesting ones.

Ref. [5] introduces a novel approach to reinforcement learning that leverages unsupervised auxiliary tasks. The authors demonstrate how incorporating auxiliary objectives, such as predicting future states or generating synthetic data, can significantly improve the learning efficiency and generalization capabilities of reinforcement learning agents. The proposed method achieves high performance based on various parallel models.

The authors of ref. [6] propose Efficient Neural Architecture Search (ENAS), a fast and cost-effective method for generating automatic models. ENAS creates a large computer graph where each layer represents a neural network structure, thereby encouraging all developers to share their layers. The operator is trained using gradients to find the subset that maximizes the expected value for a given set of values. At this point, the model is trained on the selected fields to reduce the acceptance loss. The distribution of parameters between sub-models enables ENAS to exhibit strong performance using less GPU time than current methods do; in fact, the GPU time required for it is 1000 times less than that under Neural Architecture Search.

In recent years, the development of new methods for data analysis has received attention. One such technology is the artificial neural network (ANN). Artificial neural networks have many attractive theoretic properties; specifically, these include the ability to detect non-predefined relations such as non-linear effects and/or interactions. The benefits of these considerations come at the cost of reduced model interpretation. Many authors have analyzed the same data using all statistical methods (e.g., logistic regression or Cox regression) and ANN according to these characteristics [7].

Uncertainties associated with the simulation and prediction of solar PV system performance can be easily and efficiently addressed through an intelligent design approach. During the decade from 2009 to 2019, artificial neural networks (ANN), fuzzy logic (FL), genetic algorithms (GA) and their hybrid models became intelligent tools for solar PV system prediction and simulation. Furthermore, there is no comprehensive review on the forecasting and modeling of solar photovoltaic systems using ANN, FL, GA and their hybrid models from this decade [8].

In ref. [9], the authors focus on neural networks that can learn to control behavior according to leadership goals and learn how to create management strategies or goals. The essence of the operation management system consists of four parts, namely the forecasting network, operating production network, control network and optimization network. This method and how to view it are described and explained in this article.

The authors provide an overview of recent developments in deep learning (RL). This paper starts with the concepts of deep learning and reinforcement learning, including test beds. It then discuss deep Q-networks (DQNs) and their extensions, default methods, process optimization, costs, and planning. Next, we talk about attention and memory, unsupervised learning, and learning to learn. It will discuss various applications of reinforcement learning, including gaming (notably AlphaGo), robotics, communication systems (also known as chatbots), machine translation, speech recognition, neural network design, personal web applications, healthcare, finance, and music production. Authors also cites unreviewed topics/papers. After listing the RL project, the author closes with a comment [10].

High-level data can be converted into low-level code by training a multilayer neural network with a small central layer to generate high-level vectors. Gradient descent can be used to tune the weights in an "autoencoder" network, but only if the initial weights are close to the optimal solution. They describe an efficient weighting algorithm that allows deep network coders to learn low-level codes that outperform principal component analysis as a tool for data dimensionality reduction [11,12].

The book "Neural Networks and Deep Learning" covers old and new models of deep learning. The main topic is the theory and algorithm of deep learning. The concepts and algorithms of neural networks are important for understanding the fundamentals in order

to understand the basic concepts of neural architecture design in various applications. Why are neural networks effective? In what ways do they perform better than random machine learning does? Does depth matter? Why is it so difficult to train neural networks? What are the problems? The book also covers a wide range of applications to better understand how neural architectures can be used to solve various problems, including applications in various fields such as dynamical systems, machine learning, image interpretation, image segmentation, dynamic game learning, and information analysis [13].

Since the article is a study of the mathematical model of ANN, within the framework of the literature review below, in the introduction, key works on elementary ANN models are presented, starting from the time of discovery and the first studies.

Minsky and Papert's book is the first example of mathematical analysis aimed at uncovering the true limits of a class of computing systems that can be viewed as models of the brain. Now, new mathematical tools, physicists' interest in the theory of random objects, new views and mental models of brain function, and the development of fast computers capable of simulating networks of automata have given new importance to perceptrons. The authors observe a big data problem related to communication: the difficulty of understanding exactly how individual "things" and "agents" appear in a network. Advances in this area can be linked to what the authors call "social thinking" [14].

Rosenblatt's work was supported as part of an internal research program by Cornell Aeronautical Laboratory, Inc. The concepts discussed have their origin in some of the author's independent studies in the field of physiological psychology, in which the goal was to formulate an analogue of the brain that is useful in analysis. As a result, the initial concept of the perceptron was obtained—a recent product of this research program; further efforts of the author were directed toward establishing the technical and economic feasibility of the perceptron [15].

Using the tools of critical theory, Stephen Judd proposes a comprehensive definition of participatory research in interaction networks. His work carefully reveals the computational challenges of training neural networks and examines how certain design principles can or cannot alleviate these problems. When more neurons are used, new questions arise and provide new insights into strategies that lead to the creation of artificial and biological connections. He accepts new scientific theories. His work outlines key ideas, outlines general learning problems and looks at the computational challenges of tasks, reviews current learning theory, describes textbook learning models, and more. With alternative models, other than interaction models, research begins. The following chapters establish the coherence of e-learning contexts, explain the implications of this coherence, and present several sequences that have implications for different specific contexts. Judd discusses the problem of shallow networks and the unique characteristics of the family, discusses the problem of the ability of neural networks to maintain stability, and summarizes the results, implications, and implications [16].

In ref. [17], the authors describe a new method for the learning, training and networking of neuronal units. The method reduces the difference between the actual network vector and the target vector by adjusting the correlation measure in the network. Internal "hidden" units that do not have partial inputs or outputs become important for learning due to changes in weights, and the behavior in the problem is captured through the interaction of these units. The ability to create new features differentiates reduction from earlier simpler methods such as the perceptron-switching process [17].

For a more general introduction to the topic of neural networks, the book by Simon S. Haykin was considered; it is a comprehensive guide to the mathematical foundations of neural networks. The book covers a wide range of topics, including supervised and unsupervised learning, deep learning, optimization algorithms, and various types of neural networks such as feed-forward, recurrent, and convolutional networks [18].

Kevin P. also provides a comprehensive introduction to machine learning. Murphy uses probabilistic models and assumptions as methods of connection. Combining breadth and depth, this overview provides background information on topics such as probability,

optimization, and parallelism, and discusses recent developments in the field, including standard deviation, stable L1, and deep learning [19].

The practical aspects of implementation based on modern libraries were considered in studies in the book by Aurélien Géron.

This bestselling book uses simple examples, small projects, and Python programming (Scikit-Learn, Keras, and TensorFlow) to help readers understand the concepts and tools for building intelligent systems. Author Aurélien Géron explores a variety of approaches, from linear regression all the way to deep neural networks [20].

In conclusion, this introduction highlights the diverse range of publications and research endeavors focused on neural networks. These studies span various domains, from incorporating unsupervised auxiliary tasks to improve reinforcement learning, to automating the design of efficient neural architectures for image classification, and applying generative adversarial networks for video synthesis. Each of these contributions showcases the continuous advancements and innovations in the field of neural networks, pushing the boundaries of what is possible in machine learning and artificial intelligence. By exploring new techniques, algorithms, and architectures, researchers strive to enhance the learning capabilities, efficiency, and generalization of neural networks, leading to improved performance and practical applications in a wide array of domains. As we delve further into the articles linked above, we gain deeper insights into the specific approaches and findings that contribute to the overall progress of neural network research.

One of the fields of application of the ANN is the task of data recovery, which is subjected to distortion as a result of external interference during transmission through communication channels, as well as that received from sources of analog nature.

In addition, in some cases, a critical parameter of the system is its performance, for example, in solving computational problems in real-time systems, such as process control systems, automation, SCADA systems, tomographs and others.

One area of using of ANN is machine vision. Machine vision is the ability of computers to extract information and meaning from images and videos. With the help of neural networks, computers can distinguish and recognize images in the way that humans do. Machine vision is used in several fields, such as visual recognition in unmanned cars so they can react to road signs and other road users, content moderation to automatically remove unsafe or inappropriate content from image and video archives, facial recognition to identify people and recognize attributes such as open eyes, glasses and facial vegetation, and image labeling to identify brand logos, clothing, protective gear and other image details. Also, it can be used in natural language processing (NLP) tasks. NLP is the ability to process natural, human-generated text. Neural networks help computers extract information and meaning from textual data and documents. NLP has such applications as automated virtual agents and chatbots.

In connection with the given tasks and working conditions, the application of a fast algorithm of data recovery on a set of initial samples seems to be feasible and have applied value.

The purpose of this work is to investigate and improve an original fast algorithm for recovering information distorted by noise based on the work in [21], where a numerical study of the influence of noise level, the number and size of samples and the dimensionality of the coefficient  $w$  on the recovery efficiency is carried out.

The analytical study of the restoration algorithm was carried out, as a result of which it was possible to reveal the mechanism of operation of this method, to find a matrix-free method of data restoration, to improve the accuracy of restoration taking into account the preservation of the values of weight coefficients on the main diagonal of the matrix  $W$ .

## 2. Materials and Methods

This work presents a study of the ANN algorithm for recovering noisy information, consisting of the stages formatting, training, noising and recovery from [21].

2.1. Formation of Samples for ANN Training

To test the working algorithm from [21], the initial samples were formed in the form of two-dimensional arrays filled with the values  $-1$  and  $1$ . For clarity, they were selected in a pattern similar to the Cyrillic letters “E” (Figure 1), “O” (Figure 2) and “III” (Figure 3):

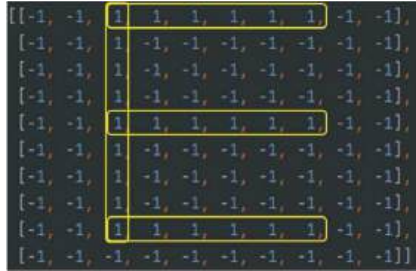


Figure 1. Sample letter «E».

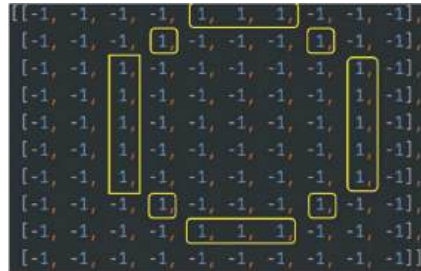


Figure 2. Sample letter «O».

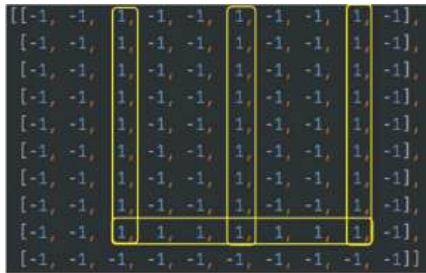


Figure 3. Sample letter «III».

2.2. ANN Training on the Generated Samples

The ANN training procedure is performed by calculating the weight coefficients,  $w_{ij}$ , characterizing the connection of neurons (1). Moreover, within the framework of the model [21], it is assumed that this coefficient is equal to zero for the same neuron.

$$w_{ij} = \begin{cases} \sum_{k=1}^m a_i^k a_j^k, & i \neq j, i, j = \overline{1, n} \\ 0, & i = j \end{cases} \quad (1)$$

where  $w_{ij}$ —weight value of the connection between neurons  $i$  and  $j$ ;

$n$ —number of neurons in ANN;

$m$ —number of samples used to train the network;

$a_i^k$ — $i$ -th element of the  $k$ -th training sample.

When calculating the coefficients,  $w_{ij}$ , two-dimensional tables with training samples are converted into strings, after which they are transposed in the original algorithm and the expressions  $a_i^k a_j^k$  are calculated for each sample. Further, summation is performed over all  $m$  samples.

As a result, a matrix of weights,  $W$ , with dimension  $n \times n$  is formed. In this case, the value  $n = 100$ —according to the total number of neurons in the samples of the letters “E”, “O”, and “III”.

A graphical representation of the overall matrix of coupling coefficients and separate ones for the three samples are presented in the figures (Figures 4–7).

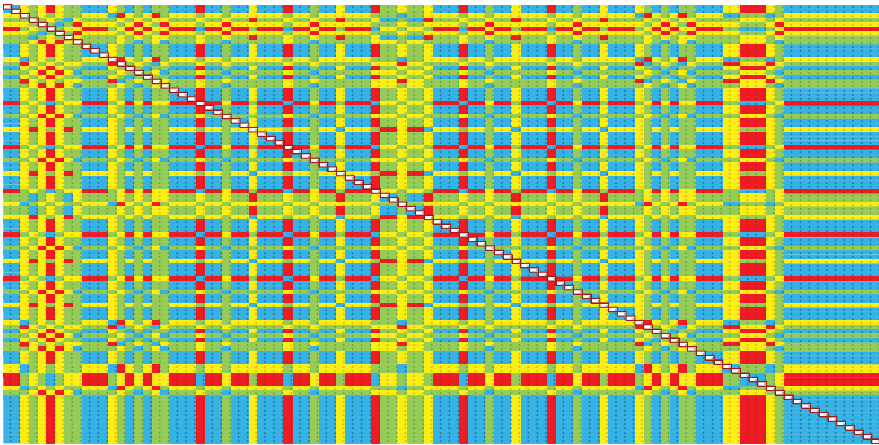


**Figure 4.** The total matrix of weights,  $W$ . The red color of the cell corresponds to the value of the sums of weights equal to  $-3$ . Yellow:  $-1$ ; white:  $0$ ; green:  $1$ ; blue:  $3$ .

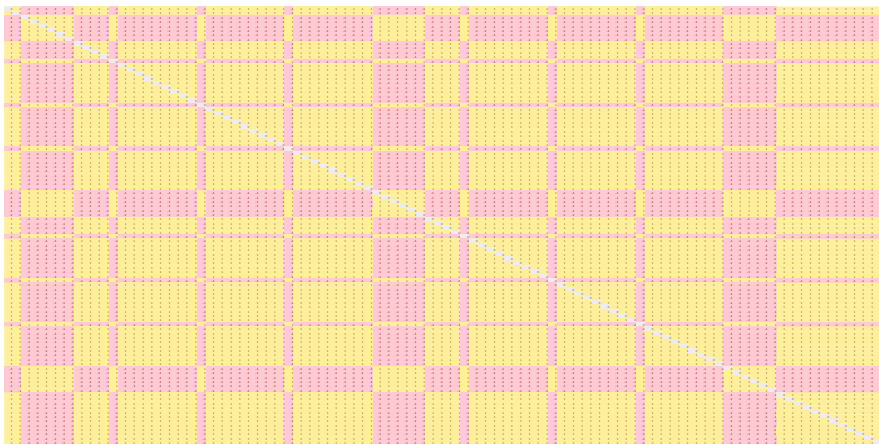


**Figure 5.** Matrix of weights for letter «E». Yellow:  $1$ ; white:  $0$ ; pink:  $-1$ .

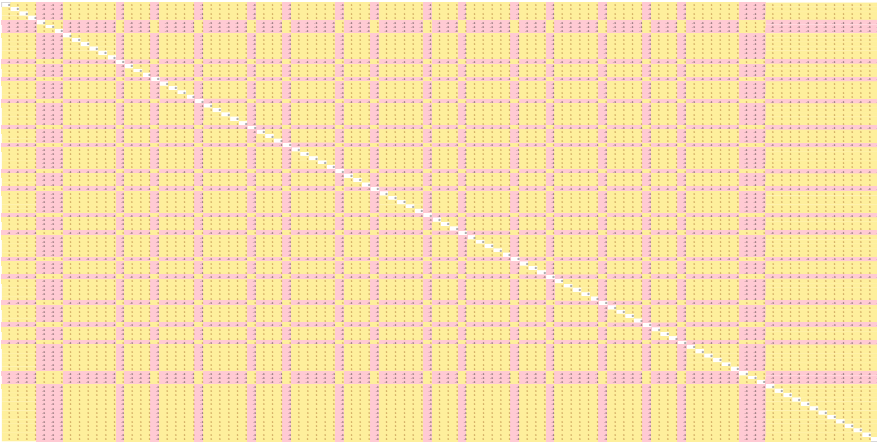


**Figure 6.** Matrix of weights for letter «O». Yellow: 1; white: 0; pink: -1.

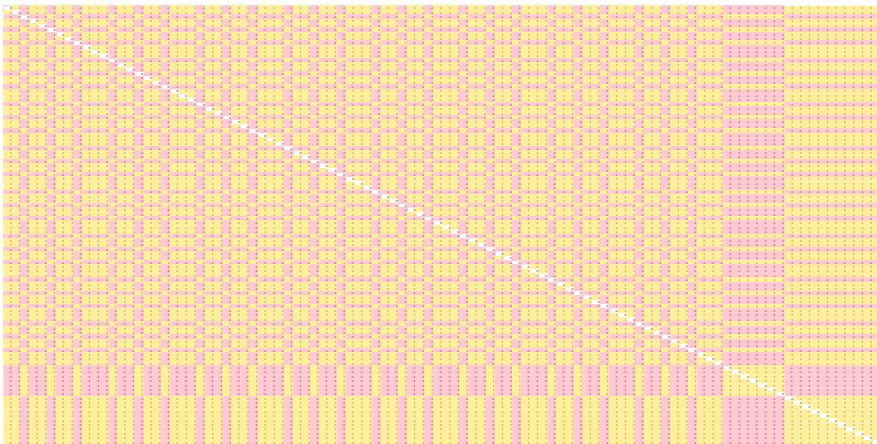


**Figure 7.** Matrix of weights for letter «III». Yellow: 1; white: 0; pink: -1.

### 2.3. Sample Noise and Recovery

For the algorithm of obtaining a noisy image, one of the original samples is selected, then  $(num * n)$  times the node state is changed from -1 to 1 if its value is -1, otherwise the value does not change. The value  $num$  is set during testing and determines the final level of sample noisiness.

The restoration of sample element  $a_i^r$  is defined by the following expression (2):

$$a_i^r = f\left(\sum_{j=1}^n w_{ji} a_j(t)\right) \quad (2)$$

where  $f$  is the activation function (3):

$$f(x) = \begin{cases} 1, & \text{for } x > 0 \\ -1, & \text{for } x \leq 0 \end{cases} \quad (3)$$

Thus, to perform the recovery operation of a single element it is necessary to form a matrix of weight coefficients,  $W$ , of size  $n*n$  elements, and then conduct its backward reduction to the recoverable matrix of  $n$  elements.

For increasing the dimensionality of neuron connectivity coefficients,  $w$ , with this approach, we will need a proportional increase in the dimensionality of matrix  $W$ . For example, to connect three elements of ANN it is necessary to calculate the  $w_{jik}$  coefficients for matrix  $W$ , containing  $n*n*n$  elements, which will significantly increase the computational complexity of the algorithm.

The computational scheme is presented in Figure 8.

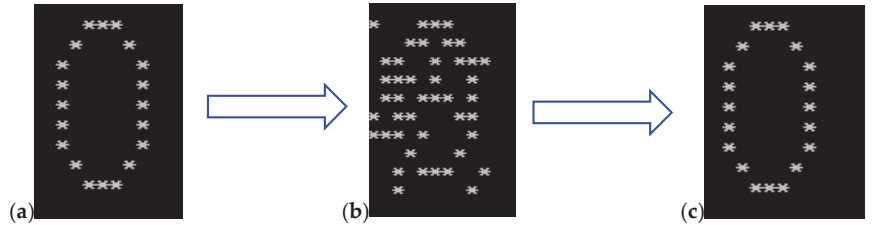


**Figure 8.** Graphical representation of sample processing. (a) Shaping, (b) noising, and (c) recovery. Symbol \* used for presentation of initial noised and recovery samples.

### 3. Results

#### 3.1. Results of Numerical Investigation of the Reconstruction Algorithm

Recovery testing was carried out with a sequential increase in the noise factor of 1% from 0% to 100%. In total, 100 tests were carried out, in each of which the percentage of deviations of the restored sample from the original was calculated and averaged (Figure 9).

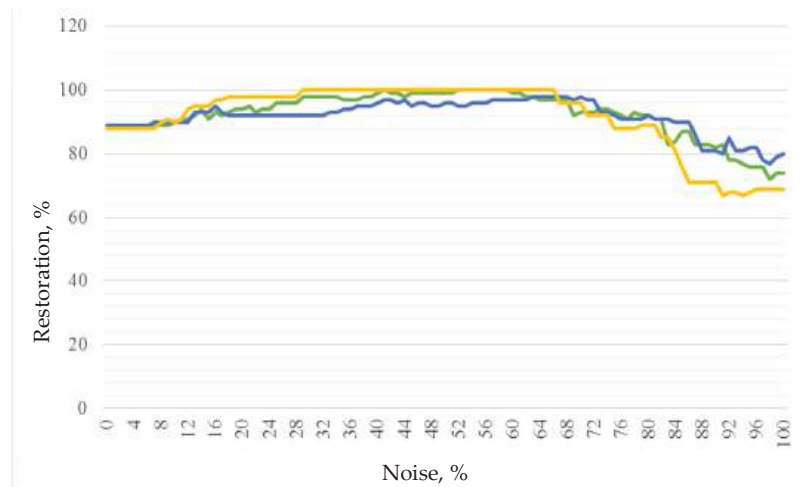


**Figure 9.** Detailed recovery results. Green corresponds to the letter “E”, blue corresponds to the letter “O”, and yellow corresponds to the letter “III”.

Based on the data obtained, the following conclusions can be drawn:

The algorithm at any level of noise is able to recover at least 60% of the data for the samples.

The sample of the letter “Sh” with a high level of noise is the worst-restored, but with an average level of noise, it has the highest average recovery percentage compared to that of other samples. This is due to the large amount of useful information.

In general, all symbols recover equally well at 35–60% noise and have significant recovery errors at noise percentages less than 20 and those greater than 65.

The choice of elements subjected to noise has a significant effect on the result of restoration. With the same level of noise, with the random selection of different points, the results of restoration can be radically different.

### 3.1.1. Recovery Error Analysis

**Sample letter «E»** (typical errors are shown in Figure 10):

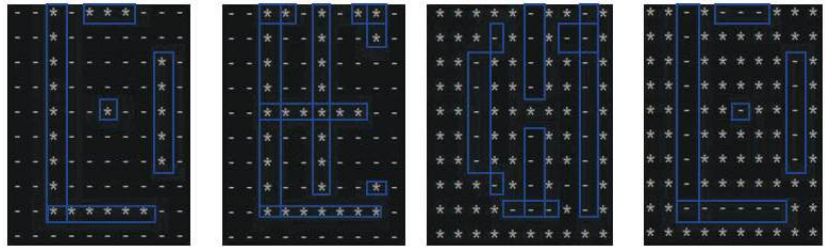


**Figure 10.** Typical errors of the sample letter «E»—from left to right—with characteristic errors 1, 2, 3 and 4. Symbol \* used for presentation of initial noised and recovery samples.

With a low percentage of noise (0–30%), the algorithm restores the image with an error of 1;

At a noise level from 30% to 65%, as a result of the algorithm, the initial letter «E» is often successfully restored;

At 70% noise, the algorithm restores the image with an error of 2; at 80% noise, it restores the image with an error of 3; at 85% noise, it restores the image with an error of 2, at 90% there is an erroneous recovery of another sample, “Letter O”; at 90% noise, it restores the image with an error of 3; at 100% noise, it restore the image with an error of 4 (inverted error 1).

**Sample letter «O»** (typical errors are shown in Figure 11):

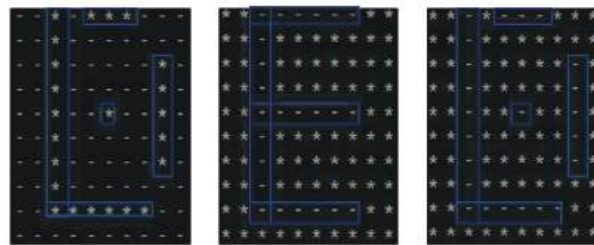


**Figure 11.** Typical errors of the sample letter «O»—from left to right—with errors 1, 2, and 3. Symbol \* used for presentation of initial noised and recovery samples.

With a low percentage of noise (0–25%), the algorithm restores the image with an error of 1;

With a noise level of 25% to 70%, as a result of the algorithm, the initial letter “O” is often successfully restored;

At 75% and 80% noise. it is almost possible to restore the sample with minor artifacts; up to 100% noise the sample is restored with an error of 2, and at 100% noise, the sample is restored with an error of 3 (inverted error 1).

**Sample letter W** (typical errors are shown in Figure 12):

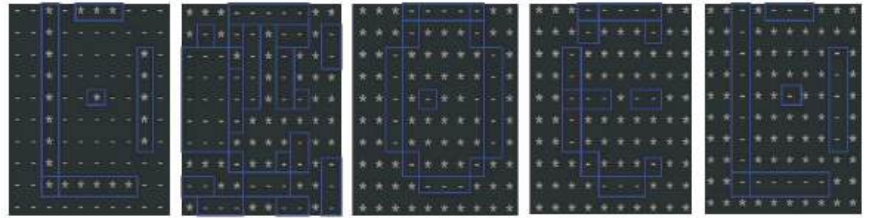


**Figure 12.** Typical errors of the sample letter «III»—from left to right—with errors 1, 2, 3, 4, and 5. Symbol \* used for presentation of initial noised and recovery samples.

Up to 15% noise, there is an error of 1;  
 From 20% to 80% as a result of the algorithm, the initial letter III is often successfully restored;

At 70% noise, the restoration is similar to that with an error of 2;

At 85–95% noise, there is an error of 3 and an error of 4.

At 100% noise, there is an error of 5 (inverted error 1).

Based on the results of this study, the following conclusion can be drawn:

Under low noise, the algorithm often does not work correctly, since all elements are equal to it at the time of training, and it draws an image that is common to all samples.

With medium noise, as a result of the algorithm, the initial sample is often successfully restored. With high noise, recovery occurs with errors, and sometimes restores erroneous samples, since in noise it is impossible to uniquely determine the original sample among the many samples on which the model was trained.

### 3.1.2. Influence of the Number of Samples on the Recovery Result

For this study, three additional data samples with a matrix size of  $10 \times 10$  were introduced. The original samples have not been changed, and their graphical and numerical representation can be seen in Section 2.2. We give a graphical and numerical representation of the embedded samples below (Figure 13).

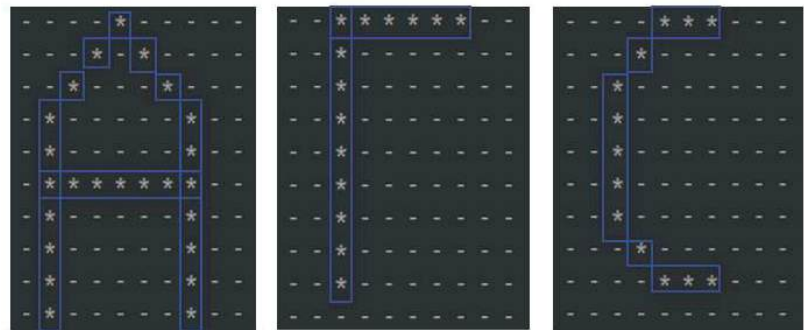


**Figure 13.** Graphic representation of the sample—letters «A», «Г», and «C». Symbol \* used for presentation of initial noised and recovery samples.

To build a graph for each of the six samples, the percentage of recovery was determined at various noise levels. The data obtained are shown in Figure 14.

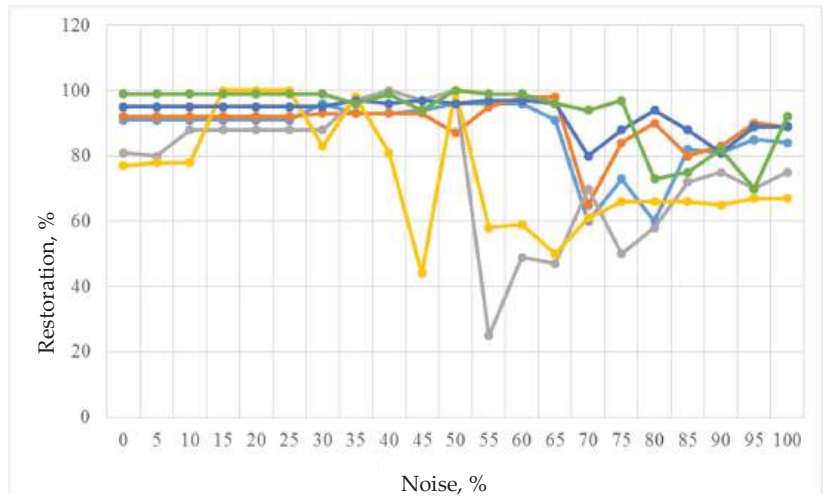


**Figure 14.** The results of recovering different data samples (blue—letter «E»; orange—letter «O»; gray—letter «S»; yellow—letter «A»; blue—letter «G»; green—letter «C»).

Based on the results obtained, it can be concluded that with an increase in the number of initial samples, the accuracy of restoring each sample has decreased. Namely, for sample E, from 50 to 60% of noise, the program produces the letter «E» that is underdrawn to varying degrees, and after 60%, various artifacts begin to appear during restoration or other samples begin to be restored.

For the sample «O» with up to 50% noise, the program produces the letter «O», which is underdrawn to varying degrees, and at 55–65% noise, the recovery percentage is large, and almost always gives the correct answer, though sometimes a couple of elements are missing, and then it gives a strongly underdrawn sample.

With this set of samples, the algorithm works best with the «Г» sample, restoring about 80% of the information for any percentage of noise. Worst of all, with the «III» sample, with a noise of about 55%, only 25% of the information can be restored. This is due to the overlap of other samples. The larger the area of the object that needs to be restored, the worse the restoration is.

### 3.1.3. Influence of Sample Matrix Sizes on Signal Recovery

For this study, the initial data samples were changed—their size was increased to that of a 40 × 40 matrix (Figure 15).

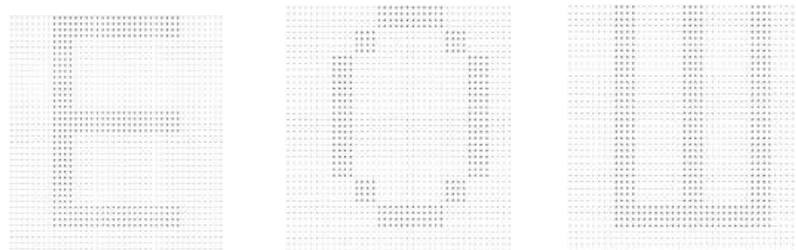


**Figure 15.** Graphical representation of 40 × 40 samples. From left to right: Letter «E», Letter «O», and Letter «III».

To construct a graph with both standard and enlarged samples, several runs of the program were performed for each sample with different noise levels and the final recovery result was obtained.

A graph for standard matrix sizes is shown in Figure 16, and a graph for enlarged ones is shown in Figure 17.

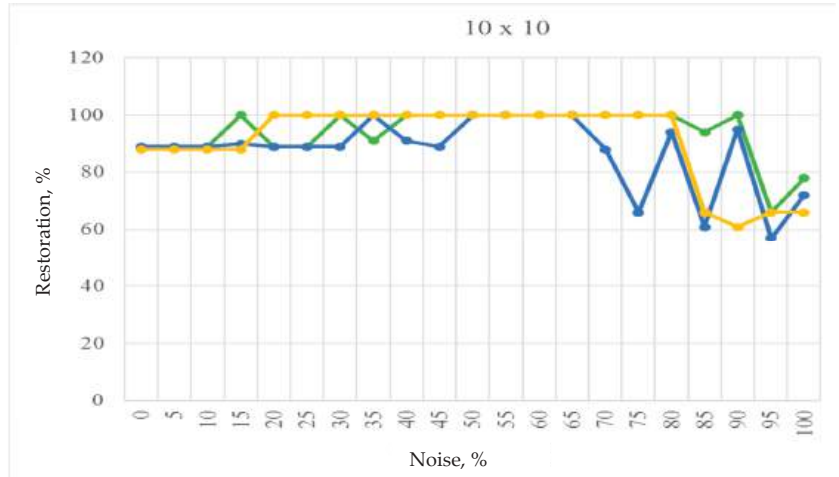


Figure 16. Restoration of standard samples (10 × 10). Green—«E»; blue—«O»; yellow—«III».

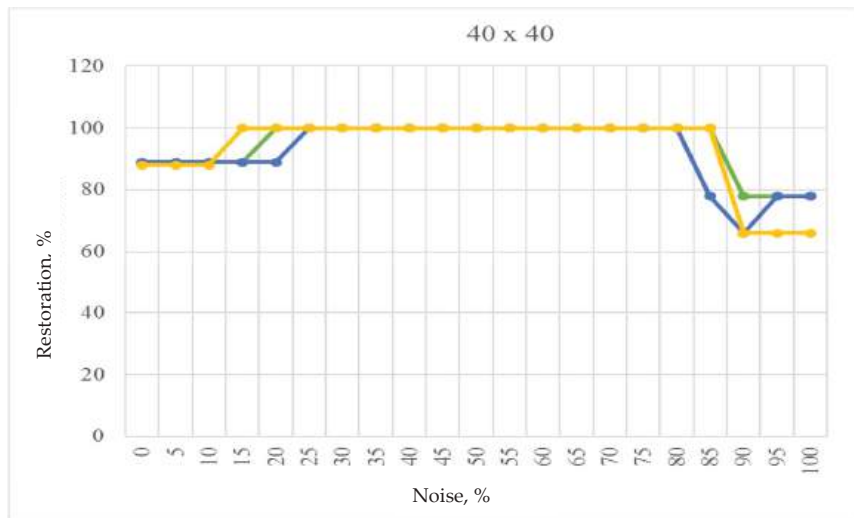


Figure 17. Restoration of enlarged samples (40 × 40). Green—«E»; blue—«O»; yellow—«III».

Based on the data obtained, the following conclusions can be drawn:

The restoration of enlarged samples is generally better; the completion of the restoration of the sample (100%) occurs at noise values from 25% to 80%, with a complete restoration of the original samples in the noise range from 50% to 65%.

This is due to the low number of samples and the large amount of data being recovered, as the data have less of an overlap in the weighting matrix.

### 3.1.4. Influence of the Dimensionality of the Matrix of Weight Coefficients, $w$

Consider the mathematical model of the neural network. Consider expression (1) for finding weight coefficients. If the dimensionality of the matrix of weight coefficients,  $w$ , increases, we obtain the following expression (4).

$$w_{ijl} = \begin{cases} \sum_{k=1}^m a_i^k a_j^k a_l^k, & i \neq j \neq l, \text{ for } i, j, l = \overline{1, n} \\ 0, & \text{for } i = j \text{ or } i = l \text{ or } j = l \end{cases} \quad (4)$$

For each sample,  $x$ , a three-dimensional matrix is created by multiplying the elements at positions  $i, j, l$  ( $w_i[i][j][l] = x[i] * x[j] * x[l]$ ), and then the resulting three-dimensional matrices are added to create the final matrix of weights: ( $w[i][j][l] = w_{i0}[i][j][l] + w_{i1}[i][j][l] + \dots + w_{im}[i][j][l]$ ).

To evaluate the effectiveness of increasing the dimensionality of the coefficients,  $w$ , of the weight matrix, the noise is increased in steps of 5%, and then the recovery algorithm is executed and the number of errors is calculated. As in the previous cases, the recovery percentage is determined by a character-by-character comparison of the unnoised sample with the recovered one (Figure 18).

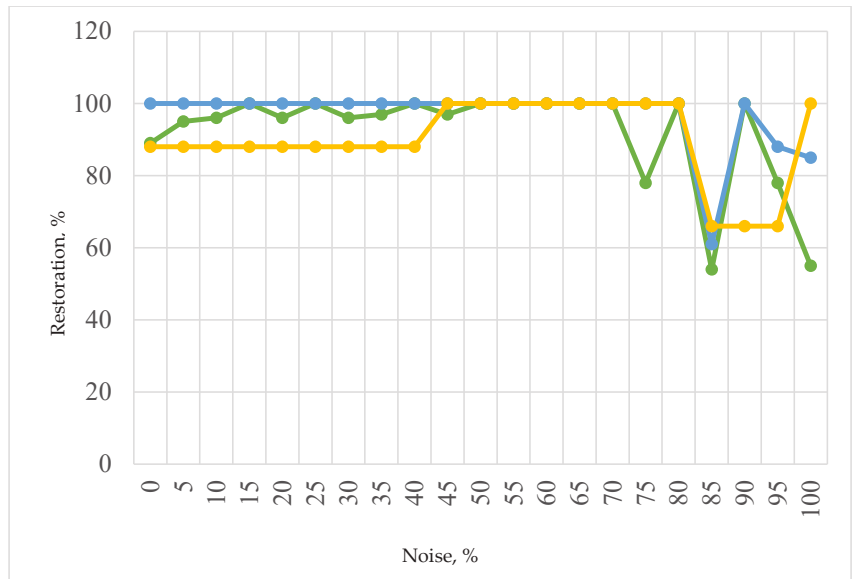


**Figure 18.** Results of sample reconstruction with the connection coefficient,  $w$ , of three neurons. Green—letter “E”; blue—letter “O”; yellow—letter “S”.

It is worth noting that these calculations are much more demanding on computer performance than the standard weighting factor matrices are, since approximately 4,000,000 computational operations are required, compared to the standard 40,000 for the standard matrix view.

However, the recovery results will be comparable to those of the original algorithm. Successful recovery occurs in the noise range of 50–70%. Significant artifacts are also noticeable, mainly due to the odd dimensionality of the matrix, inverted restoration of the sample occurs. This problem can be solved by counting the amount of useful and useless information and comparing it during the playback stage after applying the threshold function. If there is more useful information than useless information, it is necessary to invert the output, and thus the output information will be reconstructed more accurately.

Also, if the recovery percentage is 0 (no value matches the sample), then inverting the output will produce a 100% recovery.

However, for some samples within the proposed algorithm, the recovery is more successful than that for others. Namely, the letter «O» was restored in the range of 0–80%. It was also erroneously recovered when trying to recover other samples with strong noise.

The analysis revealed that the accuracy of image reconstruction did not increase, while the computational requirements became many times higher. Thus, increasing the dimensionality of weighting coefficient matrices,  $w$ , has no effect on the quality of problem solving.

For the downsizing case’s analysis, expression 4 for finding the weight coefficients will take the following form (5).

$$w_{ij} = \sum_{k=1}^m a_{ij}^k \text{ for } i = \overline{1, n} \tag{5}$$

To analyze recovery efficiency, 1000 test runs were performed with a noise step of 5%, and then the average recovery percentage for each level of noise was calculated (Figure 19).

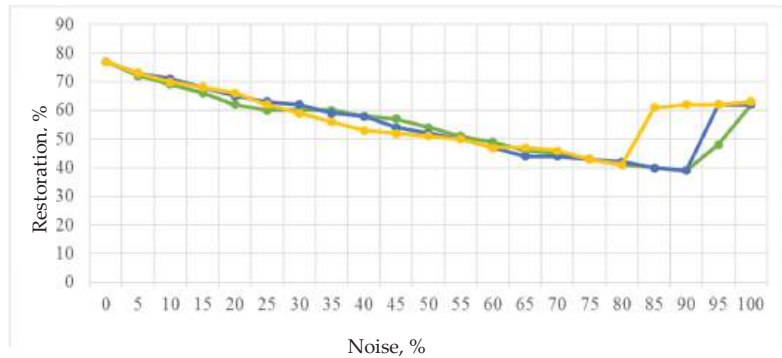


Figure 19. Results of image reconstruction in the case of a one-dimensional matrix of weight coefficients,  $w$ . Green—«E»; blue—«O»; yellow—«W».

When using this algorithm for all the tests, the original sample was not restored to 100%. Often, the algorithm produces noise that is not similar to that of the desired sample. In addition, there is a tendency for the percentage of recovery to decrease proportionally to the level of noise.

The presented modification of the algorithm is also not applicable to improve the considered neural network, since it is not able to perform the required recovery tasks.

### 3.2. Investigation of the Mathematical Model

#### 3.2.1. Hypothesis Statement

For this study, let us change the formulation of the problem

- (1) Samples will be noisy in any way, and the data may be distorted, losing information;
- (2) The main diagonal of the matrix of weight coefficients is not zeroed, because it increases the uncertainty of sample recovery and degrades the quality of the algorithm.

#### 3.2.2. Investigation of the Hypothesis: The Possibility of Obtaining a Reconstructed Image without Forming a Matrix of Weight Coefficients

**Formulation of Hypothesis:** «A matrixless way to calculate  $a_i^r$  exists»

Substitute the expression for the matrix of weighting coefficients (1) into the expression for sample element recovery (2):

$$\begin{aligned}
 a_i^r &= f\left(\sum_{j=1}^n w_{ji} a_j(t)\right) = f\left(\sum_{j=1}^{25} a_1 a_j a_j^n\right) = \\
 &= f(a_1 * a_1 * a_1^n + a_1 * a_2 * a_2^n + a_1 * a_3 * a_3^n + \dots + a_1 * a_{25} * a_{25}^n) = \\
 &= f(a_1(a_1 * a_1^n + \dots + a_{25} * a_{25}^n))
 \end{aligned}
 \tag{6}$$

Thus, we can see that there is a constant expression (7),

$$a_1 * a_1^n + \dots + a_{25} * a_{25}^n,
 \tag{7}$$

which does not change depending on the data being changed. The sum of products shows the ratio of coincidence of values in cells in the original and noisy samples. If the biggest part coincides, the value will be positive (the original image is restored), otherwise it will be negative (the inverted image is restored).

The sign and value of the sum vary depending on the ratio of noisy to original values of the corresponding elements of the samples.

The weighting matrix can be omitted on the grounds that expression (7) is a constant for the original and noisy sample, which can be calculated separately from the values of the original signal, **Q.E.D.**

Block diagrams of the original [21] and improved recovery algorithms are presented below in Figure 20.

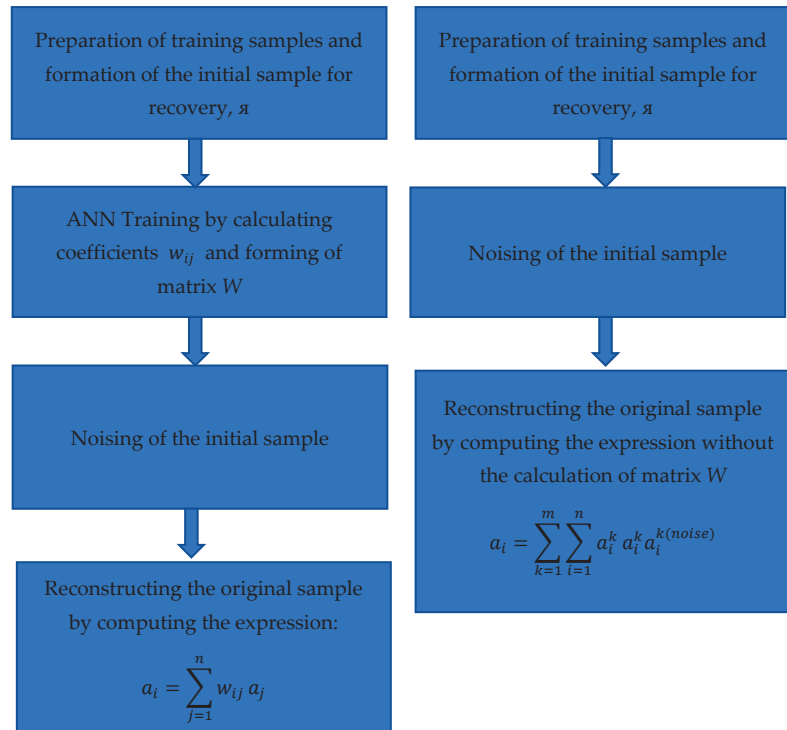


**Figure 20.** On the left is the original algorithm for the restoration of the noisy image from [21]. On the right is the improved algorithm, with matrix-free computation.

### 3.2.3. Identifying the Nature of the Recovery Mechanics

Let us investigate the constant expression (6) and find its mathematical meaning. Considering the case for several samples, the multiplication of elements will look as follows:

$$a_1 = f \left( \sum_{j=1}^m a_j^n \left( \sum_{k=1}^n a_1^k a_j^k \right) \right) \tag{8}$$

where  $n$  is the number of samples.

Then, for three samples the multiplication will look as follows (9):

$$a_1 = f \left( \sum_{j=1}^{36} \left( a_1^1 a_j^1 + a_1^2 a_j^2 + a_1^3 a_j^3 \right) a_j^n \right) \tag{9}$$

if  $n = 3$ , then  $a_1^3 = f \left( \sum_{j=1}^{36} \left( a_1^1 a_j^1 a_j^n + a_1^2 a_j^2 a_j^n + a_1^3 a_j^3 a_j^n \right) \right)$ .

The multiplication of  $a_j^k a_j^\omega$  estimates the degree of sample matching (Pearson correlation).

Thus, we can conclude that for any sample, the contribution will be determined by the sum of the products of the coefficients of values in the cells of the original and noisy sample in the range  $[-n, n]$ .

### 3.2.4. Investigation the Influence of the Dimensionality of the Matrices $w$

Consider the cases of multidimensionality for matrices of weight coefficients in the case where the dimensionality of the connection of the weight coefficients is increased to four (10):

$$\begin{aligned} a_1^r &= f \left( \sum_{j=1}^n \sum_{k=1}^n a_1 a_j^1 a_k^1 a_j^n \right) = \\ &= f \left( a_1 \left( a_1^1 (a_1^1 a_1^n + \dots + a_{25}^1 a_{25}^n) \right) + a_2^1 \left( a_1^1 a_1^{HyM} + \dots + a_{25}^1 a_{25}^n \right) + a_{25}^1 (a_1^1 a_1^n + \dots + a_{25}^1 a_{25}^n) \right) = \\ &= f \left( a_1 (a_1^1 + a_2^1 + \dots + a_{25}^1) (a_1^1 a_1^n + \dots + a_{25}^1 a_{25}^n) \right) \end{aligned} \tag{10}$$

It can be noted that  $a_1^1 + a_2^1 + \dots + a_n^1$  is a constant expression.

Then, for the four-dimensional case, by analogy, the element recovery will be determined by the following expression (11):

$$a_1^r = f \left( (a_1 (a_1 + \dots + a_{25}))_j * (a_1 + \dots + a_{25})_k * (a_1 a_1^n + \dots + a_{25} a_{25}^n)_m \right) \tag{11}$$

Thus, multiplication by a constant multiplier before the expression takes place. This multiplier has no effect on the nature and rate of recovery. As a consequence, it does not make sense to increase the dimensionality.

In the case of problems of this kind, we can avoid forming weighting factor matrices by multiplying the expression for the recovery function by a constant multiplier of the form  $n$ , where  $n^k$  is the number of elements, and  $k$  is the difference between the new and the initial value of the dimensionality of the weighting factor relationship,  $w$ .

### 3.2.5. Effect of Zeroing of Coefficient, $w$ , on the Main Diagonal

To clearly demonstrate the work of the algorithm, we present it in an expanded form: Figure 21 shows its work with the zeroing of the main diagonal, and Figure 22 shows its work without zeroing. One sample is used in the analysis.



of this or that sample in order to analytically represent the influence of this or that sample on the recovery result.

Also, Figure 23 shows the process of reconstruction of the noisy sample. The resulting noisy image differed from the three original images, which were restored using the algorithm optimized to the third sample.

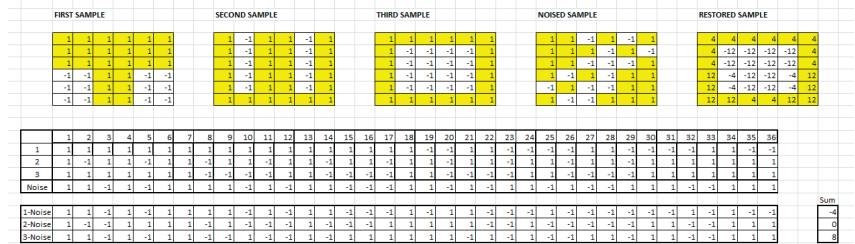


**Figure 23.** Noise reconstruction based on three samples using an optimized algorithm. **Model interpretation:** in the case of several samples, the reconstructed image will depend on the sum of products  $(a_{ij} * a_{ij}^n)$  for all three samples, and the determining influence on the element value in the cell will depend on the total correlation/anti-correlation of the original and noisy samples. In the case of a single sample, it will be recovered (either as the original or inverted original sample), depending on if the sign Sum  $(a_{ij} * a_{ij}^n)$  is in the range  $[-n, n]$  and actually describes the Pearson correlation coefficient.

**4. Conclusions**

This work presents a study of a mathematical model of a high-speed single-layer artificial neural network applied to the problems of information recovery as a result of interference of various natures—for example, as a result of the influence of electromagnetic noise during transmission and the receipt of data via analog channels, which is an urgent task in communication systems.

The formation of samples of the considered model of the neural network in order to visualize and simplify the study was implemented in the form of two-dimensional square arrays of various sizes with signal values of  $\pm 1$ . Next, the weight coefficients of interaction between individual nodes (neurons) of the samples formed for training were calculated by calculating the weight coefficients,  $w$ . After the completion of the training stage for all samples, a noisy sample was generated and further restored based on the weight coefficients,  $w$ .

The implementation and study of the described algorithm was carried out in the programming languages Python and C++, as a result of which the numerical modeling of the recovery efficiency of the described neural network was carried out for various values of the ANN parameters: (1) noise factor values, (2) the number of samples for training, (3) elements in the sample, and (4) dimensions of the coupling coefficients,  $w$ .

A study of the mathematical model of the described neural network is presented, as a result of which a number of key results were obtained:

- (1) The essence of this class of neural networks and the mechanism of influence of the original and noisy samples on the final result of information recovery in the nodes are identified.
- (2) A method has been analytically proven to improve the speed of the information recovery algorithm, which allows this operation to be carried out without the formation of an intermediate matrix of weight coefficients,  $W$ . Using a matrix-free image recovery method will allow us to move from a power exponent of the increase in the number of operations with an increase in the dimension of the coupling coefficient,  $w$ , toward multiplying the sums of products of elements of the original and noisy samples by a constant factor.

- (3) It has been proven that zeroing the weight coefficients located on the main diagonal of the matrix  $W$  worsens the result of data recovery due to the formation of artifacts on the resulting sample, which is why it is proposed to calculate them similarly to other elements.
- (4) It is proved that an increase in the dimension of the coupling coefficients,  $w$ , does not lead to an improvement in the quality of data recovery and the initial dimension of the model has an optimal value.
- (5) The calculation algorithm has been improved by eliminating matrix transposition operations by using a string representation of data.

**Author Contributions:** Conceptualization: K.K.; methodology: K.K., D.N. and K.M.; software: D.N. and K.M.; validation: K.K., D.N. and K.M.; formal analysis: K.K., D.N. and K.M.; investigation, K.K., D.N. and K.M.; resources: D.N. and K.M.; data curation: K.K., D.N. and K.M.; writing—original draft preparation: D.N.; writing—review and editing: K.K.; visualization: D.N., K.M.; supervision: K.K.; project administration: K.K.; funding acquisition, K.K. All authors have read and agreed to the published version of the manuscript.

**Funding:** This research was funded by RSF (project no. 22-71-10095).

**Data Availability Statement:** The data presented in this study are available on request from the corresponding author. The data are not publicly available due to privacy.

**Conflicts of Interest:** The authors declare no conflict of interest.

## References

1. Goodfellow, I.; Bengio, Y.; Courville, A. *Deep Learning*; MIT Press: Cambridge, MA, USA, 2016; pp. 27–54.
2. LeCun, Y.; Bengio, Y.; Hinton, G. Deep learning. *Nature* **2015**, *521*, 436–444. [CrossRef] [PubMed]
3. Schmidhuber, J. Deep Learning in Neural Networks: An Overview. *Neural Netw.* **2015**, *61*, 85–117. [CrossRef] [PubMed]
4. Krizhevsky, A.; Sutskever, I.; Hinton, G.E. ImageNet classification with deep convolutional neural networks. *Adv. Neural Inf. Process. Syst.* **2012**, *25*, 1097–1105. [CrossRef]
5. Jaderberg, M.; Mnih, V.; Marian Czarnecki, W.; Schaul, T.; Leibo, J.Z.; Silver, D.; Kavukcuoglu, K. Reinforcement Learning with Unsupervised Auxiliary Tasks. *arXiv* **2016**, arXiv:1611.05397.
6. Hieu, P.; Melody, G.; Barret, Z.; Quoc, L.; Jeff, D. Efficient Neural Architecture Search via Parameters Sharing. In Proceedings of the 35th International Conference on Machine Learning, Stockholm, Sweden, 10–15 July 2018; pp. 4095–4104.
7. Daniel, J.S. Conference on Prognostic Factors and Staging in Cancer Management: Contributions to Artificial Neural Networks and Other Statistical Methods. *Medicine* **2001**, *91*, 1589–1697.
8. Kunal, S.G.; Simon, J.; Lee, M.-Y. Special Issue: Smart Energy Technologies. *Int. J. Energy Res.* **2021**, *45*, 6–35.
9. Pao, Y.H.; Phillips, S.M.; Sobajic, D.J. Neural-net computing and the intelligent control of systems. *Int. J. Control* **1992**, *56*, 263–289. [CrossRef]
10. Li, Y. Deep Reinforcement Learning: An Overview. *arXiv* **2018**, arXiv:1701.07274.
11. Kriesel, D. Neural Networks. Available online: [https://www.dkriesel.com/\\_media/science/neuronalenetze-en-zeta2-2col-dkrieselcom.pdf](https://www.dkriesel.com/_media/science/neuronalenetze-en-zeta2-2col-dkrieselcom.pdf) (accessed on 9 June 2023).
12. Hinton, G.; Salakhutdinov, R. Reducing the Dimensionality of Data with Neural Networks. *Science* **2006**, *313*, 504–507. [CrossRef] [PubMed]
13. Charu, C. *Aggarwal, Neural Networks and Deep Learning A Textbook*; Springer: Berlin/Heidelberg, Germany, 2018; pp. 1–493.
14. Minsky, M.; Papert, S. *Perceptrons: An Introduction to Computational Geometry*; MIT Press: Cambridge, MA, USA, 1969; Volume 258, pp. 1–311.
15. Rosenblatt, F. *The Perceptron, a Perceiving and Recognizing Automaton Project Para*; Cornell Aeronautical Laboratory: Buffalo, NY, USA, 1957; pp. 1–33.
16. Stephen, J. *Neural Network Design and the Complexity of Learning, A Bradford Book*; A Bradford Book: West Yorkshire, UK, 1990; pp. 1–170.
17. Rumelhart, D.E.; Hinton, G.E.; Williams, R.J. Learning representations by back-propagating errors. *Nature* **1986**, *323*, 533–536. [CrossRef]
18. Haykin, S. *Neural Networks: A Comprehensive Foundation*; Prentice Hall: Upper Saddle River, NJ, USA, 1998; pp. 1–842.
19. Kevin, P. *Murphy, Machine Learning: A Probabilistic Perspective (Adaptive Computation and Machine Learning Series)*; The MIT Press: Cambridge, MA, USA, 2012; pp. 1–1104.

20. Géron, A. *Hands-On Machine Learning with Scikit-Learn, Keras, and TensorFlow: Concepts, Tools, and Techniques to Build Intelligent Systems*; O'Reilly Media: Sebastopol, CA, USA, 2022; pp. 1–861.
21. Kasatikov, N.N.; Brekhov, O.M.; Zhelanov, S.A. Neural network programming for pattern recognition. *Sci. Bus. Ways Dev.* **2021**, *2021*, 104–110.

**Disclaimer/Publisher's Note:** The statements, opinions and data contained in all publications are solely those of the individual author(s) and contributor(s) and not of MDPI and/or the editor(s). MDPI and/or the editor(s) disclaim responsibility for any injury to people or property resulting from any ideas, methods, instructions or products referred to in the content.

Article

# Building of a Mathematical Model for Solving the Elastic–Gas-Dynamic Task of the Gas Lubrication Theory for Petal Bearings

Sergey Surovtcev <sup>1</sup>, Elena Zadorozhnaya <sup>1,\*</sup>, Nadezhda Khozenyuk <sup>1</sup> and Oleg Mashkov <sup>2</sup>

<sup>1</sup> Department of Motor Transport, Institute of Engineering and Technology, South Ural State University, 76 Prospekt Lenina, 454080 Chelyabinsk, Russia; surovtcsv@susu.ru (S.S.); khozeniukna@susu.ru (N.K.)  
<sup>2</sup> Joint Stock Company “Special Design Bureau “Turbina”, 2-b, Prospekt Lenina, 454007 Chelyabinsk, Russia  
\* Correspondence: zadorozhnaiea@susu.ru; Tel.: +7-904-811-17-77

**Abstract:** Petal gas bearings are widely used in industrial turbine installations. However, there are practically no mathematical models that take into account the nonlinear dependence of the elastic element deformations of the gas-dynamic bearing on the pressure. It is very difficult to obtain a converged solution with a given accuracy in an acceptable time. On this basis, a mathematical model of the motion of a gas-dynamic bearing with a petals package was proposed. The model takes into account the pressure dependence of the elastic element deflections of the bearing, as well as the bearing design features and its elastic elements. A feature of solving the presented task was the joint solution of two subtasks: gas lubrication and deformations of the elastic elements of the bearing. The problem was that the contact areas of the elastic elements are not known in advance. The search for deflections or the formulation of the elasticity problem was based on the Lagrange variational principle. Petals are in the shape of thin cylindrical shells. The solution was achieved by minimizing the potential energy of the system of deformed petal shells using the first-order gradient method. The solution to the gas-dynamics problem was achieved by applying an explicit finite-difference approximation in time. To implement the proposed model, a numerical algorithm was developed to solve the related tasks of dynamics and elasticity by combining the methods of variational calculus, optimization, and an explicit finite-difference time scheme. The order of accuracy of convergence of the solution corresponded to  $10^{-5}$ . The study demonstrated that the load-carrying capability of the bearing increased by 2–4 times with an increase in the number of petals. The results of experimental studies allowed us to estimate the interval for the ascent speed of the rotor, which was used as the initial conditions for numerical modeling.

**Keywords:** elastic–gas-dynamic task; first-order gradient method; variational principle of lagrange; finite difference method; petal bearing

**MSC:** 76N15; 76M20; 70H03

**Citation:** Surovtcev, S.; Zadorozhnaya, E.; Khozenyuk, N.; Mashkov, O. Building of a Mathematical Model for Solving the Elastic–Gas-Dynamic Task of the Gas Lubrication Theory for Petal Bearings. *Mathematics* **2023**, *11*, 2901. <https://doi.org/10.3390/math11132901>

Academic Editor: Xiangmin Jiao

Received: 7 June 2023

Revised: 22 June 2023

Accepted: 27 June 2023

Published: 28 June 2023



**Copyright:** © 2023 by the authors. Licensee MDPI, Basel, Switzerland. This article is an open access article distributed under the terms and conditions of the Creative Commons Attribution (CC BY) license (<https://creativecommons.org/licenses/by/4.0/>).

## 1. Introduction

Modern turbomachine engineering demands the creation of bearings that ensure the stable, long-term rotation of a rotor at speeds of approximately 100,000 rpm and high temperatures, with large temperature differences within the rotor assembly, potential rotor imbalance, and base vibrations. Gas bearings with solid surfaces, fluid bearings, and rolling bearings are not effective under such conditions.

Initially, strip bearings were developed as a solution to create bearings with pliable surfaces. However, due to the tendency of the strips to stretch, their significant malleability, and their inability to compensate for distortions, they have not found significant application as high-speed rotor bearings.

The development of a petal gas-dynamic bearing (PGDB) that combines the idea of a bearing with a pliable surface and a bearing with self-aligning sector inserts dates back to 1963. A review of archival research focused on assessing the load characteristics quantitatively and the problem of ignoring accurate physical models in engineering practice is presented in [1]. The stages of the development of gas-lubricated support structures are discussed in more detail in [2]. Meanwhile, the current state of gas supports is considered in [3], in which deeper research and systematization of experimental data are suggested. The study in [4] provides an overview of the current state of gas bearing development in China. It highlights the application aspects of related technologies, such as coatings, production of elastic elements, and thermal regulation. The study in [5] provides an overview of various models for the study of static and dynamic characteristics, and the authors formulate the key points and useful factors for overcoming rotor instability.

The main improvement areas of PGDBs include increasing the load-bearing capacity, reducing the starting torque, improving dynamic characteristics, and increasing durability. The characteristic features of improvement are an increase in the petal layer in the package, various geometric deviations on the support nodes, and additional elastic elements.

The influence of the standard deviation and arithmetic mean deviation of the surface profile on the startup characteristics of bearings made of metal rubber-bump foil is explored in [6]. In contrast, Wang et al. [7] created a model of unsteady lubrication with mixed air and wear for non-Gaussian surfaces. This model was able to predict the wear of the foil upper surface during startup. Liu et al. [8] presented a model capable of analyzing the temperature distribution of the foil surface when the bearing was operated under conditions of ambient heat dissipation.

Unlike the previous works, [9] investigated the influence of bearing compliance, external load, acceleration time, and contact rigidity on tribological properties during startup. A transitional model taking into account the rarefaction of air was also presented in this source. The connected problem of gas-dynamics (finite volume method) and elasticity (variational approach) was solved.

Researchers created and analyzed a digital double of a thrust bearing in [10]. The research was carried out using commercial software, and the experimental stand was used to analyze the performance characteristics of a specific bearing configuration.

The authors in [11–13] describe the dynamic and static characteristics of impact-type radial bearings, to which [14–16] are devoted. Within recent studies, simplified models that take into account the influence of the support parameters on the gaps between elastic elements are presented. Investigating different configurations of radial bearings in [17], Li et al. developed a complex static structural model of a gas foil bearing with multiple sliding beams and studied the bearing characteristics. The authors then investigated the dynamic characteristics of this bearing with complex contact constraints in the following work [18]. The analysis of design features affecting the nonlinear characteristics of the rotor and its stability was carried out.

The literature review presented above shows that the dynamic characteristics of bearings made of bump film have already been adequately studied. However, these developments may not be applicable to PGDBs due to the elastic elements having a completely different structure, making it necessary to study the dynamic characteristics of such bearings for their wider application.

In this article, a mathematical model has been constructed to study the dynamic characteristics of PGDBs, with a particular focus on the nonlinear dependency present in the bearing–rotor system. The Lagrange variational principle was employed to incorporate contact mechanics into the study of petal bearing dynamics, which makes it possible to further study dynamic characteristics with complex contact constraints. Additionally, models for the perturbations of elastic elements are presented, which are nonlinearly related to the equations of the gas film and the rotor’s motion.

The novelty of this study lies in the formulation of a mathematical model for PGDBs that considers nonlinear dependencies for the first time. The first static results of a load

characteristics study for a flat bearing model are also established, whilst an experiment was conducted to study the rotor separation rate in relation to such a bearing.

## 2. Task of Calculating the Load Characteristics of Petal Bearings

The rotor maintains a constant angular velocity, with the rotation axis remaining stationary in relation to the housing. The radial load on the rotor remains constant over time and is balanced by the bearing reaction. The lubricating layer is present between the journal surface and the petals' elastic surfaces, which are either rigidly or pivotally fixed to one edge of the bush. The other edges of the petals rests freely on the adjoining petals and there are no breaks in the lubricating layer. The magnitude of the bearing reaction is equal to the main vector of the pressure forces generated in the lubricating layer during the journal's rotation. This value is called the load capacity of the bearing, and the dependence of the load capacity on the eccentricity of the journal is called the load characteristic of the PGDB.

Solving the equilibrium task involves determining the reaction value for a given equilibrium position of the rotation axis and a given angular velocity of the rotor, i.e., the load capacity. By using constructed dependencies of the load capacity on journal displacement and the angular velocity, we can determine the equilibrium position of the rotation axis at a given load on the rotor and a certain rotation speed. Additionally, we can determine whether the bearing is capable of balancing the given load on the rotor.

The elasticity task, or determining the elastic reactions of the petals that balance a given load on the rotor with a non-rotating journal, has independent significance due to the petals' reduced rigidity in the "lubricating layer—elastic shells" system. The package of petals determines the system's rigidity as a whole and the load characteristics type of the bearing. The dependence of the petals' elastic reaction on the journal displacement with a non-rotating rotor is called the static load characteristic of the bearing.

### 2.1. Initial Equations in the Pressure Task

The clearance shape in the bearing significantly determines the pressure distribution in the lubricating layer of a gas-dynamic-type bearing. In a petal bearing, one of the boundaries of the lubricating layer is deformed by the pressure developed in the layer. Finding the reactions of such a bearing requires a joint solution of the pressure task in the layer and the deformation task of the petals under pressure. This task falls into the class of elastic–gas-dynamic tasks.

The gas movement in the clearance is determined by the combined action of pressure, mass, and viscosity forces. While mass forces in the gas are relatively small, viscosity forces become significant in a thin clearance that narrows in the direction of the journal surface's relative velocity ( $\bar{V}$ ) with a sufficiently high relative velocity.

When examining the lubricant's flow within the bearing clearance, the following conditions are assumed:

1. The thickness of the lubricating layer ( $h$ ) is significantly smaller than the length of the layer ( $l$ ):

$$h/l \ll 1. \quad (1)$$

In a petal bearing, the value of  $h/l$  may be greater than in an ordinary gas-dynamic bearing, but condition (1) is still satisfied with  $h/l \cong 10^{-3} \dots 10^{-2}$ .

2. The thermal regime in the lubricating layer is isothermal. In this case, the density ( $\rho$ ) and the gas pressure ( $p$ ) are related by the equation of state through the coefficient  $k_T$ :

$$\rho = k_T \cdot p. \quad (2)$$

3. When the lubricant's flow is laminar, the forces of inertia of the lubricant can be neglected. This assumption is related to the estimation of the Reynolds number ( $Re$ )

for the layer and the assumption that the thickness of the lubricating layer changes smoothly enough:

$$Re = \rho v h^2 / \mu l_c < 1, \tag{3}$$

where  $v$  is the characteristic speed,  $\mu$  is the dynamic viscosity of the surroundings, and  $l_c$  is the layer length. Condition (3) is mostly assumed for PGDBs, but it is worth noting that local values of  $Re$  for the area taken in the vicinity of the left boundary of the layer (Figure 1) can have values of the order of one.

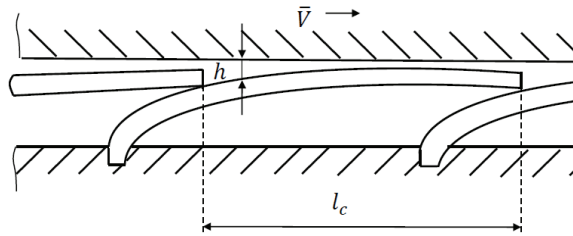


Figure 1. Bearing scheme.

Conditions (1)–(3) are commonly accepted in the gas lubrication theory. It should be noted that they are not always absolutely fulfilled in the aggregate for PGDBs.

By making assumptions (1)–(3) while considering the Navier–Stokes equation together with the continuity equation, the pressure distribution in dimensionless quantities from the Reynolds equation can be found:

$$d/d\varphi \left( h^3 p \frac{dp}{d\varphi} - \Lambda p h \right) = 0, \tag{4}$$

where  $\varphi$  is the radial coordinate,  $\Lambda$  is the compressibility parameter of the medium,  $h$  is the thickness of the lubricating layer; and  $p$  is the gas pressure.

Given that the clearance on the left border of the layer is large (in the order of the petal thickness) in a bearing with overlapping petals, the boundary conditions for pressure are taken as conditions for open borders:

$$p_B = 1. \tag{5}$$

When considering the lubricant’s flow in the bearing’s clearance, we assume that the boundary conditions (5) can contain inaccuracies that are difficult to estimate. This is because the gas flow in the boundary region at the high surface movement speeds of the journal does not strictly satisfy condition (3), so the ratio (3) may be violated and there is a drastic change in the layer thickness. Constantinescu’s results [19] suggested that during lubrication inertial effects are locally manifested in regions with sudden changes in layer thickness, which do not significantly affect the pressure distribution. It is assumed that inaccuracies in the boundary conditions (5) will affect the lubrication flow locally in marginal areas without significantly changing the pressure distribution’s integral characteristics.

2.2. Variational Approach to Solving the Elasticity Task

In the petal shell system, the conditions of the petals’ contact with the limiters of their movements are not known in advance, and the contact areas can change their positions when the journal is moving. To solve the problem of finding the equilibrium configuration of a system of elastic, deformed shells, a variational approach is required.

The petals can be treated as a system that is mechanically subordinate to one-sided connections expressed by inequalities. The system of active forces is determined by a combination of internal elastic forces and external load forces. The virtual movements,  $\delta W_I$ , of the petals’ points from the equilibrium configuration with contacts are one-sided, and the reactions of one-sided connections are co-directed with virtual movements (Figure 2).

Now the most common principle of balance of a mechanical system must be considered—the principle of virtual displacements for systems with one-way connections.

For the  $l$ -th petal:

$\delta A_l^{elast}$  is the virtual operation of elastic forces, and  $\delta A_l^n$  ( $n = 2$ ) is the virtual operation of the specified load forces to be determined.

In accordance with the principle of virtual displacements from an equilibrium configuration, it is necessary and sufficient to require the fulfillment of the condition:

$$\delta A_l^{elast} + \delta A_l^n \leq 0 \tag{6}$$

for one-way virtual displacements in the area with contacts, and the condition:

$$\delta A_l^{elast} + \delta A_l^n = 0 \tag{7}$$

in the area without contacts.

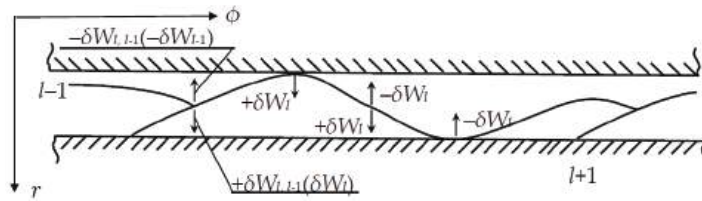


Figure 2. Movements of the petals.

To define the potential energy, virtual differentials of potential deformation energy ( $\delta E_{def.l}$ ) and potential load energy ( $\delta E_l^n$ ) are introduced:

$$\delta E_{def.l} = -\delta A_l^{elast}, \tag{8}$$

$$\delta E_l^n = -\delta A_l^n. \tag{9}$$

When solving the elasticity task, the load is considered independent of the desired deflections. So, the external forces in the considered equilibrium task are potential. The following equation is introduced:

$$\delta E_{def.l} + \delta E_l^n = \delta (E_{def.l} + E_l^n) = \delta E_l, \tag{10}$$

where  $E_l$  is the total potential energy of the petal.

The virtual displacement principle conditions (6) and (7) can be expressed as equation:

$$\delta E_l \geq 0, \tag{11}$$

for one-way virtual displacements on contacts, and equation

$$\delta E_l = 0, \tag{12}$$

for two-way virtual displacements in an open area (without contacts). In Equations (11) and (12)  $\delta E_l$  represents the variation of the potential energy when the petal moves from the equilibrium configuration to the adjoining one, allowed by connections.

The elastic contact of adjoining petals  $l$  and  $l - 1$  (Figure 2) can occur as either one-way virtual movements,  $\delta W_l, \delta W_{l-1}$ , where the condition must be met for each of the petals (11), or as two-sided joint variations,  $\pm \delta W_{l,l-1}$ , which are assumed during elastic contact. In the equilibrium deformed configuration of the petal shell system, the potential energy of the system must be stationary, which is equal to the sum of the potential energies of the petals:

$$\delta E = \delta \left( \sum_{l=1}^n E_l \right) = 0. \tag{13}$$

It was proven in previous work [20] that for a linearly elastic body with retaining limitations, the second variation of the potential energy is  $\delta^2 E \geq 0$ .

The equilibrium configuration can be obtained using the Lagrange principle, which states that for an elastic body system constrained by limitations (contact task), the system’s potential energy must reach its lowest value in the range of acceptable connections of elastic displacements for a particular configuration to be balanced in the task.

### 3. Calculation of the Load Capacity of the Petal Gas-Dynamic Bearing

In this study, the following assumptions were made:

1. The petal is a thin elastic cylindrical shell, for which the Kirchhoff–Love hypotheses are valid;
2. The median line of the petal is inextensible;
3. Elastic displacements of the petal are considered small, and the deflection problem is viewed as geometrically linear;
4. The surfaces limiting the elastic displacements of the petals (the surfaces of the shaft and the bushing) are smooth and absolutely rigid;
5. The axis of the pin is parallel to the bearing axis;
6. The gas layer is thin, inertia-less, isothermal, continuous, and laminar.

#### 3.1. Bearing Geometry

The task of determining the load-carrying capability of a bearing of finite dimensions was considered. A cylindrical coordinate system,  $O\varphi z$ , was introduced in reference to the bearing’s bushing (Figure 3). The median surface ( $r_0$ ) of the undeformed petal is described by the following relationship:

$$r_0 = r_0(\varphi, z). \tag{14}$$

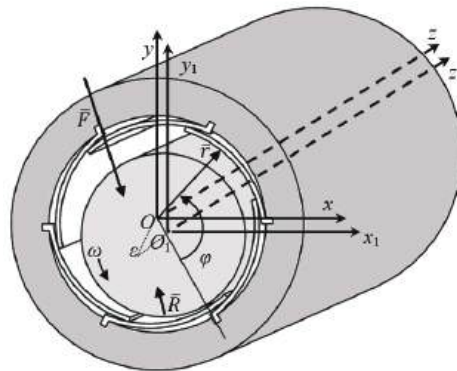


Figure 3. Diagram of the radial bearing with a package of  $n$  petals.

Moreover, the ratios are fair:

$$|\partial r_0 / \partial z| \ll 1; |\partial r_0 / \partial \varphi| \ll r_0. \tag{15}$$

If conditions (15) are met, the Lamé coefficients of the median surface can be represented as:

$$A_\varphi = \sqrt{r_0^2 + (\partial r_0 / \partial \varphi)^2} \cong r_0(\varphi, z); A_z = \sqrt{1^2 + (\partial r_0 / \partial z)^2} \cong 1. \tag{16}$$

It also follows from conditions (15) that for a point arbitrarily taken on the median surface of the lobe, the angle ( $\gamma$ ) between the normal to the surface ( $\vec{n}$ ) and the radius vector ( $\vec{r}_B$ ) drawn to this point is small. Assuming that the normal movements of the median

surface of the petal,  $W(\varphi, z)$ , coincide with the radius vector ( $\bar{r}_B$ ), then the equation of the deformed surface can be expressed as:

$$r(\varphi, z) = r_0(\varphi, z) + W(\varphi, z). \tag{17}$$

For the deformed median surface of the petal, the normal to the median surface and the radius vector ( $\bar{r}_B$ ) are also considered to coincide for any point on the petal surface.

3.2. The System of Restrictions for Deflections

The geometric relations in the bearing naturally determine the restriction system for deflections, with the following conditions:

1. Clearance,  $H(\varphi, z)$ , between the surfaces of the journal and the petal is given by:

$$H(\varphi, z) = r_0(\varphi, z) + W(\varphi, z) - 0.5\delta - R_j - e(\varphi, z) \geq H_{min}, \tag{18}$$

where  $\delta$  is the petal thickness,  $R_j$  is the radius of the journal (shaft), and  $e$  is the eccentricity of the journal displacement.

2. No cutting into the surface of the bearing bushing:

$$R_B - 0.5\delta - r_0(\varphi, z) - W(\varphi, z) \geq 0, \tag{19}$$

where  $R_B$  is the bearing bushing radius.

3. Mutual non-penetration of the surfaces of adjoining petals  $l, l'$ :

$$r_{0l}(\varphi_l, z) + W_l(\varphi_l, z) - \delta - r_{0l'}(\varphi_{l'}, z) - W_{l'}(\varphi_{l'}, z) \geq 0 \tag{20}$$

From conditions (18) and (19), the following restriction system on deflections is obtained:

$$W^- \leq W \leq W^+ \tag{21}$$

where

$$W_l^- (\varphi_l, z) = \begin{cases} R_j + e(\varphi_l, z) + h_{min} + 0.5\delta_0 - r_0(\varphi_l, z), & \varphi_l \in [\varphi_3; \varphi_1] \\ R_j + e(\varphi_l, z) + h_{min} + 1.5\delta_0 - r_0(\varphi_l, z), & \varphi_l \in [0; \varphi_3] \end{cases}, \tag{22a}$$

$$W_l^+ (\varphi_l, z) = \begin{cases} R_j - 0.5\delta_0 - r_0(\varphi_l, z), & \varphi_l \in [0; \varphi_2] \\ R_j - 1.5\delta_0 - r_0(\varphi_l, z), & \varphi_l \in [\varphi_2; \varphi_1] \end{cases}, \tag{22b}$$

$\delta_0$  is the petal thickness without coating,  $\varphi_1$  is the petal angle,  $\varphi_2$  is the angle from the overlap point of  $l - 1$  petal and  $l + 1$ , and  $\varphi_3$  is the petal  $l - 1$  overlap angle of petal  $l$ .

Expressions (20)–(22) define the geometric limitation system on the petal deflections.

3.3. Boundary Conditions for Deflections

In the  $\varphi, z$  coordinate plane, the petal occupies an area of  $S$  with border  $C = \sum_{i=1}^4 C_i$  (Figure 4).

The boundary conditions on the petal contour can be defined as:

- (a) on the line  $C_4$  attachment of the petal with the bushing

$$W_l (0, z) = 0, \tag{23}$$

with the rigid attachment

$$\partial W_l(0, z) / \partial \varphi = 0, \tag{24}$$

with the hinge mount for bending moment

$$M_\varphi = D(\chi_\varphi + \nu\chi_z) = 0, \tag{25}$$

where  $\nu$  is Poisson’s ratio.

(b) on line  $C_1, C_3$  for bending moments

$$M_z = D(\chi_\varphi + \nu\chi_z)|_{z=0} = 0. \tag{26}$$

$$z = L$$

(c) on line  $C_2$  for leaning edge

$$M_\varphi = D(\chi_\varphi + \nu\chi_z) = 0. \tag{27}$$

It follows from (23) that for the petal attachment line  $C_4$

$$W''_{zz} = 0. \tag{28}$$

For line  $C_1, C_3$  from (26) the following is obtained

$$\chi_z = -\nu\chi_\varphi. \tag{29}$$

In points  $K_1 = C_1 \cap C_4; K_4 = C_3 \cap C_4$

$$\chi_\varphi = 0. \tag{30}$$

For line  $C_2$  condition (27) is satisfied and, therefore

$$\chi_\varphi = -\nu\chi_z. \tag{31}$$

For points  $K_3 = C_2 \cap C_3; K_2 = C_1 \cap C_2$  from (25), (29), the following is obtained

$$\chi_\varphi = 0; \chi_z = 0. \tag{32}$$

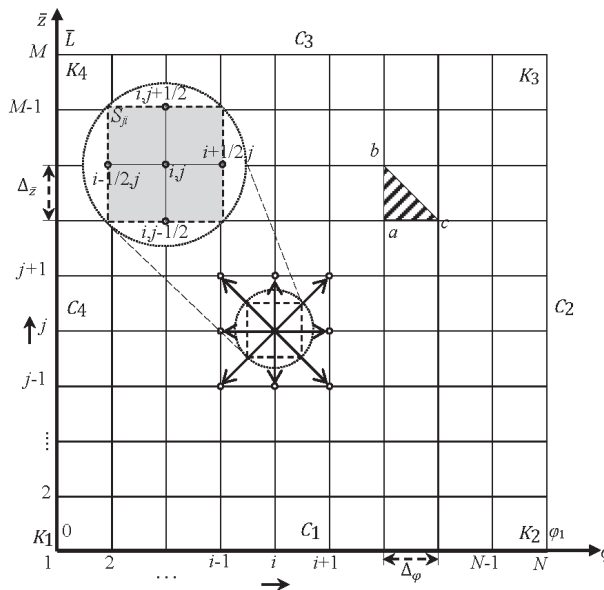


Figure 4. Division of the petal with a grid.

### 3.4. Potential Energy of the Petals Package

Considering the petal as a thin ( $\delta/L \leq 0.01$ ), linearly elastic shell with constant thickness, for which the Kirchhoff–Love hypotheses are accepted, an inaccuracy of the

order  $(\delta/L)$  can be introduced, where  $L$  is a minimum linear size of the median surface. In this case, the deformation energy of the shell bending is equal to:

$$E_{def} = D/2 \iint_S [(\chi_\varphi + \chi_z)^2 - 2(1 - \nu)(\chi_\varphi\chi_z - \chi_{\varphi z}^2)] A_\varphi A_z d\varphi dz, \tag{33}$$

where

$$\chi_\varphi = 1/A_\varphi \partial/\partial\varphi (-1/A_\varphi \partial W/\partial\varphi - U/R_\varphi); \chi_z = 1/A_z \partial/\partial z (V/R_z - 1/A_z \partial W/\partial z); \tag{34a}$$

$$\chi_{\varphi z} = 1/2 [A_z/A_\varphi \partial/\partial\varphi (1/A_z (-1/A_z \partial W/\partial z)) + A_\varphi/A_z \partial/\partial z (1/A_\varphi (U/R_z - 1/A_\varphi \partial W/\partial\varphi))], \tag{34b}$$

$1/R_z$  and  $1/R_\varphi$  are the main curvatures of the median surface, and  $U$  and  $V$  are the velocities in the directions  $\varphi$  and  $z$ , accordingly.

Moreover

$$1/R_z \rightarrow 0. \tag{35}$$

Considering the condition of inextensibility of the median surface as

$$1/A_\varphi \partial U/\partial\varphi + W/R_\varphi = 0, \tag{36}$$

the following is obtained

$$\partial U/\partial\varphi = -A_\varphi/R_\varphi W \tag{37}$$

and considering the conditions (16), the following is obtained

$$\chi_\varphi = -(1/r_0^2 \partial^2 W/\partial^2 \varphi + W/R_\varphi^2); \chi_z = -\partial^2 W/\partial z^2; \chi_{\varphi z} = -1/r_0 \partial^2 W/\partial\varphi \partial z. \tag{38}$$

Substituting (38) into (33),  $E_f$  for the system of petal can be found

$$E_f = D/2 \sum_{l=1}^n \iint_S [(1/r_0^2 \partial^2 W_l/\partial\varphi^2 + W_l/R_n^2 + \partial^2 W_l/\partial z^2)^2 - 2(1 - \nu) ((1/r_0^2 \partial^2 W_l/\partial\varphi^2 + W_l/R_n^2) \partial^2 W_l/\partial z^2 - 1/r_0^2 (\partial^2 W_l/\partial z^2)^2)] r_0 \varphi dz, \tag{39}$$

where  $\nu$  is the Poisson's ratio of the petal material.

The external load for the shell system is the excess pressure,  $Q(\varphi, z)$ , the potential of which is equal to:

$$E_P = -\sum_{l=1}^n \iint_F Q_l W_l r_0 d\varphi dz, \tag{40}$$

where  $Q_l = p_l - p_a$  is the excess pressure of the lubricating layer of petal  $l$ ;  $p_l$  is the pressure in the lubricating layer of petal  $l$ ; and  $p_a$  is the ambient pressure.

The potential energy of the shell system is equal to the sum of the bending deformation energy ( $E_f$ ) (39) and the potential of the external load ( $E_P$ ) (40):

$$E = E_P + E_f. \tag{41}$$

### 3.5. Approximation of the Potential Energy

The expression of the potential energy ( $E$ ) (41) in dimensionless quantities is given by:

$$\bar{E} = E/p_n H^* R_j^2 \tag{42}$$

where  $H^*$  is the montage clearance.

In the area  $S = (0; \varphi_1) \times (0; L)$  where petal coordinates  $\varphi, z$  change, a grid  $\omega_{\varphi z}$  is introduced:

$$\omega_{\varphi z} = \begin{cases} \varphi_i = (i - 1) \cdot \Delta_\varphi, & \Delta_\varphi = \varphi_l/N - 1; i = \overline{1, N}, \\ z_j = (j - 1) \cdot \Delta_z, & \Delta_z = \bar{L}_n/M - 1; j = \overline{1, M}, \end{cases} \tag{43}$$

where  $\bar{L}_n = L/R_j$  is the dimensionless length of the bearing bushing.

Integration is carried out on triangular elements  $abc$  (Figure 4). On the selected element, the integrand function ( $f_{ji}$ ) is approximated by a plane that passes through the relevant nodal points:

$$\iint_{S_{\Delta abc}} f(\varphi, z) d\varphi dz = \Delta_\varphi \Delta_z / 6 (f(a) + f(b) + f(c)) + \bar{O} (\Delta_\varphi^2 + \Delta_z^2), \tag{44}$$

where  $f(a)$ ,  $f(b)$ , and  $f(c)$  are values of the function at the vertices of the triangle  $abc$  (Figure 4).

Using (44), the potential energy ( $\bar{E}$ ) can be replaced with finite-difference analog  $\{\bar{E}\}$ :

$$\bar{E} \cong \{\bar{E}\} = \sum_{l=1}^n \{\bar{E}\}_l = \sum_{l=1}^n \sum_{j=1}^M \sum_{i=1}^N \lambda_{ji} f_{ji} \tag{45}$$

where  $\lambda_{ji} = \begin{cases} 2, & \text{when } i = 1 : j = 1, j = M; j = j_c \\ 1, & \text{when } i = N : j = 1, j = M; \\ 4, & \text{when } i = N; j = j_c; \\ 6, & \text{when } 2 \leq i \leq N - 1, 2 \leq j \leq M - 1; \\ 3, & \text{in other cases.} \end{cases}, j_c \text{ is petal symmetry line.}$

$$f_{ji} = r_{oji} (\bar{D} / 2 [(a_{ji} + b_{ji})^2 - 2(1 - \nu)(a_{ji} \cdot b_{ji} - c_{ji}^2)] - q_{ji} W_{ji}), \tag{46}$$

where  $\bar{D} = DH^* / p_a R_j^4$  is the dimensionless coefficient of cylindrical rigidity,  $D = E_y \delta_0^3 / 12(1 - \nu^2)$  is the coefficient of cylindrical rigidity of the petal,  $E_y$  is Young's modulus (modulus of elasticity) of the petal material, and

$$c_{ji} = \begin{cases} \begin{cases} W_{j+i+1} - W_{j+i-1} - W_{j-1+i} + W_{j-1-i} / 4\Delta_\varphi \Delta_z, & \left| \begin{array}{l} j = \overline{2, M-1} \\ i = \overline{2, N-1}' \end{array} \right. \\ W_{j+i+1} - W_{j+i-1} - W_{j+1} + W_{j-1} / r_{oji} \cdot 2\Delta_\varphi \Delta_z, & \left| \begin{array}{l} j = 1 \\ i = \overline{2, N-1}' \end{array} \right. \\ W_{j+i+1} - W_{j-1} - W_{j-1+i} + W_{j-1-i} / r_{oji} \cdot 2\Delta_\varphi \Delta_z, & \left| \begin{array}{l} j = M \\ i = \overline{2, N-1}' \end{array} \right. \\ W_{j+i+1} - W_{j-1+i} / r_{oji} \cdot 2\Delta_\varphi \Delta_z, & \left| \begin{array}{l} j = \overline{2, M-1} \\ i = 1 \end{array} \right. \text{ (hinging} \\ & \text{mounting)} \\ 0, & i = 1 \text{ (rigid mounting)}; \\ W_{j+i+1} - W_{j+1} / r_{oji} \cdot \Delta_\varphi \Delta_z, & \left| \begin{array}{l} j = 1 \\ i = 1' \end{array} \right. \\ W_{j+i} - W_{j+i-1} - W_{j+1} + W_{j-1} / r_{oji} \cdot \Delta_\varphi \Delta_z, & \left| \begin{array}{l} j = 1 \\ i = N' \end{array} \right. \\ W_{j+1} - W_{j-1+i} / r_{oji} \cdot \Delta_\varphi \Delta_z, & \left| \begin{array}{l} j = M \\ i = 1' \end{array} \right. \\ W_{ji} - W_{j-1} - W_{j-1} + W_{j-1-i} / r_{oji} \cdot \Delta_\varphi \Delta_z, & \left| \begin{array}{l} j = M \\ i = N' \end{array} \right. \end{cases} \end{cases} \tag{47}$$

$$b_{ji} = \begin{cases} \begin{cases} W_{j-1} - 2W_{ji} + W_{j+1} / \Delta_z^2, & \left| \begin{array}{l} j = \overline{2, M-1} \\ i = \overline{2, N-1}' \end{array} \right. \\ 0, & i = 1, \left| \begin{array}{l} j = 1 \\ i = 1' \end{array} \right. \left| \begin{array}{l} j = M \\ i = 1' \end{array} \right. \\ -\nu a_{ji}, & j = 1, \left| \begin{array}{l} j = M \\ i = \overline{2, N-1}' \end{array} \right. \end{cases} \end{cases} \tag{48}$$

$$a_{ji} = \begin{cases} W_{j,i-1} - 2W_{ji} + W_{j,i+1}/r_{\sigma ji}^2 \Delta \varphi^2 + W_{ji}/R_{\sigma}^2, & \left. \begin{matrix} j = \overline{1, M} \\ i = \overline{2, N-1} \end{matrix} \right\} \\ 0, & \left. \begin{matrix} i = N, & \left. \begin{matrix} j = 1 & | & j = M \\ i = 1' & | & i = 1' \end{matrix} \right\} \end{matrix} \right\} \text{(hinging mounting)} \\ -\nu b_{ji}, & \left. \begin{matrix} j = \overline{2, M-1} \\ i = N \end{matrix} \right\} \\ 8W_{j2} - W_{j3}/r_{\sigma ji}^2 \cdot 2\Delta \varphi^2, & \left. \begin{matrix} j = \overline{2, M-1} \\ i = 1 \text{ (rigid mounting)} \end{matrix} \right\} \end{cases} \quad (49)$$

Obviously, for any node  $j, i$  there is some finite set of nodes  $\{g, e\}$ , for which  $f_{g,e} = f_{g,e}(W_{ji})$ . This set of nodes forms a 9-point pattern.

Considering the selected areas of influence, the values of gradients at the nodes of variation are determined by:

$$\partial l / \partial W_{ji} = \sum_g \sum_e \lambda_{ge} \partial f_{ge} / \partial W_{ji}, \quad (50)$$

where

$$\partial f_{ge} / \partial W_{ji} = \bar{D} / 2r_{0ge} [2(a_{ge} + b_{ge})(\partial a_{ge} / \partial W_{ji} + \partial b_{ge} / \partial W_{ji}) - 2(1 - \nu)(b_{ge} \partial a_{ge} / \partial W_{ji} + a_{ge} \partial b_{ge} / \partial W_{ji}) - 2c_{ge} \partial c_{ge} / \partial W_{ji}] - \partial / \partial W_{ji} (q_{ge} W_{ge} r_{0ge}).$$

The task of determining the equilibrium deformed configuration for the petal shell system is posed as the task of determining the smallest value (infE) of the shell system’s potential energy under known limitations (18)–(22) and the given external load.

### 3.6. Calculation of the Pressure in the Lubricating Layer

To determine the stationary pressure distribution in the lubricating layer, the idea of calculating the time setting was used. The equation for the pressure distribution in a non-stationary form can be written as:

$$\partial / \partial \varphi \left( h^3 p \frac{\partial p}{\partial \varphi} - \Lambda p h \right) + \partial / \partial z \left( h^3 p \frac{\partial p}{\partial z} \right) = \partial (ph) / \partial t, \quad (51)$$

where the boundary conditions for the pressure of the open boundaries layer are:

$$p(\varphi = 0, z) = p(\varphi = \varphi_1, z) = p(\varphi, z = 0) = p(\varphi, z = L) = 1. \quad (52)$$

It is indicated that

$$U_\varphi = h^3 p \frac{\partial p}{\partial \varphi} - \Lambda p h, \quad U_z = h^3 p \frac{\partial p}{\partial z} \quad (53)$$

For an arbitrary internal node  $i, j$  of a grid  $\omega_{\varphi z}$  an area  $S_{ji} : [\varphi_{i-1/2}; \varphi_{i+1/2}] \times [z_{j-1/2}; z_{j+1/2}]$  is selected, within which Equation (51) is integrated, taking into account (53):

$$\int_{\varphi_{i-1/2}}^{\varphi_{i+1/2}} \int_{z_{j-1/2}}^{z_{j+1/2}} (\partial U_\varphi / \partial \varphi + \partial U_z / \partial z) d\varphi dz = \int_{\varphi_{i-1/2}}^{\varphi_{i+1/2}} \int_{z_{j-1/2}}^{z_{j+1/2}} \partial (hp) / \partial t d\varphi dz. \quad (54)$$

In the left part of Equation (54), using Green’s formula, it is proceeded to the contour integral and, taking into account the specified bypass direction (Figure 4), the following is obtained:

$$\int_{\varphi_{i-1/2}}^{\varphi_{i+1/2}} \int_{z_{j-1/2}}^{z_{j+1/2}} (\partial U_\varphi / \partial \varphi + \partial U_z / \partial z) d\varphi dz = \oint U_\varphi dz - U_z d\varphi \quad (55a)$$

$$\oint U_\varphi dz - U_z d\varphi = \left( \{U_\varphi\}_{j,i+1/2} - \{U_\varphi\}_{j,i-1/2} \right) \Delta z + \left( \{U_z\}_{j+1/2,i} - \{U_z\}_{j-1/2,i} \right) \Delta \varphi \quad (55b)$$

where

$$\{U_\varphi\}_{j,i,\pm 1/2} = h_{j,i,\pm 1}^3 p_{j,i,\pm 1} + h_{j,i}^3 p_{j,i}/2 \cdot p_{j,i,\pm 1} - p_{j,i}/\Delta_\varphi - \Delta p_{j,i,\pm 1} h_{j,i+1} + p_{j,i} h_{j,i}/2, \tag{56a}$$

$$\{U_z\}_{j,\pm 1/2,i} = h_{j,\pm 1,i}^3 p_{j,\pm 1,i} + h_{j,i}^3 p_{j,i}/2 \cdot p_{j,\pm 1,i} - p_{j,i}/\Delta_z. \tag{56b}$$

The right part of Equation (54) is approximated by the expression:

$$\int_{\varphi_{i-1/2}}^{\varphi_{i+1/2}} \int_{z_{j-1/2}}^{z_{j+1/2}} \partial(hp)/\partial t \, d\varphi dz = \Delta_\varphi \Delta_z h_{j,i} p_{j,i}^{k+1} - p_{j,i}^k / \Delta_t, \tag{57}$$

where  $k$ —is the layer number by time.

Referring the left part of Equation (54) to the  $k$ -th time layer, an explicit scheme for integrating the equation in time (51) is obtained:

$$h_{j,i} p_{j,i}^{k+1} - p_{j,i}^k / \Delta_t = \{U_\varphi\}_{j,i+1/2}^k - \{U_\varphi\}_{j,i-1/2}^k / \Delta_\varphi + \{U_z\}_{j+1/2,i}^k - \{U_z\}_{j-1/2,i}^k / \Delta_z, \tag{58}$$

with the approximation order  $O\left(\Delta_\varphi^2 + \Delta_z^2 + \Delta_t\right)$ . Scheme (58) is explicit because  $p_{j,i}^{k+1}$  are expressed explicitly through  $p_{j,i}^k$ .

The stability of the scheme is guaranteed by the choice of the step  $\Delta_t$ :

$$\Delta_t \leq 1/2 (ph^2)_{\max}^{(1/\Delta_\varphi^2 + 1/\Delta_z^2)}, \tag{59}$$

where  $(ph^2)_{\max} = (R_B - R_j - \delta) / H^*$  is achieved at the inlet to the lubricating layer at  $\varphi = \varphi_3$ .

The stability analysis of the scheme in accordance with  $\Delta_t$  was conducted on a grid,  $\omega_{\varphi z}$ , while varying the parameters (43)  $N \times M = 17 \times 11 \dots 35 \times 30$ . The scheme achieved stable convergence when the values of  $N \times M = 24 \times 17$  were reached.

According to the described methodology, an algorithm was developed (Figure 5) for solving a joint elastic–gas-dynamic task:

1. Input of initial data and calculation parameters of the structure.
2. Construction of input values of pressure distribution and deflections.
3. Determination of the equilibrium configuration of the deformed petals package.
4. Based on the obtained deflection distribution, the clearance value is determined, according to which the pressure distribution  $p^{(k+1)}$  is determined.
5. Determination of  $W^{(k+1)}(p^{(k+1)})$  and  $h^{k+1}(W^{(k+1)})$ .
6. Checking the convergence condition:

$$|p^{(k+1)} - p^{(k)} / p^{(k+1)}| < \varepsilon, \tag{60}$$

at which the iterative process ends.

7. If condition (60) is not met, then the pressure distribution relaxation procedure is performed:  $p^{(k+2)} = a \cdot p^{(k+1)} + (1 - a) \cdot p^{(k)}$ , followed by step 3.

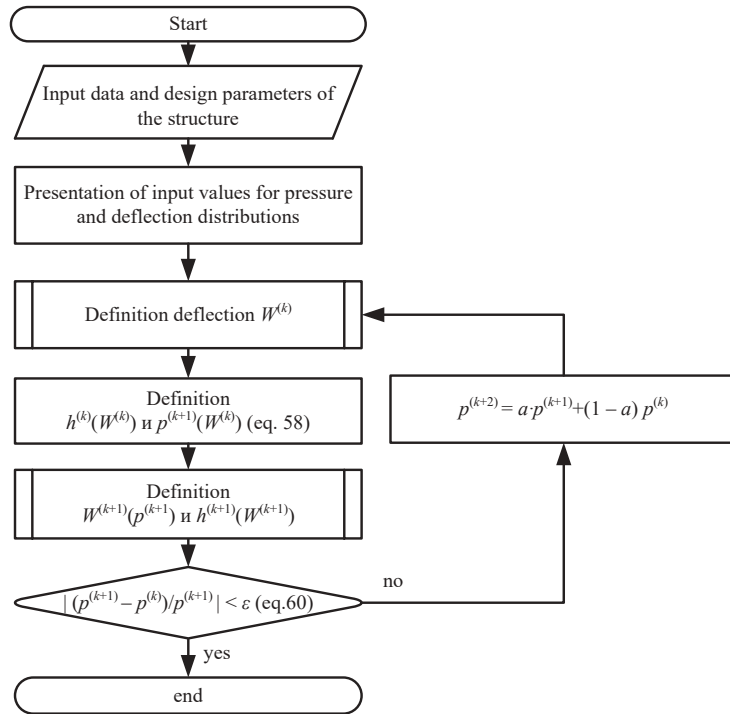


Figure 5. Scheme of the algorithm for solving the elastic–gas-dynamic task.

To accelerate the convergence of the iterative “pressure–deflection” process at the given journal position, a relaxation technique can be used to determine the deflections:

$$W_{in}^{n+1} = (1 - \alpha) \cdot W_{in}^n + \alpha \cdot W_{out}^n, \tag{61}$$

where  $W_{in}$  is the input deflection value,  $W_{out}$  is the output deflection value,  $n$  is an iteration number, and  $\alpha$  is the relaxation coefficient (different from the pressure relaxation coefficient).

### 3.7. Load Capacity of the Bearing and the Task of Dynamics

The projections  $(F_x, F_y)$  of the main vector of excess pressure forces acting on the journal are defined by:

$$\begin{bmatrix} F_x \\ F_y \end{bmatrix} = \sum_{l=1}^n \int_0^L \int_{\varphi_3}^{\varphi_1} R_j Q_l \begin{bmatrix} \sin(\varphi_2(l-1) + \varphi_0 - \varphi) \\ \cos(\varphi_2(l-1) + \varphi_0 - \varphi) \end{bmatrix} d\varphi dz. \tag{62}$$

Using an approximation (44) and the grid  $\omega_{\varphi z}$ , the following is obtained in dimensionless quantities:

$$\begin{bmatrix} F_x \\ F_y \end{bmatrix} = p_a R_j^2 \Delta_\varphi \Delta_z / 6 \sum_{l=1}^n \sum_{j=1}^M \sum_{i=1}^N \lambda_{ji} Q_{lji} \begin{bmatrix} \sin(\varphi_2(l-1) + \varphi_0 - \varphi) \\ \cos(\varphi_2(l-1) + \varphi_0 - \varphi) \end{bmatrix}. \tag{63}$$

The module of the main vector of pressure forces (load characteristic):

$$F = \sqrt{F_x^2 + F_y^2}. \tag{64}$$

The angle of the journal position

$$\beta = \arctg F_x / F_y. \tag{65}$$

To determine the trajectory of the journal center, the equation for calculating the dynamic characteristics can be presented as a system of equations in dimensionless form obtained by projecting the corresponding forces on the coordinate axes  $x_1$  and  $y_1$  (Figure 3):

$$\begin{cases} \bar{m} \ddot{\bar{x}}(t) = \bar{R}_x + \bar{F}(t)\omega^2 \sin(\omega t), \\ \bar{m} \ddot{\bar{y}}(t) = \bar{R}_y + \bar{F}(t)\omega^2 \cos(\omega t) - \bar{C}, \end{cases} \tag{66}$$

where  $\bar{m} = m\omega^2 H^* / 2p_a L R_j$  is the dimensionless mass of the rotor;  $\bar{x} = x / H^*$ ,  $\bar{y} = y / H^*$  are dimensionless coordinates of the center of the journal;  $\bar{R} = \vec{R} / 2p_a L R_j$ ,  $\bar{R}_x$ ,  $\bar{R}_y$  are dimensionless projections of the reaction force of the lubricating layer;  $\bar{F} = \vec{F}(t) / 2p_a L R_j$  is the dimensionless external force acting on the journal; and  $\bar{C} = mg / 2p_a L R_j$  is the dimensionless gravity of the rotor directed in the opposite direction of the  $Oy$  axis.

3.8. Implementation of the Mathematical Model

At the initial stage, the considered spatial mathematical model (in the space  $\mathbb{R}^3$ ) was reduced to a flat model in the space  $\mathbb{R}^2$ . The considered flat bearing model had parameters:  $R_j = 25$  mm;  $\bar{R}_p = 1.6$ ;  $\delta = 0.176$  mm;  $L = 50$  mm;  $\bar{l} = 1.8$ ;  $H^* = 1$  mm; and  $\omega = 8000, c^{-1}$ .

At the first stage of numerical modeling, an unloaded bearing was studied with the journal in a central position ( $e = 0$ ), while varying the number of petals  $n = 6, 8, 10$ . Pressure values (Figure 6) and the thickness of the lubricating layer (Figure 7) were determined in the region of radial angle variation  $\varphi_3 \leq \varphi \leq \varphi_1$  (area without overlap between petal  $l$  and previous petal  $l - 1$ ).

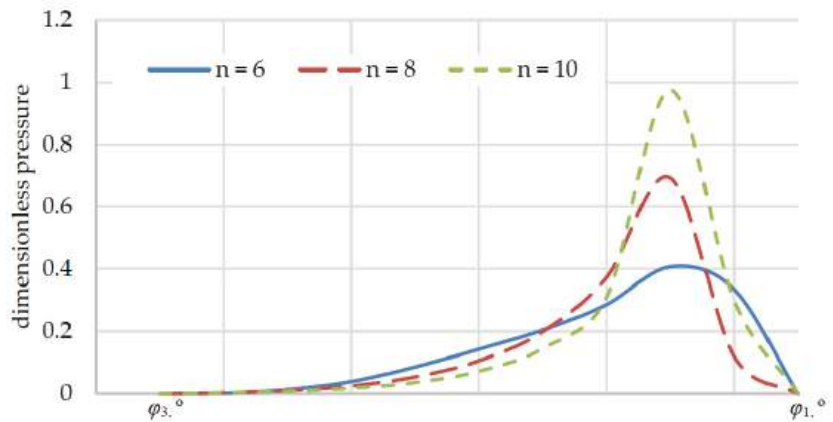


Figure 6. Distribution of dimensionless pressure over the bearing area of the petal.

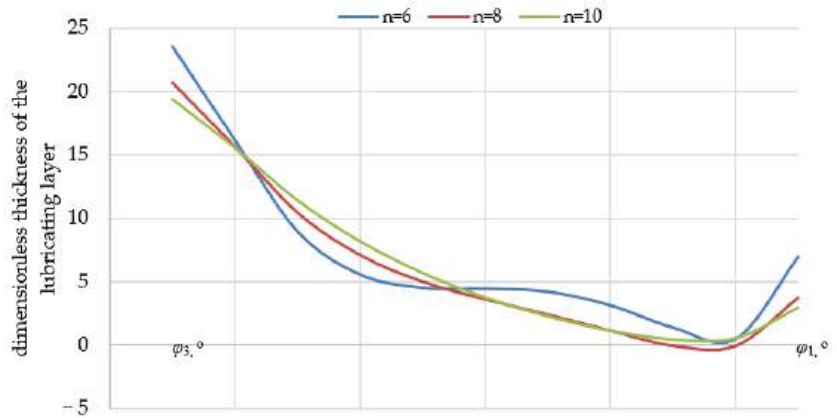


Figure 7. Distribution of the dimensionless thickness of the lubricating layer.

Additionally, with a different number of petals ( $n$ ), the dependence of the load capacity ( $F$ ) of the bearing on the eccentricity of the shaft ( $e$ ) was obtained (Figure 8).

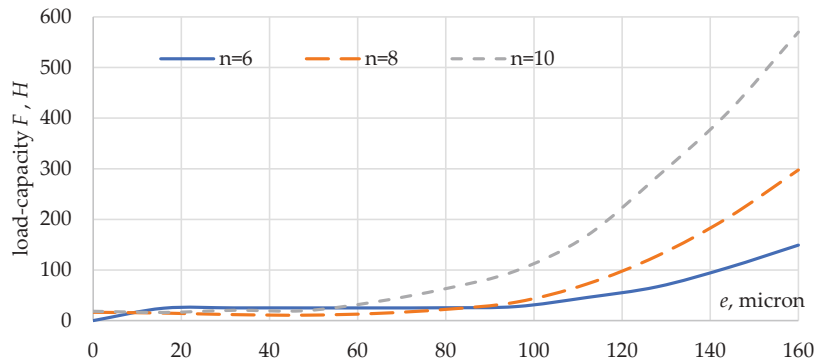


Figure 8. Dependence of load characteristics on eccentricity ( $e$ ).

Based on the results, it could be concluded that increasing the number of petals ( $n$ ) in the package from 6 to 10 led to almost a two-fold increase in the load characteristic value.

The methodology presented in this article had several advantages, including fast convergence, no need for high computational capabilities (a PC was sufficient), and a calculation accuracy of  $10^{-5}$ . A further increase in accuracy did not lead to an improvement in results.

This methodology can be used to optimize parametric studies of PGDB load characteristics.

The described technique and obtained results were used to estimate the rate of ascent of the bearing in the PGDB for various levels of shaft loading.

#### 4. Experimental Studies

The shaft ascent rate was studied in order to obtain the experimental characteristics of the bearing–rotor system. The experiment was carried out on the installation (Figure 9), that was developed at SCB “Turbina”. The gas-dynamic bearing was operated at the critical rotor speed while maintaining specific parameters: the outer radius of the bushing was 36.5 mm; the inner radius of the bearing bushing was 28.975 mm; the bearing length was 76 mm; the radius of the bending petals was 45 mm; the thickness of the petal was 0.15 mm; and the coating of the petals was 12...20 microns.

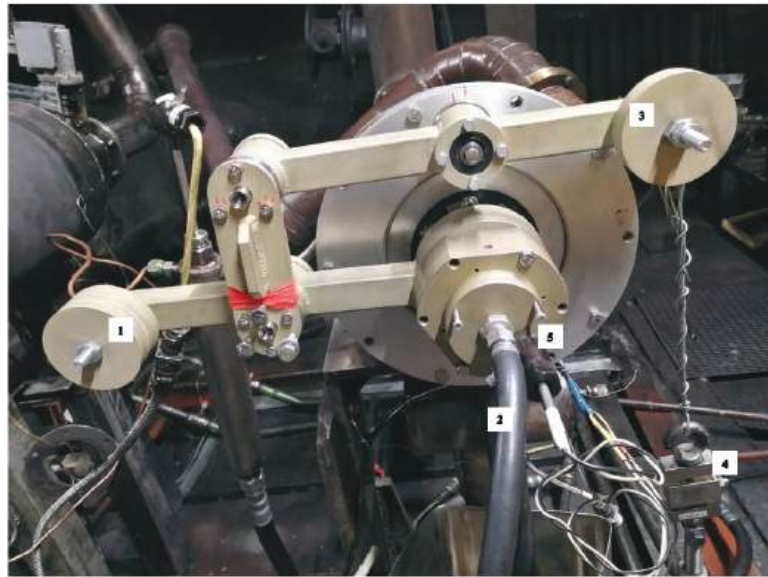


**Figure 9.** Appearance of the test installation of gas-dynamic bearings.

The installation setup (Figure 9) involved a turbocharger shaft equipped with a PGDB, which was fitted with a biaxial structure weighing 5661 kg along with adjustable masses  $m_1$  and  $m_2$ , fixed to the pins (1, 3) of the turbine (2) and on the bearing bushing. A speed sensor (5) and an air-cooling system ( $P = 2.84$  kPa) were also connected to the structure. The strain gauge force sensor (4) was connected to a pin with mass  $m_2$ .

Initially, the PGDB “lay” on the shaft driven by an axial rolling bearing. By increasing the rotor speed, an air wedge effect was created in the bearing causing it to “emerge”, thus creating an air clearance between the shaft surface and the petals package. At the moment of ascent, the force sensor (4) showed the maximum (peak) value.

During the experiments, the number of loads fixed on pins (1) and (3) changed. After loading, the shaft was accelerated with an increase in the number of rotations to 30,000 rpm. Each experiment included several parallel experiments. The results of the experiment and the values of the ascent velocity are summarized in Table 1.

**Table 1.** Experimental results.

Experiment No.	Number of Launches	Radial Load, kg	Radial Load, H	Specific Pressure, kPa	Maximum Value of the Friction Force, kgf	Maximum Value of the Friction Moment, N*m	Minimum Bearing Ascent Speed, rpm
1	3	4.73	46.40	14.40	0.76	1.19	8800
2	3	5.67	55.60	17.20	0.70	1.10	8300
3	4	6.61	64.80	20.00	0.70	1.10	8600
4	3	10.67	104.60	32.40	2.42	3.79	11,000

According to the results of experiment 1, the loading force of the journal was dependent on the angular velocity during acceleration (Figure 10) and braking (Figure 11):

In experiments 1, 2, and 3, steady ascent of the rotor was observed. In the fourth experiment (exp. 4), it was decided to test the maximum load that the bearing could withstand.

During experiment 4.2, the bearing surfaced, but it began to descend on the 13th s. The maximum value of the force measured by the dynamometer was 2.42 kgf, so it was decided to stop testing under such load.

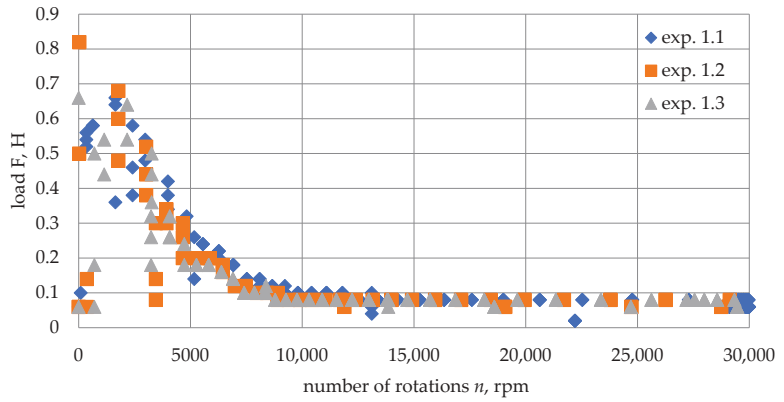


Figure 10. Dependence of the bearing load on the number of rotations, at  $m_1 = 1.316$  kg;  $m_2 = 0.752$  kg.

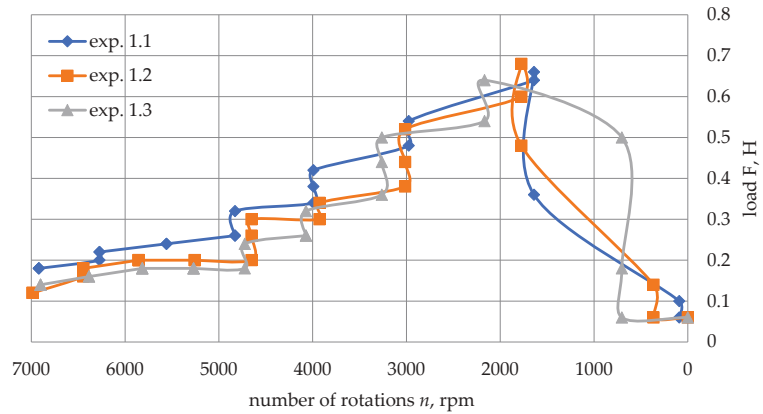


Figure 11. Dependence of the bearing load on the number of rotations during shaft deceleration, at  $m_1 = 1.316$  kg;  $m_2 = 0.752$  kg.

External inspection revealed carbon deposits on the petals of the gas-dynamic bearing (Figure 12), making them unsuitable for further testing.



Figure 12. Disassembled bearing after maximum loading.

## 5. Conclusions

1. The advantage of the presented model is the joint solution of the elastic and gas-dynamic subtasks. This approach allows the processes occurring in the shaft-bearing system to be fully analyzed and to obtain results that are close to a real-life scenario.
2. A mathematical model for the motion of a petal gas-dynamic bearing with the petals package was proposed. The model takes into account the pressure dependence of the deflection values of the elastic elements and the design features. To implement the proposed model, a numerical algorithm was developed for solving the related task of gas-dynamics and elasticity by combining the methods of variational calculus, optimization, and an explicit finite-difference time scheme. The order of accuracy of convergence of the solution corresponded to  $10^{-5}$ . The study demonstrated that the load-carrying capability of the bearing increased by 2–4 times with an increase in the number of petals.
3. The developed calculation algorithm makes it possible to conduct research optimizing the characteristics of the rotor bearing. This will ensure stable rotation of the rotor at a given speed.
4. The results of the experimental studies allowed us to estimate the interval for the ascent speed of the rotor, which was used as the initial conditions for numerical modeling. This approach made it possible to avoid preliminary parametric studies and greatly facilitated the numerical modeling of the process.
5. Further research should be conducted to clarify the experimental results and their correlation with the results of the numerical experiment, increase the dimension of the grid, and control the convergence rate of the methods. These steps will increase the accuracy of the calculation in an acceptable time frame and enable construction of the journal trajectory in the bearing clearance space within a given time interval.

**Author Contributions:** Conceptualization, S.S. and E.Z.; Methodology, S.S., E.Z. and N.K.; Validation, S.S.; Formal Analysis, S.S.; Investigation, S.S.; Resources, E.Z. and S.S.; Data collection, S.S.; Writing original drafts, S.S. and E.Z.; Writing-Review and Editing, E.Z. and S.S.; Visualization, S.S.; Experimentation, S.S. and O.M.; Oversight, N.K.; Project Administration, E.Z.; Funding Acquisition, E.Z. and S.S. All authors contributed significantly to the completion of this manuscript by conceiving and developing the study, as well as writing and improving the paper. All authors have read and agreed to the published version of the manuscript.

**Funding:** This work was financially supported by Ministry of Science and Higher Education of the Russian Federation (FENU-2023-0013).

**Data Availability Statement:** Not available.

**Conflicts of Interest:** The authors declare no conflict of interest.

## References

1. San Andrés, L. A Review of Turbine and Compressor Aerodynamic Forces in Turbomachinery. *Lubricants* **2023**, *11*, 26. [CrossRef]
2. Surovtsev, S.V. Evolution of Gas Lubricated Bearings. *Bull. South. Ural. State Univ. Ser. Mech. Eng. Ind.* **2021**, *21*, 37–48. (In Russian) [CrossRef]
3. Gu, L.; Guenat, E.; Schiffmann, J. A Review of Grooved Dynamic Gas Bearings. *Appl. Mech. Rev.* **2020**, *72*, 10802. [CrossRef]
4. Hou, Y.; Zhao, Q.; Guo, Y.; Ren, X.; Lai, T.; Chen, S. Application of Gas Foil Bearings in China. *Appl. Sci.* **2021**, *11*, 6210. [CrossRef]
5. Khamari, D.S.; Kumar, J.; Behera, S.K. A Review on Modeling and Stability Aspects of Gas Foil Bearing Supported Rotors. *Tribol. Ind.* **2023**, *45*, 12–33. [CrossRef]
6. Zhang, C.; Ao, H.; Jiang, H.; Zhou, N. Investigations on start-up performances of novel hybrid metal rubber-bump foil bearings. *Tribol. Int.* **2020**, *154*, 106751. [CrossRef]
7. Wang, C.; Wang, X.; Hu, Y. Investigation on Start-Up Performance of Gas Foil Bearing Considering Wear Topography Evolution of Non-Gaussian Surface. *Tribol. Int.* **2023**, *177*, 108003. [CrossRef]
8. Liu, X.; Li, C.; Du, J.; Nan, G. Thermal Characteristics Study of the Bump Foil Thrust Gas Bearing. *Appl. Sci.* **2021**, *11*, 4311. [CrossRef]
9. Wu, F.; Hu, Y. Theoretical Investigations on Tribological Properties of Air Foil Thrust Bearings during Start-Up Process. *Lubricants* **2023**, *11*, 94. [CrossRef]

10. Yu, T.-Y.; Wang, P.-J. Simulation and Experimental Verification of Dynamic Characteristics on Gas Foil Thrust Bearings Based on Multi-Physics Three-Dimensional Computer Aided Engineering Methods. *Lubricants* **2022**, *10*, 222. [CrossRef]
11. Bonello, P.; Hassan, M.F.B. An Experimental and Theoretical Analysis of a Foil-Air Bearing rotor system. *J. Sound. Vib.* **2018**, *413*, 395–420. [CrossRef]
12. Park, J.; Sim, K. A Feasibility Study of Controllable Gas Foil Bearings with Piezoelectric Materials via Rotordynamic Model Predictions. *J. Eng. Gas Turbines Power* **2018**, *141*, 21027. [CrossRef]
13. Martowicz, A.; Bryła, J.; Staszewski, W.J.; Ruzzene, M.; Uhl, T. Nonlocal Elasticity in Shape Memory alloys Modeled Using Peridynamics for Solving Dynamic Problems. *Nonlinear Dyn.* **2019**, *97*, 1911–1935. [CrossRef]
14. Feng, K.; Cao, Y.; Yu, K.; Guan, H.; Wu, Y.; Guo, Z. Characterization of a Controllable Stiffness Foil Bearing with Shape Memory Alloy Springs. *Tribol. Int.* **2019**, *136*, 360–371. [CrossRef]
15. Arghir, M.; Benckroun, O. A Simplified Structural Model of Bump-Type Foil Bearings Based on Contact Mechanics Including Gaps and Friction. *Tribol. Int.* **2019**, *134*, 129–144. [CrossRef]
16. Xu, Z.; Li, C.; Du, J. Modeling and Static Characteristics Study of the Double-Layer Bump Gas Foil Bearing. *Tribol. Int.* **2021**, *164*, 107202. [CrossRef]
17. Li, C.; Du, J.; Yao, Y. Study of load carrying mechanism of a novel three-pad gas foil bearing with multiple sliding beams. *Mech. Syst. Signal. Process.* **2020**, *135*, 106372. [CrossRef]
18. Li, C.; Du, J.; Li, J.; Xu, Z. Linear Stability and Nonlinear Rotor Responses of the Gas Foil Bearing with Multiple Sliding Beams. *Proc. Inst. Mech. Eng. Part. C J. Mech. Eng. Sci.* **2023**, *in press*. [CrossRef]
19. Constantinescu, V.N. Closure to “Discussion of ‘On the Influence of Inertia Forces in Turbulent and Laminar Self-Acting Films’”. *ASME J. Lubr. Technol.* **1970**, *92*, 473–480. [CrossRef]
20. Timoshenko, S.P.; Gere, T.M. *Theory of Elastic Stability*; McGraw-Hill: New York NY, USA, 1959.

**Disclaimer/Publisher’s Note:** The statements, opinions and data contained in all publications are solely those of the individual author(s) and contributor(s) and not of MDPI and/or the editor(s). MDPI and/or the editor(s) disclaim responsibility for any injury to people or property resulting from any ideas, methods, instructions or products referred to in the content.

Article

# A Method for Mathematical Modeling of Hydrodynamic Friction of Plunger Pairs with Consideration of Microgeometry

Konstantin Gavrilov <sup>1,\*</sup>, Yuriy Rozhdestvenskii <sup>2</sup> and Ildar Umurzakov <sup>1</sup>

<sup>1</sup> Department of Wheeled and Tracked Vehicles, Institute of Engineering and Technology, South Ural State University, 76 Prospekt Lenina, 454080 Chelyabinsk, Russia; asp22uik733@susu.ru

<sup>2</sup> Department of Motor Transport, Institute of Engineering and Technology, South Ural State University, 76 Prospekt Lenina, 454080 Chelyabinsk, Russia; rozhdestvenskiyv@susu.ru

\* Correspondence: gavrilovkv@susu.ru; Tel.: +89-507-420-117

**Abstract:** The fuel injection system heavily relies on the high-pressure fuel pump, which plays a critical role in its overall performance. The fuel pump plunger is subjected to high levels of stress and experiences irregular lubrication during dynamic loads, causing premature wear. In the industrial sector, laser surface micro-texturing has been utilized to reduce friction and enhance anti-wear properties, and its positive impact has been supported by both theoretical and experimental evidence. This article presents a method for determining the hydromechanical characteristics of plunger pairs under conditions of hydrodynamic friction. The microgeometry of friction surfaces was taken into account through the cavitation effect of the lubricating fluid, described by the modified Reynolds equation. Software was developed according to the proposed method. The developed software can be used to analyze the contacting surfaces of plunger pairs and evaluate their tribotechnical characteristics based on the microgeometry parameters of the friction surfaces. The article also discusses the impact of the microgeometry parameters on the quality criteria of the hydromechanical characteristics of the plunger pairs. Computational examples are given for the analysis of contacting surfaces of plunger pairs separated by a lubrication layer. The technical characteristics are evaluated depending on the parameters of the microgeometry of the roughness of the friction surfaces. The influence of the microgeometry parameters on the quality criteria of the hydromechanical characteristics of the plunger pairs is presented.

**Keywords:** surface asperities interaction; Markov process; tribological parameters

**MSC:** 62M02; 74A55; 74F10

**Citation:** Gavrilov, K.; Rozhdestvenskii, Y.; Umurzakov, I. A Method for Mathematical Modeling of Hydrodynamic Friction of Plunger Pairs with Consideration of Microgeometry. *Mathematics* **2023**, *11*, 2637. <https://doi.org/10.3390/math11122637>

Academic Editor: Efstratios Tzirtzilakis

Received: 16 May 2023

Revised: 2 June 2023

Accepted: 7 June 2023

Published: 9 June 2023



**Copyright:** © 2023 by the authors. Licensee MDPI, Basel, Switzerland. This article is an open access article distributed under the terms and conditions of the Creative Commons Attribution (CC BY) license (<https://creativecommons.org/licenses/by/4.0/>).

## 1. Introduction

Currently, there is a pressing need to improve the quality and performance of high-pressure fuel pumps and enhance environmental emission standards.

Friction reduction is a key issue for mechanical engineering. It is necessary to achieve high efficiency, reliability, economy, and ease of operation. Friction is the main cause of energy loss and mechanical system failures. Globally, friction in an engine is a part of power loss, determining its efficiency, although in piston internal combustion engines (ICE), approximately 30% of energy is spent on overcoming friction losses [1,2].

The second significant factor affecting the efficiency of hydraulic plunger pairs is mechanical damage, such as wear of mating surfaces, sticking, and plunger misalignment [3–5].

Common rail (CR) fuel injection systems provide better fuel economy, lower emissions, and higher power and form an integral part of modern engines [6,7]. Pump elements are exposed to high loads due to fuel compression under high pressure. The high-pressure fuel pump (HPP) is one of the most important elements of the CR system, the performance of which directly affects the performance of the whole system [8]. An increase in fuel pressure at the top of the plunger cylinder, combined with regularly varying speeds, requires the

accurate lubrication of the plunger pair [9]. An increase in pressure leads to more plunger wear and less lubrication, which negatively affects the efficiency of the fuel system [10,11]. Some authors say that the workflow of the HPP is poorly studied [12].

Most of the current research in this field focuses on one or several parameters of microgeometry, and improving one parameter may lead to the deterioration of others. To achieve the most effective prediction of microgeometry utilization in plunger pairs, a mass conservation algorithm was employed in conjunction with the search for optimal microgeometric parameters.

In recent years, the use of textured surfaces to reduce friction and improve the anti-wear properties of tribological couplings has been gaining popularity [13–15]. Laser surface texturing is widely used in the industry, and its positive effects have been theoretically predicted and experimentally confirmed [16–18].

Laser texturing improved the hydrodynamic lubrication of mechanical seals, positively influenced the change in load capacity and friction coefficient, and reduced wear as compared to nontextured friction surfaces [19,20].

A lubrication model has been created that takes into account the surface roughness of textured cylinder liners [21]. The special topography created on the surface of the cylinder liners improved the lubricating capability and reduced wear.

A wear prediction model based on Markov chains has been developed [22]. This model is effective in the development of new machine components and the modification of existing assemblies.

Laser texturing also affects the plunger surface to improve the seal and reduce plunger wear in diesel engines. The results of tribological tests showed that the depth of the greatest wear decreased by 72.4% and the average roughness decreased by 22.6%. Engine rig tests revealed that the number of fuel leaks decreased by 73.1%. The test results showed that the average coefficient of friction decreased by 27.8%. Figure 1 illustrates an example of plunger surface texturing [23,24].

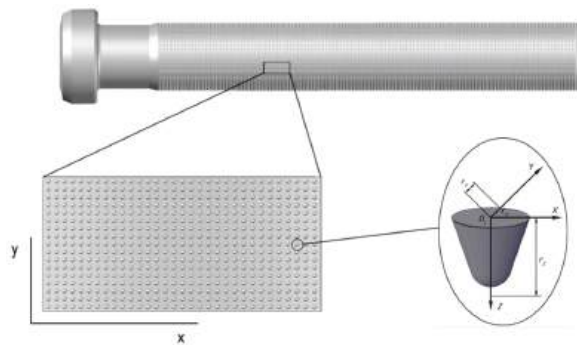


**Figure 1.** An example of plunger surface texturing.

Improving the efficiency of an HPP plunger pair by texturing the plunger surface is a relevant issue. This study evaluates the texturing effect on the hydromechanical characteristics of the plunger pair to increase the energy efficiency of the fuel system in ICE.

Also worth mentioning is the research conducted in the field of modifying friction pairs by using new materials [25,26].

## 2. Idea: Simple Discrete Model

Figure 2 schematically shows the arrangement of micro-dimples on the surface of the plunger. The illustration depicts the unfolded surface of the plunger with a microgeometry relief in the form of ellipsoidal indentations.

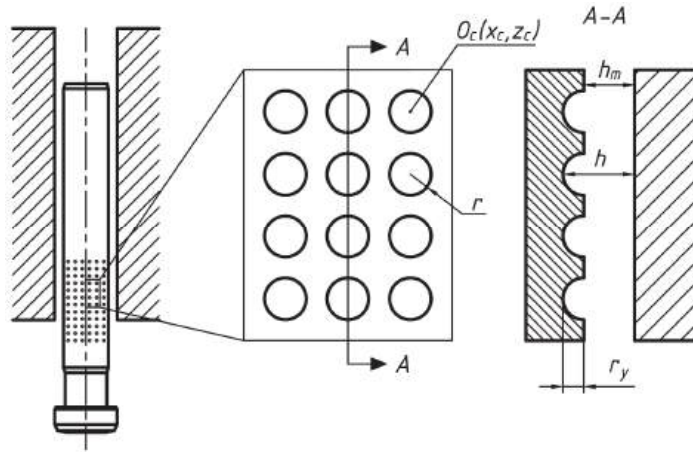


**Figure 2.** Accounting for micro-roughness in the lubricating layer.

The consideration of micro-roughness is performed using the following equation:

$$h = \begin{cases} \frac{r_y}{r} \sqrt{r^2 - (x - x_c)^2 - (z - z_c)^2}, & \text{if } \sqrt{x^2 + z^2} \leq r \\ h_m, & \text{if } \sqrt{x^2 + z^2} > r \end{cases} \quad (1)$$

where  $h$ —thickness of the oil film in any position;  
 $h_m$ —minimum thickness of the film;  
 $r$ —radius of the dimple;  
 $r_y$ —depth of the dimple;  
 $x, z$ —coordinates within the dimple cell;  
 $x_c, z_c$ —cell center coordinates.

Thus, when the computational grid intersects the micro-dimple region (Figure 2), the minimum thickness of the lubricating layer will be increased by the depth of the micro-dimple at that grid point.

In turn, the minimum thickness of the lubricating layer will be determined as follows:

$$h_m = r_0 - (r_p + e \cos \alpha) = h_0 - e \cos \alpha \quad (2)$$

where  $e$ —eccentricity of the plunger pairs;  
 $r_0$ —inner diameter of the plunger sleeve;  
 $r_p$ —radius of the plunger;  
 $h_0 = r_0 - r_p$ —thickness of the oil film in the radial direction when the plunger pair is concentric;

$\alpha$ —angle of application of the force on the crankshaft journal.

The micro-dimple filling density  $D$  is determined by the formula:

$$D = \frac{100 \cdot d^2}{H^2} \quad (3)$$

where  $d$ —micro-dimple diameter;

$H = (l + d)$ —cell height.

Therefore, the distance between micro-dimple  $l$  (Figure 3) can be determined as follows:

$$l = \sqrt{\frac{100 \cdot d^2}{D}} - d \quad (4)$$

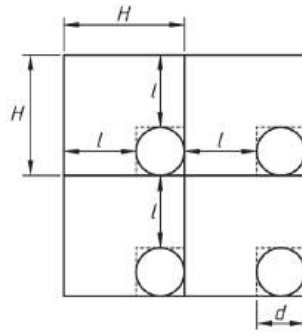


Figure 3. Distribution of micro-dimples.

### 3. Generalization of the Model

The contact surface of the plunger is oriented in a circumferential direction, as shown in Figure 2. Curvature is neglected here because the magnitude of the diametral clearance (3–4 μm) is sufficiently small compared to the plunger diameter.

To determine the hydrodynamic pressures and lubricating film reaction, a modified Reynolds equation incorporating the boundary conditions of Jakobson–Floberg–Olsson (JFO) was utilized:

$$\frac{\partial}{\partial \varphi} \left[ \frac{\bar{h}^3 \bar{\beta}}{12 \bar{\mu}_s} g(\theta) \frac{\partial \theta}{\partial x} \right] + \frac{\partial}{\partial \bar{z}} \left[ \frac{\bar{h}^3 \bar{\beta}}{12 \bar{\mu}_s} g(\theta) \frac{\partial \theta}{\partial \bar{z}} \right] = \frac{w}{2} \frac{\partial}{\partial x} (\bar{h} \theta) + \frac{\partial}{\partial \tau} (\bar{h} \theta), \tag{5}$$

where  $\bar{\beta} = \beta \psi^2 / \mu_0 \omega_0$ —dimensionless compressibility coefficient of the lubricant;

$\bar{\beta}$ —dimensional value of the compressibility coefficient of the lubricant;

$g(\theta)$ —switching function between the active region and the cavitation region:

$$g(\theta) = \begin{cases} 1, & \text{if } \theta \geq 1; \\ 0, & \text{if } \theta < 1, \end{cases} \tag{6}$$

where  $g(\theta) = 1$ —active region;

$g(\theta) = 0$ —cavitation region.

The remaining notations in Equation (5) correspond to the notations used in Reference [27].

The degree of lubricating gap fill  $\theta$  has a dual meaning. In the active region (pressure region where  $p > 0$ )  $\theta = \rho / \rho_c$ ,  $\rho_c$  is the lubricant density at the cavitation pressure  $p_c$ . In the cavitation area, where  $p \leq 0$ ,  $p = p_c$ ,  $\rho = \rho_c$ ; in this case, the degree of gap fill  $\theta$  characterizes the relative amount of lubricating material in the lubricating gap of the tribosystem. Hydrodynamic pressures and the degree of gap fill are related by the following expression:

$$\bar{p} = \bar{p}_c + g(\theta) \bar{\beta} \ln \theta. \tag{7}$$

The system of algebraic equations resulting from Equation (3) in the Elrod algorithm [28] was solved using the point iterative Gauss–Seidel method with respect to the fill factor  $\theta_{ij}$ . The switching function  $g$  was updated simultaneously at all grid nodes after completing a full iteration cycle. A dimensionless compressibility coefficient of the lubricating fluid  $\beta$  equal to 40 was chosen as the most acceptable value in terms of stability for the iterative procedure.

From the analysis of information sources, it is known that the Elrod algorithm and similar mass conservation algorithms for lubricant in the bearing lubrication film have drawbacks related to numerical instability in solving the system of algebraic equations derived from Equation (5). Additionally, the obtained calculation results depend on the values of  $\beta$ , especially at high eccentricities typical for heavily loaded bearings in thermal engines.

To solve the problem of mathematical modeling of micro-roughness on the plunger surface, a modified Elrod equation has been developed, expressed as follows:

$$\frac{\partial}{\partial \varphi} \left[ \frac{h^3}{12\bar{\mu}_e^*} \frac{\partial}{\partial x} (g\Phi) \right] + \frac{1}{a^2} \frac{\partial}{\partial z} \left[ \frac{h^3}{12\bar{\mu}_e^*} \frac{\partial}{\partial z} (g\Phi) \right] = \frac{w_{21}}{2} \frac{\partial}{\partial z} \left\{ \bar{h} [1 + (1-g)\Phi] \right\} + \frac{\partial}{\partial \tau} \left\{ \bar{h} [1 + (1-g)\Phi] \right\}, \quad (8)$$

where  $\bar{h} = h/h_0$ ;  $\bar{\mu}_e^* = \mu_e^*/\mu_0$ ;  $-a \leq \bar{z} \leq a = z/R$ ;

$a = B/2R$ ;  $\tau = \omega_0 t$ ;  $w_{21} = (w_2 - w_1)/(\omega_0 R)$ ;

$\bar{h}$ ,  $\bar{\mu}_e^*$ —dimensionless lubricating film thickness and dimensionless effective viscosity of the lubricant;

$B$ ,  $R$ —height and radius of the plunger;

$\mu_e^*$ —effective viscosity of the lubricant corresponding to the temperature  $T_e^*$ ;

$\mu_0$ ,  $h_0$ ,  $\omega_0$ —viscosity of the lubricant, the typical thickness of the lubricating film at the central position of the pin, and the rotational speed of the pin, respectively;

$\bar{w}_{21}$ —dimensionless linear velocity of the pin's movement;

$g$ —switching function.

The missing notations are provided in Reference [28].

#### 4. The Equation of Motion for a Plunger Pair

Figure 4 shows the reactions of forces acting on the plunger.

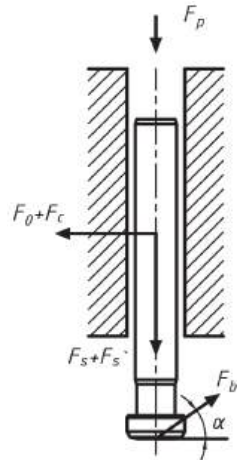


Figure 4. Forces acting on the plunger.

The equation of equilibrium is given as follows:

$$F_0 + F_c = F_b \cdot \cos \alpha, \quad (9)$$

where  $F_0$ —initial lubricating film reaction;

$F_c$ —lubricating film reaction at minimum lubricating film thickness;

$F_b$ —crankshaft force;

$\alpha$ —angle of application of crankshaft force.

$$F_p + F_s + F_{s'} = F_b \cdot \sin \alpha \quad (10)$$

where  $F_p$ —fuel injection force;

$F_s$ —spring force;

$F_{s'}$ —compression spring force.

The equation of radial balance for the plunger can be expressed as follows:

$$m \frac{\partial^2 c}{\partial t^2} = F_0 + F_c - F_b \cos \alpha \tag{11}$$

where  $m$ —mass of the plunger;  
 $c$ —instantaneous minimum oil film thickness;  
 $\alpha$ —angle of force on the distributor shaft.

**5. Results of Modeling**

Parametric studies were conducted using the developed software “Microgeometry of Plunger Pairs for Fuel Injection Pumps”, based on the calculation methodology described above. The results of the program are shown in Figure A1 of Appendix A. The software used is a modified version of the software previously used for accounting for micro-dimples in diesel engine pistons, and its validation is presented in Figure 5 [29]. The initial parameters of the plunger pair characteristics and the diesel fuel characteristics are provided in Tables 1 and 2, respectively.

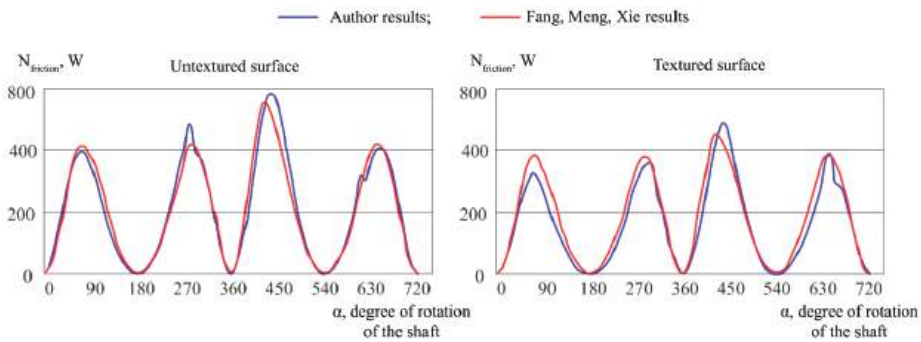


**Figure 5.** The dependency of friction losses in the piston on the crankshaft rotation angle of the diesel engine.

**Table 1.** Initial parameters of the geometry and operating conditions of the plunger pair.

Diameter of Plunger, mm	Mass of Plunger, grams	Length of Working Part of Plunger, mm	Eccentricity, mm	Rotational Speed of Shaft, RPM	Average Velocity of Plunger, m/s
11.0	56.0	55.60	3.5	3300	0.77

**Table 2.** Parameters of diesel fuel.

Density, kg/m <sup>3</sup>	Thermal Capacity, joule/K·kg	Coefficient of Thermal Conduction, W/m·K	Coefficient of Dynamic Viscosity, Pa·s
730	2090	0.149	0.0024

A total of 80 parametric measurements of the hydrodynamic characteristics were performed with different microgeometry parameters (Figure 6), including a variant with its complete absence. Then, six microgeometry variants with average values of the hydrodynamic characteristics were selected (Table 3). These results are presented in Figure 4 as squares.

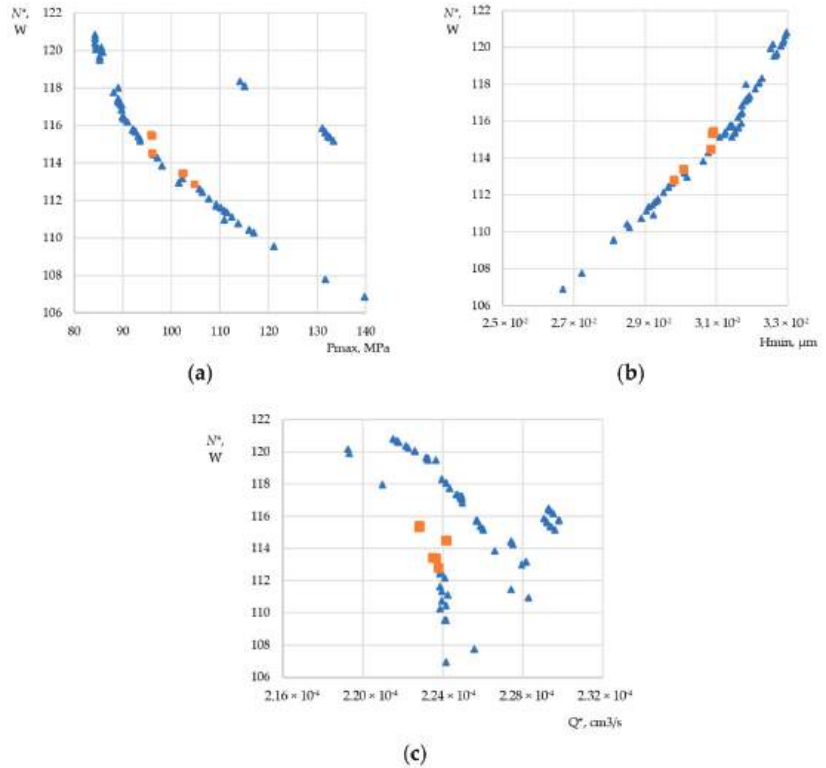


**Figure 6.** Reflection of the average friction losses of the parametric results (six selected variants highlighted with squares): (a) in the projection of maximum pressures; (b) in the projection of minimum lubricating film thickness; (c) in the projection of fuel leakage.

**Table 3.** Parametric results of the hydrodynamic characteristics of the fuel injection pump plunger pair.

№	Varied Parameters					Quality Criteria (Hydrodynamic Characteristics)				
	$X_1,$ m	$X_2,$ m	$d,$ m	$r_y,$ m	$D,$ %	$h_{min}^*,$ μm	$p_{max}^*,$ MPa	$N^*,$ W	$Q^*,$ cm <sup>3</sup> /s	
1	$0.1533 \times 10^{-1}$	$0.4378 \times 10^{-1}$	$1.19 \times 10^{-5}$	$4.76 \times 10^{-6}$	37.5599	$3.01 \times 10^{-2}$	102.651	113.384	$2.20 \times 10^{-4}$	
2	$0.1583 \times 10^{-1}$	$0.4444 \times 10^{-1}$	$1.22 \times 10^{-5}$	$4.89 \times 10^{-6}$	38.8817	$2.98 \times 10^{-2}$	105.045	112.774	$2.21 \times 10^{-4}$	
3	$0.1375 \times 10^{-1}$	$0.4166 \times 10^{-1}$	$1.08 \times 10^{-5}$	$4.33 \times 10^{-6}$	33.3326	$3.08 \times 10^{-2}$	96.340	114.463	$2.19 \times 10^{-4}$	
4	$0.1535 \times 10^{-1}$	$0.4380 \times 10^{-1}$	$1.19 \times 10^{-5}$	$4.76 \times 10^{-6}$	37.6066	$3.01 \times 10^{-2}$	102.724	113.369	$2.20 \times 10^{-4}$	
5	$0.1370 \times 10^{-1}$	$0.4161 \times 10^{-1}$	$1.08 \times 10^{-5}$	$4.32 \times 10^{-6}$	33.2203	$3.09 \times 10^{-2}$	96.306	115.307	$2.18 \times 10^{-4}$	
6	$0.1361 \times 10^{-1}$	$0.4148 \times 10^{-1}$	$1.07 \times 10^{-5}$	$4.30 \times 10^{-6}$	32.9657	$3.09 \times 10^{-2}$	95.989	115.406	$2.18 \times 10^{-4}$	
7	Plunger pair without microgeometry					$3.31 \times 10^{-2}$	85.603	121.908	$2.17 \times 10^{-4}$	

The variable parameters of the microgeometry were the following:  $X_1$  and  $X_2$ —the start and the end points of the texturing area, respectively;  $d$ —the diameter of the micro-cavities;  $r_y$ —the depth of the micro-cavities;  $D$ —the density of surface filling with micro-cavities.

The following quality criteria were selected:  $h_{min}^*$ , μm—minimum lubricating film thickness per cycle;  $p_{max}^*$ , MPa—maximum lubricating film pressure per cycle;  $N^*$ , W—average friction losses;  $Q^*$ , cm<sup>3</sup>/s—average fuel leakage.

For a graphical representation of changes in hydrodynamic characteristics in the tribosystem depending on the angle of rotation of the distributor shaft of the fuel injection pump (HPFP), the following parameters were chosen:  $N_{friction}$ —change in average fric-

tion losses;  $P_{max}$ —change in average lubricating film pressure;  $H_{min}$ —change in average lubricating film thickness;  $Q$ —change in maximum fuel leakage.

For better visualization, a graphical comparison of the hydrodynamic characteristics of the plunger pair without using the surface microgeometry and the results considering the surface with micro-dimples are presented in Figure 7. To compare the hydromechanical characteristics, results 1, 2, and 7 (without texturing) of Table 3 were selected.

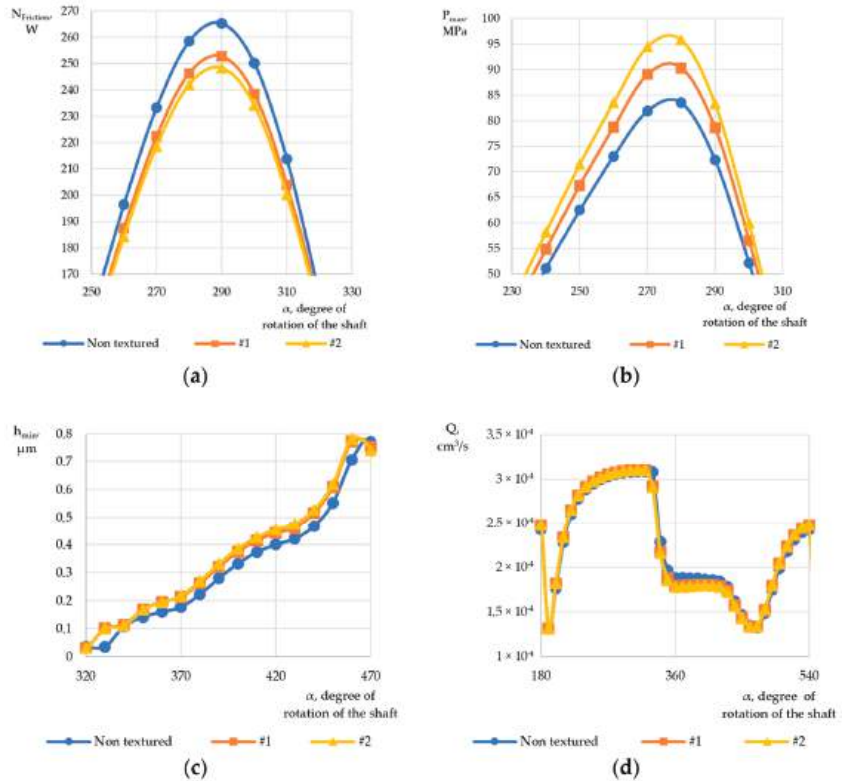


**Figure 7.** Variation in hydrodynamic characteristics depending on the angle of rotation of the shaft of the injection pump: (a) change in friction losses; (b) change in maximum pressures of the lubricating film; (c) change in minimum thickness of the lubricating film; (d) change in fuel leaks.

The graphs shown in Figure 6 indicate a positive effect of applying laser microgeometry to the plunger. Using microgeometry reduced friction losses by 7.5%, while fuel leaks increased by 2.1%. The minimum thickness of the lubricating film decreased by 9%, and the maximum pressure of the lubricating film increased by 20%, which positively affected the load-carrying capacity of the tribosystem.

### 6. Conclusions

1. A mathematical model considering micro-dimples with variable parameters on the surfaces of plunger pairs has been presented.
2. Based on the provided methodology, software has been developed, and the computational grid has been modified to increase its density and allow for significantly smaller values of microgeometry parameters to be used in the calculations.
3. Based on the results of the performed parametric investigations of the microgeometry of the plunger pair in the “Microgeometry of Plunger Pair for Fuel Injection Pump” program implemented in Visual Fortran, the following conclusions can be drawn: the

maximum feasible computational grid size is 12,000 by 7500 cells, enabling the specification of micro-dimple diameters of approximately 5 μm. The depth of the micro-dimples was varied from 2 to 6 μm (with no minimum restrictions).

4. Based on numerous results of the parametric investigations, it can be concluded that texturing has a positive impact on plunger pairs. Out of the total number of calculations exceeding 135 units, two compromise options were identified. In these cases, friction losses were reduced by 7.5%, and the load-carrying capacity of the lubricating film was increased by raising the pressure in the lubricating film by 20%.

5. The results will be further utilized in the design of new high-pressure fuel pumps for common rail systems.

**Author Contributions:** Conceptualization, K.G.; Methodology, K.G. and Y.R.; Validation, K.G. and Y.R.; Formal Analysis, K.G.; Investigation, K.G. and Y.R.; Resources, K.G. and I.U.; Data Collection, K.G.; Writing—Original Draft Preparation, K.G.; Writing—Review and Editing, I.U.; Visualization, K.G. and I.U.; Supervision, K.G.; Project Administration, K.G., Y.R. and I.U.; Funding Acquisition, K.G., Y.R. and I.U. All of the authors contributed significantly to the completion of this article, conceiving and designing the review, and writing and improving the paper. All authors have read and agreed to the published version of the manuscript.

**Funding:** This work was supported by a grant from the Russian Science Foundation No. 23-29-10042, accessed on 20 April 2023 (<https://rscf.ru/project/23-29-10042/>).

**Institutional Review Board Statement:** Not applicable.

**Informed Consent Statement:** Not applicable.

**Data Availability Statement:** There are no data applicable in this study.

**Acknowledgments:** The authors thank South Ural State University (SUSU) for supporting them.

**Conflicts of Interest:** The authors declare no conflict of interest.

Appendix A

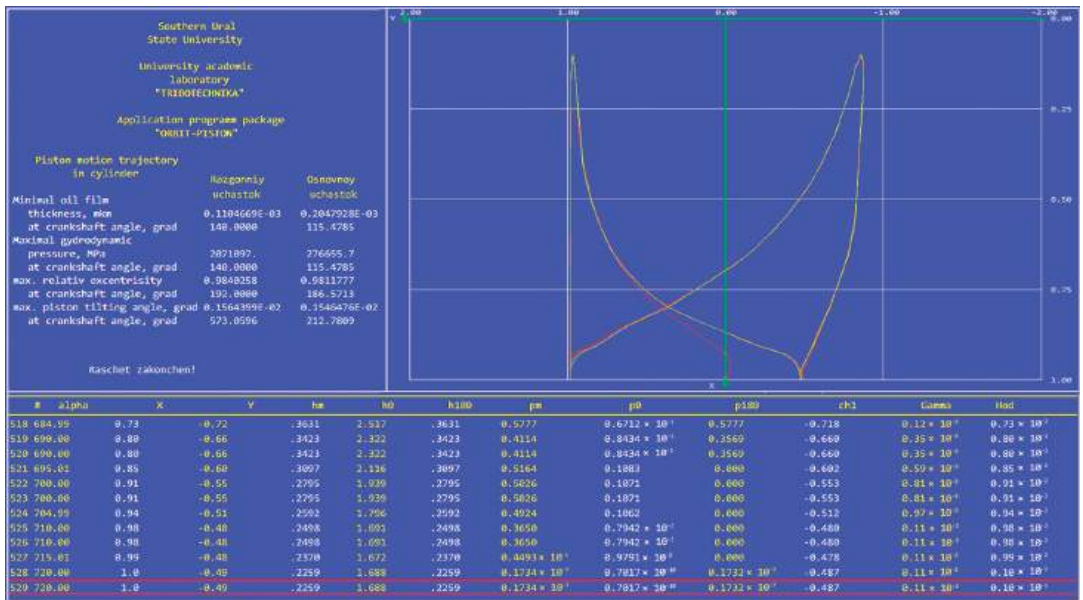


Figure A1. Program window with parametric calculation results.

## References

1. Knauder, C.; Allmaier, H.; Sander, D.E.; Salhofer, S.; Reich, F.M.; Sams, T. Analysis of the journal bearing friction losses in a heavy-duty diesel engine. *Lubricants* **2015**, *3*, 142–154. [CrossRef]
2. Holmberg, K.; Andersson, P.; Nylund, N.O.; Mäkelä, K.; Erdemir, A. Global energy consumption due to friction in trucks and buses. *Tribol. Int.* **2014**, *78*, 94–114. [CrossRef]
3. Brazhenko, V.N.; Mochalin, E.V.; Jian-Cheng, C. Mechanical Admixture Influence in the Working Fluid on Wear and Jamming of Spool Pairs from Aircraft Hydraulic Drives. *J. Frict. Wear* **2020**, *41*, 526–530. [CrossRef]
4. Brazhenko, V. The Influence of Contaminated Hydraulic Fluid on the Relative Volume Flow Rate and the Wear of Rubbing Parts of the Aviation Plunger Pump. *Aviation* **2019**, *23*, 43–47. [CrossRef]
5. Liu, S.; Zhang, Y.; Ai, C.; Ge, Y.; Li, Z.; Zhu, Y.; Hao, M. A new test method for simulating wear failure of hydraulic pump slipper pair under high-speed and high-pressure conditions. *Front. Energy Res.* **2023**, *10*, 1096633. [CrossRef]
6. Zhang, Q.; Fu, Y.; Yuan, Z.; Song, Z. Multi-medium running induced piston pump erosion. *Sci. Technol. Rev.* **2012**, *30*, 44–48.
7. Teoh, Y.H.; How, H.G.; Masjuki, H.H.; Nguyen, H.-T.; Kalam, M.A.; Alabdulkarem, A. Investigation on particulate emissions and combustion characteristics of a common-rail diesel engine fuelled with Moringa oleifera biodiesel-diesel blends. *Renew. Energy* **2019**, *136*, 521–534. [CrossRef]
8. Huang, J.L.; Xu, H.; Sun, S.Y.; Wang, D. Influence of fuel injection system's optimization on performance of diesel engine and its injection parameter reoptimization. *J. Dalian Marit. Univ.* **2017**, *43*, 2–108.
9. Zhao, J.; Fu, Y.; Ma, J.; Fu, J.; Chao, Q.; Wang, Y. Review of cylinder block/valve plate interface in axial piston pumps: Theoretical models, experimental investigations, and optimal design. *Chin. J. Aeronaut.* **2021**, *34*, 1–134. [CrossRef]
10. Segu, D.Z.; Hwang, P. Effectiveness of multishape laser surface texturing in the reduction of friction under lubrication regime. *Ind. Lubr. Tribol.* **2016**, *68*, 116–124. [CrossRef]
11. Sun, J.; Zhang, X.; Zhu, J.; Gao, Y.; Wang, H.; Zhao, X.; Teng, Q.; Ren, Y.; Zhu, G. On the lubrication characteristics of piston ring under different engine operation conditions. *Ind. Lubr. Tribol.* **2019**, *72*, 101–108. [CrossRef]
12. Cavallo, M.; Frattini, E.; Palmieri, F. *Fuel Influence on Single-Piston Common Rail Pump Performance*; SAE Technical Paper 2021; N° 2021-24-0063; SAE International: Warrendale, PA, USA, 2021. [CrossRef]
13. Chen, L.; Ren, L.Q.; Zhao, Y.; Zhou, H. The wear-resistance of 3Cr2W8V steel with cave pit non-smooth processed by laser. *J. Bionic Eng.* **2008**, *5*, 34–39. [CrossRef]
14. Lee, Y.H.; Schuh, J.K.; Ewoltdt, R.H.; Allison, J.T. Simultaneous design of non-Newtonian lubricant and surface texture using surrogate-based multiobjective optimization. *Struct. Multidiscip. Optim.* **2019**, *60*, 99–116. [CrossRef]
15. Singh, A.; Patel, D.S.; Ramkumar, J.; Balani, K. Single step laser surface texturing for enhancing contact angle and tribological properties. *Int. J. Adv. Manuf. Technol.* **2019**, *100*, 1253–1267. [CrossRef]
16. Fukagai, S.; Le, M.; Lewis, R. Tribological aspects to optimize traction coefficient during running-in period using surface texture. *Wear* **2019**, *424*, 223–232. [CrossRef]
17. Etsion, I.; Sher, E. Improving fuel efficiency with laser surface textured piston rings. *Tribol. Int.* **2009**, *42*, 542–547. [CrossRef]
18. Kovalchenkova, A.; Ajayi, O.; Erdemir, A.; Fenske, G.; Etsion, I. The effect of laser surface texturing on transitions in lubrication regimes during unidirectional sliding contact. *Tribol. Int.* **2005**, *38*, 219–225. [CrossRef]
19. Etsion, I.; Halperin, G. A laser surface textured hydrostatic mechanical seal. *Tribol. Trans.* **2002**, *45*, 430–434. [CrossRef]
20. Etsion, I.; Kligerman, Y.; Halperin, G. Analytical and experimental investigation of laser-textured mechanical seal faces. *Tribol. Trans.* **1999**, *42*, 511–516. [CrossRef]
21. Yin, B.; Zhou, H.; Xu, B.; Hekun, J. The influence of roughness distribution characteristic on the lubrication performance of textured cylinder liners. *Ind. Lubr. Tribol.* **2019**, *71*, 483–493. [CrossRef]
22. Gavrilov, K.; Rozhdestvenskii, Y.; Umrzakov, I. The Construction of Models of Rough Surfaces' Interaction: Markov's Approach. *Mathematics* **2022**, *10*, 3607. [CrossRef]
23. Jia, H.; Zhou, Z.; Yin, B.; Zhou, H.; Xu, B. Effect of compound texture on lubrication and sealing performance of plunger pump. *Lubr. Sci.* **2020**, *33*, 43–59. [CrossRef]
24. Jia, H.; Zhou, Z.; Yin, B.; Zhou, H.; Xu, B. Influence of microdimple on lubrication performance of textured plunger pump. *Ind. Lubr. Tribol.* **2021**, *73*, 4–571. [CrossRef]
25. Sinong, X.; Xiuqing, H.; Yinfei, Y.; Liang, L.; Ning, H.; Hanlong, L. Feasible fabrication of a wear-resistant hydrophobic surface. *Appl. Surf. Sci.* **2019**, *463*, 923–930.
26. Puzanov, A.; Simakov, A.; Kosorukova, O.; Kotov, V. Perspectives using synthetic corundum in hydraulic drives. *J. Phys. Conf. Ser.* **2021**, *1925*, 012021. [CrossRef]
27. Prokopyev, V.N.; Gavrilov, K.V. Optimization of parameters of lightly loaded sliding bearings. *Probl. Mech. Eng. Mach. Reliab.* **2007**, *5*, 79–86. (In Russian)

28. Gavrilov, K.V.; Izzatulloev, M.A.; Gritsenko, P.S.; Tsveshko, I.R. Influence of lubrication source location on hydro-mechanical characteristics of lightly loaded bearings in thermal engines. *Vestnik of South Ural State University. Ser. Mech. Eng.* **2019**, *19*, 3–21. (In Russian)
29. Fang, C.; Meng, X.; Xie, Y. A piston tribodynamic model with deterministic consideration of skirt surface grooves. *Tribol. Int.* **2017**, *110*, 232–251. [CrossRef]

**Disclaimer/Publisher’s Note:** The statements, opinions and data contained in all publications are solely those of the individual author(s) and contributor(s) and not of MDPI and/or the editor(s). MDPI and/or the editor(s) disclaim responsibility for any injury to people or property resulting from any ideas, methods, instructions or products referred to in the content.

Article

# Horizontal Axis Wind Turbine Weather Vane Aerodynamic Characteristics: Delayed Detached Eddy Simulation and Experimental Approach

Evgeny V. Solomin \* and Gleb N. Ryavkin

Department of Electric Power Generation Stations, Network and Supply Systems,  
South Ural State University (National Research University), Chelyabinsk 454080, Russia

\* Correspondence: solominev@susu.ru

**Abstract:** The known differential yaw error of horizontal axis wind turbines is clearly linked to weather vane fluctuations, arising out of the deflection of the onrushing wind flow from the rotating blades. Since the problem has not been resolved as the control systems still present this problem, it should be considered as an actual difficulty requiring deeper studies of the weather vane's aerodynamic features, including the modeling of its deviations. This paper focuses on the computational fluid dynamics and experimental study of the aerodynamic characteristics of the weather vane located on the nacelle top of horizontal axis wind turbines. Computational fluid dynamics simulation is based on the  $k-\omega$  Shear Stress Transport turbulence model and the Delayed Detached Eddy Simulation. The numerical simulation and laboratory experiment arrangements are demonstrated in detail. The new scientific results obtained during the research include the validation of the numerical experiment, demonstration of the differences in forming the wake structures for the used models on the studied angles of attack and comparison of the mean values of the moment and power spectral densities for all cases, which demonstrated a good correlation between the Delayed Detached Eddy Simulation data and the experiment. The time spent on the preparation of numerical experiments using different models was accurately estimated, to give an understanding of man-hour resources. The obtained moment values for the weather vane are applied for further mathematical modeling of the systems intended for the reduction in the differential yaw error. The applicability of the Delayed Detached Eddy Simulation approach was proved by the simulation of the aerodynamic characteristics of complexly streamlined bodies, but at the same time, it showed an extended calculation period. The results obtained during the study expand upon the experience of using numerical simulation when studying horizontal axis wind turbines and may be used to build mathematical models of yaw control systems.

**Citation:** Solomin, E.V.; Ryavkin, G.N. Horizontal Axis Wind Turbine Weather Vane Aerodynamic Characteristics: Delayed Detached Eddy Simulation and Experimental Approach. *Mathematics* **2023**, *11*, 1834. <https://doi.org/10.3390/math11081834>

Academic Editors: James M. Buick and Umberto Morbiducci

Received: 1 March 2023

Revised: 5 April 2023

Accepted: 7 April 2023

Published: 12 April 2023

**Keywords:** wind energy; horizontal axis wind turbine; yaw system; weather vane; computational fluid dynamics; Delayed Detached Eddy Simulation

**MSC:** 76F65



**Copyright:** © 2023 by the authors. Licensee MDPI, Basel, Switzerland. This article is an open access article distributed under the terms and conditions of the Creative Commons Attribution (CC BY) license (<https://creativecommons.org/licenses/by/4.0/>).

## 1. Introduction

Wind power currently covers a considerable share of electricity generation in a number of countries. Global annual investments in the renewable energy segment reached USD 259 billion in 2022 as announced in [1].

The increase in electricity generation is one of the main goals of wind power developers around the world. In general, there are two ways that could be used in this area. There is a simple but the expensive method, which is to increase the installed capacity of wind farms, and this approach is working. The global wind power growth from 2020 to 2021 was estimated to be 93 gigawatts according to the Global Wind Energy Council [2]. Another method is to improve a single installation. Works in this area are concentrated primarily on

the increment in the wind turbine's lifetime, and improvements in the aerodynamic and electrodynamic characteristics of the components, especially the rotor and generator.

One of the main problems in the operation of horizontal axis wind turbines is the permanent determination of the direction of the wind flow since the electric generation of any wind turbine depends on the swept area and reaches its maximum when the onrushing air flow vector is perpendicular to the wind rotor plane it rotates in. When the wind direction changes, the yaw control system reads as an appeared error, and if and when it is sensitive enough, then the system gives a command to turn the nacelle with the rotor to the right position. The accurate yawing reduces the power losses and, at the same time, structural loads, which may shorten the wind turbine's lifetime significantly.

Scientists from countries with developed wind power have continue their research to improve the accuracy of rotor orientation. Kim and Dalhoff (2014) in [3] presented a patent analysis of the state of the field, showing that the main directions of development are focused on the design of new types of mechanisms and control systems to reduce stress. Newer researches have not really changed the areas of development but are more concerned with the intelligent control issues such as advanced model predictive control (Song, 2019) [4] and neural-network-based fault detection systems for pitch and yaw control (El-Mallawany, 2019) [5]. The intelligent systems presented in these studies have huge potential in terms of the installations of the next generation, but they still have a number of disadvantages associated with the limited set of cases for training.

A new type of orientation sensor, LiDAR (light detection and ranging), presented by Scholbrock et al. (2015) in [6] showed great potential for its usage in wind farm yaw control systems and is currently being used for megawatt-class installations. However, the huge disadvantage of this type of yaw control is its high cost. The authors also noted that the differences in positioning accuracy with classical-weather-vane-based systems can be neglected by the implementation of a bias correction function.

Another research team was involved in a project that intended to study of the nature of the yawing differential (periodically changing) error caused by the deflection of the air flow by the rotating blades [7–10]. A mathematic compensator, built-in as a separate block in the control software, was developed for this case on the basis of studying the behavior of a weather vane. This approach led to a decrease in the error of yawing by up to 2 degrees. The study focused on mathematical simulation based on aerodynamic data obtained by experimental and numerical methods.

Due to the lack of aerodynamic data for a weather vane in open sources, this article presents both an experimental and a numerical study along with a comparison of the approaches to reach a conclusion about the feasibility of their usage for studying a wind turbine's operation. Being able to obtain the aerodynamic characteristics of a complex streamlined body that are close to real, is still a common problem in many research areas. However, it can be resolved partly or in full by numerical simulation. The main modeling approaches for obtaining the required data on different levels are as follows:

- Solution of Reynolds-averaged Navier–Stokes equations (RANS). The  $k-\epsilon$  and  $k-\omega$  Shear Stress Transport (SST) turbulence models are the most commonly used in engineering projects;
- Large eddy simulation (LES);
- Detached eddy simulations (DES) and different modifications;
- Direct numerical simulation (DNS) approach, which is used primarily in the academic area, while not being practical enough for engineering calculations.

DES is the most promising method, rapidly developing and acquiring various modifications such as Detached DES (DDES), Zonal DES (ZDES), etc. [11,12]. At the moment, the application of the method affects the study of the geometry of simple and medium complexity. In the research [13], two modifications of DES (DDES and Zonal DES) were studied using the examples with channel flow and profile flow on a small angle of attack (AoA), and showed a significant advantage of the DDES approach over ZDES. In paper [14], a mesh study of iced wings was performed with good correspondence between the data ob-

tained from DDES and the experiment, and, in addition, some valuable recommendations regarding the construction of a computational grid were given. According to the literature analysis, the most used modification is Delayed Detached Eddy Simulation (DDES). It is worth noting that most of the studies were performed on the Spalart–Allmaras (SA) modification of DES. The SA model, in some cases, loses in terms of the accuracy of the description of the boundary flows of the  $k$ - $\omega$  SST model; therefore, a modification of the  $k$ - $\omega$  SST is preferable. As a consequence, the  $k$ - $\omega$  SST modification of DDES was used in the present study based on the ANSYS Fluent software package.

The project is divided into several stages. First, we give a short theory of the DDES approach using governing equations. Here, we describe the geometry and finite volume mesh preparation process, including mesh zones, highlighting the boundary layer modeling and spatial resolution assessment, as well as the boundary conditions and time step selections. This contains some new elements in the preparation of a numerical experiment, such as a hybrid approach to the creation of a computational grid and the study of its resolution. Such details are often overlooked when describing the method. Second, we give a description of the experiment. Finally, we present the results of the research with analysis. We also make a conclusion on the applicability of computational fluid dynamics (CFD) for this specific case with some other general conclusions. Further research steps are also proposed on the basis of the material presented in this article.

## 2. Delayed Detached Eddy Simulation

DES was first introduced in 1997 by Spalart [15]. This approach was designed to mitigate the next shortcomings of the Reynolds-averaged Navier–Stokes (RANS) and Large Eddy Simulation (LES) methods:

- The inability of RANS to provide an acceptable accuracy when calculating flows with large separation zones;
- The high computational cost of LES. To resolve the boundary layer, which contains a lot of small energy-carrying vortices, appropriate spatial and temporal resolution is required.

Notwithstanding these, both of the methods are widely used in engineering and scientific projects due to their main advantages:

- RANS is capable of a quite accurate resolving of the boundary layer with a low computational cost as reported in [16,17];
- LES demonstrates a physically close representation of turbulence in accordance with [18].

According to these statements, DES was developed as a hybrid approach that uses RANS in the near-wall region and LES for the stall one. This approach demonstrates a good agreement with the experimental data presented in [19]. It has a good ratio of performance to computational costs and is therefore widely used on modern personal computers.

The well-known problem of DES is grid-induced separation, the physics of which is described in [20]. The Delayed Detached Eddy Simulation (DDES) was introduced to mitigate this problem according to [21].

### 2.1. Theory

In this research, the Shear Stress Transport  $k$ - $\omega$  formulation of DDES was employed as recommended in [22]. This approach is described by Equations (1) and (2), showing a good ratio of compliance between the experimental data and calculation cost, compared with another modern LES approach [23].

Turbulence kinetic energy:

$$\frac{\partial k}{\partial t} + \frac{\partial k}{\partial x_j} (\bar{v}_j k) = P^k - \beta^* k \omega + \frac{\partial}{\partial x_j} \left[ \left( \nu + \frac{\nu_t}{\sigma_k} \right) \frac{\partial k}{\partial x_j} \right], \quad (1)$$

Specific dissipation rate:

$$\frac{\partial \omega}{\partial t} + \frac{\partial \omega}{\partial x_j} (\bar{v}_j \omega) = \frac{\partial}{\partial x_j} \left[ \left( v + \frac{v_t}{\sigma_\omega} \right) \frac{\partial \omega}{\partial x_j} \right] + \alpha \frac{P^k}{v_t} - \beta \omega^2 + 2(1 - F_1) \frac{\sigma_\omega \omega^2}{\omega} \frac{\partial k}{\partial x_i} \frac{\partial \omega}{\partial x_i} \quad (2)$$

The selected model is suitable for simulating both parts of the boundary layer: outer with the  $k-\varepsilon$  model in a free-flow zone, thus avoiding the known problem of the standard  $k-\omega$  model being too sensitive to the free-stream condition as per [24], and inner by  $k-\omega$ , with better behavior on adverse pressure gradients.

The action mechanism of  $k-\omega$  SST DDES is based on using the «switch» in a modified dissipation term (3):

$$\varepsilon = -\beta^* k \omega \rightarrow \beta^* k \omega \cdot F_{DES}, \quad F_{DES} = \left[ \max \left( \frac{L_t}{C_{DES} \Delta}, 1 \right) - 1 \right] \quad (3)$$

where  $\Delta$ —largest cell size (4):

$$\Delta = \max(\Delta_x, \Delta_y, \Delta_z), \quad (4)$$

$f_{DES}$ —shielding function and  $L_t$  is the turbulent length scale (5):

$$L_t = \frac{\sqrt{k}}{\beta^* \cdot \omega}, \quad (5)$$

Thus, when  $f_{DES} = 0$  and/or  $C_{DES} \Delta > L_t$ , the solution is obtained by means of RANS. Otherwise, Large Eddy Simulation is used.

### 2.2. Studied Geometry

The geometry under study is a HAWT weather vane (Figure 1) of the following size: 0.25 m × 0.02 m × 0.06 m. Since the bottom part of the vane rack does not influence torque occurrence but generates an additional turbulence that complicates calculation, it was decided not to consider it in the numerical simulation.

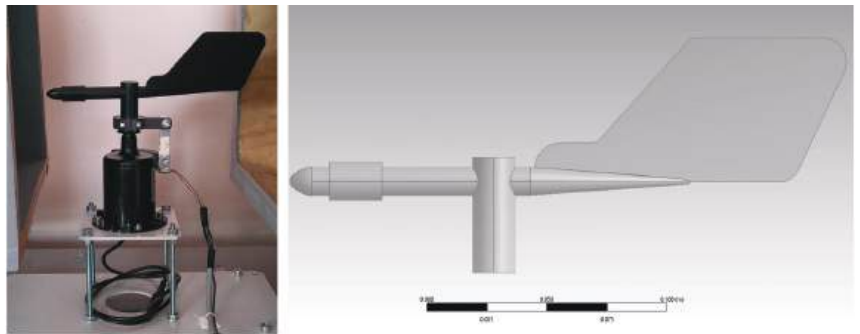


Figure 1. Photo of horizontal axis wind turbine weather vane and its 3D model.

### 2.3. Mesh Preparation

The finite volume method starts from dividing the study area into simple geometric shapes. The structure of the cells to be analyzed by computer has a setting with a simple function inside each. Thus the more cells, the more accurate the calculation is. At the same time, the growth in the number of cells is accompanied by an increase in time and cost of computer resources. When working with CFD, the problem often appears in the determination of optimal ratio between the accuracy of solution and the resources spent to obtain it. The following description presents the process of generating optimal mesh for simulation.

### 2.3.1. Mesh Regions' Description

According to [25], it is advisable to highlight zones where the proper mesh should be generated in all of them. The geometry can then be analyzed, identifying the corresponding zones, as shown in Figure 2.

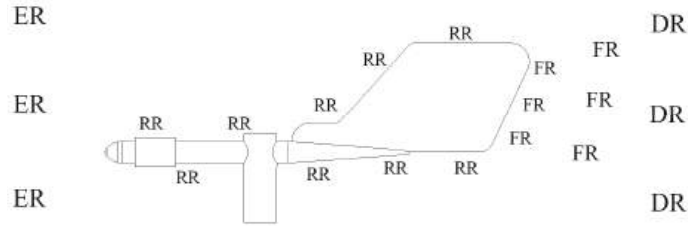


**Figure 2.** Weather vane flow regions: ER—Euler region, RR—RANS region, FR—Focus region, DR—Departure region.

The Euler region (ER) is a place with almost no disturbance of the flow, so there is no need for a dense mesh. The RANS region (RR) includes viscous and outer regions (not indicated due to their small sizes). This part has the same mesh requirements as basic RANS modeling faces. As soon as the disturbance of flow caused by obstacles appears, the LES region (LR) is involved. LES region consists of Focus region (FR) and Departure (DR) region. FR is a zone of high turbulence because of strong separation effects. To achieve a good resolution in all mesh directions, the cells in FR should be of a cubic form. DR is an extension of FR and does not require 100% of turbulence structures to be resolved; thus, the mesh is incremented, allowing RANS to be switched on.

### 2.3.2. Hybrid Approach

The mesh model for the flow streaming around the weather vane is difficult to study using hexahedral cells, i.e., structured mesh. That is why a hybrid mesh was used for the current study.

The hybrid mesh (Figure 3) represents a tetrahedral mesh with prismatic layer in the geometrical area to be studied, and hexahedral mesh in the rest of the region. To create this mesh, the computational domain was divided into blocks, in which the mesh sizes were set according to the region types (Figure 2).

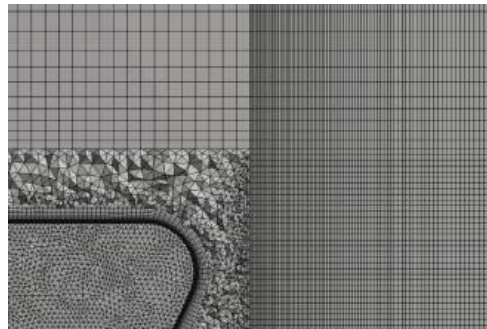


**Figure 3.** Hybrid mesh in weather vane tail area.

### 2.3.3. Boundary Layer

Meshes required for implementation of DDES in the near-wall region, coincide with meshes required for solving the RANS equations. They are considerably larger than the meshes needed for calculating a small near-wall vortices in the framework of LES. Thus, the preparation of mesh in the near-wall region was made according to RANS concept.

The thickness of the boundary layer (BL) was calculated using the Schlichting Formula (6) for a developed turbulent BL and was further used to create the inflation layer.

$$h = 0.37 \cdot l \cdot \left( \frac{1}{\text{Re}_l^{1/5}} \right), \quad (6)$$

$$\text{Re} = U_\infty \cdot l \cdot \frac{\rho}{\mu}$$

where  $U_\infty$ —stream velocity,  $l$ —characteristic size,  $\rho$ —air density equal to 1.225 kg/m<sup>3</sup>,  $\mu$ —dynamic viscosity is  $1.85 \times 10^{-5}$  kg/m s.

To ensure the required value of  $y^+ = 1$  (location of the first cell in viscous sublayer), thickness of first near-wall cell was calculated using formula (7):

$$\Delta y = \frac{y^+ \mu}{\rho U_\tau}, \quad (7)$$

where  $U_\tau$ —friction velocity (8):

$$U_\tau = \sqrt{\frac{\tau_\omega}{\rho}}, \quad (8)$$

where  $\tau_\omega$ —wall shear stress (9):

$$\tau_\omega = 0.5 \cdot C_f \cdot \rho \cdot U_\infty^2, \quad (9)$$

#### 2.4. Spatial Resolution

Mesh resolution has crucial influence on the accuracy of the calculation results as reported in [26–28]. To create a mesh with good resolution, it is necessary to conduct a preliminary RANS simulation. This also provides valuable data, such as pressure and velocity fields for subsequent transient simulation, accelerating final calculations. Thus, all steady simulations are performed until convergence reaches value  $1 \times 10^{-4}$  of residuals and stabilization of monitored values, such as mass flow rate on outlet.

In accordance with the recommendation of Pope in [29], about 80% of resolved turbulence kinetic energy (TKE) should be achieved for better quality of solution. According to Young-Person's Guide [25], it is necessary to have at least 5 cells on turbulent length scale (5) to resolve such level of turbulent kinetic energy.

As a result, a finite volume mesh was iteratively refined in weather vane bounded area to have at least 5 cells per  $L_t$  in FR volume. Changing resolution fields with mesh refinement for AoA = 15° case can be seen in Figure 4.

As can be seen from Figure 4, it was not possible to achieve 100% coverage of FR mesh with the required resolution. The tail stall region near wall has low resolution, which should not affect further simulation due to calculation of a near-wall layer by RANS  $k-\omega$  SST forces. Rest of FR has resolution of about required value of 5. The same preparation of mesh was fulfilled for all other cases.

#### 2.5. Temporal Resolution

It should be noted that temporal resolution has to match the spatial one. The Courant–Friedrichs–Lewy condition (10) is used to evaluate the correctness of chosen time step in transient calculations:

$$C = \frac{U_\infty \cdot \Delta t}{\Delta x}, \quad (10)$$

where  $U_\infty$ —magnitude of velocity,  $\Delta t$ —is time step,  $\Delta x$ —characteristic length, equal to the pitch of mesh at the trailing edge of weather vane.

The value of Courant number is equal to 1, which means that one time step particle motion corresponds to one mesh step. An acceptable estimation of Courant number for calculations of complex aerodynamics is considered to be a value that does not exceed '1' in FR. According to this assessment, the integration step was set up during the simulation to achieve the required Courant–Friedrichs–Lewy CFL level.

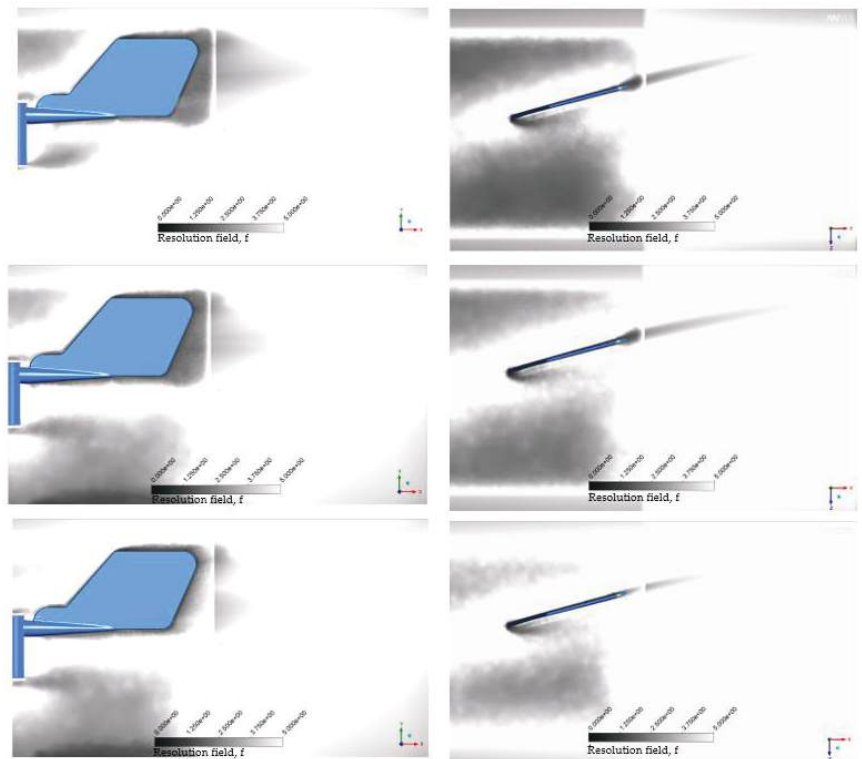


**Figure 4.** Consistent mesh refinement for obtaining acceptable resolution in the separation region (angle of attack =  $15^\circ$ ). The scale is displayed in the vane plane and in the ZX plane at middle-line of tail.

The total time of each simulation was 5 complete passes of the air mass through the computational domain. The observed values were averaged for the last two passes.

### 2.6. Boundary Conditions

The domain of  $2\text{ m} \times 0.5\text{ m} \times 0.5\text{ m}$  size includes both inlet and outlet. The study was made at flow rate of  $10\text{ m/s}$  from inlet since this speed is optimal for the operation of most megawatt-class HAWTs. A zero-pressure outlet was used with a reverse flow from neighborhood-cell condition turned on to enhance a solver robustness. No-slip wall condition, applied for all walls, implies a zero roughness.

### 2.7. Monitors Setup

The axial torque was monitored during simulation. To monitor the convergence, in addition to the residuals and CFL in FR, stabilization of the mass flow rate was monitored through outlet.

## 3. Experimental Research

The experimental study was performed using a small-size aerodynamic pipe (Figure 5a). The air flow is moved in a closed looped tunnel, driven by centrifugal fan (1). The wind tunnel has an open working area (2) with the following dimensions:  $300\text{ mm} \times 300\text{ mm} \times 250\text{ mm}$ . The open working area ensures the constancy of the total pressure and eliminates the influence of the walls on the measured characteristics, which contributes to the similarity of the experimental conditions and real object. This pipe was calibrated by measuring the wind speed at 9 cross-sectional positions (Figure 5b) using a telescopic anemometer probe (Figure 5c). The

required air flow velocity was achieved by changing the rotation speed of the suction turbine by frequency controller. The torque (force) on the vane shaft was measured by strain gauge providing accuracy up to 0.01 g. The reading frequency was set to 1 kHz.

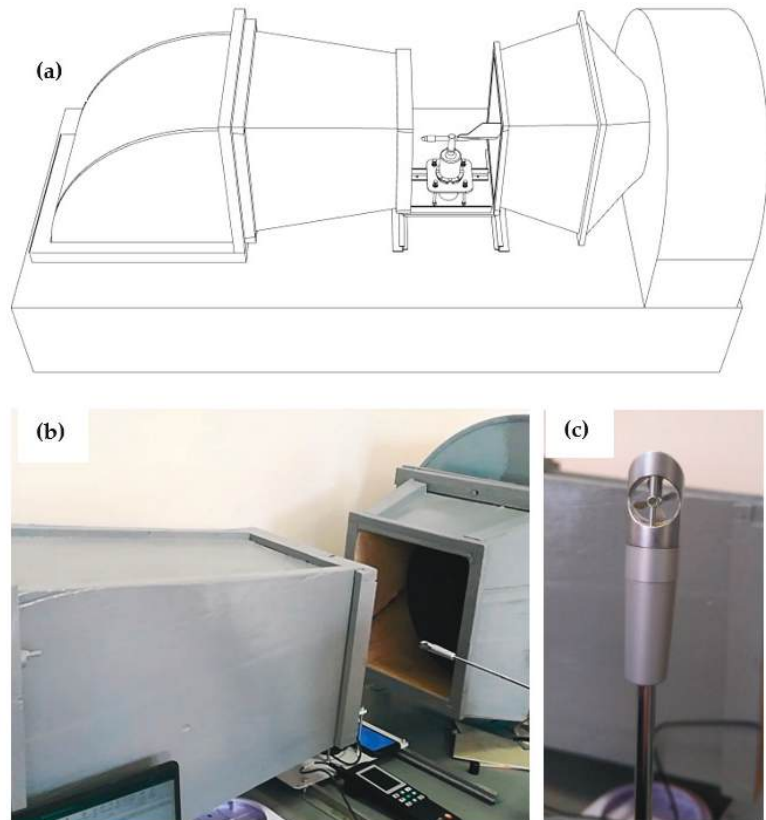


**Figure 5.** Aerodynamic pipe overall sketch (a), working area for the wind velocity measurements (b) and anemometer probe (c).

Next, the results and discussion are presented to finalize the research.

#### 4. Results and Discussion

Validation of the spatial resolution starts with an evaluation of the  $Y_{plus}$  value on the weather vane's surface. Table 1 consists of  $Y_{plus}$  data for all cases studied in this work. The readings satisfy the following condition: the first near-wall cell enters the viscous sublayer, excluding the usage of near-wall functions by the solver.

The second part of the table shows the values of the Courant number in the FR. During the simulation, the size of the time step was adjusted depending on the volume-averaged CFL. As the angle of attack increases, the CFL increases as well, so a reduction in the time step corresponding to the design case is required. Compliance with the requirements for the CFL value was achieved on optimized meshes with a gradual decrease in the time step from  $1 \times 10^{-3}$  to  $1 \times 10^{-4}$ .

In the obtained data, there is a sharp increase in the volume-averaged Courant number at a 15 degrees angle of attack, and a slight decrease at 20 degrees. This phenomenon can be explained by the transition from a near-separated flow around to a developed turbulent one at an  $AoA = 45^\circ$ , with periodic stall (lower and upper edges with swirling vortex

shedding, absent in the  $k-\omega$  SST case), which disappears with an increase in the angle of attack, turning to a stable one over the entire surface of the weather vane (Figure 6).

**Table 1.** Yplus, Courant–Friedrichs–Lewy number and turbulence kinetic energy ratio in Focus Region distribution.

AoA	Yplus			CFL in FR			TKE Ratio
	Min	Max	Face Avg.	Min	Max	Face Avg.	FR Avg.
0°	0.021	0.846	0.328	0.300	7.795	0.699	89.1%
5°	0.032	0.941	0.366	0.273	8.342	0.718	65.4%
10°	0.037	1.056	0.395	0.229	9.029	0.726	64.5%
15°	0.042	0.961	0.400	0.258	9.390	0.961	49%
20°	0.057	1.07	0.435	0.246	6.825	0.855	51%
45°	0.065	1.082	0.440	0.137	7.475	1.052	71%

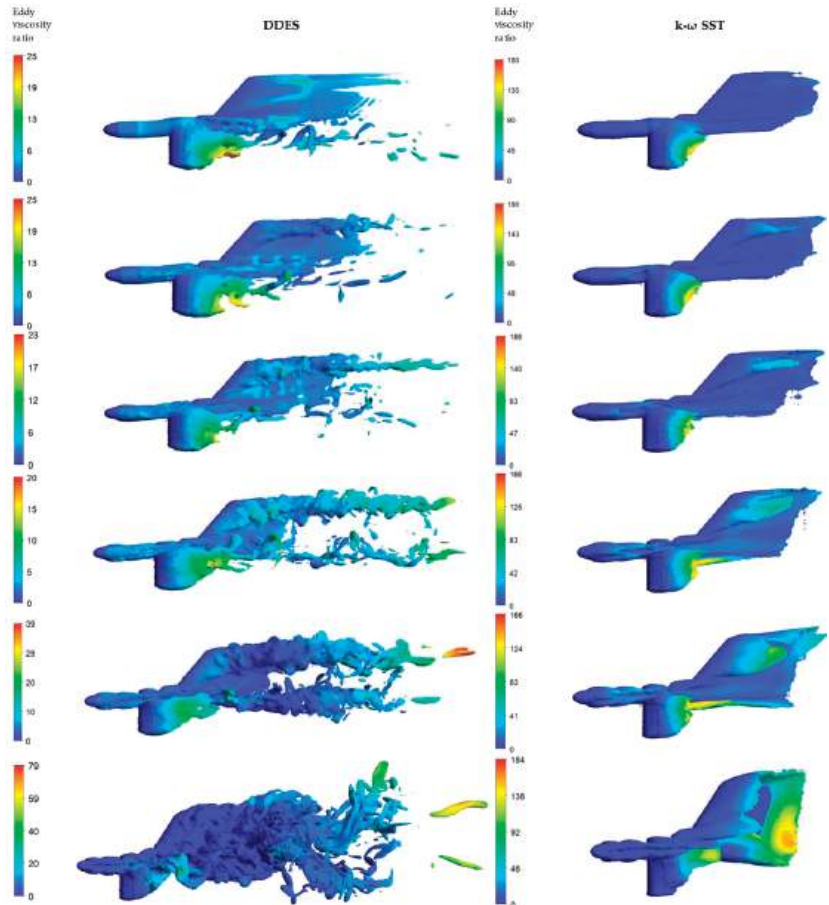


**Figure 6.** Delayed Detached Eddy Simulation (left) and  $k-\omega$  Shear Stress Transport (right) development of vortex structure behind horizontal axis wind turbine’s vane, isosurface of vorticity colored by eddy viscosity ratio.

The next point in the validation of the spatial resolution is to determine the level of resolved TKE. As was previously noted, it is advisable for this to be higher than 80%, which is indicated to achieve good quality of the simulation. The level of resolved turbulence was estimated by calculating the ratio of the resolved turbulence  $k_{res}$  to the sum of the resolved and modeled components in the FR.

The reduced percentage of TKE resolution was probably obtained due to the inaccurate preliminary estimation of the spatial resolution when creating the mesh due to the non-100% correspondence of the shape of the cells to the cube. However, the used meshes give a relatively high level of resolution, and the resulting moment values are in good compliance with the experimental values (Figure 7).

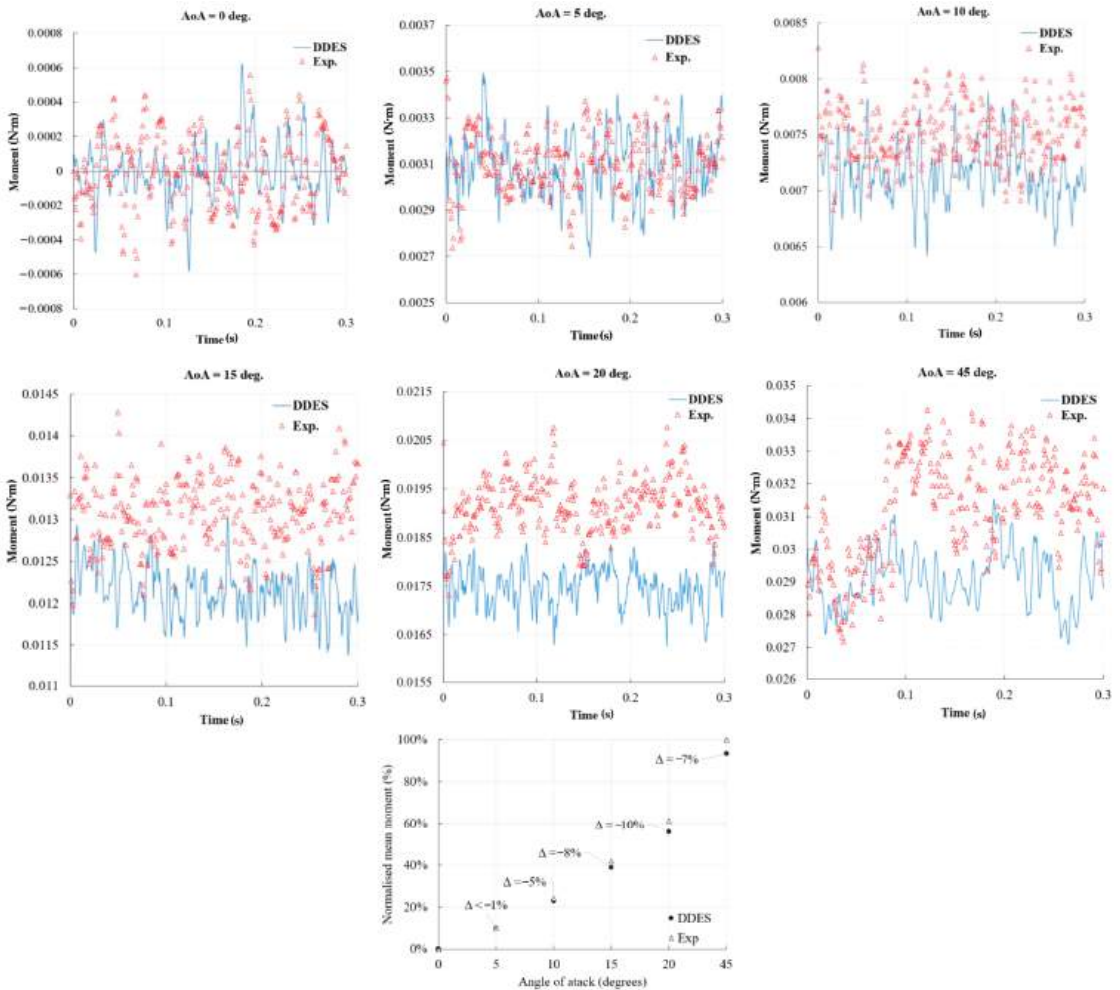


**Figure 7.** Instantaneous moment for measured cases and normalized mean moment from angle of attack.

In addition to the above-described validation steps, an integral error was determined in accordance with the methodology presented in [30,31]. The calculation took into account the usage of the second-order scheme and a maximum error level of 1%. The results are summarized in Table 2.

**Table 2.** Accumulated error and reliability estimation for calculated cases.

AoA	Accumulated Error, %	Reliability ( $\frac{n_{max}}{n}$ )
0	$8.73333 \times 10^{-5}$	17,481.5
5	$6.5029 \times 10^{-5}$	31,530.06
10	$6.5029 \times 10^{-5}$	31,530.06
15	$5.13081 \times 10^{-5}$	50,648.49
20	$5.13081 \times 10^{-5}$	50,648.49
45	$4.02481 \times 10^{-5}$	82,309.1

According to the results obtained, it can be argued that the accumulated error is small, and due to the high value of reliability (ratio of maximum allowable number of time steps to actual number), the numerical simulation can be significantly extended without the significant impact of errors, if necessary.

For the analysis of the experimental and numerical data, power spectral density (PSD) graphs were obtained using Welch's method (Figure 8). The comparison showed the similarity in the frequencies of weather vane oscillations caused by the shedding of vortices with different kinetic energies, which indicates the similarity in the aerodynamics of the vortices simulated in CFD and obtained from the experiment. For the cases requiring most computation, the biggest difference is observed in the high-frequency spectrum (100–1000 Hz) with low amplitude, which in numerical simulation corresponds to frequencies of the smallest eddies modeled by the subgrid model. According to the Kolmogorov turbulent cascade, these vortices have low energy and do not strongly affect the characteristics. For angles of attack of 10, 15, 20 and 45 degrees, there is a noticeable increasing the difference in the mid-frequency part of the spectrum (10–100 Hz). In the low-frequency spectrum, the greatest deviation is observed for angles of 15 and 20 degrees, and the angle of attack of 45 degrees shows a smaller level of deviation. Thus, the obtained differences in the averaged values are explained by the differences in low- and mid-frequency spectra. It is also necessary to take into account the influence of the flow pulsations in the wind tunnel due to the open type of working area. The pulsations introduce additional fluctuations to the kinetic energy of the flow, which in turn affects the shape of the boundary layer and the subsequent difference in aerodynamic characteristics. From the CFD point of view, the error can be explained by the insufficient resolution of the grid, and as a consequence, by the lowered turbulent kinetic energy ratio. To obtain similar PSDs in these areas, a significant mesh refinement and decrease in time step are required, which transfers the simulation into the DNS class.

In addition, an assessment of the time spent on the preparation and calculation of the numerical experiment and the full-scale one was performed during the study. The DDES preparation time consists of three main steps.

The first stage is the preparation of the geometry. In the case of RANS and DDES, it takes the same time and directly depends on its complexity.

At the second stage, the finite volume mesh is prepared. RANS requires a mesh independence test, which requires several meshes with different densities. To prepare the final DDES mesh, it is not advisable to perform mesh independence tests due to excessive time costs. In this study, we applied a method, according to which the optimal mesh resolution was obtained based on the results of preliminary RANS modeling with successive mesh refinement in FR. As noted above, the preliminary RANS simulations also allow speeding up of the DDES. Thus, the preparation of the final mesh requires approximately the same refinement steps, but for DDES, this procedure is associated with a large number of operations.

The third stage is the simulation. DDES, compared to RANS  $k-\omega$  SST, requires several thousand time steps to obtain statistically averaged values, each of which converge to the required level of residuals for several iterations per time step. Steady-state aerodynamic

performance in RANS rarely requires more than 500 iterations. It is important to note the need to monitor the Courant number in the FR for DDES, setting the time step according to the observed values.

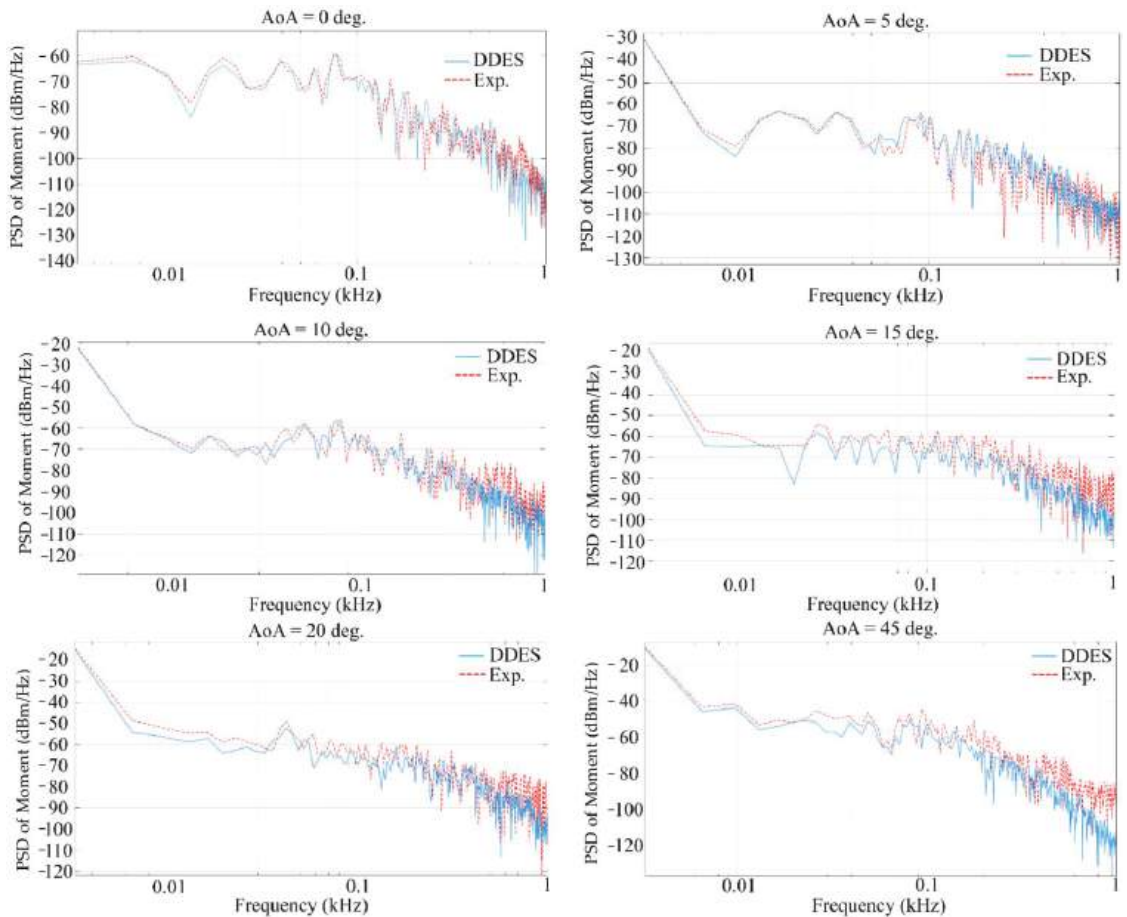


**Figure 8.** Power spectral density of moment for all angles of attack.

The value of the time costs that cannot be estimated includes the time of loading the results for processing in a postprocessor, which is significantly higher for DDES due to the larger amount of data.

The final distribution of time costs in the preparation of one design case is summarized in Table 3.

**Table 3.** Reynolds-averaged Navier–Stokes and Delayed Detached Eddy Simulation time costs single case.

Stage №	RANS k- $\omega$ SST (h)	DDES (h)
1	3	3
2	7	10
3	5	26
Total:	15	39 (+260%)

## 5. Conclusions

In this paper, the numerical simulation of the weather vane of a horizontal axis wind turbine was performed to obtain the most accurate aerodynamic characteristics at the lowest possible computational costs. To assess the numerical approach, the previous works in this area, related to Detached Eddy Simulation and its modifications, were analyzed. Studies on the geometry of simple and medium complexity have shown the advantage of using Detached Eddy Simulation modification. Unfortunately, in these works, the stage of the preparation of computational grids, as well as the numerical experiment itself, was overlooked or poorly detailed. To fill up the research gap, the Delayed Detached Eddy Simulation was used. It was prepared in accordance with the recommendations given in the literature, using new techniques for the preparation of numerical modeling: a hybrid grid, validation with the study of the degree of resolution of the grids with further iterative correction of low-quality regions. The analysis of the simulation of weather vane aerodynamics showed a positive result in general. The following are the key findings:

- When creating a finite volume mesh for the design case where the angle of attack =  $5^\circ$ , the required resolution was achieved on sufficiently large grids (5 and 5 cells compared to 1 and 6 at angle of attack =  $10^\circ$ ). The presence of large stall zones leads to significant increases in mesh density (2 and 6 cells for angle of attack =  $45^\circ$ ).
- The largest deviations from the experimental values were obtained for calculated cases at 15 and 20 degrees with the worst turbulence kinetic energy resolution values. However, the error did not exceed 10%, so the recommendation about the need for 80% turbulence kinetic energy resolution can be revised towards lower values to save resources.
- A significant difference in aerodynamic coefficients between Delayed Detached Eddy Simulation and k-w Shear Stress Transport is noticeable starting from low angles of attack because for bluff bodies, the rate of formation of turbulent structures does not allow a second model to adequately reflect the aerodynamics of the studied geometry. The use of the Reynolds-averaged Navier–Stokes to obtain aerodynamic coefficients is reasonable in the absence of strong vortex formation only.
- Delayed Detached Eddy Simulation requires more time to prepare a mesh, and set up and run the simulation. The preparation and calculation of just one case takes approximately 2.5 to 4 times longer than Reynolds-averaged Navier–Stokes. The usage of Delayed Detached Eddy Simulation for urgent applications remains questionable.

The current increase in computer performance leads to the fact that computing power at the moment can allow partial transition to hybrid approaches in aerodynamic calculations of medium complexity. Thus, the modeling approach considered in this article, as well as the results obtained and the conclusions drawn, can already be applied in the engineering practice of numerical modeling for the renewable energy, aircraft and architecture industries.

At the end of this conclusion, it has to be noted that although Delayed Detached Eddy Simulation is more expensive both in terms of preparation and computing resources, the shortcomings can be neglected when using the recommendations of the developers and the described preparation methodology.

Further research of authors can be directed towards a mathematical modeling of yaw control dynamic systems with the usage of the gained results to improve the yaw error compensators algorithms.

**Author Contributions:** Conceptualization and methodology, E.V.S.; software, G.N.R.; validation, G.N.R. and E.V.S.; formal analysis, E.V.S.; investigation, E.V.S. and G.N.R.; resources, G.N.R.; data curation, E.V.S.; writing—original draft preparation, G.N.R.; writing—review and editing, E.V.S.; visualization, G.N.R.; supervision, E.V.S.; project administration, E.V.S.; funding acquisition, E.V.S. and G.N.R. All authors have read and agreed to the published version of the manuscript.

**Funding:** This research was funded by the Russian Science Foundation, grant number 23-11-20016.

**Data Availability Statement:** Data are available upon request to the corresponding author.

**Conflicts of Interest:** The authors declare no conflict of interest.

### Nomenclature and Abbreviation

The following abbreviations are used in this article:

HAWT	Horizontal axis wind turbine
CFD	Computational fluid dynamics
SST	Shear Stress Transport
DES	Detached Eddy Simulation
DDES	Delayed Detached Eddy Simulation
ZDES	Zonal Detached Eddy Simulation
LES	Large Eddy Simulation
SA	Spalart–Allmaras
LiDAR	Light detection and ranging
RANS	Reynolds-averaged Navier–Stokes
DNS	Direct numerical simulation
ER	Euler region
RR	RANS region
LR	LES region
FR	Focus region
DR	Departure region
BL	Boundary layer
TKE	Turbulence kinetic energy
CFL	Courant–Friedrichs–Lewy
AoA	Angle of attack
PSD	Power spectral density

The following nomenclature are used in this article:

$k$	Turbulent kinetic energy
$P_k$	Production term
$w$	Specific dissipation rate
$t$	Time
$\nu$	Kinematic viscosity
$\nu_t$	Kinematic turbulent viscosity
$\alpha, \beta^*, \beta, \sigma_k, \sigma_w$ and $\sigma_{w2}$	Model coefficients
$F_1$	Switch function of $k$ - $\omega$ SST
$\varepsilon$	Dissipation
$C_{DES}$	DES model constant
$\Delta$	largest cell size
$f_{DDES}$	Shielding function
$L_t$	Turbulent length scale
$h$	Boundary layer
$Re$	Reynolds number
$U_\infty$	Stream velocity
$l$	Characteristic size
$\rho$	Air density
$\mu$	Dynamic viscosity
$y^+$	Dimensionless distance from the wall
$U_\tau$	Friction velocity
$\tau_w$	Wall shear stress
$C_f$	Friction coefficient
$\Delta t$	Time step
$\Delta x$	Pitch of the mesh
$n$	Actual number of time steps
$n_{max}$	Maximum allowable number of time steps

## References

- Lee, J.; Zhao, F. Global Wind Report 2022. Available online: <https://gwec.net/wp-content/uploads/2022/03/GWEC-GLOBAL-WIND-REPORT-2022.pdf> (accessed on 21 February 2023).
- REN21, 2021, Renewables 2021 Global Status Report (Paris: REN21 Secretariat). Available online: [https://www.ren21.net/wp-content/uploads/2019/05/GSR2021\\_Full\\_Report.pdf](https://www.ren21.net/wp-content/uploads/2019/05/GSR2021_Full_Report.pdf) (accessed on 21 February 2023).
- Kim, M.-G.; Dalhoff, P.H. Yaw Systems for wind turbines—Overview of concepts, current challenges and design methods. *J. Conf. Ser.* **2014**, *524*, 012086. [CrossRef]
- Song, D.; Li, L.; Yang, J.; Joo, Y.H. A Model predictive control for the yaw control system of horizontal-axis wind turbines. *Energy Procedia* **2019**, *158*, 237–242. [CrossRef]
- El-Mallawany, A.R.; Shaaban, S.; Hafiz, A.A. A neural networking based fault detection system for pitch and yaw control of a HAWT under different operating conditions. *Energy Rep.* **2022**, *8*, 13101–13113. [CrossRef]
- Scholbrock, A.; Fleming, P.; Wright, A.; Slinger, C.; Medley, J.; Harris, M. *Field Test Results from LIDAR Measured Yaw Control for Improved Yaw Alignment with the NREL Controls Advanced Research Turbine* (No. NREL/CP-5000-63202); National Renewable Energy Lab. (NREL): Golden, CO, USA, 2014.
- Solomin, E.V. Centrifugal Controller of Rotation Frequency for Vertical Axis Wind Turbine. *J. King Saud Univ. Eng. Sci.* **2022**. [CrossRef]
- Solomin, E.V.; Ryavkin, G.N.; Sirotkin, E.A. Determination of Maximum Deflection Angles of a HAWT Yawing System Weather Vane Based on the Solution of the Equations of Moments. In Proceedings of the ICIEAM 2022, Sochi, Russia, 20 May 2022. [CrossRef]
- Solomin, E.V.; Terekhin, A.A.; Martyanov, A.S.; Kovalyov, A.A.; Ismagilov, D.R.; Ryavkin, G.N.; Kulganatov, A.Z.; Pogorelov, B.T. Evaluation of influence of turbulence models on the vortex formation processes modeling in wind power. *J. Samara State Tech. Univ.* **2022**, *26*, 339–354. [CrossRef]
- Solomin, E.V.; Terekhin, A.A.; Martyanov, A.S.; Shishkov, A.N.; Kovalyov, A.A.; Ismagilov, D.R.; Ryavkin, G.N. Horizontal axis wind turbine yaw differential error reduction approach. *Energy Convers. Manag.* **2022**, *254*, 115255. [CrossRef]
- Wang, G.; Tang, Y.; Gao, Y.; Liu, Y. Evaluation of DDES based on SST  $k-\omega$  Model with Different Shielding Functions for Tip Leakage Flow in Turbomachinery. In Proceedings of the GPPS Xi'an21 Conference, Xi'an, China, 18 October 2021. [CrossRef]
- Deck, S. Recent improvements in the Zonal Detached Eddy Simulation (ZDES) formulation. *Theor. Comput. Fluid Dyn.* **2011**, *26*, 523–550. [CrossRef]
- Cengiz, K.; Özyörük, Y. Experiences with two detached eddy simulation approaches through use of a high-order finite volume solver. *Int. J. Numer. Methods Fluids* **2020**, *92*, 899–921. [CrossRef]
- Huck, V.; Morency, F.; Beaugendre, H. Grid study for Delayed Detached Eddy Simulation's grid of a pre-stalled wing. In Proceedings of the CASI Aero 2019—Canadian Aeronautics and Space Institute's AERO 2019 Conference, Laval, QC, Canada, 14–16 May 2019.
- Spalart, P.R. Comments on the Feasibility of LES for Wings and on the Hybrid RANS/LES Approach. In Proceedings of the First AFOSR International Conference on DNS/LES, Ruston, LO, USA, 4–8 August 1997; pp. 137–147.
- Garbaruk, A.V.; Sagittariu, M.H.; Travin, A.K.; Shur, M.L. *Modern Approaches to Turbulence Modeling*; Polytechnic Publishing House: St. Petersburg, Russia, 2016.
- Menter, F.R. *Turbulence Modeling for Engineering Flows*; Ansys, Inc.: Canonsburg, PA, USA, 2011.
- Tavakol, M.M.; Abouali, O.; Yaghoubi, M. Large eddy simulation of turbulent flow around a wall mounted hemisphere. *Appl. Math. Model.* **2015**, *39*, 3596–3618. [CrossRef]
- Strelets, M. Detached eddy simulation of massively separated flows. In Proceedings of the 39th Aerospace Sciences Meeting and Exhibit, Reno, NV, USA, 8–11 January 2001.
- Menter, F.R.; Kuntz, M. Adaptation of eddy-viscosity turbulence models to unsteady separated flow behind vehicles. In *The Aerodynamics of Heavy Vehicles: Trucks, Buses, and Trains*; Springer: Berlin/Heidelberg, Germany, 2004.
- Spalart, P.; Deck, S.; Shur, M.; Squires, K.; Strelets, M.K.; Travin, A. A New Version of Detached-Eddy Simulation, Resistant to Ambiguous Grid Densities. *Theor. Comput. Fluid Dyn.* **2006**, *20*, 181–195. [CrossRef]
- Gritskevich, M.S.; Garbaruk, A.V.; Schütze, J.; Menter, F.R. Development of DDES and IDDES formulations for the  $k-\omega$  shear stress transport model. *Flow Turbul. Combust.* **2012**, *88*, 431–449. [CrossRef]
- Geng, F.; Kalkman, I.; Suiker, A.; Blocken, B. Sensitivity analysis of airfoil aerodynamics during pitching motion at a Reynolds number of  $1.35 \times 10^5$ . *J. Wind Eng. Ind. Aerodyn.* **2018**, *183*, 315–332. [CrossRef]
- Menter, F.R. Influence of freestream values on  $k-\omega$  turbulence model predictions. *AIAA J.* **1992**, *30*, 1657–1659. [CrossRef]
- Spalart, R. *Young-Persons Guide to Detached-Eddy Simulation Grids*; Technical Report NASA CR-2001-211032; NASA: Washington, DC, USA, 2001.
- Vatsa, V.N.; Lockard, D.P.; Spalart, P.R. Grid sensitivity of SA-based delayed-detached-eddy-simulation model for blunt-body flows. *AIAA J.* **2017**, *55*, 2842–2847. [CrossRef]
- Morton, S.A.; Forsythe, J.R.; Squires, K.D.; Wurtzler, K.E. Assessment of unstructured grids for detached-eddy simulation of high Reynolds number separated flows. In Proceedings of the 8th ISGG Conference, Honolulu, HI, USA, June 2002.
- Georgiadis, N.J.; Rizzetta, D.P.; Fureby, C. Large-Eddy Simulation: Current Capabilities, Recommended Practices, and Future Research. *AIAA J.* **2010**, *48*, 1772–1784. [CrossRef]

29. Pope, S.B. *Turbulent Flows*; Cambridge University Press: Cambridge, UK, 2000; 771p.
30. Smirnov, N.N.; Betelin, V.B.; Nikitin, V.F.; Stamon, L.I.; Altoukhov, D.I. Accumulation of Errors in Numerical Simulations of Chemically Reacting Gas Dynamics. *Acta Astronaut.* **2015**, *117*, 338–355. [CrossRef]
31. Smirnov, N.N.; Betelin, V.B.; Shagaliev, R.M.; Nikitin, V.F.; Belyakov, I.M.; Deryuguin, Y.N.; Aksenov, S.V.; Korchazhkin, D.A. Hydrogen fuel rocket engines simulation using LOGOS code. *Int. J. Hydrogen Energy* **2014**, *39*, 10748–10756. [CrossRef]

**Disclaimer/Publisher's Note:** The statements, opinions and data contained in all publications are solely those of the individual author(s) and contributor(s) and not of MDPI and/or the editor(s). MDPI and/or the editor(s) disclaim responsibility for any injury to people or property resulting from any ideas, methods, instructions or products referred to in the content.



Article

# Measuring and Modelling the Concentration of Vehicle-Related PM<sub>2.5</sub> and PM<sub>10</sub> Emissions Based on Neural Networks

Vladimir Shepelev <sup>1,\*</sup>, Aleksandr Glushkov <sup>2</sup>, Ivan Slobodin <sup>1</sup> and Yuri Cherkassov <sup>3</sup>

<sup>1</sup> Department of Automobile Transportation, South Ural State University (National Research University), 454080 Chelyabinsk, Russia

<sup>2</sup> Department of Mathematical and Computer Modeling, South Ural State University (National Research University), 454080 Chelyabinsk, Russia

<sup>3</sup> Department of Transport and Service, M. Dulatov Kostanay Engineering and Economic University, Kostanay 110000, Kazakhstan

\* Correspondence: shepelevvd@susu.ru

**Abstract:** The urban environment near the road infrastructure is particularly affected by traffic emissions. This problem is exacerbated at road junctions. The roadside concentration of particulate (PM<sub>2.5</sub> and PM<sub>10</sub>) emissions depends on traffic parameters, meteorological conditions, the characteristics and condition of the road surface, and urban development, which affects air flow and turbulence. Continuous changes in the structure and conditions of the traffic flow directly affect the concentration of roadside emissions, which significantly complicates monitoring and forecasting the state of ambient air. Our study presents a hybrid model to estimate the amount, concentration, and spatio-temporal forecasting of particulate emissions, accounting for dynamic changes in road traffic structure and the influence of meteorological factors. The input module of the model is based on data received from street cameras and weather stations using a trained convolutional neural network. Based on the history of emission concentration data as input data, we used a self-learning Recurrent Neural Network (RNN) for forecasting. Through micromodeling, we found that the order in which vehicles enter and exit an intersection affects the concentration of vehicle-related emissions. Preliminary experimental results showed that the proposed model provides higher accuracy in forecasting emission concentration (83–97%) than existing approaches.

**Keywords:** vehicle-related emissions; recurrent neural networks (RNN); convolutional neural network (CNN); traffic; deep learning

**MSC:** 68T07; 68T45; 91B76; 62R07

**Citation:** Shepelev, V.; Glushkov, A.; Slobodin, I.; Cherkassov, Y.

Measuring and Modelling the Concentration of Vehicle-Related PM<sub>2.5</sub> and PM<sub>10</sub> Emissions Based on Neural Networks. *Mathematics* **2023**, *11*, 1144. <https://doi.org/10.3390/math11051144>

Academic Editor: Georgios Tsekouras

Received: 11 January 2023

Revised: 19 February 2023

Accepted: 23 February 2023

Published: 25 February 2023



**Copyright:** © 2023 by the authors. Licensee MDPI, Basel, Switzerland. This article is an open access article distributed under the terms and conditions of the Creative Commons Attribution (CC BY) license (<https://creativecommons.org/licenses/by/4.0/>).

## 1. Introduction

The growing density of urban populations and the increasing number of vehicles have nearly incapacitated road networks, which are unable to provide proper mobility given urban infrastructural restrictions. This increases the number and severity of traffic jams, leading to negative social, environmental, and economic consequences. Real-time optimization and control of traffic signals is a key strategy for managing traffic congestion and improving traffic conditions in urban areas [1,2]. Adaptive control of traffic signals is based on real-time traffic data, allowing for proper adjustment to signal timing in response to changes in the traffic flow [3,4]. The Transport Demand Management (TDM) strategy is also focused on controlling traffic congestion and its negative effects. This strategy is based on the implementation of various measures to effectively redistribute travel demand, such as developing comfortable public transport; promoting the use of active transport facilities, paid parking, and entrance fees to high-traffic areas; developing alternative routes; etc. A distinctive advantage of TDM is its low cost and flexible implementation in various conditions. The introduction of TDM contributes to sustainable transport development,

reduces costs (fuel, time), reduces traffic congestion, improves road safety, and reduces traffic-related harmful emissions [5–7].

Given the importance of adaptive traffic light control for urban mobility, many signal control methods have been developed and successfully implemented. However, these solutions are not always effective, since they do not take into account environmental aspects, which are largely determined by the dynamic structure of the traffic flow and meteorological factors [8,9]. At the same time, accurate situational forecasting of the road situation that accounts for environmental factors enables traffic control systems to make appropriate decisions. This is a key factor in effective traffic management. Given the influence and variability of different factors on the organization of sustainable traffic, a methodology for collecting, assessing, and forecasting the dynamic and environmental parameters of traffic flows must be developed.

This paper focuses on forecasting the concentration of particulate (PM<sub>2.5</sub> and PM<sub>10</sub>) emissions at urban signal-controlled intersections. We propose and implement a new data collection system, using the latest advances in vehicle detection and tracking to assess traffic-related emissions, that takes into account vehicle type and driver behavior. The scientific novelty of our study is the real-time assessment and modeling of the concentrations of vehicle-related emissions based on a method that includes the parallel decomposition of artificial neural networks (hybrid model). The input module of the hybrid model based on the optimized You Only Look Once (YOLOv4) recurrent neural network is responsible for collecting, interpreting, and aggregating traffic data to model the formation of maximum ground level emission concentrations, taking into account weather factors. The hybrid model architecture uses the advantage of the rapid obtaining of a large bulk of data by a convolutional neural network on the influence of traffic parameters and meteorological factors on the formation of emission concentrations. The forecasting module based on the Long Short-Term Memory (LSTM) recurrent neural network received continuous feature extraction to improve the accuracy of forecasting the distribution of concentrations of harmful emissions, taking into account spatio-temporal correlations (urban development).

We verified our model through laboratory tests and simulations and provided empirical evidence that the proposed solution is sufficiently accurate and can be further used as a launching point for other high-level models.

In the Literature Review section, we review scientific publications on emissions assessments and forecasting. The Materials and Methods section describes our approach to assessing and collecting parametric data on traffic-related emissions. The Experiment and Verification section presents an evaluation report and details of the experiment. The Discussion and Results section analyzes and generalizes the obtained results. Finally, the Conclusions section reviews the main results of the study and highlights areas of further research.

### *Literature Review*

Growing road traffic density has become the main source of serious negative economic and environmental impact in large cities [10,11]. Several studies have found that poor urban areas are exposed to a higher adverse environmental impact, which affects the health of residents [12–14]; environmental inequality has thus been identified. The problem is more complicated and related to urban planning (dense building development), as well as complex economic and social structures. It is relevant to use a system of effective road traffic management, taking into account environmental aspects, that does not require the deployment of expensive infrastructure for highly populated areas. However, there are traffic-related environmental problems even in small settlements that develop clear urban dynamics and, at the same time, devote insufficient effort and funds to sustainable traffic management [15].

Many studies have also identified the hottest spots in terms of vehicle-related emissions in the urban environment [16–18]. Signal-controlled intersections and road junctions

are the main sources of emissions due to low traffic capacity, long idle periods, and the traffic patterns (acceleration, deceleration, waiting) in these areas.

The driver's behavior significantly affects the time and nature of crossing at an intersection. The situation is especially aggravated by mixed traffic, when the driver finds it difficult to decide on the nature of movement in the so-called dilemma area due to fear of a traffic accident occurring [19–21].

With the advent of new engineering structures and solutions, modern cities are growing not only in width, but also in height. High-rise buildings standing along highways form canyons with accumulating pollutants and a lack of natural ventilation, which contributes to the dispersion of harmful emissions [22–24]. Nevertheless, the levels of street pollution can vary significantly depending on various factors: wind direction and speed, vehicle composition and movement speed, the dimensions of street buildings, degree of landscaping, etc. One study [25] developed a set of urban indicators to quantify the spatial patterns of urban districts and better describe the urban structure.

Over the past decade, there has been a steady increase in the number of studies assessing the concentrations of ultrafine PM<sub>2.5</sub> particles and their impact on the population in urban transport microenvironments [26]. In this paper, the authors conclude that air quality is not uniform in the urban environment; pedestrians and cyclists who choose a low traffic route are exposed to fewer pollutants than people traveling by car.

The main tool for assessing air pollution concentration in urban areas is the Operational Street Pollution Model (OSPM) [27]. However, OSPM has a substantial drawback—it requires hourly background concentration measurements, including those from households, industrial enterprises, etc. Mensink and Cosemans [28] combined the OSPM with the Gaussian Immission Frequency Distribution Model (IFDM) to obtain a more realistic map of pollutant concentrations in the urban environment. A comparison of the simulated and measured data (for NO<sub>2</sub> and PM<sub>10</sub>) showed an accuracy of up to 15%, which is in line with EU directives.

Some researchers have focused on completing an inventory of vehicle-related emissions, accounting for the emission of volatile organic compounds resulting from evaporation. Luo et al. [29] used the Comprehensive Air-quality Model with extensions (CAMx) to comprehensively quantify PM<sub>2.5</sub> and O<sub>3</sub> concentrations in China. The study also assessed public health risks from long-term exposure to these pollutants.

The chemical mass balance (CMB) model consists of a set of linear equations and is used to determine the contribution of various emission sources at the measurement site. This method is based on the assumption that the composition of emissions is constant over time, chemicals do not react with each other, the number of sources is less than or equal to the number of emission types, measurement uncertainties are random, and all emission sources are known. The CMB model [30,31] was used to determine the chemical components of PM<sub>2.5</sub> and PM<sub>10</sub> in a typical Chinese coastal city. As a result, seasonal fluctuations in the dominant sources of pollution were detected: soil dust was more prevalent in winter, while exhaust gasses were more prevalent in spring.

Many sensor-based devices are being deployed in cities to collect data on the state of the ambient air, which constitute the Internet of Things (IoT) for smart cities [32,33]. These sensors are able to accumulate and store only the necessary data from the collected dataset. Hu et al. [34] focused on the lack of 100% availability of data from the Internet of Vehicles (IoV) related to accidental disconnections due to inclement weather (or for other reasons), which leads to incomplete and sparse traffic data. Incomplete data create a traffic planning and forecasting problem. Therefore, Hu et al. proposed a method for short-term traffic flow forecasting based on data from a digital twin of current road traffic.

Yu et al. [35] determined the distribution of pollutants from the traffic flow in a three-dimensional space in a tunnel and along a highway using unmanned aerial vehicles equipped with PM<sub>2.5</sub> sensors. They modeled air quality using the California Gaussian Linear Source Dispersion Model (CALINE4) and the Computational Fluid Dynamics (CFD)

fluid model. A comparison of the simulated and measured data showed that the proposed model for predicting pollutant emissions is effective.

The US Environmental Protection Agency (USEPA) [36] uses various models to study air pollution to understand the formation of air pollutant mixtures and their atmospheric movement: the Community Multiscale Air Quality Modeling System (CMAQ), Air Quality Dispersion Model (AERMOD), MOVES (Motor Vehicle Emission Simulator), mobile device emissions model for air quality analysis, and multimedia and multi-stress modeling to help understand the relationship between the environment and the distribution of pollutants.

The AERMOD is recommended by the USEPA for designing roads and intersections and is also actively used to assess the dispersion and concentration of vehicle-related harmful emissions [37–39]. Thus, the authors of [37] studied the impact of the introduction of cordon pricing on the concentration of PM 2.5 in a downtown area and used the AERMOD to reveal a positive effect both outdoors (the concentration decreased by 7–13%), and indoors. Researchers united the MOVES, AERMOD, and CALINE4 models into MOVES-Matrix [38], a high-performance emission dispersion modeling system. The highly computational model that was developed performs 200 times more calculations than the MOVES and can work with various data sources for hotspot analysis.

Dispersion models require a huge amount of different data for calculations and are time-consuming. Therefore, the authors of [39] developed a link screening methodology to reduce the time spent on calculations without affecting accuracy. Thus, the AERMOD simulation time with the proposed model is only 0.2–1.1% of the conventional AERMOD simulation. Despite all the advantages of the considered models, they are not designed for the real-time assessment of the concentrations of vehicle-related harmful emissions, which does not provide for quick environmental risk management.

New technologies output large data volumes which are successfully and effectively processed by a neural network. The neural network has intelligent data processing functions and can learn, memorize, and forecast data. It is irreplaceable in complex systems with a high degree of unpredictable factors, such as road traffic. Therefore, neural networks have become widely used in research over the past decade.

Teng et al. [40] proposed the use of a new hybrid model combining a bidirectional neural network with long short-term memory to accurately forecast vehicle-related PM<sub>2.5</sub> concentration. The developed model shows trends of PM<sub>2.5</sub> levels over a period of 6 to 24 h and performs very well.

The forecast of vehicle-related pollutant emissions in the urban environment relies primarily on the road traffic forecast. Many studies develop predictive models of urban traffic. Shuai et al. [41] developed a model based on the information on vehicles collected using vehicle communications. Vehicle behavior is considered to be a stochastic process by the queue theory. The model helps to reduce the travel time and standing time of vehicles.

Shang et al. [42] proposed an interesting solution for building a high-precision traffic volume forecasting model using an ensemble deep graph reinforcement learning network. The final version of the model was obtained by combining two neural networks, which allowed the authors to achieve better results than several dozen models developed by various researchers.

The wavelet-attention-based traffic prediction method built on the analysis of weather conditions (temperature, wind speed, rain, visibility, and humidity) identified temporal correlations between road traffic and weather conditions and thereby improved the forecasting of traffic parameters [43].

Gu et al. [10] used a recurrent neural network in a traffic flow prediction model to better express the temporal and spatial characteristics of traffic flow. A deep learning method based on recurrent neural networks [44–46] produced more accurate traffic prediction based on big data.

Classification of recent publications is depicted in Table 1.

**Table 1.** Classification of studies by emissions from traffic.

Models	Types of Models	Studies and Year	Input Data
Traffic management models	Adaptive control of traffic light signals	Lee et al. [1] Wang et al. [2] Fusco et al. [4]	<ul style="list-style-type: none"> <li>Real-time traffic from surveillance cameras,</li> <li>Internet of Vehicles.</li> </ul>
	Modeling Driver Behavior	Pathivada and Perumal [19] Najmi et al. [20] Calvi et al. [21]	<ul style="list-style-type: none"> <li>Video recording of the driver's decision.</li> </ul>
Air quality models	Operational Street Pollution Model	Berkowicz et al. [27] Mensink and Cosemans [28]	<ul style="list-style-type: none"> <li>Pollutants from the source to the receptor,</li> <li>The recirculation component the urban background.</li> </ul>
	Comprehensive Air-quality Model	Luo et al. [21]	<ul style="list-style-type: none"> <li>Surface characteristics,</li> <li>Initial and boundary conditions,</li> <li>Emission rates various meteorological fields.</li> </ul>
	Chemical mass balance	Gao et al. [30] Song et al. [31]	<ul style="list-style-type: none"> <li>Speciated profiles of sources,</li> <li>Corresponding ambient data from analyzed samples collected at a single receptor site.</li> </ul>
Dispersion models for predicting air pollutant concentrations	CALINE4	Yu et al. [35] Air Quality Modeling [36]	<ul style="list-style-type: none"> <li>Traffic emissions,</li> <li>Site geometry meteorology.</li> </ul>
	AERMOD	Baghestani et al. [37] Liu et al. [38] Kim et al. [39]	<ul style="list-style-type: none"> <li>Surface meteorological data,</li> <li>Upper air soundings,</li> <li>Data from on-site instrument towers.</li> </ul>
	CMAQ	Hembeck et al. [47] Wang et al. [48]	<ul style="list-style-type: none"> <li>Meteorology from a WRF38 simulation,</li> <li>Regional emission inputs.</li> </ul>

After studying the relevant literature, we can conclude that measuring and accurately forecasting traffic flows is still a challenge due to the limited input data and high uncertainty of dynamic processes.

## 2. Materials and Methods

The entire developed program can be divided into two subsystems. The first is a monitoring system; the second is a forecasting system. The input data for the monitoring system is a video stream from a camera. The vehicle detection module receives this video stream and, using the YOLOv4 neural network and the Simple Online and Realtime Tracking (SORT) tracker, detects and tracks the vehicle over a series of frames. The movement path of these vehicles is broken down and imported into the Emissions module. The Emissions module calculates the average speed of traffic flows, idle time, and pollutant emissions by the movement directions and categories based on the obtained vehicle movement paths. It also calculates the maximum concentration, taking into account weather factors across the entire study area. The calculated data are aggregated into 20-min time intervals and stored in the PostgreSQL database. The LSTM subsystem for forecasting the number of vehicles and emissions trains the neural network based on the data obtained from the PostgreSQL database after their normalization. Training is performed in manual mode on command. The resulting weights are used for forecasting based on the normalized data also obtained from the database. Figure 1 shows a flowchart of the developed software system. More detailed information on emission calculation, concentration, and prediction algorithms is described in the following sections.

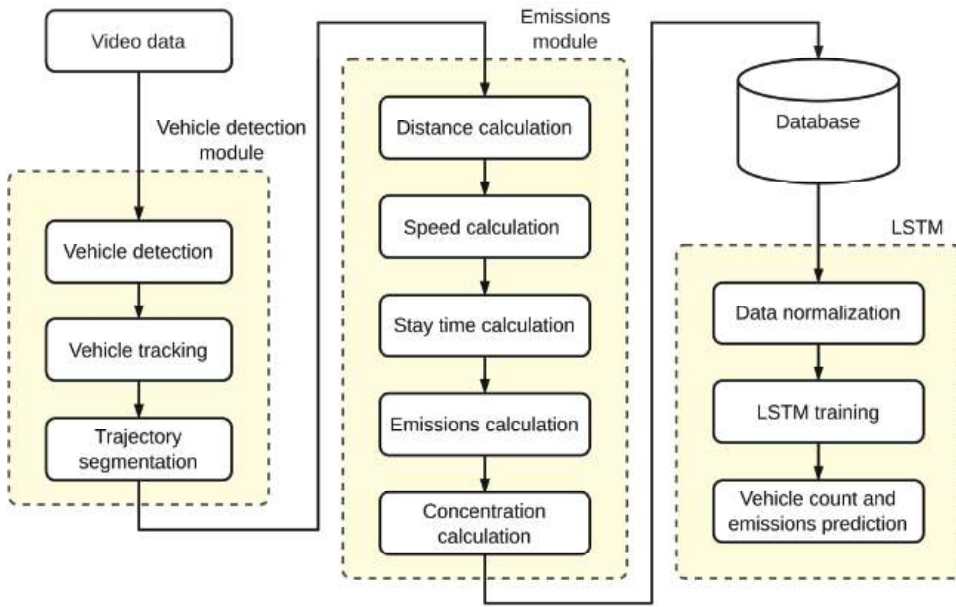


Figure 1. A flowchart of the developed program.

The quantitative assessment of traffic-related emissions is an important component of urban air quality design. Emissions levels change based on the number and type of vehicles and their dynamic performance (speed) [49,50]. Traffic-related emissions are primarily determined by the main characteristics of the traffic flow, such as the number of vehicles, speed, and standing time at the intersection [51,52]. Building prediction models on a dataset of many variables with relatively few observations can provide less accurate predictions and limit the performance of deep learning models [53].

In the first stage of this study, our primary goal was to develop a dynamic model to collect accurate data on road traffic parameters within the largest sections of the road network. We trained and modified the YOLOv4 convolutional neural network to collect high-quality dynamic data on individual vehicle movement parameters such as vehicle type, speed, and idling time [54–57]. We used low-resolution urban street cameras, allowing us to collect data within an area of up to 40,000 m<sup>2</sup>. Figure 2 shows how the YOLOv4 neural network detects and tracks moving objects (vehicles) from street camera feeds.



Figure 2. Collection of data on traffic flow parameters using the YOLOv4 neural network.

Collecting data from street cameras makes it possible to track the movement and individual dynamic parameters of vehicles over a long period and across large sections of the road network. This approach requires significantly fewer sensors and less server power while greatly improving the accuracy of vehicle-related emissions assessments.

2.1. A Methodology for Calculating the Amount of Finely Dispersed Pollutant Emissions from Traffic Flows

Studies and verification measurements were carried out near signal-controlled intersections, which are more highly exposed to harmful exhaust gases from traffic flows. In the initial stage of the study, we focused on collecting and analyzing data on the amount and concentration of emissions over 20-min intervals. This approach makes it possible to obtain a stable trend of the concentration in the control area and respond promptly to environmental changes to avoid reaching the maximum permissible concentrations of harmful substances in the ambient air. The amount of finely dispersed emissions of the *i*-th vehicle-related pollutant within a signal-controlled intersection over 20 min ( $M_{L_i}^{Stop}$ ) can be calculated using the formula [58,59]:

$$M_{L_i}^{Stop} = \frac{P_c}{60} \cdot \sum_1^{N_c} \sum_1^k (M'_{L_{i,k}} \cdot G_{kl}), \tag{1}$$

where  $P_c$  is the duration of red and yellow traffic lights over 20 min, in s;  $N_c$  is the number of red and yellow traffic light cycles over 20 min;  $k$  is the number of vehicle groups;  $M'_{L_{i,k}}$  is the specific emission of the *i*-th pollutant generated by vehicles of the *k*-th group in queue at the red light, in g/min; and  $G_{kl}$  is the number of vehicles of the *k*-th group in the queue at the end of each red light cycle.

Table 2 shows the specific emissions of CO and PM2.5 pollutants by vehicle group.

**Table 2.** Specific emissions of the *i*-th vehicle-related pollutant [58].

Vehicle Group Name	Group Number	Emissions (g/min)	
		CO	PM2.5
Cars	I	0.17	0.011
Vans and minibuses weighing up to 3.5 tons	II	1.00	0.033
Trucks weighing 3.5 to 12 tons	III	1.00	0.220
Trucks weighing over 12 tons	IV	2.00	0.450
Buses weighing over 3.5 tons	V	0.90	0.120

The emission of the *i*-th pollutant generated over a 20 min period by vehicles moving in a given direction at an intersection when the traffic light turns green ( $M_{L_i}^{Go}$ ) is calculated as:

$$M_{L_i}^{Go} = L^I \sum_1^{N'_c} \sum_1^k M^L_{k,i} \cdot G_{k_{go}} \cdot r_{V_{k,i}}, \tag{2}$$

where  $L^I$  is the distance traveled by vehicles in one direction at green traffic signals over 20 min, including the length of the vehicle queue formed at red and yellow traffic signals and the length of the corresponding intersection area, in km;  $N'_c$  is the number of cycles of the green traffic light over 20 min;  $M^L_{k,i}$  is the specific running exhaust emission of the *i*-th pollutant generated by the vehicles of the *k*-th group, in g/min;  $G_{k_{go}}$  is the number of vehicles of each *k*-th group passing through the intersection in one direction during the green traffic light;  $r_{V_{k,i}}$  is the correction factor accounting for the mean speed of the vehicle flow  $V_{k,i}$  (in km/h) on a particular road (or a section thereof) [58–60].

Table 3 shows the specific running exhaust emission of the *i*-th vehicle-related pollutant [58–60].

**Table 3.** Specific running exhaust emissions of the *i*-th vehicle-related pollutant [58].

Vehicle Group Name	Group Number	Emissions (g/min)	
		CO	PM2.5
Cars	I	0.90	$0.55 \times 10^{-2}$
Vans and minibuses weighing up to 3.5 tons	II	4.60	$3.70 \times 10^{-2}$
Trucks weighing 3.5 to 12 tons	III	5.30	0.37
Trucks weighing over 12 tons	IV	5.60	0.44
Buses weighing over 3.5 tons	V	3.90	0.15

The total amount of emissions in g/s of the *i*-th pollutant generated by vehicles moving in a particular direction at a signal-controlled intersection is calculated as the sum of the emissions produced at green and red/yellow traffic signals, divided by 1200. The presented method only calculates the amount of vehicle-related emissions from exhaust pipes. We used specific running coefficients according to the COPERT method [60] to determine particulate matter (PM2.5 and PM10) emissions produced from the road, brake pads, and tire wear.

The following coefficients are used in the method:

- I—passenger vehicles;
- II—vehicles with a load capacity up to 3.5 tons;
- III—heavy-duty vehicles (over 3.5 tons).

We classified the specific running coefficients for three types of vehicles according to the COPERT method into five groups based on their load capacity (Table 4).

**Table 4.** Specific running coefficients by types of vehicles [58–60].

Vehicle Type	Vehicle Type, per COPERT	PM2.5 (g/min)			PM10 (g/min)		
		Brake Pad Wear	Tire Wear	Road Surface Wear	Brake Pad Wear	Tire Wear	Road Surface Wear
I	I	0.00293	0.00449	0.00405	0.00735	0.00642	0.00750
II	II	0.00456	0.00710	0.00405	0.01147	0.01014	0.00750
III	III	0.01277	0.01887	0.02052	0.03209	0.02696	0.03800
IV	III	0.01277	0.01887	0.02052	0.03209	0.02696	0.03800
V	III	0.01277	0.01887	0.02052	0.03209	0.02696	0.03800

*2.2. Method Used to Calculate the Concentration of Finely Dispersed Pollutant Emissions from Traffic Flows*

The maximum ground level one-time concentration of pollutants ( $C_M$ ), when the gas-air mixture (GAM) is released from a single point source with a round mouth, is achieved at a dangerous wind speed  $u_m$  at a distance  $x_m$  from the emission source and determined by the formula [59]:

$$C_M = \frac{A \cdot M \cdot F \cdot m \cdot n \cdot \eta}{H^2 \cdot \sqrt[3]{V_1 \cdot \Delta T}}, \tag{3}$$

where *A* is a coefficient which depends on the temperature stratification of the atmosphere and determines the conditions for horizontal and vertical pollutant dispersion in the air; *M* is the mass of pollutants emitted into the ambient air per unit of time (emission rate), in g/s; *F* is a dimensionless coefficient accounting for the settling rate of pollutants (gaseous and aerosols, including solid particles) in the ambient air; *m* and *n* are calculated dimensionless coefficients which account for the conditions of output from the mouth of the emission source;  $\eta$  is a dimensionless coefficient accounting for the influence of terrain features and urban development; *H* is the height of the emissions source, in m;  $V_1$  is the gas-air mixture consumption, in m<sup>3</sup>/s; and  $\Delta T$  is the difference between the temperature of the emitted GAM and the ambient air temperature.

The gas-air mixture consumption ( $V_1$ ) is calculated as [59]:

$$V_1 = \frac{\pi \cdot D^2}{4} \cdot \omega_0, \tag{4}$$

where  $D$  is the diameter of the mouth of the emission source, in m; and  $\omega_0$  is the mean speed of the GAM release from the mouth of the emission source, in m/s.

A dangerous wind speed  $u_m$  takes into account the following parameters:  $H$ ,  $V_1$ ,  $\omega_0$  and  $D$  [59].

The maximum ground level concentration ( $c_{m,u}$ ) at a given wind speed ( $u$ ) is calculated as:

$$c_{m,u} = r \cdot c_m$$

$$r = 0.67 \cdot \frac{u}{u_m} + 1.67 \cdot \left(\frac{u}{u_m}\right)^2 - 1.34 \cdot \left(\frac{u}{u_m}\right)^3 \text{ when } \frac{u}{u_m} \leq 1, \tag{5}$$

$$r = \frac{3 \cdot (u/u_m)}{2 \cdot (u/u_m)^2 - u/u_m + 2} \text{ when } \frac{u}{u_m} > 1$$

The maximum ground level concentration at a given wind speed  $u$  at a distance  $x$  from the source along the emission plume axis and  $y$  perpendicular to the emission plume axis are calculated as:

$$c = s_1 \cdot c_m \tag{6}$$

$$c_y = s_2 \cdot c \tag{7}$$

where  $s_1$  and  $s_2$  are the coefficients dependent upon  $x$  and  $y$ .

The values of coefficient  $A$  depend on the geographical region and are given in Table 5.

**Table 5.** Values of coefficient  $A$  [59].

#	Region	Coefficient A
1	Republic of Buryatia and Trans-Baikal Territory	250
2	Regions of the European part of the Russian Federation south of 50 °N, other regions of the Lower Volga territory, Asian part of the Russian Federation, except for those indicated in Items 1 and 3 of this Table	200
3	European part of the Russian Federation and the Urals from 50 °N to 52 °N inclusive, except for the areas falling into this zone, listed in Items 1 and 2 of this Table, as well as for the areas of the Asian part of the Russian Federation located north of the Arctic Circle and west of the meridian 108 °e.	180
4	European part of the Russian Federation and the Urals north of 52 °N (except for the center of the European part of the Russian Federation)	160
5	Vladimir, Ivanovo, Kaluga, Moscow, Ryazan, and Tula regions	140

### 3. Experiment and Verification

This section presents a methodology for determining the amount of emissions from vehicles in real time, taking into account meteorological conditions. A prediction model using a recurrent neural network is also proposed and its statistical reliability is verified.

#### 3.1. Implementation of the Algorithm to Calculate the Amount and Concentration of Emissions from Mobile Emission Sources

To calculate the amount and concentration of emissions from a single mobile source, the movement of the object (a vehicle) is divided into intervals of 5 s (Figure 3). The coordinates of the mobile emission source are set as the center of the distance travelled in 5 s. The time the vehicle spends in queue at the traffic light is also taken into account. When a vehicle is in queue, the length of the resulting 5-s segment will be equal to 0. This method of segmentation was chosen because shorter time intervals and smoother paths provide higher computational capacity. This implementation is sufficient for the real-time calculation of emissions and concentration with the required accuracy. A series of screenshots (frames) are taken for each car. The frame time, current speed, and location of

the vehicle is added to the frame each time the vehicle is detected by the neural network. When the difference in time between the first and last frame exceeds 5 s, the network builds the path of the vehicle and calculates the amount and concentration of emissions based on the entire series, after which the series is cleared and filled again.

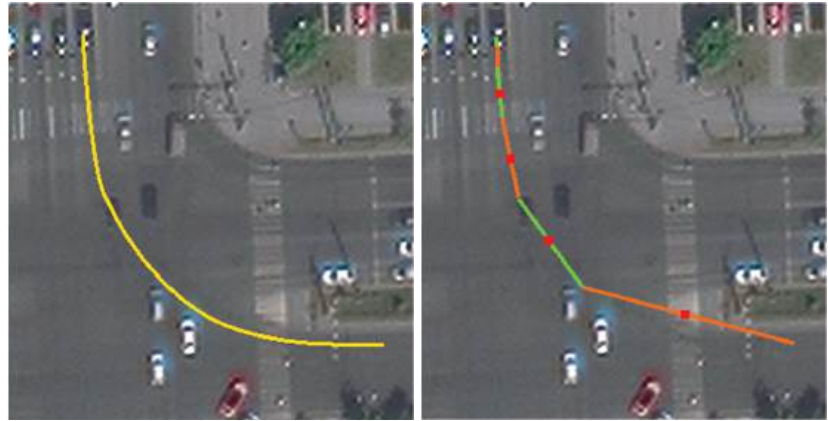


**Figure 3.** The path of a mobile emissions source and the same path broken into 5-s segments.

We have updated our method to track each vehicle throughout the entire field of view of the camera rather than following traffic light signals. The algorithm for calculating the amount of emissions has been adjusted accordingly. In the current implementation, the emission of the  $i$ -th pollutant from one vehicle is calculated as:

$$M = P \cdot M_p + L \cdot M_L \cdot r_V, \tag{8}$$

where  $M$  is the total amount of emissions for one vehicle (taking into account both the intervals when the vehicle is standing and when it is moving), in g;  $P$  is the idling time of the vehicle, in min;  $M_p$  is the specific emission of the  $i$ -th pollutant of the vehicle in the  $k$ -th group (used to calculate idle emissions), in g/min;  $L$  is the distance traveled by the vehicle, in km;  $M_L$  is the specific running exhaust emission of the  $i$ -th pollutant produced by the vehicle in the  $k$ -th group (the mileage emission used to calculate driving emissions), in g/km; and  $r_V$  is a correction factor accounting for the mean vehicle speed.

To convert the emissions into g/s, the resulting  $M$  value is divided by the vehicle tracking time [61]. Thus, emissions are calculated in real time for each vehicle every 5 s. The total amount of emissions produced by a vehicle is calculated as the sum of emissions at all intervals of its movement.

The following parameters were chosen to calculate the maximum ground level concentration of vehicle-related pollutants:

- $A = 160$  for Chelyabinsk;
- $F = 1$  (gaseous pollutants and fine aerosols with a diameter of no more than  $10\mu\text{m}$ );
- $\eta = 1$  (terrain features and urban development are not taken into account);
- $H = 2$  m (minimum source height);
- $T_{GAM} = 100$  °C;
- $D$  is the distance traveled by the vehicle;
- $\omega_0 = 0.01$  m/s (since the vehicle exhaust pipe is directed horizontally, we used the minimum vertical speed of the air–water mixture).

Data on air temperature, wind speed, and wind direction were obtained from OpenWeather [62].

To calculate the emission concentration and distribution at the chosen intersection, we divided the intersection into a  $20 \times 20$  grid of  $20 \times 20$  m squares (Figure 4). Then, we

calculated the concentration in each of the areas from each last unaccounted movement interval for each vehicle (Figure 5). The middle of the movement interval was taken as the GAM source. The concentration in each square was calculated at the moment when the emissions cloud reached the square. This delay was calculated by dividing the distance from the source to a square by the wind speed. Then the concentrations were summed up inside their areas. Figure 6 visualizes the distribution of the CO concentration at the intersection, accounting for the effects of wind. The maximum ground level pollutant concentration across the entire intersection is equal to the maximum pollutant concentration across all areas.



Figure 4. Grid of 20 × 20 m squares at an intersection in Chelyabinsk, Russia.

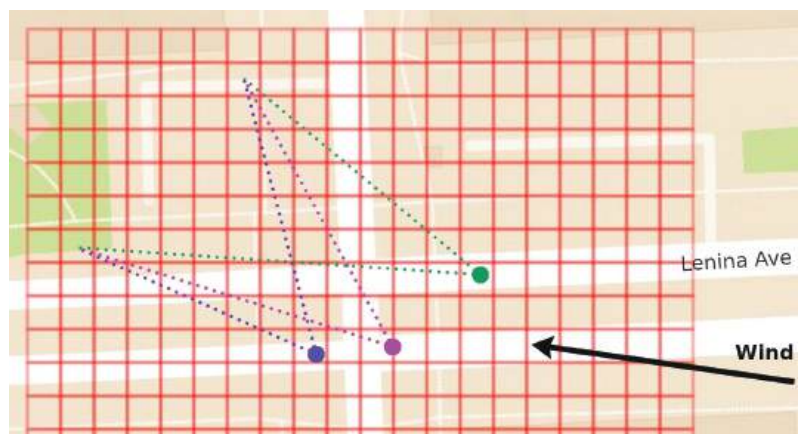
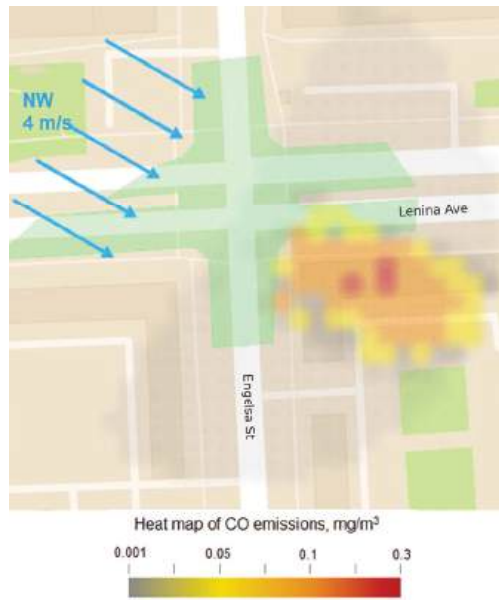


Figure 5. Calculation of the concentration from vehicles to the centers of the squares.



**Figure 6.** Calculated CO concentration in each area of the grid.

### 3.2. Forecasting the Number of Vehicles

Long short-term memory is a deep learning technique that can be used to obtain more accurate time series [44,45]. We implemented a serial encoder-decoder model with a Recurrent Neural Network (RNN) to forecast particulate matter in urban environments. The model was trained using emission concentration statistics and transport and meteorological data. The forecasts were in good agreement with the measurements, indicating the applicability of the system and its great potential for producing high-quality real-time forecasts of urban air pollutants. The recurrent neural network, unlike other networks, can highlight the features of each element, accounting for the connections between elements [63,64]. The vector  $H$  (Figure 7) of a cell in an RNN describes the current inner state of the network and contains memories of all the studied elements. These cells are collected in a sequence, representing a time series. Each cell transfers its inner state to a subsequent cell.

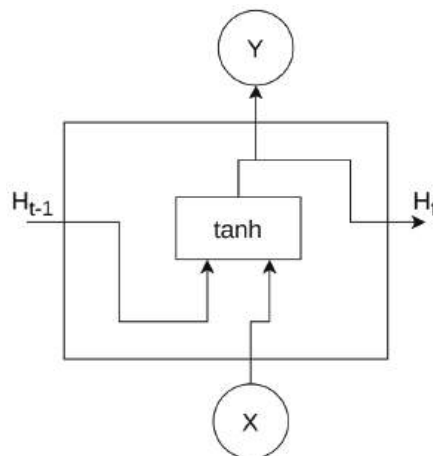


**Figure 7.** Schematic of an RNN cell.

These neurons cannot memorize data vectors above a certain size. The LSTM model was proposed to solve this problem. The existing cell was supplemented with one more inner state  $S$ , as well as the ability to extract the most significant features from the input data and decide what has a greater influence on the inner state and what is sent to the output. An example of an LSTM cell is shown in Figure 8.

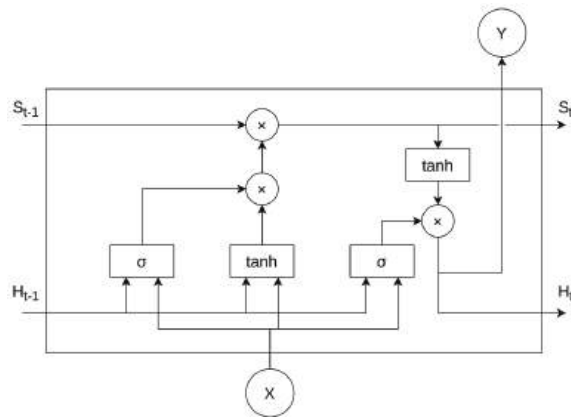


**Figure 8.** Schematic of an LSTM cell.

We implemented an RNN in the Keras library of the Python programming language. The dataset was formed from 1000 records from the database containing the aggregate number of vehicles in all directions and all categories over 20-min intervals. These 1000 20-min intervals amount to roughly two weeks. The data were divided into training and test samples in the ratio of 85% to 15%, respectively.

A vector of 72 24-h intervals with one parameter (the number of vehicles) was chosen as the input data of the neural network used as the basis for training and forecasting.

A vector of 24 8-h time intervals with one parameter (the number of vehicles) was chosen as the output data (forecasted value).

All input and output data were converted to the interval  $[0, 1]$  for normalization. The number of vehicles was divided by the maximum value of 2500 across the entire dataset for each 20-min time interval.

The mean absolute error (*mae*) of determining the number of vehicles was chosen to assess the quality of the neural network.

The following lawyers were used:

- LSTM (a recurrent layer);
- Dropout with rate = 0.2 (a layer that prevents retraining by ignoring randomly selected neurons during training);
- Dense (an output layer that changes the shape of the data into the desired form).

Eighteen options were tested with different parameters as the neural network configuration:

- Number of LSTM layers: 1, 2, 3;
- Number of neurons in each of the LSTM layers: 50, 100, 300, 500, 750, 1000.
- The number of learning epochs was 500.

The results of experimental training of 18 neural network configurations are shown as distribution fields of the error in calculating the number of vehicles (mean absolute error) and the network training time depending on the number of LSTM layers and neurons in each layer (Figure 9).

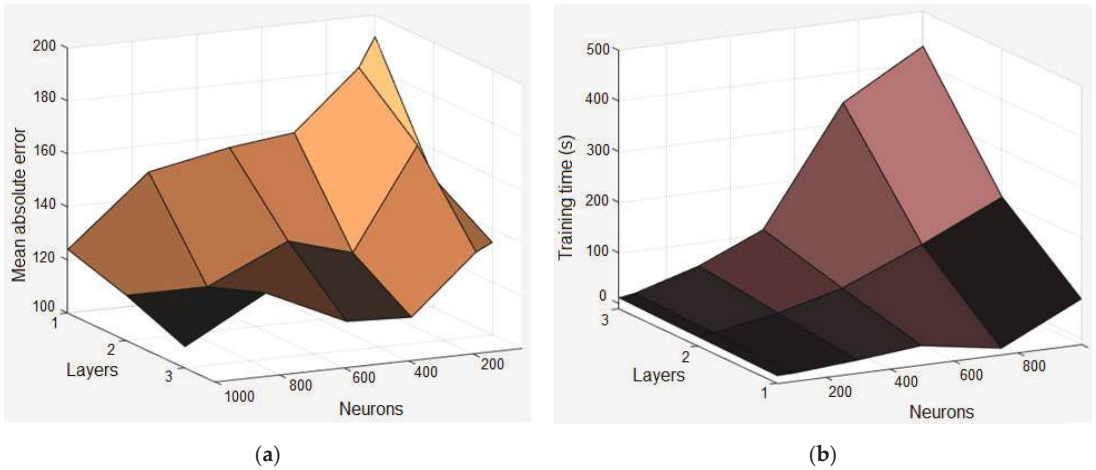


**Figure 9.** Distribution fields: (a) for the mean square error  $m_{ae}$  of calculating the number of vehicles; (b) for the training time of a three-layer neural network.

Testing showed that Configuration 15 with three layers and 300 neurons in each layer showed the minimum values of mean and maximum absolute errors. We found that configurations with fewer layers and neurons do not cope well with the task. Configurations of three layers with 750 and 1000 neurons are ineffective and spend too much time on training.

Figure 10 shows the forecasted number of vehicles produced by Configuration 15 for two conjugated 8-h time intervals.

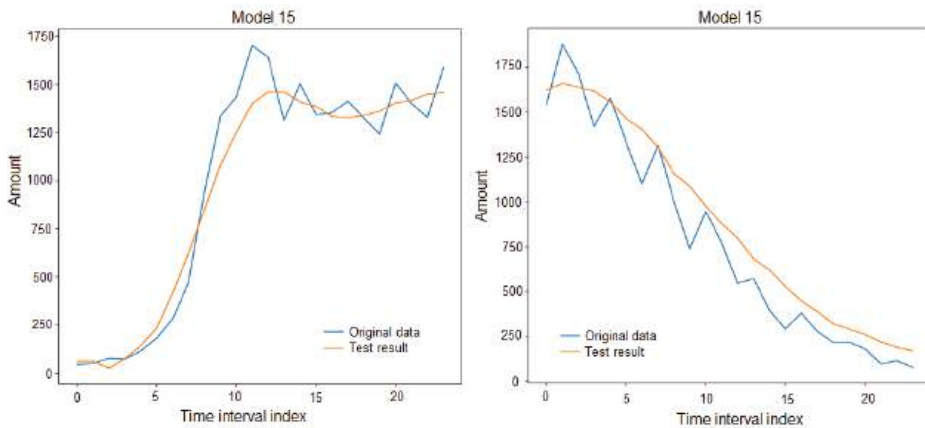


**Figure 10.** Number of vehicles measured over two time periods, and the number of vehicles forecasted by the neural network over the same periods.

Statistical analysis of the forecasted and actual number of vehicles showed a mean square deviation of 210 vehicles in a 20-min measurement interval, which is 34.7% (coefficient of variation) less than the mathematical forecast. Although this forecast deviation is rather high, it does not invalidate the model, but rather characterizes the amplitude of random deviations. The main significant factor is the cumulative number-of-vehicles basis during the experiment.

Figure 11 compares the forecasted and measured total traffic flow volume (number of vehicles) over 48 20-min intervals (16 h in total). The calculation showed an increase in the

forecast values of the number of vehicles from the actual number of 42,345 to 44,120 units, which is only 4.2% of the deviation.

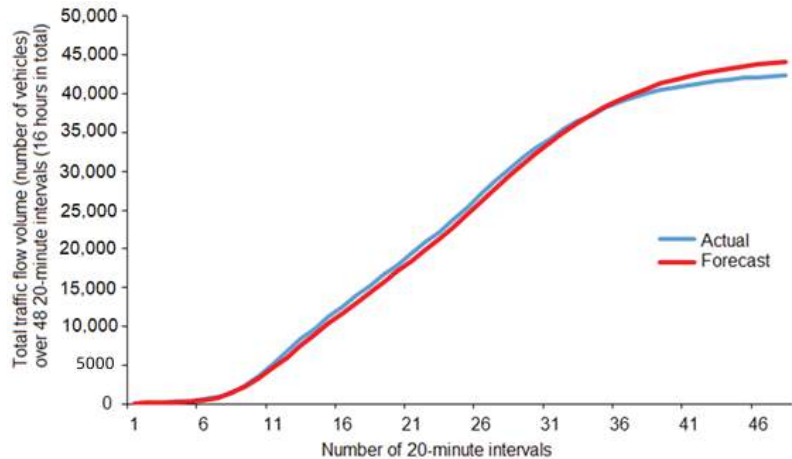


**Figure 11.** Actual and forecast total traffic flow volume (number of vehicles) over 48 20-min intervals (16 h in total).

A check of the differences using the non-parametric chi-square test (SPSS package) confirmed that there are no statistically significant differences between the forecast and actual daily emissions (error level = 54%, which considerably exceeds the difference significance threshold of 5%). Based on the deviation analysis, we can conclude that the RNN produces statistically reliable predictions of the number of vehicles passing through an intersection over a given period.

### 3.3. Forecasting the Amount of Emissions

An array of 72 intervals of 20 min was chosen as the input data of the neural network for training and forecasting. The input data have three parameters: PM2.5 emissions, the day of the week, and the time interval index. Thus, the shape of the two-dimensional array of input data was (72, 3). An array of 72 20-min intervals with one parameter (amount of PM2.5 emissions) was chosen as the output data (forecast value). The shape of the two-dimensional array of output data was (72, 1).

All input and output data were converted to the interval [0, 1] for normalization. The amount of PM2.5 emissions was divided by the maximum value of 30 across the entire dataset for each 20-min time interval. Each day of the week was assigned a value between zero and six, where zero was Monday and six was Sunday, and divided by six. Each 20-min interval was assigned a value between 0 and 71, where 0 was the time interval of 0:00–0:20, and 71 was the interval of 23:40–00:00, and divided by 71.

To find the best neural network configuration, we implemented a program that generates several configurations, trains each of them, conducts tests, and evaluates performance.

The mean squared error (*mse*), the average absolute error (*mae*), and the maximum absolute error (*Mae*) were chosen to assess the quality of the neural network.

The following layers were chosen to create configurations:

- LSTM (a recurrent layer);
- Dropout with rate = 0.2 (a layer that prevents retraining by ignoring randomly selected neurons during training). This layer follows each LSTM layer;
- Dense (an output layer that changes the shape of the data into the desired form).

We tested 32 configuration options with different parameters:

- Number of LSTM layers: 1, 2, 3, 4;

- Number of neurons in each of the LSTM layers: 50, 100, 250, 400, 600, 800, 1000, and 1200.

The number of learning epochs was 500.

Figure 12 shows the results of experimental training for 32 neural network configurations as distribution fields of the forecasting error and the training time depending on the number of LSTM layers and neurons in each layer.

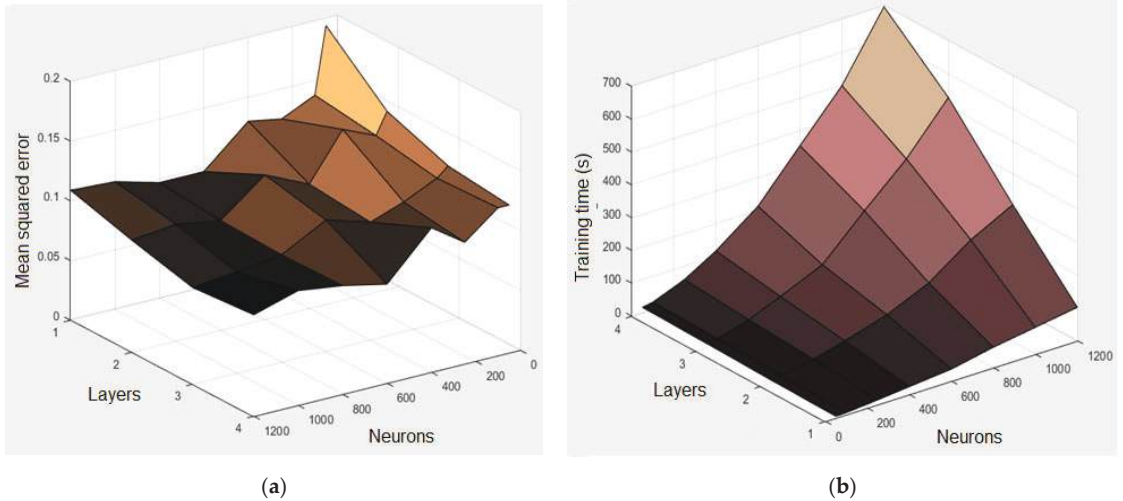


**Figure 12.** Distribution fields: (a) for the mean square error *mse* of calculating the amount of PM<sub>2.5</sub> emissions; (b) for the training time of a four-layer neural network.

Configuration 24, with three layers and 1200 neurons in each layer (*mse* = 0.081; time = 527 s) showed the minimum *mse* errors. However, this configuration spends too much time on learning and operation. Configuration 29, with four layers and 600 neurons in each layer (*mse* = 0.083; time = 212 s) is one of the most optimal. It produces predictions with nearly the same quality as Configuration 1, but 2.5 times faster.

Statistical analysis of the forecasting accuracy (*mse*) of various network configurations showed that the area of significant differences begins with errors of more than 0.108 (Pearson's nonparametric chi-square test). Fifteen out of the thirty-two tested configurations fall into this area of statistically equal accuracy values. Configuration 29 again has the minimum forecast time, which is the main criterion for a real-time system. We ultimately chose Configuration 29 of the RNN, with four layers and 600 neurons, to forecast PM<sub>2.5</sub> emissions.

Figure 13 presents the PM<sub>2.5</sub> emissions forecasted by Configuration 29 with the original data in grams over 24 h (72 intervals of 20 min).

Statistical analysis of the forecast and measured emissions data in the neural network showed a 1.26-g mean square deviation in the 20-min measurement interval. This is, on average, 18.5% per day (coefficient of variation) less than the forecasted value. Although this deviation is quite a high deviation, the daily amount of emissions remains the main significant factor.

Figure 14 compares the total emissions of PM<sub>2.5</sub> particulate matter on a cumulative daily basis. The daily forecast value was only 6.25% less than the actual recorded value (448 g and 477.5 g, respectively).

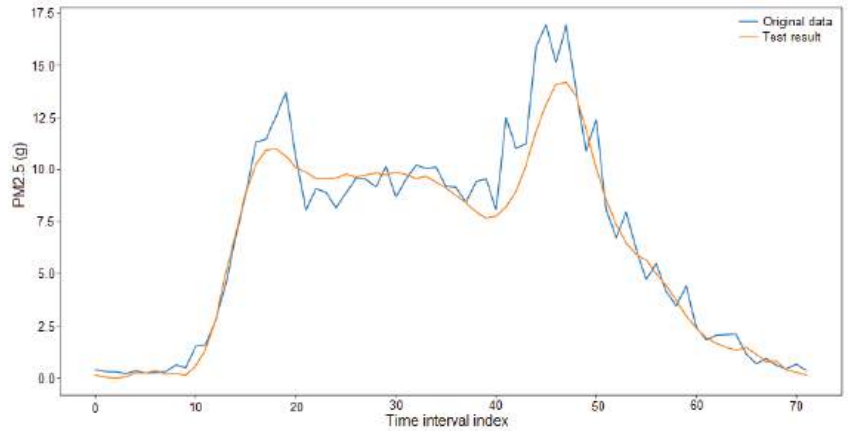


Figure 13. Measured PM2.5 emissions over 24 h and PM2.5 emissions forecasted by the neural network.

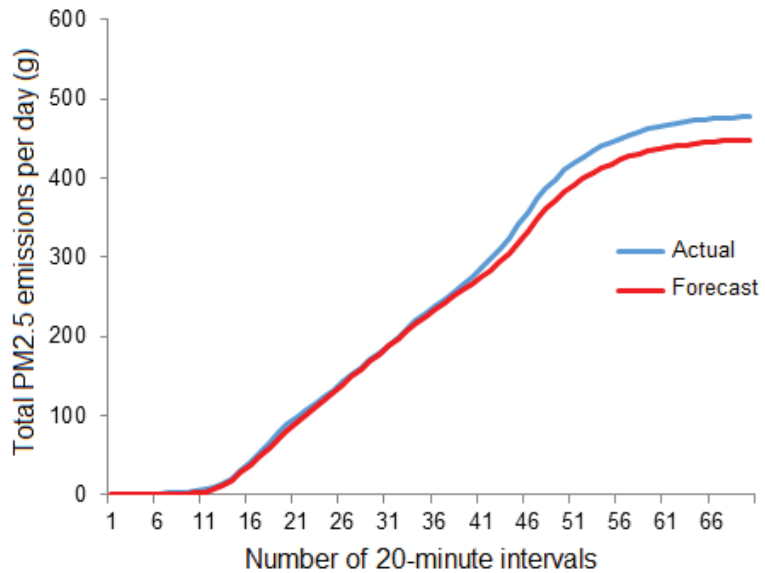


Figure 14. Actual and forecasted cumulative PM2.5 emissions.

A non-parametric chi-square test confirmed that the difference between the forecast and actual daily volume of emissions was not statistically significant (error level = 34%, which considerably exceeds the difference significance threshold of 5%). We can conclude that the recurrent neural network produces statistically reliable forecasts of PM2.5 emissions.

#### 4. Discussion and Results

To assess the reliability and quality of the above system for monitoring the amount of emissions and the atmospheric concentration of harmful substances from traffic flows, analytical work was performed to compare the model calculations of emissions with laboratory measurements made by the Regional State Institution Center for Environmental Monitoring of the Chelyabinsk Region.

The results of the laboratory measurements of pollutant emissions were read from the reports of the Center for Environmental Monitoring (CEM). The measurements were made within the intersection of Engelsa Street and Lenina Avenue. The laboratory measurements of PM<sub>2.5</sub> and PM<sub>10</sub> emissions were recorded using a standard meter—a DustTrack 8533 dust analyzer [65]. The device measures only one type of emissions and features a rigid, calculated connection of the other type with it.

Notably, the CEM reports also record meteorological conditions corresponding to the measurement time, which can serve as a basis for further studying the influence of meteorological conditions on the concentration of pollutants within the intersection, provided that the volume of measurements is sufficient. However, unfortunately, instrumental measurements are a rather laborious procedure; three 20-min measurements are routinely performed within one day in the morning and afternoon, no more than once a week.

The proposed system based on a recurrent neural network has the following undeniable advantages: calculation results are provided in real time; there is no grouping of data into 20-min intervals, since the calculations are linked only to instantaneous data of the recorded traffic flow at the intersection. However, this gives rise to the main drawback of the calculation system—it does not take into account the general background of atmospheric pollution by industrial emissions. Notably, in our case, the analyzed intersection is located in an environmentally friendly urban area with minimum industrial emissions.

Figures 15 and 16 present the results of comparing the predicted emissions of PM<sub>2.5</sub> and PM<sub>10</sub> particulate matter with the CEM instrumental data based on 14 control measurements.

According to a visual comparison of the concentrations, a stable lower value of the predicted emissions of particulate matter indicates the presence of similar emissions from the urban industrial enterprises. These deviations can act as their evaluation measure.

The significant unstable deviations observed in the graphs are explained by several random factors in instrumental measurements, such as the single passage of heavy vehicles with an unbalanced engine; sharply changing weather conditions; measuring instrument error floating in time. These factors cannot be minimized by averaging statistical algorithms due to the complexity and laboriousness of instrumental measurements.

The main trend seen in the graphs is a similar nature of changes in emissions both during instrumental measurements and computational forecasting, which is a good confirmation of the quality of the developed system for the dynamic monitoring of emissions.

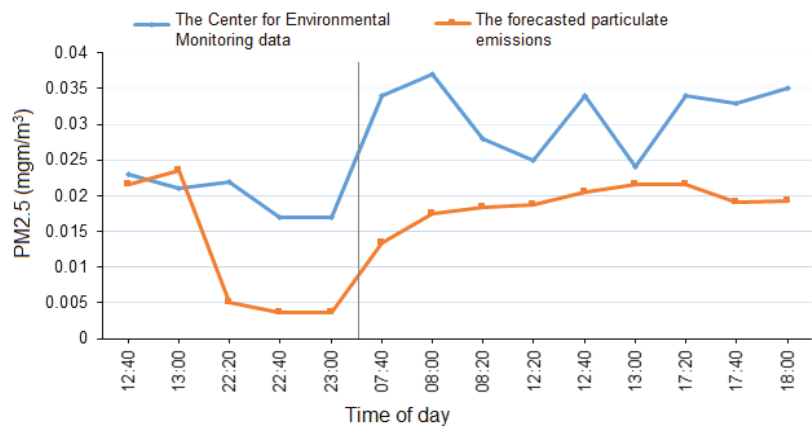
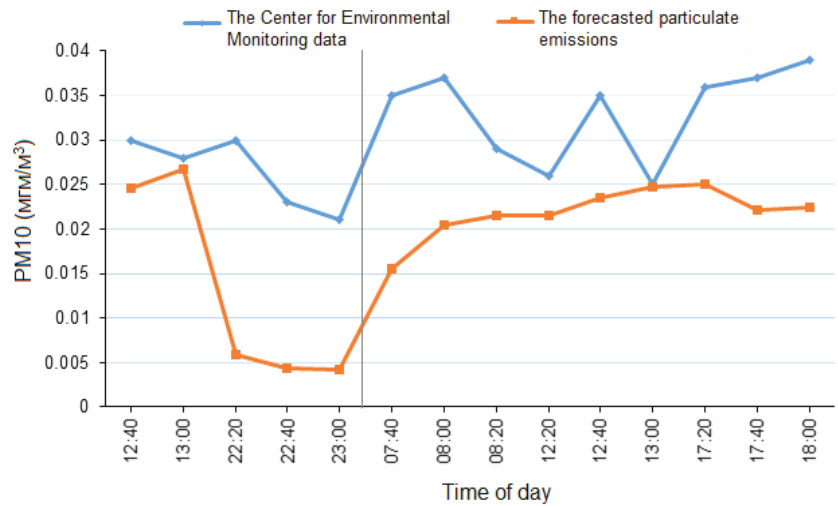


Figure 15. Comparison of the forecasted and actual PM<sub>2.5</sub> emission concentrations.



**Figure 16.** Comparison of the forecasted and actual PM10 emission concentrations.

The problem of separating emissions generated by various sources—industrial enterprises and motor traffic flows—is relevant and highly-demanded for identifying the reasons for exceeding maximum pollutant concentrations. In the results of the study (see Figure 12), a visible decrease in the predicted values of vehicle-related emissions versus the actual total emissions is observed in the time interval from 13.00 to 16.00 local time (from the 40th to the 50th twenty-minute interval), which exactly corresponds to the maximum industrial emissions. Nevertheless, at urban intersections, the main share of pollutions is still attributed to urban vehicles, which is confirmed by a perfect match of the actual and predicted emissions in the morning and evening. This is in good agreement with a priori estimates of minimum industrial emissions at that time. Notably, the analyzed intersection belongs to an environmentally friendly urban area with minimum industrial emissions.

With the wider commercialization of vehicle to vehicle (V2V), intelligent transportation systems are better able to reduce the negative impact of emissions on the urban environment by structuring and shaping traffic flows. Various sensors and systems designed to monitor urban transport and emissions are appearing. These devices often have overlapping functions, which require major computational capability and maintenance costs. Our approach is based on using the existing network of urban street cameras as sensors for data collection. Considering the worsening environmental situation in cities, monitoring tools alone are no longer sufficient; accurate forecasting methods and solutions to manage environmental risks are crucial. The presented hybrid model can effectively improve the accuracy of deep learning neural network models to forecast the amount and concentration of air pollutants. The optimized architecture of the combined YOLOv4 and LSTM neural networks uses far fewer computational resources and imposes minimal requirements on the number and characteristics of outdoor cameras used as sensors. Future research will expand this methodology to not just assess and forecast emissions, but also to model the dynamic structure of road traffic to reduce the negative environmental impact of vehicles.

### 5. Conclusions

Signal-controlled intersections are one of the most popular urban intersection structures. The traffic congestion which inherently occurs at such intersections leads to increased emissions concentrations.

Most applicable methods for assessing and forecasting emission concentrations do not fully consider the influence of road traffic heterogeneity and the behavior exhibited by

drivers when following another type of vehicle. Many models do not account for the road infrastructure either. These omissions lead to major differences in forecasted emissions.

This study proposes a hybrid model that combines convolutional and recurrent neural networks to produce more accurate evaluations and forecasts of the amount and concentration of vehicle-related pollutants. The advantage of the proposed model is that it collects, interprets, and aggregates individual vehicle characteristics as mobile emission sources. This allows the model to account for driver behavior, including how drivers behave when following vehicles of various types. This aspect has been ignored in previous studies. The accuracy of the model is supported by high-quality monitoring of road traffic and by selecting features which account for spatiotemporal correlations (urban development). We collected 12,000 video frames from over 650,000 marked vehicles to train and evaluate the detector. The collected data covers more than 20 intersections with different viewing angles, occlusion levels, and major scale differences. The proposed system can count and classify vehicles by the direction of movement with an average percentage error of less than 6%. The module of the hybrid model for data collection and interpretation is a good solution for extracting the necessary data to forecast the amount of emissions while accounting for individual vehicle parameters. The hybrid model uses the advantages of the fast data extraction of a convolutional neural network and incorporates the efficiency of the long-term feature extraction of an LSTM recurrent neural network.

The proposed model successfully forecasted the amount and maximum ground level concentration of finely dispersed emissions and exceeded the forecasting accuracy of competing models.

Our methodology represents an evolution in modeling and assessment methods. The proposed model assesses driver behavior, vehicle type, and environmental factors (the influence of meteorological predictors and the features of transport infrastructure) on vehicle-related emissions. Our model can build next-generation datasets, which will support the development of sustainable transport systems. The proposed approach makes a qualitative transition from measuring emissions with expensive sensors to more informative, accurate, and efficient digital solutions.

**Author Contributions:** Conceptualization, A.G. and V.S.; methodology, V.S.; software, I.S.; validation, Y.C.; investigation, I.S.; resources, A.G.; writing—original draft preparation, V.S.; writing—review and editing, V.S.; visualization, Y.C.; supervision, A.G. All authors have read and agreed to the published version of the manuscript.

**Funding:** This research received no external funding.

**Institutional Review Board Statement:** Not applicable.

**Data Availability Statement:** Not applicable.

**Conflicts of Interest:** The authors declare no conflict of interest.

## References

1. Lee, S.; Younis, M.; Murali, A.; Lee, M. Dynamic local vehicular flow optimization using real-time traffic conditions at multiple road intersections. *IEEE Access* **2019**, *7*, 28137–28157. [CrossRef]
2. Wang, J.; Jiang, S.; Qiu, Y.; Zhang, Y.; Ying, J.; Du, Y. Traffic signal optimization under connected-vehicle environment: An overview. *J. Adv. Transp.* **2021**, *2021*, 3584569. [CrossRef]
3. Yau, K.-L.A.; Qadir, J.; Khoo, H.L.; Ling, M.H.; Komisarczuk, P. A survey on Reinforcement learning models and algorithms for traffic signal control. *ACM Comput. Surv.* **2017**, *50*, 1–38. [CrossRef]
4. Fusco, G.; Gentile, G.; Meschini, P. Urban traffic signal optimization. In *Intelligent Transport Systems (ITS): Past, Present and Future Directions*; Nova Science Publishers, Inc.: Hauppauge, NY, USA, 2017.
5. Toan, D.T.; Lam, H.S.; Meng, M.; Wong, D.Y. Travel demand management policies: A case study of Singapore and transferability potentials for Hanoi. *Case Stud. Transp. Policy* **2023**, *11*, 100934. [CrossRef]
6. Giuliano, G. Transportation Demand Management: Promise or Panacea? *J. Am. Plan. Assoc.* **1992**, *58*, 327–335. [CrossRef]
7. Habibian, M.; Kermanshah, M. Coping with congestion: Understanding the role of simultaneous transportation demand management policies on commuters. *Transp. Policy* **2013**, *30*, 229–237. [CrossRef]

8. Li, H.; Andrews, G.E.; Savvidis, D.; Daham, B.; Ropkins, K.; Bell, M.; Tate, J. Impact of driving cycles on greenhouse gas (GHG) emissions, global warming potential (GWP) and fuel economy for SI car real world urban driving. *SAE Int. J. Fuels Lubr.* **2009**, *1*, 1320–1333. [CrossRef]
9. Boubaker, S.; Rehim, F.; Kalboussi, A. Impact of intersection type and a vehicular fleet's hybridization level on energy consumption and emissions. *J. Traffic Transp. Eng.* **2016**, *3*, 253–261. [CrossRef]
10. Gu, Z.-Y.; Chen, C.; Zheng, J.-J.; Sun, D.-H. Traffic flow prediction based on STG-CRNN. *Kongzhi Yu Juece/Control Decis.* **2022**, *37*, 645–653. [CrossRef]
11. Adams, M.D.; Kanaroglou, P.S. Mapping real-time air pollution health risk for environmental management: Combining mobile and stationary air pollution monitoring with neural network models. *J. Environ. Manag.* **2016**, *168*, 133–141. [CrossRef]
12. Brazil, N. Environmental inequality in the neighborhood networks of urban mobility in US cities. *Proc. Natl. Acad. Sci. USA* **2022**, *119*, e2117776119. [CrossRef] [PubMed]
13. Colmer, J.; Hardman, I.; Shimshack, J.; Voorheis, J. Disparities in PM 2.5 air pollution in the United States. *Science* **2020**, *369*, 575–578. [CrossRef] [PubMed]
14. Bell, M.L.; Ebisu, K. Environmental Inequality in Exposures to Airborne Particulate Matter Components in the United States. *Environ. Health Perspect.* **2012**, *120*, 1699–1704. [CrossRef]
15. Balsa-Barreiro, J.; Morales, A.J.; Lois-González, R.C. Mapping Population Dynamics at Local Scales Using Spatial Networks. *Complex* **2021**, *2021*, 8632086. [CrossRef]
16. Fernandes, P.; Salamati, K.; Roupail, N.M.; Coelho, M.C. Identification of emission hotspots in roundabouts corridors. *Transp. Res. Part D Transp. Environ.* **2015**, *37*, 48–64. [CrossRef]
17. Coelho, M.C.; Farias, T.L.; Roupail, N.M. Effect of roundabout operations on pollutant emissions. *Transp. Res. Part D Transp. Environ.* **2006**, *11*, 333–343. [CrossRef]
18. Guo, R.; Zhang, Y. Exploration of correlation between environmental factors and mobility at signalized intersections. *Transp. Res. Part D Transp. Environ.* **2014**, *32*, 24–34. [CrossRef]
19. Pathivada, B.K.; Perumal, V. Modeling Driver Behavior in Dilemma Zone under Mixed Traffic Conditions. *Transp. Res. Procedia* **2017**, *27*, 961–968. [CrossRef]
20. Najmi, A.; Choupani, A.; Aghayan, I. Characterizing driver behavior in dilemma zones at signalized roundabouts. *Transp. Res. Part F Traffic Psychol. Behav.* **2019**, *63*, 204–215. [CrossRef]
21. Calvi, A.; Petrella, C. An evaluation of the effectiveness of countermeasures for improving the safety of dilemma zones: A driving simulator study. *Transp. Res. Part F Traffic Psychol. Behav.* **2022**, *87*, 295–312. [CrossRef]
22. Zhang, Y.; Gu, Z.; Yu, C.W. Large eddy simulation of vehicle induced turbulence in an urban street canyon with a new dynamically vehicle-tracking scheme. *Aerosol Air Qual. Res.* **2017**, *17*, 865–874. [CrossRef]
23. Voordeckers, D.; Meysman, F.J.R.; Billen, P.; Tytgat, T.; Van Acker, M. The impact of street canyon morphology and traffic volume on NO<sub>2</sub> values in the street canyons of Antwerp. *Build. Environ.* **2021**, *197*, 107825. [CrossRef]
24. Zheng, X.; Yang, J. CFD simulations of wind flow and pollutant dispersion in a street canyon with traffic flow: Comparison between RANS and LES. *Sustain. Cities Soc.* **2021**, *75*, 103307. [CrossRef]
25. Hermosilla, T.; Palomar-Vázquez, J.; Balaguer-Beser, Á.; Balsa-Barreiro, J.; Ruiz, L.A. Using street based metrics to characterize urban typologies. *Computers. Environ. Urban Syst.* **2014**, *44*, 68–79. [CrossRef]
26. Kaur, S.; Nieuwenhuijsen, M.J.; Colville, R.N. Fine particulate matter and carbon monoxide exposure concentrations in urban street transport microenvironments. *Atmos. Environ.* **2007**, *41*, 4781–4810. [CrossRef]
27. Berkowicz, R.; Winther, M.; Ketzel, M. Traffic pollution modelling and emission data. *Environ. Model. Softw.* **2006**, *21*, 454–460. [CrossRef]
28. Mensink, C.; Cosemans, G. From traffic flow simulations to pollutant concentrations in street canyons and backyards. *Environ. Model. Softw.* **2008**, *23*, 288–295. [CrossRef]
29. Luo, Z.; Wang, Y.; Lv, Z.; He, T.; Zhao, J.; Wang, Y.; Liu, H. Impacts of vehicle emission on air quality and human health in china. *Sci. Total Environ.* **2022**, *813*, 152655. [CrossRef] [PubMed]
30. Gao, X.; Wu, J.; Zhang, H.; Zhang, W.; Dai, Q.; Gong, P. Contributions of vehicle emissions to PM<sub>2.5</sub> in roadside microenvironments. *Zhongguo Huanjing Kexue/China Environ. Sci.* **2021**, *41*, 5086–5093.
31. Song, N.; Xu, H.; Bi, X.; Wu, J.; Zhang, Y.; Yang, H.; Feng, Y. Source Apportionment of PM<sub>2.5</sub> and PM<sub>10</sub> in Haikou. *Res. Environ. Sci.* **2015**, *28*, 1501–1509. [CrossRef]
32. Teng, H.; Liu, Y.; Liu, A.; Xiong, N.N.; Cai, Z.; Wang, T.; Liu, X. A novel code data dissemination scheme for Internet of Things through mobile vehicle of smart cities. *Future Gener. Comput. Syst.* **2019**, *94*, 351–367. [CrossRef]
33. Shahrour, I.; Xie, X. Role of internet of things (IoT) and crowdsourcing in smart city projects. *Smart Cities* **2021**, *4*, 1276–1292. [CrossRef]
34. Hu, C.; Fan, W.; Zeng, E.; Hang, Z.; Wang, F.; Qi, L.; Bhuiyan, M.Z.A. Digital twin-assisted real-time traffic data prediction method for 5G-Enabled Internet of Vehicles. *IEEE Trans. Ind. Inform.* **2022**, *18*, 2811–2819. [CrossRef]
35. Yu, S.; Chang, C.T.; Ma, C.M. Simulation and measurement of air quality in the traffic congestion area. *Sustain. Environ. Res.* **2021**, *31*, 26. [CrossRef]
36. Air Quality Modeling. Available online: <https://www.epa.gov/air-research/air-quality-modeling> (accessed on 9 February 2023).

37. Baghestani, A.; Tayarani, M.; Allahviranloo, M.; Gao, H.O. Cordon Pricing, Daily Activity Pattern, and Exposure to Traffic-Related Air Pollution: A Case Study of New York City. *Atmosphere* **2021**, *12*, 1458. [CrossRef]
38. Liu, H.; Xu, X.; Rodgers, M.O.; Xu, Y.; Guensler, R.L. MOVES-Matrix and distributed computing for microscale line source dispersion analysis. *J. Air Waste Manag. Assoc.* **2017**, *67*, 763–775. [CrossRef]
39. Kim, D.; Liu, H.; Rodgers, M.O.; Guensler, R. Development of roadway link screening model for regional-level near-road air quality analysis: A case study for particulate matter. *Atmos. Environ.* **2020**, *237*, 117677. [CrossRef]
40. Teng, M.; Li, S.; Xing, J.; Song, G.; Yang, J.; Dong, J.; Zeng, X.; Qin, Y. 24-Hour prediction of PM<sub>2.5</sub> concentrations by combining empirical mode decomposition and bidirectional long short-term memory neural network. *Sci. Total Environ.* **2022**, *821*, 153276. [CrossRef]
41. Shuai, C.; Wang, W.; Xu, G.; He, M.; Lee, J. Short-Term traffic flow prediction of expressway considering spatial influences. *J. Transp. Eng. Part A Syst.* **2022**, *148*, 04022026. [CrossRef]
42. Shang, P.; Liu, X.; Yu, C.; Yan, G.; Xiang, Q.; Mi, X. A new ensemble deep graph reinforcement learning network for spatio-temporal traffic volume forecasting in a freeway network. *Digit. Signal Process. A Rev. J.* **2022**, *123*, 103419. [CrossRef]
43. Nasser, A.; Simon, V. Wavelet-attention-based traffic prediction for smart cities. *IET Smart Cities* **2022**, *4*, 3–16. [CrossRef]
44. Bai, Y.; Li, Y.; Wang, X.; Xie, J.; Li, C. Air pollutants concentrations forecasting using back propagation neural network based on wavelet decomposition with meteorological conditions. *Atmos. Pollut. Res.* **2016**, *7*, 557–566. [CrossRef]
45. Baskar, P.K.; Kaluvan, H. Long short-term memory (LSTM) recurrent neural network (RNN) based traffic forecasting for intelligent transportation. *AIP Conf. Proc.* **2022**, *2435*, 020039. [CrossRef]
46. Kong, X.; Zhang, J.; Wei, X.; Xing, W.; Lu, W. Adaptive spatial-temporal graph attention networks for traffic flow forecasting. *Appl. Intell.* **2022**, *52*, 4300–4316. [CrossRef]
47. Hembeck, L.; Dickerson, R.R.; Canty, T.P.; Allen, D.J.; Salawitch, R.J. Investigation of the Community Multiscale air quality (CMAQ) model representation of the Climate Penalty Factor (CPF). *Atmos. Environ.* **2022**, *283*, 119157. [CrossRef]
48. Wang, M.; Zhang, Y.; Fung, J.C.H.; Lin, C.; Lau, A.K.H. A novel hybrid clustering model of region segmentation to fuse CMAQ simulations with observations. *Atmos. Environ.* **2022**, *278*, 119062. [CrossRef]
49. Du, W.; Chen, L.; Wang, H.; Shan, Z.; Zhou, Z.; Li, W.; Wang, Y. Deciphering urban traffic impacts on air quality by deep learning and emission inventory. *J. Environ. Sci.* **2023**, *124*, 745–757. [CrossRef] [PubMed]
50. Glushkov, A.; Shepelev, V. Development of reliable models of signal-controlled intersections. *Transp. Telecommun.* **2021**, *22*, 417–424. [CrossRef]
51. Qin, D.; Gao, C. Control measures for automobile exhaust emissions in PM<sub>2.5</sub> governance. *Discret. Dyn. Nat. Soc.* **2022**, *2022*, 8461406. [CrossRef]
52. Shepelev, V.; Kostyrchenko, V. Modeling the Operation of Signal-Controlled Intersections with Different Lane Occupancy. *Mathematics* **2022**, *10*, 4829. [CrossRef]
53. Hoque, J.M.; Erhardt, G.D.; Schmitt, D.; Chen, M.; Chaudhary, A.; Wachs, M.; Souleyrette, R.R. The changing accuracy of traffic forecasts. *Transportation* **2022**, *49*, 445–466. [CrossRef]
54. Shepelev, V.; Glushkov, A.; Fadina, O.; Gritsenko, A. Comparative Evaluation of Road Vehicle Emissions at Urban Intersections with Detailed Traffic Dynamics. *Mathematics* **2022**, *10*, 1887. [CrossRef]
55. Shepelev, V.; Aliukov, S.; Glushkov, A.; Shabiev, S. Identification of distinguishing characteristics of intersections based on statistical analysis and data from video cameras. *J. Big Data* **2020**, *7*, 46. [CrossRef]
56. Shepelev, V.; Zhankaziev, S.; Aliukov, S.; Varkentin, V.; Marusin, A.; Marusin, A.; Gritsenko, A. Forecasting the passage time of the queue of highly automated vehicles based on neural networks in the services of cooperative intelligent transport systems. *Mathematics* **2022**, *10*, 282. [CrossRef]
57. Shepelev, V.; Glushkov, A.; Bedych, T.; Glushchenko, T.; Almetova, Z. Predicting the traffic capacity of an intersection using fuzzy logic and computer vision. *Mathematics* **2021**, *9*, 2631. [CrossRef]
58. Order of the Ministry of Natural Resources and Ecology of the Russian Federation No. 804 Dated November 27, 2019 “On Approval of the Methodology for Determining Emissions of Pollutants into the Atmospheric air from Mobile Sources for Conducting Summary Calculations of Atmospheric Air Pollution”. Available online: <https://www.garant.ru/products/ipo/prime/doc/73240708/> (accessed on 7 November 2022).
59. Order of the Ministry of Natural Resources and Ecology of the Russian Federation No 273 Dated June 6, 2017 “On Approval of Methods for Calculating the Dispersion of Emissions of Harmful (Polluting) Substances in the Atmospheric Air”. Available online: <https://docs.cntd.ru/document/456074826> (accessed on 7 November 2022).
60. Ntziachristos, L.; Gkatzoflias, D.; Kouridis, C.; Samaras, Z. COPERT: A European road transport emission inventory model. In Proceedings of the 4th International ICSC Symposium, Thessaloniki, Greece, 28–29 May 2009; Springer: Berlin/Heidelberg, Germany, 2009; pp. 491–504. [CrossRef]
61. Ntziachristos, L.; Samaras, Z. COPERT III: Computer Programme to Calculate Emissions from Road Transport-Methodology and Emission Factors. *European Topic Centre on Air Emissions*; EEA: Copenhagen, Denmark, 2000.
62. Weather Forecasts, Newscasts and History in a Fast and Elegant Way. Available online: <https://openweathermap.org/> (accessed on 30 August 2022).
63. Vlahogianni, E.I.; Karlaftis, M.G.; Golias, J.C. Short-term traffic forecasting: Where we are and where we’re going. *Transp. Res. Part C Emerg. Technol.* **2014**, *43*, 3–19. [CrossRef]

64. Zeng, Y.; Chen, J.; Jin, N.; Jin, X.; Du, Y. Air quality forecasting with hybrid LSTM and extended stationary wavelet transform. *Build. Environ.* **2022**, *213*, 108822. [CrossRef]
65. DustTrak™ DRX Aerosol Monitor 8533. Available online: <https://tsi.com/products/aerosol-and-dust-monitors/aerosol-and-dust-monitors/dustrak%E2%84%A2-drx-aerosol-monitor-8533/> (accessed on 17 August 2022).

**Disclaimer/Publisher's Note:** The statements, opinions and data contained in all publications are solely those of the individual author(s) and contributor(s) and not of MDPI and/or the editor(s). MDPI and/or the editor(s) disclaim responsibility for any injury to people or property resulting from any ideas, methods, instructions or products referred to in the content.

Article

# Investigation of the Convergence of a Multi-Grid Algorithm for Solving the Task of Pressure in the Thin Lubricating Film of the Non-Newtonian Fluid

Elena Zadorozhnaya \*, Igor Levanov, Igor Mukhortov and Vlad Hudyakov

Department of Motor Transport, Institute of Engineering and Technology, South Ural State University, 76 Prospekt Lenina, 454080 Chelyabinsk, Russia

\* Correspondence: zadorozhnaiea@susu.ru; Tel.: +7-904-811-17-77

**Abstract:** The article describes a multi-grid algorithm for integrating the Reynolds equation for hydrodynamic pressures in the lubricating film of a heavy-loaded journal bearing. This equation is the basic one in solving the tasks of designing friction units of piston- and rotary machines. Lubrication sources of various configurations in the form of grooves and holes located on the friction surfaces were taken into account. The version of the multi-grid algorithm developed by the authors is based on Brandt's work. At each level of grids, not only the convergence of the solution is controlled, but also the rate of convergence. The pressure equation was approximated by finite differences using the control volume method and passed to a system of algebraic equations, which were solved by the Seidel method. Bessel formulas were used as the interpolation operator. The function for taking into account the non-Newtonian properties of the lubricant is based on the power law. Comparison of the developed algorithm with other versions showed high efficiency. The use of multi-grid algorithms makes it possible to perform multi-variant calculations of the dynamics of heavily loaded bearings. As a result of the calculations, the characteristics of the connecting rod bearing of the heat engine, as well as the multilayer bearing of the turbocharger, are presented.

**Keywords:** multi-grid algorithm; hydrodynamic pressures; journal bearing; non-Newtonian fluids; highly viscous boundary layer

**Citation:** Zadorozhnaya, E.; Levanov, I.; Mukhortov, I.; Hudyakov, V. Investigation of the Convergence of a Multi-Grid Algorithm for Solving the Task of Pressure in the Thin Lubricating Film of the Non-Newtonian Fluid. *Mathematics* **2023**, *11*, 54. <https://doi.org/10.3390/math11010054>

Academic Editor: Hovik Matevosian

Received: 23 November 2022

Revised: 15 December 2022

Accepted: 20 December 2022

Published: 23 December 2022



**Copyright:** © 2022 by the authors. Licensee MDPI, Basel, Switzerland. This article is an open access article distributed under the terms and conditions of the Creative Commons Attribution (CC BY) license (<https://creativecommons.org/licenses/by/4.0/>).

**MSC:** 65M50; 65M06; 74A55

## 1. Introduction

In the classical hydrodynamic theory of lubrication, the movement of fluid in a thin lubricating film of tribo-units is described by three fundamental laws [1–3]:

- preservation of momentum in a limited volume of liquid;
- preservation of mass in the form of a flow continuity equation;
- preservation of energy, which reflects the equality of the change in time of the total energy of the allocated volume of liquid and the superposition of the work of the mass forces applied to this volume, and the amount of heat supplied from an external source per unit time.

For heavily loaded tribo-units, the equations of motion of their moving elements are added to the equations compiled on the basis of conservation laws.

Theories and methods for studying hydrodynamic tribo-units are characterized by a set of methods for solving interrelated tasks [4–6]:

1. Solving the equations of dynamics of multi-mass mechanical systems, including the equations of motion of moving elements of tribo-units to determine the trajectory of the center of the journal in the bearing.

2. Solutions to tasks of continuous medium dynamics for determining pressures in a lubricating layer separating friction surfaces of non-ideal geometry with an arbitrary law of their motion.
3. Assessment of the thermal state of the system “shaft-lubricating film-bush”.
4. Determination and optimization of integral hydro-mechanical characteristics of bearings.

A comprehensive solution of the above tasks is the main condition for creating tribounits with an increased capacity and reliability that meet modern requirements and working conditions.

However, the joint solution of these tasks causes great difficulties, since it requires the development of highly efficient mathematical techniques and methods, algorithms and calculation technologies.

Usually, various methods for solving tasks of dynamics are divided into two main groups: numerical methods of continuum mechanics and methods for modeling multi-mass mechanical systems. Typical representatives of the first class are the finite element method (FEM) or the finite difference method (FDM), which is mainly used for calculations involving all kinds of deformable structures, viscous liquids and gases [7–9].

The algorithm presented in the article can be used to evaluate the performance of various friction units of machines and mechanisms, including: multilayer plain bearings of turbocharger rotors; heavily loaded crankshaft bearings of an internal combustion engine; piston-ring-cylinder connection; diesel engine bearings and large steam turbine bearings.

## 2. Formulation of the Problem/Literature Review

The Reynolds equation is the basic one when calculating the performance of multilayer plain bearings of lightly loaded turbocharger rotors, determining their stability characteristics [10], as well as when calculating the hydro-mechanical characteristics of heavily loaded bearings of thermal machines and mechanisms. Wear resistance, thermal stress, fatigue life of the antifriction layer of liners directly or indirectly depend on the hydro-mechanical characteristics of the bearings. The Reynolds equation for hydrodynamic pressures in a thin lubricating film in a coordinate system fixed on a bearing is written as [11]:

$$\frac{\partial}{\partial \varphi} \left[ F \bar{\rho} \bar{h}^{n+2} \frac{\partial \bar{p}}{\partial \varphi} \right] + \frac{1}{a^2} \frac{\partial}{\partial \bar{z}} \left[ F \bar{\rho} \bar{h}^{n+2} \frac{\partial \bar{p}}{\partial \bar{z}} \right] = \frac{\partial}{\partial \varphi} \{ F_{\omega} \bar{\rho} \bar{h} \} + \frac{\partial}{\partial \tau} (\bar{\rho} \bar{h}) . \tag{1}$$

Here  $\bar{z} = 2z/B$ ,  $-1 < \bar{z} < 1$ ,  $a = B/2r$ ,  $\bar{t} = \omega_0 t$ ,  $\bar{p} = (p - p_a) \cdot \psi^2 / \mu_0 \omega_0$ ,  $\bar{\rho} = \rho / \rho_0$ ;  $\bar{\mu} = \mu / \mu_0$ ;  $\bar{h} = h/h_0$ ;  $\psi = h_0/r$ ;  $\bar{\omega} = \omega / \omega_0$ ;  $\tau = \omega_0 t$ ,  $h$  is lubricating layer thickness;  $\mu$  is effective (calculated) lubricant viscosity;  $h_0, \mu_0, \rho_0, \omega_0$  is characteristic thickness of the lubricating film, lubricant viscosity, density, journal rotation speed;  $p, p_a$  is hydrodynamic and atmospheric pressure;  $\omega$  is absolute angular velocity of rotation of the journal;  $r, B$  is bearing radius and width

$$F = \left( \bar{\phi}_2 - \frac{\bar{\phi}_1}{\bar{\phi}_0} \bar{\phi}_1 \right), F_{\omega} = \bar{\omega}_1 + \bar{\omega}_{21} \left( 1 - \frac{\bar{\phi}_1}{\bar{\phi}_0} \right), \bar{\phi}_k = \int_0^1 \frac{y^k}{\bar{\mu}} d\bar{y}.$$

Dimensionless lubricating film thickness  $\bar{h}$  and its derivative  $\partial \bar{h} / \partial \tau$  are determined by the formulas  $\bar{h} = 1 - \chi \cos(\varphi - \delta)$ ,  $\partial \bar{h} / \partial \tau = -\dot{\chi} \cos(\varphi - \delta) - \chi \dot{\delta} \sin(\varphi - \delta)$ , where  $\chi = e/h_0$ ,  $e$  is absolute eccentricity of the journal center;  $\dot{\chi}, \dot{\delta}$  are derivatives with respect to dimensionless time.

When integrating Equation (1) in region  $\Omega = (\varphi \in 0.2\pi; \bar{z} \in -a, a)$ , the Swift–Stieber boundary conditions are most often used, which are written in the form of the following restrictions on the function  $\bar{p}(\varphi, \bar{z})$ :

$$\begin{aligned} \bar{p}(\varphi, \bar{z} = \pm a) &= \bar{p}_a; \bar{p}(\varphi, \bar{z}) = \bar{p}(\varphi + 2\pi, \bar{z}); \bar{p}(\varphi, \bar{z}) \geq 0, \\ \bar{p}(\varphi, \bar{z}) &= \bar{p}_S \text{ on } (\varphi, \bar{z}) \in \Omega_S, S = 1, 2 \dots S^*, \end{aligned} \tag{2}$$

where  $\Omega_S$  is lubrication source area where the pressure is constant and equal to the supply pressure  $p_s$ ,  $S^*$ —number of sources.

The scan of the lubricating film in the presence of lubrication sources of various shapes on the friction surface is shown in Figure 1, where axis  $O\varphi$  coincides with the axis of symmetry of the lubricating film. Loops  $S_\alpha$  and  $S_\beta$  limit, respectively, closed (not in contact with the ends of the bearing) and open (in contact with the ends) grooves;  $S_\gamma$  is the square introduced into the design model to approximate the contour of the hole.

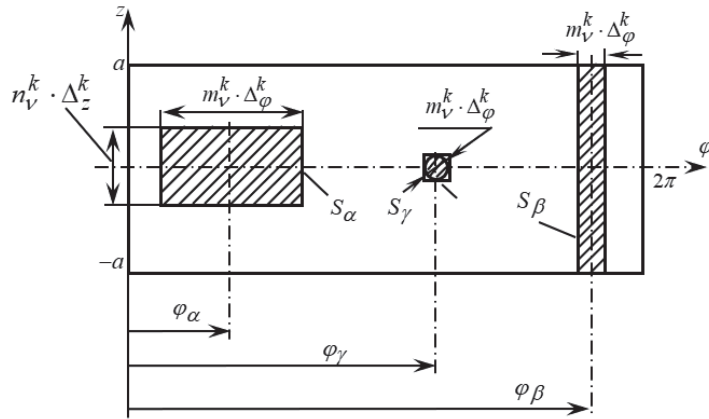


**Figure 1.** The scan of the lubricating film in the presence of lubrication sources of various shapes on the friction surface.

In closed grooves, i.e., in areas  $S_\alpha$  that include boundaries  $\partial S_\alpha$ ,  $\alpha = 1, 2, \dots, \alpha^*$ , the pressure is set equal to the supply pressure  $p_s$ . In open grooves, i.e., in areas  $S_\beta$ ,  $\beta = 1, 2, \dots, \beta^*$ , the change in the dimensionless pressure along the coordinate  $z$  is described by a linear function  $p_\beta(\varphi \in S_\beta, z) = p^- + 0.5(p^+ - p^-) \cdot (z + a)/a$ , where  $p^\pm$  are the dimensionless pressures at the endfaces, i.e., at  $z = \pm a$ . In particular, if an excess  $z = -a$  pressure is maintained at  $p_s$ , and the end  $z = a$  connects with the atmosphere ( $p^+ = 0$ ), this equation will take the form  $p_\beta(\varphi \in S_\beta, z) = p_s - 0.5p_s(z + a)/a$ .

The set of restrictions on the function  $p(\varphi, z)$  for the bearing with lubrication sources will be written for the moment in the form.

$$p(\varphi, z) = p(\varphi + 2\pi, z) = \begin{cases} \geq 0, \Omega \in (0 \leq \varphi \leq 2\pi, -a \leq z \leq a); \\ p^\pm, z = \pm a; \\ p_v(\varphi, z) \in S_v, v = 1, 2, \dots, \bar{v}, \bar{v} = \alpha, \beta, \gamma. \end{cases} \tag{3}$$

The location of the sources is given by the coordinates of their geometric centers (angles  $\varphi_\alpha, \varphi_\beta, \varphi_\gamma$ ), and their length by the formulas:

$$b_{v\varphi}^k = m_v^k \cdot \Delta_\varphi^k, b_{vz}^k = n_v^k \cdot \Delta_z^k, m_v^k = \text{int}(b_\varphi / \Delta_\varphi^k), n_v^k = \text{int}(b_z / \Delta_z^k) \tag{4}$$

where  $b_\varphi^k, b_z^k$  are dimensionless extensions of sources in the direction of the axes  $\varphi$  and  $z$  on the grid  $k$ ;  $\Delta_\varphi^k, \Delta_z^k$  are grid step sizes  $k$ ;  $m_v^k, n_v^k$  are scale factors.

Recently, preference has been increasingly given to numerical-analytical methods based on finite-difference approximation of differential operators of a boundary value task with free boundaries, which make it possible to obtain solutions for bearings of arbitrary geometry. Among the numerical methods, the most widely used methods are finite difference methods (FDM) [12–14] and variation difference methods using finite element (FEM) [15–18] approximating models.

Numerical methods based on finite-difference approximation of the boundary value task of hydrodynamic pressure make it possible to obtain solutions for bearings with a complex geometry of the lubricating layer, and to take into account the presence of lubricant sources on the friction surface; the algorithms for their implementation are flexible and universal.

The Reynolds Equation (1) after its difference approximation is reduced to a system of algebraic equations, which, taking into account restrictions (2), is usually solved by the iterative Seidel method, and less often using one of the well-known modifications of the method of longitudinal-transverse sweeps [19]. The algorithm for implementing restrictions (2) is that each time during iterations at some point in the region  $\Omega$  the condition  $\bar{p} > 0$  is not met, the pressure at this point is reset to zero. This technique was used by El-Bach and El-Tayeb [20] when calculating the pressure field in a bearing lubricated with carbonated lubricants.

An economical way to find a solution to Equation (1) is associated with the use of multi-grid algorithms [21], in which the carrier region  $\Omega$  is approximated by a sequence of rectangular grids  $S^1, S^2, \dots, S^{\bar{k}}$ , with appropriate step sizes

$$S^k = \begin{cases} \varphi_i = \Delta_\varphi(i - 1); i = 1, \dots, M^k; M^k = M \cdot 2^{(k-1)}; \Delta_\varphi^k = 2\pi / M^k; \\ z_j = -a + \Delta_z(j - 1); j = 1, \dots, N^k; N^k = N \cdot 2^{(k-1)} + 1; \Delta_z^k = 2a / N^k; \\ k = 1, \dots, \bar{k}. \end{cases} \quad (5)$$

where  $M$  and  $N$  is number of discretization nodes of the plane  $\Omega$  in coordinate directions  $\varphi$  and  $z$  on the first (largest) grid;  $\bar{k}$  is number of grids (sampling levels);  $\Delta_\varphi^k$  and  $\Delta_z^k$  are grid steps by coordinates  $\varphi$  and  $z$ :  $\Delta^{(1)} = 2\Delta^{(2)} = 4\Delta^{(3)} = \dots = 2^{\bar{k}-1}\Delta^{(\bar{k})}$ .

When using multi-grid algorithms [21–24], the time spent on integrating the Reynolds equation is reduced by several orders of magnitude. In this regard, the popularity of multi-grid algorithms for integrating second-order equations, to which the Reynolds equation belongs, is understandable. The idea of multi-grid algorithms was first presented in the work of P.P. Fedorenko [23] and further developed by Brandt [21,24]. The effectiveness of their application was demonstrated in the works of V.N. Prokopiev et al. [25,26], who showed that the use of multi-grid algorithms for integrating the Reynolds equation reduces the time spent by dozens of times [25]. The authors of [27] successfully considered geometric multi-grid methods that use information about grids of different nesting levels to solve nonlinear tasks described by parabolic type equations. They showed that a significant advantage of nonlinear multi-grid methods is the absence of the need for linearization and the construction of Jacobians, which somewhat simplifies the software implementation of these algorithms.

Among the numerical methods for solving equations for pressures in a thin lubricating layer, not only FDM, but also FEM have received the most widespread use in recent years in the literature. In the work of Byung-Jik Kim and Kyung-Woong Kim [28], the Reynolds equation was solved by the finite element method. FEM have found wide application for statically loaded bearings in solving EHD lubrication tasks [28–30] due to the extremely simple docking of hydrodynamic and elastic subproblems. The disadvantage of such calculations is the excessive cost of resources for the solution.

More than 1000 billion floating point operations per second (1 TFLOPS) of computing power is required to solve many of today’s tasks. A large number of computational algorithms using the sequential programming model have been developed at present. However, it is not always possible to create an efficient parallel algorithm to implement many of them.

Often, to obtain an approximate solution with high accuracy, a grid with a high density of nodes is used, while the calculation time increases significantly, and thus the use of multiprocessor computers becomes relevant to reduce the calculation time. For example, D.V. Degi and A.V. Starchenko [31], when solving the task of the flow of a viscous incompressible fluid in a cavity with a moving top cover, used the obtained property of

parallel algorithms to speed up calculations on grids with more than  $10^6$  nodes by several tens of times. There are other works [32–34] that use the power of supercomputers to solve engineering tasks, including tasks of hydrodynamics. It was noted in [33] that the development of software packages for solving hydroaerodynamic tasks, such as ANSYS CFX, ANSYS FLUENT, STAR-CD, FlowVision, etc., has reached a high level of efficiency, accuracy, and flexibility. All these packages allow solving tasks of continuum mechanics using models built on the basis of the Navier–Stokes equations. However, the difficulty of using such powerful and, for the most part, commercial packages is due to the need to simultaneously solve the tasks of hydrodynamics, the theory of elasticity, heat transfer, etc. There are also tasks with the correct assignment of boundary conditions, matching of input and output data when using different packages. This is especially noticeable when solving elasto-hydrodynamic tasks requiring the use of iterative procedures.

Methods for solving tasks on pressure in a thin lubricating layer, for the most part, are designed to find the pressure distribution in a Newtonian fluid layer. The rheological properties of any fluid in shear are fully characterized by its viscosity. The viscosity of a lubricant is practically the only parameter that can be used to characterize and take into account the rheological behavior of a lubricant when determining hydrodynamic pressures using the Reynolds equation. Therefore, the task of substantiating the mathematical model of viscosity is fundamental. Existing attempts to apply these methods for a lubricant with non-Newtonian properties lead to an unjustified increase in the calculation time and simplification of the applied mathematical models.

### 3. The Ideology of Multi-Grid Algorithms for Integrating Second-Order Differential Equations

Equation (1) with conditions (2) in the grid domain  $S^k$  with grid steps  $\Delta_\varphi^k$  and  $\Delta_z^k$  is approximated by finite differences and with difficulties in the form of a difference equation.

$$L^k \bar{p}^k = F^k, \tag{6}$$

where  $L$  is a differential operator, and  $L^k \bar{p}^k$  are the expressions corresponding to it, including values  $\bar{p}^k$  at neighboring nodes,  $F^k$  is the right side of Equation (1).

Task (4) with a constraint  $\bar{p} \geq 0$  is called the linear complementarity task and is solved by any iterative method in two stages.

The solution of complementarity tasks is considered in detail in [23,35].

Firstly, after the  $s$ -th iteration, the preliminary pressure value is found.

$$\bar{p}^{k,s+1/2} = \bar{p}^{k,s} + \Delta \bar{p}^{k,s+1} \tag{7}$$

and then its projection

$$\bar{p}^{k,s+1} = \max\left(0, \bar{p}^{k,s+1/2}\right) \tag{8}$$

Such a two-stage iterative method is hereinafter referred to as the projection method.

The simplest version of the multi-grid algorithm studied by the author implements R.P. Fedorenko [23] and looks like this. We start the solution on the first (largest) grid. The convergent solution of Equation (6) is found using projection iterations (7, 8), achieving the specified accuracy. The resulting solution is transferred to the grid of the next finer level

$$\bar{p}^{k+1} = I_k^{k+1} \bar{p}^k, \tag{9}$$

where the symbol  $I_k^{k+1}$  means the interpolation operation from  $S^k$  to  $S^{k+1}$  and is used as an initial approximation to find a convergent solution, which is then passed to the next lower level, etc. This algorithm is called the direct multi-grid algorithm (DM) [23,24].

The modern version of the multi-grid algorithm for integrating second-order differential equations, which includes the Reynolds equation, developed in collaboration, is based on the A. Brandt scheme and is further called AMA (multi-grid adaptive algorithm).

As in the direct multi-grid algorithm, the solution obtained on a coarse grid  $k$  is interpolated to a finer grid  $(k + 1)$  and used as an initial approximation for the solution obtained using this intermediate grid.

A series of projection iterations is carried out on the grid  $(k + 1)$  to suppress the high-frequency components of the error (smoothing the errors of the solution  $V^{k+1}$ ). After each iteration, the convergence of the solution is controlled

$$\left\| \nabla \bar{p}^k \right\|_s \leq \varepsilon^k, \tag{10}$$

as well as the rate of convergence

$$\left\| \nabla \bar{p}^k \right\|_s / \left\| \nabla \bar{p}_{prev}^k \right\|_s \leq \eta \tag{11}$$

Here, the operator  $\|\bullet\|_s$  is a pre-selected norm,  $\varepsilon$  is a small number,

$$\nabla \bar{p}^k = \bar{p}^{k,s+1} - \bar{p}^{k,s}, \nabla \bar{p}_{prev}^k = \bar{p}^{k,s} - \bar{p}^{k,s-1} \tag{12}$$

$\eta = 0.5$  is theoretical rate of convergence.

If, after several projection iterations, condition (10) is not satisfied, but condition (11) is met, which means the convergence slows down, we switch to a coarser grid, i.e., grid of the previous level. On a coarse grid, we determine the correction that needs to be made to the smoothed approximate solution  $\bar{p}^{k+1}$  obtained on the grid  $(k + 1)$ .

We replace the equation on a fine grid.

$$L^{k+1}(\bar{p}^{k+1} + V^{k+1}) - L^{k+1}\bar{p}^{k+1} = \tilde{r}^{k+1}, \tag{13}$$

where

$$\tilde{r}^{k+1} = (F^{k+1} - L^{k+1}\bar{p}^{k+1}) \tag{14}$$

is the residual.

By equivalent equation on a coarse grid

$$L^{k+1}(I_{k+1}^k \bar{p}^k + V^k) - L^k(I_{k+1}^k \bar{p}^k) = \tilde{I}_{k+1}^k \tilde{r}^{k+1} \tag{15}$$

Here  $I_{k+1}^k$  and  $\tilde{I}_{k+1}^k$  are interpolation operators (optionally) from  $S^{k+1}$  to  $S^k$ . To avoid the appearance of additional nonlinear terms in Equation (14), instead of  $V^k$ , we introduce a new unknown  $w^k$ , which represents the sum of the initial (preliminary) approximation  $\tilde{p}^{k+1} = \bar{p}_{prev}^{k+1}$  and correction  $V^{k+1}$  on a coarse grid.

As a result, Equation (15) takes the form

$$L^k w^k = f^k, \tag{16}$$

where

$$f^k = L^k(I_{k+1}^k \tilde{p}^k) + \tilde{I}_{k+1}^k \tilde{r}^{k+1}. \tag{17}$$

Note that not solution  $w^k$  itself, but function  $V^k = w^k - I_{k+1}^k \tilde{p}^k$  is an approximation on a coarse grid of a smoothed function  $V^k$  defined on  $(k + 1)$  grid. Therefore, if  $w^k$  is the solution to Equation (15), then the approximation found earlier on a fine grid is refined using the ratio:

$$\bar{p}_{ref}^{k+1} = \bar{p}_{prev}^{k+1} + I_k^{k+1}(w^k - I_{k+1}^k \bar{p}_{prev}^k) \tag{18}$$

#### 4. Difference Approximation of the Reynolds Equation for Non-Newtonian Fluids

To integrate Equation (1) with constraints (2) or (3), uniform grid domains (4) were introduced.

The grid with the number  $(k + 1)$  is the result of splitting the cells of the  $k$ -th grid in half. The ratio between the sizes of grid cells of adjacent levels

$$\Delta^{(1)} = 2\Delta^{(2)} = 4\Delta^{(3)} = 2^{\bar{k}-1}\Delta^{(\bar{k})}$$

Equation (1) in divergent form takes the form:

$$\frac{\partial B}{\partial \varphi} + \frac{\partial C}{\partial z} = M(\varphi, \bar{t}), \tag{19}$$

where

$$B = \left(\bar{\varphi}_2 - \frac{\bar{\varphi}_1}{\bar{\varphi}_0}\bar{\varphi}_1\right)\bar{h}^{n+2}\frac{\partial \bar{p}}{\partial \varphi}; \quad C = \left(\bar{\varphi}_2 - \frac{\bar{\varphi}_1}{\bar{\varphi}_0}\bar{\varphi}_1\right)\bar{h}^{n+2}\frac{\partial \bar{p}}{\partial z}; \tag{20}$$

$$M(\varphi, \bar{z}) = \left(\bar{\omega}_1 + \bar{\omega}_{21}\left(1 - \frac{\bar{\varphi}_1}{\bar{\varphi}_0}\right)\right)\frac{\partial \bar{h}}{\partial \varphi} - \dot{\chi} \cos(\varphi - \delta) - \chi \dot{\delta} \sin(\varphi - \delta) + \frac{\partial \bar{h}}{\partial \bar{t}}.$$

When constructing difference algorithms for the numerical differential solution of tasks, it is important that the construction of the finite-difference scheme be conservative, i.e., correctly reflecting the main backbones (mass, heat, energy, etc.) underlying the original differential task.

Integrating Equation (19) over the area  $S_{ij}$  (Figure 2), and passing in its left side to the contour integral, we obtain a conservative scheme in the form.

$$\left(B_{i+\frac{1}{2},j} - B_{i-\frac{1}{2},j}\right)\frac{1}{\Delta \varphi} + \left(C_{i,j+\frac{1}{2}} - C_{i,j-\frac{1}{2}}\right)\frac{1}{\Delta z} = M_{ij}, \tag{21}$$

where

$$B_{i\pm\frac{1}{2},j} = \left(\left(\bar{\varphi}_2 - \frac{\bar{\varphi}_1}{\bar{\varphi}_0}\bar{\varphi}_1\right)\bar{h}^{n+2}\frac{\partial \bar{p}}{\partial \varphi}\right)_{i\pm\frac{1}{2},j}^{m+1}; \tag{22}$$

$$C_{i,j\pm\frac{1}{2}} = \left(\left(\bar{\varphi}_2 - \frac{\bar{\varphi}_1}{\bar{\varphi}_0}\bar{\varphi}_1\right)\bar{h}^{n+2}\frac{\partial \bar{p}}{\partial z}\right)_{i,j\pm\frac{1}{2}}^{m+1}; \tag{23}$$

$$M_{ij} = \left(\bar{\omega}_1 + \bar{\omega}_{21}\left(1 - \frac{\bar{\varphi}_1}{\bar{\varphi}_0}\right)\right)\frac{\Delta h}{\Delta \varphi} - \dot{\chi} \cos(\varphi - \delta^{m+1}) - \chi \dot{\delta} \sin(\varphi - \delta^{m+1}) + \frac{\Delta h}{\Delta t} \tag{24}$$

and the index  $(m + 1)$  denotes the time layer.

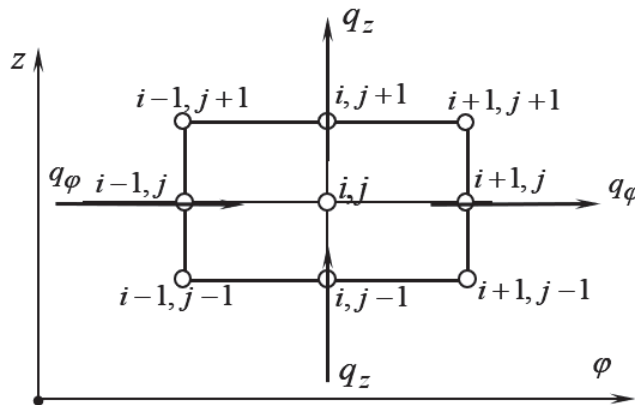


Figure 2. Node numbering by area for discretization of the Reynolds equation.

Approximating the spatial derivatives by central differences, we find (subscripts  $(m + 1)$  omitted):

$$a_{ij}\bar{p}_{ij} + a_{i-1,j}\bar{p}_{i-1,j} + a_{i+1,j}\bar{p}_{i+1,j} + a_{i,j-1}\bar{p}_{i,j-1} + a_{i,j+1}\bar{p}_{i,j+1} = b_{ij}. \tag{25}$$

Here

$$\begin{aligned} a_{i-1,j} &= \frac{1}{\Delta_z^2} \left( \left( \bar{\phi}_2 - \frac{\bar{\phi}_1}{\bar{\phi}_0} \bar{\phi}_1 \right) \bar{h}^{n+2} \right)_{i-\frac{1}{2},j}; & a_{i+1,j} &= \frac{1}{\Delta_z^2} \left( \left( \bar{\phi}_2 - \frac{\bar{\phi}_1}{\bar{\phi}_0} \bar{\phi}_1 \right) \bar{h}^{n+2} \right)_{i+\frac{1}{2},j}; \\ a_{i,j-1} &= \frac{1}{\Delta_x^2} \left( \bar{\phi}_2 - \frac{\bar{\phi}_1}{\bar{\phi}_0} \bar{\phi}_1 \right) \bar{h}_i^{n+2}; & a_{i,j+1} &= \frac{1}{\Delta_x^2} \left( \bar{\phi}_2 - \frac{\bar{\phi}_1}{\bar{\phi}_0} \bar{\phi}_1 \right) \bar{h}_i^{n+2}; \\ a_{ij} &= -(a_{i-1,j} + a_{i+1,j} + a_{i,j-1} + a_{i,j+1}); & b_{ij} &= M_{ij}. \end{aligned}$$

The system of linear algebraic Equation (25) is a detailed record of the operator Equation (6), and the ideology of multi-grid algorithms described above was used to solve it.

The set of restrictions on the function  $p(\varphi, z)$  for the bearing with lubrication sources is used in the form (3).

In multi-grid algorithms for integrating the Reynolds equation on a coarse (first) grid, the sources were specified as pressure lines for the groove and points for the hole. On the second and third grids, the sizes of the sources were calculated by Equation (4), and thus, their boundaries could be set with the accuracy of the sizes of the cells of the finest grid  $\Delta_\varphi^k, \Delta_z^k$ .

When solving Equation (1), the non-Newtonian properties that modern lubricants have are taken into account.

### 5. Modeling Non-Newtonian Properties of Lubricants

Lubricant is an integral element of the design of many friction units. Traditionally, when modeling friction units, the viscosity-temperature properties of lubricants are taken into account. However, modern oils are structurally complex substances and their rheological behavior differs from that of a Newtonian fluid. The main feature of the rheological behavior of many oils is the nonlinearity of the dependence of viscosity on shear rate, which must be taken into account when calculating the hydromechanical characteristics of friction units, for example, rotor bearings of turbochargers of internal combustion engines. Thus, there was a need for a complex rheological model of the lubricant. This model should take into account viscosity as a function of lubricant temperature, hydrodynamic pressure in a thin lubricant layer and shear rate:

$$\mu(T, p, \dot{\gamma}) = \begin{cases} \mu_1 \cdot C_1 e^{(C_2/(T+C_3))+\beta(T) \cdot p}, & 1 \leq \dot{\gamma} \leq 10^2; \\ (I_2)^{(n(T)-1)/2} \cdot C_1 e^{(C_2/(T+C_3))+\beta(T) \cdot p}, & 10^2 \leq \dot{\gamma} \leq 10^6; \\ \mu_2 \cdot C_1 e^{(C_2/(T+C_3))+\beta(T) \cdot p}, & \dot{\gamma} > 10^6, \end{cases} \tag{26}$$

where  $\dot{\gamma} = \sqrt{I_2}$ ,  $I_2 = (\partial V_x / \partial y)^2 + (\partial V_z / \partial y)^2$ ,  $C_1, C_2, C_3$  are constants, which reflect empirical features of the lubricant.

At Section 1 in the range of shear rates from 1 to  $10^2 \text{ s}^{-1}$  the oil behaves as a Newtonian fluid with a viscosity  $\mu_1$ . At Section 2 in the range of shear rates from  $10^2$  to  $10^6 \text{ s}^{-1}$  it is characteristic that the decrease in viscosity follows a power law. In Section 3, where the shear rate is greater than  $10^6 \text{ s}^{-1}$ , the oil behaves as a Newtonian fluid with the viscosity  $\mu_2$ .

The effect of natural or synthetic surfactants on the rheological behavior of oils in thin films is of great technical interest. In order to take into account the phenomenon of formation of a boundary layer on the metal surfaces of friction units, the following rheological model was proposed [36–39]:

$$\mu_i = \mu_0 + \mu_s \exp(h_i / l_h) \tag{27}$$

where  $\mu_s$  is the parameter representing the conditional value of viscosity at infinitesimal distance from the limiting surface. We assume that the viscosity of hydrocarbon oils near a solid surface is equal to the viscosity of solid paraffin.

Dependence (27) in this case describes the change in viscosity  $\mu(h)$  with distance of  $h_i$  from the metal surface.

In a layer limited by two surfaces, possible distinctions between the adsorptive properties and the structuring influence of various materials need to be considered. These distinctions are described by parameters  $l_{h1}, l_{h2}$

$$\mu_i = \mu_0 + \mu_s \left( \exp\left(\frac{-h_i}{l_{h1}}\right) + \exp\left(\frac{h_i - h}{l_{h2}}\right) \right) \tag{28}$$

Calculation of  $h_s$  and  $l_h$  is carried out by numerical methods proceeding from:

$$\begin{cases} \mu_{ef} = \mu(\mu_0, h, h_s, l_h) \\ F(\mu_{ef}, h_s) = F_{\min}. \end{cases} \tag{29}$$

The model of the additive interaction of the adsorptive layers (28) allows us to explain a number of experimental data. It can be also used for an explanation of the dependence of the viscosity of suspensions on the sizes of particles. However, this model does not consider the interaction of the adsorptive layers formed on two surfaces. Therefore, it can be applied only at thickness values of the lubricant layer which considerably exceed  $2h_s$ , i.e., in the presence of a lubricant with the usual viscosity.

With further increase of loading inevitably there is an interaction of the adsorptive layers as described in [37,38].

Thus, the value of viscosity across the thickness of the lubricating layer varies from value  $\mu_s$ , which lies within  $[10^4 \dots 10^6]$  Pa·s, to the values of viscosity in the middle of the lubricating layer  $\mu^*(T, p, \dot{\gamma})$ . Figure 3 schematically shows the change in the viscosity of the lubricant along the  $y$  coordinate, directed along the normal to the friction surface. Coordinate  $y_1$  corresponds to the value of the boundary lubricating layer  $h_s$ . Coordinate  $x$  corresponds to the change in the angular  $\varphi$  coordinate.

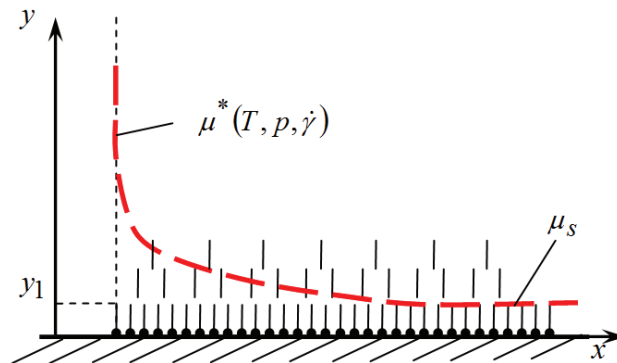


Figure 3. Lubricant viscosity change over layer thickness.

Generalizing models (26) and (28), we write down the rheological model for the viscosity of the lubricant at each point of the discrete grid in three coordinates  $(\varphi, z, y)$  characterizing the position of the elementary volume of the lubricant enclosed between two friction surfaces,

$$\mu = \mu^*(T, p, \dot{\gamma}) + (1 - \vartheta)\mu_s \exp(-y_k/l_h), \quad y_k = 0 \dots h, \quad \vartheta = \begin{cases} 0, & h_{\min} < h_{crit.} \\ 1, & h_{\min} \geq h_{crit.} \end{cases} \tag{30}$$

where  $\mu^*(T, p, \dot{\gamma})$  is determined by expression (26).

When solving technical tasks of modeling friction units with lubrication, the influence of the boundary lubricating layer appears only at those moments of time when the calculated minimum layer thickness becomes less than the allowable value  $\text{inf}h_{\text{min}} < h_{\text{crit}}$ , i.e., with a possible transition from the hydrodynamic friction mode to the mixed one.

When calculating the field of hydrodynamic pressures in a thin lubricating layer of non-Newtonian fluids (Equation (1)), the viscosity model (30) takes into account the non-Newtonian properties of the lubricant and presence of adsorption layers.

**6. Numerical Implementation of Multi-Grid Algorithms**

To determine the discretization parameters, namely, the number of discretization nodes of the region  $S^k$  (Equation (5)) along the coordinate directions  $\varphi$  and  $\bar{z}$ , the number of grids (sampling levels) and the size of the grid steps along the coordinates, we used the calculated values of the hydromechanical characteristics obtained by solving the system of algebraic Equation (25) by the Gauss–Seidel projection method with varying calculation accuracy  $\varepsilon$ . As reference values of hydromechanical characteristics, we used the calculation results obtained in [26] for a given accuracy  $\varepsilon = 10^{-6}$  on a fine mesh with the number of nodes  $M^{\bar{k}} = 192$ ,  $N^{\bar{k}} = 49$ .

The characteristics were calculated for the symmetrical bearing with a dimensionless width  $a = 0.5$  at  $\bar{\mu} = 1$ ,  $\bar{\omega}_{21} = 1$ ,  $\delta = 0$  as a function of the relative eccentricity  $\chi$  and the parameter  $\bar{q} = 2\chi/|\bar{\omega}_{21}|$ .

Taking into account the symmetry of the diagram of hydrodynamic pressures relative to the axis  $\bar{z}$ , only the region  $0 \leq \bar{z} \leq a$  was considered. The initial array of values  $p_{ij}(\varphi, \bar{z})$  was assumed to be zero, and in expression (10) the norm was used:

$$\|\nabla \bar{p}^{\bar{k}}\|_s = \frac{\left| \sum_{i,j} \bar{p}_{ij}^{s+1} - \sum_{i,j} \bar{p}_{ij}^s \right|}{\sum_{i,j} \bar{p}_{ij}^s} \tag{31}$$

The integrals required to calculate the characteristics were calculated using the Simpson method. The maximum hydrodynamic pressure  $\bar{p}_{\text{max}}$  and the coordinate  $\varphi_{\text{max}}$  corresponding to it were determined in two stages. Initially, at  $\bar{z} = 0$ , by enumeration over all nodes of the grid of a given level, node  $\varphi_i$  was found, in which  $\bar{p}$  is maximum. At the second stage  $\bar{p}_{\text{max}}$  and  $\varphi_{\text{max}}$  were clarified. To do this, in the vicinity of the  $i$ -th node, using the approximate differentiation formula based on the Lagrange interpolation formula, we determined the derivative

$$\frac{\partial \bar{p}}{\partial \varphi} = \frac{1}{\Delta_\varphi} \left[ \frac{1}{2} \bar{p}_{i-1} (2\eta - 3) - \bar{p}_i (2\eta - 2) + \frac{1}{2} \bar{p}_{i+1} (2\eta - 1) \right],$$

where  $\eta = (\varphi - \varphi_{i-1})/\Delta_\varphi$ —interpolation step.

By equating the derivative  $\partial \bar{p}/\partial \varphi$  to zero, the relative value  $\eta_{\text{max}}$  was determined, by which point  $\varphi_{\text{max}}$  is separated from point  $\varphi_{i-1}$ :

$$\eta_{\text{max}} = \frac{\bar{p}_{i+1} - 4\bar{p}_i + 3\bar{p}_{i-1}}{2(\bar{p}_{i+1} - 2\bar{p}_i + \bar{p}_{i-1})}.$$

The maximum pressure  $\bar{p}_{\text{max}}$  was calculated using Newton’s interpolation formula

$$\bar{p}_{\text{max}} = \bar{p}_{i-1} + (\bar{p}_i - \bar{p}_{i-1})\eta_{\text{max}} + \frac{1}{2}(\bar{p}_{i+1} - 2\bar{p}_i + \bar{p}_{i-1})\eta_{\text{max}}(\eta_{\text{max}} - 1),$$

and the coordinate corresponding to it, from the obvious relation

$$\varphi_{\text{max}} = \varphi_{i-1} + \eta_{\text{max}}\Delta_\varphi$$

All calculations were performed with rougher termination criteria for the number of iterations:  $\varepsilon = 10^{-4}$ ;  $\varepsilon = 10^{-3}$ . It was found that at  $\varepsilon = 10^{-3}$ , the relative errors  $\Delta$  of calculating the dimensionless lubricant consumption  $\bar{Q}$  at  $\chi \geq 0.9$  can reach 15%; for other characteristics, these errors do not exceed 5%. At  $\varepsilon = 10^{-4}$ , the errors in determining all the characteristics of the lubricating layer are not higher than 2.5%. As the grid level decreases ( $M^{\bar{k}} = 96$ ,  $N^{\bar{k}} = 25$  and  $\varepsilon = 10^{-4}$ ), the errors increase and at  $\chi = 0.975$  they reach the value of 5%. In the operating range of eccentricities  $0.1 \leq \chi \leq 0.95$ , the relative errors in determining all characteristics do not exceed 3%. Similar results were obtained for other values  $a$  from the range  $0.25 \leq a \leq 1.5$ . Taking this into account, the sizes of  $\Delta_\varphi$  and  $\Delta_z$  cells of the finest grid ( $\bar{k} = 3$ ) were selected from condition  $M^{\bar{k}} = 96$ ,  $N^{\bar{k}} = 25$ ; in expression (10), which controls the convergence according to the norm (31),  $\varepsilon^{\bar{k}} = 10^{-4}$  was taken. On the intermediate grid ( $k = 2$ ), the number of grid nodes was reduced to  $(M^k \times N^k) = (48 \times 13)$ , and on the first ( $k = 1$ ), the coarsest mesh, up to  $(M^k \times N^k) = (24 \times 7)$ .

In the DM algorithm, convergence criterion  $\varepsilon^{\bar{k}} = 10^{-4}$  remained unchanged at the second and first discretization levels. In the AMA algorithm, when moving from the third to the second grid, according to the criterion of slowing down the convergence rate (11) in expression (10),  $\varepsilon^k = \tilde{\delta} \|\nabla p^{k+1}\|$ . The value of  $\tilde{\delta} = 0.125$  was selected by numerical experiments from the range recommended by Brandt.

As operator  $I_k^{k+1}$  for transferring grid functions from the coarse grid (the lower level) to the fine grid (the higher level), locally one-dimensional linear or cubic interpolation operators are usually used.

However, linear interpolation did not provide sufficient accuracy. The use of cubic interpolation led to the appearance of unwanted negative values of the interpolated function. A rather simple and accurate method of interpolation turned out to be a method based on Bessel formulas (numbering of nodes is shown in Figure 4):

$$\begin{aligned} f_{\frac{1}{2}} &= \frac{1}{16}[f(-1) + 9f(0) + 9f(1) - f(2)] ; \\ f_{\frac{3}{2}} &= \frac{1}{16}[f(-1) - 5f(0) + 15f(1) + 5f(2)] ; \\ f_{-\frac{1}{2}} &= \frac{1}{16}[f(2) - 5f(1) + 15f(0) + 5f(-1)] . \end{aligned} \tag{32}$$

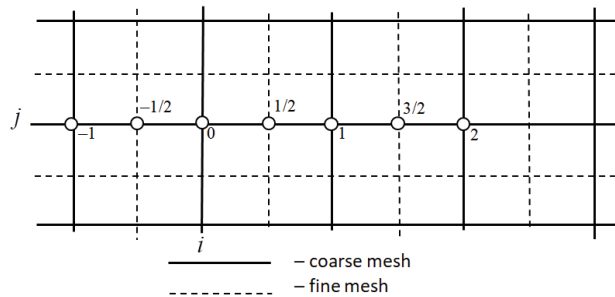


Figure 4. Node numbering when transferring grid functions from the coarse grid to the fine one.

When switching from the coarse to the fine grid, the values of the function at coinciding nodal points (points with integer numbers in Figure 4) are preserved. At points belonging only to a fine grid (points with fractional numbers in Figure 4), the values of the functions are recalculated first in the direction of axis  $\varphi$ , and then  $\bar{z}$ . At points adjacent to the boundaries of the integration region, formulas for  $f_{-1/2}$  and  $f_{3/2}$  are applied, and at other points—for  $f_{1/2}$ .

Inequality  $\bar{p}_i(\varphi_i, \bar{z}_i) \geq 0$  from conditions (2) requires that  $\bar{p}^k$  be non-negative at every point. Condition (3) ensures that  $\bar{p}^{k+1}$  is non-negative at each iteration.

Moreover, with an appropriate choice of operator  $I_{k+1}^k$ , approximations  $\bar{p}^k$  are also non-negative. However, Equation (16) does not preserve non-negativity when returning

from  $S^k$  to  $S^{k+1}$ , which was observed when debugging the algorithm. Of course, all negative components of  $\bar{p}_{ij}$  are set to zero already at the first projection iteration by  $S^{k+1}$ , but, nevertheless, their appearance slowed down the convergence. To ensure the non-negativity of hydrodynamic pressures immediately after returning from the grid  $S^k$ , after the calculation according to Equation (18), the AMA initially using the following procedure was provided:

$$p^{k=1} = \begin{cases} p_{ref}^{k+1}, & \text{if } p_{ref}^{k+1} \geq 0; \\ p_{prev}^{k+1}, & \text{if } p_{ref}^{k+1} < 0. \end{cases}$$

An alternative procedure, which turned out to be more efficient, is written as

$$\bar{p}^{k=1} = \begin{cases} \bar{p}_{ref}^{k+1}, & \text{if } \bar{p}_{ref}^{k+1} \geq 0; \\ 0, & \text{if } \bar{p}_{ref}^{k+1} < 0. \end{cases} \tag{33}$$

In the DM algorithm, all negative values of  $\bar{p}^{k+1}$  from Equation (9) are set to zero. In the developed version of AMA, the same operators for transferring solutions and residuals from fine grids to coarse ones ( $I_{k+1}^k = \bar{I}_{k+1}^k$ ) were used. Five- and nine-dot operators were tested:

$$I_{k+1}^k \equiv \frac{1}{16} \begin{bmatrix} 0 & 2 & 0 \\ 2 & 8 & 2 \\ 0 & 2 & 0 \end{bmatrix}, \quad \frac{1}{16} \begin{bmatrix} 1 & 2 & 1 \\ 2 & 4 & 2 \\ 1 & 2 & 1 \end{bmatrix}$$

The latter expression is ultimately preferred. Thus, in AMA, the recalculation of grid functions  $\tilde{\theta} = \bar{p}, \tilde{\tau}$  when transferring from the fine grid to the coarser grid is performed by the formula

$$\tilde{\theta}^k = I_{k+1}^k \tilde{\theta}^{k+1} = \frac{1}{16} [\tilde{\theta}_{i-1,j-1}^{k+1} + 2\tilde{\theta}_{i-1,j}^{k+1} + \tilde{\theta}_{i-1,j+1}^{k+1} + 2\tilde{\theta}_{i,j-1}^{k+1} + 4\tilde{\theta}_{i,j}^{k+1} + 2\tilde{\theta}_{i,j+1}^{k+1} + \tilde{\theta}_{i+1,j-1}^{k+1} + 2\tilde{\theta}_{i+1,j}^{k+1} + \tilde{\theta}_{i+1,j+1}^{k+1}]. \tag{34}$$

The scheme of the final version of the AMA is shown in Figure 5.

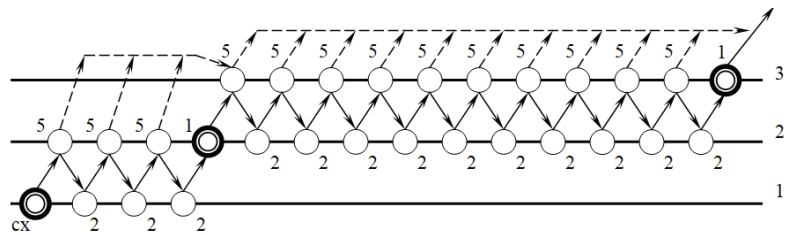


Figure 5. Scheme of the multi-grid AMA algorithm.

Different levels of the grid are marked with numbers 1, 2, 3. The maximum allowable numbers of iterations at each level are marked with numbers next to the circles. The converged solution is shown by double lines.

In accordance with the scheme of the AMA algorithm, the search for the solution started on the grid of the lowest level ( $k = 1$ ) (the largest grid) and was performed until the convergence condition (10) was satisfied. With the help of the interpolation operator (32), the converged solution was transferred as an initial approximation to the second level, where iterations and estimation of the convergence rate (11) at each step continued.

If the convergence rate slowed down or all the iterations provided by the AMA algorithm were performed, and the solution was not yet obtained, the transition to the coarse grid (34) was performed, where Equation (16) was solved for the corrections. Then the return to the fine mesh (18) was carried out, and so on, until a solution is found on the second level grid. From numerical experiments it was found that the number of cycles

(returns to the coarse grid) required to obtain the solution on the second grid does not exceed three.

If the solution is obtained before all three cycles are completed, then the remaining cycles are simply not executed, and this solution is considered obtained and transferred to the third level grid as the initial approximation. On the third grid, the described procedure is repeated, but the allowable number of cycles is increased to ten. In practice, in most cases, two or three cycles are enough to find the solution on the third grid.

The effectiveness of multi-grid algorithms can be judged by estimating the total number of conventional units  $\Sigma CU$ , which is to a certain extent proportional to the time spent on obtaining the solution. A conventional unit is the “price” of one iteration on the finest grid. Approximately, i.e., without taking into account the “price” of auxiliary operations, for example, the transfer of grid functions from fine grids to large ones and back is the “price” of one iteration on the grid  $k$ :

$$(YE)_k = 4^{(k-\bar{k})} \tag{35}$$

Thus, the total “price” (in conventional units) of the solution obtained using  $k$  grids is determined by summing the number of iterations  $It_k$  on grids with weight factors defined by relation (34).

For an algorithm with three grid levels (three-grid algorithm)

$$\sum YE = \frac{1}{16}It_1 + \frac{1}{4}It_2 + It_3 \tag{36}$$

The number of iterations on grids and the total number of conventional units for various algorithms for solving the Reynolds equation are presented in Tables 1 and 2, from which it follows that multi-grid algorithms are more than an order of magnitude more efficient than single grid ones in terms of time consumption. The adaptive algorithm (AMA) is about twice as efficient as the DM algorithm.

**Table 1.** Comparison of the efficiency of algorithms for solving the Reynolds equation.

$q$	The Total “Price”	Dimensionless Eccentricity, $\chi$						
		0.1	0.3	0.5	0.7	0.9	0.95	0.975
<b>Single Grid Algorithm</b>								
-2.0	$\Sigma CU = It_3$	735	743	747	747	741	738	737
0.0	$\Sigma CU = It_3$	727	716	691	641	528	464	408
2.0	$\Sigma CU = It_3$	721	699	662	593	430	345	272
<b>Three Grid DM Algorithm</b>								
-2	$It_1$	38	38	38	38	38	38	37
	$It_2$	50	49	46	45	40	36	34
	$It_3$	49	45	42	33	32	30	28
	$\Sigma CU$	63.87	59.62	55.87	46.62	44.37	41.37	38.81
0	$It_1$	37	36	35	33	27	24	21
	$It_2$	10	9	14	21	39	37	32
	$It_3$	2	2	6	6	63	70	62
	$\Sigma CU$	6.81	6.5	11.68	13.31	74.43	80.75	71.31
2	$It_1$	37	36	34	31	23	18	15
	$It_2$	7	8	19	36	43	36	28
	$It_3$	2	2	2	4	75	77	64
	$\Sigma CU$	6.06	6.25	8.87	14.93	87.18	87.12	71.93

**Table 2.** Comparison of the efficiency of algorithms for solving the Reynolds equation.

$q$	The Total "Price"	Dimensionless Eccentricity, $\chi$						
		0.1	0.3	0.5	0.7	0.9	0.95	0.975
<b>Adaptive AMA Algorithm with Three Grids</b>								
−2	$It_1$	44	44	44	42	42	42	43
	$It_2$	23	24	26	19	19	19	21
	$It_3$	17	17	17	12	17	17	14
	$\Sigma CU$	25.5	26.75	26.25	19.37	24.37	24.37	21.93
0	$It_1$	39	38	39	37	33	32	27
	$It_2$	7	7	12	17	30	34	29
	$It_3$	2	2	5	7	27	32	28
	$\Sigma CU$	6.18	6.12	10.43	13.56	36.56	42.5	36.93
2	$It_1$	39	38	38	37	31	26	21
	$It_2$	7	7	12	17	34	34	29
	$It_3$	2	2	2	4	32	35	32
	$\Sigma CU$	6.18	6.12	7.37	10.56	42.43	45.12	40.56

**7. Examples of Using the Multi-Grid Algorithm**

The use of multi-grid algorithms makes it possible to perform calculations of complexly loaded tribo-units, taking into account the non-Newtonian properties of modern lubricants.

For multilayer plain bearings of a turbocharger, hydrodynamic pressure diagrams were calculated in the internal lubricating layer of the support with various types of lubrication sources on the bushing surface. The calculation results are shown in Figures 6–8 ( $\chi = 0.5$ ;  $E = 0$ ;  $G = 1$ ;  $a = 0.5$ ).

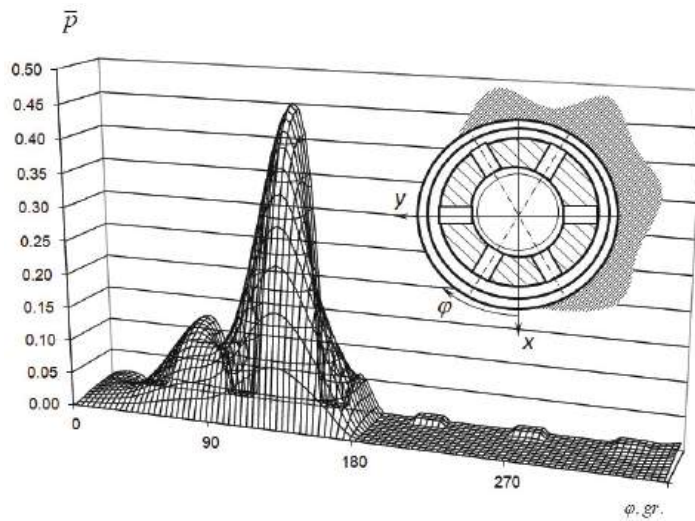


**Figure 6.** Diagram of hydrodynamic pressures in the lubricating layer with six holes.

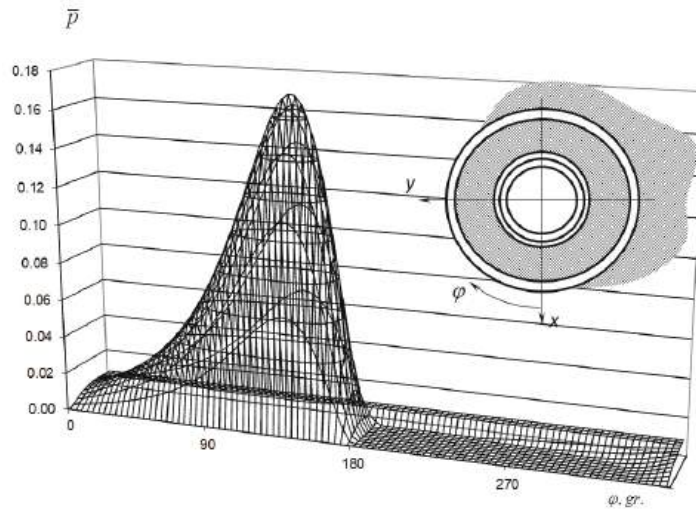


**Figure 7.** Diagram of hydrodynamic pressures in the lubricating layer with the circumferential groove.

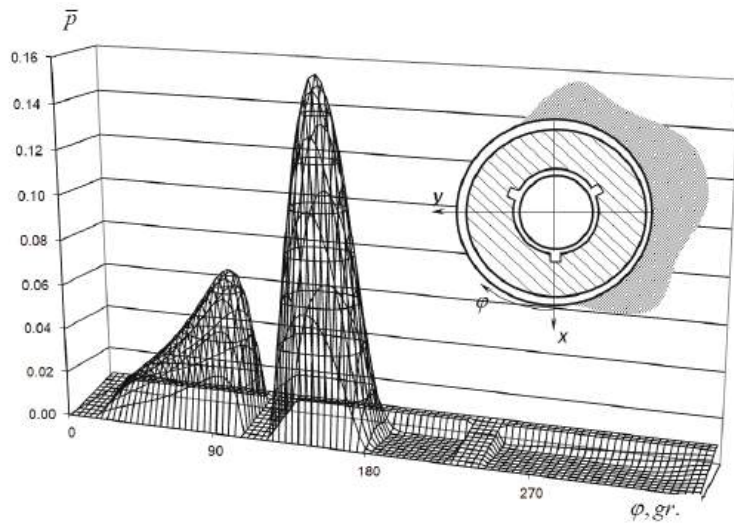


**Figure 8.** Diagram of hydrodynamic pressures in the lubricating layer with three longitudinal grooves.

The algorithm described above has been successfully applied to calculate the dynamics of a flexible asymmetric turbocharger rotor. Turbochargers of different dimensions were considered. For example, Turbochargers –7, 8, ... 23. In these designs, the diameters of the shafts varied from 8 to 16 mm. The ratio of external and internal clearances is varied from 1.8 to 2.4. The rotor speed was varied from 10,000 rpm to 200,000 rpm.

To obtain a converged stable trajectory of the rotor in the space of the bearing clearance, it is necessary to take 30,000–40,000 time steps. The use of the developed algorithm makes it possible to reduce the calculation time by 8–10 times. For example, to calculate one variant of the dynamics of the Turbochargers –8 rotor at a speed of 90,000 rpm on a fine

(third) grid, 7 h must be spent. Using the adaptive algorithm reduces the calculation time to 40 min.

The authors have experience in using an adaptive algorithm to calculate the dynamics of large-sized steam turbine bearings (bearing diameter is 0.6 m; radial clearance is 1.15 mm; bearing width is 0.335 m; rotor speed is 3000 rpm).

In addition, the adaptive algorithm was used to calculate the hydromechanical characteristics (pressure, friction losses, minimum lubricating layer thickness, lubricant consumption, etc.) of the ICE crankshaft plain bearings.

The use of the multi-grid AMA algorithm makes it possible to evaluate the effect of a high-viscosity boundary layer on the hydromechanical characteristics of heavily-loaded tribo-units. For this, the bearing of the lower head of the engine connecting rod with a dimension of 13/15 was calculated. The results were obtained for two calculation options:

1. The lubricant is considered as a Newtonian fluid, the temperature in the lubricant layer is constant,  $T = 100\text{ }^{\circ}\text{C}$ , the boundary layer is not taken into account.
2. The lubricant is considered as a Newtonian fluid, the temperature in the lubricating layer is constant,  $T = 100\text{ }^{\circ}\text{C}$ , the presence of a boundary layer with parameters  $\mu_s = 10^6\text{ Pa}\cdot\text{s}$ ,  $l_h = 56\cdot 10^{-9}\text{ m}$ , obtained experimentally is taken into account.

The number of nodes along the thickness of the lubricating layer was assumed to be 300. The calculation results are shown in Table 3.

**Table 3.** Evaluation of the influence of a high-viscosity boundary layer on the hydromechanical characteristics of heavily loaded tribo-units.

Hydromechanical Characteristics	Calculation Option 1	Calculation Option 2	Relative Error $\delta, \%$
Mean integral power loss due to friction $N, W$	601.2	722.9	20.2
Mean-integral value of the temperature of the lubricating layer, $T, \text{ }^{\circ}\text{C}$	107.3	115.4	7.6
Mean integral end flow through tribo-unit $Q, \text{ l/s}$	0.01818	0.01479	18.6
Mean integral value of the minimum thickness of the lubricating layer $h_{\min}, \mu\text{m}$	4.048	5.006	23.7
Maximum hydrodynamic pressure in the lubricating layer for the loading cycle $\text{supp}_{\max}, \text{ MPa}$	276.9	292.6	5.7
The smallest value of the minimum thickness of the lubricating layer for the loading cycle $\text{inf}h_{\min}, \mu\text{m}$	2.215	2.638	19.1

As can be seen from the results obtained, when the high-viscosity boundary layer is taken into account in the calculation process, hydromechanical characteristics are obtained, the values of which differ significantly from similar data obtained without taking into account the adsorption layer. Due to the influence of the highly viscous boundary layer, friction losses increase by 20%, and the thickness of the lubricating layer increases by 23%.

### 8. Conclusions

1. To solve the Reynolds equation when determining the field of hydrodynamic pressures, an adaptive multi-grid algorithm based on a finite-difference approximation of differential operators of a boundary value task with free boundaries is presented. The application of this algorithm makes it possible to obtain the field of hydrodynamic pressures in the lubricating layer of heavily loaded tribo-units with irregular geometry, taking into account the presence of various shaped lubricant supply sources on the friction surfaces.

2. In the course of numerical studies, the best ratios of the number of nodes  $M$  and  $N$  of the discretization of region  $S^k$  along the coordinate directions  $\varphi$  and  $\bar{z}$ , as well as  $\bar{k}$ —the discretization level, were established. To obtain a solution with an accuracy of

$\varepsilon = 10^{-4}$ , it is necessary to discretize the carrier area of the tribo-unit in such a way that the number of nodes on the last (finest) grid is not less than  $M^{\bar{k}} = 96$ ,  $N^{\bar{k}} = 25$ . The number of iterations on the finest grid compared to the single-grid method is reduced from 500 to 3 ... 5. In this case, the relative errors in calculating the field of hydrodynamic pressures in the lubricating layer of a non-Newtonian fluid do not exceed  $10^{-4}$ , and the errors in determining all characteristics of the lubricating layer do not exceed 2.5%. The maximum level discretization to achieve a given precision of  $\varepsilon = 10^{-4}$  is 3.

3. The algorithm has been developed for calculating hydrodynamic pressures in the lubricating layer, taking into account the non-Newtonian properties of the lubricant, in particular, the dependence of viscosity on shear rate and pressure.

4. The results obtained showed that taking into account high-viscosity layers leads to an increase in the calculated minimum thickness of the lubricating layer by 40–45%, temperature by 6–7%, and maximum hydrodynamic pressures by 4–5%.

The complexity of performing multivariant calculations was that in order to be able to take into account the adsorbed high-viscosity layer, it is necessary to increase the number of grid nodes to at least 300 in the process of constructing a discrete grid over the thickness of the lubricating layer. With a larger partition, it is impossible to obtain a result reflecting the effect of the adsorbed layer, since the thickness of this layer for different types of lubricants ranges from 0.3 to 10 microns.

**Author Contributions:** Conceptualization, E.Z.; Methodology, E.Z., I.M. and I.L.; Validation, E.Z.; Formal Analysis, E.Z.; Investigation, E.Z. and I.L.; Resources, E.Z. and I.L.; Data collection, E.Z., I.M. and I.L.; Writing original drafts, E.Z. and I.L.; Writing—Review and Editing, E.Z. and V.H.; Visualization, V.H.; Oversight, I.L.; Project Administration, E.Z.; Funding Acquisition, E.Z. and I.L. All authors contributed significantly to the completion of this manuscript by conceived and developed the study, and wrote and improved the paper. All authors have read and agreed to the published version of the manuscript.

**Funding:** This research was funded by the Russian Science Foundation grant number 22-29-20156.

**Data Availability Statement:** Not available.

**Acknowledgments:** The authors thank South Ural State University (SUSU) for supporting.

**Conflicts of Interest:** The authors declare no conflict of interest.

## References

1. Cameron, A. *Theory of Lubricants in Engineering*; Mashgiz: Moscow, Russia, 1962; 296p.
2. Kodnir, D.S. *Contact Hydrodynamic Lubrication of Machine Parts*; Mashinostroenie: Moscow, Russia, 1976; 632p.
3. Korovchinsky, M.V. *Theoretical Foundations of the Operation of Journal Bearings*; Mashgiz: Moscow, Russia, 1959; 403p.
4. Rozhdestvensky, Y.; Lazarev, E.; Doikin, A. Effect of the Heat Insulating Coating of the Piston Crown on Characteristics of the piston-Cylinder Liner Pair. *Procedia Eng.* **2016**, *150*, 541–546. [CrossRef]
5. Prokopiev, V.N.; Boyarshinova, A.K.; Gavrilov, K.V. Algorithm of mass conservation during calculating the dynamics of loaded sliding supports. *Probl. Mech. Eng. Reliab. Mach.* **2004**, *4*, 32–38.
6. Zakharov, S.M.; Zharov, I.A. Tribological criteria for assessing the performance of internal combustion engines crankshafts journal bearings. *Fric. Wear* **1996**, *17*, 606–615.
7. Vorozhtsov, E.V. *Difference Methods for Solving Problems of Continuum Mechanics*; Publishing House of NSTU: Nizhny Novgorod, Russia, 1998; 86p.
8. Dmitrienko, Y.I. *Nonlinear Continuum Mechanics*; Fizmatlit Publishing House: Moscow, Russia, 2009; 624p.
9. Prosvetov, G.I. *Continuum Mechanics*; Alfa-Press Publishing House: Moscow, Russia, 2011; 112p.
10. Zadorozhnaya, E.A.; Cherneyko, S.V.; Kurochkin, M.I. A study the axial and radial rotor stability of the turbo machinery with allowance the geometry of the surface and properties of the lubricating fluid. *Tribol. Ind.* **2015**, *37*, 455–463.
11. Rozhdestvensky, Y.; Gavrilov, K.; Doikin, A. Forced Diesel Piston Tribological Parameters Improvement. *Procedia Eng.* **2017**, *206*, 647–650. [CrossRef]
12. Petrushev, A.S. *Difference Schemes and Their Analysis*; MIPT Publishing House: Moscow, Russia, 2004; 89p.
13. Jagadeesha, K.M.; Nagaraju, T.; Sharma, S.C.; Jain, S.C. 3D Surface Roughness Effects on Transient Non-Newtonian Response of Dynamically Loaded Journal Bearings. *Tribol. Trans.* **2012**, *55*, 32–42.
14. Yang, Y.-K.; Jeng, M.-C. Analysis of Viscosity Interaction and Heat Transfer on the Dual Conical-Cylindrical Bearing. *Tribol. Trans.* **2004**, *47*, 77–85. [CrossRef]

15. Ebrat, O.; Mourelatos, Z.P.; Vlahopoulos, N.; Vaidyanathan, K. Calculation of Journal Bearing Dynamic Characteristics Including Journal Misalignment and Bearing Structural Deformation. *Tribol. Trans.* **2004**, *47*, 94–102. [CrossRef]
16. Nagaraju, T.; Sharma, S.C.; Jain, S.C. Performance of Externally Pressurized Non-Recessed Roughened Journal Bearing System Operating with Non-Newtonian Lubricant. *Tribol. Trans.* **2003**, *46*, 404–413. [CrossRef]
17. Khushnood, S.; Malik, A.; Rashid, B.; Azim, R.A. Experimental and Finite Element Analysis of Hydrodynamic Lubrication of Rotary Diesel Fuel Injection Pump. *Tribol. Lubr. Eng.* **2004**, *2*, 1015–1024.
18. Kim, T.-J.; Han, J.-S. Comparison of the Dynamic Behavior and Lubrication Characteristics of a Reciprocating Compressor Crankshaft in Both Finite and Short Bearing Models. *Tribol. Trans.* **2004**, *47*, 61–69. [CrossRef]
19. Alimov, I.; Pirnazarova, T.; Kholmatova, I. On a numerical method for solving the hydrodynamic problem of underground leaching. *J. Phys. Conf. Ser.* **2019**, *1260*, 102001. [CrossRef]
20. El-Butch, A.M.A.; El-Tayeb, N. Surface Roughness Effects on Thermo-Hydrodynamic Lubrication of Journal Bearings Lubricated with Bubbly Oil. *Tribol. Lubr. Eng.* **2004**, *2*, 999–1006. [CrossRef]
21. Brant, A.; Cryer, C.W. Multigrid Algorithms for the Solution of Linear Complementarity. Problems Arising from Free Boundary Problems. *SIAM/J. Sci. Stat. Comput.* **1983**, *4*, 655–684. [CrossRef]
22. Samarsky, A.A.; Nikolaev, E.S. *Methods for Solving Grid Equations*; Science: Moscow, Russia, 1978; pp. 73–103.
23. Fedorenko, R.P. On the rate of convergence of one iterative process. *Zh. Vychisl. Mat. Mat. Fiz.* **1964**, *4*, 559–564.
24. Brant, A. Multi-Level Adaptive Solution to Boundary. Value Problems. *Math. Comput.* **1977**, *31*, 333–390. [CrossRef]
25. Prokopiiev, V.N.; Boyarshinova, A.K.; Zadorozhnaya, E.A. Multinet integration algorithms of Reynolds equation in the dynamics problems of complex-loaded plain bearings. *Probl. Mech. Eng. Reliab. Mach.* **2005**, *5*, 16–21.
26. Prokopiiev, V.N.; Boyarshinova, A.K.; Zadorozhnaya, E.A. Adaptive multigrid algorithm for integrating the Reynolds equation for hydrodynamic pressures in the lubricating layer of heavily loaded journal bearings. *Bull. SUSU* **2001**, *6*, 61–67.
27. Maksimov, D.Y.; Filatov, M.A. Study of Nonlinear Multigrid Methods for Solving Single-Phase Filtration Problems. M.V. Keldysh IPM 2011, 26. Preprints. Available online: <http://library.keldysh.ru/preprint.asp?id=2011-43> (accessed on 1 September 2019).
28. Byung-jik, K.; Kyung-Woong, K. Thermo-Elastohydrodynamic Analysis of Connecting Rod Bearing in Internal Combustion Engine. *J. Tribol.* **2001**, *123*, 444–454.
29. Olson, E.G.; Booker, J.F. EHD Analysis with Distributed Structural Inertia. *Trans. ASME* **2001**, *123*, 463–468. [CrossRef]
30. Genka, O. Solution of an elastic-hydrodynamic problem for dynamically loaded connecting rod bearings. In *Problems of Friction and Lubrication*; American Society of Mechanical Engineers: New York, NY, USA, 1985; Volume 3, pp. 70–76.
31. Degi, D.V.; Starchenko, A.V. Numerical solution of the Navier-Stokes equations on computers with parallel architecture. *Bull. Tomsk State Univ. Math. Mech.* **2012**, *2*, 88–98.
32. Bogoslovsky, N.N.; Esaulov, A.O.; Starchenko, A.V. Parallel implementation of the SIMPLE CFD algorithm. In *Siberian School Seminar on Parallel Computing*; Tomsk University Press: Tomsk, Russia, 2002; pp. 118–124.
33. Vasiliev, V.A.; Nitsky, A.Y.; Kraposhin, M.V.; Yuskin, A.V. Investigation of the possibility of hydroaerodynamic problems parallel computing using the open source software package OpenFOAM. In *Supercomputer Technologies and Open Source Software: A Scientific Articles Collection*; Chelyabinsk State University Publishing House: Chelyabinsk, Russia, 2013; pp. 19–26.
34. Shirkovich, D.G. *Femap & Nastran: Engineering Analysis by the Finite Element Method*; DMK Press: Moscow, Russia, 2008; 704p.
35. Popov, L.D. *Introduction to the Theory, Methods and Economic Applications of Complementarity Problems: Textbook*; Publishing House of the Ural University: Yekaterinburg, Russia, 2001; 124p.
36. Mukhortov, I.V.; Usoltsev, N.A.; Zadorozhnaya, E.A.; Levanov, I.G. Improved model of rheological properties of the boundary layer of lubricant. *Friect. Lubr. Mach. Mech.* **2010**, *5*, 8–19.
37. Mukhortov, I.V. *Multilayer Adsorption Lubricants and Its Inclusion in the Theory of Fluid Friction*; Bulletin SUSU series “Engineering”; SUSU Publishing Center: Chelyabinsk, Russia, 2011; Volume 18, pp. 62–67.
38. Mukhortov, I.; Zadorozhnaya, E.; Levanov, I. Multimolecular adsorption lubricants and its integration in the theory fluid friction. In Proceedings of the STLE 68th STLE Annual Meeting & Exhibition, Detroit Marriott at the Renaissance Center, Detroit, MI, USA, 5–9 May 2013; pp. 147–149.
39. Mukhortov, I.; Zadorozhnaya, E.; Levanov, I.; Pochkaylo, K. The influence of poly-molecular adsorption on the rheological behaviour of lubricating oil in a thin layer. *FME Trans.* **2015**, *43*, 218–222.

**Disclaimer/Publisher’s Note:** The statements, opinions and data contained in all publications are solely those of the individual author(s) and contributor(s) and not of MDPI and/or the editor(s). MDPI and/or the editor(s) disclaim responsibility for any injury to people or property resulting from any ideas, methods, instructions or products referred to in the content.



Article

# Modeling the Operation of Signal-Controlled Intersections with Different Lane Occupancy

Viacheslav Morozov <sup>1,\*</sup>, Vladimir Shepelev <sup>2</sup> and Viktor Kostyrchenko <sup>3</sup>

- <sup>1</sup> Department of Road Transport Operation, Industrial University of Tyumen, 625000 Tyumen, Russia
- <sup>2</sup> Department of Automobile Transportation, South Ural State University (National Research University), 454080 Chelyabinsk, Russia
- <sup>3</sup> Department of Road Transport and Technological Systems, Industrial University of Tyumen, 625000 Tyumen, Russia
- \* Correspondence: morozov1990\_72@mail.ru; Tel.: +7-982-943-59-40

**Abstract:** In many cities of the world, the problem of traffic congestion on the roads remains relevant and unresolved. It is especially noticeable at signal-controlled intersections, since traffic signalization is among the most important factors that reduce the maximum possible value of the traffic flow rate at the exit of a street intersection. Therefore, the development of a methodology aimed at reducing transport losses when pedestrians move through signal-controlled intersections is a joint task for the research and engineering community and municipalities. This paper is a continuation of a study wherein the results produced a mathematical model of the influence of lane occupancy and traffic signalization on the traffic flow rate. These results were then experimentally confirmed. The purpose of this work is to develop a method for the practical application of the mathematical model thus obtained. Together with the obtained results of the previous study, as well as a systems approach, traffic flow theory, impulses, probabilities and mathematical statistics form the methodological basis of this work. This paper established possible areas for the practical application of the previously obtained mathematical model. To collect the initial experimental data, open-street video surveillance cameras were used as vehicle detectors, the image streams of which were processed in real time using neural network technologies. Based on the results of this work, a new method was developed that allows for the adjustment of the traffic signal cycle, considering the influence of lane occupancy. In addition, the technological, economic and environmental effects were calculated, which was achieved through the application of the proposed method.

**Keywords:** traffic flow rate; lane occupancy; signal-controlled intersections; traffic signalization; neural network technologies

**MSC:** 76A30; 90B20; 90B22; 93-10

**Citation:** Morozov, V.; Shepelev, V.; Kostyrchenko, V. Modeling the Operation of Signal-Controlled Intersections with Different Lane Occupancy. *Mathematics* **2022**, *10*, 4829. <https://doi.org/10.3390/math10244829>

Academic Editor: Andrea Scozzari

Received: 23 November 2022  
 Accepted: 14 December 2022  
 Published: 19 December 2022

**Publisher’s Note:** MDPI stays neutral with regard to jurisdictional claims in published maps and institutional affiliations.



**Copyright:** © 2022 by the authors. Licensee MDPI, Basel, Switzerland. This article is an open access article distributed under the terms and conditions of the Creative Commons Attribution (CC BY) license (<https://creativecommons.org/licenses/by/4.0/>).

## 1. Introduction

Increasing the efficiency of traffic organization in cities in terms of economic and environmental damage remains one of the most pressing transport problems [1]. Finding an optimal solution to the current situation is an unresolved problem not only for local governments, but also for research and engineering communities.

In a broad sense, traffic congestion is a consequence of another problem—the constant increase in the level of motorization, especially in terms of individual cars, and delays in the development of the urban road network. In other words, it is a consequence of the disproportion between transport demand and transport supply [2]. At the same time, global experience shows that transport supply will never be able to satisfy, especially exceed, transport demand [1]. As a result, traffic congestion is formed when cars move along the city’s road network. By investigating traffic congestion, the authors of this article understand the phenomenon in which the traffic flow rate in the subsequent section of the

road network, for some reason, becomes lower than in the preceding section where these traffic flows are formed [3,4].

Among the existing approaches to resolving this problem, the most promising is the use of intelligent transport systems [5–16]. Traffic flow management on the road is implemented here through automated traffic control systems, some of the main elements of which are vehicle detectors, specialized software and additional peripheral equipment such as servers and fiber optic lines, inter alia. The adoption of an operational or strategic decision on the duration of a permissive traffic light signal for a given traffic flow is carried out on the basis of constantly incoming data regarding various characteristics of traffic flows [16–18].

Based on the definition of traffic congestion established by the authors of this work, it is advisable that flow rate be taken as a key indicator of the traffic flow management process [3,4]. In general, the traffic flow rate at the entrance of the considered section of the road network shows the transport demand or “request for traffic” [19] in terms of moving through this section using various vehicles. In turn, the values of the traffic flow rate at the exit of the intersection studied represent the amount of transport demand satisfied due to the adoption of certain traffic management measures.

However, the traffic flow rate indicator alone is not enough to assess the traffic situation and make a decision to adjust the traffic signal cycle. This is because in the case of measuring the traffic flow rate using a vehicle detector, its values can tend toward or be equal to zero not only in the case of traffic congestion, but also in the actual absence of vehicles on the lane studied [19,20]. In order to resolve this uncertainty, data on the traffic flow rate needs to be further compared with its concentration either in space or in time [20–22].

Until the second half of the twentieth century, the fundamental theory of traffic flows, as the main measure of traffic flow concentration, determined only its spatial characteristic—density [21]. However, thanks to the development of information technologies, it has become possible to measure traffic flow concentration not only in space, but also in time via lane occupancy [22–29]. Previously, the author of the current study developed and experimentally confirmed a two-factor mathematical model of the process of changing traffic flow rate under the influence of lane occupancy and traffic signal cycle [3]. This allows us to move on to the next stage of the study, namely, to develop a method for the practical application of the mathematical model obtained, and to evaluate the effectiveness of the method.

#### *Literature Review*

There are various traffic signal control systems: traditional (using fixed cycles), based on historical traffic data at a particular intersection; adaptive (using cycle duration variation throughout the day depending on the traffic flow rate); and intelligent (as an integral part of the ITS), operating in real-time when the duration of the cycle and its phases varies depending on the traffic flow rate and the queue of vehicles waiting for a permissive signal [12,30].

Coordinating traffic light operation can significantly reduce the negative consequences of an increased number of vehicles on the roads in an urban environment (fuel consumption and environmental load, car accidents, noise levels, etc.). However, this is sometimes impossible due to the different distances between intersections [31]. Drive quality deteriorates even when the traffic flow rate is low, since the number of stops and waiting times increases. An extended coordination model was proposed in [31], where the cycle duration was set taking into account the total capacity of intersections and the distances between them.

In order to optimize traffic light operation, a model of the dynamic sequence of phases aimed at ordering the phases of a traffic light depending on the traffic flow rate was proposed in [32]. The traffic flow rate is determined using various types of sensors, and the choice of their location affects the effectiveness of the results.

In order to avoid congestion and irregular queues at intersections, a number of researchers propose the automatic setting of traffic light phase duration depending on the size of the vehicle queues at intersections [33–35].

Traffic flow is characterized by stochasticity and is a complex system in which many elements interact: drivers, the environment and road conditions. The interaction of these elements is contradictory. As such, traffic flow does not easily lend itself to traditional mathematical modeling. In this case, the methods required are those which take into account the “fuzziness” of the source data. This possibility is provided by fuzzy modeling methods. Using fuzzy logic methods, researchers have optimized the operation of traffic lights, thus reducing delay time and queue length at intersections [36–38].

The introduction of new technologies aimed at traffic optimization, reducing the number of traffic jams and smoothing the movement of vehicles, with a minimum number of stops and delays on the way, can significantly reduce fuel consumption. As a result, it can reduce emissions of harmful substances into the atmosphere. Yang et al. [39] calculated that the implementation of speed-guided intelligent transportation systems (SG-ITS) reduced emissions of nitrogen oxides, carbon monoxide, total hydrocarbons and particulate matter in Beijing by 15.9%, 20.5%, 23.9 % and 22.5%, respectively. Alrawi [40] studied the effect of introducing ITS on environmental problems in the city and found that the widespread use of ITS throughout the entire road network reduced harmful emissions almost two-fold.

In order to improve the efficiency of traffic lights at intersections, various approaches and methods are used: optimization, fuzzy logic, linear programming, etc.

Table 1 shows the common methods of regulating the operation of traffic lights.

**Table 1.** Traffic light control methods and their main results.

Method	Positive Results
Neural network model for controlling traffic signal lights [30]	To reduce average delay time
Model of the dynamic sequence of phases [31]	To decrease the average number vehicles waiting in queues (by approximately 21%)
A waiting time model for vehicles [33]	To avoid queues that are too long and uneven or unfair at all lanes of the intersection
Fuzzy logic model [36]	To decrease the average waiting time of vehicles To decrease average queue length
Traffic-actuated optimization signal fuzzy control [37]	To reduce queue length To reduce the overall delay time of vehicles
Agent-based modeling system [38]	To reduce waiting time To reduce the number of vehicles stopping at an intersection To increase vehicles’ speed
Speed-guided intelligent transportation system [39]	To reduce the total vehicle-related exhaust emissions of nitrogen oxide, carbon monoxide, total hydrocarbons and particulate matter To alleviate urban traffic congestion

Most recent studies on optimizing the adaptive regulation of traffic light cycles at intersections are aimed at reducing the queue and delay times of vehicles (Table 1). After a detailed study of the presented methods, we noted that there is a need to develop a more effective methodology to solve the existing problems and make changes associated with the adaptive setting of traffic signalization. The real-time collection of high-quality initial data is the most important aspect of optimizing the effectiveness of any decision-making system, and is lacking in most of the previous studies under discussion. The development of functions and the selection and adjustment of lane occupancy parameters are essential for increasing the traffic capacity of signal-controlled intersections and reducing the negative impact of traffic on the urban environment.

This study presents a method aimed at preventing the formation of traffic congestion on urban signal-controlled intersections. This goal is achieved by managing traffic flows through the adjustment of traffic light control cycles based on established and experi-

mentally confirmed mathematical models of the influence of lane occupancy on traffic flow rate.

**2. Materials and Methods**

*2.1. Influence of Lane Occupancy on Traffic Flow Rate When Moving through Urban Signal-Controlled Intersections*

The problem of traffic congestion formation is one of the most complex problems for transport systems in many cities and, unfortunately, it is still unresolved. Existing approaches and numerous attempts to resolve it show that this problem may well remain unresolved in the near future [1]. However, the resources and efforts of the engineering and research communities, as well as governments, are currently being employed in a variety of ways to attempt to at least reduce the negative effects of traffic congestion.

Current scientific and practical experience has shown that the creation of a sustainable urban transport system, regardless of the chosen priorities (road construction, the development of public transport, etc.) is impossible without the use of intelligent transport systems [5–16]. In terms of traffic flow management, the functionality of these systems is implemented by adjusting traffic light cycles at signal-controlled city intersections [12,16–18,30].

From the point of view of the authors of the current paper, the most significant indicator in management is traffic flow rate [3,4,19–21]. The authors argue their position by stating that the formation of traffic congestion, in essence, can be represented as a result of decreased traffic flow rate in a section of the urban road network in relation to the previous one [3,4].

However, decreased traffic flow can occur both due to the formation of traffic congestion and due to the actual absence of vehicles on the lane studied [3,4,19–21]. Thus, uncertainty and an additional problem have arisen which do not allow full implementation of the process of traffic flow management on the urban road network.

In order to resolve this uncertainty, authors have resorted to using an additional indicator of the state of the traffic flow—its concentration in time [3,4,20–29].

At the previous research stage, the authors of the current paper managed to establish the regularity of the influence of lane occupancy on the traffic flow rate at the exit of a controlled city intersection. This regularity was also found to be described by a quadratic two-factor mathematical model [3]:

$$Q = (b\theta - a\theta^2)M_S\lambda, \tag{1}$$

where  $Q$  is the traffic flow rate at the exit of the controlled intersection (cars/hour);  $\theta$  is lane occupancy (%);  $a, b$  are model parameters (1/%);  $M_S$  is the saturation flow (the maximum possible value of the traffic flow rate; cars/hour); and  $\lambda$  is the ratio of the permitting traffic signal duration to the total duration of the traffic signal cycle.

In order to confirm the mathematical model developed (1), experimental studies were carried out which allowed us to determine the values of its parameters and verify its adequacy with a probability of at least 0.9. Table 2 presents the final results of the experiments.

**Table 2.** Results of experimental studies to determine the parameters of the model (1) and verify its adequacy.

Traffic Direction	Model Parameters <i>a</i> , 1/%	<i>b</i> , 1/%	Saturation Flow $M_S$ , cars/Hour	Optimal $\theta$ , %	Correlation Coefficient <i>R</i>	Student's <i>t</i> -Test	Determination Coefficient $R^2$	Average Approximation Error, %	Fisher's Variance Ratio <i>F</i>
Left-turn	$342 \times 10^{-6}$	$370 \times 10^{-4}$	1760	62	0.90	12.5	0.82	8.92	2.02
Forward	$360 \times 10^{-6}$	$383 \times 10^{-4}$	1906	48	0.86	9.68	0.74	11.83	1.71
Right-turn	$334 \times 10^{-6}$	$364 \times 10^{-4}$	1695	68	0.82	7.94	0.69	11.97	1.66

Since the mathematical model developed (1) is two-factor, the surface presented in Figure 1 will be its most visual graphical representation.

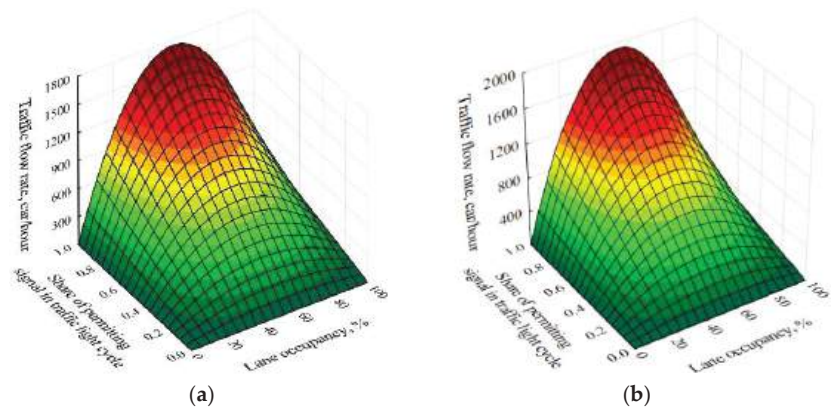


**Figure 1.** The combined influence of lane occupancy and traffic light cycle on the traffic flow rate: (a) in a left-turn; (b) forward directions of the traffic flow.

From the point of view of the authors, the following results, obtained at the previous research stage, are identified as the most significant. By their physical meaning, the values of the lane occupancy indicator, which is the main and, so far, the only indicator for assessing the concentration of traffic flow in time, are always strictly in the range of 0 to 100%. When lane occupancy assumes a minimum allowable value equal to 0%, it indicates that there are no vehicles in the lane under consideration. On the contrary, a maximum allowable value of lane occupancy equal to 100% indicates that there are vehicles in the traffic lane under consideration and that the movement of the traffic flow has been completely stopped during the entire measurement period. In practice, such a cessation of traffic can occur for a number of reasons, among which the most common are the formation network congestion inside an intersection, a vehicle stopping in a traffic lane due to breakdown and, as a result, blocking the movement of the rest of the traffic flow moving along the same lane, or a traffic accident, *inter alia*.

Among the results obtained, the most significant from the point of view of the authors is that a new optimization criterion was established for managing traffic flows at controlled city intersections. This criterion is the optimal value of lane occupancy at which the maximum possible value of the traffic flow rate at the exit of the controlled intersection is achieved.

This is explained by the fact that as the value of lane occupancy increases, the traffic flow rate also increases. The joint increase in the values of these indicators occurs only from zero to the maximum point. Finding the values of the studied traffic flow indicators in this sector indicates a surplus in the capacity of the section of the road network under consideration. In the future, this can be used as a reserve for redistributing time between different directions of traffic flow.

However, after reaching the optimal value of lane occupancy and with its subsequent increase to 100%, the traffic flow rate only decreases from its maximum to zero. After the optimal value of lane occupancy is reached, its subsequent increase no longer causes an increase, but a decrease in the intensity of the traffic flow. This is preconditioned by the physical meaning of the model (1) and directly affected by the indicator of lane occupancy itself. In aggregates, this also indicates a decrease in the traffic capacity.

Thus, the results obtained at the previous stage of the study established that a further increase in the efficiency of the traffic organization of city road networks will be associated with the management of traffic flows by optimizing the operation of controlled intersections according to the criterion of the optimal value of lane occupancy.

## 2.2. Main Methodological Stages of Further Research and Their Rationale

Since the purpose of this study is to develop a practical application for the established patterns and subsequent evaluation of the effectiveness of the measures proposed, from the point of view of the authors, the main stages of the study should be as follows:

1. Determining the area of practical application of the mathematical model (1), which describes the process of changing the traffic flow rate under the influence of lane occupancy at urban controlled intersections. First of all, this stage implies general analysis of existing methods for the development of traffic light control cycles. Based on the results of the analysis, an existing method is selected, which can serve as a base for further research.
2. The next stage, from the point of view of the authors, should be aimed at improving the basic method, taking into account the mathematical model (1).
3. This stage, according to the authors, will consist in determining the sequence of the main stages of the proposed method, taking into account lane occupancy.
4. The final stage of this study will be an assessment of the effectiveness of the proposed method.

## 2.3. Determination of the of Practical Application Area of the Research Results

Traffic flow management in cities is carried out by changing the duration of traffic lights at signal-controlled intersections. Therefore, the main area for practical application of the results of the study is the adjustment of the traffic signal cycles of controlled intersections, taking into account the different incidences of lane occupancy.

Currently, there are various methods for developing and adjusting traffic signal cycles [11,41–44]. The F. Webster method can be considered the main method for designing the operation of signal-controlled intersections.

The main steps of this method are:

1. Collecting the initial data on the existing traffic organization scheme and the geometric characteristics of the intersection, including traffic and pedestrian flow monitoring.
2. Analyzing the data obtained, and developing and adjusting the traffic management scheme and the scheme for the traffic priority of vehicles and pedestrians.
3. Determining the saturation flow  $M_S$  (cars/hour).
4. Determining the values of the phase coefficients  $y$ .
5. Determining the duration of the intermediate timings  $t_{interm}$  (s).
6. Determining the duration of the traffic signal cycle  $T_C$  (s).
7. Determining the duration of the main timings  $t_{main}$  (s).
8. Checking the results obtained in paragraphs 5 and 7 according to compliance with the minimum required time for the movement of pedestrian flows, and adjusting the results obtained, if necessary.

The method [44] is adequate and quite applicable in the initial design of traffic lights. However, in situations where, due to an excess of lane occupancy, there is a decrease in traffic flow rate at the exit of the controlled intersection [3,4], it is not possible to adjust the traffic signal cycle according to the existing F. Webster method [44].

In this regard, in order to develop a new method, the existing procedure for determining the traffic signal cycle needs to be analyzed and improved, taking into account the results of the study.

### 2.3.1. Initial Data Collection

Street video surveillance cameras were used as road detectors [45], since they provide a larger viewing angle to detect vehicles in the entire functional area of the intersection and adjacent road sections under dynamic conditions (Figure 2). Street cameras are usually located on the facades of residential buildings with an elevation angle of 30–60° to the horizon and a height of 14–40 m. The video streams of these cameras support a resolution of 1920 × 1080 pixels and provide stable transmission at 25 frames per second. The

determination of the occupancy and traffic intensity along the lanes from the video stream provides a solution to complex problems arising from the non-perpendicular direction of the camera view center and the large number of possible traffic scenarios. We used an optimized YOLOv4 recurrent neural network and the open-source Sort library to process the video streams, in order to detect and track multiple objects in video sequences [16]. In order to detect vehicles in control zones, we applied a method based on mapping coordinates from the camera image onto the space of the geographical coordinates using perspective transformations [46,47]. As a result of the experiment, we determined that the maximum time spent detecting a vehicle for one frame was 0.066 s.



Figure 2. An example of processing an input image and marking the boundaries of the control zones.

In order to assess the occupancy and traffic intensity along the lanes, we determined the time when the vehicle entered the control zone and calculated the accumulated distance  $d_i$  before it left the measured zone at each  $i$ -th step of obtaining a frame from the video stream (Figure 3). The first step is to get the coordinates of the screen from the tracker. The second is the transformation of coordinates into geographical and calculation.

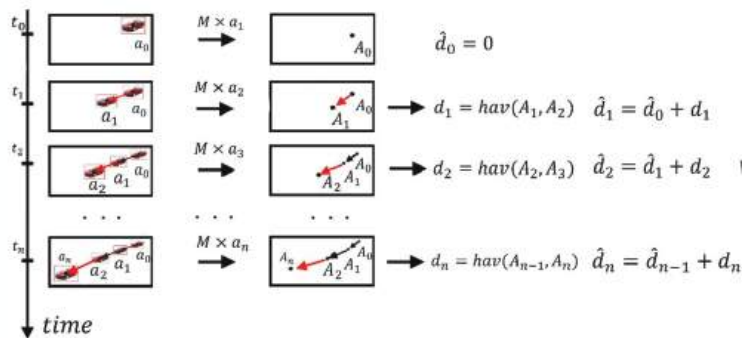
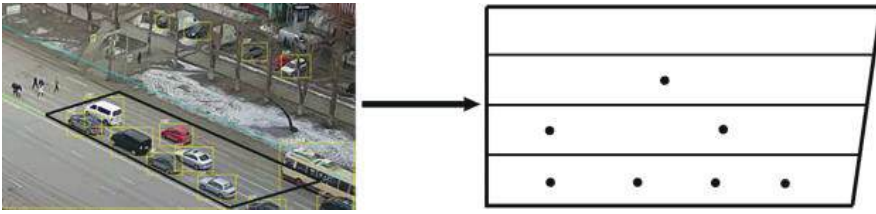
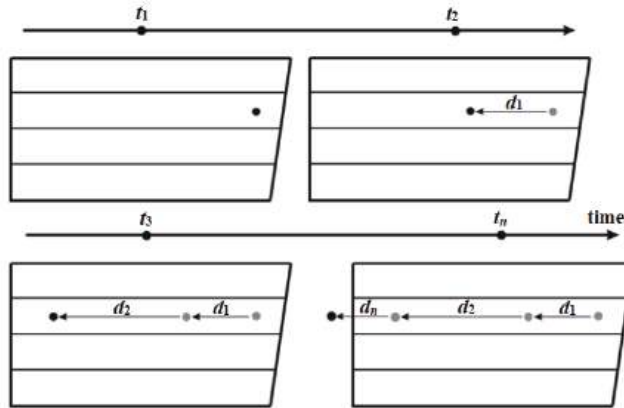


Figure 3. Matrix of perspective transformation to determine the time spent by the vehicle within the control zone, where  $a_i$  is the coordinates of a specific vehicle;  $d_i$  is the distance between two points; and  $t_i$  is the time between frames.

The processing of each video stream frame while updating the data on the distance traveled by the vehicle allows use of the proposed method in real-time traffic control tasks (Figures 4 and 5).



**Figure 4.** Transportation of vehicle screen coordinates into geographic coordinates using perspective transformation.



**Figure 5.** Vehicle movement on a series of frames, where  $x_i$  and  $y_i$  are the coordinates of a specific vehicle;  $d_i$  is the distance between two points; and  $t_i$  is the time between frames.

In order to assess the occupancy and traffic intensity along the lanes for each vehicle, we calculated the total time of its stay in the control zone (Figure 4). To this end, the location of the vehicle in the control zone was determined at each time interval. If the current  $(x_i, y_i)$  and the previous coordinate  $(x_{i-1}, y_{i-1})$  are located in the zone, the time spent in the zone is taken as equal to the time between frames  $t_i$  and considered in the total time (Figure 5). If one of the coordinates,  $(x_i, y_i)$  or  $(x_{i-1}, y_{i-1})$ , is beyond the control zone, the speed of the vehicle in this section is calculated using the formula:

$$u_i = \frac{\sqrt{(x_i - x_{i-1})^2 + (y_i - y_{i-1})^2}}{t_i} \tag{2}$$

The time spent by the vehicle in the zone is calculated using the formula:

$$t' = \frac{\sqrt{(x'_i - x'_{i-1})^2 + (y'_i - y'_{i-1})^2}}{u_i} \tag{3}$$

where  $(x', y')$  are the coordinates of the intersection of the travel path and the zone.

Lane occupancy is calculated using the following formula:

$$\theta = \frac{\sum_{i=1}^{n-k} t_i + \sum_{j=1}^k t'_j}{T} \tag{4}$$

where  $\theta$  is lane occupancy (%);  $n$  is the number of frames during which the vehicle was partially or fully in the control zone;  $k$  is the number of frames during which the vehicle was

partially in the control zone;  $t_i$  is the time between frames (s);  $t_j'$  is the time during which the vehicle was in the control zone between frames, (s); and  $T$  is the measurement duration (s).

### 2.3.2. Analysis of the Data Obtained, Adjustment of the Scheme of Traffic Organization and Traffic Priority of Vehicles and Pedestrians

The traffic priority of vehicles and pedestrians, the maximum permitted speed and the direction of movement of vehicles in lanes, as well as the location of pedestrian crossings, are significant factors affecting the level of road safety. Therefore, in order to further develop the method to prevent reductions in the level of road safety, the authors introduce an additional restriction in terms of changing the traffic organization scheme and traffic priority of vehicles and pedestrians at a signalized intersection.

### 2.3.3. Determination of the Saturation Flow and Phase Coefficients

Saturation flow  $M_S$  is determined by a calculation method based on the geometric characteristics of the considered intersection. The calculation method is adopted to determine the value of  $M_S$ , which also allows it to reflect the effects of the geometric characteristics of the road network [19,41].

Further, the obtained calculation results will allow for determination of the coefficient  $y$  for each phase of the traffic signal cycle as the ratio of the traffic flow intensity to the value of the saturation flow.

### 2.3.4. Determination of the Duration of Intermediate Timings

The duration of intermediate timings in each phase of the traffic light cycle is determined according to the formula [11,19,41,44]:

$$t_{intermi} = \frac{u_a}{7.2 \cdot a_T} + \frac{3.6(l_i + l_a)}{u_a}, \tag{5}$$

where  $t_{intermi}$  is the duration of the intermediate timing of the  $i$ -th phase of the traffic signal cycle (s);  $u_a$  is the average speed of vehicles on the approach to the intersection without braking (km/h);  $a_T$  is the average deceleration of the vehicle when the prohibiting signal is turned on ( $m/s^2$ );  $l_i$  is the distance from the “stop line” road marking to the farthest conflict point moving in the direction in the  $i$ -th phase of the traffic signal cycle (m);  $l_a$  is the most common value of the length of the vehicle in the flow (m); and the constants 7.2 and 3.6 are necessary for the transition to common measurement units of distance and time.

In practice,  $a_T$  can be considered a constant in a range of values from 3 to 4  $m/s^2$ . The values  $u_a$ ,  $l_a$  and  $l_i$  are also considered constants within each phase of traffic signal control. The key operation in performing calculations is the correct determination of the distance  $l_i$ . Unlike the durations of permitting (prohibiting) traffic signals, which can dynamically change throughout the day according to changes in transport demand, the duration  $t_{intermi}$  primarily depends on the geometric characteristics of the road network. Therefore,  $t_{intermi}$  can be considered constant and independent of the transport demand at the controlled intersection under consideration.

### 2.3.5. Determination of the Duration of the Traffic Signal Cycle

Based on the values obtained of the phase coefficients and the duration of the intermediate timings, we can calculate the optimal duration of the traffic signal cycle as follows [11,19,41,44]:

$$T_C = \frac{1.5T_L + 5}{1 - \sum_{i=1}^n y_i}, \tag{6}$$

where  $T_C$  is the duration of the traffic signal cycle (s);  $T_L$  is the total duration of the lost time in the cycle (s);  $y_i$  is the phase coefficient of the  $i$ -th phase of the traffic signal cycle;  $n$  is the number of phases in a traffic signal cycle; and the coefficients 1.5 and 5 are the reserve of the traffic light cycle time and the green signal according to [44,48–52].

### 2.3.6. Determination of the Duration of the Main Timing of the Traffic Signal Cycle

The obtained value of the cycle duration allows us to determine the duration of the main timing of each phase of the traffic signal cycle [11,19,41,44]:

$$t_{maini} = \frac{(T_C - T_L)y_i}{\sum_{i=1}^n y_i}, \tag{7}$$

where  $t_{maini}$  is the duration of the main timing of the  $i$ -th phase of the traffic signal cycle (s).

### 2.3.7. Verification of Calculations, Taking into Account the Movement of Pedestrian Flows

According to (5) and (7), the calculations for traffic flows must be compared with the minimum required duration of the main and intermediate timings for pedestrian flows [11,19,41,44]:

$$t_{intermi,ped} = \frac{B_{Wi,ped}}{4u_{ped}}, \tag{8}$$

$$t_{maini,ped} = \frac{B_{Wi,ped}}{u_{ped}} + 5, \tag{9}$$

where  $t_{intermi,ped}$  is the minimum required duration of the intermediate timing for the pedestrian direction in the  $i$ -th phase of the traffic signal cycle (s);  $u_{ped}$  is the speed of the pedestrian flow (m/s);  $B_{Wi,ped}$  is the width of the carriageway crossed by pedestrians in the  $i$ -th phase of the traffic signal cycle (m);  $t_{maini,ped}$  is the minimum required duration of the signal of the main timing for the pedestrian direction in the  $i$ -th phase of the traffic signal cycle (s); 4 is used to correct the speed of pedestrian traffic in order to have time to leave the carriageway during the green signal; and 5 is the additional time laid down to minimize the influence of possible additional factors on the change in the speed of pedestrian flow [11,19,41,44].

For the values obtained according to (5) and (7), the following conditions must be satisfied:

$$t_{intermi} \geq t_{intermi,ped}, \tag{10}$$

$$t_{maini} \geq t_{maini,ped}, \tag{11}$$

Satisfying the conditions in (10) and (11) is necessary to ensure the safe movement of pedestrians. Therefore, if the results of calculations according to (5) and (7) do not satisfy conditions (10) and (11), the duration of the main and intermediate timings for traffic flows are taken to be equal to (8) and (9), respectively.

### 2.3.8. Evaluation of Signal-Controlled Intersection Efficiency

A technological indicator of signal-controlled intersection efficiency is the average delay of vehicles when passing through the intersection [11,19,20,41,44]:

$$\begin{cases} d_j = \frac{T_C(1-\lambda_i)^2}{2(1-\lambda_i x_j)} + \frac{x_j^2}{2Q_{j,enter}(1-x_j)} - 0.65 \left(\frac{T_C}{Q_{j,enter}^2}\right)^{\frac{1}{3}} x_j^{2+5\lambda_i}, \\ x_j = \frac{Q_{j,enter}}{M_{Sij}\lambda_i}. \end{cases} \tag{12}$$

where  $d_j$  is the average delay of each vehicle in the  $j$ -th direction of movement (s/car);  $T_C$  is the duration of the traffic signal cycle (s);  $\lambda_i$  is the ratio of the permitting traffic signal duration to the total duration of the traffic signal cycle of the  $i$ -th phase of the traffic signal cycle;  $x_j$  is the degree of saturation of the  $j$ -th traffic direction;  $Q_{j,enter}$  is the car traffic flow rate of the  $j$ -th direction at the entrance of the controlled intersection (cars/hour);  $M_{Sij}$  is the saturation flow in the  $i$ -th phase of the  $j$ -th traffic direction of vehicles (cars/hour); and 2, 1 and 0.65 are the coefficients that were obtained by F. Webster [44] based on analytical and experimental studies. The first term in (12) takes into account the regularly arriving

part of the traffic flow. The second term additionally takes into account the random nature of the arrivals. The third term adjusts at least 10% of the possible error in the calculation of the delay compared to the actual experimental values.

The average delay  $d$  represents the average time that each vehicle is forced to remain idle when passing through the intersection due to the operation of the traffic signal controls.

2.4. Development of a Method for Improving the Efficiency of Traffic Management at Signal-Controlled City Intersections, Taking into Account Lane Occupancy

Based on the results of the analysis of the method [44] for the development of the operating mode of the controlled intersection and taking into account the restrictions introduced to prevent a decrease in the level of road safety, the key stages of the developed method will be to adjust the following parameters of the traffic signal cycle: the phase coefficients  $y$ , the total duration of the traffic signal cycle  $T_C$  and the duration of the main timings of the cycle phases  $t_{main}$ .

2.4.1. Adjustment of Phase Coefficients, Taking into Account Lane Occupancy

Taking into account (1), Formula (7) will have the form:

$$y_{i\theta} = \begin{cases} \max(Q_{ik,enter} / M_{Sik}), & \text{when } \theta_j < \theta_{j,opt} \\ \max(Q_{ik,enter} / Q_{ij\theta,exit}), & \text{when } \theta_{j,opt} \leq \theta_j < 100' \end{cases} \quad (13)$$

where  $y_{i\theta}$  is the phase coefficient of the  $i$ -th phase of the traffic signal cycle, taking into account lane occupancy;  $Q_{ik,enter}$  is the traffic flow rate at the entrance of the controlled intersection in the  $i$ -th phase along the  $k$ -th car traffic lane (cars/hour);  $Q_{ij\theta,exit}$  is the traffic flow rate at the exit of the controlled intersection in the  $i$ -th phase along the  $j$ -th car traffic lane, influenced by the occupancy of the  $j$ -th lane (cars/hour);  $M_{Sik}$  is the saturation flow in the  $i$ -th phase of the  $k$ -th traffic direction of vehicles (cars/hour);  $\theta_j$  is the occupancy of the  $j$ -th lane at the exit of the signal-controlled intersection (%);  $\theta_{j,opt}$  is the optimal lane occupancy at which the maximum value  $Q_{ij,exit}$  is realized in the  $i$ -th phase along the  $j$ -th lane, determined as a result of theoretical and experimental studies [1] (%).

It should be noted that a special case for (13) is a situation in which  $\theta = 100\%$  for the traffic lane under consideration at the signal-controlled intersection. Based on the results of theoretical studies in [1], it was found that this situation indicates a complete cessation of traffic flow along the lane under consideration. The value of the traffic flow rate at the exit of the signal-controlled intersection along this lane will be equal to zero, which was also revealed as a result of theoretical studies and was experimentally confirmed. Therefore, when such a situation occurs, the cycle should be adjusted, taking into account the exclusion of this lane from the calculations based on the complete loss of its functionality.

2.4.2. Determination of Optimal Traffic Signal Cycle Duration, Taking into Account Lane Occupancy

The values of the phase coefficients, adjusted for lane occupancy, make it possible to determine the optimal duration of the traffic signal cycle:

$$T_{C\theta} = \frac{1.5T_L + 5}{1 - \sum_{i=1}^n y_{i\theta}}, \quad (14)$$

where  $T_{C\theta}$  is the duration of the traffic signal cycle, taking into account lane occupancy (s), and  $y_{i\theta}$  is the phase coefficient of the  $i$ -th phase of the traffic signal cycle, taking into account lane occupancy.

An Additional Problem in Determining the Optimal Duration of the Traffic Signal Cycle and a Method of Solving It

The results of the analysis showed that at present, the movement of traffic flows on the road networks of cities is characterized by a significant excess of transport demand in

relation to transport supply. This indicates that, according to the F. Webster method [44], the calculated value  $\sum_{i=1}^n y_i \geq 1$ . If  $\sum_{i=1}^n y_i \rightarrow 1$  according to (7), the duration of the traffic signal cycle  $T_C \rightarrow \infty$ , and if  $\sum_{i=1}^n y_i > 1$  the value of  $T_C < 0$  at any  $T_L$ , which makes it unusable for further practical application. In order to confirm this argument, a process occurs that involves changing the value of the optimal duration of the traffic signal cycle depending on the lost time and the sum of the phase coefficients; this is shown in Figure 6.

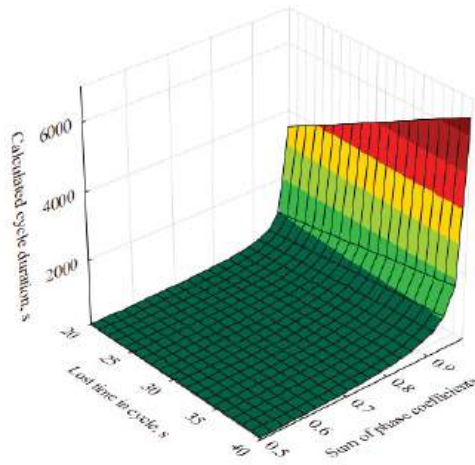


**Figure 6.** Optimal traffic signal cycle duration, obtained via the F. Webster method [44], depending on the values of the sum of the phase coefficients and the lost time.

Thus, an additional task arises to determine the boundaries of the values of the minimum and maximum duration of the traffic signal cycle.

Determining the minimum allowable duration of the traffic signal cycle does not cause any difficulties. The structure of any traffic signal cycle can be represented as follows:

$$T_C = \sum_{i=1}^n t_{maini} + T_L, \tag{15}$$

As indicated earlier, the value of  $T_L$  largely depends on the geometric characteristics of the street intersection, is not subject to constant and dynamic change and it is directly related to the level of safety of road users. In this connection, the value of  $T_L$  within the framework of a single traffic signal cycle can be considered a constant. Therefore, the structure of the minimum allowable duration of the traffic signal cycle can be represented as follows:

$$T_{C,min} = \sum_{i=1}^n t_{maini,min} + T_L, \tag{16}$$

where  $T_{C,min}$  is the minimum allowable duration of the traffic signal cycle (s); and  $t_{maini,min}$  is the minimum allowable duration of the main timing of the  $i$ -th phase of the traffic signal cycle (s).

In turn,  $t_{main,min}$  in each phase can be limited by the minimum required duration  $t_{main,ped}$  of the signal of the main timing in the pedestrian direction, which is determined according to (9). If in the phase under consideration, only the transport is moving,  $t_{main,min}$  should be at least 7 s. This is due, firstly, to the purpose of ensuring the passage of at least one vehicle, which may be randomly present at the controlled intersection. Secondly, it is necessary to maintain the priority of traffic and pedestrian flows at the controlled intersection in order to ensure the safety of vehicles and pedestrians.

When determining the minimum allowable duration of the traffic signal cycle, there is no need to provide any reserve; this is because a situation where the duration of the traffic signal cycle is minimal is rather typical for inter-peak time, when transport demand tends to zero and there is no need to provide any time reserve. Therefore, it is also advisable to consider the formula for determining the minimum duration of the traffic signal cycle [11,19,41,44]:

$$T_{C,\min} = \frac{T_L}{1 - \sum_{i=1}^n y_i}, \tag{17}$$

Thus, based on (16) and (17) and taking into account (13), when adjusting the traffic signal cycle, taking into account the influence of lane occupancy, the value of the sum of phase coefficients must at least satisfy the condition:

$$\sum_{i=1}^n y_{i\theta} \geq 1 - T_L / (\sum_{i=1}^n t_{maini,\min} + T_L), \tag{18}$$

According to (14), it is also possible to determine the boundaries of the maximum allowable values of the sum of the phase coefficients:

$$\sum_{i=1}^n y_{i\theta} \leq 1 - (1.5T_L + 5) / T_{C\theta,\max}, \tag{19}$$

where  $T_{C\theta,\max}$  is the maximum duration of the traffic signal cycle, taking into account lane occupancy (s).

Based on the results of the analyses of previously performed studies, the authors of this work have not been able to find a single approach that guarantees a positive result for determining the optimal duration of the traffic signal cycle for a fully loaded, and especially overloaded, controlled intersection.

Therefore, for the developed method, the authors of this paper propose considering  $T_{C\theta,\max}$  as a constant that is determined by engineers and researchers independently based on their goals and priorities, as well as available reserves and resources.

In this paper, the authors decide to limit the maximum allowable duration of the traffic signal cycle  $T_{C\theta,\max}$  to 160 s. This limit was set by Tyumen traffic engineers so that the waiting time for traffic in pedestrian flows in any redistribution of time in the traffic signal cycle does not exceed 120 s (2 min) and does not provoke pedestrians to violate traffic rules [47].

Thus, the duration of the traffic signal cycle should be within the following limits:

$$\begin{cases} T_{C\theta,\min} \leq T_{C\theta} \leq T_{C\theta,\max}, \\ 1 - T_L / (\sum_{i=1}^n t_{maini,\min} + T_L) \leq \sum_{i=1}^n y_{i\theta} \leq 1 - (1.5T_L + 5) / T_{C\theta,\max}, \\ T_{C\theta,\max} := \text{const.} \end{cases} \tag{20}$$

Therefore, if the sum of the phase coefficients obtained on the basis of (13) exceeds the maximum allowable value, it is necessary to forcibly limit it according to (20) and adjust the value of each phase coefficient. To do this, in the opinion of the authors, it is advisable to identify the specific weight of each phase coefficient of the total amount:

$$\alpha_i = \frac{y_{i\theta}}{\sum_{i=1}^n y_{i\theta}}, \tag{21}$$

where  $\alpha_i$  is the specific weight of the phase coefficient of the  $i$ -th phase of the traffic signal cycle, taking into account lane occupancy.

The value of  $\alpha_i$  will be applied as a correction factor and will allow us to save the specific weight of each phase coefficient, the value of which will be forcibly limited if additional adjustment is necessary:

$$\begin{cases} \sum_{i=1}^n y_{i\theta} := \sum_{i=1}^n y_{i\theta,cor}, \text{ when } \sum_{i=1}^n y_{i\theta} > 1 - (1.5T_L + 5)/T_{C\theta,max}, \\ \sum_{i=1}^n y_{i\theta,cor} = 1 - (1.5T_L + 5)/T_{C\theta,max}, \\ y_{i\theta,cor} = \alpha_i \sum_{i=1}^n y_{i\theta,cor}, \\ T_{C\theta,max} := \text{const.} \end{cases} \quad (22)$$

where  $y_{i\theta,cor}$  is the corrected value of the phase coefficient of the  $i$ -th phase of the traffic signal cycle, taking into account lane occupancy.

The dependence of the maximum value of the sum of phase coefficients on lost time in a traffic signal cycle, with a different limit set on the maximum duration of the traffic signal cycle, is shown graphically in Figure 7.

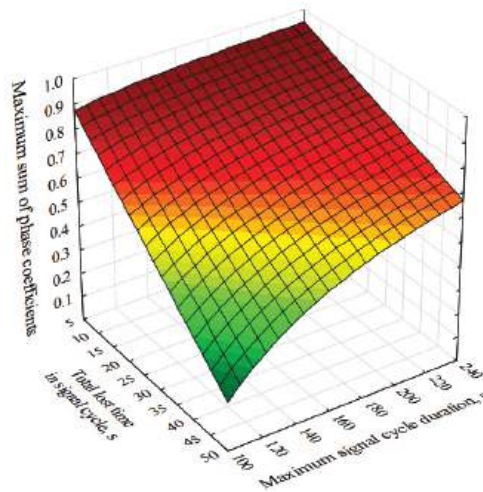


**Figure 7.** The dependence of the maximum value of the sum of phase coefficients on lost time and the maximum duration of the traffic signal cycle.

2.4.3. Determination of the Duration of the Main Timings of the Traffic Signal Cycle Phases, Taking into Account Lane Occupancy

The obtained values of the duration of the traffic signal cycle and the phase coefficients will allow us to determine the duration of the main timing of each phase of the traffic signal cycle, taking into account the influence of lane occupancy:

$$t_{maini\theta} = \frac{(T_{C\theta} - T_L)y_{i\theta}}{\sum_{i=1}^n y_{i\theta}}, \quad (23)$$

where  $t_{maini\theta}$  is the duration of the main timing of the  $i$ -th phase of the traffic signal cycle, taking into account lane occupancy.

3. Results

3.1. Determination of the Main Stages of the Method for Improving the Efficiency of Traffic Management at Signal-Controlled Urban Intersections, Taking into Account Lane Occupancy

Ultimately, the developed method will include the following key stages.

### 1. Collecting the initial data:

The initial experimental data were collected during working hours on weekdays, taking into account several requirements and restrictions. In order to achieve maximum purity of the experiment, we chose a signal-controlled intersection where the movement of trucks is prohibited and priority lanes are provided for the movement of shuttle buses. The movement on the remaining lanes is organized strictly in one of three possible directions, i.e., only straight, only to the right, or only to the left. There are no conflict points at the studied intersection during the forward movement and turning of traffic flows. The conflict or collision of vehicles and pedestrians at a workable traffic light is not possible, since a separate movement phase is provided for pedestrians. In addition, we took into account the limitations regarding the usability of the model (1) [3]: the initial data were collected in the absence of any precipitation and with clear visibility during daylight hours.

According to the technology developed for initial data collection, data were obtained on the occupancy of lanes and the traffic flow rate at the intersection under study. The total sample is presented in Figure 8.

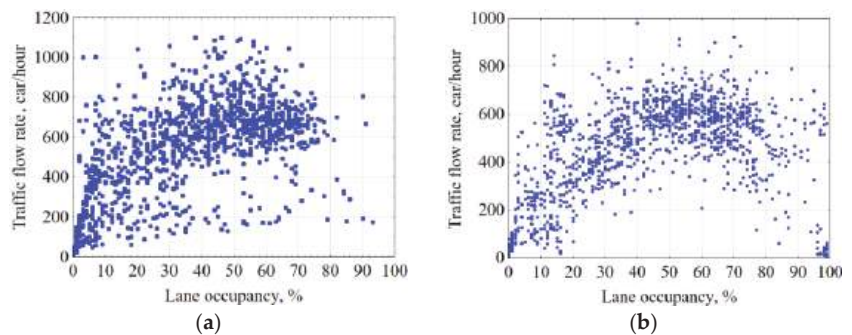


**Figure 8.** Cumulative sample of initial data on traffic flow rate and occupancy of lanes in (a) left-turn and (b) forward directions of traffic flow.

### 2. Determining the minimum allowable duration of the main and intermediate timings and the boundaries of the duration of the traffic signal cycle.

At this stage, we calculated the values of the intermediate timings and the minimum duration of the main timings for the vehicle and pedestrian directions ( $t_{interm}$ ,  $t_{main,min}$  and  $t_{interm,ped}$ ,  $t_{main,ped}$ , respectively). A decision was made to choose the minimum allowable duration of the intermediate and main timings of each phase in order to ensure the safety of all road users. A calculation was conducted and a limit was introduced on the minimum and maximum allowable duration of the traffic signal cycle ( $T_{C,min}$  and  $T_{C,max}$ , respectively).

### 3. Predicting the maximum possible traffic flow rate at the exit of the signal-controlled intersection.

At the same time as the previous stage, we calculated the value of the saturation flow  $M_S$  and the share  $\lambda$  of the permitting signal for the vehicle directions of the current traffic signalization cycle. Based on the results of the calculations, as well as the data collected on occupancy  $\theta$ , the maximum possible value of the traffic flow rate for each of the lanes at the exit of the controlled intersection  $Q_{exit}$  was predicted. In order to do this, for each operating mode of traffic lights, the experimental data were grouped according to Sturges' formula [53,54] for the number of intervals  $k$  within a range  $\delta$  of lane occupancy  $\theta$  (%). Within the range, the type of distribution was determined [55], which, in most cases, corresponded to the normal distribution (Figure 9a). Using the least-square method [54,56], the regularity of the influence of lane occupancy on the traffic flow rate was established, the graphical representation of which is the regression line in Figure 9b.

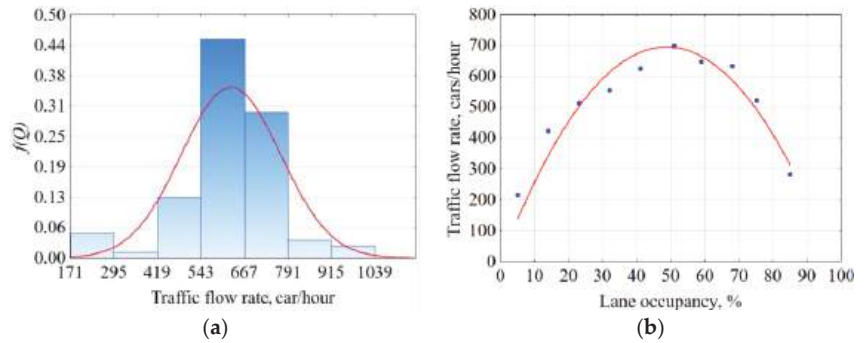


**Figure 9.** The histogram and the corresponding distribution function. (a) The regularity of the influence of lane occupancy on the traffic flow rate. (b) For the traffic lights’ operating mode from 09:00 to 15:00 and from 19:00 to 23:00,  $\lambda = 0.38$ .

Similarly, the initial data were processed for the other modes of operation of the controlled intersection under study, operating on weekdays during the working hours of the day. Thus, for each operating mode of the controlled intersection, the maximum possible values of the traffic flow rate in the directions of movement and the optimal values of lane occupancy were predicted.

4. Determining the efficiency of traffic management at the controlled intersection with an active traffic signal cycle.

Taking into account the authors’ notion of the definition of such a phenomenon as traffic congestion, in this work, it is recommended that the traffic flow rate be taken as a key indicator to assess the effectiveness of traffic management. From the point of view of the authors, it is obvious that during the formation of a traffic jam, the value of the traffic flow rate changes at the entrance and exit of the considered system of transport nodes. Therefore, within the boundaries of the controlled intersection under consideration, the following statements are true:

$$\begin{cases} Q_{enter} \geq Q_{exit}, \\ Q_{enter}, Q_{exit} \geq 0. \end{cases} \tag{24}$$

where  $Q_{enter}$  and  $Q_{exit}$  are, respectively, the traffic flow rates at the entrance and exit of the controlled intersection (cars/hour).

It is also obvious that in the most favorable outcome, the traffic flow rate at the exit of the controlled intersection tends to the value of the flow at the entrance, but under no circumstances can it be greater. This observation allows us to represent the desired objective function of maximizing the flow rate in relative terms:

$$E = \frac{Q_{exit}}{Q_{enter}} \rightarrow \max, E = [0 : 1] \tag{25}$$

The value  $E = 1$  indicates the full satisfaction of the transport demand at the considered controlled intersection. Therefore, the current traffic signal cycle is optimal and no adjustment is required. In this case, the movement of traffic flows needs to be remonitored, in order to update the data on lane occupancy  $\theta$  and traffic flow rate on the approach to the intersection  $Q_{enter}$ , and then, returned to the predicting stage. When  $E < 1$ , there is a risk of traffic congestion; to prevent this, it is necessary to adjust the traffic signal cycle.

A special case for (25) would be a situation in which there is no traffic demand at all on the approach to the controlled intersection under consideration. In this case, according to the theory of limits, the efficiency value obtained by (25) is considered to be undefined on the entire number line [53]. In such a situation, the duration of the main timings of the

phases of the traffic signal cycle should be adjusted to the minimum allowable duration, the values of which are determined considering the limits identified earlier in this paper.

#### 5. Finding reserve adjustments.

An analysis was conducted of the data on lane occupancy at the exit of the controlled intersection. A decision was made on the further expediency of adjusting the traffic signal cycle. This requires that at least one of the traffic lanes in each direction be less than 100% occupied. Otherwise, it is not advisable to adjust the traffic light cycle. In order to prevent the formation of traffic congestion, the movement of vehicles at the previous controlled intersection needs to be limited by increasing the duration of the prohibitory signal or reducing the permitting signal to the minimum allowable value in directions that can facilitate the inflow of vehicles to fully occupied lanes. After that, additional monitoring of the movement of traffic flows needs to be carried out. The traffic flow rate data on the approach to the intersection  $Q_{enter}$  and lane occupancy  $\theta$  also need to be updated, and then, returned to the prediction stage.

#### 6. Adjusting the traffic signal cycle.

Based on the results obtained at the previous stages, the phase coefficients  $y_\theta$  were determined, as well as the duration of the traffic signal cycle  $T_{C\theta}$  and the duration of the main timings of the phases  $t_{\theta main}$ , taking into account the actual influence of the occupancy of the lanes. The adjusted cycle was put into action.

#### 7. Analyzing the results of the adjustment.

After the cycle was introduced, the proposed adjustment was assessed. The change in the efficiency of traffic management, i.e., the difference  $\Delta E$  between the value of the share of satisfied transport demand after and before the adjustment, was analyzed. The value of  $\Delta E > 0$  indicates that there has been an increase in the efficiency of traffic management  $E$  and, therefore, the adjustment has been successful. If the proposed measures did not bring the expected result, like in paragraph 5 of this method, arriving vehicles at the approach to the intersection need to be limited and additional monitoring of the movement of traffic flows carried out. The traffic flow rate data on the approach to the intersection  $Q_{enter}$  and lane occupancy  $\theta$  need to be updated, and then, returned to the stage of predicting the rate of the outgoing traffic flow.

In contrast to the existing recommendations on the development of the operating modes of controlled intersections, when developing a traffic signal cycle according to the method proposed, not only is the presence of reserves due to incomplete loading of the road network taken into account, but it is also predicted that the maximum possible traffic flow rate at the exit of controlled intersections will decrease due to the influence of lane occupancy.

### 3.2. Evaluation of the Efficiency of the Developed Method

#### 3.2.1. Evaluation of Technological Efficiency

When analyzing formula (12) to determine the average delay of the basic method of F. Webster [44], it should be noted that the product  $M_S \lambda$  in the denominator of the degree of saturation  $x$  reflects the capacity of the controlled intersection, and hence, the maximum traffic flow rate  $Q_{exit}$  at the exit from it. Taking into account the results of the study [1], when determining the delay, we must also take into account lane occupancy, since the limitation of  $Q_{exit}$  occurs not only due to the presence of traffic signalization means, but also due to the influence of lane occupancy  $\theta$ . Thus, the determination of the degree of saturation and the average delay of vehicles passing through a controlled

intersection, taking into account the limitation of the maximum  $Q_{exit}$  due to the influence of lane occupancy, will have the form:

$$\begin{cases} d_{j\theta} = \frac{T_{C\theta}(1-\lambda_i)^2}{2(1-\lambda_i x_{j\theta})} + \frac{x_{j\theta}^2}{2Q_{j,enter}(1-x_{j\theta})} - 0.65\left(\frac{T_{C\theta}}{Q_{j,enter}^2}\right)^{\frac{1}{3}} x_{j\theta}^{2+5\lambda_i}, \\ x_{j\theta} = \begin{cases} \frac{Q_{j,enter}}{M_{Sij}\lambda_i}, & \text{when } \theta_j < \theta_{j,opt} \\ \frac{Q_{j,enter}}{(b\theta_j - a\theta_j^2)M_{Sij}\lambda_i}, & \text{when } \theta_j \in [\theta_{j,opt} : 100] \end{cases} \end{cases} \quad (26)$$

where  $d_{\theta_j}$  is the average delay of each vehicle in the  $j$ -th lane, taking into account lane occupancy (s/car), and  $x_{\theta_j}$  is the degree of saturation of the  $j$ -th lane, taking into account lane occupancy.

A special case for determining the degree of saturation would be a situation in which  $\theta_j = 100\%$ . In this case, the movement of vehicles along the lane is completely stopped. In other words,  $Q_{exit} = 0$  veh./h. Therefore, when such a situation occurs, it is proposed to exclude the lane from the calculations, and redistribute the incoming traffic evenly to the remaining lanes, along which the direction of movement of cars corresponds to the direction of movement along the fully occupied lane.

The determination of the average movement delay for each vehicle, performed according to (26), will determine the total delay for all vehicles passing through the controlled intersection:

$$T_{D\theta} = \sum_{j=1}^n d_{j\theta} Q_{j,enter}, \quad (27)$$

where  $T_{D\theta}$  is the total delay in the movement of cars passing through the controlled intersection, taking into account lane occupancy (s).

The value of  $T_{D\theta}$  can be interpreted as the total idle time or the total time loss for cars, caused by the operation of traffic signalization at the intersection. Therefore, the technological effect of the application of the developed method will be as follows:

$$\Delta T_D = T_D - T_{D\theta} \quad (28)$$

where  $\Delta T_D$  is the technological effect of reducing the total delay in the movement of cars, obtained as a result of applying the developed method (s), and  $T_D$  is the total delay in the movement of cars at the controlled intersection with the current traffic signal cycle before the application of the developed method (s).

Figure 10 graphically presents a comparative analysis of the current operating mode of the signal-controlled intersection and the results of adjusting the traffic light cycle according to the methodology developed, using one of the working days as an example.

### 3.2.2. Evaluation of Economic Efficiency

In the opinion of the authors, the economic effect of the application of the developed method will primarily be expressed in decreased fuel consumption in the idle mode of the engine, which will be realized due to a reduction in the downtime of cars when passing through a controlled intersection:

$$G_{\Delta T_D} = G_{idle} \Delta T_D, \quad (29)$$

where  $G_{\Delta T_D}$  is the total fuel consumption at idle for the time period  $\Delta T_D$  (l), and  $G_{idle}$  is the nominal fuel consumption of an idle car (L/hour).

### 3.2.3. Evaluation of Environmental Efficiency

The authors believe that the environmental effect of the application of the developed method will be expressed as a reduction in emissions of the harmful substances CO, CH, NO<sub>x</sub> and SO<sub>2</sub>, which will be implemented by reducing downtime at idle speed of the car engine when driving through a signal-controlled intersection. Based on the results of

studies previously conducted in this area [57–66], it seems possible to assess the expected environmental effect as follows:

$$m_{\Delta T_D} = \sum_{i=1}^n g_{i,idle} \Delta T_D, \tag{30}$$

where  $m_{\Delta T_D}$  is the total reduction in emissions of the harmful substances CO, CH, NO<sub>x</sub> and SO<sub>2</sub> over a period of time  $\Delta T_D$ (kg);  $g_{i,idle}$  is the specific emission of the  $i$ -th harmful substance (CO, CH, NO<sub>x</sub> or SO<sub>2</sub>) (kg/h); and  $\Delta T_D$  is the technological effect of reducing the total delay in the movement of cars, obtained as a result of applying the developed method (hours).

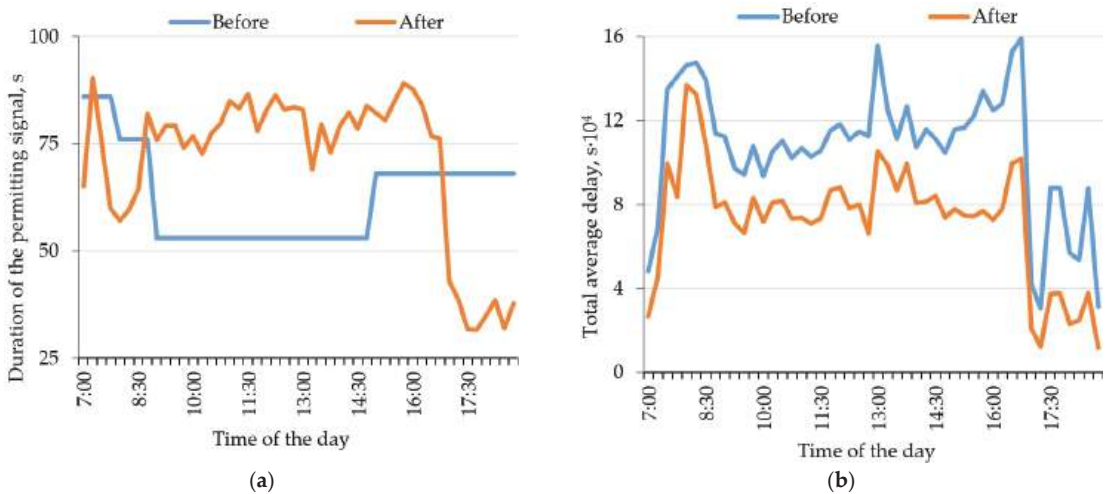


**Figure 10.** Operation of the regulated intersection before and after adjustment: (a) the duration of the resolving signal of the left-turn direction; (b) the total average delay of vehicles.

Table 3 presents an example of evaluating the efficiency of the proposed solutions for one of the studied days of the week when the initial data were collected.

**Table 3.** Comparative analysis of the efficiency of the signal-controlled intersection under the current operating parameters of traffic lights and the adjustment of the cycle according to the developed methodology using an example of the left-turn direction of traffic flow.

Time	Total Average Delay (h)			Economic Losses due to Fuel Consumption (USD)			Pollutant Emissions (kg)		
	Before	After	$\Delta$	Before	After	$\Delta$	Before	After	$\Delta$
7:00	26.74	14.86	11.88	15.23	8.47	6.77	1.99	1.10	0.88
10:00	52.01	39.89	12.11	29.62	22.72	6.90	3.86	2.96	0.90
13:00	86.50	58.42	28.08	49.27	33.28	15.99	6.43	4.34	2.09
16:00	69.32	40.34	28.98	39.48	22.98	16.51	5.15	3.00	2.15

The data presented in Table 3 show that the application of the proposed methodology will improve the efficiency of signal-controlled intersections in all respects by an average of 35% compared to the current mode.

According to preliminary calculations, the adjustment of traffic signal cycles at the regulated intersection will reduce the total average delay in the movement of vehicles by about 127 h per working day of the week. Thus, with an average fuel cost of 95, or USD 0.64, per 1 L in Tyumen (price for the first quarter of 2022 [56]), the expected economic

effect if this methodology will be more than USD 70 per 1 working day of the week. For signal-controlled intersections that are not equipped with the necessary equipment to apply the developed method, the payback period will be approximately 3.5 calendar years. The estimated reduction in emissions of harmful substances, in total, will be more than 1.6 kg for one working day of the week.

#### 4. Discussion

The authors of this study suggest that one of the ways of resolving the problem of traffic congestion is through the management of traffic flows at signal-controlled intersections that are equipped with automated traffic control systems [16–18] and form part of a single urban intelligent transport system [5–16]. Decision-making regarding the particular duration of traffic signals in this concept will be based on the initial data of traffic flow rate, obtained in real time using street video surveillance cameras and neural network technologies [3,4,9,16,41].

However, the use of the traffic flow rate indicator alone is not enough to implement the control process, since both in the case of a traffic congestion and in the event of an actual decrease in transport demand in the studied lane, the detector will record a drop in the traffic flow rate value. This leads to uncertainty and does not allow the implementation of the control process. In order to resolve this uncertainty, the authors use an indicator of the concentration of traffic flow in time—lane occupancy. This indicator is essentially an indicator of the state of traffic flow, embodying the specific amount of time, from the total time resource of the lane, that the traffic flow spends on moving along the city's road network, including acceleration, movement, deceleration and stopping [3].

The lane occupancy indicator was determined as the most useful. At the previous stage of the work, the authors conducted a study wherein the results established and experimentally confirmed a two-factor mathematical model of the effect of lane occupancy and the traffic signal cycle on the traffic flow rate [3]. The authors acknowledge that, like any other results of the study, the mathematical model obtained also has a number of limitations, and, for example, does not take into account the negative impact of environmental conditions and the quality of the road surface. However, from the point of view of the authors, the mathematical model developed is significant and allows us to continue studying both its refinement in terms of factors previously unaccounted for, and its practical application.

As a basis for developing a method for the practical application of the previously obtained mathematical models [31], the method presented in the works of F. Webster [44] was chosen. Based on the results of a detailed analysis of the method of F. Webster, a drawback was identified which does not allow for the application of this technique in modern conditions. Thus, if the transport demand exceeds the capacity of the road network, a traffic signal cycle cannot be developed using the original method. In this situation, the estimated duration of the cycle either takes on an infinitely large and unrealizable value in practice, or has no physical meaning at all, taking on a negative value. This drawback is clearly presented by the authors in Figure 6. Unfortunately, according to the authors, it is not possible to find an absolutely ideal solution in this case. As one of the solutions, the authors proposed consideration of the maximum allowable cycle duration as a constant value to be determined by an engineer or researcher, depending on the available reserves and resources, as well as their goals and objectives. This decision can be justified by the fact that in the current traffic conditions in cities, in the event of traffic congestion and the absence of any reserves for the redistribution of time in the traffic signal cycle, it will still not be possible to satisfy the entire transport demand in the road network. The authors suggest that a definitive solution to this problem is possible only when the complete redistribution of transport demand, from individual transport to alternative modes of transportation, is taken into account. However, this approach, firstly, requires long-term strategic decisions, and secondly, it still does not exclude the formation of traffic congestion due to stochastic factors, which also requires prompt adjustment of the traffic signal cycles of controlled intersections.

The authors also acknowledge that the achievement of the indicated effects of the application of the developed method can be guaranteed only if it is subject to a number of limits. These limits were justifiably introduced at the previous stage of this study during the development of the mathematical models [3]. In this regard, the positive effect of the application of the method can be realized under the condition that vehicles are moving on a dry road surface, in the absence of ice, precipitation and fog.

Vehicles moved at the intersection in strictly defined directions, where traffic flows were homogeneous and consisted only of cars. At the same time, the movement of vehicles was organized in such a way as to exclude conflict points for traffic flows moving forward and turning. Thus, the use of the proposed methodology at urban signal-controlled intersections with traffic conditions that differ from those presented in the study may require additional calibration of the mathematical models.

Therefore, improving the obtained method—taking into account the influence of various environmental conditions, the state of the road surface, the priority of public transport and other factors that can be established in the aggregate—will be an area of further research in the near future.

The prospects of the proposed methodology can be achieved through the proposed neural network technology for collecting and processing the initial data. Depending on the viewing angle, outdoor cameras track and classify vehicles within road sections of up to 500 m. Precise and informative monitoring of the dynamic parameters of traffic flows and lane distribution enables proactive adjustment of traffic lights, taking into account the individual characteristics of intersections.

## 5. Conclusions

The proposed method, developed on the basis of F. Webster, enables changes in traffic flow rate due to the influence of lane occupancy at urban controlled intersections to be taken into account. The developed method is based on mathematical models [3] which allow significant advancement of the existing fundamental provisions for designing operating modes for controlled intersections.

Firstly, the new method, in contrast to the existing one, takes into account the change in the maximum possible value of the traffic flow rate at the exit of the controlled intersection due to the deviation of lane occupancy from its optimal value [3,4]. In turn, this indicates either a shortage or a surplus in the traffic capacity of the road network and allows prompt real-time adjustment of the traffic light cycle at the controlled intersection in question.

Second, a detailed analysis of the basic method of F. Webster also revealed that it has another significant drawback which, in principle, does not allow its use in modern traffic conditions in cities. With all the coherent logic of the original methodology, the calculation results obtained by it are inadequate or completely devoid of physical meaning for controlled intersections with high traffic demand. This drawback was eliminated by introducing a limit on the maximum allowable duration of the traffic light control cycle, determining the specific weight of each phase coefficient and adjusting their values, taking into account the indicated limitation.

Thirdly, in order to collect initial data on the required characteristics of traffic flows, the authors proposed an approach that consists of processing a video image received in real time from street surveillance cameras using an optimized recurrent neural network. The advantage of this approach is significant reduction in the monetary costs required for the collection of the initial data, since each street video surveillance camera is able to replace all the necessary vehicle detectors. In addition, reducing the time required to process video information makes it possible to increase the efficiency of not only monitoring the initial situation itself, but also managing traffic flows in real time.

Fourthly, it was not possible to adequately assess the efficiency of the traffic light cycle using the basic method of F. Webster, since Formula (12) for determining transport delay also did not take into account the decrease in the maximum possible traffic flow rate due to the influence of lane occupancy. In this regard, the original formula for determining the

transport delay was also refined (29). This allowed for correct assessment of the efficiency of the proposed solutions. According to the preliminary results, the application of the proposed method will make it possible to realize positive technological, economic and environmental effects at urban controlled intersections.

Ultimately, a new method was developed and presented, aimed at improving the efficiency of traffic management at urban signal-controlled intersections through the real-time adjustment of traffic light cycles.

Meanwhile, we note that the accurate and situational assessment of lane occupancy is essential to ensuring effective traffic control at signal-controlled intersections. These preliminary experimental studies have shown that even when taking into account the introduced restrictions, the use of the proposed methodology can reduce the total delay of vehicles by an average of 3%. Therefore, in our future research, we will obtain more suitable parameters for adjusting traffic lights, taking into account the individual characteristics of intersections.

**Author Contributions:** Conceptualization, V.M.; methodology, V.M.; validation, V.M., V.S. and V.K.; initial data collection technology, V.S.; as author of the vast majority of the previous research stage, V.M. determined the areas of its practical application, analyzed the most common method of designing controlled intersections, identified its strengths and weaknesses, and developed a new method based on it; economic efficiency evaluation, V.M. and V.S.; environmental efficiency evaluation, V.M. and V.K. All authors have read and agreed to the published version of the manuscript.

**Funding:** This research received no external funding.

**Institutional Review Board Statement:** Not applicable.

**Informed Consent Statement:** Not applicable.

**Acknowledgments:** This article was prepared as part of the implementation of a state assignment in the field of science for scientific projects carried out by teams of researchers in scientific laboratories of higher educational institutions subordinate to the Russian Ministry of Education and Science, on the project: "New patterns and solutions for the functioning of urban transport systems in the paradigm "Transition from owning a personal car to mobility as a service"" (No. 0825-2020-0014, 2020–2022).

**Conflicts of Interest:** The authors declare no conflict of interest.

## References

1. Vuchic, V.R. *Transportation for Livable Cities*, 1st ed.; Routledge: New York, NY, USA, 2017; p. 378.
2. Shepelev, V.; Aliukov, S.; Nikolskaya, K.; Shabiev, S. The capacity of the road network: Data collection and statistical analysis of traffic characteristics. *Energies* **2020**, *13*, 1765. [CrossRef]
3. Morozov, V.; Larkov, S. Formation of the Traffic Flow Rate under the Influence of Traffic Flow Concentration in Time at Controlled Intersections in Tyumen, Russian Federation. *Sustainability* **2021**, *13*, 8324. [CrossRef]
4. Morozov, V.; Larkov, S. The application of lane occupancy parameter for solving tasks of traffic management. *Transp. Res. Procedia* **2018**, *36*, 520–526. [CrossRef]
5. Zhankaziev, S. Current trends of road-traffic infrastructure development. *Transp. Res. Procedia* **2017**, *20*, 731–739. [CrossRef]
6. Asensio, Á.; Blanco, T.; Blasco, R.; Marco, Á.; Casas, R. Managing emergency situations in the smart city: The smart signal. *Sensors* **2015**, *15*, 14370–14396. [CrossRef]
7. Cottrill, C.; Derrible, S. Leveraging big data for the development of transport sustainability indicators. *J. Urban Technol.* **2015**, *22*, 45–64. [CrossRef]
8. Errampalli, M.; Chalumuri, R.S.; Nath, R. Development and evaluation of an integrated transportation system: A case study of Delhi. *Proc. Inst. Civ. Eng. Transp.* **2018**, *171*, 75–84. [CrossRef]
9. Karmanov, D.S.; Zakharov, D.A.; Fadyushin, A.A. Evaluation of changes in traffic parameters for various types of traffic signal regulation. *Transp. Res. Procedia* **2018**, *36*, 274–280. [CrossRef]
10. Krivolapova, O. Algorithm for Risk Assessment in the Introduction of Intelligent Transport Systems Facilities. *Transp. Res. Procedia* **2017**, *20*, 373–377. [CrossRef]
11. Moroz, B.I.; Udovyyk, I.M.; Shvachych, G.G.; Pasichnik, A.M.; Miroshnichenko, S.V. Intelligent system of traffic light control with dynamic change phases of traffic flows on controlled intersections. *Sci. Rev.* **2019**, *1*, 11–17. [CrossRef]
12. Nguyen, D.D.; Rohács, J.; Rohács, D.; Boros, A. Intelligent Total Transportation Management System for Future Smart Cities. *Appl. Sci.* **2020**, *10*, 8933. [CrossRef]

13. Petrov, A.I.; Kolesov, V.I.; Petrova, D.A. Theory and Practice of Quantitative Assessment of System Harmonicity: Case of Road Safety in Russia before and during the COVID-19 Epidemic. *Mathematics* **2021**, *9*, 2812. [CrossRef]
14. Rodríguez, D.A.; Levine, J.; Agrawal, A.W.; Song, J. Can information promote transportation-friendly location decisions? A simulation experiment. *J. Transp. Geogr.* **2010**, *19*, 304–312. [CrossRef]
15. Shepelev, V.D.; Glushkov, A.I.; Almetova, Z.V.; Mavrin, V.G. A study of the travel time of intersections by vehicles using computer vision. In Proceedings of the 6th International Conference on Vehicle Technology and Intelligent Transport Systems, Online, 2–4 May 2020; pp. 653–658.
16. Shepelev, V.; Zhankaziev, S.; Aliukov, S.; Varkentin, V.; Marusin, A.; Marusin, A.; Gritsenko, A. Forecasting the Passage Time of the Queue of Highly Automated Vehicles Based on Neural Networks in the Services of Cooperative Intelligent Transport Systems. *Mathematics* **2022**, *10*, 282. [CrossRef]
17. Khazukov, K.; Shepelev, V.; Karpeta, T.; Shabiev, S.; Slobodin, I.; Charbadze, I.; Alferova, I. Real-time monitoring of traffic parameters. *J. Big Data* **2020**, *7*, 84. [CrossRef]
18. Winter, H.; Serra, J.; Nesmachnow, S.; Tchernykh, A.; Shepelev, V. Computational intelligence for analysis of traffic data. In Proceedings of the Communications in Computer and Information Science, Online, 9–11 November 2020; Volume 1359, pp. 167–182. [CrossRef]
19. National Academies of Sciences, Engineering, and Medicine. *Highway Capacity Manual: A Guide for Multimodal Mobility Analysis*, 7th ed.; The National Academies Press: Washington, DC, USA, 2022.
20. Gordon, R.L.; Tighe, W. *Traffic Control Systems Handbook*; U.S. Department of Transportation, Federal Highway Administration: Washington, DC, USA, 2005.
21. Gerlough, D.L.; Huber, J.H. *Traffic Flow Theory: A Monograph*; Transportation Research Board National Research Council: Washington, DC, USA, 1975.
22. Larin, O.N.; Dosenko, V.A. Use of a Phase Transition Concept for Traffic Flow Condition Estimation. *Transp. Telecommun.* **2014**, *15*, 315–321. [CrossRef]
23. Athol, P. Interdependence of Certain Operational Characteristics Within a Moving Traffic Stream. *Highw. Res. Rec.* **1965**, *72*, 58–87.
24. Banks, J.H. Freeway Speed-Flow-Concentration Relationships: More Evidence and Interpretations. *Transp. Res.* **1989**, *1225*, 53–60.
25. Hall, F.L.; Gunter, M.A. Further Analysis of the Flow-Concentration Relationship. *Transp. Res.* **1986**, *1901*, 1–9.
26. Hall, F.L.; Hurdle, V.F.; Banks, J.H. Synthesis of recent work on the nature of speed-flow and flow-occupancy (or density) relationships on freeways. *Transp. Res.* **1992**, *1365*, 12–18.
27. Hurdle, V.F.; Datta, P.K. Speeds and Flows on an Urban Freeway: Some Measurements and a Hypothesis. *Transp. Res.* **1983**, *905*, 127–137.
28. Hurdle, V.F.; Merlo, M.I.; Robertson, D. Study of speed-flow relationships on individual freeway lanes. *Transp. Res.* **1997**, *1591*, 7–13. [CrossRef]
29. Pushkar, A.; Hall, F.L.; Acha-Daza, J.A. Estimation of Speeds from Single-Loop Freeway Flow and Occupancy Data Using the Cusp Catastrophe Theory Model. *Transp. Res.* **1994**, *1457*, 149–157.
30. Araghi, S.; Khosravi, A.; Johnstone, M.; Creighton, D. Intelligent Traffic Light Control of Isolated Intersections Using Machine Learning Methods. In Proceedings of the 2013 IEEE International Conference on Systems, Man, and Cybernetics, Manchester, UK, 13–16 October 2013; pp. 3621–3626. [CrossRef]
31. Tresler, F. A proposed model of extended coordination for the traffic light control at intersections. *Commun. Comput. Inf. Sci.* **2012**, *329*, 240–248. [CrossRef]
32. Gunes, F.; Bayrakli, S.; Zaim, A.H. Smart Cities and Data Analytics for Intelligent Transportation Systems: An Analytical Model for Scheduling Phases and Traffic Lights at Signalized Intersections. *Appl. Sci.* **2021**, *11*, 6816. [CrossRef]
33. Harahap, E.; Darmawan, D.; Fajar, Y.; Rachmiatie, A. Modeling and simulation of queue waiting time at traffic light intersection. *J. Phys. Conf. Ser.* **2019**, *1188*, 012001. [CrossRef]
34. Leverents, E.; Andronov, R.; Anufrieva, T. Simulation of queue length and vehicle delays on signal-controlled intersection. *MATEC Web Conf.* **2018**, *170*, 05010. [CrossRef]
35. Li, X.; Khattak, A.J.; Kohls, A.G. Signal phase timing impact on traffic delay and queue length—a intersection case study. In Proceedings of the Winter Simulation Conference (WSC), Washington, DC, USA, 11–14 December 2016; pp. 3722–3723. [CrossRef]
36. Adak, M.F.; Balta, M. Fuzzy Logic-based Adaptive Traffic Light Control of an Intersection: A Case Study. In Proceedings of the 5th International Symposium on Multidisciplinary Studies and Innovative Technologies (ISMST), Ankara, Turkey, 21–23 October 2021; pp. 394–398. [CrossRef]
37. Talab, H.S.; Mohammadkhani, H. Design Optimization Traffic Light Timing Using the Fuzzy Logic at a Diphasic’s Isolated Intersection. *J. Intell. Fuzzy Syst.* **2014**, *27*, 1609–1620. [CrossRef]
38. Yusuf, A.M.H.; Yusuf, R. Adaptive Traffic Light Controller Simulation for Traffic Management. In Proceedings of the 6th International Conference on Interactive Digital Media (ICIDM), Bandung, Indonesia, 14–15 December 2020; pp. 1–5. [CrossRef]
39. Yang, Z.; Peng, J.; Wu, L.; Ma, C.; Zou, C.; Wei, N.; Zhang, Y.; Liu, Y.; Andre, M.; Li, D.; et al. Speed-guided intelligent transportation system helps achieve low-carbon and green traffic: Evidence from real-world measurements. *J. Clean. Prod.* **2020**, *268*, 122230. [CrossRef]
40. Alrawi, F. The importance of intelligent transport systems in the preservation of the environment and reduction of harmful gases. *Transp. Res. Procedia* **2017**, *24*, 197–203. [CrossRef]

41. Branston, D. Some factors affecting the capacity of signalized intersection. *Traffic Eng. Control* **1979**, *20*, 390–396.
42. Gorodokin, V.; Almetova, Z.; Shepelev, V. Procedure for calculating on-time duration of the main cycle of a set of coordinated traffic lights. *Pap. Present. Transp. Res. Procedia* **2017**, *20*, 231–235. [CrossRef]
43. Glushkov, A.; Shepelev, V. Development of reliable models of signal-controlled intersections. *Transp. Telecommun.* **2021**, *22*, 417–424. [CrossRef]
44. Webster, F.V.; Cobbe, B.M. *Traffic Signals*; Road Research Technical Paper N56; HMSQ: London, UK, 1966.
45. Video observation: Online broadcast. Available online: <https://stream.is74.ru> (accessed on 8 February 2022).
46. Fedorov, A.; Nikolskaia, K.; Ivanov, S.; Shepelev, V.; Minbaleev, A. Traffic Flow Estimation with Data from a Video Surveillance Camera. *J. Big Data* **2019**, *6*, 73. [CrossRef]
47. Tyumen City Transport. Available online: <https://tgt72.ru/> (accessed on 8 February 2021). (In Russian).
48. Keilson, J. Introduction to the Theory of Queues. *Technometrics* **1963**, *5*, 286. [CrossRef]
49. Krishnamoorthy, A.; Joshua, A.N.; Vishnevsky, V. Analysis of a k-Stage Bulk Service Queuing System with Accessible Batches for Service. *Mathematics* **2021**, *9*, 559. [CrossRef]
50. Ma, F.-Q.; Fan, R.-N. Queuing Theory of Improved Practical Byzantine Fault Tolerant Consensus. *Mathematics* **2022**, *10*, 182. [CrossRef]
51. Minkevičius, S.; Katin, I.; Katina, J.; Vinogradova-Zinkevič, I. On Little's Formula in Multiphase Queues. *Mathematics* **2021**, *9*, 2282. [CrossRef]
52. Tsitsiashvili, G. Construction and Analysis of Queuing and Reliability Models Using Random Graphs. *Mathematics* **2021**, *9*, 2511. [CrossRef]
53. Hubbard, J.H.; Hubbard, B.B. *Vector Calculus, Linear Algebra, and Differential Forms: A Unified Approach*, 6th ed.; Matrix Editions: Ithaca, NY, USA, 2015; p. 818.
54. Sturges, H. The choice of a class-interval. *J. Am. Stat. Assoc.* **1926**, *21*, 65–66. [CrossRef]
55. Bhattacharya, G.K.; Johnson, R.A. *Statistical Concepts and Methods*; John Wiley & Sons: New York, NY, USA, 1977; p. 639.
56. Federal State Statistics Service. Available online: <https://eng.rosstat.gov.ru> (accessed on 17 December 2021).
57. Boulter, P.G.; Latham, S. *Emissions Factors 2009: Report 5—A Review of the Effects of Fuel Properties on Road Vehicle Emissions*; RL Report PPR358; TRL Limited: Wokingham, UK, 2009.
58. Chainikov, D.; Chikishev, E.; Anisimov, I.; Gavaev, A. Influence of Ambient Temperature on the CO<sub>2</sub> Emitted with Exhaust Gases of Gasoline Vehicles. In Proceedings of the VII International Scientific Practical Conference “Innovative Technologies in Engineering”, Yurga, Russia, 19–21 May 2016; Volume 142, p. 12109. [CrossRef]
59. Magaril, E. Increasing the efficiency and environmental safety of vehicle operation through improvement of fuel quality. *Int. J. Sustain. Dev. Plan.* **2015**, *10*, 880–893. [CrossRef]
60. Magaril, E.; Magaril, R.; Abrzhina, L. Environmental Assessment of the Measures Increasing the Sustainability of Motor Transport. *IOP Conf. Ser. Earth Environ. Sci.* **2017**, *72*, 012003. [CrossRef]
61. Magaril, E.; Abrzhina, L.; Belyaeva, M. Environmental damage from the combustion of fuels: Challenges and methods of economic assessment. *WIT Trans. Ecol. Environ.* **2014**, *190*, 1105–1115. [CrossRef]
62. Parsaev, E.V.; Malyugin, P.N.; Teterina, I.A. Methodology for the calculation of emissions for non-stationary transport flow. *Russ. Automob. Highw. Ind. J.* **2018**, *15*, 686–697. (In Russian) [CrossRef]
63. Schiavon, M.; Redivo, M.; Antonacci, G.; Rada, E.C.; Ragazzi, M.; Zardi, D.; Giovannini, L. Assessing the air quality impact of nitrogen oxide and benzene from road traffic and domestic heating and the associated cancer risk in an urban area of Verona (Italy). *Atmos. Environ.* **2015**, *120*, 234–243. [CrossRef]
64. Stroe, C.-C.; Panaitescu, V.N.; Ragazzi, M.; Rada, E.C.; Ionescu, G. Some considerations on the environmental impact of highway traffic. *Rev. Chim.* **2014**, *65*, 152–155.
65. Zakharov, D.; Magaril, E.; Rada, E.C. Sustainability of the Urban Transport System under Changes in Weather and Road Conditions Affecting Vehicle Operation. *Sustainability* **2018**, *10*, 2052. [CrossRef]
66. Ertman, S.; Ertman, J.; Zakharov, D. Adaptation of urban roads to changing of transport demand. *E3S Web Conf.* **2016**, *6*, 01013. [CrossRef]

Article

# The Construction of Models of Rough Surfaces' Interaction: Markov's Approach

Konstantin Gavrilov <sup>1,\*</sup>, Yuriy Rozhdestvenskii <sup>2</sup> and Ildar Umurzakov <sup>1</sup>

<sup>1</sup> Department of Wheeled and Tracked Vehicles, Institute of Engineering and Technology, South Ural State University, 76 Prospekt Lenina, 454080 Chelyabinsk, Russia

<sup>2</sup> Department of Motor Transport, Institute of Engineering and Technology, South Ural State University, 76 Prospekt Lenina, 454080 Chelyabinsk, Russia

\* Correspondence: gavrilovkv@susu.ru; Tel.: +7-8-950-742-01-17

**Abstract:** This article shows that the change of rough surfaces in the way of their contact interaction can be analyzed using the theory of Markov's processes. In the framework of existing models, this problem cannot be solved. In this article, the idea of reducing to Markov's model is shown on a simple discrete scheme, which is then generalized. The approach was applied to the analysis of the friction process, to the fatigue failure mode, in which the surface element changes after multiple contacts, possibly many millions. The Kolmogorov-Feller's equations for the model of this regime were presented and the model of the influence of lubrication is offered. A calculated example of estimating the evolution of surfaces separated by a lubricant layer is given. Additionally, the technical characteristics as functions of the friction path and the load were evaluated.

**Keywords:** surface asperities interaction; Markov process; tribological parameters

**MSC:** 62M02; 74A55; 74F10

**Citation:** Gavrilov, K.; Rozhdestvenskii, Y.; Umurzakov, I. The Construction of Models of Rough Surfaces' Interaction: Markov's Approach. *Mathematics* **2022**, *10*, 3607. <https://doi.org/10.3390/math10193607>

Academic Editor: Yury Shestopalov

Received: 5 September 2022

Accepted: 29 September 2022

Published: 2 October 2022

**Publisher's Note:** MDPI stays neutral with regard to jurisdictional claims in published maps and institutional affiliations.



**Copyright:** © 2022 by the authors. Licensee MDPI, Basel, Switzerland. This article is an open access article distributed under the terms and conditions of the Creative Commons Attribution (CC BY) license (<https://creativecommons.org/licenses/by/4.0/>).

## 1. Introduction

The interaction of rough surfaces determines many processes in electrical and heat engineering in the transmission of electrical and thermal energy, through mobile and fixed contacts, friction, lubrication and wear processes in mechanical engineering, the automobile industry, engine building and other industries [1–4]. These processes determine the performance and service life of the main tribo-assemblies and units. The aim of this article is to show that the change of rough surfaces in the way of their contact interaction can be analyzed by using the theory of Markov's processes.

The fundamental idea of Markov's process is as follows: the future depends only on the present and does not depend on the past.

Interaction characteristics depend on many factors, first of all, on surface microgeometry, the physical characteristics of materials, as well as regime and force factors [5,6]. The relief of a rough surface represents a function random in space. The problems of interaction contacting surfaces are most actively considered in mechanics [5,7,8] and are caused by the processes of friction and wear. It is known that the interaction process is a complex process of physico-chemical and molecular mechanics, and it is not possible to describe it without reasonable simplifications, therefore, various models of the friction process have become widespread [7,9–12]. It is widely recognized that existing methods are not perfect, and work in this direction continues.

Most analysis methods are based on functions that are random in their spatial argument. Gauss functions are used starting with work [13], as well as functions composed of projections of a certain shape in such a way as to have a given law of distribution of heights; this approach is first proposed in work [14]. Considering [15,16], the shapes of protrusions are in the form of columns, hemispheres, wedges, etc. An important engineering task is to

calculate the change of the surfaces during the process of friction and the corresponding friction characteristics. Existing models of friction do not solve this problem.

This article describes an approach in which each of the two surfaces is represented by a set of protrusions. Each ledge is described by its random state (a set of selected characteristics, for example, the height and radius of curvature of the vertex). Each surface is described by the probability distribution on the set of states. When the surfaces move mutually, the interaction of the elementary protrusions has a place, and the result for the two projections describes a two-dimensional function of interaction, which is considered known. The state of the fixed ledge at the next moment is determined by the previous state, and the accidental impact of the ledge of another surface. If the effects are independent, the process of state change can be considered Markov's, and its change is described by difference, differential or integro-differential equations (depending on the assumptions). By counting distribution recurrently, the results of time-varying distribution are received, which are determined by the desired characteristics of the interaction. Choosing different variants of what is the state of the projection, and what is the function of interaction, models of varying complexity and accuracy are obtained. This approach to the analysis of the interaction of surfaces (in particular, for friction) has not been described in the literature; the only exceptions are the work of the authors, [17–20]; this work generalizes on previous ones.

In the second section, the idea of reducing to the Markov model is shown in a simple discrete scheme. Each of the surfaces consist of projections arranged in "orderly rows" at the same distance from each other, and these distances are the same on two surfaces; mutual movement occurs discretely: shift, interaction, shift, interaction, etc.; the state of the projection is its random height, which changes under the influence of the projections of another surface. The process of changing the state of the ledge is a Markov's chain, if the disturbances are random and independent. The entire surface is characterized by the distribution of probabilities on a set of the heights of projections, for the probability distribution recurrent recalculation in time is fair. The distribution of heights determines such characteristics as surface contact area, the average height of the protrusions, the frictional force, and wear, etc., so that we can assess the change in the surface over time and the characteristics of the interaction can be assessed.

In the third section, the model is generalized: it is assumed that the location of the projections is random, the characteristics of the location for the two surfaces are different, and the mutual movement is continuous. The protrusion state is a multidimensional random variable value (for example, three-dimensional: height, radius of curvature of the protrusion vertex, temperature). The state changes under the influence of the protrusions of another surface, and the height plays a special role since the interaction of the protrusions occurs only under the condition of contact. Under some assumptions, the state change process is considered to be Markov's, for the distribution of the process is still a fair recurrent recalculation in time. Technical characteristics can be estimated by distribution.

In the fourth section, the approach is applied to the analysis of the fatigue failure mode resulting from repeated contact of the projections; the load is assumed to be constant. Fatigue failure is modeled by the fact that there is a low probability of separation of the particle after the contact of the projections, and the height of the projection is reduced by, generally speaking, a random variable.

The fifth section provides a computational example of the evolution of surfaces (distributions) separated by a lubricant layer. The technical characteristics as functions of the friction and load path are evaluated. The wear of the main bearing of the crankshaft of the diesel engine is estimated.

## 2. Idea: Simple Discrete Model

In the work [17], the model of change of a surface during the time is offered. The surface is represented by a set of projections with random heights (and with very flat tops), Figure 1, located at a distance along the line of motion, which reflects the interaction of two friction surfaces.

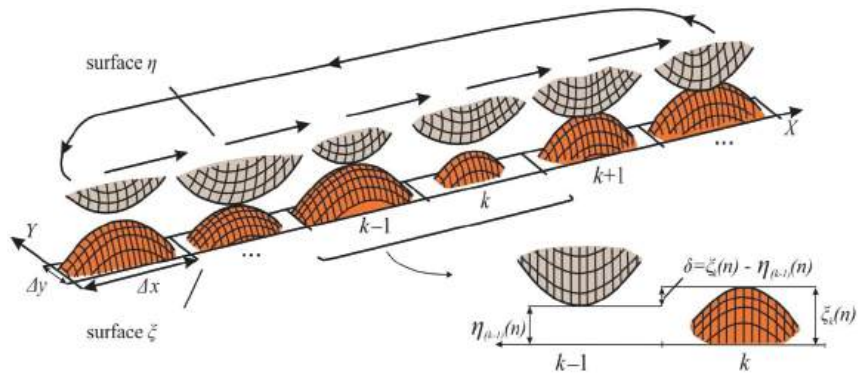


**Figure 1.** Model surface and the shift pattern. If limit distributions  $p^*$  and  $q^*$  exist, they are obtained from a system of nonlinear equations.

Movement appears discrete: in one step with an interval  $\tau = \Delta s / V$  there is a progress with a speed  $V$  on one element  $\Delta s$  and interaction of opposite ledges. The height  $\xi$  of the projection of the lower surface is exposed to moving projections with random independent heights of the upper surface. The result  $\xi_k(n + 1)$  of interaction at the element step  $n + 1$  with the number  $k$  depends on  $\xi_k(n)$  and the level  $\eta_{k-1}(n)$  of the neighboring element:

$$\xi_k(n + 1) = \Phi(\xi_k(n), \eta_{k-1}(n)), \tag{1}$$

Let us fix any element with a number and simplify the recording:

$$\xi_{n+1} = \Phi(\xi_n, \eta_n), \tag{2}$$

If we consider the sequence  $\eta_n, n = 0, 1, 2, \dots$  to be independent random variables, then the sequence  $\xi_n, n = 0, 1, 2, \dots$  is Markov's. It is given that not only the upper sequence  $\eta_n$  acts on the lower protrusion with height  $\xi_n$ , but also on any fixed protrusion of the upper surface with a level  $\eta_n$ , the sequence  $\xi_n$  acts, and it is possible for any element of the upper surface to write similarly:

$$\eta_{n+1} = \Psi(\eta_n, \xi_n), \tag{3}$$

Functions  $\Phi$  and  $\Psi$  set the mechanism of interaction between the two projections. The choice of functions  $\Phi$  and  $\Psi$  can implement various schemes of interaction. These two general relations define Markov's sequences  $\{\eta_n\}$  and  $\{\xi_n\}$  changes in heights and the evolution of the corresponding distributions  $p_n(x)$  and  $q_n(y)$ . By introducing a discretization on the level of the vertices of the projections, we obtain a simple Markov's chain with the following recalculation of the distributions:

$$\begin{aligned} p_{n+1} &= p_n \Pi_{\xi}(q_n, \Phi), \\ q_{n+1} &= q_n \Pi_{\eta}(p_n, \Psi), \end{aligned} \tag{4}$$

where  $\Pi_{\xi}, \Pi_{\eta}$ —matrix of transition probabilities that depend on the distributions  $p_n(x), q_n(y)$  and transformation functions  $\Phi$  and  $\Psi$ ;  $p_n$  and  $q_n$ —vectors of the row distributions. The matrix elements (transition probabilities from  $x$  to  $y$ ) in general for  $\xi_n$  in (2) are defined as follows:

$$\begin{aligned} \pi_{\xi_n}(x, y) &\equiv P\{\xi_{n+1} = y | \xi_n = x\} = \\ &= P\{\Phi(x, \eta_n) = y\} = \sum_{z: \Phi(x, z) = y} q_n(z), \end{aligned} \tag{5}$$

Similarly, for  $\eta_n$  in (3):

$$\begin{aligned} \pi_{\eta_n}(x, y) &\equiv P\{\eta_{n+1} = y | \eta_n = x\} = \\ &= P\{\Psi(x, \xi_n) = y\} = \sum_{z: \Psi(x, z) = y} p_n(z), \end{aligned} \tag{6}$$

$$\begin{aligned} p^* &= p^* \Pi_{\xi}(q^*, \Phi), \\ q^* &= q^* \Pi_{\eta}(p^*, \Psi). \end{aligned} \tag{7}$$

In the idea to trace the evolution of the process according to the scheme (1), (7) was detailed and implemented as a modeling program of the protrusions' interaction; the results are described in [17,18]. A fatigue cycle distribution based on Markov chains has been presented in the following work [21]. The transformation functions  $\Phi$  and  $\Psi$ , adopted there, reflect the process of elastic and plastic deformations under constant load, as well as fatigue failure. The implementation of the model on a computer allows, through the physical properties of materials, the characteristics of the initial roughness and the applied normal pressure to evaluate the characteristics of friction in time. The results of the program are shown in Figures A1 and A2 of Appendix A. The application and efficiency of this approach are shown in [19,20,22].

With the help of the described model, the evolution of distributions is observed not by simulation modeling, but by the usual for Markov's processes recalculation of distributions, similar to (4).

### 3. Generalization of the Model

It is assumed that the mutual movement is continuous, the location of the projections is random, and the characteristics of the location for the two surfaces are different. The state of the surface protrusion (conditionally lower) will be considered as a two-dimensional random variable  $\xi = (\xi_1, \xi_2)$ , (dimension, as it is clear from the following, is easy to increase) where  $\xi_1$ —is the height,  $\xi_2$ —is another parameter, for example, the radius of curvature of the vertex. Component  $\xi_1$ —height plays a special role, because the fact of interaction between the protrusions is determined by the intersection of the protrusions. The state of the protrusion on the other (conditionally, upper) surface will be considered similarly  $\eta = (\eta_1, \eta_2)$ .

To fix any protrusion of the lower surface, it is exposed to the flow of moving protrusions of the upper surface with random locations and heights. Note that the interaction of protrusions (as a result of mechanical contact) occurs only between the highest protrusions, the share of which, according to the assumption, is one percent. Additionally, take into account that the flow of outputs of a random process for a certain high level  $x$  (when the probability of exceeding the level is small) is approximately Poisson's. These circumstances allow us to assume that the flow of contacts (interactions) for a protrusion with a level  $\xi_1(t) = x_1$  is Poisson, so the flow parameter  $\lambda_{\eta}(x_1, t)$  is equal to the average number of events per unit time:

$$\lambda_{\eta}(x_1, t) = (V / \Delta s_{\eta}) F_{\eta 1}(x_1, t), \tag{8}$$

where  $\Delta s_{\eta}$ —is the average distance between the projections of the upper surface;  $V$ —the rate of slippage;  $V / \Delta s_{\eta}$ —the number of passing projections per unit time;  $F_{\eta 1}(x_1, t)$ —the conditional probability of contact, equal to the distribution function of a random variable, which defines as:

$$\begin{aligned} P\{\delta(t) = \xi_1(t) - \eta_1(t) > 0 | \xi_1(t) = x_1\} = \\ = P\{\eta_1(t) > x_1\} = \int_{-\infty}^{x_1} q_1(z, t) dz = F_{\eta 1}(x_1, t) \end{aligned} \tag{9}$$

If the contact moments  $t_1, t_2, \dots, t_k, \dots$ —are Poisson's, and the corresponding states  $\eta(t_1), \eta(t_2), \dots, \eta(t_k), \dots$  are independent, then the process  $\xi(t)$  is two—dimensional

Markov’s with jumps. It is very important that the moments of contact are determined only by heights, and therefore—distributions:

$$\begin{aligned} p_1(x_1, t) &= \int p_\xi(x_1, x_2; t) dx_2 \\ q_1(x_1, t) &= \int q_\eta(x_1, x_2; t) dx_2 \end{aligned} \tag{10}$$

where  $p_\xi(x_1, x_2; t)$ ,  $q_\eta(x_1, x_2; t)$ —are distributions of two-dimensional random variables, respectively,  $\xi(t) = (\xi_1(t), \xi_2(t))$  and  $\eta(t) = (\eta_1(t), \eta_2(t))$ .

Due to the proposed Poisson’s belonging, the conditional probability for a protrusion with a height level  $\xi_1(t) = x_1$  to get a contact in a short time  $\Delta t$  is  $\hat{p} = \lambda_\eta(x_1, t)\Delta t + o(\Delta t)$ .

It can be recorded for  $\xi_1(t + \Delta t)$  provided to  $\xi_1(t) = x_1$ :

$$\begin{cases} \xi(t + \Delta t) = \xi(t) + \\ \Delta W_\xi(\xi_t, \eta_t) \text{ with probability } \hat{p}, \\ 0 \text{ with probability } 1 - \hat{p}, \end{cases} \tag{11}$$

where  $\xi_t, \eta_t$ —is a simplified designation for  $\xi(t), \eta(t)$ ;  $\Delta W_\xi(\xi_t, \eta_t)$ —abrupt change of state, a random variable (in our case, two-dimensional, and depending on the result of the interaction of the projections with the states  $\xi_t$  and  $\eta_t$ ) with distribution  $h(y|x) \equiv h(y_1, y_2|x_1, x_2)$  of the transition from  $x = (x_1, x_2)$  into  $y = (y_1, y_2)$ .

For Markov’s processes with jumps, at  $\Delta t \rightarrow 0$  for density  $p_\xi(y, t)$  the Kolmogorov-Feller’s equation is fair:

$$\frac{\partial p_\xi(y, t)}{\partial t} = -\lambda_\eta(y, t)p_\xi(y, t) + \int_{-\infty}^{\infty} \lambda_\eta(x, t)p_\xi(x, t)h_\xi(y/x)dx \tag{12}$$

Which in the two-dimensional case is written as:

$$\begin{aligned} \frac{\partial p_\xi(y_1, y_2, t)}{\partial t} &= -\lambda_\eta(y_1, t) \\ &\cdot p_\xi(y_1, y_2, t) + \int \lambda_\eta(x_1, t)p_1(x_1, t) \\ &\cdot [\int h_\xi(y_1, y_2|x_1, x_2)dx_2]dx_1 \end{aligned} \tag{13}$$

where  $p_1(x_1, t)$  determines by (10).

This formula (13) can be used for Markov processes with jumps at 1  $\Delta t \rightarrow 0$ .

Such reasoning can lead to any ledge of upper surface and records the ratio analogous to (13), [23]. There are also other related details about Equation (13).

Equation (13) has to be solved numerically, moving to the discretization in time and states. As it is so small, the probability for any protrusion to achieve more than one impact can be neglected. Let’s denote:  $t_n = n\Delta t$ ,  $\eta_n = \eta(t_n)$ ,  $n = 0, 1, 2, \dots$ . For two-dimensional processes  $\xi_n$  and  $\eta_n$  can be written the ratio (1) with the only difference that the values  $\xi_n, \eta_n$  and functions  $\Phi, \Psi$ —are two-dimensional [24].

#### 4. The Process of Friction: A Model of Fatigue Fracture, Taking into Account the Lubricant

##### 4.1. Mode without Lubrication

The model for this very important regime of fatigue failure at constant load is considered in [19]. It is assumed that the process of fatigue failure leads to the fact that with multiple contacts of the projections, the separation of the material particle occurs, and the height of the protrusion decreases by a certain amount, generally speaking, it is random. The condition of the projection is considered to be a one-dimensional parameter—the height (or rather, the level of a node). The ratio (2) takes the form (with precision  $o(\Delta t)$ ):

$$\xi_{n+1} = \Phi(\xi_n, \eta_n) = \xi_n - W_\xi \cdot \varepsilon_\xi(\delta_n) + h_n/2, \tag{14}$$

if  $\xi_n = x$ , so

$$\varepsilon_{\xi_n}(\delta_n) = \begin{cases} 1, & \text{with probability } P_{W_\xi} \lambda_\eta(x, t) \Delta t, \\ 0, & \text{with probability } 1 - P_{W_\xi} \lambda_\eta(x, t) \Delta t. \end{cases} \quad (15)$$

This entry means that if the contact occurs, i.e., the value of the contact intersection is  $\delta_n = \xi_n - \eta_n > 0$  (the probability of this event is  $\lambda_\eta(x, t_n) \Delta t$ ), then the probability of destruction is  $P_{W_\xi}$ . The decrease in height occurs by the value  $W_\xi$ ;  $\varepsilon_{\xi_n}(\delta_n)$  is a random variable; the flow parameter:

$$\lambda_\eta(x, t_n) = (V / \Delta s_\eta) F_\eta(x, t_n), \quad (16)$$

according to (8) at  $x_1 = x$ . The value  $h_n$  of the approximation of surfaces is introduced to ensure the condition of the constant force of resistance to a constant external load (this non-random value, defined below, is a functional of the distributions  $p_n$  and  $q_n$ ; explanation: with a decrease of the height the resistance force falls, and under the action of a constant normal load the surfaces converge; for the purposes of symmetry, the approximation is provided by a half value for each surface). Adding a constant  $h_n/2$  shifts the distribution of  $(n + 1)$  moment, so it is convenient to make Markov’s recalculation without taking it into account, and then shift the distribution. The ratio (3) takes the form similar to (16) (with obvious difference in increment signs). In [10] this scheme is analyzed, transition probabilities for Markov’s chains  $\xi_n$  and  $\eta_n$  are derived, and the conversion ratio  $p_n$  in  $p_{n+1}$  and  $q_n$  in  $q_{n+1}$  are obtained. There is also derived a formula for convergence  $h_n$ . In addition, in [10] the question of determining the incremental way of friction  $\Delta L$  in terms of distributions is solved.

It is assumed, that the effect of lubrication, [24], consists mainly in the following:

- the presence of grease in the gap of the two contacting bodies, as a result of the load, leads to the appearance of the field of hydrodynamic pressures and, accordingly, the appearance of the reaction of the lubricant layer, which counteracts the external load, and therefore the load in the lubricated contact of the counterbody decreases;
- as a result, the lubricant “pushes” the surfaces, and the number of contacts (the proportion of the contact surface) decreases;
- the molecular (adhesion) component of the friction force of solids disappears;
- the convergence of the surfaces at some moment ends, as well as wear, because there is a hydrodynamic mode of friction, due to a decrease of roughness. The onset of the hydrodynamic regime is estimated by the criterion  $\lambda$  [5] (p. 275):

$$\lambda = h_{\min} / (R_{z1} + R_{z2}), \quad (17)$$

where  $R_{z1}, R_{z2}$ —are the parameters of roughness of working surfaces, determined experimentally using a profilometer. When  $\lambda > 3$ , the hydrodynamic regime of friction comes; the wear ends.

#### 4.2. Definition of Initial Convergence $D_0$

Before starting the calculations of the mechanical contact,  $d$  is great,  $P_k(d) = 0$ . At the convergence (reduction of  $d$ ) increase the proportion of  $P_k(d)$  contacts, and elastic counter force  $F_{elast}(d)$ ; if  $F_{elast}(d) + F_{oil}(d) < F_N$ , so the convergence continues until equality

$$F_{elast}(d) + F_{oil}(d) = F_N, \quad (18)$$

moreover

$$\begin{aligned} F_{elast}(d) &= P_k(d) S c M \delta E, \\ F_{oil}(d) &= (1 - P_k(d)) S \sigma_{oil}, \end{aligned} \quad (19)$$

where  $d$ —the distance between the surfaces (the value of convergence);  $P_k(d)$ —the proportion of the surface of the mechanical contact, depending on the  $d$  convergence;  $S$ —nominal

area of interface surfaces;  $P_k(d)S$ —surface area of mechanical contact;  $(1 - P_k(d))S$ —the surface area of the lubricant;  $\sigma_{oil}$ —the pressure under which the lubricant is supplied (this value is an order of magnitude less than the pressure due to the load);  $E$ —elastic modulus,  $c$ —constant (in Hooke’s law,  $c = 1/L$ ,  $L$ —is the height of the rod, i.e., protrusion),  $M$ —number of contact projections.

The external load  $F_N$  is balanced by the elastic force of the contact lugs  $F_{elast}(d)$  and the pressure force of the lubricant  $F_{oil}(d)$ . When wear  $P_k(d)$  increases, and due to the preservation of the balance of forces (14), the  $d$  convergence decreases, and so it will be until the moment of hydrodynamic regime.

4.3. Scheme of Plastic Deformation

The described approach was also used in [16] to estimate the change of surfaces in the run-in mode when plastic deformations act. The following scheme is adopted: if the contact intersection is  $\delta \leq \Delta$ ,  $\Delta > 0$  where  $\Delta$ —is the threshold of elasticity (i.e., the maximum value  $\delta$  of the elastic (recoverable) deformation), then the change of the element height does not occur; if  $\delta > \Delta$  then the total decrease in elevation  $D_\xi + D_\eta$  takes place on the value  $\delta - \Delta$ . This value is distributed between  $D_\xi$  and  $D_\eta$  depending on the ratios of physical properties of materials. The dependence  $D_\xi(\delta)$  is assumed to be random; it is believed that the change in height ( $\delta - \Delta$ ) occurs only for one element: with probability  $P_m$  for  $\xi_m$  and with probability  $1 - P_m$ —for  $\eta_m$ . For this scheme, transition probability matrices for  $\xi_m$  and  $\eta_m$  are defined in [16]. There are also calculations with elastic and plastic deformations and fatigue failure under the action of a constant load; the evolution of distributions over time, the influence of the load, the threshold of elasticity, and the initial distributions on the limit distributions and roughness are analyzed there. In work [19] the described approach is used for the analysis of wear process of the piston of the diesel engine, and the estimation of the parameters of friction defining its resource is made. There is also the choice of the sampling interval for the recalculation of the distributions was substantiated, which had greatly accelerated the numerical evaluation of the model by a change of the matrix of transition probabilities.

5. Results of Modeling

The described approach differs from the known ones by the possibility of obtaining estimates of the changes in characteristics over time. In this section, a specific example demonstrates how the method works to obtain the required time dependencies. It is considered a mate “crankshaft—main bearing” of the diesel engine. Changes in time of friction characteristics, such as roughness, average contact area, average contact intersection, friction coefficient and wear, are estimated. The dependence of these characteristics on the applied load is also estimated. The initial data are given in Table 1 and below in the text. The data of Table 1 were obtained experimentally and from reference books.

Table 1. Initial parameters of mating surfaces.

Parameters	Crankshaft Journal (Surface $\eta$ )	Half-Bearing (Surface $\xi$ )
$R_a$ —arithmetic mean deviation of the profile, $\mu\text{m}$	0.083	1.099
Standard deviation $(1.25R_a)$ , $\mu\text{m}$	0.103	1.373
$\Delta s$ —the average distance between the projections, $\mu\text{m}$	18	30
$E$ —the Young’s modulus, GPa	200	75
$\nu$ —Poisson ratio	0.28	0.31
$\sigma_T$ —yield point, MPa	4250	1200

The nominal area of the contact area  $S$  (this is a small part of the cylindrical surface along the generatrix with an angle of about 10 degrees), taking into account the pulsating load, is determined by the engineers as the value  $S = 22.62 \text{ cm}^2$  the maximum permissible minimum thickness of the lubricant layer is  $h_{\min} = 1 \text{ }\mu\text{m}$ . The probability of failure  $P_W$  for the half-bearing is taken to be  $4 \cdot 10^{-7}$ , and  $10^{-9}$  for the crankshaft journal, i.e., a hundred times less, because it is made of a much harder material, and it is known that its surface is practically unchanged. The initial distribution densities  $p_0(x)$  and  $q_0(x)$  for the heights of the surface protrusions  $\xi$  (half-bearing) and  $\eta$  (crankshaft journal) were, respectively, approximated by shifted and stretched beta-distributions (density  $C(a, b)x^{a-1}(1-x)^{b-1}$ ,  $x \in [0, 1]$ ). Parameters  $a$  and  $b$  were selected on the base of profilograms so that after the shift and stretching in the desired height range to ensure the equality of the first two moments. For  $p_0(x)$  (half-bearing) it is received:  $a = 1.82$ ;  $b = 1.86$ . For  $q_0(x)$  (crankshaft journal):  $a = 1.71$ ;  $b = 4.60$ .

Analyzed coupling works in the hydrodynamic regime of friction most of the time, but in some points in time, characterized by increased load, it goes to mixed and boundary friction regimes (with regards to these regimes, see for example [5], p. 274), which determine resource coupling. In the considered computational model, first, for a short time, the coupling operates in the run-in mode, then—in the fatigue failure mode (boundary mode), after which the hydrodynamic friction mode occurs. The run-in time is less than 1% of the considered friction path. Boundary friction ranged from 30 to 40% of the friction path depending on the load.

Figure 2a shows the initial densities of the distribution  $p_0(x)$ ,  $q_0(x)$  of the peak levels of the lower and upper surfaces; the level scale of the peaks of the treads is rigidly connected with the half-bearing to observe the change in the distribution of the half-bearing  $p(x)$ . The levels of the protrusion peaks of the half-bearing (curve  $p_0(x)$ ) are in the range from 2.5  $\mu\text{m}$  to 8.5  $\mu\text{m}$ ; the levels of the crankshaft journal protrusion peaks are in the range from 8.2  $\mu\text{m}$  to 8.7  $\mu\text{m}$ . The normal force is taken to be 90 kN.

The operating mode is characterized by elastic and plastic deformations. Let us omit the description of this mode, because in our case this mode takes a negligible fraction of time; it is described in [15,16]. The convergence of the two surfaces and, as a consequence, an increase in the contact area (i.e., the number of contacting protrusions) and a decrease in stress, occurs almost due to plastic deformations. When they stop, this mode ends. The corresponding moment is seen in Figure 2b: a small “jump” in the distribution shows that a part of the protrusions has undergone plastic deformation, and changes in height; this distribution is the initial to analyze the mode of fatigue failure; accordingly, the height distribution  $q(x)$  of the shaft protrusions is shifted by the amount  $\sim 0.3 \text{ }\mu\text{m}$  in the surface of the half-bearing. On all the charts of Figure 2, vertices of peak density distributions are not shown, they are above the boundary of the figure; significant are not the peaks of peak density, but the location of the peaks on the horizontal axis of the levels of projection peaks.

The fatigue failure mode described in Section 3, and caused by the separation of the particle under multiple interactions, begins. Figure 2b shows the distribution after 240 km of friction; it can be seen that the distribution has changed significantly. The separation of the particles reduces the height of the projections, part of the height of the half-bearing from the upper levels goes to lower, forming a large proportion of projections with almost equal heights (this is the peak on the curve 4  $p(x)$  in the vicinity of the 6 microns level); distribution  $q(x)$ , respectively, almost unchanged shifted towards the half-bearing at 2.5 microns. The distribution shift  $q(x)$  is determined by maintaining a constant load. The shift also determines the amount of wear. This slow mode ends when the roughness becomes so small that the condition (“lambda criterion”) of transition to the hydrodynamic friction regime is satisfied [5], (p 275):

$$\lambda = h_{\min} / (R_{z1} + R_{z2}) > 3, \quad (20)$$

where  $h_{\min}$ —the minimum thickness of the lubricant layer,  $R_{z1}$ ,  $R_{z2}$ —surface roughness.

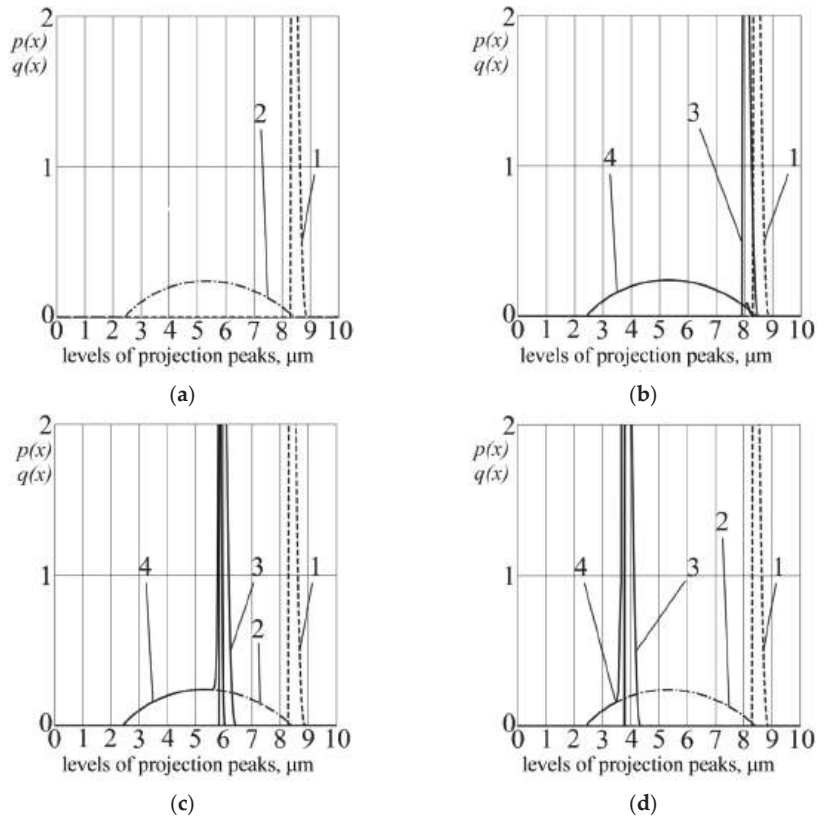


**Figure 2.** The distribution of heights (a) the initial density distribution, (b) after running, (c) friction way  $L = 240$  km, (d) friction way  $L = 1200$  km (the moment of the end of the work): 1—initial  $q_0(x)$  (crankshaft journal); 2—initial  $p_0(x)$  (half-bearing); 3—current  $q(x)$ ; 4—current  $p(x)$ .

Fatigue failure mode stops. The distributions corresponding to this point are shown in the Figure 2d. The hydrodynamic regime starts, and the wear intensity decreases to zero, i.e., the convergence of the surfaces is terminated. Modeling of transient, without a doubt, a smooth process, requires additional analysis; in the given calculations the transition is described in conditional (spasmodic) form.

Friction characteristics were calculated at three values of normal force: 10, 30, 90 kN. Figures 3 and 4 show the dependence of friction way. They show the possibility for engineers to quantify and compare the characteristics changing in the process of friction. As you can see, they agree with the known (qualitatively) dependences: the greater is the applied load, the faster the surface of the half-bearing smooths (Figure 3a); the proportion of contacting protrusions  $P\{\delta > 0\}$  increases faster (Figure 3b), i.e., the proportion of contact area; the transition to the hydrodynamic regime comes faster (“lambda criterion”  $\lambda$ , Figure 3c), intensive wear occurs (Figure 4b,c). Let us note that the parameter that determines the rate of change of the surface can be determined once by comparing the estimated time of the resource with empirically known.

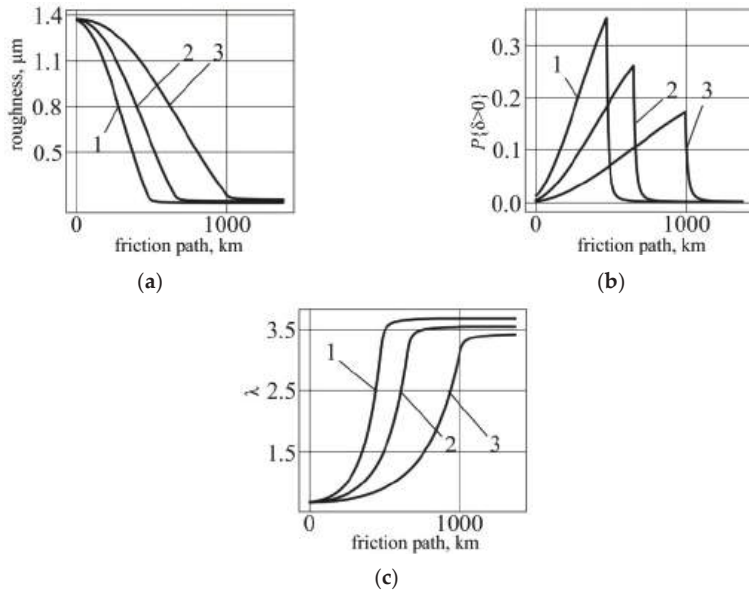


**Figure 3.** Friction characteristics (a) roughness of the bottom surface, (b) contact area share, (c) criterion  $\lambda$  of the lubrication mode: 3—load 10 kN; 2—load 30 kN; 1—load 90 kN.

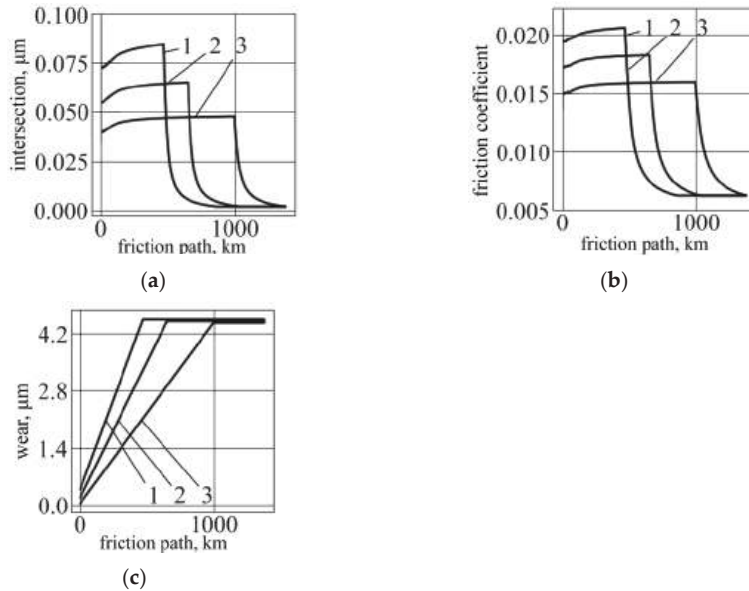


**Figure 4.** Friction characteristics (a) average contact intersection, (b) friction coefficient, (c) wear of half-bearing surface: 3—load 10 kN, 2—load 30 kN, 1—load 90 kN.

## 6. Conclusions

An approach to modeling changes in rough surfaces during their interaction is described in a general form. Using the developed method, a computational analysis of the “crankshaft journal-liner” interface of a diesel engine was performed. Taking into account the necessary initial data obtained experimentally and taken from reference materials, an

assessment was made of the change in the distribution of the heights of the liner irregularities. The evaluation was carried out depending on the friction path corresponding to the mode of operation of the diesel engine. Based on the calculation results, the following conclusions can be drawn. The proportion of high protrusions of the liner surface is small. They are subjected to pressure in excess of the yield strength. The height range for the shaft 0.5 microns is an order of magnitude narrower than for the liner. It can be seen that after running-in, the surface of the liner has undergone plastic deformation. The fatigue failure mode is caused by the separation of particles during multiple interactions, part of the liner heights from the upper levels moves to lower ones. The height shift of the liner determines the amount of wear. The described processes made it possible to calculate the coupling friction characteristics under three characteristic load conditions of a diesel engine: 10, 30, and 90 kN.

With an increase in load, the surface of the liner is smoothed out faster, and the proportion of the contact area increases faster; the transition to hydrodynamic friction occurs faster, and wear occurs more intensively. Thus, using the developed model in the future, it is possible to estimate the resource of a hydrodynamic interface operating in hydrodynamic and boundary friction modes. Such tribological couplings, in particular, include bearings of crankshafts of internal combustion engines, parts of the cylinder-piston group, as well as the couplings of high-pressure fuel pumps.

**Author Contributions:** Conceptualization, K.G.; methodology, K.G. and Y.R.; validation, K.G. and Y.R.; formal analysis, K.G.; investigation, K.G. and Y.R.; resources, K.G. and I.U.; data collection, K.G.; writing—original draft preparation, K.G.; writing—review and editing, I.U.; visualization, K.G. and I.U.; supervision, K.G.; project administration, K.G., Y.R. and I.U.; funding acquisition, K.G., Y.R. and I.U. All of the authors contributed significantly to the completion of this article, conceiving, and designing the review, writing, and improving the paper. All authors have read and agreed to the published version of the manuscript.

**Funding:** The work was carried out with the financial support of the Ministry of Science and Higher Education of the Russian Federation in a comprehensive project to create a high-tech production “Creation of a high-tech production of a unified family of vehicles “Arctic Bus” for the organization of safe transportation of passengers and mobile social facilities in the Far North in low temperatures (up to minus 50 °C) to ensure the connectivity of territories The Arctic Zone of the Russian Federation” under Agreement No. 075-11-2021-058 dated 25.06.2021. (Identifier of the state contract 000000S407521QLY0002) between the Ministry of Science and Higher Education of the Russian Federation and the URAL Automobile Plant Joint Stock Company in cooperation with the Main Contractor of research and development work—the Federal State Autonomous Educational Institution of Higher Education “South Ural State University (National Research University)”.

**Institutional Review Board Statement:** Not applicable.

**Informed Consent Statement:** Not applicable.

**Data Availability Statement:** Not applicable.

**Acknowledgments:** The authors thank South Ural State University (SUSU) for support.

**Conflicts of Interest:** The authors declare no conflict of interest.

### Appendix A

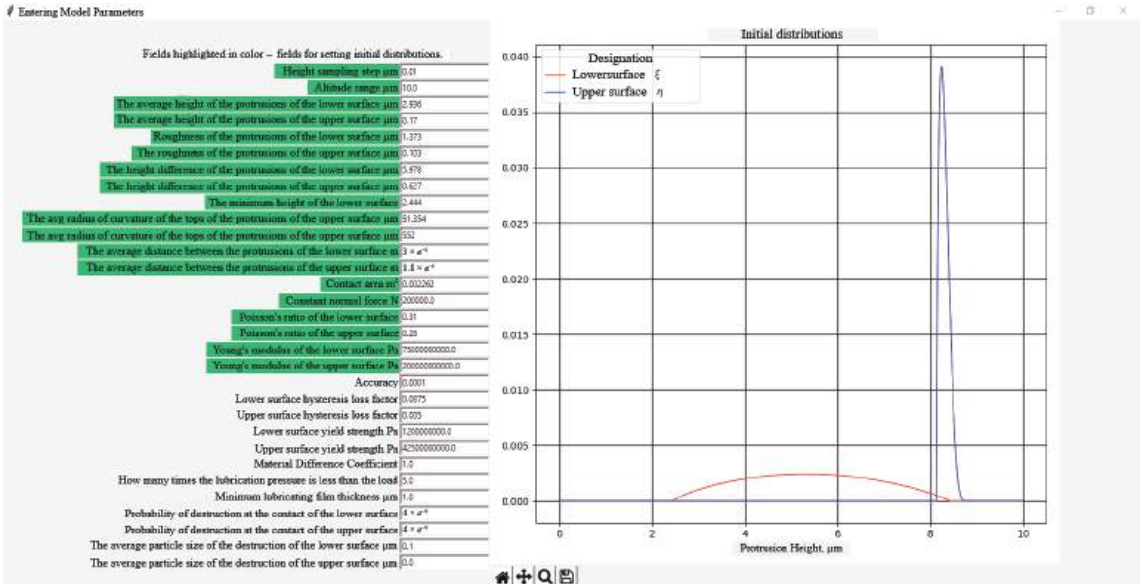


Figure A1. Program window with initial data input and height distribution.

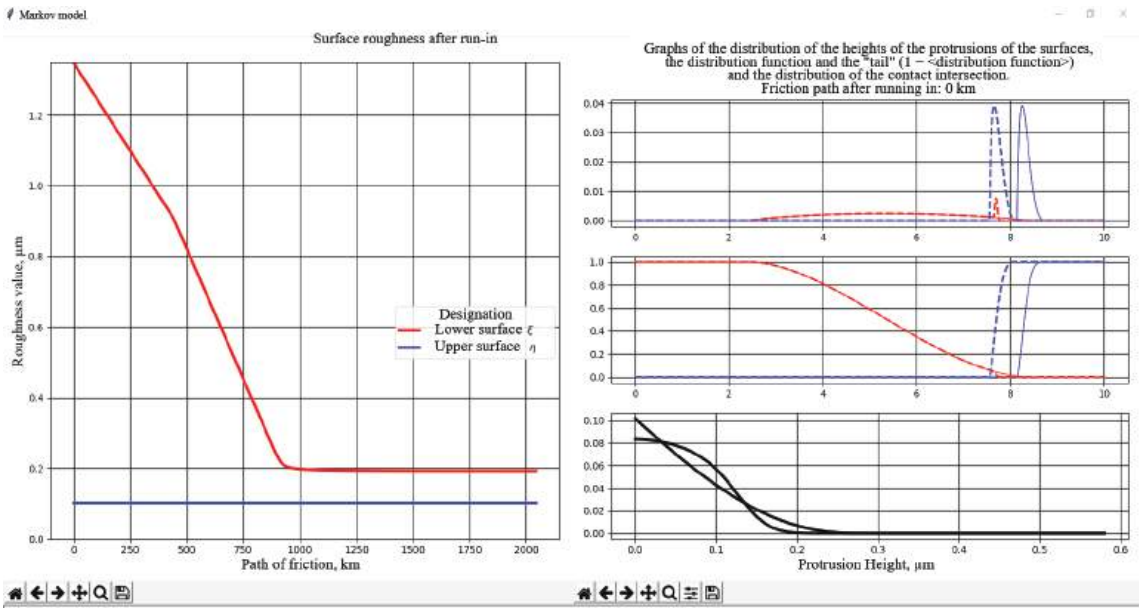


Figure A2. Program window reflecting friction characteristics.

### References

1. Vencl, A.; Rac, A. Diesel engine crankshaft journal bearings failures: Case study. *Eng. Fail. Anal.* **2014**, *44*, 217–228. [CrossRef]
2. Javorova, J.; Mazdrakova, A.; Andonov, I.; Radulescu, A. Analysis of HD journal bearings considering elastic deformation and non-Newtonian Rabinowitsch fluid model. *Tribol. Ind.* **2016**, *38*, 186–196.

3. Holmberg, K.; Andersson, P.; Erdemir, A. Global energy consumption due to friction in passenger cars. *Tribol. Int.* **2012**, *47*, 221–234. [CrossRef]
4. Zadorozhnaya, E.A.; Mukhortov, I.V.; Levanov, I.G. The use of non-Newtonian models of lubricating fluids in the calculation of complexly loaded friction units of piston and rotor machines. *Fric. Lubr. Mach. Mech.* **2011**, *7*, 22–30. (In Russian)
5. Al-Samieh, M.F.A. Surface roughness effects for Newtonian and non-Newtonian lubricants. *Tribol. Ind.* **2019**, *41*, 56–63. [CrossRef]
6. Vorlaufer, G.; Ilincic, S.; Franek, F.; Pauschitz, A. Wear Quantification by Comparison of Surface Topography Data. In *Encyclopedia of Tribology*; Wang, Q.J., Chung, Y.-W., Eds.; Springer: Boston, MA, USA, 2012; pp. 4087–4093. [CrossRef]
7. Novotny, P. Mixed lubrication solution of dynamically loaded radial slide bearings. *Tribol. Ind.* **2017**, *39*, 82–89. [CrossRef]
8. Popov, V.L. *Contact Mechanics and Friction Physics*; Phymathlit: Moscow, Russia, 2013. (In Russian)
9. Lazarev, V.; Gavrilov, K.; Doikin, A.; Sequard-Base, J.; Vorlaufer, G. Estimation of the Tribotechnical Parameters of the “Piston Skirt-Cylinder Liner” Contact Interface from IC-Engine for Decreasing the Mechanical Losses. In Proceedings of the 1st International Conference on Energy Production and Management in the 21st Century: The Quest for Sustainable Energy, Ekaterinburg, Russia, 23–25 April 2014; WIT Transactions on Ecology and the Environment: Southampton, UK, 2014; Volume 190, pp. 625–635. [CrossRef]
10. Amor, M.B.; Belgith, S.; Mezlini, S. Finite element modeling of RMS roughness effect on the contact stiffness of rough surfaces. *Tribol. Ind.* **2016**, *38*, 392–401.
11. Gavrilov, K.; Doikin, A.; Izzatulloev, M.; Goritskiy, Y. Numerical Model of Mechanical Interaction of Rough Surfaces of Journal Bearings of Piston Engine. In *Lecture Notes in Mechanical Engineering, ICIE, Proceedings of the 4th International Conference on Industrial Engineering, Moscow, Russia, 15–18 May 2018*; Radionov, A., Kravchenko, O., Guzeev, V., Rozhdestvenskiy, Y., Eds.; Springer: Berlin/Heidelberg, Germany, 2019. [CrossRef]
12. Zhu, S.; Sun, J.; Li, B.; Zhao, X.; Wang, H.; Teng, Q.; Ren, Y.; Zhu, G. Stochastic models for turbulent lubrication of bearing with rough surfaces. *Tribol. Int.* **2019**, *136*, 224–233. [CrossRef]
13. Greenwood, J.A.; Williamson, J.B.P. Contact of Nominally Flat Surfaces. *Proc. R. Soc. Ser. A* **1966**, *295*, 300–319. [CrossRef]
14. Nayak, P.R. Random process model of rough surfaces. *J. Lubr. Technol.* **1971**, *93*, 398–407. [CrossRef]
15. Dyomkin, N.B. *Contacting Rough Surfaces*; Science: Moscow, Russia, 1970. (In Russian)
16. Kragelsky, I.V.; Dobychny, M.N.; Kombatov, V.S. *Basics of Calculations for Friction and Wear*; Mechanical Engineering: Moscow, Russia, 1977. (In Russian)
17. Tigetov, D.; Goritskiy, Y. Markov model of mechanical interaction of rough surfaces in the process of friction. *Fric. Lubr. Mach. Mech.* **2010**, *3*, 4–13. (In Russian)
18. Goritskiy, Y.; Glavatskih, S.; Brazhnikova, Y. Markov model of interaction of rough surfaces. *Fric. Lubr. Mach. Mech.* **2014**, *2*, 11–20. (In Russian)
19. Gavrilov, K.; Goritskiy, Y.; Ismailova, Y.; Rozhdestvenskiy, Y.; Doikin, A. A numerical model for mechanical interaction of rough surfaces of the “piston-cylinder liner” tribosystem. *FME Trans.* **2015**, *43*, 249–253. [CrossRef]
20. Gavrilov, K.; Goritskiy, Y.; Migal, I.; Izzatulloev, M. A numerical model for estimation of service life of tribological systems of the piston engine. *Tribol. Ind.* **2017**, *39*, 329–333. [CrossRef]
21. Benasciutti, D.; Tovo, R. On fatigue cycle distribution in nonstationary switching loadings with Markov chain structure. *Probab. Eng. Mech.* **2010**, *25*, 406–418. [CrossRef]
22. Goritskiy, Y.; Gavrilov, K.; Ismailova, Y.; Shevchenko, O. Markov model for changing rough surfaces during mechanical interaction. *Bull. MPEI* **2017**, 112–125. (In Russian) [CrossRef]
23. Goritskiy, Y.; Gavrilov, K.; Migal, I. The construction of models of rough surfaces’ interaction: Markov’s approach. *Bull. MPEI* **2019**, 114–123. (In Russian) [CrossRef]
24. Rozhdestvenskiy, Y.; Zadorozhnaya, E. A simulation of the thermal state of heavily loaded tribo-units and its evaluation. *Bull. South Ural State Univ. Ser. Math. Model. Program.* **2014**, *7*, 51–64. [CrossRef]



Review

# A Review of Mathematical Models of Macroeconomics, Microeconomics, and Government Regulation of the Economy

Veniamin Mokhov <sup>1</sup>, Sergei Aliukov <sup>2,\*</sup>, Anatoliy Alabugin <sup>1</sup> and Konstantin Osintsev <sup>3</sup>

- <sup>1</sup> Department of Digital Economy and Information Technology, School of Economics and Management, South Ural State University, 76 Prospekt Lenina, 454080 Chelyabinsk, Russia; mokhovvg@susu.ru (V.M.); alabuginaa@susu.ru (A.A.)
- <sup>2</sup> Department of Automotive Engineering, Institute of Engineering and Technology, South Ural State University, 76 Prospekt Lenina, 454080 Chelyabinsk, Russia
- <sup>3</sup> Department of Energy and Power Engineering, Institute of Engineering and Technology, South Ural State University, 76 Prospekt Lenina, 454080 Chelyabinsk, Russia; osintcevk@susu.ru
- \* Correspondence: aliukovsv@susu.ru

**Abstract:** This review analyzes articles on the mathematical modeling of economic facts and processes. Mathematical modeling of the economy has rapidly developed in the past and current centuries. This is explained by the fact that, firstly, economics does not tolerate full-scale experiments, secondly, mathematical modeling significantly improves the accuracy of research results, and, finally, thirdly, economics becomes a science only when it is based on mathematics. The article presents an overview of the main methods of economic modeling used in scientific research over the past twenty years. The review does not claim to cover all areas, methods, and models used in scientific research in the field of economics. This cannot be done in one article. Mathematical modeling of only three sections of economic theory is considered: macroeconomics, microeconomics, and state regulation of the economy. The review of research methods and models in the microeconomics section, which are available in the scientific research toolkit but have already been described in the macroeconomics section, has been omitted. Only effective, practice-tested models are used in the Review. We hope that this review will be useful to scientists involved in the indirect study of economic phenomena and processes.

**Keywords:** modeling; model; macroeconomics; microeconomics; sources; review

**MSC:** 37N40

**Citation:** Mokhov, V.; Aliukov, S.; Alabugin, A.; Osintsev, K. A Review of Mathematical Models of Macroeconomics, Microeconomics, and Government Regulation of the Economy. *Mathematics* **2023**, *11*, 3246. <https://doi.org/10.3390/math11143246>

Academic Editor: Chuangyin Dang

Received: 25 June 2023  
 Revised: 16 July 2023  
 Accepted: 19 July 2023  
 Published: 24 July 2023



**Copyright:** © 2023 by the authors. Licensee MDPI, Basel, Switzerland. This article is an open access article distributed under the terms and conditions of the Creative Commons Attribution (CC BY) license (<https://creativecommons.org/licenses/by/4.0/>).

## 1. Introduction

Improving the accuracy and reliability of the results of economic research is achieved on the basis of mathematics. In recent decades, mathematical modeling has become the main instrumental method for the indirect study of economic facts and processes.

A formalized mathematical description of stable quantitative laws of the economy has been actively conducted since the eighteenth century. Obviously, this review could not describe all the retrospective mathematical methods and models of the economy but it took the main ones, the most frequently used and tested by practice over the last two decades of the current century.

By analogy with the existing division of economic theory into macroeconomics, microeconomics, and state regulation of the economy, the Review provides an overview of the main methods of mathematical modeling in such a structural division.

## 2. Modeling of Macroeconomics

Table 1 presents the mathematical modeling of macroeconomics.

**Table 1.** Mathematical modeling of macroeconomics.

Method	Model	References
1. Statistical models of macroeconomics	Macroeconomic production functions	[1,2]
	Leontief model	[3,4]
2. Dynamic models of macroeconomics with discrete time	Dynamic Keynesian model	[5,6]
	Samuelson–Hicks model	[7,8]
	Dynamic Leontief model	[9,10]
	Neumann model	[11,12]
3. Linear dynamic systems	Linear dynamic element	[13,14]
	Multiplier	[15,16]
	Accelerator	[17,18]
	Inertial link	[19,20]
	Transmission function	[21,22]
	Oscillating link	[23,24]
4. Nonlinear dynamic systems	Dynamic element of a nonlinear dynamic system	[25,26]
	Nonlinear dynamic Keynesian model	[27,28]
	Market cycles in economy	[29,30]
	Optimal control of dynamic systems	[31,32]
	Pontryagin maximum principle	[33,34]
5. Small-sector nonlinear dynamic models of macroeconomics	Solow model	[35,36]
	The golden rule of accumulation	[37,38]
	One-sector model of optimal economic growth	[39,40]
	Three-sector model of the economy	[41,42]

Economics is an applied science; therefore, mathematical models of the economy arose as a result of the urgent need for social development. We agree that not all limitations reflecting the specifics of the objects of study are taken into account in the models. However, without models, as a rule, research is simply impossible.

1.1. Macroeconomic production functions. In macroeconomic production functions, the economy is considered as an unstructured unit, the input of which is resources and the output is the final product of the functioning of the economy. In this case, the resources are considered as arguments, and the final product is a function. In practice, the Cobb–Douglas production function is most often used:

$$F(K, L) = A \cdot K^\alpha \cdot L^{1-\alpha},$$

where  $A > 0$ —coefficient of neutral technical progress;  $\alpha \in (0, 1)$ —the coefficient of elasticity of output for capital  $K$ ; and  $(1 - \alpha)$  is for labor  $L$ .

With time-invariant parameters of the production function, the mathematical model is static [1,2].

1.2. Leontief model. In the Leontief model, the economy is structured and consists of a finite number of autonomous industries which produce one kind of product. For its production in a particular industry, its own product and products from other industries are used. The amount of products consumed for the production of a unit of product of the industry under study is taken into account by means of direct cost coefficients. These coefficients do not depend either on time or on the scale of production. Gross outputs of

industries that ensure the production of the final product are determined according to the matrix of coefficients of direct costs for a given final product [3,4].

2.1. Dynamic Keynesian model. The gross output of the  $i$ -th product for the year  $x_i$  is divided into two parts: production consumption in all industries and nonproductive consumption. The net output of the  $i$ -th product is:

$$x_i - \sum_{j=1}^n a_{ij}x_j, \quad i = 1, \dots, n,$$

where  $\sum_{j=1}^n a_{ij}x_j$ —production consumption of the  $i$ -th product by all industries.

If we equate the net output of each  $i$ -th product and the final demand for it  $y_i$ , then a system of equations is formed:

$$x_i - \sum_{j=1}^n a_{ij}x_j = y_i, \quad i = 1, \dots, n,$$

which constitutes the static Leontief model.

Conclusion: Static macroeconomic models are still the best tool for system analysis of resource support for the production of products and services.

Linear dynamic models of macroeconomics with discrete time are represented by the dynamic Keynesian model, the dynamic Samuelson–Hicks model, the dynamic Leontief model, and the Neumann model. Here, mathematical methods and research models consider the economy as a simply connected system with discrete time.

In the dynamic Keynesian model, the economy is treated as a single dynamic element  $Y$ , and a time-varying endogenous variable is gross domestic product ( $GDP$ ).  $GDP$  consists of four parts: nonproductive consumption fund  $C$ ; gross private domestic investment  $I$ ; government expenditures on the purchase of goods and services  $G$ , and net exports  $E$ . In the model, the economy is considered closed; thus, net exports equal zero and government expenditures are allocated to consumption and accumulation:

$$Y = C + I.$$

The model assumes that the demand for investment goods is constant and the demand for consumer goods in the next year is a linear function of the current year's  $GDP$ :

$$C_{t+1}^D = \underline{C} + cY_t,$$

where  $c$  is the lower limit of the nonproductive consumption fund;  $0 < c < 1$ —marginal propensity to consume. Dynamic Keynesian model arises if we equate the planned output of end-use goods with the projected demand for them:

$$Y_{t+1} = \underline{C} + cY_t + I.$$

This model can only be used for analysis and short-term forecasting of the economy. It is not suitable for long-term forecasting, since it does not reflect the reproduction process of capital. From a mathematical point of view, this model is a first-order linear finite-difference equation [5,6].

2.2. Samuelson–Hicks model. The Samuelson–Hicks model, at certain values of the parameters, is an oscillatory link and, in another case, it is represented by two first-order linear dynamic elements connected in series. The difference between the Samuelson–Hicks model and the dynamic Keynesian model is the rejection of the investments constancy

and their introduction as a variable part, which is proportional to the GDP growth of the current year compared to the previous year:

$$Y_{t+1} = \underline{C} + cY_t + r(Y_t - Y_{t-1}) + I,$$

where  $r$ —acceleration coefficient,  $0 < r < 1$ .

From a mathematical point of view, the Samuelson–Hicks model is a second-order linear finite-difference equation. To find solutions of the dynamic model, finite-difference equations and Laurent transformations [7,8] are used.

2.3. Dynamic Leontief model. Leontief dynamic model of input–output balance reflects the reproduction process; thus, it is applicable to study the behavior of the economic system over sufficiently long time intervals while maintaining the technological structure [9,10].

2.4. Neumann model. The Neumann model is a generalization of the Leontief model, as it allows the production of one product in different ways. The model represents  $n$  products and  $m$  methods of their production, each  $j$ -th method is defined by the cost column vector  $a_j$  and the output column vector  $b_j$  per unit of process intensity:

$$a_j = \begin{pmatrix} a_{1j} \\ a_{2j} \\ \vdots \\ a_{nj} \end{pmatrix}, b_j = \begin{pmatrix} b_{1j} \\ b_{2j} \\ \vdots \\ b_{nj} \end{pmatrix}.$$

Cost and output matrices are formed from the input and output vectors:

$$A = (a_1, a_2, \dots, a_m), B = (b_1, b_2, \dots, b_m).$$

The input coefficients  $a_{ij}$  and output  $b_{ij}$  are non-negative. The implementation of any process requires the costs of at least one product, i.e., for each  $j$  there is at least one  $i$  such that  $a_{ij} > 0$ , and each product can be produced in at least one way, i.e., for each  $i$  there is some  $j$  such that  $b_{ij} > 0$ . Thus, each column of matrix  $A$  and each row of matrix  $B$  must have at least one positive element.

The Neumann model describes a closed economy in which the products produced in the previous production cycle (year  $t - 1$ ) are used to produce products in the next production cycle (year  $t$ ):

$$Ax_t \leq Bx_{t-1}, x_t \geq 0, t = 1, 2, \dots, T,$$

where  $y_t = Ax_t$ —cost vector for a given process intensity vector  $x_t$ :

$$x = \begin{pmatrix} x_1(t) \\ x_2(t) \\ \vdots \\ x_m(t) \end{pmatrix}$$

$z_t = Bx_{t-1}$ —output vector.

It is assumed that the initial stock vector  $Bx_0 > 0$  is given [11,12].

Neither the Leontief model nor the Neumann model is suitable for reflecting scientific and technological progress. In addition, these models do not reflect the reproductive process. Therefore, they can only be used for operational forecasting.

Conclusion: Dynamic models of macroeconomics with discrete time are not suitable for the analysis of reproduction and reflection of scientific and technological progress but

can be successfully used for operational and short-term forecasting of economic processes and phenomena.

3.1. Linear dynamic element. The main results in the study of dynamic systems with continuous time were obtained in the study of technical systems within the framework of the theory of automatic control. The apparatus of differential equations was used as the main mathematical toolkit. The obtained scientific results of research are now successfully used in the economy.

A linear dynamic element of the  $n$ -th order is given by a linear differential equation [13,14]:

$$\sum_{j=0}^n a_j y^{(j)} = \sum_{i=0}^n b_i x^{(i)}.$$

3.2. Multiplier. Most often, there are elements of the zero order (multiplier, accelerator) and the first order (inertial link) seen in practice.

The multiplier is a linear static link given by the equation:

$$a_0 y = b_0 x \text{ or } y = \alpha x, \alpha = \frac{b_0}{a_0},$$

where  $\alpha$  is the amplification factor (multiplier) [15,16].

3.3. Accelerator. The accelerator is a zero-order differentiator, the output of which is proportional to the input speed. For example, investment  $I$  can be expressed in terms of the rate of  $GDP$  change as follows:

$$I = r \frac{dY}{dt},$$

where  $r$  is the acceleration coefficient, i.e., an increase in the need for investment with an increase in  $GDP$  per unit [17,18].

3.4. Inertial link. The inertial link is given by a first-order differential equation [19,20]:

$$a_1 \frac{dy}{dt} + a_0 y = x(t).$$

3.5. Transmission function. The concept of the transfer function of a dynamic element is associated with the operator method for solving a differential equation.

The transfer function of series-connected elements is the relation of the output and input images:

$$G(s) = \frac{Y(s)}{X(s)} = \frac{Y_2(s)}{X_1(s)} = \frac{G_2(s)Y_1(s)}{X_1(s)} = G_1(s)G_2(s).$$

Thus, the transfer function of series-connected elements is equal to the product of their transfer functions.

The transfer function of parallel-connected elements with a summing link is equal to the sum (difference) of the transfer functions of the elements [21,22]:

$$G(s) = \frac{Y(s)}{X(s)} = \frac{Y_1(s) \pm Y_2(s)}{X(s)} = G_1(s) \pm G_2(s).$$

3.6. Oscillating link. An oscillatory link is used to model cyclical processes in the economy. The oscillatory link is given by a second-order differential equation:

$$a_2 \frac{d^2 y}{dt^2} + a_1 \frac{dy}{dt} + a_0 y = \sum_{i=0}^n b_i x^{(i)}(t)$$

with a negative discriminant made up of the coefficients on the left side of the equation [23,24].

$$a_1^2 - 4a_2 a_0 < 0$$

Conclusion: The apparatus of differential equations in the analysis of linear dynamic systems should be used to model cyclical processes in the economy.

4.1. Dynamic element of a nonlinear dynamic system. Dynamic systems are called nonlinear if they contain at least one nonlinear element.

The method of analysis of a nonlinear system depends on the type of nonlinearity. There are two main approaches: direct solution of nonlinear equations of a dynamic system by numerical integration on a computer and linearization of the system and the subsequent use of methods for studying linear dynamic systems.

Schematically, using a dynamic element as an example, it looks as follows. The dynamic element equation has the form:

$$F(y, y', \dots, y^{(n)}, x, x', \dots, x^{(n)}) = 0.$$

This equation has a solution with respect to the highest derivative:

$$y^{(n)} = f(y, y', \dots, y^{(n-1)}, x, x', \dots, x^{(n)}),$$

followed by a transition to a system of differential equations with respect to variables  $y_1, \dots, y_n$ :

$$\begin{aligned} y_1 &= y, \\ \frac{dy_1}{dt} &= y_2, \\ &\vdots \\ \frac{dy_{n-1}}{dt} &= y_n, \\ \frac{dy_n}{dt} &= f(y, y', \dots, y^{(n)}, x, x', \dots, x^{(n)}). \end{aligned}$$

Next, it is necessary to obtain an analytical or numerical solution of an equation or a system of differential equations [25,26].

4.2. Nonlinear dynamic Keynesian model. The nonlinear Keynesian dynamic model can be represented as a first-order nonlinear dynamic link:

$$\frac{dy}{dt} = f(y, I),$$

that is, *GDP* growth rate ( $y$ ) is a function of *GDP* and investment. In the linear case:

$$f(y, I) = \underline{c} - (I - c)y + I.$$

It is obvious that

$$\frac{\partial f}{\partial y} < 0, \quad \frac{\partial f}{\partial I} > 0$$

therefore, the rate of *GDP* growth slows down with an increase in *GDP* and it increases with an increase in investment.

Let us suppose that at  $t = 0$ , investments were equal to  $I_0$  and the system was in some equilibrium state  $(y_E^0, I_0)$ , the first component of which is determined from the equation of a nonlinear dynamic link:

$$f(y_E^0, I_0) = 0.$$

With an increase in investment from  $I_0$  to  $I = I_0 + \Delta I$ ,  $\Delta I > 0$ , the system will satisfy the equation

$$\frac{dy}{dt} = f(y, I), \quad y(0) = y_E^0.$$

Let us represent *GDP* as a sum of constant and variable parts:

$$y(t) = y_E^0 + \eta(t), \quad \eta(t) > 0, \quad \eta(0) = 0.$$

The variable part  $\eta(t)$  satisfies the equation

$$\frac{dy}{dt} = f(y_E^0 + \eta, I_0 + \Delta I), \eta(0) = 0.$$

If the investment increment  $\Delta I$  is relatively small, then, with the evolutionary nature of the function  $f(y, I)$ , the variable part  $\eta(t)$  is also relatively small; so, the right side of the last equation can be expanded in the vicinity of the point  $(y_E^0, I_0)$  in a Taylor series, discarding terms of the second and higher orders:

$$\frac{dy}{dt} = \frac{\partial f}{\partial y}(y_E^0, I_0)\eta + \frac{\partial f}{\partial I}(y_E^0, I_0)\Delta I, \eta(0) = 0.$$

After transferring the term containing  $\eta$  to the left side and dividing both parts by  $\frac{\partial f}{\partial y}(y_E^0, I_0)$ , we get the equation of the inertial link:

$$T \frac{d\eta}{dt} + \eta = \alpha \Delta I, \eta(0) = 0,$$

where  $\frac{1}{T} = -\frac{\partial f}{\partial y}(y_E^0, I_0)$ —generalized propensity to accumulate in the initial state;

$$\alpha = -\frac{\frac{\partial f}{\partial I}(y_E^0, I_0)}{\frac{\partial f}{\partial y}(y_E^0, I_0)} > 0.$$

From the last equation, it follows that the variable part of GDP will be equal to:

$$\eta(t) = \alpha \Delta I (1 - e^{-\frac{t}{T}}),$$

and GDP in general will change following the dependence:

$$y(t) = y_E^0 + \alpha \Delta I (1 - e^{-\frac{t}{T}}),$$

in this case, the new equilibrium state of GDP will be equal to [27,28]:

$$y_E = \lim_{t \rightarrow \infty} y(t) = y_E^0 + \alpha \Delta I = y_E^0 - \frac{\frac{\partial f}{\partial I}(y_E^0, I_0)}{\frac{\partial f}{\partial y}(y_E^0, I_0)} \Delta I$$

4.3. Market cycles in economy. Nonlinear multiply connected systems have seven types of stability and can have several equilibrium states. The state of equilibrium in such systems can be either a fixed point or a closed trajectory (limit cycle). In both cases, particular solutions of differential equations are used.

Market cycles in the economy are described by a second-order linear dynamic model and are studied using a continuous analogue of the Samuelson–Hicks model or a continuous analogue of the nonlinear Goodwin model.

The Goodwin model [29,30] assumes that capital intensity  $k$ , population growth rate  $n$ , and labor productivity  $\gamma$  remain constant:

$$k = \frac{K_t}{Y_t} = const,$$

where  $K_t$ —capital (fixed and current assets);  $n = \frac{N_{t+1} - N_t}{N_t} = const$ , where  $N_t$ —population in year  $t$ ;  $\gamma = \frac{y_{t+1} - y_t}{y_t} = const$ ,  $y_t = \frac{Y_t}{L_t}$ —labor productivity,  $Y_t$ —GDP,  $L_t$ —the number of employees.

The model has two endogenous variables,  $\lambda_t$  and  $\delta_t$  : where  $\lambda_t = \frac{L_t}{N_t}$  – the share of employed people in the total population;  $\delta_t = \frac{w_t L_t}{Y_t} = \frac{w_t}{y_t}$  – the share of the consumption fund in GDP,  $w_t$  is the annual wage rate.

The continuous analogue of the nonlinear Goodwin model has the form:

$$\begin{cases} \frac{d\delta}{dt} = (a\lambda - a_0)\delta \\ \frac{d\lambda}{dt} = (-b\delta + b_0)\lambda' \end{cases}$$

where  $a = \frac{\alpha}{1+\gamma} > 0$ ,  $a_0 = \frac{\alpha_0}{1+\gamma} > 0$ ;  $b = \frac{1}{k(1+\gamma)(1+n)} > 0$ ,  $b_0 = \frac{1-k[\gamma-n(1+\gamma)]}{k(1+\gamma)(1+n)}$ .

4.4. Optimal control of dynamic systems. The control of a dynamic system is understood as a direct impact on the system in order to achieve a given result. Optimal control is understood as a choice from a set of alternative options for such control, which, according to a given criterion, is optimal. As an optimality criterion, a certain functional of the phase and control trajectories is chosen, which is subject to maximization (minimization).

The behavior of any nonlinear multiply connected system is described by the following equations of motion:

$$\frac{dy_i}{dt} = f_i(y, x, t), y_i(0) = y_i^0, i = 1, \dots, n,$$

where  $y$  – vector of phase coordinates that specifies the state of the system;  $x$  – vector of external (input) setting and (or) disturbing influences on the system;  $y_i^0$  – initial values of phase variables.

If the disturbing actions are negligible, some of the setting actions become control actions, and others are given known functions of time; then, we arrive at the following equations for the controlled dynamic system:

$$\frac{dy_i}{dt} = f_i(y, u, t), y_i(0) = y_i^0, i = 1, \dots, n,$$

where  $u$  – vector of control parameters,  $u \in U$ ;  $U$  – area of acceptable values of control parameters.

The control trajectory (control)  $u(t)$  is called admissible if it is piecewise continuous, continuous at the discontinuity points on the left:

$$u(\tau) = u(\tau - 0) = \lim_{\substack{i \rightarrow \tau \\ t < \tau}} u(t),$$

and, moreover, for any  $tu(t) \in U$ .

If the control law is given, i.e., an admissible control trajectory  $u(t)$  is defined, then the equations for the phase variables take the form:

$$\frac{dy_i}{dt} = f_i(y, u(t), t), y_i(0) = y_i^0, i = 1, \dots, n,$$

thus, for any initial conditions  $y(0) = y^0$ , the solution is uniquely determined.

As an optimality criterion, a certain functional of the phase and control trajectories is chosen, which is subject to maximization (minimization) [31,32].

4.5. Pontryagin maximum principle. The necessary conditions for solving such a problem are given by the Pontryagin maximum principle [33,34].

The Pontryagin maximum principle is applied to a general control problem of the form

$$\begin{aligned} \max_{u(t) \in U} \int_0^T f_0(y, u, t) dt + F(y^T, T), \\ \frac{dy}{dt} = f(y, u, t), y(0) = y^0, \end{aligned}$$

where  $y = \begin{pmatrix} y_1 \\ \vdots \\ y_n \end{pmatrix}$ —column vector of phase variables that determine the state of the dynamic system;

$f(y, u, t) = \begin{pmatrix} f_1(y, u, t) \\ \vdots \\ f_n(y, u, t) \end{pmatrix}$ —column vector of the right parts of the equations of the system;

$y^0, y^T$ —initial and final values of the state vector;

$u = \begin{pmatrix} u_1 \\ \vdots \\ u_n \end{pmatrix}$ —column vector of control parameters;

$U$ —area of possible values of control parameters;

$f_1(y, u, t)$ —integrand of the control criterion.

The functions  $f_i(y, u, t), F(y^T, T)$  are continuous and differentiable with respect to each argument. If the equation  $u(t)$  is defined, then the trajectory of the system  $y(t)$  is uniquely defined for a given initial condition  $y(0) = y^0$ . The search for the trajectory of the system, corresponding to the optimal control, is reduced to finding the saddle point of the Lagrange function in a nonlinear programming problem.

Conclusion: Economic phenomena and processes are characterized by nonlinearity. However, the use of the mathematical method of system linearization makes it possible to apply methods for studying linear dynamic systems for the analysis of economic entities.

### 5.1. Solow model. Small-sector nonlinear dynamic models of macroeconomics.

Nonlinear small-sector models are used to study long-term trends, growth factors, and assess the consequences of options for macroeconomic decisions.

The base model is the one-sector Solow model [35,36]. In this model, the economic system is considered as a single unstructured whole that produces one universal product. In this case, the product can be both consumed and invested. The model in its most aggregated form reflects the process of reproduction and allows for the analyzing of the relationship between consumption and accumulation in general terms.

The state of the economy is given by five endogenous variables:

$X$ —GDP;

$C$ —nonproductive consumption fund;

$I$ —investments;

$L$ —the number of employees;

$K$ —basic production assets.

The model uses three exogenous indicators:

$\nu$ —annual growth rate of the number of employees;

$\mu$ —the share of fixed production assets retired during the year;

$\rho$ —the rate of accumulation (share of gross investment in GDP).

Exogenous indicators are within the following limits:  $-1 < \nu < 1, 0 < \mu < 1, 0 < \rho < 1$ .

It is assumed that endogenous variables change over time, while exogenous indicators are constant.

The Solow model in absolute terms would be:

$$L = L_0 e^{\nu t}; \frac{dK}{dt} = -\mu K + \rho X; K(0) = K_0;$$

$$X = F(K, L); I = \rho X; C = (1 - \rho)X.$$

This model takes into account two aggregated products (means of production and commodities) and two sectors. The first sector produces means of production, the second, consumer goods.

5.2. The golden rule of accumulation. The Solow model solves the problem known as the “Golden Rule of Accumulation” [37,38]. Its essence boils down to the fact that in a stationary mode, with a proper choice of the rate of accumulation, in a relatively short period of time after the start of the transition process, it is possible to maximize per capita consumption. Genuinely:

$$c^E(p) = (1 - p)A(k^E)^\alpha = (1 - p)A \left[ \frac{\rho A}{\lambda} \right]^{\frac{\alpha}{1-\alpha}} = B[g(\rho)]^{\frac{1}{1-\alpha}},$$

where  $B = \left[ \frac{A}{\lambda^\alpha} \right]^{\frac{1}{1-\alpha}}$ ,  $g(\rho) = \rho^\alpha(1 - \rho)^{1-\alpha}$ .

Thus, per capita consumption  $c$  is entirely determined by the function  $g(\rho)$ .

We have

$$\frac{dg}{d\rho} = \left( \frac{\rho}{1 - \rho} \right)^\alpha \frac{\alpha - \rho}{\rho},$$

Therefore  $\frac{dc^E}{d\rho} > 0$  for  $\rho < \alpha$ ,  $\frac{dc^E}{d\rho} < 0$  for  $\rho > \alpha$ .

Thus, the highest average per capita consumption is achieved at  $\rho^* = \alpha$ , i.e., the rate of accumulation should be equal to the elasticity of output for funds.

5.3. One-sector model of optimal economic growth. With  $\rho = const$  and current consumption per employee  $c(t) = C(t)/L(t)$ , the Solow model is transformed into a one-sector model of optimal economic growth [39,40]:

$$\frac{dk}{dt} = f(k) - (\mu + \nu)k - c, \quad k(0) = k_0,$$

since the quantity  $\rho f(k)$  in the Solow model is replaced by  $f(k) - c(t)$ . The last equation is the main equation of the controlled system.

Specific consumption  $c(t)$  is considered as a control parameter. Its admissible trajectory, as it is customary in optimal control theory, can be any piecewise continuous trajectory that satisfies the boundary condition:

$$0 < \underline{c} \leq c(t) \leq f(k(t)),$$

where  $\underline{c}$ —maximum permissible lower limit of specific consumption.

The task of the governing body of the economic system is to choose the value of current consumption in such a way that, over a long period of time, the discounted utility from consumption would be maximum:

$$\int_0^\infty e^{-\delta t} u(c(t)) dt \rightarrow max,$$

where  $\delta$ —the discount rate by which future utilities are reduced to the present (assuming that immediate consumption is more important than distant consumption);  $u(c)$  is the consumption utility function.

5.4. Three-sector model of the economy. The process of reproduction is reflected in more details by a three-sector model of the economy, in which there are three aggregated products (objects of labor, means of labor, and consumer goods), and each of the three sectors produces its own product; namely, the material sector produces objects of labor, capital creating produces means of labor, and the consumer produces consumer goods [41,42].

When constructing a three-sector model of the economy, the following assumptions were made:

1. The technological structure is considered constant and is set using linearly homogeneous neoclassical production functions

$$X_i = F_i(K_i, L_i),$$

where  $X_i, K_i, L_i$ —output, fixed production assets and the number of people employed in the  $i$ -th sector;

2. The total number of employed  $L$  in the manufacturing sector changes with a constant growth rate  $\nu$ ;
3. There is no investment lag;
4. The depreciation coefficients of fixed production assets  $\mu_i$  and direct material costs  $\alpha_i$  of the sectors are constant;
5. The economy is closed, i.e., foreign trade is not considered;
6. The time  $t$  changes continuously.

Assumption (2) in discrete time has the following form ( $t$  is the number of the year):

$$\frac{L(t+1) - L(t)}{L(t)} = \nu,$$

And, upon transition to continuous time, it takes the form of a differential equation

$$\frac{dL}{dt} = \nu L, L(0) = L^0,$$

which has a solution:

$$L = L^0 e^{\nu t}.$$

From assumptions (3, 4), it follows that the change over the year of the fixed production assets of the  $i$ -th sector consists of two parts: depreciation ( $\mu_i K_i$ ) and growth due to gross capital investments ( $+I_i$ ), i.e.,

$$K_i(t+1) - K_i(t) = -\mu_i K_i(t) + I_i(t), i = 0, 1, 2,$$

or in continuous time

$$K_i(t + \Delta t) - K_i(t) = -[\mu_i K_i(t) + I_i(t)]\Delta t,$$

with  $\Delta t \rightarrow 0$  we obtain differential equations for the main production assets of the sectors

$$\frac{dK_i}{dt} = -\mu_i K_i + I_i, K_i(0) = K_i^0, i = 0, 1, 2.$$

Thus, under the assumptions made, the three-sector model of the economy (with the signs of time omitted) in absolute terms takes the form:

$L = L(O)e^{\nu t}$ —number of employees;

$L_0 + L_1 + L_2 = L$ —distribution of the employed by sectors;

$\frac{dK_i}{dt} = -\mu_i K_i + I_i, K_i(0) = K_i^0, i = 0, 1, 2$ —dynamics of funds by sectors;

$X_i = F_i(K_i, L_i), i = 0, 1, 2$ —output by sectors;

$X_1 = I_0 + I_1 + I_2$ —distribution of products of the fund-creating sector;

$X_0 = a_0 X_0 + a_1 X_1 + a_2 X_2$ —distribution of products of the material sector.

With the help of a three-sector model, conditions are identified under which the economy falls into stagnation or balanced economic growth. It is proved that in a stationary state a three-sector economy has a technological optimum. Therefore, any change in the stationary state of the economy as a result of an external influence or a control decision can be assessed as positive if there has been a movement towards the optimum point and negative otherwise.

Conclusion: Based on the basic one-sector Solow model, an arsenal of models has been developed and recommended for a small-sector study of the state of the economy and determining its technological optimum.

### 3. Modeling of Microeconomics

Table 2 presents mathematical modeling of macroeconomics.

**Table 2.** Mathematical modeling of microeconomics.

Method	Model	References
6. Consumer behavior models	Consumer preferences and utility function	[43,44]
	Consumer behavior model	[45,46]
7. Producer behavior models	Firm model	[47,48]
	Duopoly model	[49,50]
8. Models of interaction between consumers and producers	Equilibrium price model	[51,52]
	Walrasian model	[53,54]

6.1. Consumer preferences and utility function. The household (consumer) is an important concept in microeconomics. The main problem in the study of consumer behavior is to establish the magnitude of his demand for purchased goods and services at given prices and his income.

A consumer’s decision to buy a certain set of goods can be mathematically represented as a choice of a specific point in the space of goods. Let  $n$  be a finite number of goods under consideration;  $x = (x_1, \dots, x_n)^T$ —column vector of volumes of goods purchased by the consumer for a certain period at given prices and income for the same period. The space of goods is the set of possible sets of goods  $x$  with non-negative coordinates:

$$C = \{x : x \geq 0\}.$$

In consumer choice theory [43,44], it is assumed that each consumer initially has his own preferences on some subset of the product space  $X \subset \{x : x \geq 0\}$ . This means that, for every pair  $x \ni X, y \ni Y$ , one of three relations takes place:

- $x \succ y$ —set  $x$  is preferred over  $y$ ;
- $x \prec y$ —set  $x$  is less preferred than  $y$ .

$x \sim y$ —for the consumer, both sets have the same degree of preference. Preference relations have the following properties:

- if  $x \succ y, y \succ z$ , then  $x \succ z$  (transitivity);
- if  $x \succ y$ , then  $x \succ y$  (unsaturation: a larger set is always preferable to a smaller one).

The preference relations of each consumer can be represented in the form of a preference indicator, i.e., a utility function  $u(x)$  such that  $x \succ y$  implies  $u(x) > u(y)$  and  $x \sim y$  implies  $u(x) = u(y)$ . For each consumer, such a representation is multivariate. The introduction of a utility function makes it possible to replace preference relations with the usual relations between numbers: greater than, less than, and equal to.

6.2. Consumer behavior model. In the model of consumer behavior [45,46], it is assumed that the consumer always seeks to maximize his utility and is constrained only by limited income:

$$\max_{x \in \delta \cap X} u(x) = \max_{px \in M} u(x)$$

This conditional extremum problem reduces to finding the unconditional extremum of the Lagrange function:

$$L(x) = u(x) + \lambda(M - px).$$

Necessary conditions for a local extremum:

$$\sum_{j=1}^n p_j x_j^* = M,$$

$$\frac{\partial L}{\partial x_i} = \frac{\partial u}{\partial x_i}(x_i^*) - \lambda^* p_i = 0, \quad i = 1, \dots, n.$$

These conditions really determine the maximum point, since the matrix  $U$  is negative definite.

Conclusion: The developed mathematical arsenal allows for the determination of the behavior of the consumer—his preferences and usefulness in the face of budget constraints—not on a qualitative but on a quantitative level.

7.1. Firm model. When studying the behavior of a manufacturer in the firm model [47,48], it is assumed that a manufacturing firm produces one type of product or several types but with a constant structure;  $X$  is the number of units of one type of product or the number of multiproduct units.

Each of the three aggregated types of resources (labor  $L$ , funds  $K$ , and materials  $M$ ) has a certain number of varieties.

The technology of a firm is determined by its production function, which expresses the relationship between resource inputs and output:

$$X = F(x),$$

where  $x = (x_1, \dots, x_n)$ —a column vector of possible costs for various types of resources.

It is assumed that  $F(x)$  is twice continuously differentiable and neoclassical. Moreover, the matrix of its second derivatives is negative definite.

If the price of a unit of production is equal to  $p$ , and the price of a unit of a resource of the  $j$ -th type is  $w_j$ ,  $j = 1, \dots, n$ , then each cost vector  $x$  corresponds to a profit

$$\Pi(x) = pF(x) - wx,$$

where  $w = (w_1, w_2, \dots, w_n)$ —row vector of resource prices.

In the presence of a natural restriction on nonnegativity of the sizes of resources involved in production, the problem of maximizing profit takes the form:

$$\max_{(x \geq 0)} [pF(x) - wx].$$

This is a nonlinear programming problem with  $n$  non-negativity conditions  $x \geq 0$ . The necessary conditions for its solution are the Kuhn–Tucker conditions:

$$\begin{aligned} \frac{\partial \Pi}{\partial x} &= p \frac{\partial F}{\partial x} - w \leq 0, \\ \frac{\partial \Pi}{\partial x} x &= \left( p \frac{\partial F}{\partial x} - w \right) x = 0, \\ x &\geq 0. \end{aligned}$$

If all types of resources are used in the optimal solution, i.e.,  $x^* > 0$ , then the solution of the problem takes the form:

$$p \frac{\partial F(x^*)}{\partial x} = w \text{ or } p \frac{\partial F(x^*)}{\partial x_j} = w_j, \quad j = 1, \dots, n,$$

that is, the optimal point, the value of the marginal product of a given resource, must be equal to its price.

7.2. Duopoly model. In the most general case of the duopoly model [49,50], two competitors produce one type of product in accordance with their production function

$$X_i = F_i(x^i), \quad i = 1, 2.$$

The price of products depends on both issues:

$$p = p(X_1, X_2),$$

and, as output increases, the price falls:

$$\frac{\partial p}{\partial X_1} < 0, \quad \frac{\partial p}{\partial X_2} < 0.$$

The resource price also depends on the volume of its purchases  $x_j^1, x_j^2$  by the first and second firms:

$$w_j = w_j(x_j^1, x_j^2), \quad j = 1, \dots, n,$$

where prices rise as demand increases:

$$\frac{\partial w_j}{\partial x_j^1} > 0, \quad \frac{\partial w_j}{\partial x_j^2} > 0.$$

Every firm seeks to maximize its profits. For example, the first firm should act as follows:

$$\max_{(X_1, x_1^1, \dots, x_n^1)} \left[ p(X_1, X_2)X_1 - \sum_{j=1}^n w_j(x_j^1, x_j^2)x_j^1 \right]$$

on condition  $X_1 = F_1(x_1^1, \dots, x_n^1)$ .

The Lagrange function for this problem has the form:

$$\begin{aligned} L(X_1, x^1, \lambda) &= p(X_1, X_2)X_1 - \sum_{j=1}^n w_j(x_j^1, x_j^2)x_j^1 + \lambda(F_1(x_1^1, \dots, x_n^1) - X_1), \\ \frac{\partial L}{\partial X_1} &= p(X_1, X_2) + X_1 \frac{\partial p}{\partial X_1} + X_1 \frac{\partial p}{\partial X_2} \frac{\partial X_2}{\partial X_1} - \lambda = 0, \\ \frac{\partial L}{\partial x_j^{(1)}} &= -w_j(x_j^1, x_j^2) - x_j^1 \frac{\partial w_j}{\partial x_j^1} - x_j^1 \frac{\partial w_j}{\partial x_j^2} \frac{\partial x_j^2}{\partial x_j^1} + \lambda \frac{\partial F_1}{\partial x_j^1} = 0, \quad j = 1, \dots, n, \\ \frac{\partial L}{\partial \lambda} &= F_1(x_1^1, \dots, x_n^1) - X_1 = 0. \end{aligned}$$

Eliminating  $\lambda$ , we get the  $(n + 1)$  equation for determining the strategy  $X_1, x_1^1, \dots, x_n^1$  of the first firm:

$$\begin{aligned} \left[ p(X_1, X_2) + \left( X_1 \frac{\partial p}{\partial X_1} + X_1 \frac{\partial p}{\partial X_2} \frac{\partial X_2}{\partial X_1} \right) \frac{\partial F_1}{\partial x_j^1} \right] &= w_j + x_j^{(1)} \left( \frac{\partial w_j}{\partial x_j^1} + \frac{\partial w_j}{\partial x_j^2} \frac{\partial x_j^2}{\partial x_j^1} \right), \quad j = 1, \dots, n, \\ X_1 &= F_1(x_1^1, \dots, x_n^1) \end{aligned}$$

The solution of these equations depends on  $\frac{\partial X_2}{\partial X_1}$  and  $\frac{\partial x_j^2}{\partial x_j^1}$ ,  $j = 1, \dots, n$ . The latter equations represent the expected response of the second firm to the strategy  $X_1, x_1^1, \dots, x_n^1$  of the first firm. Under different assumptions about this response, different solutions to the competitors' problem will be obtained in the duopoly model.

Conclusion: Based on the production functions, the above models allow for the determination of the optimal strategy of the company in a competitive environment.

8.1. Equilibrium price model. Models for establishing an equilibrium price in the processes of interaction between consumers and producers are based on the assumption that price changes depend on the difference between supply and demand: if demand is higher than supply, then the price increases; otherwise, it decreases.

The most well-known model for establishing an equilibrium price in the market for one product is the "cobweb" one [51]. In this model, demand is characterized by a decreasing

aggregate demand function  $\Phi(p)$ , while supply is characterized by an increasing aggregate supply function  $\psi(p)$ . These functions are defined and continuous for all  $p > 0$ . Moreover,

$$\lim_{p \rightarrow 0} \Phi(p) = \infty, \quad \lim_{p \rightarrow \infty} \Phi(p) = 0,$$

$$\lim_{p \rightarrow 0} \psi(p) = 0, \quad \lim_{p \rightarrow \infty} \psi(p) = \infty.$$

The state of equilibrium is characterized by the equality of supply and demand:

$$\Phi(p) = \psi(p),$$

notably, by virtue of the assumptions made, the last equation has a unique solution  $p^E$ , so that the equilibrium state

$$\Phi(p^E) = \psi(p^E) = x^E$$

is unique.

The “cobweb” model makes it possible to implement the process of iterative approximation to the equilibrium price. Let us assume that at the initial moment of time the price  $p_0$  is set, while the demand turned out to be less than the supply:

$$\Phi(p_0) < \psi(p_0),$$

then, in the model, we lower the price to a level at which demand will be equal to supply at the initial price:

$$\Phi(p_1) = \psi(p_0).$$

At the new price  $p_1$ , demand exceeds supply:

$$\Phi(p_1) > \psi(p_1),$$

therefore, we raise the price to the level  $p_2$ , at which

$$\Phi(p_2) = \psi(p_1),$$

and so on. Thus, the process described by the recurrent relation  $\Phi(p_i) = \psi(p_{i-1})$ ,  $i = 1, 2, \dots$ , converges.

To determine the forecast values of the equilibrium price in the world’s youngest energy market in Russia, according to the data of 2004–2017, a recurrent neural network was built and tested in seven federal districts [52]. The simulation results for two districts are shown in Figures 1 and 2. Simulation made it possible to obtain a high accuracy of the forecast. The error for all districts was less than 2%. High-precision forecasting ensures that energy consumers operate in an equilibrium market with relatively low tariffs.

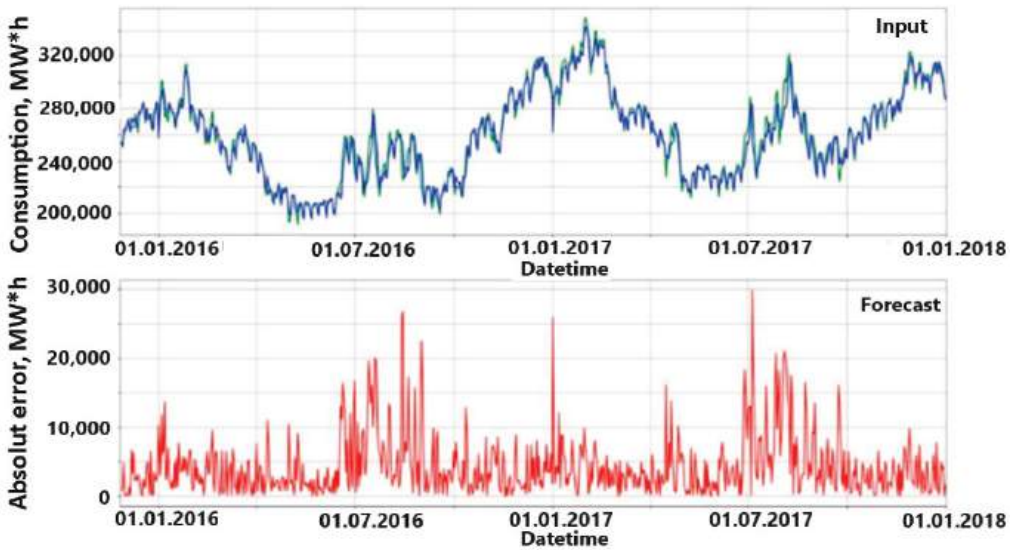


Figure 1. The results of the run on the test dataset for the Southern Federal District.

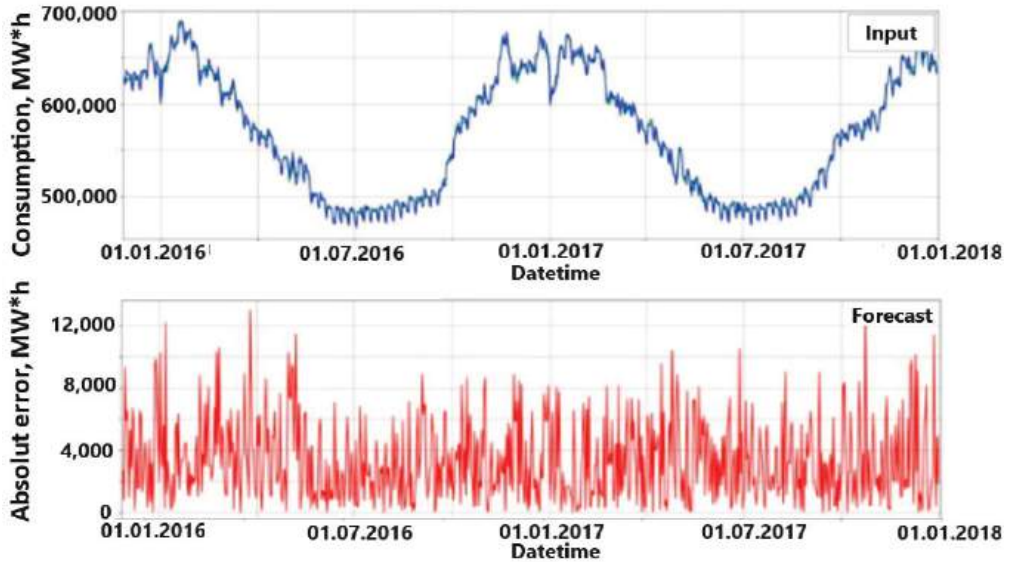


Figure 2. The results of the run on the test dataset for the Siberian Federal District.

8.2. Walrasian model. The Walrasian model [53,54] considers an economy with  $I$  consumers ( $i = 1, \dots, I$ ),  $m$  producers ( $k = 1, \dots, m$ ), and  $n$  types of goods ( $j = 1, \dots, n$ ). The row vector of prices will be denoted through  $p = (p_1, \dots, p_n)$  and the column vector of goods—through  $x = (x_1, \dots, x_n)$ .

Each consumer has income  $K(p)$  and has his own preference field for goods, which can be specified as a utility function  $u(x)$ . If we denote the set of possible sets of goods

available to the consumer at prices  $p$  by  $X(p) = \{x^* : x \in X, px \leq K(p)\}$ ,  $X$  is the domain of definition of  $u(x)$ ; then, the consumer-demand function is given by the following way:

$$\Phi(p) = \begin{cases} x^* : x \in X(p), u(x^*) = \max_{x \in X(p)} u(p) \\ 0, u(x^*) \neq \max_{x \in X(p)} u(p), \end{cases}$$

i.e., the demand function is the set of available goods, each of which maximizes consumer utility at given prices  $p$ . It is assumed that the income of each consumer consists of two parts: the income  $pb_i$  from the sale of the initial stock of goods  $b_i$  and the income  $I_i p$  as a result of the consumer’s participation in production, i.e.,  $K_i(p) = pb_i + I_i p$ .

Each manufacturer (firm) is set by its technological capabilities. Let us denote the input–output column vector of the  $k$ -th producer by  $y_k = (y_{k1}, \dots, y_{kn})$ : the positive components of this vector define the firm’s output; the negative components define the costs. Therefore, the dot product  $py_k$  represents the profit of the firm. The technological capabilities of a firm are defined as the set of admissible input–output vectors  $Y_k$ . This set is called the production possibilities set.

The distribution of production is carried out by choosing the input–output vector  $y_k$  from the technological set of production possibilities  $Y_k$  for each producer  $k = 1, \dots, m$ . The sum  $Y = \sum_{k=1}^m y_k$  represents the overall production process. Distribution of consumption is carried out by choosing a consumption menu  $x_i \in X_i, i = 1, \dots, l$  by each consumer. The sum  $x = \sum_{i=1}^l x_i$  is a vector of aggregate demand, some components of which may be negative if they represent supply (for example, labor).

The joint distribution of production and consumption is understood as such a set of consumption vectors and input–output vectors  $(x_1, \dots, x_l, \dots, x_l, y_1, \dots, y_k, \dots, y_m)$ ,  $x_i \in X_i, y_k \in Y_k$ , for which the aggregate demand matches the total offer:

$$x = \sum_{i=1}^l x_i = b + \sum_{k=1}^m y_k = b + y.$$

The set  $(x_1^*, \dots, x_l^*, \dots, x_l^*, y_1^*, \dots, y_k^*, \dots, y_m^*, p^*)$  defines a competitive equilibrium in the Walrasian model if

$$x_i^* \in \Phi_i(p^*), i = 1, \dots, l, y_k^* \in \psi_k(p^*), k = 1, \dots, m,$$

$$\sum_{k=1}^m y_k^* + b \geq \sum_{i=1}^l x_i^*,$$

$$p \left( \sum_{k=1}^m y_k^* + b \right) = p^* \sum_{i=1}^l x_i^*.$$

In this case,  $p^*$  is called the vector of competitive prices, and the last two equations are called the Walras’s law.

Conclusion: The above mathematical models are of great practical importance in the processes of establishing an equilibrium price in the interactions of consumers and producers.

Despite the fact that most of the considered mathematical models of macroeconomics and microeconomics were developed relatively long ago, at the beginning and in the middle of the last century, they have not lost their relevance to the present day and are widely demanded by practitioners in the study of economic phenomena and processes. This is evidenced by a far from complete list of references cited.

#### 4. Modeling the Regulation of the Economy

Table 3 presents mathematical modeling of regulation of the economy.

**Table 3.** Mathematical modeling of regulation of the economy.

Method	Model	References
9. Mathematical models of market economy	Modeling the labor market	[55,56]
	Modeling the money market	[57,58]
	Financial market models	[59,60]
	Forecasting currency crises and financial risks	[61,62]
10. Modeling inflation	Modeling inflation	[63,64]
	Impact of inflation on production	[65,66]
11. Mathematical models of state regulation of the economy	Taxes in a three-sector economy	[67,68]
	Impact of higher taxes on production and consumption	[69,70]
12. Modeling foreign trade	Model of an open three-sector economy	[41,71]
	Conditions for entering the foreign market	[72,73]
	The golden rule of foreign trade	[74,75]
	The impact of foreign trade on the national economy	[76,77]
13. Modeling the goal of social development	Mathematical theory of public choice	[78,79]
	Models of cooperation and competition	[80,81]
	Simulation of scientific and technological progress	[82,83]

9.1. Modeling the labor market. The labor market is described using three dependencies: demand functions, supply functions, and equilibrium conditions [55,56]. In equilibrium, the marginal product of labor in value terms is equal to the wage rate:

$$p \frac{\partial F}{\partial L} = w,$$

where  $p$ —product price;  $F = F(K, L)$ , wherein  $K$ —funds, and  $L$ —number of employees.

Assuming that all factors of production, except labor, are fixed, we obtain the necessary condition for the maximum profit:

$$\frac{\partial \Pi}{\partial L} = p \frac{\partial F}{\partial L} - w = 0.$$

9.2. Modeling the money market. The theory of demand for money in the classical model is based on the hypothesis that the total demand for money  $M^D$  (is a function directly proportional to money income):

$$M^D = kY_p,$$

$Y_p$ —gross domestic product. Money offer ( $M^S$ ) considered as a fixed, exogenously given, quantity [57].

In this way, the further analysis of a portfolio should be moved from the rather obvious two-dimensional “profitability-risk” analysis to three-dimensional “profitability-reliability—riskiness” analysis. Thus, analyzing the surface from one side, there is a set of guarantees, from another, a set of survival functions. As a result, this surface provides all the information for decisions’ possibility, profitability, reliability, and riskiness levels evaluation. Thus, it becomes clear that an investor is directly interested in two investment features. This is the profitability possibilities and guarantee, or reliability of each possibility,

which is measured in probability  $p$ , that possible profitability  $\xi$  will be not smaller than our selected profitability  $x$ .

$$\bar{F}(x) = P\{\xi \geq x\} p$$

Thus, we can see that an investor, in principle, should fully know the probability distribution of profitability possibilities

$$F(x) = P\{\xi < x\}$$

Often, if the mean value of possibilities and possibilities' variance is given, the probability distribution of these possibilities is also known. However, it is not always the case. Usually, knowing mean value and variance does not allow for describing fully the probability distribution and, in turn, the reliability and survival function

$$\bar{F}(x) = 1 - F(x)$$

Also, and what is especially important, investor's risk usually goes beyond assets and portfolio riskiness and this riskiness is only one of the factors influencing the extent of investor's risk. At that time, reliability of outcome entirely rests on the profitability possibilities distribution function [58].

9.3. Financial market models. Suppose that a loan is provided in the amount of  $S(0)$  with the condition that the amount of  $S(T)$  be returned in time  $T$ . Per unit of loan, the lender will receive a profit:

$$r_T = \frac{S(T) - S(0)}{S(0)}.$$

The value of  $r_T$  is called the efficiency of a financial transaction or the interest rate.

Another indicator of the effectiveness of a financial transaction is the discount—the ratio of profit to the amount returned:

$$d_T = \frac{S(T) - S(0)}{S(T)}.$$

These values are in the following ratios:

$$r_T = \frac{d_T}{1 - d_T}.$$

If we consider the flow of payments from the standpoint of one of the participants, then the result of such a distributed operation can be measured by bringing all payments to the initial point in time. This value is called net present value:

$$NPV = \sum_{k=1}^N S_k \frac{1}{(1+r)^{t_k}},$$

where  $S_k$ —payments on the interval  $[1,N]$ ;  $r$ —discount rate; and  $t_k$ —time of payment.

Consider the problem of optimizing a portfolio of securities. Let there be  $n$  types of securities from which the investor forms a portfolio. These papers are characterized by efficiency  $R_1, R_2, \dots, R_n$ , which are random variables with known mathematical expectations  $MR = m_i$  and the known covariance matrix  $B = \|cov(R_i, R_j)\|$ , in particular  $cov(R_i, R_j) = DR_i = \sigma_i^2$ .

If the investor has distributed his capital in shares  $\Theta_i$ ,  $0 \leq \Theta_i \leq 1$ ,  $\sum_{i=1}^n \Theta_i = 1$ , into different securities, then the efficiency of the formed portfolio

$$R_p = \sum_{i=1}^n \Theta_i R_i,$$

Moreover, this random efficiency has the following mathematical expectation and variance:

$$MR_p = M\left(\sum_{i=1}^n \Theta_i R_i\right) = \sum_{i=1}^n \Theta_i MR_i = \sum_{i=1}^n \Theta_i m_i,$$

$$\sigma_p^2 = DR_p = D\left(\sum_{i=1}^n \Theta_i R_i\right) = cov\left(\sum_{i=1}^n \Theta_i R_i, \sum_{j=1}^n \Theta_j R_j\right) = \sum_{i=1}^n \sum_{j=1}^n \Theta_i \Theta_j cov(R_i, R_j).$$

Distribution  $(\Theta_1, \dots, \Theta_n), 0 \leq \Theta_i \leq 1, \sum_{i=1}^n \Theta_i = 1$  is called the portfolio structure. As a result, we obtain the following task of optimizing a portfolio of securities:

$$\begin{aligned} \min \sum_{i=1}^n b_{ij} \Theta_i \Theta_j, & \quad b_{ij} = cov(R_i, R_j), \\ & \quad \sum_{i=1}^n \Theta_i = 1, \\ & \quad \sum_{i=1}^n m_i \Theta_i = m_p, \\ & \quad \Theta_1 \geq 0, \dots, \Theta_n \geq 0, \end{aligned}$$

where  $m_p$  – the value of the average portfolio efficiency chosen by the investor.

This is the problem of minimizing a quadratic form in  $n$  variables  $\Theta_1, \dots, \Theta_n$ , related by two relations

$$\sum_{i=1}^n \Theta_i = 1, \sum_{i=1}^n m_i \Theta_i = m_p,$$

as well as conditions  $\Theta_i \geq 0, i = 1, \dots, n$ , i.e., a Markowitz quadratic programming problem. Its solution using the Lagrange function in mathematical economics is known [59,60].

9.4. Forecasting currency crises and financial risks. The following probabilistic model can be used to predict the logarithmic gain (per day) of financial assets:

$$\begin{aligned} \delta_t &= \zeta_t + \zeta_t^n, \quad t = 0, 1, \dots, \\ \zeta_t &= \mu + \sigma_t \varepsilon_t, \quad \zeta_t^n = \eta_t J_t, \\ \ln \sigma_t^2 &= a_0 + a_1 \ln \sigma_{t-1}^2 + a_2 \left| \frac{\varepsilon_{t-1}}{\sigma_{t-1}} \right| + a_3 \frac{\varepsilon_{t-1}}{\sigma_{t-1}} + \zeta_t, \\ \varepsilon_t &\sim N(0, 1), \quad cov(\varepsilon_t, \varepsilon_{t'}) = 0 \text{ при } t \neq t', \quad \eta_t = \begin{pmatrix} 0 & 1 \\ 1-p & p \end{pmatrix}, \\ J_t &\sim N(y, \gamma), \quad M \zeta_t = 0. \end{aligned}$$

According to this model, the logarithmic profit has two components: regular  $\zeta_t$ , generated by “long money”, and jumping  $\zeta_t^n$ , generated by “short money”.

In the regular component, the average is close to zero  $\mu \approx 0$ ; the standard deviation  $\sigma_t$  is determined from the statistical ratio established from the past data, while  $\varepsilon_t, t = 0, 1, 2, \dots$ , is a sequence of uncorrelated standard normal values. Thus, the regular component is a mixture of normal distributions.

At any time  $t$ , with a probability of  $1 - p$ , the jump component does not appear and, with a probability  $p$ , there is a jump in the average value  $y$  with a standard deviation  $\gamma$ .

Model parameters  $\mu, a_0, a_1, a_2, a_3, p, y, \gamma$  are determined using the maximum likelihood method and other mathematical and statistical methods based on actual data:  $\mu, a_0, a_1, a_2, a_3$  – by time series  $\gamma_t, \sigma_t, t = 1, T$ ;  $p, \Theta, \gamma$  – over a subset of time points  $\hat{T}$ , in which the jumps took place, according to the following formulas:

$$\hat{p} = \frac{T^t}{T}, \hat{y} = \frac{1}{T^t} \sum_{i \in \hat{T}} \Theta_i, \hat{y}^2 = \frac{1}{T^t - 1} \sum_{i \in \hat{T}} (\Theta_i - \hat{\Theta})^2,$$

where  $T^t$ —the number of time points at which the jumps took place. If, at time  $t$ , the portfolio is formed  $V = V_t$  out of  $n$  assets  $\left(\Theta_i = \frac{V_i}{V}, \sum_{i=1}^n V_i = V\right)$ , then the logarithmic profit of the portfolio at the next moment of time will be equal to

$$\delta_{i+1} = \sum_{i=1}^n \Theta_i \delta_{i+1}^i,$$

where  $\delta_{i+1}^i$ —predicted value of the logarithmic profit of the  $i$ -th asset.

The potential amount of loss is considered as a risk  $L_{i+1}$ , the corresponding quantile  $K_q$ , corresponding to the probability  $q$  :

$$\begin{aligned} L_{i+1} &= -V_i K_q \sqrt{\Theta \Sigma \Theta'} > 0, \\ P\{\delta_{i+1}^i < K_q\} &= q, K_q < 0, \end{aligned}$$

where  $\Theta = (\Theta_0, \dots, \Theta_n)$ —portfolio structure vector;  $\Sigma$ —covariance matrix of logarithmic asset returns [61,62].

Conclusion: At the conceptual level, a comparison was made between the monetarist and Keynesian approaches to forecasting and regulating the market economy in the context of the segments of the economy: labor, monetary and financial, and credit. The model for forecasting financial risks and currency crises is given.

10.1. Modeling inflation. Consider three common generalized autoregressive conditional heteroscedasticity (GARCH) models that are employed to model inflation uncertainty. First, consider a standard one, namely the GARCH model (referred to as GARCH hereinafter):

$$\begin{aligned} \pi_t &= \alpha + \epsilon_t, \epsilon_t \sim N(0, \sigma_t^2) \\ \sigma_t^2 &= \beta + \gamma \sigma_{t-1}^2 + \delta \epsilon_{t-1}^2, \end{aligned}$$

where  $\pi_t$  is the inflation rate,  $\sigma_0^2$  is constant, and  $\epsilon_t = 0$ . To make sure the variance process is always stationary, we impose the restriction  $\gamma + \delta < 1$ . It can be clearly seen that the conditional variance  $\sigma_t^2$  representing a proxy for the inflation volatility is determined by past data and the model parameters.

Another common GARCH model that is widely used in modelling inflation uncertainty is the GARCH-GJR model. The GARCH-GJR model accounts for asymmetric (leverage) effects of positive and negative disturbances on the conditional variance. The conditional variance equation is defined as follows:

$$\sigma_t^2 = \beta + \gamma \sigma_{t-1}^2 + [\delta + \theta 1(\epsilon_{t-1} < 0)] \epsilon_{t-1}^2,$$

where  $1(\cdot)$  denotes an indicator function. The parameter  $\theta$  captures the asymmetric effect: if  $\theta > 0$ , a negative shock would have a greater impact on inflation uncertainty; if  $\theta < 0$ , a negative shock would lower inflation uncertainty; and if  $\theta = 0$ , there is no asymmetric effect documented and, thus, this specification becomes the standard GARCH model.

The last one we consider is the GARCH in mean model (referred to as GARCH-M) which accounts for potential volatility feedback on the inflation rates:

$$\pi_t = \alpha + \lambda \sigma_t^2 + \epsilon_t; \epsilon_t \sim N(0, \sigma_t^2),$$

$$\sigma_t^2 = \beta + \gamma \sigma_{t-1}^2 + \delta (\pi_{t-1} - \alpha - \lambda \sigma_{t-1}^2)^2.$$

The effect of inflation volatility on inflation itself is captured by the parameter  $\lambda$ : when  $\lambda > 0$ , inflation uncertainty has a positive impact on the inflation rate; when  $\lambda < 0$ , inflation uncertainty has a negative impact on the inflation rate; and when  $\lambda = 0$ , inflation

uncertainty has no impact on the inflation rate and, thus, this specification reduces to the standard GARCH model [63,64].

10.2. Impact of inflation on production. There are two points of view regarding the impact of inflation on production. Keynesians believe that controlled inflation is the source of growth. Monetarists believe that controlled inflation causes a short-term increase in production, which then stops. Both approaches are based on the premise that the behavior of prices lags somewhat behind changes in the money supply. Keynesians argue their position from the condition of maximum profit at the national level:

$$p \frac{\partial F}{\partial K} = r,$$

where  $p$ —price level;

$F(K, L)$ —production function of the national economy;

$r$ —a rate of return roughly equal to the interest rate.

If there is more money, then the interest rate must decrease; therefore, the marginal product of capital must decrease  $\frac{\partial F}{\partial K}$ , what is observed with the growth of capital. Thus, a fall in the rate of profit leads to a decrease in the marginal product of capital, which causes an increase in the demand for investment goods and, as a result, production increases and unemployment decreases.

The reasoning of the monetarists is based on the main macroeconomic equation and the pricing equation:

$$\pi - \pi_{-1} = \lambda (y_{-1} - y^E),$$

where  $\pi, \pi_{-1}$ —growth rates of prices (inflation rate) at the current and past points in time;

$$y = \log Y, y^E = \log Y^E,$$

where  $Y^E Y$ ,  $Y^E$ —current and established volumes of GDP.

Let us introduce the notation:

$p = \log P, m = \log M, e = \log Y$ . Then, the main macroeconomic equation can be written as:

$$p = m - y + const.$$

Taking the difference of the last equations at adjacent times, we get:

$$p - p_{-1} = m - m_{-1} - (y - y_{-1})$$

or

$$\pi = \dot{m} - (y - y_{-1}),$$

where  $\pi = (p - p_{-1})$ —the rate of price growth or the rate of inflation;

$m = (m - m_{-1})$ —the growth rate of the money supply.

To study the effect of inflation on production, the following system of equations is considered:

$$\begin{cases} \pi = \pi_{-1} + y - y^E, \\ \pi = \frac{1}{2}(\dot{m} + \pi_{-1} + y - y^E). \end{cases}$$

Steady state  $\dot{m} = 0, y = y_{-1} = y^E, \pi = 0$  [65,66].

Conclusion: The mathematical study of the mechanism of the emergence and self-sustaining of inflation using a three-sector model of the economy is given. The study of inflation is based on the main macroeconomic equation, according to which the supply of money and the demand for them are in dynamic equilibrium.

11.1. Taxes in a three-sector economy. Since the three-sector economy is considered as closed, the gross income of each sector is spent in the following four main areas: for the purchase of materials; for the purchase of investment goods; for the payment of salaries

and bonuses; for the payment of taxes. Therefore, the balances of income and expenditure of the sectors will be written as follows:

$$\begin{aligned} p_0X_0 &= p_0a_0X_0 + p_1s_0X_1 + w_0L_0 + t_0X_0, \\ p_1X_1 &= p_0a_1X_1 + p_1s_1X_1 + w_1L_1 + t_1X_1, \\ p_2X_2 &= p_0a_2X_2 + p_1s_2X_1 + w_2L_2 + t_2X_2, \end{aligned}$$

where  $p_i$ —product price  $i$ -th sector;

$w_i$ —wages with bonuses per one employed in the  $i$ -th sector;

$s_i$ —the share of the  $i$ -th sector in the distribution of products of the fund-creating sector;

$t_i$ —tax rate per unit of output of the  $i$ -th sector.

Using the commodity output of the sectors, we transform the cost balances to the form:

$$\begin{aligned} p_0(1 - a_0)X_0 &= p_1s_0X_1 + w_0L_0 + t_0X_0, \\ p_1(1 - s_1)X_1 &= p_1a_1X_1 + w_1L_1 + t_1X_1, \\ p_2X_2 &= p_0a_2X_2 + p_1s_2X_1 + w_2L_2 + t_2X_2. \end{aligned}$$

Let us add up these balances and move to the left side all the terms containing the prices for the products of the sectors as a multiplier:

$$p_0[(1 - a_0)X_0 - a_1X_1 - a_2X_2] + p_1X_1(1 - s_0 - s_1 - s_2) + p_2X_2 = \sum_{i=0}^2 w_iL_i + \sum_{i=0}^2 t_iX_i.$$

Since there are material and investment balances:

$$\begin{aligned} (1 - a_0)X_0 &= a_1X_1 + a_2X_2, \\ s_0 + s_1 + s_2 &= 1, \end{aligned}$$

then the coefficients at prices  $p_0, p_1$  are equal to zero; therefore, as a result, we obtain a balance of supply and demand for commodities [67,68]:

$$p_2X_2 = \sum_{i=0}^2 w_iL_i + \sum_{i=0}^2 t_iX_i.$$

11.2. Impact of higher taxes on production and consumption. In a closed economy, the only source of consumption is the own production of consumer goods. Therefore, it is the behavior of specific outputs of sectors that determines consumption.

The regulatory impact of the state is to change tax rates in all three sectors of the economy:  $dt_0, dt_1, dt_2$ . The direct impact of this impact is presented in the form of a pseudo-increment in the tax burden:

$$d\hat{t}^p = \sum_{i=0}^2 x_i dt_i.$$

There will be an increase in taxes if the pseudo increment is positive:  $d\hat{t}^p > 0$ . In particular, this situation includes the usual increase in taxes in the sectors of the economy:  $dt_0 > 0, dt_1 > 0, dt_2 > 0$ .

Since  $v > 0, d\hat{t}^p > 0$ , then the sign of  $ds_2$  is determined by the sign of the expression

$$\hat{v}(s_2) = \sum_{i=0}^2 a_i v_i(s_2) t_i x_i(s_2),$$

wherein  $\hat{v}(0) = 0, \hat{v}(1) = 0$  and, of the three terms of the last sum, only the last can be negative for  $s_2 < s_2^*$ , so for  $s_2 > s_2^* \hat{v}(s_2) > 0$ .

When studying the sign  $\hat{v}(s_2)$  for  $0 < s_2 < s_2^*$ , the following circumstances must be taken into account:  $s_2$  all functions  $v_i(s_2)$  are growing and  $v_2(s_2) < 0$ ,  $s_2 < s_2^*$ ,  $v_2(s_2^*) = 0$ ; specific output  $x_0(s_2)$  at  $s_1^0 > a_1$  first increases, then reaches a maximum at  $s_2 = \hat{s}_2^*$ , after which it decreases and  $x_2(s_2)$  is growing. Therefore, near  $s_2 = 0$ , generally speaking, it is possible  $\hat{v}(s_2) < 0$ . However, in most cases of practical interest,  $s_2$  differs significantly from zero, since the situation  $s_2 = 0$  is “production for production”; so  $\hat{v}(s_2) > 0$  at  $s_2 > \underline{s}_2$  ( $\hat{v}(\underline{s}_2) = 0$ ).

At  $\hat{v} > 0$ , tax increase  $\left(\sum_{i=0}^2 x_i dt_i > 0\right)$  leads to the overflow of investment resources into the consumer sector ( $ds_2 > 0$ ); so, when  $s_2 < \hat{s}_2^*$ , this has the effect of increasing the production of consumer goods and at  $s_2 > \hat{s}_2^*$ —reduction in production.

The production of investment goods is reduced with an increase in taxes since the overflow of investment resources into the consumer sector ( $ds_2 > 0$ ) occurs primarily at the expense of the fund-creating sector  $\left(\frac{ds_1}{s_1} = -\frac{q_1}{q_2} \cdot \frac{ds_2}{s_2}; q_1 > 0, q_2 > 0\right)$ . Production of materials at  $s_2 > \hat{s}_2^*$  is also declining, although the tax burden on capital-goods sectors may be reduced.

The situation of “redistribution of the tax burden” is characterized by equality:

$$(x_0 dt_0 + t_0 dx_0) + (x_1 dt_1 + t_1 dx_1) + (x_2 dt_2 + t_2 dx_2) = 0,$$

in which each of the brackets is the actual change in the tax burden on the corresponding sector [69,70].

Conclusion: The fiscal function of taxes consists in the tax burden, determined by the state’s expenses for its functions. Mathematical models provide a search for the optimal tax burden for business entities.

12.1. Model of an open three-sector economy. When forming the model of an open three-sector economy, the following changes are introduced into the model of a closed three-sector model of the economy:

- in the income part of the investment balance, the term  $Y_1$  is added—the import of investment goods;
- in the expenditure part of the material balance, the term  $Y_0$  is added—the export of materials;
- on the consumer market, along with its own production  $X_2$ , imports of consumer goods  $Y_2$  are added;
- finally, the foreign trade balance is added.

As a result, the model of an open three-sector economy takes the following form.

The technological structure is in the form of linearly homogeneous production functions:

$$X_i = F_i(K_i, L_i), \quad i = 0, 1, 2.$$

Dynamics of the total number of employees:

$$L = L(0)e^{vt}.$$

Dynamics of sectors of fixed production assets:

$$\frac{dK_i}{dt} = -\mu K_i + I_i, \quad K_i = K_i(0), \quad i = 0, 1, 2.$$

Labor balance:

$$L = L_0 + L_1 + L_2.$$

Investment balance:

$$X_1 + Y_1 = I_0 + I_1 + I_2.$$

Material balance:

$$(1 - a_0)X_0 = a_1X_1 + a_2X_2 + Y_0.$$

Foreign trade balance:

$$q_0Y_0 = q_1Y_1 + q_2Y_2,$$

where  $q_0, q_1, q_2$ —world prices for products of the material, capital creating, and consumer sectors.

We introduce the following relative indicators:

$\theta_i = \frac{L_i}{L}$ ,  $s_i = \frac{I_i}{X_i + Y_i}$ —shares of the  $i$ -th sector in the distribution of labor and investment resources;

$f_i(k_i) = \frac{F_i(K_i, L_i)}{L_i}$ —industry productivity of the  $i$ -th sector;

$x_i = \frac{X_i}{L}$ —economic productivity of the  $i$ -th sector;

$k_i = \frac{K_i}{L_i}$ —capital–labor ratio of one employed in the  $i$ -th sector;

$y_0 = \frac{Y_0}{L}$ —net export of materials per employee;

$y_1 = \frac{Y_1}{L}$ —net import of investment goods per employee;

$y_2 = \frac{Y_2}{L}$ —net imports of consumer goods per employee.

Then the model of an open three-sector economy in relative terms will be written as follows:

$$\begin{aligned} x_i &= \theta_i f_i(k_i), \quad i = 0, 1, 2; \\ \frac{dk_i}{dt} &= -\lambda_i k_i + \frac{s_i}{\theta_i} (x_1 + y_1), \quad \lambda_i = \mu_i + v; \\ k_i(0) &= \frac{K_i(0)}{\theta_i L(0)}, \quad i = 0, 1, 2; \\ \theta_0 + \theta_1 + \theta_2 &= 1, \quad \theta_i \geq 0, \quad i = 0, 1, 2; \\ s_0 + s_1 + s_2 &= 1, \quad s_i \geq 0, \quad i = 0, 1, 2; \\ (1 - a_0)x_0 &= a_1x_1 + a_2x_2 + y_0, \quad y_0 \geq 0; \\ q_0y_0 &= q_1y_1 + q_2y_2, \quad y_1 \geq 0, \quad y_2 \geq 0. \end{aligned}$$

In the given notation of the model, internal cost balances are not considered, since their form depends on the type of behavior of the sectors, whether they act in cooperation or compete with each other [41,71].

12.2. Conditions for entering the foreign market. The expediency of the entry of the national economy into the world market is possible under the following options: without changing the existing distribution of resources, i.e., only by regulating the components of foreign trade and with a change in the existing distribution of resources. Both options are possible if the economy is in a state of autarky, i.e., when the volume of foreign trade is small. From a mathematical point of view, this means that it is possible to linearize nonlinear dependencies by discarding quadratic terms and terms of a higher order (with respect to  $y_i$ ,  $i = 0, 1, 2$ ).

Since  $y_0, y_2$  enter the model in a linear way, it is necessary to linearize only the specific outputs of sectors that depend on  $y_i$  nonlinearly.

When the national economy enters the world market without changing the existing distribution of resources, i.e., with constant  $\theta_i, s_i$ , the specific outputs of the sectors will be:

$$x_1 = x_1^0 + \frac{\alpha_1 y_1}{(1 - \alpha_1)}, \quad x_i = x_i^0 + \frac{\alpha_i x_i^0 y_1}{(1 - \alpha_1)x_1^0}, \quad i = 0, 2.$$

Let us substitute the last expression into the material balance equation:

$$(1 - a_0) \left[ x_0^0 + \frac{\alpha_0 x_0^0 y_1}{(1 - \alpha_1)x_1^0} \right] = a_1 \left[ x_1^0 + \frac{\alpha_1 y_1}{(1 - \alpha_1)} \right] + a_2 \left[ x_2^0 + \frac{\alpha_2 x_2^0 y_1}{(1 - \alpha_1)x_1^0} \right] + y_0,$$

but in a state of autarky  $(1 - a_0)x_0^0 = a_1x_1^0 + a_2x_2^0$ , therefore,

$$y_0 = \frac{y_1}{(1 - \alpha_1)x_1^0} \left[ \alpha_0(1 - a_0)x_0^0 - \alpha_1a_1x_1^0 - \alpha_2a_2x_2^0 \right].$$

Since  $\alpha_0 < \alpha_1$ ,  $\alpha_0 < \alpha_2$ , then the expression in square brackets is negative, so  $y_0 < 0$ , i.e., a small import of machinery and equipment in the amount  $y_i$  cannot be compensated by the corresponding export of materials. Thus, the entry of a resource-based national economy into the world market strengthens its focus on raw materials, since it requires the transfer of additional resources to the material sector.

For the expediency of foreign trade according to the second option, the following two conditions must be met:

$a_1q_0 \geq (1 + \gamma)q_1$  (the cost of selling materials needed to produce a unit of investment goods is not less than the cost of acquiring such a unit with a load  $\gamma$ );

$$\frac{\alpha_0 + b_0/b_1}{\alpha_1} > \delta_2.$$

These two conditions, which ensure  $dx_1 + dy_1 > 0$ , are quite strict, especially the second condition, according to which the shares of labor and investment resources  $(\theta_1, s_1)$  directed to the fund-creating sector should be as follows:

$$(1 - \alpha_0)\theta_1 \geq \alpha_0\theta_0, (1 - \alpha_1)s_1 \geq \alpha_1s_0,$$

i.e., much higher than observed values in the real economy. Therefore, the first option is more appropriate [72,73].

12.3. The golden rule of foreign trade. The “golden rule of foreign trade” is understood as such a choice of structural and foreign trade parameters  $(\theta, s, y)$ , in which all balances and specific consumption are met to the maximum. Specific consumption is formed as the sum of domestic production and imports of consumer goods per employee. The problem is posed and solved in a stationary state and in specific indicators.

The model of an open three-sector economy in a stationary state, with Cobb–Douglas production functions and in specific indicators, is written as follows.

Economic productivity of sectors:

$$x_i = B_i\theta_i^{1-\alpha_i}s_i^{\alpha_i}y_i^{\alpha_i}(x_1 + y_1)^{a_i}, B_i = A_i\lambda_i^{-a_i}, i = 0, 1, 2.$$

Labor balance:

$$\theta_0 + \theta_1 + \theta_2 = 1, \theta_i \geq 0.$$

Investment balance:

$$s_0 + s_1 + s_2 = 1, s_i \geq 0.$$

Material balance:

$$(1 - a_0)x_0 = a_1x_1 + a_2x_2 + y_0, y_0 \geq 0.$$

Foreign trade balance:

$$q_0y_0 = q_1y_1 + q_2y_2,$$

where  $y_0$ —specific export of materials;

$y_1, y_2$ —specific import of investment and consumer goods;

$q_0, q_1, q_2$ —world market prices for materials, investment, and consumer goods;

$a_0, a_1, a_2$ —coefficients of direct material costs of the material, fund creating, and consumer sectors.

In this model, endogenous variables (i.e., determined by means of the model) are  $(\theta, s, y) = (\theta_0, \theta_1, \theta_2, s_0, s_1, s_2, y_0, y_1, y_2)$ . These nine endogenous variables are linked by

four balance ratios (labor, investment, material, and foreign trade), so there are five degrees of freedom in their change. These degrees of freedom can be used to select the endogenous variables to maximize the specific consumption  $c(\theta, s, y) = x_2(\theta, s, y) + y_2$ .

Thus, we arrive at the following nonlinear programming problem:

$$\max_{(\theta, s, y)} \left[ B_2 \theta_2^{1-a_2} s_2^{a_2} (x_1 + y_1)^{a_2} + y_2 \right]$$

when fulfilling the restrictions set by labor, investment, material, and foreign trade, in which  $x_i = x_i(\theta, s, y)$  are given by the ratios indicated in the national economic productivity of the sectors.

By introducing five free variables (according to the number of degrees of freedom), the problem of nonlinear programming is reduced to the problem of finding the unconditional maximum of a function of five variables. In connection with the leading role of investments in the development of the economy, it is reasonable to include  $\theta_i, s_i$ , and  $y_i$  among the free variables.

If the shares of resources  $\theta_1, s_1$  directed to the fund-creating sector are set, then when the specified restrictions are met, the material and consumer sectors are left with  $(1 - \theta_1)$  labor and  $(1 - s_1)$  investment resources. Let us introduce variables  $h, i$ , characterizing the distribution of these residual resources between the material and consumer sectors:

$$\begin{aligned} \theta_0 &= (1 - lh)(1 - \theta_1), \quad \theta_2 = lh(1 - \theta_1), \\ s_0 &= (1 - h)(1 - s_1), \quad s_2 = h(1 - s_1), \end{aligned}$$

where  $lh, h$  are the share of the consumer sector in the distribution of labor and investment resources inherited by the material and consumer sectors and  $l$  can be interpreted as the relative labor supply of investment resources directed to the consumer sector.

For any  $l, h(0 \leq h \leq 1)$ , the distribution of resources determined by them satisfies the labor and investment balances, while the specific outputs of the material and consumer sectors are transformed to the form [74,75]:

$$\begin{aligned} x_0 &= B_0 (1 - lh)^{1-a_0} (1 - h)^{a_0} (1 - \theta_1)^{1-a_0} (1 - s_1)^{a_0} (x_1 + y_1)^{a_0}, \\ x_2 &= B_2 l^{1-a_2} h (1 - \theta_1)^{1-a_2} (1 - s_1)^{a_2} (x_1 + y_1)^{a_2}. \end{aligned}$$

12.4. The impact of foreign trade on the national economy. Consider a situation where the national economy is already integrated into the world market. With  $\theta_1 = s_1$ , the specific outputs of the sectors will take the form:

$$\begin{aligned} x_0 &= B_0 (1 - h)(1 - s_1)(x_1 + y_1)^{a_0}, \\ x_1 &= B_1 x_1 (x_1 + y_1)^{a_1}, \\ x_2 &= B_2 h(1 - s_1)(x_1 + y_1)^{a_2}. \end{aligned}$$

Let the specific import of machinery and equipment increase by  $dy_1$ ; then (with the same import of consumer goods), the specific export of raw materials and other materials must increase by a certain amount  $dy_0$  in order to compensate for the increase in import, while, according to the foreign trade balance:

$$q_0 dy_0 = q_1 dy_1.$$

If the country adheres to the policy of industrial security, then an increase in the output of materials can only be achieved by transferring resources from the consumer sector to the material sector while maintaining the share of the fund-creating sector in the distribution of resources (the first option). If the economy is sufficiently industrialized, then the growth in the output of materials can also be achieved by reducing the share of the fund-creating sector in the distribution of resources (second option). A combination of these two structural policy options is also possible [76,77].

Conclusion: With a given technological mode, based on the criterion of maximizing stationary specific consumption, it is advisable for countries with an underdeveloped manufacturing industry to export as much raw materials and materials as the technological capabilities of the material sector allow. For countries with a sufficiently developed manufacturing industry, there is a critical level of export of raw materials, which it is not advisable to exceed.

13.1. Mathematical theory of public choice. There are many approaches to establishing a public-choice criterion. One of these is the determination of the economic optimum according to Pareto. The Pareto optimal is understood as such a state of the economy in which an acceptable redistribution of products and costs is impossible, leading to an increase in the utility of some without reducing the utility of others.

Consider the public-choice problem in the following aggregated form: there are two types of resources, two types of goods, two types of consumers. For definiteness, by resources we will understand the main production assets  $K$  and the number of employees  $L$ , by goods: food products  $X_i$  and nonfood products  $Y_i$ ; by consumers, two large social divisions that together make up the whole society. These divisions differ in their product preferences. Each of the two goods is produced by its own sector of the economy with its own neoclassical production function:

$$X_i = F_i(K_i, L_i), \quad i = 1, 2,$$

it is assumed that the sector of the economy that produces this type of product includes all industries, subsectors, and industries that not only produce goods of this type but also ensure their release.

It is assumed that funds and labor can move freely between the food and nonfood sectors, in accordance with the available resources  $K, L$ :

$$\begin{aligned} K_1 + K_2 &= K, \\ L_1 + L_2 &= L. \end{aligned}$$

The overall picture of the output of goods and the distribution of resources can be depicted on the production Edgeworth–Bowley diagram (Figure 3). The rectangle  $O_1LO_2K$ , whose side lengths correspond to the availability of resources, can be called a resource allocation rectangle for this reason. Each of its points has coordinates  $(K_1, L_1)$  in the first coordinate system and coordinates  $(K_2, L_2)$  in the second coordinate system. Since the lengths of the sides of the rectangle are  $K, L$ , then, at any of its points, balances of resource consumption are performed.

Thus, each point of the resource allocation rectangle is characterized by six indicators:

$$(K_1, L_1, K_2, L_2, X_1, X_2),$$

and

$$K_1 + K_2 = K, \quad L_1 + L_2 = L, \quad X_1 = F_1(K_1, L_1), \quad X_2 = F_2(K_2, L_2).$$

Since the production functions of the sectors are neoclassical, their isoquants are convex functions (each in its own coordinate system). When viewed on an Edgeworth–Bowley diagram, the isoquants of the first function remain convex, while the isoquants of the second function in the  $O_1$  coordinate system become concave. Therefore, each specific isoquant of the first function can be in the following relationship with a specific isoquant of the second function:

- do not intersect at any point;
- intersect at two points;
- touch.

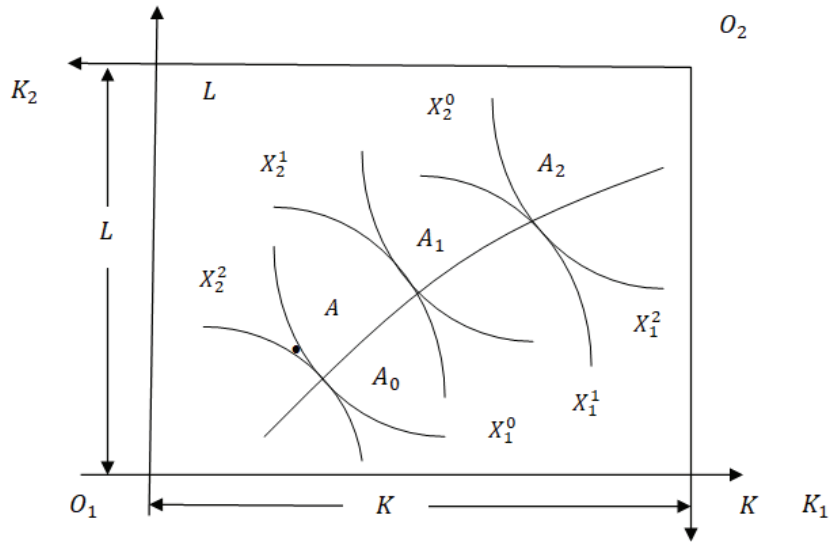


Figure 3. Resource allocation rectangle.

Curve  $A_0A_1A_2$ , composed of points of contact isoquant sectors, is called the production curve. All points of this curve characterize such states of the economy when more than any one product cannot be produced without reducing the production of another product. Thus, all points on this curve are Pareto optimal.

From the condition of contact of isoquants at some point  $(K_1, L_1, K_2, L_2, X_1, X_2)$ , it follows that  $gradF_1(K_1, L_1)$  is collinear with  $gradF_2(K_2, L_2)$ :

$$S_K^1(L_1, K_1) = \frac{\frac{\partial F_1}{\partial L_1}(K_1, L_1)}{\frac{\partial F_1}{\partial K_1}(K_1, L_1)} = \frac{\frac{\partial F_2}{\partial L_2}(K_2, L_2)}{\frac{\partial F_2}{\partial K_2}(K_2, L_2)} = S_K^2(L_2, K_2),$$

i.e., on the production curve, the marginal rates of replacement of sectoral resources are equal [78,79].

13.2. Models of cooperation and competition. Consider, for simplicity, a cooperation and competition model for only two persons with a finite number of strategies for each player:  $G = \{M, N; A, B\}$  where  $M = \{1, \dots, m\}; N = \{1, \dots, n\}$  are sets of strategies for the first and second players,  $A = \|a_{ij}\|; B = \|b_{ij}\|$  are payoff functions of the first and second players.

The basis of such a bimatrix (including cooperative) game is the bimatrix:

$$(A, B) = (a_{ij}, b_{ij}),$$

where  $a_{ij}$ —the payoff of the first player, when the first player uses the pure strategy  $i$ , and the second player uses the pure strategy  $j, i = 1, \dots, m, j = 1, \dots, n; b_{ij}$ —the payoff of the second player under the same conditions.

If  $b_{ij} = -a_{ij}$ , then we come to the usual game of two persons with zero sum.

In addition to pure strategies, mixed ones are considered:

$$p = (p_1, \dots, p_m), q = (q_1, \dots, q_n),$$

where  $p_i$ —the probability of the first player using the  $i$ -th strategy,  $i = 1, \dots, m; q_j$ —the probability of the second player using the  $j$ -th strategy,  $j = 1, \dots, n$ .

When players use mixed strategies  $p, q$  their average payoffs are respectively equal to

$$u_1(p, q) = \sum_{i,j} a_{ij} p_i q_j, \quad u_2(p, q) = \sum_{i,j} b_{ij} p_i q_j.$$

Exodus  $(p^*, q^*)$  is called Pareto optimal if for any  $p, q$

$$u_1(p^*, q^*) \geq u_1(p, q^*), \quad u_2(p^*, q^*) \geq u_2(p, q).$$

Exodus  $(p, q)$  dominates the outcome  $(p', q')$  if

$$u_i(p', q') \leq u_i(p, q), \quad i = 1, 2.$$

A strategy is called maximin if it provides the player with the maximum of the minimum payoffs (guaranteed payoff)

$$v_1 = \max_p \min_q u_1(p, q),$$

$$v_2 = \max_q \min_p u_2(p, q).$$

A bimatrix game in which negotiations between participants are not allowed is called noncooperative. In such a game, it is preferable for each player to adhere to a cautious (maximum) strategy that provides a guaranteed win. On the contrary, a matrix game is called cooperative if negotiations and joint actions of participants are allowed in it.

The solution of a cooperative game is reduced to finding the optimal, in a certain sense, joint strategy  $P^*$  among joint strategies:

$$P = \|p_{ij}\|, \quad \sum_{i,j} p_{ij} = 1, \quad p_{ij} \geq 0,$$

$$u_1(P) = \sum_{i,j} a_{ij} p_{ij}, \quad u_2(P) = \sum_{i,j} b_{ij} p_{ij}.$$

It should be noted that the desired joint strategy  $P = \|p_{ij}\|, \sum_{i,j} p_{ij} = 1$  can be obtained, for example, as a result of the following joint actions of players:

$$p_i = \sum_{j=1}^n p_{ij}, \quad i = 1, \dots, m, \quad q_j(i) = \frac{p_{ij}}{p_i}, \quad j = 1, \dots, n.$$

The whole set of joint strategies  $P$  forms a convex hull of points  $(a_{ij}, b_{ij}), i = 1, \dots, n$  on surface  $(u_1, u_2)$ . A point  $(u_1, u_2)$  dominates a point  $(\tilde{u}_1, \tilde{u}_2)$  if  $u_1 \geq \tilde{u}_1, u_2 \geq \tilde{u}_2$ . A subset of points in a convex hull is Pareto optimal if none of them dominates the other. This subset is called the negotiation set.

The choice of a certain point among the points of the negotiation set is the result of negotiations and compromise between the two players. One way to find such a compromise is the Nash algorithm. According to this algorithm, the optimal point is the point of the negotiation set at which the product of the gain increments of the first and second players reaches its maximum. This product is called the Nash function:

$$\max(u_1 - v_1)(u_2 - v_2),$$

$$(u_1, u_2) \in T.$$

This or that compromise choice of a specific point of the negotiation set determines the optimal solution of the corporate game [80,81]

$$(u_1^*, u_2^*), u_1^* = \sum_{i,j} p_{ij}^* a_{ij}, \quad u_2^* = \sum_{i,j} p_{ij}^* b_{ij}.$$

13.3. Simulation of scientific and technological progress. In evolutionary models of scientific and technological progress (STP), the economy is considered as one unstructured whole and is described by a production function with coefficients drifting in time. At the same time, a slow increase in resource productivity as a result of scientific and technical progress is reflected by including an exponent in the coefficient of neutral technical progress:

$$X_t = A_0 e^{\lambda t} K_t^{\alpha_K} L_t^{\alpha_L}, \quad A(t) = A_0 e^{\lambda t},$$

where  $\lambda$ —measure of NTP.

This approach has been developed and differentiated:

1. Labor-increasing progress:

$X_t = F(K_t, L_t^*)$ ,  $L_t^* = A_L(t)L_t$ —how many units of labor would be required if there were no scientific and technical progress;

2. Capital-increasing progress:

$X_t = F(K_t^*, L_t)$ ,  $K_t^* = A_K(t)K_t$ —how many units of funds would be required if there were no scientific and technological progress;

3. Resource-increasing progress:

$$X_t = F(K_t^*, L_t^*), \quad K_t^* = A_K(t)K_t, \quad L_t^* = A_L(t)L_t.$$

4. Product-increasing progress:

$$X_t = A(t)F(K_t, L_t),$$

where  $A(t)$ ,  $A_L(t)$ ,  $A_K(t)$ —some growing functions of time are generally exponents ( $A(t) = e^{\lambda t}$ ).

The use of exponentials when changing the NTP is advisable when the corresponding function  $A(t)$  grows with an approximately constant growth rate  $\lambda$ , then  $A(t) = (1 + \lambda) \approx e^{\lambda t}$ , the latter is true for a small value of  $\lambda$ . This is the case when progress is evolutionary.

Technical progress is called neutral if it does not change the ratio of the values of certain parameters. There is neutrality according to Hicks, Harrod, and Solow.

Progress is Hicks neutral if, for a given capital–labor ratio, the marginal rate of replacement of labor by funds is constant for any output:

$$s_0 = \frac{\frac{\partial X}{\partial L}}{\frac{\partial X}{\partial K}} = \frac{\frac{\partial F}{\partial L^*}}{\frac{\partial F}{\partial K^*}} \cdot \frac{e^{\lambda_L t}}{e^{\lambda_K t}} = \frac{\frac{\partial F}{\partial L^*}}{\frac{\partial F}{\partial K^*}} \text{ at } \lambda_L = \lambda_K;$$

Therefore, Hicks neutrality means that progress is resource increasing with  $\lambda_L = \lambda_K$  or that progress is product increasing.

Progress is Harrod neutral if the marginal product of funds does not change:

$$\frac{\partial X}{\partial K} = \frac{\partial F}{\partial K'}$$

therefore, Harrod’s neutrality means that progress is labor increasing:

$$X = F\left(K, e^{\lambda_L t} L\right).$$

Progress is Solow neutral if the marginal product of labor does not change:

$$\frac{\partial X}{\partial L} = \frac{\partial F}{\partial L'}$$

therefore, Solow neutrality means that progress is capital increasing:

$$X = F(e^{\lambda \kappa t} K, L).$$

The model for changing the technological structure takes into account that the rearmament processes in different production subsystems can take place asynchronously. Let the production functions of the old and new production methods be given:

$$F_0(K, L) = A_0 K_0^{\alpha_0} L_0^{1-\alpha_0}, F_1(K, L) = A_1 K_1^{\alpha_1} L_1^{1-\alpha_1};$$

moreover, at the same costs, the output of the new method is significantly larger than the old one, i.e.,

$$F_1(K, L) \gg F_0(K, L).$$

Let us assume that the retirement rates are the same for the old and new methods, i.e.,  $\mu_0 = \mu_1 = \mu$ . In addition, let us assume that labor resources are also constant, i.e.,  $L(t) = L = const$ , there are no investment lags within each method.

Since the old method has exhausted itself, by the beginning of the rearmament it was already in stationary mode; therefore:

$$k_0 = (A_0 \rho_0 / \mu_0)^{t(1-\alpha_0)}, x_0 = A_0 (k_0)^{\alpha_0}, i_0 = \rho_0 x_0, c_0 = (1 - \rho_0) x_0.$$

We will assume that the investment of the old method in the creation of a new method occurs with a fixed lag  $\tau$ . If the specific consumption can be reduced to the level  $\underline{c}$ ,  $\underline{c} < c_0$ , then the released capacities can be used to produce the means of labor for the new method and, due to the presence of a lag, investments are made at the time  $t - \tau$ ; funds are deposited at time  $t$ , i.e.,  $V(t) = I(t - \tau)$ .

During time  $\tau$ , the total investment will be  $L(c_0 - \underline{c})t$ ,  $t < \tau$ .

The transitional period  $0 < t < T$  is divided into three stages.

Accumulation stage ( $0 < t < \tau$ ). Accumulation occurs due to the reduction of specific consumption to the minimum allowable level. There is no return on investment in the new method yet, so only the old method works:

$$k(t) = k_0, x(t) = x_0, c(t) = \underline{c}, i(t) = c_0 - \underline{c}, I(t) = (c_0 - \underline{c})Lt, V(t) = 0.$$

Stage of return of savings ( $\tau < t < 2\tau$ ). Accumulations of the old method into the new one begin to return and the old method stops accumulating for the new one; therefore  $c_0(\tau) = c_0$ ; in addition, the new method accumulates for itself (without lag):

$$k(t) = \theta_0 k_0 + \theta_1 k_1, x(t) = \theta_0 k_0 + \theta_1 A_1 k_1^{\alpha_1}, c(t) = \theta_0 c_0 + \theta_1 (1 - \rho_1) A_1 k_1^{\alpha_1}, \\ c(t) = \theta_0 c_0 + \theta_1 (1 - \rho_1) A_1 k_1^{\alpha_1},$$

where  $k_1$  – capital–labor ratio adopted for the transitional period of the new method

$$k_0 \leq k_1 \leq k_1^0, k_1^0 = \left[ \frac{\rho_1 A_1}{\mu} \right]^{\frac{1}{1-\alpha_1}}$$

stationary capital–labor ratio of the new method at the rate of accumulation  $\rho_1$ ;  $\theta_1 = \frac{L_1}{L}$ ,  $i = 0, 1$  – the share of the  $i$ -th method in the use of labor resources.

New mode funds satisfy the differential equation

$$\frac{\partial K_1}{\partial t} = -\mu K_1 + \rho_1 A_1 k_1^{\alpha_1} L_1^{1-\alpha_1} + (c_0 - \underline{c})L, K_1(\tau) = 0.$$

Since  $K_1 = k_1 L_1$ , then the last equation goes into the equation

$$\frac{dL_1}{dt} = -\mu L_1 + \rho_1 A_1 k_1^* L_1 + \frac{(c_0 - \underline{c})L}{k_1}, \quad L_1(t) = 0,$$

or

$$\frac{dL_1}{dt} = bL_1 + d, \quad L_1(t) = 0,$$

where  $b = \mu \left[ (k_1^0/k_1)^{1-\alpha_1} - 1 \right]$ ,  $d = \frac{(c_0 - \underline{c})L}{k_1}$ .

The share of the new way in the use of ore resources grows exponentially, starting from  $\theta_1(t) = 0$ . The moment of the end of the transition process  $T$  is determined from the equation  $\theta_1(t) = 1$ , which means the end of the overflow of labor resources into a new way.

At  $T < 2\tau$ , an accelerated transient process takes place, which ends already at the second stage, while:

$$\frac{(c_0 - \underline{c}) \left[ e^{b(T-\tau)} - 1 \right]}{\mu k_1 \left[ (k_1^0/k_1)^{1-\alpha_1} - 1 \right]} = 1,$$

where

$$T = \tau + \frac{\ln \left\{ 1 + \frac{\mu k_1 \left[ (k_1^0/k_1)^{1-\alpha_1} - 1 \right]}{c_0 - \underline{c}} \right\}}{\mu \left[ (k_1^0/k_1)^{1-\alpha_1} - 1 \right]}.$$

If the capital–labor ratio  $k_1$  is close to  $k_1^0$ , or the difference between the initial and the minimum allowable specific consumption  $c_0 - \underline{c}$  is large enough, then the last condition will be written as follows:

$$k_1 < \tau(c_0 - \underline{c}).$$

Otherwise, a slow transient process takes place, which ends at  $T > 2\tau$ , i.e., ends in the third stage.

The equation for funds in this case will take the form:

$$\frac{dK_1}{dt} = -\mu K_1 + \rho_1 A_1 k_1^{\alpha_1} L_1^{1-\alpha_1}, \quad K_1(2\tau) = dk_1 \frac{e^{bt} - 1}{b},$$

or for new way workforce

$$\frac{dL_1}{dt} = bL_1, \quad L_1(2\tau) = d \frac{e^{bt} - 1}{b}.$$

The last equation has the following solution:

$$L_1(t) = d \frac{e^{bt} - 1}{b} e^{(b-2\tau)t} = \frac{(c_0 - \underline{c})L \left( e^{bt} - 1 \right) e^{(b-2\tau)t}}{\mu k_1 \left[ (k_1^0/k_1)^{1-\alpha_1} - 1 \right]},$$

where

$$\theta_1(t) = \frac{(c_0 - \underline{c}) \left( e^{bt} - 1 \right)}{\mu k_1 \left[ (k_1^0/k_1)^{1-\alpha_1} - 1 \right]} e^{(b-2\tau)t}.$$

The condition  $\theta_1(t) = 1$  gives the following expression for the end time of the transient:

$$T = 2\tau + \frac{1}{\delta} \ln \left\{ 1 - \frac{\mu_1 k_1 \left[ (k_1^0/k_1)^{1-\alpha_1} - 1 \right]}{(c_0 - \underline{c}) \left( e^{bt} - 1 \right)} \right\}.$$

After the old method is completely replaced from the time  $t = T$ , the usual transition process begins in the Solow model for the new method from the capital–labor ratio  $k_1(T) = k_1$  to the stationary capital–labor ratio  $k_1^E$  [82,83].

Conclusion: The formalized expression of the goal of social development at the conceptual level comes down to improving the wellbeing of members of society, creating comfortable and safe living conditions, and increasing life expectancy. The socially oriented policy of the state ensures an increase in the birth rate and a decrease in the death rate. In models of optimal economic growth, the Pareto optimality criterion is most often used.

## 5. Conclusions

To date, the most effective methods for studying the economy are methods based on the mathematical apparatus. This is explained by the fact that the economy does not tolerate full-scale experiments and the best methods of indirect study of economic phenomena and processes are mathematical models. Starting with the world's first economic and mathematical model of the social economy, Francois Quesnay, which was published in 1758, the arsenal of mathematical models of the economy has become extremely extensive. Obviously, this review could not describe all the retrospective mathematical methods and models of the economy, but took the main ones, the most frequently used and tested by practice over the last two decades of the current century. The review contains an analysis of articles and a description of some studies in the field of mathematical modeling of macroeconomics, microeconomics, and state regulation of the economy. We hope that this article will be useful to undergraduates, specialists, and graduate students who study economic phenomena using mathematical methods and models.

It is currently difficult to accurately determine the prospect of using the above models. Apparently, in the near future there will be a change in the paradigm of the economy, which will objectively require the development of new conceptual models.

**Author Contributions:** Conceptualization, V.M. and A.A.; Methodology, V.M. and S.A.; Validation, V.M., A.A., and K.O.; Formal Analysis, A.A. and K.O.; Investigation, V.M.; Resources, V.M. and A.A.; Data Collection, V.M. and S.A.; Writing-Original Draft Preparation, V.M.; Writing-Review and Editing, S.A. and A.A.; Visualization, V.M. and S.A.; Supervision, A.A.; Project Administration, S.A. and K.O.; Funding Acquisition, V.M. and K.O. All of the authors contributed significantly to the conception, design, and completion of this review, writing, and improving the paper. All authors have read and agreed to the published version of the manuscript.

**Funding:** This research received no external funding.

**Institutional Review Board Statement:** Not applicable.

**Informed Consent Statement:** Not applicable.

**Data Availability Statement:** There are no data applicable in this study.

**Acknowledgments:** The authors thank South Ural State University (SUSU) for its support.

**Conflicts of Interest:** The authors declare no conflict of interest.

## References

1. Koshkin, G.; Kitayeva, A. Nonparametric identification of static and dynamic production functions. *IAENG Int. J. Appl. Math.* **2011**, *41*, 228–234.
2. Mokhov, V.; Stakhanov, K. Modelling the innovation activity of an enterprise. *Bulletin of the South Ural State University. Ser. Math. Model. Program. Comput. Softw.* **2016**, *9*, 130–134.
3. Guilhoto JJ, M. Input-Output Analysis: Theory and Foundations. *Munich Pers. RePEc Arch.* **2011**, 32566, 72.
4. Akhabbar, A. The Case against “Indirect” Statistical Inference. *Hist. Political Econ.* **2021**, *53* (Suppl. S1), 259–292. [CrossRef]
5. Busato, M.I.; Reif, A.C.; Possas, M.L. Uma tentativa de integração entre Keynes e Kalecki: Investimento e dinâmica. *Braz. J. Political Econ.* **2019**, *39*, 509–526. [CrossRef]
6. Bruun, C. Rediscovering the Economics of Keynes in an Agent-Based Computational Setting. *New Math. Nat. Comput.* **2016**, *12*, 77–96. [CrossRef]
7. Myagotina, E.D.; Tregub, I.V. Application of the Samuelson—Hicks model in the conditions of modern economy Case of Bhutan. *Mezhdunarodnaja Jekonomika World Econ.* **2021**, *5*, 404–413. [CrossRef]
8. Ovchinnikov, A.V. On the Behavior of Solutions of a Modified Samuelson—Hicks Model with Two Accelerators. *J. Math. Sci.* **2016**, *216*, 722–724. [CrossRef]

9. Miernyk, W.H. Leontief and dynamic regional models. In *Wassily Leontief and Input-Output Economics*; Cambridge University Press: Cambridge, UK, 2004; pp. 90–101. [CrossRef]
10. Kurz, H.D.; Salvadori, N. The dynamic Leontief model and the theory of endogenous growth. *Econ. Syst. Res.* **2000**, *12*, 255–265. [CrossRef]
11. Heikkinen, T. A study of degrowth paths based on the von Neumann equilibrium model. *J. Clean. Prod.* **2020**, *251*, 119562. [CrossRef]
12. Detemple, J.; Rindisbacher, M. Dynamic asset allocation: Portfolio decomposition formula and applications. *Rev. Financ. Stud.* **2010**, *23*, 25–100. [CrossRef]
13. Jančařík, A. Dynamic models. In *Proceedings of the European Conference on e-Learning, ECEL*; Academic Conferences Limited: Reading, UK, 2015; pp. 264–271. [CrossRef]
14. Cervinek, O.; Pettermann, H.; Todt, M.; Koutny, D.; Vaverka, O. Non-linear dynamic finite element analysis of micro-strut lattice structures made by laser powder bed fusion. *J. Mater. Res. Technol.* **2022**, *18*, 3684–3699. [CrossRef]
15. Piironen, P.T.; Raghavendra, S. A Nonsmooth Extension of Samuelson’s Multiplier-Accelerator Model. *Int. J. Bifurc. Chaos* **2019**, *29*, 1930027. [CrossRef]
16. Omran, Q.K.; Humood, K.A.; Mahmood, T. A new truncation algorithm of low hardware cost multiplier. *Period. Eng. Nat. Sci.* **2022**, *10*, 188–194. [CrossRef]
17. Dassios, I.K.; Zimbidis, A.A.; Kontzalis, C.P. The Delay Effect in a Stochastic Multiplier–Accelerator Model. *J. Econ. Struct.* **2014**, *3*, 52. [CrossRef]
18. Madaleno, M.; Nathan, M.; Overman, H.; Waights, S. Incubators, accelerators and urban economic development. *Urban Stud.* **2022**, *59*, 281–300. [CrossRef]
19. Grigorenko, N.; Luk’yanova, L. Optimal control and positional controllability in a one-sector economy. *Games* **2021**, *12*, 11. [CrossRef]
20. Long, B.; Zeng, W.; Rodriguez, J.; Guerrero, J.M.; Hu, J.; Chong, K.T. Enhancement of Voltage Regulation Capability for DC-Microgrid Composed by Battery Test System: A Fractional-Order Virtual Inertia Method. *IEEE Trans. Power Electron.* **2022**, *37*, 12538–12551. [CrossRef]
21. Löschenbrand, M. A transmission expansion model for dynamic operation of flexible demand. *Int. J. Electr. Power Energy Syst.* **2021**, *124*, 106252. [CrossRef]
22. Capozzi, B.; Low, J.Z.; Xia, J.; Liu, Z.F.; Neaton, J.B.; Campos, L.M.; Venkataraman, L. Mapping the Transmission Functions of Single-Molecule Junctions. *Nano Lett.* **2016**, *16*, 3949–3954. [CrossRef]
23. Buzsáki, G.; Draguhn, A. Neuronal oscillations in cortical networks. *Science* **2004**, *304*, 1926–1929. [CrossRef] [PubMed]
24. Stryzhnev, A.G.; Shykha, A.A. Methods of reduction of control objects models containing oscillating and forcing links. *Syst. Anal. Appl. Inf. Sci.* **2019**, *1*, 50–57. [CrossRef]
25. Roy, S.; Rana, D. Machine Learning in Nonlinear Dynamical Systems. *Resonance* **2021**, *26*, 953–970. [CrossRef]
26. Nan, G.; Tang, M.; Chen, E.; Yang, A. Nonlinear dynamic mechanism of rolling element bearings with an internal clearance in a rotor-bearing system. *Adv. Mech. Eng.* **2016**, *8*, 1–9. [CrossRef]
27. Mutanov, G. *Mathematical Methods and Models in Economic Planning, Management and Budgeting*; Springer: Berlin/Heidelberg, Germany, 2015. [CrossRef]
28. Farmer, L.E. The discretization filter: A simple way to estimate nonlinear state space models. *Quant. Econ.* **2021**, *12*, 41–76. [CrossRef]
29. Grassetti, F.; Guzowska, M.; Michetti, E. A dynamically consistent discretization method for Goodwin model. *Chaos Solitons Fractals* **2020**, *130*, 109420. [CrossRef]
30. Coşkun, S. Informal employment and business cycles in emerging market economies. *J. Macroecon.* **2022**, *74*, 103452. [CrossRef]
31. Eichmeir, P.; Nachbagauer, K.; Lauß, T.; Sherif, K.; Steiner, W. Time-Optimal Control of Dynamic Systems Regarding Final Constraints. *J. Comput. Nonlinear Dyn.* **2021**, *16*, 031003. [CrossRef]
32. Chen, X.; Zhu, Y. Optimal control for multistage uncertain random dynamic systems with multiple time delays. *ISA Trans.* **2022**, *129*, 171–191. [CrossRef]
33. Arutyunov, A.V.; Karamzin, D.Y.; Pereira, F. Pontryagin’s maximum principle for constrained impulsive control problems. *Nonlinear Anal. Theory Methods Appl.* **2012**, *75*, 1045–1057. [CrossRef]
34. Boscain, U.; Sigalotti, M.; Sugny, D. Introduction to the Pontryagin Maximum Principle for Quantum Optimal Control. *PRX Quantum* **2021**, *2*, 030203. [CrossRef]
35. Brock, W.A.; Taylor, M.S. The Green Solow model. *J. Econ. Growth* **2010**, *15*, 127–153. [CrossRef]
36. Yerznkyan, B.H.; Gataullin, T.M.; Gataullin, S.T. Solow models with linear labor function for industry and enterprise. *Montenegrin J. Econ.* **2021**, *17*, 111–120. [CrossRef]
37. Dombi, M. The golden rule of material stock accumulation. *Environ. Dev.* **2022**, *41*, 100638. [CrossRef]
38. Asch, J.; Bourget, O.; Cortés, V.; Fernandez, C. Energy-Time Uncertainty Principle and Lower Bounds on Sojourn Time. *Ann. Henri Poincaré* **2016**, *17*, 2513–2527. [CrossRef]
39. Mahroji, D.; Indrawati, M. Analisis sektor unggulan dan spesialisasi regional kota bandar lampung. *J. Ekobis Ekon. Bisnis Manaj.* **2020**, *9*, 01–08. [CrossRef]
40. Tognoli, M. A Model for Optimal Economic Lockdown to Contain Epidemic. *J. Econ. Res. Rev.* **2022**, *2*, 133–140.

41. Zhang, W.-B. A Three-Sector Spatial Growth Model of a Small Open Economy with Capital Accumulation. *J. Econ. Integr.* **2009**, *24*, 248–274. [CrossRef]
42. Kislitsyn, E.V.; Gorodnichev, V.V. Simulation of development of individual heavy industry sectors. *Bus. Inform.* **2021**, *15*, 59–77. [CrossRef]
43. Li, S.; Chen, R.; Yang, L.; Huang, D.; Huang, S. Predictive modeling of consumer color preference: Using retail data and merchandise images. *J. Forecast.* **2020**, *39*, 1305–1323. [CrossRef]
44. Sepúlveda, W.S.; Maza, M.T.; Uldemolins, P.; Cantos-Zambrano, E.G.; Ureta, I. Linking Dark Chocolate Product Attributes, Consumer Preferences, and Consumer Utility: Impact of Quality Labels, Cocoa Content, Chocolate Origin, and Price. *J. Int. Food Agribus. Mark.* **2022**, *34*, 518–537. [CrossRef]
45. Jisana, T.K. Consumer behaviour models: An overview. *Sai Om J. Commer. Manag.* **2014**, *1*, 34–43.
46. Mandel, N.; Rucker, D.D.; Levav, J.; Galinsky, A.D. The Compensatory Consumer Behavior Model: How self-discrepancies drive consumer behavior. *J. Consum. Psychol.* **2017**, *27*, 133–146. [CrossRef]
47. Martynenko, A.V.; Vikharev, S.V. A firm model with strict regulation and management influence on profit. *Math. Notes NEFU* **2020**, *27*, 39–53. [CrossRef]
48. Mokhov, V.; Chebotareva, G. Mathematical Modeling and Analysis Activities of PJSC “Fortum”. Bulletin of the South Ural State University. Ser. Math. Model. Program. Comput. Softw. **2022**, *15*, 111–117.
49. Chen, J.; Wang, X.; Liu, J. Corporate social responsibility and capacity sharing in a duopoly model. *Appl. Econ. Lett.* **2021**, *28*, 512–517. [CrossRef]
50. Ren, J.; Sun, H.; Xu, G.; Hou, D. Convergence of output dynamics in duopoly co-opetition model with incomplete information. *Math. Comput. Simul.* **2023**, *207*, 209–225. [CrossRef]
51. Baqaee, D.R.; Farhi, E. The Microeconomic Foundations of Aggregate Production Functions. NBER Working Paper n.25293. 2019. Available online: <http://www.nber.org/papers/w25293.pdf> (accessed on 26 January 2020).
52. Zagrebina, S.A.; Mokhov, V.G.; Tsimbol, V.I. Electrical energy consumption prediction is based on the recurrent neural network. *Procedia Comput. Sci.* **2019**, *150*, 340–346. [CrossRef]
53. Deride, J.; Jofré, A.; Wets, R.J.B. Solving Deterministic and Stochastic Equilibrium Problems via Augmented Walrasian. *Comput. Econ.* **2019**, *53*, 315–342. [CrossRef]
54. Gowdy, J.; Hall, C.; Klitgaard, K.; Krall, L. What every conservation biologist should know about economic theory. *Conserv. Biol.* **2010**, *24*, 1440–1447. [CrossRef]
55. Fields, G.S.; Song, Y. A Theoretical Model of the Chinese Labor Market. *SSRN Electron. J.* **2021**, *7278*, 1–48. [CrossRef]
56. Kant, J.D.; Ballot, G.; Goudet, O. Worksim: An agent-based model of labor markets. *J. Artif. Soc. Soc. Simul.* **2020**, *23*, 1–39. [CrossRef]
57. Cassola, N.; Morana, C. Modelling Short-Term Interest Rate Spreads in the Euro Money Market. *SSRN Electron. J.* **2021**. [CrossRef]
58. Rutkauskas, A.V.; Miečinskiene, A.; Stasytyte, V. Investment decisions modelling along sustainable development concept on financial markets. *Technol. Econ. Dev. Econ.* **2008**, *14*, 417–427. [CrossRef]
59. Cafferata, A.; Tramontana, F. A financial market model with confirmation bias. *Struct. Change Econ. Dyn.* **2019**, *51*, 252–259. [CrossRef]
60. Wray, C.M.; Bishop, S.R. A financial market model incorporating herd behaviour. *PLoS ONE* **2016**, *11*, e0151790. [CrossRef]
61. Alaminos, D.; Peláez, J.I.; Salas, M.B.; Fernández-Gámez, M.A. Sovereign debt and currency crises prediction models using machine learning techniques. *Symmetry* **2021**, *13*, 652. [CrossRef]
62. Chatzis, S.P.; Siakoulis, V.; Petropoulos, A.; Stavroulakis, E.; Vlachogiannakis, N. Forecasting stock market crisis events using deep and statistical machine learning techniques. *Expert Syst. Appl.* **2018**, *112*, 353–371. [CrossRef]
63. Le, H. Modelling inflation dynamics: A Bayesian comparison between GARCH and stochastic volatility. *Econ. Res.-Ekon. Istraz.* **2023**, *36*, 2112–2136. [CrossRef]
64. Caraka, R.E.; Sugiyarto, W. Inflation Rate Modelling in Indonesia. *Etikonomi* **2016**, *15*, 111–124. [CrossRef]
65. Lotfi, E.; Babrzadeh, S.; Khosravi, A. Sensitivity analysis of economic variables using neuro-fuzzy approach. *Sci. Iran.* **2020**, *27*, 1352–1359. [CrossRef]
66. Sek, S.K. Impact of oil price changes on domestic price inflation at disaggregated levels: Evidence from linear and nonlinear ARDL modeling. *Energy* **2017**, *130*, 204–217. [CrossRef]
67. Raja Wahab RA, S.; Bakar, A.A. Digital economy tax compliance model in Malaysia using machine learning approach. *Sains Malays.* **2021**, *50*, 2059–2077. [CrossRef]
68. Selvakkumar, S.; Limmeechokchai, B. Low carbon society scenario analysis of transport sector of an emerging economy-The AIM/Enduse modelling approach. *Energy Policy* **2015**, *81*, 199–214. [CrossRef]
69. Kaenchan, P.; Puttanapong, N.; Bowonthumrongchai, T.; Limskul, K.; Gheewala, S.H. Macroeconomic modeling for assessing sustainability of bioethanol production in Thailand. *Energy Policy* **2019**, *127*, 361–373. [CrossRef]
70. Demczuk, A.; Padula, A.D. Using system dynamics modeling to evaluate the feasibility of ethanol supply chain in Brazil: The role of sugarcane yield, gasoline prices and sales tax rates. *Biomass Bioenergy* **2017**, *97*, 186–211. [CrossRef]
71. Mosikari, T.J.; Eita, J.H. Modelling asymmetric relationship between exports and growth in a developing economy: Evidence from Namibia. *South Afr. J. Econ. Manag. Sci.* **2020**, *23*, 10. [CrossRef]

72. Kovbatiuk, M.V.; Shkliar, V.V.; Kovbatiuk, H.O. The Strategies for Entering International Markets by Levels of Management. *Probl. Econ.* **2022**, *4*, 156–162. [CrossRef]
73. Bortnikova, M.; Chyrkova, Y. Formation of the generalized technology for the enterprise adaptive competitive strategy development in conditions of entering new foreign markets. *Economics. Finances. Law* **2021**, *11/3*, 13–16. [CrossRef] [PubMed]
74. Gehrels, F. Optimizing International Investment and Trade Under Golden Rule Conditions. *Atl. Econ. J.* **2012**, *40*, 127–131. [CrossRef]
75. Welfens PJ, J. Innovation, inequality and a golden rule for growth in an economy with Cobb-Douglas function and an R&D sector. *Int. Econ. Econ. Policy* **2015**, *12*, 469–496. [CrossRef]
76. Melnichuk, O. The impact of foreign trade on the functioning of the national economy. *Sci. Opin. Econ. Manag.* **2020**, *2*. [CrossRef]
77. Sadiq, M.; Usman, M.; Zamir, A.; Shabbir, M.S.; Arif, A. Nexus between economic growth and foreign private investment: Evidence from Pakistan economy. *Cogent Econ. Finance.* **2021**, *9*, 1–16. [CrossRef]
78. Althouse, B.M.; Bergstrom, T.C.; Bergstrom, C.T. A public choice framework for controlling transmissible and evolving diseases. *Proc. Natl. Acad. Sci. USA* **2010**, *107* (Suppl. S1), 1696–1701. [CrossRef] [PubMed]
79. Kanazawa, S. The savanna principle. *Manag. Decis. Econ.* **2004**, *25*, 41–54. [CrossRef]
80. Shi, X.; Shi, L.; Zhou, Q.; Chen, K.; Cheng, Y. Bipartite Flocking for Cucker-Smale Model on Cooperation-Competition Networks Subject to Denial-of-Service Attacks. *IEEE Trans. Circuits Syst. I Regul. Pap.* **2022**, *69*, 3379–3390. [CrossRef]
81. Zhou, W.; Xing, Z.; Cui, H.; Li, Y. Analysis of a stochastic cooperation-competition model. *Adv. Differ. Equ.* **2018**, *2018*, 74. [CrossRef]
82. Mazurov, M.E. Modeling of scientific and technical progress. *Stat. Econ.* **2015**, *5*, 108–110. [CrossRef]
83. Boichenko, E.; Martynovych, N.; Shevchenko, I. Cognitive modeling concepts of sustainable development of society. *Probl. Ekorozwoju* **2021**, *16*, 158–165. [CrossRef]

**Disclaimer/Publisher’s Note:** The statements, opinions and data contained in all publications are solely those of the individual author(s) and contributor(s) and not of MDPI and/or the editor(s). MDPI and/or the editor(s) disclaim responsibility for any injury to people or property resulting from any ideas, methods, instructions or products referred to in the content.

Review

# Mathematical Models in High-Temperature Viscometry: A Review

Inna Elyukhina

Institute of Engineering and Technology, South Ural State University, Lenin Ave, 76, 454080 Chelyabinsk, Russia; inna.elyukhina@susu.ac.ru

**Abstract:** We systematize and review the mathematical models for use in oscillating-cup viscometry to solve different problems: for analysis of fluid flow and viscometer oscillations, for estimation of rheological constants and density, and for study without taking into account the traditional assumptions of this method. The full model for the cup and bob viscometer and a model for the oscillating-plate viscometer are also considered.

**Keywords:** oscillating-cup viscometer; mathematical model; nonlinear oscillations

**MSC:** 76-10

## 1. Introduction

The oscillating-cup viscometer has been the dominant technique for high-temperature melts (liquid crystals, molten metals and alloys, semiconductors, salts, etc.) since the middle of the 20th century up to the present day. These devices are constructed by researchers for measurements in both engineering (nuclear energetics, metallurgical industry) and physics (e.g., [1–12]). The advantages of this technique are related to high melting points, chemical activity, and low melt viscosity. These advantages include design simplicity, ease of use in an inert atmosphere with inactive materials, absence of an immersion probe, precise measurement of oscillation parameters, absolute technique, and small specimen volumes, i.e., isothermality, among others.

Traditionally, the mathematical model for the viscometer is built with some assumptions. The method can be used beyond them, and not taking them into account can lead to measurement errors. Viscometric data on metal melts contain enough contradictions (e.g., the review in [13]), and the question of their reasons is a principal one for condensed matter physics. Experimental uncertainty and error analysis are the main problems for this method [14–16]. Furthermore, the study of the non-Newtonian behavior of metal melts is actively discussed in experiments with serially produced rotational viscometers [17,18]. However, they are not mainly suitable for high-temperature studies, and discrepancies in the data of different authors can reach three orders of magnitude for the same melts and shear rates [19,20]. These discrepancies are also observed for the oscillating-cup method that is traditionally used for Newtonian fluids. The theory needs revision to find the sources of these discrepancies, develop an effective mathematical model, and analyze its assumptions.

The oscillating-cup viscometer is a right circular cylinder (1) filled with a fluid (2) and suspended from a thin torsion member (3), so it performs oscillations about the vertical axis (Figure 1). The viscometer usually works in damped mode. In this paper, we discuss this mode by default, and the forced mode is considered a specific case. Schematic views or photos of a viscometer are given, e.g., in [21–26].

**Citation:** Elyukhina, I. Mathematical Models in High-Temperature Viscometry: A Review. *Mathematics* **2023**, *11*, 2300. <https://doi.org/10.3390/math11102300>

Academic Editors: Sergei Viktorovich Aliukov, Anatoliy Alekseevich Alabugin and Konstantin Vladimirovich Osintsev

Received: 10 April 2023

Revised: 9 May 2023

Accepted: 10 May 2023

Published: 15 May 2023



**Copyright:** © 2023 by the author. Licensee MDPI, Basel, Switzerland. This article is an open access article distributed under the terms and conditions of the Creative Commons Attribution (CC BY) license (<https://creativecommons.org/licenses/by/4.0/>).

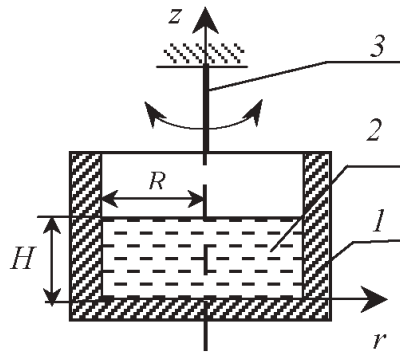


Figure 1. Schematic view.

The main experimental parameters are the following: (i) the fluid properties: density  $\rho$  and rheological constants, e.g., the kinematic viscosity  $\nu$  for Newtonian fluids; (ii) the viscometer parameters: the natural period  $\tau_0$  and the decrement  $\delta_0$  of oscillations for the fluid mass  $M = 0$ , the inertia moment  $K$  of the empty viscometer with respect to its axis; the geometric characteristics: the height  $H$  and the radius  $R$  of the fluid sample; (iii) the parameters of oscillations, e.g., the logarithmic decrement  $\delta$  and the period  $\tau$  of the steady linear oscillations in the damped mode.

These parameters give three dimensionless groups:  $A = 0.5MR^2/K$ ,  $\zeta_0 = R/d$ , and  $\chi = H/R$ , where the boundary-layer thickness is  $d = \sqrt{\nu/\theta}$ , with  $\theta$  being the angular frequency. The period  $\tau > \tau_0$  and decrement  $\delta > \delta_0$  are due to a larger effective moment of inertia and extra dissipation of mechanical energy in the presence of viscous friction, respectively.

In the general case, the model for the oscillating-cup experiments includes the partial differential equations for the fluid flow: the momentum conservation equation, the mass conservation equation and the rheological constitutive equation, and the coupled nonlinear equation of the cup oscillations. We give the simplified models obtained from the general model by using the different assumptions and systematize the solutions and applications of the results obtained from them. We review both the classical problems and the working equations for linear fluids (viscous and viscoelastic) and the novel trends in oscillating-cup viscometry for nonlinear fluids, for higher amplitudes of oscillations, etc.

The models are used in the direct and inverse problems of viscometry to study fluid properties and to model the oscillation law, respectively. The last one includes an analysis of the features for the flow and cup oscillations, an experimental design, and parameter identification in experiments with metal melts.

## 2. Full Axisymmetric Case

We take the case of an axially symmetric fluid flow in the oscillating-cup viscometer. The mass and momentum conservation equations have the form

$$\frac{\partial \vartheta_r}{\partial r} + \frac{\vartheta_r}{r} + \frac{\partial \vartheta_z}{\partial z} = 0, \tag{1}$$

$$\rho \left( \frac{\partial \vartheta_r}{\partial t} + \vartheta_r \frac{\partial \vartheta_r}{\partial r} + \vartheta_z \frac{\partial \vartheta_r}{\partial z} - \frac{\vartheta_\phi^2}{r} \right) = -\frac{\partial p}{\partial r} + \frac{\partial \sigma_{rr}}{\partial r} + \frac{\partial \sigma_{rz}}{\partial z} + \frac{\sigma_{rr} - \sigma_{\phi\phi}}{r}, \tag{2}$$

$$\rho \left( \frac{\partial \vartheta_\phi}{\partial t} + \vartheta_r \frac{\partial \vartheta_\phi}{\partial r} + \vartheta_z \frac{\partial \vartheta_\phi}{\partial z} + \frac{\vartheta_r \vartheta_\phi}{r} \right) = \frac{\partial \sigma_{r\phi}}{\partial r} + \frac{\partial \sigma_{\phi z}}{\partial z} + 2 \frac{\sigma_{r\phi}}{r}, \tag{3}$$

$$\rho \left( \frac{\partial \vartheta_z}{\partial t} + \vartheta_r \frac{\partial \vartheta_z}{\partial r} + \vartheta_z \frac{\partial \vartheta_z}{\partial z} \right) = -\frac{\partial p}{\partial z} - \rho g + \frac{\partial \sigma_{rz}}{\partial r} + \frac{\partial \sigma_{zz}}{\partial z} + \frac{\sigma_{rz}}{r}. \tag{4}$$

For oscillations of the cylinder, we have the equation

$$\ddot{\alpha} = P_{\Sigma}/K, \tag{5}$$

where  $P_{\Sigma} = P + P_0 + P_f$  and  $P = -2\pi R^3 \int_0^H \sigma_{\varphi r}|_R dz + 2\pi \int_0^R (\sigma_{\varphi z}|_0 - ((a-1)\sigma_{\varphi z}|_H)) r^2 dr$ , and for the linear case of the suspension stiffness,  $P_0 = 2\delta_0 \dot{\alpha} / \tau_0 + N\alpha / K$ .

In Equations (1)–(5),  $a$  is the number of viscometer end walls ( $a = 1$  for a fluid with a free surface at  $z = H$  and  $a = 2$  for a full cylinder with a lid);  $\alpha$  is the angular displacement of the cylinder from equilibrium;  $N$  is the stiffness coefficient of the suspended wire;  $\vartheta_r$ ,  $\vartheta_{\phi}$ , and  $\vartheta_z$  are the radial, azimuthal, and axial components of the velocity vector;  $g$  is the free-fall acceleration;  $p$  is the pressure;  $P_{\Sigma}$  is the total torque of external forces acting on the viscometer about the rotation axis;  $P$  is the torque exerted by a fluid;  $P_0 = P_e + P_r$  is the torque acting also on the empty cup system;  $P_e$  is the elastic torque of the suspension torsion;  $P_r$  is the resistance torque (due to the resistance in the surrounding air and the internal friction of the suspension wire);  $P_f$  is the varying external action, e.g.,  $P_f = F \sin \omega t$ ;  $F$  and  $\omega$  are the amplitude and the angular frequency of the driving torque, respectively; for the damped oscillations,  $P_f = 0$ ;  $r$ ,  $z$ , and  $\varphi$  are the radial, axial, and angular coordinates ( $r = 0$  on the cylinder axis and  $z = 0$  on the bottom);  $\sigma_{ij}$  is the  $ij$ -th component of the extra-stress tensor  $\sigma$ ;  $t$  is the time;  $\rho = \text{const}$ ; in the forced mode, the natural frequency  $\omega_0$  of the system is found from the resonance frequency and amplitude at  $M = 0$ ; the overdot denotes the time derivative.

The model includes the initial and no-slip boundary conditions:

$$\begin{aligned} t = 0 : \vartheta_r = \vartheta_z = \vartheta_{\phi} = 0; & \text{ (i) } \alpha = \alpha_0 \sim 6^\circ, d\alpha/dT = 0, \text{ (ii) } \alpha = 0, d\alpha/dT \neq 0 (\sim \alpha_0), \\ & \text{(iii) } t \in (0, t_0): P_f \neq 0 \text{ for (i) or (ii), } t \geq t_0: P_f = 0; \\ r = 0 : \vartheta_r = \vartheta_{\phi} = d\vartheta_z/dr = 0; & r = R: \vartheta_r = \vartheta_z = 0, \vartheta_{\phi} = \dot{\alpha}R; z = 0: \vartheta_r = \vartheta_z = 0, \\ & \vartheta_{\phi} = \dot{\alpha}r; \\ z = H: \vartheta_r = \vartheta_z = 0, \vartheta_{\phi} = \dot{\alpha}r & (a = 2), \text{ and } \partial\vartheta_r/\partial z = \partial\vartheta_{\phi}/\partial z = \vartheta_z = 0 (a = 1). \end{aligned} \tag{6}$$

The equation set is supplemented with the rheological constitutive equation for the Newtonian, Bingham, and upper-convected Maxwell models [27], respectively:

$$\sigma = 2\nu\rho\mathbf{D}, \tag{7}$$

$$\sigma = (2\nu'\rho + \sigma_0/II_{\mathbf{D}})\mathbf{D} \text{ for } II_{\sigma} \geq \sigma_0; \mathbf{D} = 0 \text{ for } II_{\sigma} < \sigma_0, \tag{8}$$

$$\sigma + \lambda \overset{\nabla}{\sigma} = 2\nu\rho\mathbf{D} \tag{9}$$

where  $\mathbf{D}$  is the tensor of the deformation rates;  $II_{\mathbf{A}} = (\sum A_{ij}A_{ij}/2)^{1/2}$  is the second invariant of a tensor  $\mathbf{A}$ ;  $A_{ij}$  is the  $ij$ -th component of  $\mathbf{A}$ ;  $\lambda$  is the relaxation time;  $\nu'$  is the kinematic viscosity after yielding;  $\sigma_0$  is the yield stress.

The model is applied to analyze the secondary flows, the oscillations with higher amplitudes, and the features of the case without taking into account the traditional assumptions of the oscillating-cup method in the general case [1,28–33].

### 3. Traditional Assumptions

#### 3.1. Mathematical Model

The traditional assumptions of the oscillating-cup method [1,34] are as follows: the fluid is incompressible, the wall slip is absent, and the oscillation amplitudes are small.

In addition, the fluid flow is axisymmetric, the substantial velocity component is  $\vartheta_\phi$ , the convective terms in (2)–(4) are absent, and the model (1)–(6) has the following form:

$$\frac{d^2 \alpha}{dT^2} + \frac{\delta_0}{\pi} \frac{d\alpha}{dT} + \left(1 + \frac{\delta_0^2}{4\pi^2}\right) \alpha = P, \tag{10}$$

$$\frac{\partial U}{\partial T} = \frac{\partial \sigma_{\xi\phi}}{\partial \xi} + \frac{2\sigma_{\xi\phi}}{\xi} + \frac{\partial \sigma_{\eta\phi}}{\partial \eta}, \tag{11}$$

$$T = 0 : \alpha \sim 6^\circ, \frac{d\alpha}{dT} = 0, U = 0; \xi = \xi_0: U = \frac{d\alpha}{dT} \xi_0; \\ \xi = 0: U = 0; \eta = 0, \eta = 2\eta_0 (a = 2) \text{ or } \eta = \eta_0 (a = 1) : U = \frac{d\alpha}{dT} \xi,$$

with the rheological equation for Newtonian fluids

$$\sigma_{\xi\phi(\eta\phi)} = D_{\xi\phi(\eta\phi)}, \tag{12}$$

for the Ostwald [35]–de Waele [36] model

$$\sigma_{\xi\phi(\eta\phi)} = bD_{\xi\phi(\eta\phi)} D^{m-1}, \tag{13}$$

for the Bingham model [37] in the form

$$\sigma_{\xi\phi(\eta\phi)} = (1 + \text{Bn}/D)D_{\xi\phi(\eta\phi)} \text{ if } \sigma \geq \text{Bn}, D_{\xi\phi(\eta\phi)} = 0 \text{ if } \sigma < \text{Bn}, \tag{14}$$

for nonlinear viscoplastic fluids with the Herschel–Bulkley model in the form [38]

$$\sigma_{\xi\phi(\eta\phi)} = (bD^{m-1} + \text{Bn}/D)D_{\xi\phi(\eta\phi)} \text{ if } D \geq D_0, \sigma_{\xi\phi(\eta\phi)} = k_\sigma D_{\xi\phi(\eta\phi)} \text{ if } D < D_0, \tag{15}$$

and for the Johnson–Segalman model [39]

$$\sigma'_{\xi\phi} + \text{We} \left( \frac{\partial \sigma'_{\xi\phi}}{\partial T} + \frac{1-\gamma}{2} D_{\xi\phi} \sigma'_{\phi\phi} - \frac{1+\gamma}{2} D_{\xi\phi} \sigma'_{\xi\xi} \right) = D_{\xi\phi}, \\ \sigma'_{\phi\phi} + \text{We} \left( \frac{\partial \sigma'_{\phi\phi}}{\partial T} - (1 + \gamma) D_{\xi\phi} \sigma'_{\xi\xi} \right) = 0, \\ \sigma'_{\xi\xi} + \text{We} \left( \frac{\partial \sigma'_{\xi\xi}}{\partial T} + (1 - \gamma) D_{\xi\phi} \sigma'_{\xi\phi} \right) = 0. \tag{16}$$

In Equation (10),

$$P = -\frac{4A}{\xi_0^2 \eta_0} \int_0^{\eta_0} \sigma_{\xi\phi} |_{\xi=\xi_0} d\eta + \frac{4A}{\xi_0^4 \eta_0} \left[ \int_0^{\xi_0} \sigma_{\eta\phi} |_{\eta=0} \xi^2 d\xi - \int_0^{\xi_0} \sigma_{\eta\phi} |_{\eta=\eta_0} \xi^2 d\xi \right], \tag{17}$$

and for Ostwald–de Waele fluids

$$P = -\frac{4Ab}{\xi_0^2 \eta_0} \int_0^{\eta_0} \left( \frac{\partial U}{\partial \xi} - \frac{U}{\xi} \right) \left| \frac{\partial U}{\partial \xi} - \frac{U}{\xi} \right|^{m-1} \Big|_{\xi_0} d\eta + \frac{4Ab}{\xi_0^4 \eta_0} \left[ \int_0^{\xi_0} \left( \frac{\partial U}{\partial \eta} \right) \left| \frac{\partial U}{\partial \eta} \right|^{m-1} \xi^2 d\xi - \int_0^{\xi_0} \left( \frac{\partial U}{\partial \eta} \right) \left| \frac{\partial U}{\partial \eta} \right|^{m-1} \Big|_{\eta_0} \xi^2 d\xi \right].$$

Here

$$U = \frac{\vartheta_\phi}{dq_0}, T = q_0 t, h = \frac{H}{a}, \xi = \frac{r}{a}, \eta = \frac{\bar{z}}{a}, \eta_0 = \frac{h}{a}, q_0 = \frac{2\pi}{q_0}; \\ D_{\xi\phi} = \frac{\partial U}{\partial \xi} - \frac{U}{\xi}, D_{\eta\phi} = \frac{\partial U}{\partial \eta}, D = \sqrt{D_{\xi\phi}^2 + D_{\eta\phi}^2}; \\ b = \frac{q_0^{m-1} \kappa}{\sigma p}, \text{Bn} = \frac{\sigma_0}{\sigma p q_0}, D_0 = \frac{\text{Bn}}{k_\sigma - 1}, \text{We} = \lambda q_0, \sigma'_{\xi\phi} = \sigma_{\xi\phi} - (\mu'/\mu) D_{\xi\phi};$$

where  $Bn$  is the Bingham number;  $\kappa$  and  $m$  are the flow consistency and the behavior indexes, respectively;  $We$  is the Weissenberg number;  $\gamma$  is the slip parameter;  $\mu$  and  $\mu'$  are the dynamic polymer and solvent viscosities;  $\sigma$  is the second invariant of  $\sigma$ ; the bi-viscosity model [40] is used in (15) and  $k_\sigma$  is the model coefficient; the values of  $\sigma, P$ , etc., are dimensionless ones in contrast to (1)–(9); the parameter  $\gamma \in [0, 1]$  [41], and the affine motion is for  $\gamma = 1$  and the slip increases as  $\gamma$  decreases; the Maxwell model responds to (16) with  $\gamma = 1$  and  $\mu'/\mu \sim 0$ ;  $m < 1$  for shear-thinning fluids and  $m > 1$  for shear-thickening fluids.

For some problems, the long cylinder model with constant fluid characteristics in height can be used. This is suitable to reveal the features in special cases, e.g., to describe the features of the nonlinear behavior of the fluid with viscous, elastic, and plastic components. The mathematical modeling of the experiments includes both constructing the working viscometric equations and developing the parameter identification methods. Mainly, the exact solutions of the nonlinear partial differential equations are of interest in practice. For nonlinear cases, they are obtained on the basis of the expressions for linear fluids.

### 3.2. Features of Fluid Flow and Viscometer Oscillations

We first give some explanations for the power-law case. The function  $z(y) = y^{m-1}$  ( $y > 0, m > 0$ ) has the following features: (i)  $z(y)$  increases for  $m > 1$  and decreases for  $m < 1$ ; (ii)  $m > 1: z(y) \rightarrow 0$  as  $y \rightarrow 0$ ;  $m < 1: z(y) \rightarrow \infty$  as  $y \rightarrow 0$ ; (iii)  $m < 1: y^{m-1} > y$  for  $y < 1, y^{m-1} < y$  for  $y > 1, z(y)$  is convex downward;  $m > 2: y^{m-1} < y$  for  $y < 1, y^{m-1} > y$  for  $y > 1, z(y)$  is convex downward;  $1 < m < 2: y^{m-1} > y$  for  $y < 1, y^{m-1} < y$  for  $y > 1, z(y)$  is convex upward.

This explains the features in terms of the effective viscosity  $v_{eff}$  of power-law fluids when  $v_{eff}$  is higher or lower than the Newtonian viscosity depending on the shear rate. The dimensionless effective viscosity is equal to  $bD^{m-1}$  for the rheological model (13). The features are reflected in the character of the fluid flow: the flow penetration depth is proportional to  $v_{eff}$  and the developed flow with  $U \neq 0$  extends to a different interval from  $\xi = \xi_0$  depending on  $D$ . For example, for  $D > 1$  and for fluids with  $m < 1$ , the viscosity  $v_{eff}$  is lower than the Newtonian one, and the interval from  $\xi = 0$  with  $U \sim 0$  is wider and its boundary is closer to  $\xi_0$ . The features of fluid flows and viscometer oscillations for rheostable fluids and fluids with elastic viscoplastic components and non-affine deformations are considered in [42–44].

For fluids with plastic components, an unyielded region (zone I in Figure 2a) arises near the cylinder wall in each oscillation period. It moves to a rigid core (zone II), the radius of which increases in the next period. Some velocity profiles are given for a half-period in Figure 2b. In the rigid zones,  $\sigma < \sigma_0$  and the fluid do not flow and have a nonzero velocity with linear dependence  $dU/d\xi - U/\xi = 0$ . For the cylinder entirely filled with the unyielded region, it is equal to the product of the radial coordinate and the angular velocity. These zones correspond to the linear parts in the profiles of  $U$  and  $D_{\xi\phi}$  beginning from  $\xi = 0$  (zone I) in Figure 2b,c, to the parts with a curvature of  $D_{\xi\phi}$  at  $D_{\xi\phi} \sim 0$  (zone II) in Figure 2c, or to the intervals with  $D < D_0$  in Figure 2a. Figure 2 is carried out for the bi-viscosity model, and  $D_0$  is the value of  $D$  in the transition between the yielded and unyielded states.

Oscillations of the viscometer filled with linear fluids are isosynchronous ones without the transient, i.e.,  $\delta$  and  $\tau$  are constant in the oscillation process. In the general case of nonlinear oscillations, we determine these parameters for the period number  $N$  beginning from  $T = 0$ . It can be found by the curve fitting [30,45] or as the following:  $\delta = 2 \ln|\alpha_1/\alpha_2|$ , where  $\alpha_1, \alpha_2$  are the nearest neighboring extreme values of  $\alpha$  ( $|\alpha_1| > |\alpha_2|$ ) [46].

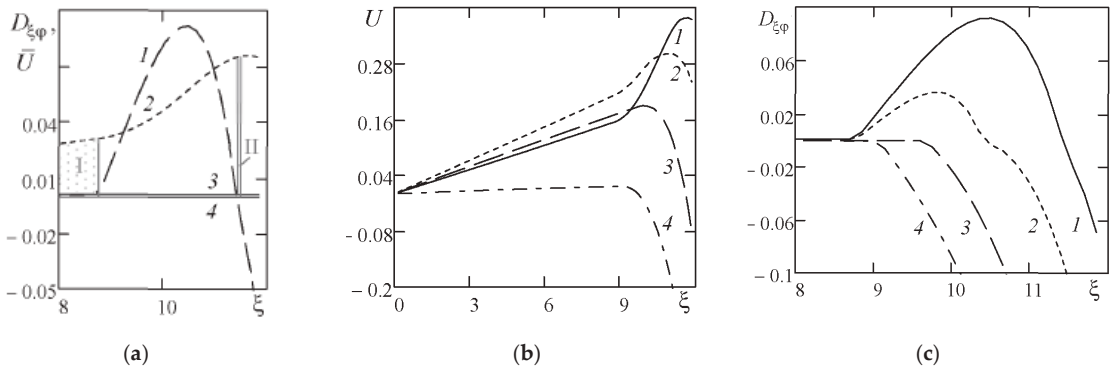


**Figure 2.** Distribution of  $D_{\xi\varphi}$  and  $U$  along the radius for Bingham fluids ( $A = 0.2$ ,  $\xi_0 = 12$ ,  $Bn = 0.4$ ,  $\chi \rightarrow 0$ ):  $D_{\xi\varphi}$  (1),  $\bar{U} = 0.2U$  (2),  $D_0$  (3),  $(-D_0)$  (4); I and II are the unyielded regions in (a); the curves are for the 10th (1, 2) and 11th (3, 4) half-periods in (b,c); (a) corresponds to 1 in (b,c).

For Newtonian fluids, when increasing the parameter  $\xi_0$  or decreasing the viscosity, the period  $\tau$  decreases mainly in  $\xi_0 \in (2, 12)$  (Figure 3). For  $\xi_0 \rightarrow 0$ , we have a rigid body, and  $\tau$  is found from the equation  $\ddot{\alpha} + 2p_0\dot{\alpha} + v^2\alpha = 0$ , where  $v^2 = N(K + MR^2/2)^{-1}$ ,  $p_0 = \delta_0/\tau_0$ . The case with  $\xi_0 \rightarrow \infty$  corresponds to the ideal fluid and  $\tau \rightarrow \tau_0$ . The decrement dependence on  $\xi_0$  has a maximum energy absorption for a certain value of  $\xi_m$ . This is determined by the prevalence of the effects of viscosity decreasing or shear rate increasing at the wall. In the boundary cases of  $\xi_0$ , the decrement  $\delta \rightarrow \delta_0$ . For the long cylinder,  $\xi_m \sim 4.3$  and  $\xi_m$  shift to larger  $\xi_0$  for smaller  $\chi$ . The intervals to the left of the peak  $\xi_m$  and for  $\xi_0 > 10$  are considered the high-viscosity and low-viscosity intervals, respectively. The curves  $\tau(\xi_0)$  and  $\delta(\xi_0)$  become steeper as the complex  $A$  increases.

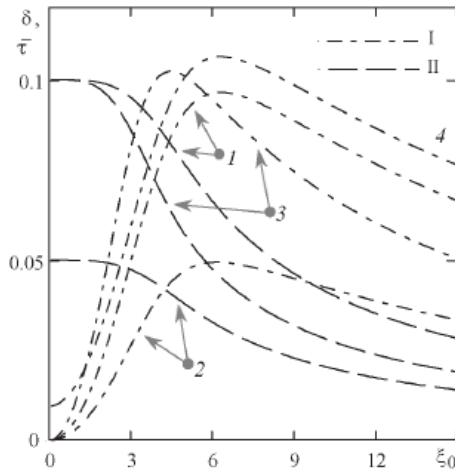


**Figure 3.** Dependences of oscillation parameters  $\delta$  (I) and  $\bar{\tau} = (\tau/\tau_0)^2 - 1$  (II) on  $\xi_0$ : 1— $A = 0.1$ ,  $\chi = 1$ ; 2— $0.05, 1, 0$ ; 3— $0.1, \infty, 0$ ; 4— $0.1, 1, 0.01$ .

For viscoplastic and pseudoplastic fluids, the amplitude of  $v_{\text{eff}}$  increases with time, i.e., the period increases and the decrement passes through the maximum (Figure 4). The decrement monotonically decreases when the value of  $\xi_{\text{eff}}$  at the beginning is smaller than  $\xi_m$ . For dilatant fluids, the opposite occurs. The special feature of the viscoplastic case is the presence of isosynchronous oscillations at the end [42], which is a response to the

viscometer being filled with a solid body. Therefore, the parameters  $\zeta_{\text{eff}} \sim 0$  and  $\delta \sim \delta_0$ ,  $\tau/\tau_0 \sim \sqrt{1+A}$ . For the numerical computation of these fluids, regularized models with high coefficients are used, and their values  $\sim 10^3$  provide an error of 0.1% in the oscillation law. Figure 5a shows how models with different coefficients and flow curves approach the behavior of Bingham fluids with  $\text{Bn} = 0.5$  and how this is reflected in the oscillation law (Figure 5b,c).

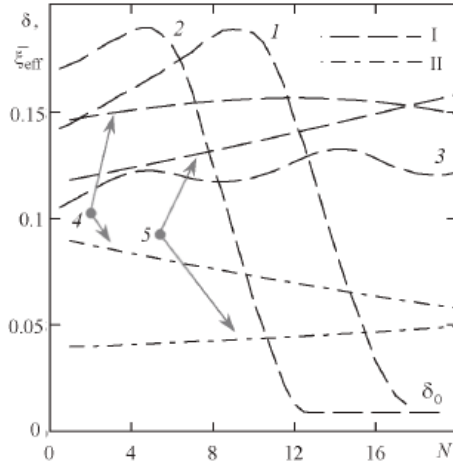


**Figure 4.** Dependences of  $\delta$  (I) and  $\bar{\zeta}_{\text{eff}} = 0.015\zeta_{\text{eff}}$  (II) on  $N$  for linear viscoplastic (1, 2), elastic viscoplastic (3), and nonlinear viscous (4, 5) fluids ( $\chi \rightarrow \infty$ ,  $b = 1$ ,  $c = 1$ ): 1— $A = 0.2$ ,  $\zeta_0 = 12$  ( $\text{Bn} = 0.2$ ); 2— $0.2$ ,  $12$  ( $\text{Bn} = 0.4$ ); 3— $0.1$ ,  $10$  ( $\text{We} = 1$ ,  $\text{Bn} = 0.5$ ); 4— $0.15$ ,  $7$  ( $m = 0.75$ ); 5— $0.2$ ,  $2$  ( $m = 1.2$ ).

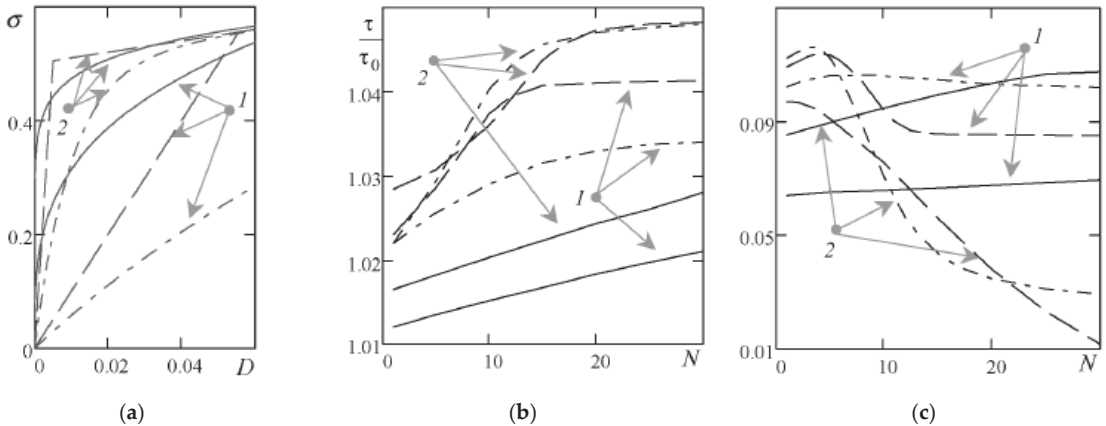


**Figure 5.** Flow curves (a) and dependences of oscillation parameters  $\tau/\tau_0$  (b) and  $\delta$  (c) on  $N$ :  $A = 0.1$ ,  $\zeta_0 = 10$ ,  $\chi \rightarrow \infty$ ,  $\delta_0 \sim 0.001$ ; bi-viscosity model (I) and exponential model (II) with model coefficients equal to 10 (I) and 100 (2); power-law pseudoplastic model (III) with  $\kappa = 0.75$  and  $m = 0.9$  (1), 1.25 and 0.7 (2).

The change in  $\tau$  and  $\delta$  has an oscillatory character in the presence of the elastic component in the rheological equation. Increasing the elastic fluid properties leads to increasing the number of extrema in these curves, which depends on the ratio of viscous and elastic wavelengths (curve 3 in Figure 6 corresponds to  $\lambda = 2.5/q_0$ ). This behavior determines the

sensitivity of the errors of estimated parameters to the errors of direct measurement (e.g.,  $\psi_{\xi_0, \delta} = |\partial \xi_0 / \partial \delta| \delta / \xi_0$ ), i.e., the error in viscosity is high at  $\xi_0 \sim \xi_m$  (Figure 7). Such features are discussed in [1,23,47]. They allow one to interpret the oscillations of a viscometer filled with nonlinear fluids in terms of features related to linear fluids. The shear rate amplitude decreases with time, and the effective viscosity  $v_{\text{eff}}$  and the parameter  $\xi_{\text{eff}}$  change. Then, the changes in the period and the decrement take place according to how these parameters change with  $\xi_0$  for linear fluids. Figures 3–7 correspond to the steady-state oscillations without the transient.

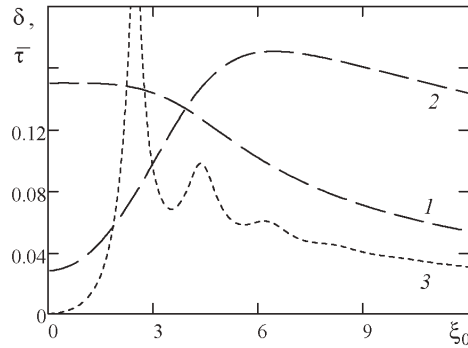


**Figure 6.** Dependences of oscillation parameters  $\bar{\tau}$  (1) and  $\delta$  (2) on  $\xi_0$  for Newtonian fluids:  $A = 0.15$ ,  $\chi = 1$ ,  $\delta_0 = 0.03$ ,  $a = 2$ ; and  $\delta$  (3) for Maxwell fluids:  $0.1, \infty, 0, 0$ .

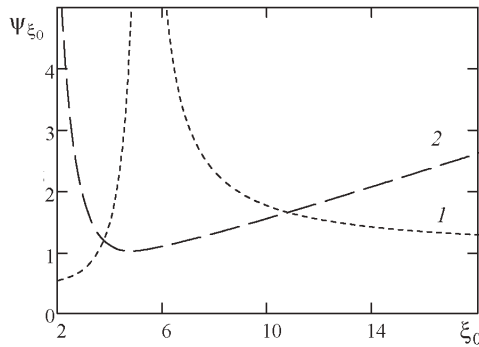


**Figure 7.** Sensitivities  $\psi_{\xi_0, \delta}$  (1) and  $\psi_{\xi_0, \lambda}$  (2) for Newtonian fluids:  $A = 0.2$ ,  $\chi = 2$ ,  $\delta_0 \sim 0$ ,  $a = 2$ .

The dependence of shear stress on shear rate, i.e.,  $\sigma_{\xi\phi} = \sigma_{\xi\phi}(D_{\xi\phi})$ , is a straight line for Newtonian fluids and an oval for Maxwell fluids in the forced mode. Hysteresis occurs (Figure 8) for nonlinear viscoelastic fluids with non-affine deformations, and there are unordered trajectories in the transient. Hence, the spectrum includes the even and odd harmonics of the fundamental frequency and the subharmonics as well. The odd harmonics only appear for nonlinear viscous fluids (Figure 9). The intensity of spectrum peaks depends on nonlinear fluid properties and experimental conditions that allow one to use the methods of Fourier-transform rheology to analyze them.

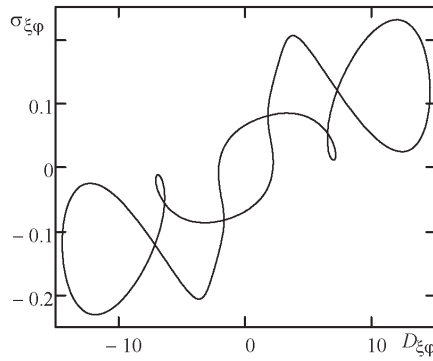


**Figure 8.** Dependence of shear stress  $\sigma_{\xi\varphi}$  on  $D_{\xi\varphi}$  at  $\xi = \xi_0$ :  $A = 0.2$ ;  $\xi_0 = 8$ ,  $We = 3$ ;  $\gamma = 0.5$ ; oscillation amplitude  $\sim 0.1$ .

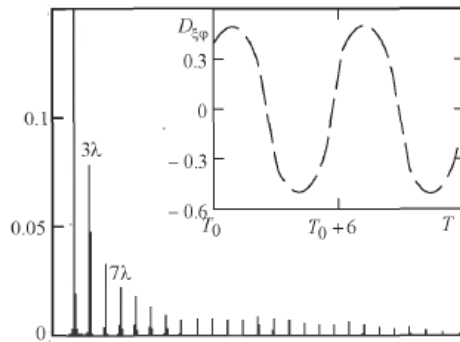


**Figure 9.** Spectrum and dependence of  $D_{\xi\varphi}$  at  $r = R$  on time:  $A = 0.1$ ,  $\xi_0 = 20$ ,  $\omega_0/\omega = 1.01$ ,  $F/K\omega_0^2 = 0.0015$ ,  $b = 1$ ,  $m = 3$ .

### 3.3. Parameter Identification

The theoretical foundations of an estimation method include both building the mathematical model and developing the identification approach. The last one consists of the following: (i) analyzing the model identifiability and observability; (ii) creating the algorithms and the objective function  $\Phi$ ; (iii) determining the covariance matrix of unknown parameters from the measurable values; (iv) testing the model adequacy; and (v) choosing the optimal experimental conditions [48]. The components of the Jacobian matrix can be constructed for power-law fluids as  $J_{11} = \partial\tau/\partial\kappa$ ,  $J_{12} = \partial\tau/\partial m$ ,  $J_{21} = \partial\delta/\partial\kappa$ ,  $J_{22} = \partial\delta/\partial m$ .

The maximum plausibility method can be used for building the function  $\Phi: \Phi(\kappa, m) = (\theta_c(\kappa, m) - \theta_e)^T \mathbf{B}_1^{-1} (\theta_c - \theta_e)$ , where  $\theta_c$ ,  $\theta_e$  are the column vectors of the calculated and experimental values of the parameters that are observable in the experiment ( $\tau$  and  $\delta$  or  $\alpha(t)$ );  $\mathbf{B}_1$  is the covariance matrix of the measurement errors (the scalar positive definite matrix:  $\det \mathbf{B}_1 \neq 0$ ,  $(j, j)$ -components equal to the variance  $\sigma_j^2$  of measurement in the  $j$ -th point). The covariance matrix of the estimated parameter errors is  $\mathbf{B}_2 = (\mathbf{L}^T \mathbf{B}_1^{-1} \mathbf{L})^{-1}$ , where the sensitivity function matrix  $\mathbf{L}$  has elements such as  $(\partial\delta/\partial\kappa)$ ,  $(\partial\delta/\partial m)$ . In the general case, this matrix includes  $l \times 2$  components, where  $l$  is the number of experimental points. The optimal experimental design is carried out based on the solution of the extremal problem  $|\mathbf{B}| \rightarrow \max$ , where  $\mathbf{B}$  includes the components  $\sum_j \sigma_j^{-2} (\partial\delta_j/\partial\kappa)^2$ ,  $\sum_j \sigma_j^{-2} (\partial\delta_j/\partial\kappa) (\partial\delta_j/\partial m)$ .

### 4. Working Equations

#### 4.1. Linear Fluids

In order to obtain the classic solution, the steady-state oscillations are considered. This is first obtained in [1] as follows:

$$\frac{L'}{K} = p \left( 1 + \frac{p_0^2 + q_0^2}{p^2 + q^2} \right) - 2p_0, \quad \frac{L''}{K} = q \left( 1 - \frac{p_0^2 + q_0^2}{p^2 + q^2} \right), \tag{18}$$

or

$$L' + L'' \frac{p}{q} = 2K(p - p_0); \tag{19}$$

$$L' = \text{Re}(L), \quad L'' = \text{Im}(L), \quad L = -2\nu M\beta \frac{J_2(\beta)}{J_1(\beta)} + 4 \frac{M}{h} \frac{k^2}{\nu} \sum_{n=1}^{\infty} \frac{\text{th}(\theta_n h)}{\mu_n^2 \theta_n^3}, \tag{20}$$

where

$$\beta = R\sqrt{\frac{k}{\nu}}, \quad \theta_n^2 = \mu_n^2 - \frac{k}{\nu}, \quad k = p + iq, \quad p = \frac{\delta}{\tau}, \quad q = \frac{2\pi}{\tau}, \quad i = \sqrt{-1};$$

$$J_2(z)/J_1(z) = \int_0^\pi \cos(z \sin y - 2y) dy / \int_0^\pi \cos(z \sin y - y) dy,$$

$J_l$  are the Bessel functions of first kind and order  $l$ ;  $L$  is the friction function determined by the relation of  $P$  to the viscometer angular velocity;  $p$  and  $q$  are the damping coefficient and the angular frequency of oscillations, respectively;  $p_0$  and  $q_0$  are  $p$  and  $q$  when  $M = 0$ ;  $\mu_n$  are the roots of the equation  $J_1(\mu_n R) = 0$ ;  $\text{Im}$  and  $\text{Re}$  are the imaginary and real parts, respectively; the formula from [49] is used for the Bessel functions. Equations (18)–(20) are obtained from (10)–(13) and (17) for oscillations of a crucible filled with a Newtonian fluid without the transient. The frequency  $q_0$  depends on the load on the wire and the temperature, i.e.,  $q_0$  needs to be measured in experiments over the whole temperature interval with the load for which the viscosity estimations are carried out. Equation (19) is preferable for calculations because of the absence of the period  $\tau_0$ .

Equation (20) is one of the exact solutions found later in [34]:

$$(s + \Delta_0)^2 + 1 + D(s) = 0, \tag{21}$$

where the roots are  $s_{1,2} = \tau_0(-\Delta \pm i)/\tau$ ,  $\Delta = \delta/(2\pi)$ . The following forms of  $D(s)$  are equivalent and suitable in different cases, including the problems for nonlinear viscous fluids:

$$D(s) = s^2 A \frac{4I_2(\sqrt{s}\xi_0)}{\sqrt{s}\xi_0 I_1(\sqrt{s}\xi_0)} + \frac{8s^3 A}{\eta_0} \sum_{n=1}^{\infty} \frac{\text{th}(s_n \eta_0)}{\mu_n^2 s_n^3},$$

$$D(s) = s^2 A \frac{\text{th}(\sqrt{s}\eta_0)}{\sqrt{s}\eta_0} + \frac{32s^3 A}{\pi^2 \xi_0^3} \sum_{m=0}^{\infty} \left[ \frac{1}{(2m+1)^2 s_m^3} \frac{I_2(s_m \xi_0)}{I_1(s_m \xi_0)} \right],$$

$$D(s) = s^2 A - 8s^3 A \sum_{n=1}^{\infty} \frac{1}{(s \mu_n')^2} \left( 1 - \frac{\text{th}(s \mu_n' \eta_0)}{s \mu_n' \eta_0} \right),$$

$$D(s) = s^2 A - \frac{8s^3 A}{\pi^2} \sum_{m=0}^{\infty} \frac{1}{(2m+1)^2} \frac{I_3(s_m \xi_0)}{I_1(s_m \xi_0) s_m^3},$$

$$D(s) = s^2 A - \frac{64s^3 A}{\pi^2} \sum_{n=1}^{\infty} \sum_{m=0}^{\infty} \frac{1}{\mu_n'^2 (2m+1)^2 (s - s_{nm})}, \tag{22}$$

where

$$\mu_n' = \mu_n R, \quad s_\mu^2 = \frac{\mu_n'^2}{\xi_0^2} + s, \quad s_m^2 = s + \left[ \frac{(2m+1)\pi}{2\eta_0} \right]^2, \quad s_{nm} = - \left[ \frac{(2m+1)\pi}{2\eta_0} \right]^2 - \frac{\mu_n'^2}{\xi_0^2};$$

$I_l$  are the modified Bessel functions of order  $l$ .

Equation sets (18) and (20), (19) and (20), and (21) and (22) have been numerically solved since the middle of the last century [50]. However, simplified relationships are often used, which can introduce inaccuracies in viscosity estimation depending on ex-

perimental conditions. A review of such expressions used to calculate the Newtonian viscosity is carried out in [1,21,28,47,51–55], among others. In addition to viscosity, the experiment model includes density, which allows one to simultaneously estimate both of these parameters [29,56,57].

For solving the equations, e.g., (18) and (20), we minimize the objective function  $\Phi$  that includes the real and imaginary parts of these equations with different weight coefficients. Calculations using  $L'$  and  $L''$  give higher sensitivity to the decrement and the period, respectively. The function  $\Phi$  is minimized on the set of  $\tau$  and  $\delta$ :  $\Phi = \Phi(\tau, \delta)$ , in the inverse viscometric task in order to model the oscillation law. For such modeling from  $t = 0$ , the transient is taken into account as, e.g., in [34]. In the direct task, the equations are used for the steady oscillations and the function  $\Phi(v) \rightarrow 0$  in order to estimate  $v$  or  $\Phi(v, \rho) \rightarrow 0$  for the simultaneous measurement of  $v$  and  $\rho$ . The complex viscosity is introduced for linear viscoelastic fluids (e.g., [23]).

#### 4.2. Nonlinear Fluids

Models (1)–(9) and (10)–(17) for nonlinear fluids are solved by numerical methods. We develop the algorithm on the basis of the approach in [58], using the analytical expressions for linear fluids in order to identify nonlinear fluid properties. This allows one to obtain solutions suitable for the practice. The exact solutions for linear fluids are applied in terms of the effective values with averaging on the time and the internal surface of the crucible. This is adequate for oscillatory viscometry with weak nonlinearity and different combinations of viscous, plastic, and elastic components. The method is effective for such unsteady flows of Bingham fluids with singularities, yielded zones, etc.

The estimates from the equations for Newtonian fluids give the values  $\delta_j$  and  $\tau_j$  for each  $j$ , where  $j$  is the measurement point number (i.e., the number of half-periods). The values are used to find the effective viscosity  $v_{\text{eff}}$  for each  $j$ , and then the unknown rheological constants are determined from the dependence  $v_{\text{eff}} = v_{\text{eff}}(D)$ . The objective function  $\Phi$  can be constructed using the least-squares method. As an example, for Bingham fluids, we have:

$$\Phi(v', \sigma_0) = \sqrt{\sum_j (v_j - v_{\text{eff}_j})^2}. \tag{23}$$

For each  $j$ , the value of  $v_j$  in (23) is calculated from viscometric Equations (18)–(20), and viscosity  $v_{\text{eff}} = v' + \sigma_0 / (2\rho D)$  is determined from the value of the shear rate averaged on the time and the surface, solving the fluid flow problem as for Newtonian fluids [59]:

$$D_j = \kappa_j D(r, z), \quad D(r, z) = \frac{|\text{Re}(i_1)| + |\text{Re}(i_2)|}{RH + 0.5R^2}, \tag{24}$$

$$i_1 = \int_0^R D_{z\phi}(r, -H, t) \exp(kt) r dr, \quad i_2 = R \int_{-H}^0 D_{r\phi}(R, z, t) \exp(kt) dz,$$

i.e.,

$$i_1 = -\frac{1}{4} \sum_l \frac{b_l \theta_l \pi R \text{th}(\theta_l H)}{\mu_l} [(J_1(\mu_l R) H_0(\mu_l R) - J_0(\mu_l R) H_1(\mu_l R))],$$

$$i_2 = -\frac{1}{2} R H i \beta q \alpha_0 j \frac{J_2(\beta)}{J_1(\beta)} - \frac{1}{2} R \sum_l \frac{b_l J_2(\mu_l R) \mu_l \text{th}(\theta_l H)}{\theta_l}, \tag{25}$$

where  $b_l = 2iq\alpha_0j(\mu_l^2/\theta_l^2 - 1)/\mu_l J_0(\mu_l R)$ . The following expressions to calculate  $H_\ell$ ,  $J_\ell$  [48], and  $\mu_l$  [23] can be used:

$$J_\ell(z) = \pi^{-1} \int_0^\pi \cos(z \sin \theta - \ell\theta) d\theta, E_\ell(z) = \pi^{-1} \int_0^\pi \sin(\ell\theta - z \sin \theta) d\theta,$$

$$H_0(z) = -E_0(z), H_1(z) = 2/\pi - E_1(z), \mu_l = 0.25\mu_l' l' R^{-1}, l' = \pi(4l + 1),$$

$$\mu_l' = 1 - \frac{6}{l'^2} + \frac{6}{l'^4} - \frac{4716}{5l'^6} + \frac{3902418}{35l'^8} - \frac{8952167292}{35l'^{10}} + \dots,$$

where  $E_\ell$  and  $H_\ell$  are the Weber and Struve functions of  $\ell$ -order, respectively;  $\bar{\kappa}$  is the coefficient of the averaging of  $\exp(-kt)$  on a time interval, i.e., on a period

$$\bar{\kappa} = \{4\pi[\exp(-3\delta/4) + \exp(-\delta/4)] + \delta[1 - \exp(-\delta)]\} (\delta^2 + 4\pi^2)^{-1}. \tag{26}$$

**5. Forced Mode**

*5.1. Linear Fluids*

As an example, we consider the case of the long cylinder and traditional assumptions. For the steady-state oscillations in the form  $\alpha = a \sin(\lambda T + \varphi)$  and for Newtonian fluids, the solution is the following:

$$\bar{a} = (L_r^2 + L_i^2)^{-0.5}, \text{tg } \varphi = -L_i/L_r, \tag{27}$$

where

$$L = s^2 + 1 + D(s), D(s) = \frac{4}{\xi_0} s A \sqrt{s} \frac{I_2(\sqrt{s}\xi_0)}{I_1(\sqrt{s}\xi_0)}, \tag{28}$$

$\bar{a} = a/\alpha_0, L = L_r + iL_i, s = \lambda i, \lambda = \omega/\omega_0; d = \sqrt{\nu/\omega_0}, \alpha_0 = F/(K\omega_0^2), U = \vartheta_\phi/(d\omega_0), T = \omega_0 t$  in the corresponding models (5), (11);  $D(s)$  is given in the form as in [34];  $\varphi$  is the phase shift between the cup oscillations and the driving force;  $\delta_0 \sim 0$ . For comparison, in the damped mode:  $L = s^2 + 1 + D(s) = 0$  (21). The working equations for linear viscoelastic fluids are in [23]. The amplitude  $\bar{a}$  does not depend on  $\alpha_0$  in the linear oscillations (e.g., for the following conditions: the fluid is Newtonian, significant secondary flows are absent, etc.).

*5.2. Nonlinear Fluids*

The steady-state oscillations of the viscometer filled with nonlinear fluids are nonlinear ones, i.e., the amplitude  $\bar{a}$  is not constant as  $\alpha_0$  changes. This allows one to identify nonlinear fluid behavior under other linear assumptions. For estimating the fluid properties, the numerical model can be used or the analytical approach can be developed as in (23)–(26) [60]. For example, for an Ostwald–de Waele fluid, the rheological state equation has the form (13):

$$\sigma_{\xi\phi} = b D_{\xi\phi} D^{m-1}, \tag{29}$$

where the second invariant  $D = |D_{\xi\phi}|$  for the long cylinder;  $b = \omega_0^{m-1} \kappa/\eta; \eta$  is a fixed value of the dynamic viscosity.

The rheological properties are estimated by the fitting procedure. The objective function  $\Phi$  takes into account the relative deviation between the measured and calculated values.  $\Phi$  is constructed by the least-squares method:  $\Phi = \sqrt{\sum (\Delta x_j/\bar{x}_j)^2}$ , where  $\Delta x_j$  and  $\bar{x}_j$  are, respectively, the absolute deviation and the average value of the observable parameter  $x$  between them in the  $j$ -th point; the weight coefficients can be introduced. Function  $\Phi$  is minimized over the set of unknown parameters, and for the fluid (29), the function  $\Phi(b, m) \rightarrow 0$ . The algorithm for estimation is the following [60]: the wall shear rate is determined based on the formula

$$D_0 = a D e^{\bar{\sigma} T}, \tag{30}$$

where

$$D = -s\sqrt{s}\zeta_0 I_2(\sqrt{s}\zeta_0)/I_1(\sqrt{s}\zeta_0), \tag{31}$$

$D = D_r + iD_i$ ,  $D_r$ ,  $D_i$  are the real and imaginary parts of  $D$ ;  $a$  is the amplitude in  $\alpha = \alpha(T)$  that is found from (27) and (28); there is a phase shift in  $\bar{s}$ .

The real part  $D_0$  of  $D_0$  (30) gives the values of the wall shear rate and can be represented as

$$D_0/a = D_r \cos(\lambda T + \varphi + \pi/2) - D_i \sin(\lambda T + \varphi + \pi/2). \tag{32}$$

We determine  $\tilde{D}_0$  as the time-averaged value of  $D_0$ . The averaging is carried out for the half-period beginning from the point  $T_0$  in time when (i)  $D_0|_{T=T_0} = 0$  and (ii) the function  $D_0 = D_0(T)$  increases in  $T = T_0$  and then for  $D_0 \geq 0$ :

$$\tilde{D}_0 = \frac{\lambda}{\pi} \int_{T_0}^{T_0+\pi/\lambda} D_0(T) dT, \tag{33}$$

where the value of  $T_0$  is found as the roots of the function  $D_0 = D_0(T)$  (32). Instead of calculating by using (33) and finding  $T_0$ , the value of  $\tilde{D}_0$  can be determined as the amplitude value of the function  $\tilde{D}_0 = \tilde{D}_0(T_0)$ . The parameter

$$\tilde{\zeta}_{\text{eff}} = \zeta_0 / \sqrt{b\tilde{D}_0^{m-1}} \tag{34}$$

allows one to interpret the nonlinear viscous behavior in terms of the parameter  $\zeta_0$  for the Newtonian model, according to which the amplitude–frequency characteristics are changed with the change in  $\tilde{\zeta}_{\text{eff}}$  in the nonlinear case. The objective function  $\Phi$  includes the difference between  $\zeta_{\text{eff}}$  and  $\tilde{\zeta}_{\text{eff}}$  in the  $j$ -th point, where (i) the value of  $\zeta_{\text{eff}}$  is found from (27) and (28) using the experimental data and  $\tilde{D}_0$  is calculated from (33); (ii)  $\tilde{\zeta}_{\text{eff}}$  is calculated from (34). Figure 10 demonstrates such estimation from the amplitude curves obtained by modeling the experiment.

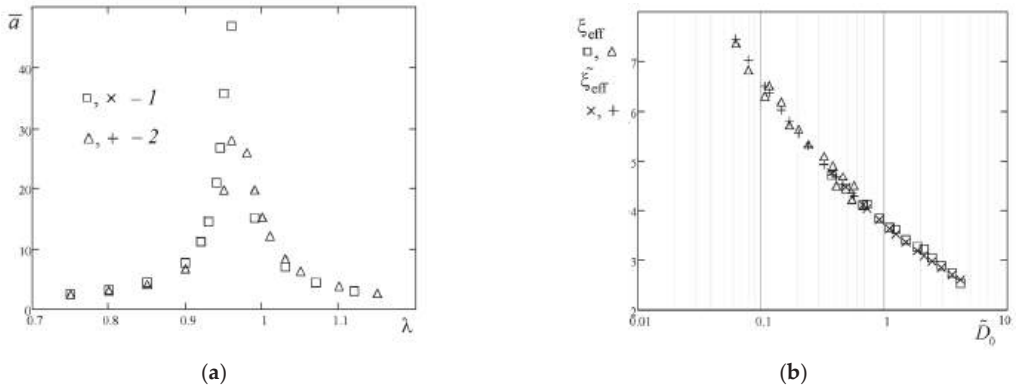


**Figure 10.** An example ( $A = 0.1$ ,  $\zeta_0 = 5$ ;  $b = 1.8$ ,  $m = 1.5$ ;  $1-\alpha_0 = 0.1$ ,  $2-0.01$ ): (a)— $\bar{a} = \bar{a}(\lambda)$ ; (b)— $\tilde{\zeta}_{\text{eff}} = \tilde{\zeta}_{\text{eff}}(\tilde{D}_0)$  and  $\zeta_{\text{eff}} = \zeta_{\text{eff}}(\tilde{D}_0)$ .

### 6. Other Models

The oscillating-cup viscometer is traditionally used for studying materials in their molten state at high temperatures. As the temperature decreases, in particular in the supercooled liquid state, the study is carried out, e.g., with the parallel plate rheometer [61,62]. Additionally, other types of viscometers, such as capillary or rotational ones, are used to analyze metal melts [1,19,21,63,64]. As an example of the methods with oscillating plates, we briefly consider the models for the vibrational and pendulum types [65]. We also

give the generalized model for cylinder viscometry [66], for which an oscillating disc or rotational devices are its special cases.

### 6.1. Oscillating Plate

The oscillating plate method refers to external flows in contrast to internal flows in oscillating-vessel viscometry. In the vibrational case, a thin plate of surface area  $S$  is fixed by means of an elastic element with the spring constant  $k$  and oscillates in its own plane due to the action of the harmonic force  $F \sin \omega t$ . The mathematical model includes the following coupled partial differential equations:

The equation of plate oscillations

$$\frac{d^2 \zeta}{dT^2} + \zeta = \sin \frac{T}{\lambda} - \Phi; \tag{35}$$

The momentum conservation equation

$$\frac{\partial U}{\partial T} = \frac{\partial \sigma_{\zeta\zeta}}{\partial \zeta}; \tag{36}$$

The initial and boundary conditions for (35), (36)

$$d\zeta/dT|_{T=0} = 0, \zeta(0) = 0, U(\zeta, 0) = 0, U(0, T) = y \frac{d\zeta}{dT}, U(\infty, T) = 0; \tag{37}$$

The rheological constitutive equation for the Ostwald–de Waele model

$$\sigma_{\zeta\zeta} = b D_{\zeta\zeta} D^{m-1}, \tag{38}$$

where

$$b = \omega_0^{m-1} \kappa / (v\rho), \zeta = xk/F, T = \omega_0 t, \lambda = \omega_0 / \omega, \omega_0^2 = k/M, \zeta = z/d, d = \sqrt{v/\omega_0}, A = Sv\rho\omega_0/F, y = F/(kd), \beta = \sqrt{2}Ay, U = V/(d\omega_0), D_{\zeta\zeta} = \frac{\partial U}{\partial \zeta}, \Phi = 2A \sigma_{\zeta\zeta}|_{\zeta=0} \tag{39}$$

$A$  is the dimensionless complex characterizing the experimental conditions and the fluid properties;  $d$  is the boundary layer thickness;  $D_{\zeta\zeta}$  is the dimensionless  $\zeta\zeta$ -th component of the tensor of the deformation rates;  $\Phi$  is the dimensionless friction force acting on the plate from the fluid;  $M$  is the mass of the suspension system;  $V$  is the component of the plate velocity directed along the axis  $X$ ;  $X$  and  $Z$  are the axes of the Cartesian coordinate system coinciding and orthogonal to the plate plane (the coordinate  $z = 0$  on the plate);  $x$  is the linear displacement of the plate from the equilibrium;  $y$  is the proportionality factor between scales along the axes  $X$  and  $Z$ ;  $\beta$  is the dimensionless viscosity; and  $\sigma_{\zeta\zeta}$  is the dimensionless  $\zeta\zeta$ -th component of the extra-stress tensor. The damping of the oscillations in the absence of a fluid and the edge effects are neglected for flow conditions  $D = |D_{\zeta\zeta}|$ .

For weakly viscous fluids, the method can be realized in the damped mode. In this case, the first term on the right side of Equation (35) is absent;  $\zeta(0) = \zeta_0$  and  $U(0, T) = \frac{d\zeta}{dT}$  take on the conditions in (37);  $\zeta = x/d$ ,  $A = Sd\rho/M$ , and  $\beta = \sqrt{2}A$  are the parameters in (39). The set of coupled Equations (35)–(39) can be solved numerically for nonlinear fluids, or an analytical approach can be applied, as in (24)–(26). For Newtonian fluids ( $b = m = 1$  in (38)) in steady-state oscillations without the transient, the solutions are as follows:

(i) for the oscillation law  $\bar{a} \sin(T/\lambda + \varphi)$  in the forced mode:

$$\bar{a} = \frac{\lambda^2}{\sqrt{1 + 2\beta\sqrt{\lambda} + \lambda^4 - 2\lambda^2 - 2\beta\lambda^2\sqrt{\lambda} + 2\beta^2\lambda}}, \text{tg } \varphi = -\frac{\beta}{\beta - (\lambda^2 - 1)/\sqrt{\lambda}}; \tag{40}$$

(ii) for the viscometric equation for the damped mode  $\xi = \xi_0 \exp[-iT(\theta - \Delta i)]$ :

$$\left[1 - (\theta - \Delta i)^2\right] - 2A\sqrt{i}(\theta - \Delta i)^{3/2} = 0, \tag{41}$$

where  $\theta = q/q_0$ ,  $\Delta = (\delta/(2\pi)) \cdot q/q_0$ ,  $q = 2\pi/\tau$ , and  $q_0 = 2\pi/\tau_0$ ;  $\xi_0$  is the dimensionless initial displacement of the plate.

In the pendulum case, a thin plate of surface area  $S$  is suspended by means of a system with a moment of inertia  $I$  and torsional stiffness  $K$ . The plate oscillates in its plane around the point of suspension. The oscillation amplitudes are small, the pendulum has a large length, and the plane-parallel motion of the plate is assumed; the edge effects are also neglected. The mathematical model has the form

$$\frac{d^2\alpha}{dt^2} + \frac{r\ell^2}{I} \frac{d\alpha}{dt} + \frac{(Mg\ell_c + K)}{I} \alpha = \frac{F\ell}{I}; \tag{42}$$

$$\frac{\partial V}{\partial t} = \frac{1}{\rho} \frac{\partial \sigma_{zx}}{\partial z}; \tag{43}$$

$$d\alpha/dt|_{t=0} = 0, \alpha(0) = \alpha_0, V(z,0) = 0, V(0,t) = d\alpha/dt \cdot \ell, V(\infty,t) = 0; \tag{44}$$

where  $\ell$  and  $\ell_c$  are the distances from the point of suspension to the center of mass of the pendulum and to the center of the plate;  $r$  is the coefficient of friction force in the absence of a fluid;  $\alpha_0$  is the initial angular displacement from equilibrium;  $D = |D_{zx}|$ ; the friction force  $F = 2S\sigma_{zx}|_{z=0}$ . In terms of the parameters:

$$x = \alpha\ell, T = \frac{2\pi}{\tau_0}t, U = \frac{V}{d} \frac{\tau_0}{2\pi}, d = \sqrt{v \frac{\tau_0}{2\pi}}, \zeta = \frac{z}{d}, \xi = \frac{x}{d}, A = \frac{S\ell^2 d \rho}{I}, \psi_{\zeta\xi} = \frac{\partial U}{\partial \zeta}, \Phi = 2A \cdot (\psi_{\zeta\xi} \cdot \phi(\psi))|_{\zeta=0}$$

Equations (42) and (43) are written as

$$\frac{d^2 \xi}{dT^2} + \frac{\delta_0}{\pi} \frac{d\xi}{dT} + \left[ \left(\frac{\delta_0}{2\pi}\right)^2 + 1 \right] \xi = \Phi; \tag{45}$$

$$\frac{\partial U}{\partial T} = \frac{\partial \psi_{\zeta\xi}}{\partial \zeta} \phi(\psi); \tag{46}$$

where  $\phi(\psi) = 1$ ,  $\phi(\psi) = \psi^{m-1}(2\pi/\tau_0)^{m-1}\kappa/(v\rho)$ ,  $\phi(\psi) = (1 + Bn/\psi)$  for  $\psi > Bn$  and  $\psi_{\zeta\xi} = 0$  for  $\psi < Bn$  for Newtonian, power-law, and Bingham fluids, respectively; the natural frequency  $\omega_0$  is excluded from the observed parameters. The model in (45), (46) is similar to the model in (35), (36) for the damped mode (with different  $A$ ), and their analyses can be combined. The oscillation parameters for the empty pendulum and vibrational viscometers are the following, respectively:

$$\tau_0^2 = \frac{4\pi^2 I^2}{I(Mg\ell_c + K) - 0.25r^2\ell^4}, \delta_0 = \frac{1}{2} \frac{r\ell^2\tau_0}{I}; \tau_0^2 = \frac{4\pi^2 M^2}{Mk - 0.25r^2}, \delta_0 = \frac{1}{2} \frac{r\tau_0}{M}. \tag{47}$$

The set (35), (36) includes the system state vector ( $U$  and  $\xi$ ), the spatiotemporal coordinates ( $\zeta$  and  $T$ ), and only parameter  $A$  characterizing the fluid properties and experimental conditions and giving the data for an optimal experimental design.

Some results calculated for the vibrational viscometer using the models are shown in Figure 11 for the forced mode and in Figure 12 for the damped mode. Figure 12 corresponds to the formula obtained from (41) by taking into account the decrement  $\delta_0$  in the absence of a fluid and introducing the  $q_0$  instead of  $\omega_0$  to determine the dimensionless parameters:

$$\tilde{F} = Q^2 Q_0^2 \left[ (1 - \tilde{\Delta}i)^2 + 2\alpha\sqrt{i}Q^{-1/2}(1 - \tilde{\Delta}i)^{3/2} + 2\tilde{\Delta}_0(i + \tilde{\Delta})Q^{-1} \right] - 1 = 0, \tag{48}$$

where

$$Q = \omega/q_0, \alpha = S\rho\tilde{a}/M, \tilde{d} = \sqrt{v/q_0}, \tilde{\Delta} = \delta/2\pi, \tilde{\Delta}_0 = \delta_0/2\pi.$$

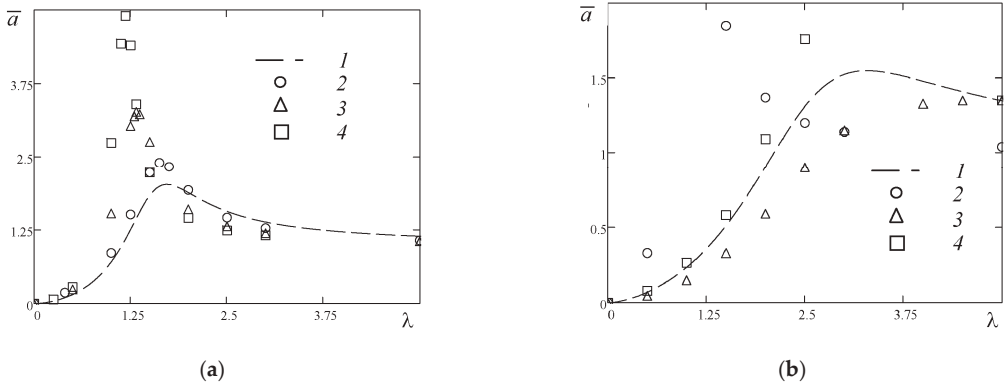


**Figure 11.** The amplitude curves for power-law fluids ( $y = 0.1$ ): (a)—for different  $b$  ( $1-b = 1, m = 1, \beta = 1$ ;  $2-b = 10, m = 2, \beta = 1$ ;  $3-b = 1, m = 2, \beta = 1$ ;  $4-b = 0.1, m = 2, \beta = 1$ ); (b)—for different  $\beta$  and  $m$  ( $1-b = 1, m = 1, \beta = 3$ ;  $2-b = 1, m = 2, \beta = 0.1$ ;  $3-b = 1, m = 0.5, \beta = 1$ ;  $4-b = 1, m = 2, \beta = 10$ ).

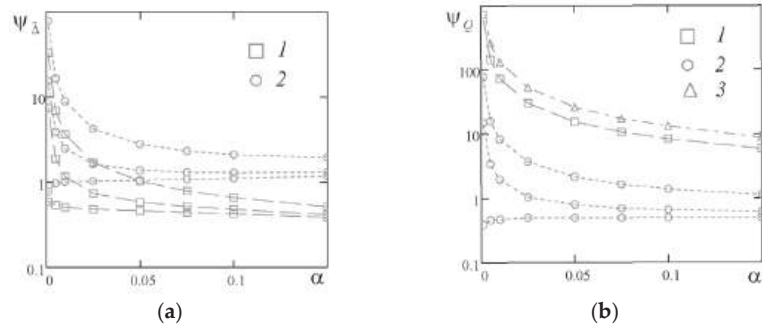


**Figure 12.** The sensitivity of  $\alpha$  to the oscillation parameters ( $1-c_1 = c_2$ ;  $2-c_1 \neq 0, c_2 = 0$ ;  $3-c_1 = 0, c_2 \neq 0$ ); the curves correspond to different  $\tilde{\Delta}_0$ , beginning from the bottom: (a)—0, 0.01, 0.05, 0, 0.01, 0.05; (b)—0, 0.01, 0.05, 0.05, 0.05.

Identification of  $\alpha$ , i.e.,  $v$  from (48), can be carry out by minimization of the function  $\tilde{f}(\alpha) = \sqrt{c_1 \text{Re}^2(\tilde{F}) + c_2 \text{Im}^2(\tilde{F})}$ . The sensitivities  $\psi_\Delta$  and  $\psi_Q$  in Figure 12 are found as the response of  $\alpha$  to a change in the oscillation parameters  $\tilde{\Delta}$  and  $Q$ .

### 6.2. General Model

Let there be two cylinders: the cup of the inner radius  $R_1$  and the height  $H_1$  and the bob of the outer radius  $R_2 < R_1$  and of the height  $H_2 \leq H_1$ . Their axes of symmetry coincide with each other, the distance between their top ends is equal to  $h$ , the investigated fluid is placed between the cylinders. The model corresponds to external and internal flows and the damped and forced modes and can be used for the rotation case with the corresponding external torque. Such a generalized viscometric model for vertical cylindrical geometry contains the following equations: the mass conservation equation

$$\nabla \cdot \mathbf{V} = 0 \tag{49}$$

and the momentum conservation equation

$$\rho \frac{DV}{Dt} = \mathbf{F}_e + \mathbf{F}_s, \mathbf{F}_e = \rho \mathbf{g}, \mathbf{F}_s = \nabla \cdot \mathbf{T}, \mathbf{T} = -p\mathbf{1} + \boldsymbol{\sigma} \tag{50}$$

for the investigated fluid and the equations for the external ( $i = 1$ ) and internal ( $i = 2$ ) cylinders

$$\ddot{\alpha}_i = P_{\Sigma i} / K_i, \tag{51}$$

where the torque applied from the fluid

$$P = (-1)^i \left[ -2\pi R_i^2 \int_0^{H_i} \sigma_{\phi r} |_{R_i} dz + 2\pi \int_0^{R_i} r^2 dr \left( \sigma_{\phi z} |_{0((H_1-H_2-h) - i=2)} - (a-1) \sigma_{\phi z} |_{H_1((H_1-h) - i=2)} \right) \right],$$

$\mathbf{F}_e + \mathbf{F}_s$  is the extensional and surface external force resulting;  $\mathbf{V}(\vartheta_r, \vartheta_\phi, \vartheta_z)$  is the velocity vector;  $\mathbf{T}$  is the Cauchy stress tensor;  $P_\Sigma = P + P_0 + P_f$  is the total external torque, where  $P_0 = P_e + P_r$ ,  $P_r = 0$  for  $i = 2$ ,  $P_f = 0$  for the damped oscillation mode;  $\alpha_i$  is the angular displacement of the cylinders from the equilibrium for oscillation mode or other position;  $\boldsymbol{\sigma}$  is the extra stress tensor;  $\sigma_{ij}$  is  $ij$ -th component of  $\boldsymbol{\sigma}$ ; the axis-symmetric case and  $\rho = \text{const}$  are considered;  $\nabla \cdot$  is the divergence;  $D/Dt$  is the substantial derivative; the coordinate origin is located at the cup bottom on the axis of symmetry. The model (49)–(51) also includes a rheological constitutive equation. The initial conditions for the bob and the cup are analogous to (6). The boundary conditions are the following:

$$\begin{aligned} r = 0 \ (z \in [0; H_1 - H_2 - h], z \in [H_1 - h; H_1]) : \vartheta_r = \vartheta_\phi = d\vartheta_z / \partial r = 0; \\ r = R_2 \ (z \in [H_1 - H_2 - h; H_1 - h]) : \vartheta_r = \vartheta_z = 0, \vartheta_\phi = \dot{\alpha}_2 R_2; \\ r = R_1 \ (z \in [0; H_1]) : \vartheta_r = \vartheta_z = 0, \vartheta_\phi = \dot{\alpha}_1 R_1; z = 0 \ (r \in [0; R_1]) : \vartheta_r = \vartheta_z = 0, \vartheta_\phi = \dot{\alpha}_1 r; \\ z = H_1 \ (r \in [0; R_1]) : \vartheta_r = \vartheta_z = 0, \vartheta_\phi = \dot{\alpha}_1 r \ (a = 2) \text{ and } \partial\vartheta_r / \partial z = \partial\vartheta_\phi / \partial z = \vartheta_z = 0 \ (a = 1); \\ z = H_1 - H_2 - h \text{ and } z = H_1 - h \ (r \in [0; R_2]) : \vartheta_r = \vartheta_z = 0, \vartheta_\phi = \dot{\alpha}_2 r. \end{aligned}$$

### 7. Conclusions

The mathematical model of the oscillating-cup experiment includes coupled nonlinear differential equations for the cylinder oscillations ((5) and (10)) and for the investigated fluid (the mass conservation Equation (1), the momentum conservation Equations (2)–(4) and (11), and the rheological constitutive Equations (7)–(9) and (12)–(16)). With different assumptions, the model can be applied to solve the following various problems: to study the secondary flows in the viscometer and to carry out the data processing for higher amplitude oscillations from the model without the usual assumptions (1)–(9); to measure the rheological properties and model the viscometric experiment in the damped ((10), (11)) and forced ((1)–(5)) modes by using both numerical methods for these equations and the developed analytical approach ((23)–(26), (30)–(34)) for nonlinear fluids, as well as the classic viscometric equations for Newtonian fluids ((18)–(22)). These models are special cases of the generalized model ((49)–(51)) for torsional viscometers with bob and cup. As an example of external viscometric flow, the oscillating plate technique is analyzed in terms of the model in (35)–(39) for the damped and forced modes.

**Funding:** This research received no external funding.

**Institutional Review Board Statement:** Not applicable.

**Informed Consent Statement:** Not applicable.

**Data Availability Statement:** Not applicable.

**Conflicts of Interest:** The authors declare no conflict of interest.

## References

- Shvidkovskiy, Y.G. *Certain Problems Related to the Viscosity of Fused Metals*; NASA-TT-F-88; GITTL: Moscow, Russia, 1962. (In Russian)
- Zhao, D.; Yan, L.; Jiang, T.; Peng, S.; Yue, B. On the viscosity of molten salts and molten salt mixtures and its temperature dependence. *J. Energy Storage* **2023**, *61*, 106707. [CrossRef]
- Pries, J.; Weber, H.; Benke-Jacob, J. Fragile-to-strong transition in phase-change material Ge<sub>3</sub>Sb<sub>6</sub>Te<sub>5</sub>. *Adv. Funct. Mater.* **2022**, *32*, 2202714. [CrossRef]
- Zhu, W.; Gulbitten, O.; Aitken, B.; Sen, S. Viscosity, enthalpy relaxation and liquid-liquid transition of the eutectic liquid Ge<sub>15</sub>Te<sub>85</sub>. *J. Non-Cryst. Solids* **2021**, *554*, 120601. [CrossRef]
- Magnusson, J.; Munro, T.; Memmott, M. Review of thermophysical property methods applied to fueled and un-fueled molten salts. *Ann. Nucl. Energy* **2020**, *146*, 107608. [CrossRef]
- Nell, S.; Yang, F.; Evenson, Z.; Meyer, A. Viscous flow and self-diffusion in densely and loosely packed metallic melts. *Phys. Rev. B* **2021**, *103*, 064206. [CrossRef]
- Brillo, J.; Arato, E.; Giuranno, D.; Kobatake, H.; Maran, C.; Novakovic, R.; Ricci, E.; Rosello, D. Viscosity of liquid Ag-Cu alloys and the competition between kinetics and thermodynamics. *High Temp. High Press.* **2018**, *47*, 417–441.
- Assael, M.J.; Kalyva, A.E.; Antoniadis, K.D.; Banish, R.M.; Egry, I.; Wu, J.; Kaschnitz, E.; Wakeham, W.A. Reference Data for the Density and Viscosity of Liquid Copper and Liquid Tin. *J. Phys. Chem. Ref. Data* **2010**, *39*, 033105. [CrossRef]
- Horne, K.; Ban, H. Sensitivity analysis of the transient torque viscosity measurement method. *Metrologia* **2015**, *52*, 1. [CrossRef]
- Jin, Y.; Cheng, J.; An, X.; Su, T.; Zhang, P.; Li, Z. Accurate viscosity measurement of nitrates/nitrites salts for concentrated solar power. *Sol. Energy* **2016**, *137*, 385–392. [CrossRef]
- Mao, Z.; Zhang, T. Numerical analysis of an improved heating device for the electromagnetically driven oscillating cup vis-cometer. *Adv. Mech. Eng.* **2017**, *9*, 10. [CrossRef]
- Nunes, V.M.B.; Lourenço, M.J.V.; Santos, F.J.V.; Nieto de Castro, C. Measurements of the Viscosity of Molten Lithium Nitrate by the Oscillating-cup Method. *Int. J. Thermophys.* **2017**, *38*, 13. [CrossRef]
- Questaed, P.; Redgrove, J. Issues concerning measurement of the viscosity of liquid metals. In Proceedings of the IUPAC Meeting, Bergen, Norway, 5–6 April 2003.
- Gruner, S.; Hoyer, W. A statistical approach to estimate the experimental uncertainty of viscosity data obtained by the oscillating cup technique. *J. Alloys Comp.* **2009**, *480*, 629–633. [CrossRef]
- Cheng, J.; Gröbner, J.; Hort, N.; Kainer, K.U.; Schmid-Fetzer, R. Measurement and calculation of the viscosity of metals—A review of the current status and developing trends. *Meas. Sci. Technol.* **2014**, *25*, 062001. [CrossRef]
- Tolbaru, D.; Popescu, A.-M.; Zuca, S. Error Analysis of the Oscillating Cup Method for Viscosity Measurements of Molten Salts. *Z. Naturforsch.* **2008**, *63*, 57–60. [CrossRef]
- Jeyakumar, M.; Hamed, M.; Shankar, S. Rheology of liquid metals and alloys. *J. Non-Newton. Fluid Mech.* **2011**, *166*, 831–838. [CrossRef]
- Malik, M.M.; Jeyakumar, M.; Hamed, M.S.; Walker, M.J.; Shankar, S. Rotational rheometry of liquid metal systems: Measurement geometry selection and flow curve analysis. *J. Non-Newton. Fluid Mech.* **2010**, *165*, 733–742. [CrossRef]
- Ritwik, R. Measuring the Viscous Flow Behaviour of Molten Metals under Shear. Ph.D. Thesis, Brunel University, London, UK, 2012.
- Elton, E.S.; Reeve, T.C.; Thornley, L.E.; Josphura, I.D.; Paul, P.H.; Pascall, A.J.; Jeffries, J.R. Dramatic effect of oxide on measured liquid metal rheology. *J. Rheol.* **2020**, *64*, 119–128. [CrossRef]
- Brooks, R.F.; Dinsdale, A.T.; Questaed, P.N. The measurement of viscosity of alloys—A review of methods, data and models. *Meas. Sci. Technol.* **2005**, *16*, 354–362. [CrossRef]
- Nunes, V.M.B.; Santos, F.J.V.; de Castro, C.A.N. A High-Temperature Viscometer for Molten Materials. *Int. J. Thermophys.* **1998**, *19*, 427–435. [CrossRef]
- Kleiman, R.N. Analysis of the oscillating-cup viscometer for the measurement of viscoelastic properties. *Phys. Rev.* **1987**, *35*, 261–275. [CrossRef]
- Zhu, P.; Lai, J.; Shen, J.; Wu, K.; Zhang, L.; Liu, J. An oscillating cup viscometer based on Shvidkovskiy algorithm for molten metals. *Measurement* **2018**, *122*, 149–154. [CrossRef]
- High-Temperature Oscillating-Cup Viscometer. Available online: <https://www.tu-chemnitz.de/physik/RND/ausruest.php.en> (accessed on 9 May 2023).
- Sakata, K.; Mukai, M.; Rajesh, G.; Arivanandhan, M.; Inatomi, Y.; Ishikawa, T.; Hayakawa, Y. Viscosity of molten InSb, GaSb, and In<sub>x</sub>Ga<sub>1-x</sub>Sb alloy semiconductors. *Int. J. Thermophys.* **2014**, *35*, 352–360. [CrossRef]
- Macosko, C.W. *Rheology: Principles, Measurements and Applications*; Wiley/VCH: New York, NY, USA, 1994.
- Grouvel, J.M.; Kestin, J. Working equations for the oscillating-cup viscometer. *Appl. Sci. Res.* **1978**, *34*, 427–443. [CrossRef]
- Nieuwoudt, J.C.; Sengers, J.V.; Kestin, J. On the theory of oscillating-cup viscometers. *Phys. A. Stat. Mech. Its Appl.* **1988**, *149*, 107–122. [CrossRef]
- Elyukhina, I.; Vikhansky, A. On the secondary flows in oscillating-cup viscometer. *Measurement* **2023**, *206*, 112267. [CrossRef]

31. Elyukhina, I.V.; Vyatkin, G.P. Evaluation of the effect of secondary flows on the oscillations of an oscillating-cup viscometer. *Dokl. Phys.* **2006**, *51*, 459–460. [CrossRef]
32. Elyukhina, I.; Vyatkin, G. Software for oscillating-cup viscometry: Verification of data reasonableness and parametric identification of rheological model. *J. Phys. Conf. Ser.* **2008**, *98*, 022011. [CrossRef]
33. Lourenço, M.J.V.; Santosó, F.J.V.; Nieto de Castro, C.A. The meniscus effect in viscosity determinations by the oscillating-cup method. *High Temp. High Press.* **2003**, *35*, 75–80.
34. Kestin, J.; Newell, G.F. Theory of oscillation type viscometers: The oscillating cup. Part I. *Z. Angew. Math. Phys.* **1957**, *8*, 433–449. [CrossRef]
35. Ostwald, W. About the rate function of the viscosity of dispersed systems. *Kolloid Z.* **1925**, *36*, 99–117. [CrossRef]
36. De Waele, A. Viscometry and plastometry. *J. Oil Color Chem. Assoc.* **1923**, *6*, 33–88.
37. Bingham, E.C. *Fluidity and Plasticity*; McGraw-Hill: New York, NY, USA, 1922.
38. Burgos, G.R.; Alexandrou, A.N.; Entov, V. On the determination of yield surfaces in Herschel–Bulkeley fluids. *J. Rheol.* **1999**, *43*, 463–483. [CrossRef]
39. Johnson, M.; Segalman, D. A model for viscoelastic fluid behavior which allows non-affine deformation. *J. Non-Newton. Fluid Mech.* **1977**, *2*, 255–270. [CrossRef]
40. Beverly, C.R.; Tanner, R.I. Numerical analysis of three-dimensional Bingham plastic flow. *J. Non-Newton. Fluid Mech.* **1992**, *42*, 85–115. [CrossRef]
41. Keentok, M.; Georgescu, A.G.; Sherwood, A.A.; Tanner, R.I. The measurement of the second normal stress difference for some polymer solutions. *J. Non-Newton. Fluid Mech.* **1980**, *6*, 303–324. [CrossRef]
42. Elyukhina, I.V. The observation and measurement of the non-Newtonian properties of high-temperature fluids using the torsional-oscillation method. *High Temp.* **2006**, *44*, 406–413. [CrossRef]
43. Vyatkin, G.P.; Elyukhina, I.V. The potential of an oscillating-cup viscometer for the analysis of elastic viscoplastic properties. *Dokl. Phys.* **2006**, *51*, 90–92. [CrossRef]
44. Elyukhina, I.V. Johnson-Segalman fluid behavior in a oscillating-cup system. *Russ. J. Phys. Chem.* **2006**, *80*, 819–822. [CrossRef]
45. Kehr, M.; Hoyer, W.; Egry, I. A New High-Temperature Oscillating Cup Viscometer. *Int. J. Thermophys* **2007**, *28*, 1017–1025. [CrossRef]
46. Elyukhina, I. Nonlinear oscillating-cup viscometry. *Rheol. Acta* **2011**, *50*, 327–334. [CrossRef]
47. Beckwith, D.A.; Newell, G.F. Theory of oscillating type viscometers: The oscillating cup. Part II. *Z. Angew. Math. Phys.* **1957**, *8*, 450–465. [CrossRef]
48. Kholpanov, L.P.; Elyukhina, I.V. Identification of the complex nonlinear processes. *Theor. Found. Chem. Eng.* **2009**, *43*, 869–880. [CrossRef]
49. Abramowitz, M.; Stegun, I.A. (Eds.) *Handbook of Mathematical Functions with Formulas, Graphs and Mathematical Tables*; Dover Publications: Mineola, NY, USA, 1972.
50. Wittenberg, L.J.; Ofte, D.; Curtiss, C.F. Fluid Flow of Liquid Plutonium Alloys in an Oscillating-Cup Viscosimeter. *J. Chem. Phys.* **1968**, *48*, 3253–3260. [CrossRef]
51. Roscoe, R. Viscosity Determination by the Oscillating Vessel Method I: Theoretical Considerations. *Proc. Phys. Soc.* **1958**, *72*, 576–584. [CrossRef]
52. Nieuwoudt, J.C. An extension of the theory of oscillating cup viscometers. *Int. J. Thermophys.* **1990**, *11*, 525–535. [CrossRef]
53. Wang, D.; Overfelt, R.A. Oscillating cup viscosity measurements of aluminum alloys: A201, A319 and A356. *Int. J. Thermophys.* **2002**, *23*, 1063–1076. [CrossRef]
54. Iida, T.; Guthrie, R.I.L. *The Physical Properties of Liquid Metals*; Clarendon Press: Oxford, UK, 1988.
55. Torklep, K.; Oye, H.A. An absolute oscillating cylinder (or cup) viscometer. *J. Phys. Sci. Instrum.* **1979**, *12*, 875–885. [CrossRef]
56. Krall, A.H.; Sengers, J.V. Simultaneous measurement of viscosity and density with an oscillating-disk instrument. *Int. J. Thermophys.* **2003**, *24*, 337–359. [CrossRef]
57. Elyukhina, I. Oscillating-cup technique for yield stress and density measurement. *J. Mater. Sci.* **2013**, *48*, 4387–4395. [CrossRef]
58. Elyukhina, I.V.; Vyatkin, G.P. Analytical method for estimating the nonlinear properties of liquids by a torsion viscosimeter. *J. Eng. Phys. Thermophys.* **2008**, *81*, 544–550. [CrossRef]
59. Elyukhina, I.V. Theoretical foundation of oscillating-cup viscometry for viscoplastic fluids. *High Temp.* **2009**, *47*, 533–537. [CrossRef]
60. Elyukhina, I.V. Oscillating-Cup Viscometer for Nonlinear Fluids in Forced Mode. *High Temp.* **2022**, *60*, 328–334. [CrossRef]
61. Parthiban, R.; Stoica, M.; Kaban, I.; Kumar, R.; Eckert, J. Viscosity and fragility of the supercooled liquids and melts from the Fe–Co–B–Si–Nb and Fe–Mo–P–C–B–Si glass-forming alloy systems. *Intermetallics* **2015**, *66*, 48–55. [CrossRef]
62. Yuan, B.; Aitken, B.; Sen, S. Structure and Rheology of Se-I Glasses and Supercooled Liquids. *J. Non-Cryst. Solids* **2020**, *544*, 120106. [CrossRef]
63. Bakhtiyarov, S.I.; Overfelt, R.A. Measurement of liquid metal viscosity by rotational technique. *Acta Mater.* **1999**, *47*, 4311–4319. [CrossRef]
64. Shpilrain, E.E.; Fomin, V.A.; Skovorodko, S.N.; Sokol, G.F. *Research on Liquid-Metal Viscosity*; Nauka: Moscow, Russia, 1983. (In Russian)

65. Elyukhina, I.V.; Vyatkin, G.P. Identification of the nonlinear viscous properties of fluids by the vibrational method. *J. Eng. Phys. Thermophys.* **2005**, *78*, 907–915. [CrossRef]
66. Elyukhina, I. Modeling the experiments in an oscillating cylinder viscometry. *AIP Conf. Proc.* **2015**, *1648*, 850077. [CrossRef]

**Disclaimer/Publisher's Note:** The statements, opinions and data contained in all publications are solely those of the individual author(s) and contributor(s) and not of MDPI and/or the editor(s). MDPI and/or the editor(s) disclaim responsibility for any injury to people or property resulting from any ideas, methods, instructions or products referred to in the content.



Review

# A Review of Methods, and Analytical and Experimental Studies on the Use of Coal–Water Suspensions

Konstantin Osintsev <sup>1</sup>, Sergei Aliukov <sup>2,\*</sup> and Anatoliy Alabugin <sup>3</sup>

<sup>1</sup> Department of Energy and Power Engineering, Institute of Engineering and Technology, South Ural State University, 76 Prospekt Lenina, 454080 Chelyabinsk, Russia

<sup>2</sup> Department of Automotive Engineering, Institute of Engineering and Technology, South Ural State University, 76 Prospekt Lenina, 454080 Chelyabinsk, Russia

<sup>3</sup> Department of Digital Economy and Information Technology, School of Economics and Management, South Ural State University, 76 Prospekt Lenina, 454080 Chelyabinsk, Russia

\* Correspondence: alysergey@gmail.com

**Abstract:** Research in the field of building mathematical models for combustion processes has been ongoing ever since the chemical reactions of combustion were first discovered. The authors of this review have systematized mathematical models of coal–water suspension (CWS) combustion processes, the sequence of analytical and experimental studies, and have also shown the global genesis of the CWS use. In addition, this review touches upon a topic that is inextricably linked with the combustion of CWS, namely their transportation from the place of coal mining to their place of thermal utilization. For developing countries, their own energy independence is in the foreground, as it is the basis for their economic independence and also a means for other sectors of their economy to be protected from the impact of market changes in fuel prices in the future spot world market. The authors of this review explored the possibility of using Kyrgyz brown coal and transporting it through a coal pipeline from a mountainous area to an industrial site for thermal utilization in specialized steam boiler units. As the economic analysis showed, for the conditions of the Republic of Kyrgyzstan, the use of CWS and coal pipelines with rising prices for natural gas is economically justified. The recommendations of the authors are used in scientific reports and methodological recommendations for the energy and mining sectors of the Republic of Kyrgyzstan, how the recommendations can also be applied to similar conditions in the highlands of Russia, China, and India.

**Keywords:** coal–water suspensions (CWS); combustion process; mathematical modeling; studies; transportation

**MSC:** 93A30

**Citation:** Osintsev, K.; Aliukov, S.; Alabugin, A. A Review of Methods, and Analytical and Experimental Studies on the Use of Coal–Water Suspensions. *Mathematics* **2022**, *10*, 3915. <https://doi.org/10.3390/math10203915>

Academic Editor: Xiangmin Jiao

Received: 9 October 2022

Accepted: 17 October 2022

Published: 21 October 2022



**Copyright:** © 2022 by the authors. Licensee MDPI, Basel, Switzerland. This article is an open access article distributed under the terms and conditions of the Creative Commons Attribution (CC BY) license (<https://creativecommons.org/licenses/by/4.0/>).

## 1. Introduction

Mathematical models of solid and gaseous fuels began to be compiled by scientists in the first half of the 20th century, when the concept of the kinetics of chemical reactions were developed. Spaulding [1], Zeldovich [2], and Williams [3] presented detailed information on the mathematical modeling for the combustion kinetics of coal–water suspensions. The researchers emphasized that the efficiency of fuel combustion depends on the thermo-physical characteristics of organic fuel [2], on the design of the burner [1], and—for solid fuel—also on the degree of grinding [3]. Verwey, Overbeck [4], and Furnas [5] laid the foundations for the mathematical description of the physical processes that occur during the combustion of colloidal mixtures, taking into account the size of the coal particles included in these mixtures. When burning liquid fuels, the forces of viscosity become important, and, for water-based suspensions, taking into account the forces of intermolecular

attraction (i.e., van der Waals forces) allows one to create more accurate mathematical models for studying the combustion of coal–water fuels. Krieger and Dougherty [6], Takano, Cambe [7], Freiling [8], and Rutgers [9] all conducted rheological studies of suspensions and attempted to create prototypes for a mathematical description of the behavior of suspensions during their combustion. The rheology of suspensions is so unusual that individual branches and institutes have taken up the mathematical description, at low temperatures, of their behavior. Yufin [10] laid the foundations for the mechanization of coal and ore mining via the hydraulic method. Jvarsheishvili [11] and Tsarnat [12] determined the controlled technical parameters of hydromechanization. Further, the work of [13] shows the features of the operation of pipelines for transporting suspensions in winter. Similar developments are considered in [14], and in the article [15]. Volkov and Gokhman summarized the developments available at that time in the field of pipeline transport for transporting suspensions over long distances. In later works [16,17], Chinese scientists studied the freezing of ballast water in a mixture of coal ore. However, that which is of the greatest interest in this area are the studies of Li, Huang, and Lv [18,19], in which the authors studied the effect of low temperatures on the movement of water inside coals and the movement of suspensions. We note the works [20,21], in which the numerical simulation of the process of transporting suspensions at low ambient temperatures was carried out. At the same time, an experimental study was carried out in [22], and an attempt was made in [23] to mathematically model the processes presented in [20,21].

In Kyrgyzstan, in the 1970–1980s of the 20th century, a technology was developed for the disposal of dispersed coal sludge. This dispersed coal sludge was polluting the environment and is formed in the processes of enrichment, hydro-extraction, and transportation of coal from a mine using pipeline transport [24]. Mathematical models have been developed for these processes, such as in models to reduce environmental pollution [25], coal combustion [26], and transportation [27]. Due to the high stability and dispersion of sludge suspensions, significant costs are required for their dehydration [28]; further, direct combustion of sludge suspensions in thermal units would solve the problem of their disposal [24]. It was assumed that, under certain conditions, this could be more profitable and more technologically advanced than the combustion of dispersed coal released by dehydration and the drying of slurry suspensions [29,30]. In techno-economic calculations of the efficiency of direct combustion, it was assumed that the cost of coal sludge is small compared to other costs for their processing into a technologically acceptable fuel [31,32].

The development of the world economy and the steady upward trend in prices for petroleum products lead to an intensive search for new technologies for processing coals [33,34], the proven reserves of which are more than 20 times greater than those of oil. Currently, in such countries as China, Japan, Italy, the USA, Sweden, and Russia, special attention is paid to water–coal suspensions [35,36] as a real alternative to liquid fuels from oil. First of all, this is due to the significant scientific and technical potential accumulated by these countries in the field of production, transportation, storage, and the combustion of coal–water fuel (CWF) in boiler plants of thermal power plants, steam-gas, and gas turbines.

In China, for the technical guidance on the introduction of water–coal fuel [37,38], the State Center for Coal-Water Suspensions of the Coal Industry was established. In 2001, China consumed more than 2.0 million tons of such suspensions [39,40] per year. Fuel preparation was carried out at eight plants with a capacity of up to 600 thousand tons per year. The consumers were thermal power plants that previously operated on fuel oil, enterprises of the chemical, metallurgical, pulp and paper, and other industries. In the next 20 years, it is planned that the capacity for the production of CWF to 100 million tons per year [41,42] will be increased.

One of the ways to increase the generation of electrical and thermal energy by the fuel and energy complex of Kyrgyzstan is to increase the share of coal in the combusted raw materials. In the future, the increase in generating capacities will also be carried out at the

expense of thermal power plants that operate on the low-grade coals of the Karakechi coal basin, as such the volume of consumption of these will increase annually.

A significant increase in the share of coal in the generation of heat and electricity in the Kyrgyz Republic requires the development of new energy and environmentally advanced technologies for the processing and burning of coal. One of the most economically justified and environmentally friendly types of fuel at large thermal power plants of the country and boiler plants is the use of suspension coal–water fuels.

It must be noted that preliminarily carried out deep demineralization of the solid phase of the coal suspension—via flotation methods—reduces the ash content of the fuel to 2–3%. According to the literature data [41,42], the conversion of demineralized coal into CWF with a fineness of less than 10  $\mu\text{m}$ , will reduce the ignition temperature, which is about 500 °C for existing CWF. Transferring demineralized coal to an ultra-dispersed state with an average particle size of less than 1  $\mu\text{m}$  will make it possible to bring the ignition temperature of the coal dispersion to the ignition temperature of diesel fuel (about 350 °C) and, at the same time, obtain the rheological properties of CWF close to those of diesel fuel [43]. This provides grounds to assume that a water–coal suspension based on coal in an ultra-dispersed state will have consumer characteristics close to conventional diesel fuel.

From the literature data [44,45], it is known that the presence of solid particles of a certain composition, concentration, shape, size, and other physicochemical and technological parameters in a liquid can significantly change, on the one hand, the initial properties of the liquid itself and, on the other hand, the properties of the filler. In this sense, the suspension is a liquid–microsolid-phase quasi-equilibrium system that has all the features of a classical composite material. Based on this, the suspension can be conditionally classified as a specific liquid-phase composite material with broad functional and technological capabilities, physicochemical, and consumer properties [44,45].

In known methods, the process of preparing various suspensions consisting of a mechanical mixture of a liquid phase (filler) is divided in time. In this case, the fractionation and dispersion of the solid product is carried out mechanically, and then it is mixed with the liquid matrix. In this case, the mixing process can be combined with the grinding of the filler, separation, and other processes. Such a sequence of actions reduces the efficiency of activation of the liquid-phase matrix by solid filler particles [44].

The functional activity of various liquids can be controlled by varying the pressure of the flow with particles, the size of the fractionation vessel, the number of fractionation stages, the diameter of the nozzle for the microheterogeneous phase, and other technological parameters of the entire process [43,46]. Thus, hydro percussion, multi-stage fractional technology makes it possible to combine the processes of formation of a highly dispersed solid phase and suspension as a whole, and to increase the functional activity of the latter.

The positive parameters of the proposed method for obtaining activated carbon suspensions include easy process controllability, production of suspensions on an industrial scale, and no restrictions on the strength characteristics of the solid phase.

The main activating factor of the proposed hydro-percussion method for obtaining activated suspensions based on highly dispersed coal particles should include the following:

- a formation of highly dispersed coal particles after multiple fractionations, directly inside the liquid matrix;
- a developed (large) surface of coal particles;
- an impact on the liquid of mechano-chemical, physical, and other processes occurring after contact with fine particles of coal.

Such processes include reusable hydrodynamic, shock-acoustic impact, etc., on the vessel surface, which, as is known, leads to the activation of the liquid matrix itself (to the possibility of the manifestation of synergistic [47] activation effects). This is explained by the fact that hydraulic shock activation of the liquid in combination with super active particles of coal (filler) can lead to the appearance of nonlinear effects in the functional properties of the final product, which its original elements (components) did not possess. In other words, the classical rule of “mixtures” may not hold, i.e., all necessary and sufficient

conditions are created for the manifestation of synergy in the properties of the suspension activated according to the proposed method.

The constant search for optimal solutions that allow the fuel and energy complex of coal-producing countries to effectively master the necessary volumes of fuel transportation at the lowest possible cost of funds is currently one of the main, and most promising, tasks for the development and further stabilization of energy markets. Each type of transportation of solid fuel has its own specific features. To determine the areas of economically viable uses of a particular type of coal transport, it is necessary to take into account various factors, including the specific properties of the transported coal. When comparing the options for transporting coal by various modes of transport, the main indicators are: the technological properties of coal, (which includes their physical and chemical characteristics, as well as including granulometric and ash composition, gas recovery, grindability coefficient, and tendency to grindability); the level of operating costs (the cost of transportation); capital investments; movement speed and delivery time; availability of transportation and throughput capabilities; maneuverability in ensuring transportation in various conditions; reliability and uninterrupted transportation, i.e., their regularity; and lastly, conditions for the efficient use of vehicles, mechanization, and automation of loading and unloading operations.

All of the above encourages researchers to develop a mathematical apparatus and also mathematical methods that would be close to cluster analysis, but would be based solely on the individual characteristics of coals and coal suspensions, taking into account the improvement in economic indicators.

The value of these indicators for each type of coal transport is different. It largely depends on the capacity and structure of the cargo flow from the deposit to the industrial site of the consumer, the distance of transportation, and a number of other factors, including the above-mentioned technological properties of coal.

One of the promising areas of transportation for solid bulk materials, which has recently been developed both in internal and external communications of industrial enterprises, is pipeline hydraulic transport.

It should be emphasized that the introduction of hydraulic transport can significantly improve technical and economic indicators; increase labor safety; reduce environmental pollution; industrial morbidity; ensure a wide range of automation of pipeline transport processes and the reliability of pipeline transport systems; and, ultimately, continuous non-overloading transport communication between supplier and consumer.

## 2. Application of Mathematical Models in CWS Combustion Processes

A mathematical model for the process of combustion of CWS in the form of suspension droplets is described in [34]. In this article, the static modes of the process are considered, and methods and a calculation scheme are proposed, which, therefore, made it possible to create a mathematical model and solve the optimization problem. The proposed methods are based on a thermodynamic description of the combustion process; further, the article calculates the heat and material balance. The solution of the optimization problem is performed for a dynamic mathematical model on the basis of the developed methods and an implemented calculation system. The combustion of droplets of a CWS was considered in a vortex furnace, and a physicochemical description of this process was given.

It is a well known fact, that climate change on our planet, specifically the impact of the greenhouse effect, is largely determined by the violation of the ozone layer from the combustion of fossil fuels. The combustion of this type of fuel is identified in modern research as one of the key factors causing climate change. The article [32] considers the properties of lignite coal and CWS using lignite coal. Based on the performed mathematical modeling, the article provides a calculation of the number of carbon dioxide molecules that arise as a result of the chemical reactions during the combustion process. In addition to this—and what is also important—is that the article provides a detailed review of publications made in recent years by scientists in the field of combustion of CWS using

brown coal. Combustion studies, and their results, in this review are considered on the example of industrial recycling furnaces. This review presents the results of theoretical and experimental studies, taking into account the thermal properties of brown coal and the CWS that is based on it. The obtained results are compared with the results of numerical calculations performed using the ANSYS computer program. The comparison showed a high degree of convergence of the results. To build a mathematical model, new methods for approximating the step and generalized functions were developed. The developed approximation methods made it possible to increase the accuracy of approximations in the use of mathematical functions that describe the thermal properties of brown coal and CWS. The developed approximation methods do not have the same drawbacks that are typical for traditional expansions of step functions (when completed with the help and application of Fourier series). These methods are universal in nature and can be used for the purposes of mathematical modeling in describing various processes and systems in a wide range of scientific and technical problems. In article [32], the developed approximation methods were mostly used, for example, in order to determine the coefficients of kinematic viscosity, ash content, and the moisture content of brown coal and CWS. This made it possible to reduce the calculation error and obtain more accurate results using mathematical modeling. Additionally, in the article, numerical modeling of the combustion processes and fuel transportation by means of hydraulic transport were performed. The article presents the results of numerical simulation; further, it also describes the procedure by which the verification of the initial data and the result of the calculations are carried out. It is also shown that the convergence of data, and their location, in the selected uncertainty band corresponds to the conditions and criteria for verifying experimental data, which are accepted in the European and Eurasian Unions.

Typically, CWS has the following composition: 60–70% coal, 30–40% water, and 1% chemical additives; further, the development of this composition was carried out in the last 20 years. The composition was an alternative to fuel oil for combustion in industrial and municipal furnaces. A numerical study of the combustion process, the flow field of the process, and the features of heat transfer in an industrial furnace during CWS combustion, were all performed in the article [35]. The study was carried out using a computer program, Fluent, for describing the hydrodynamic processes. As shown by the results of the mathematical modeling, the combustion field in the furnace has a swirling form, in which high temperature gases—expanding outward—form recirculation areas directly in the burner zones. The effect of a drop in the combustion temperature with an increase in the length of the furnace is revealed, with the highest value of the combustion temperature being observed in the burner zone. The value of the swirl of the combustion field increases at the beginning of the transition from the front wall of the furnace to the rear, but then, subsequently, decreases. The article then notes that the type of distribution, in regard to the concentration of gases CO and CO<sub>2</sub>, is mainly determined by the temperature field, namely—with an increase in temperature—the concentration of CO increases, and also the concentration of O<sub>2</sub> and CO<sub>2</sub> decreases. Moreover, the degree of loading for the boiler greatly affects the output average temperature, the maximum temperature of the furnace, and the rate of the combustion process.

The first developments that were made on the issue of the use and incineration of CWS appeared in the early 1980s. Currently, China is the largest manufacturer and user of CWS [37]. The currently, and widely, conducted studies [37] are aimed at improving dispersed fuels, their operational characteristics, and increasing the efficiency of the combustion process. In the course of research, a close correlation was established between the properties of CWS and characteristics such as the type and properties of coal raw materials. The established relationship leads to the need to take into account the purpose of the fuel in the production of CWS. For example, when burning CWS' "recycling" in pulverized boilers, conventional quality coal sludge can be used. While the solution of an important technological task is to increase the efficiency of power units, when faced with a reduced

technical minimum there is a requirement for the use of higher quality, fine coal fractions that form the pulp.

Article [38] considers the mathematical model developed by the authors, which allows one to reproduce, with a high degree of accuracy, the experimental values of the integral characteristics of the CWS droplet combustion process. These characteristics include minimum temperatures and ignition delay times (as well as the coordinates for the start of the combustion front). The combustion of droplets containing petrochemical additives is considered in a hot oxidizer stream. The paper then describes the results of the numerical simulation carried out for the process of ignition of sludge droplets, which are common waste products that arise in coal processing. In the study for various sizes of droplets with a radius ranging from 0.25 mm to 1.5 mm, various values of the flow velocity of a high-temperature oxidizing gas from 0.5 m/s to 3 m/s, gas temperatures from 700 K to 1000 K, and the ignition delay time of drops were all determined. The selected values of the radius, velocity, and temperature of the droplets were determined, with consideration in taking into account the typical conditions of the combustion chambers. The results of the study showed a good agreement between the results of mathematical modeling and the data obtained experimentally. We used the Ansys Fluent software package, which is designed for numerical simulation of the CWS droplet ignition process, to analyze this data. It was found that the deviation of the results for the numerical simulation and the experimental data, on the characteristics of the inertia of the ignition process, does not exceed 5–10%.

In article [39], the authors describe the results of their theoretical and experimental research. The article shows studies of the ignition processes of CWS in the form of single drops. The surface of the droplets is covered with a thin water film. In the course of the study, the main parameters of the fuel combustion process were determined, such as the time for complete evaporation of the water droplet coating as well as the ignition delay, as depending on the ambient temperature. The errors in the calculated values, based on the mathematical models of the combustion process developed in the article, did not exceed 5%, relative to the experimental data. The mathematical models used in the study were built on the basis of a thorough analysis of the video recordings of the CWS ignition process. Mathematical models were developed taking into account the relationships within the complex of thermophysical and thermochemical processes. The article demonstrates a solution for a multifactorial nonlinear problem concerning the phenomenon of ignition of CWS particles. Approximate analytical solutions were obtained using asymptotic methods. The theoretical and experimental studies carried out have shown the importance of taking into account the thickness of the water film covering the surfaces of the fuel droplets. Additionally, film thickness has also been proven to be one of the main parameters for determining the conditions and characteristics of the CWS ignition process. The performed studies have shown that the characteristic evaporation time of the water surface film is from 45 to 60% for the entire induction period, depending on the film thickness.

CWS is a complex solid–liquid suspension. To study its properties, there have been a large number of research papers on the production and use of CWS. Technologies for using CWS are being developed around the world in various governmental, industrial, and academic institutions. The results of research in the field of production and application of CWS over the past 30 years are described in detail in article [36]. Particular attention, in the description, is given to various aspects of the CWS combustion process—for example, the structure and properties of coal, various additives used according to the technology conditions, and the possibility of using these additives for various types of coal are all described in detail. The article shows that the characteristics of the suspension capacity of coal, and the rheological properties of the CWS that are obtained on the basis of this coal, are largely determined by the particle size distribution. The article notes that, despite alternative sources of heat and electricity and the currently popular statement about the end of the coal era, modern efficient coal combustion technologies can help to reduce emissions of pollutants into the atmosphere. This fact speaks to the benefits of using coal as an energy

source, at least until more adequate efficient and environmentally friendly alternatives are developed. In addition, the studies of the CWS combustion processes and the results of mathematical modeling obtained in these cases may be useful in the development of technologies for the use of other types of fuel. For example, we can then talk about biomass that is based on charcoal or trophy.

The new technologies for CWS incineration provide a range of good alternatives for the incineration process. These alternative possibilities fully meet modern requirements for environmental protection. Therefore, the issues of using coal suspension as an energy source undoubtedly require the most thorough of studies and further research. Study [40] can be cited as an example. This paper presents the results of a comprehensive study of continuous and cyclic CWS combustion processes. The advantages of cyclic combustion are determined by the nature of the movement of bulk coal material in the cyclic flow circuit of the fluidized bed; further, the circuit is formed by a combustion chamber, a cyclone device, and a furnace riser. As shown by the results of experimental studies, the cyclical nature of the change in the oxygen concentration for fuel combustion contributes to significant changes in the combustion mechanisms and the kinetics of the combustion process. The article developed a mathematical model for the cyclic process of fuel combustion. The initial concept of this mathematical model takes into account the cyclical nature of the change in the oxygen concentration for fuel combustion. The mathematical model helps to make predictions about the change in temperature of the inner surface of the combustion chamber and its central part. Additionally, with the help of a mathematical model, the mass loss of fuel is determined during the cyclic nature of combustion in a fluidized bed when in air.

Studies have shown that CWS is an attractive low-cost alternative fuel. The advantage of this technology is also a high degree of reliability in the transport and preparation of fuel for use. The gasification efficiency of coal–water suspension is determined by its high carbon content and low viscosity. These characteristics allow you to increase the heating rate. The CWS' fine atomization plays an important role in this. Article [47] considers the rheology of a coal–water suspension with a coal content of 30 to 60%. Moreover, power law models, specifically Casson and Herschel Buckley models, were used to study the rheology of CWS; the models also showed the pseudo-plastic behavior of the CWS. Further, the preparation of CWS was carried out using polyvinyl alcohol (PVA) and triethanolamine (TEA).

For several decades, the efforts of researchers have been directed to find a practical solution to the problem of transporting CWS through a slurry pipeline. Solving this problem requires understanding and a modeling of the complex phenomena involved. A significant increase in the computing power of computer systems and the widespread use of application software packages for computational fluid dynamics, have made it possible to collect large amounts of information at the local level regarding the flows of the suspension that is transported through the slurry pipelines. This is the main difference between modern CWS research methods and traditional approaches using simplified methods of mathematical modeling with a macroscopic description of processes. An example of this is in review article [48]. This article explores the potential of computational fluid dynamics for modeling flows in slurry pipelines. A detailed description of modern modeling methods is carried out, with a review of important publications on this topic. The main attention in the article is focused on the assessment of the potential of various methods of computational fluid dynamics. The issues of interaction between computational hydrodynamic modeling and experimental studies are considered. In addition, the main causes that create uncertainties in CFD models are considered. The article evaluates existing models in terms of their interpretive and predictive ability.

There are articles [49,50] that consider mathematical models that which make it possible to determine the optimal conditions for the ignition of promising CWS. At the same time, the criteria for optimizing the ignition of CWS, which include petrochemicals, are the minimum possible ambient temperatures and a short ignition delay time. Three optimal

regimes have been experimentally determined under which physicochemical transformations effectively occur when CWS is heated. The first mode is characterized by intensive thermal decomposition of the coal component after the evaporation of the liquid components of the fuel. The second mode is characterized by gasification of the coal component; this mode occurs under conditions that result in boiling liquid components. Then, there is a heterogeneous combustion of the solid residue. In the third mode, the gas mixture is ignited. Ignition begins directly in the vicinity of fuel particles and passes into a heterogeneous combustion of the solid residue. For the identified regimes of physicochemical transformations, the ambient temperature ranges, and other conditions for their occurrence, are established.

On the basis of the experimental data obtained and the results of their statistical processing, a mathematical model of physicochemical transformations under the heating conditions of CWS with different compositions of components was proposed. The developed model makes it possible to make predictions about the course of the combustion process. The model is built taking into account functional relationships in physical and chemical processes. The model describes inert heating, evaporation, thermal decomposition, and exothermic reaction during combustion. The obtained results of theoretical studies carried out on the basis of the proposed model helped to determine the degree of influence of the parameters on the constituent parts of the fuel, such as the heating conditions that were found to be effective modes of physicochemical transformations.

### 3. Summary

#### 3.1. Mathematical Models on the Combustion of Water–Coal Fuel

The combustion of water–coal suspensions is a heterogeneous process of chemical interaction of solid fuel with an oxidizer, and is complicated by parallel steam generation in the suspension, which significantly changes the reaction characteristics of the fuel and the conditions of heat and mass transfer both on the surface and in its volume. This leads to an intensification of the total burnout rate and high thermal stresses of the process [51].

The chain nature of the processes of oxidation and combustion of coal to a certain extent predetermines the decisive role of water and steam. The main total (final) reactions of combustion of water–coal suspensions in a gaseous oxidizer (air), are the reactions of oxidation and combustion of coal with oxygen and water vapor, as well as secondary reactions of carbon dioxide reduction, conversion of carbon monoxide, methane formation, etc. A feature of these reactions during the combustion of water–coal suspensions is their flow at a high concentration of water vapor and temperatures close to the theoretical temperatures found in the combustion of carbon.

An analysis, carried out in [52], of the reactions of oxidation and combustion of coal particles in the presence of water and water vapor, shows that moisture can intensify reactions with carbon, both through free hydroxyl radicals and also through the mechanical transfer of other oxidants dissolved in water to the coal surface. Low temperature coal oxidation reactions in the presence of water proceed with a very low activation energy. In washing out carbon dioxide, methane, and nitrogen from the coal pores and from the surface, water significantly increases the sorption capacity of coal with respect to oxygen and increases the rate of desorption of reaction products, thereby improving mass transfer on the coal surface.

It has been experimentally established that during surface combustion of a layer of a mixture of small particles of coal with water (as a result of humidity and temperature gradients), there is a continuous transport of moisture from the inner layers of the fuel to the burning surface. This, however, is complicated by the processes of evaporation of the moisture and gas formation, which is as a result of the interaction of moisture and carbon of the fuel as it warms up. The combustion process of such a mixture is accompanied by the formation of a narrow water vapor superheat zone, which is located directly behind the surface combustion zone and characterized by high thermal resistance and large gradients of temperature and water vapor concentration.

According to [52], the distinguishing features found in the ignition and combustion of a coal–water suspension drop are high concentrations of water vapor near the reaction surface; relatively large sizes of suspension droplets that react with atmospheric oxygen when compared with coal dust; and, as a consequence, the determining role of mass and heat transfer not only during the combustion of the drop, but also to a large extent during its ignition.

Immediately after the drop enters the combustion chamber, evaporation begins from its surface, which occurs at a constant temperature as per the drop and a decrease in the temperature of the medium (due to heat consumption for evaporation). Visible changes in color, volume, and the shape of the drop are absent. As the temperature rises on the surface of the droplet, the second stage begins—during which further heating of the droplet, overheating of water vapor, and interaction of the fuel with water vapor, continue. The temperature of the medium is then equalized. The drop begins to increase in volume. The reaction of fuel carbon with water and water vapor is endothermic, therefore temperatures rise. The minimum temperature of the environment at which ignition of the drops of coal–water (composed of coals of different grades) suspensions arise is different. However, it must be noted, that for all coal–water suspensions the minimum temperature is much lower than for dry coals of the same grades. Increase in droplet size is a consequence of the intense vaporization and thermal decomposition of the coal inside the droplet. An increase in the volume of the drop leads to an increase in the porosity of the dried layers, which reduces heat transfer to the central region of the drop and also reduces the rate of moisture evaporation and thermal decomposition of coal particles. The third stage begins with ignition from a drop of combustible gases, with a further increase in both the ambient temperature and the drop itself. The drop becomes lighter and, in some cases, larger in volume. Afterburning of the coke residue is the fourth (last) stage of the process. It is not much different from the burnout of a particle of dry coal, however, the burnout rate of a drop due to the highly developed specific combustion surface is greater than during the combustion of a particle of dry coal. In [53], a mathematical model was constructed on this topic.

Thus, the combustion of a drop of suspension is considered as a heterogeneous process that proceeds with a continuously changing volume and therefore composition of the fuel. This is further complicated by the process of volumetric afterburning of combustible gases, which is continuously generated from the central part of the drop.

Study [54] presents a model for the process of atomization and the combustion of suspension coal fuel. The combustion efficiency of this fuel significantly depends on the quality of its atomization [54].

The stability and completeness of fuel burnout in the combustion chamber are determined by the degree of atomization of the fuel that is introduced into the chamber and also the perfection of the aerodynamics of gas flows inside the chamber. These qualities provide reliable conditions for flame ignition and stabilization; reliable mixing of the fuel with the oxidizer and temperature distribution; as well as optimal conditions for fuel burnout throughout the entire volume of the chamber. The atomization quality of a coal–water suspension in the combustion chamber depends on the perfection of the design of the atomizer and the properties of the fuel.

It is known that the combustion of coal–water fuel differs significantly from a similar process when using pulverized coal [54]. At the same time, it is argued that the influence of the brand of coal, and its ash content on the ignition temperature and combustion stability is insignificant. However, the results of bench tests and operating experience show that when burning batches of CWF, which is prepared from highly metamorphosed coals and anthracites, a higher initial heating of the furnace space is required in order to initiate the process of fuel ignition and its further stable combustion. A similar phenomenon was also recorded when using coal–water fuel prepared from high-ash coal sludge. All of this indicates that the mechanism of spraying and the mathematical model of ignition and combustion of coal–water fuel require adjustment.

Considering the polydispersity of coal particles in CWF during spraying, pure coal particles (“drop-particles” larger than 80–100  $\mu\text{m}$ ) are formed, from which a liquid film with the finest particles breaks off due to hydrodynamic friction forces, and coal–water drops, consisting of thin particles of coal and liquid phase, are thus developed. Therefore, the mechanisms of ignition and combustion of a polydisperse flow of CWF droplets must be considered when taking into account the laws of heat and mass transfer, as well as chemical reactions that occur in liquid coal drops and ordinary coal particles [55].

Thus, it is assumed that the combustion process of sprayed CWF droplets is a combination of combustion of two model systems: coal particles with a diameter of more than 80–100  $\mu\text{m}$  and coal–water droplets with a diameter in the range of 80–100  $\mu\text{m}$ . This physical model of CWF spraying was confirmed by mathematical calculations and experimental results [55].

The experimental tests carried out showed that CWF, when prepared from coals of various grades and ash content, reliably ignite and burn effectively in a swirl furnace. The mechanical under burning of the fuel (the content of combustibles in the trapped ash particles) is no more than 3–5%. A similar indicator for layered coal furnaces is 20–60%.

The ignition temperature and the time to reach a stable regime of independent combustion of various types of CWF depend on the brand of coal and its ash content, the content of which are harmful emissions that are 3.3–4.3 times lower than the maximum allowable concentrations (for enterprises that operate in Kyrgyzstan and Russia).

The economic efficiency in the use of coal–water fuel was obtained due to the different cost of the fuel components when using CWF and when using ordinary coal in boiler houses. Moreover, payback of capital costs takes no longer than 2.5 years.

Thus, the implementation of this technology for the purposes of the combustion of coal–water fuel in swirl furnaces of small and medium-sized boilers makes it possible to obtain a significant economic effect and reduce harmful emissions in the environment.

### 3.2. *Mathematical Models of Transportation of Coal–Water Suspensions*

According to Offengenden [50], a study conducted 40 years ago, the most efficient application and use of hydraulic transport can be under the following conditions:

- when it is indispensable for any other modes of transport due to the tendency for the spontaneous combustion or due to the high water content of the fuel;
- when, due to the conditions of the terrain, it is possible to reduce the length of the pipeline transport main when compared to rail or to other modes of transport; further, while hydraulic transport is especially favorable in mountainous or rough terrain there is still an excess of geodetic height that the supplier must contend with when compared with the consumer;
- when the fuel production areas are remote from the places of its consumption, and when there is an absence, or weak development, of highways and railways;
- in the absence of large reserves of labor in the pipeline transport, as in they do not exceed 30–40% of the cost of rail and road transport.

The last few decades have been characterized by a noticeable expansion globally in the scale of pumping various kinds of hydraulic mixtures via pipeline transport.

Design studies are underway for a number of pipeline transport systems in the BRICS countries as well. The most striking recent work in this area is found in article [56] by the authors D. Das and S. Das. See also [57] by Wang, Zhao, Zhang, and Hu [58] as well as by Yi and Zhou. Features of transport are found, first of all, in the variety in properties of bulk materials, which in turn have a decisive influence on the properties and characteristics of slurry and the parameters of pressure pipeline transportation. This was studied in the United States and Europe before their attempts to completely switch to “green” energy. Articles [59–61] show the latest research at that time for these countries. However, it should be noted that strong attention to this topic has been attracted in China. In [60,62], the properties of suspensions and surfactants are studied. These properties should be used

in the future when constructing mathematical models for the motion of suspensions and individual particles.

From the current practice of preparing, transporting, and burning artificially watered solid fuels, it is possible to divide these into classes of low- and high-reactivity mixtures [63,64].

This division depends on the heat value of the original coal and the moisture content of its slurry. The economy of the second option is due to the cost of construction and operation of devices for preliminary dehydration. To take into account the specific technical capabilities of the existing boiler and furnace equipment when switching to the combustion of CWS, comprehensive studies were thus carried out in order to select the combustion technology for the Karakechi brown coal when delivered to the consumer by pipeline transport. At the same time, the following research tasks are defined:

- analysis of the combustion features of artificially watered Karakechi brown coal in a wide range of moisture content and size, this being of the initial coal particles that are based on bench studies of the combustion process in a single flame;
- determination of the conditions for stable combustion of flooded Karakeche brown coal in industrial furnaces of boiler units, taking into account the above analysis;
- analysis of the effectiveness and selection of industrial schemes for burning Karakechi brown coal based on the studies;
- selection of the optimal storage technology, intraschool transport, and supply of high-moisture Karakechi brown coal to the furnace, taking into account the studied combustion schemes.

The technique for studying the process of combustion of CWS of Karakechi brown coal is based on the study of the process in separate characteristic zones along its course.

Previously, studies of the combustion of CWS were carried out by individual authors.

In [65] Wan, Yu, Wang, and Sun, the authors who studied pyrolysis processes and suspensions, CWS were used as fuel. In [66] Li, Liu, Wang, and Cheng carried out a fairly extensive study of mixtures and suspensions. Additionally, in [67] Yao, Zhao, Chen, and Liu studied the ratio of water and coal when in suspension and the effect of their concentrations on qualitative characteristics.

A feature of the experimental studies was that the possibilities of controlling the moisture content of the supplied fuel were limited by the fluidity of the CWS at  $W^{\text{daf}} \leq 43 \dots 45\%$  [26,68]. With a further increase in humidity, starting from  $\sim 46\%$ , the mixture becomes fluid with a characteristic manifestation of viscoelastic properties inherent in non-Newtonian liquids. Atomization of such a mixture by a nozzle located in the upper cover of the combustion chamber leads to the formation of droplets, including coal particles and water.

Sampling from the combustion chamber showed that the thermal effect on the droplets of the CWS leads to the agglomeration of the initial dust particles that make up the droplet. The nature of the distribution of crushed samples of agglomerates, in terms of size, is close to the distribution of particles of the initial dust. A visual study of fuel samples of the agglomerates shows that the presence of lighter-burnt small inclusions and also the presence of large particles with obvious signs of under burning. The analysis of crushed agglomerate screenings for the content of combustible components also confirms the staging of the fuel particles burnout of the agglomerate.

In order to select effective technological schemes for the purposes of burning Karakechi brown coal that is delivered to TPPs via pipeline transport, the pipelines were modeled by utilizing the equipment of a pilot plant on a TP-35 boiler, as well as using the moisture content and fractional composition of the initial coal dust. At the same time, within the initial stages of the research, the task was set: to formulate the modeling conditions when considering the effect of the two ways that water can be introduced into the furnace. That is to say, either through nozzles that are installed through a CWS or instead through the main burners of the boiler (together with ordinary coal dust through the same nozzles and burners) while maintaining the analogy of the physical chemical characteristics of the fuel dry mass and the proportion of the water. Similar studies were also carried out by researchers from Turkey in [69] and by the authors Dinçer, Boylu, Sirkeci, and

Ateşok [70–72]. Such an approach to modeling processes on a full-scale boiler is convenient in that the conditions of geometric, kinematic, and dynamic similarity, which are all generally accepted in aerothermodynamics, are satisfied in advance. Thus, we are talking about the selection of only additional conditions that implement thermal similarity, which, due to the inadequacy of the distribution of dust and sprayed droplets in the reagent flows, will be approximate. Industrial experiments carried out on the TP-35 boiler with a steam output of 4.88 kg/s showed the fundamental possibility of thermal modeling [73].

The authors of the article themselves studied the properties of Karakechi coal, its mixture with water [63,64], and also used data on coals and mixtures previously studied by other authors [69,74]. In paper [68], as well as studies [32,33], experimental and analytical data were obtained. Below, we present the main results of research, including those obtained using mathematical modeling methods. Processing of the results was carried out as per the area of active combustion, from the nozzle exit to the zone with the maximum temperature, as well as the location that varied depending on the moisture content in the sprayed CWS and the temperature of the chamber wall. For example, at humidity  $W^{\text{daf}} = 48\%$  and wall temperature  $T_w = 1470$  K, the length of this section is  $l_f = 0.5$  m, and at  $W^{\text{daf}} = 55\%$  the same wall temperature is  $l_{\text{daf}} = 1.0$  m. Within the  $l_f$  section, a shorter section  $l_{\text{ign}}$  can be distinguished from the nozzle exit to the beginning of the flame glow. The length of this section, as a rule, was  $l_{\text{ign}} = 0.2 l_f$ . According to the values of  $l_{\text{ign}}$  and the flow rate of the reagents, the total time for heating the coke residue before the start of its active burnout was determined, and the values of  $l_{\text{comb}} = l_f - l_{\text{ign}}$ , were used to determine the burnout time of the coke residue. These results formed the basis of the methodology for assessing the influence of the moisture content of the CWS on the conditions for the combustion to proceed.

Additionally, it was interesting to note, that, from the point of view of the initial data, the mathematical models were obtained in the scientific work [74]. Here, the properties of coals were studied, and the combustion constants of coal dust were determined. When determining the combustion constants  $k_{\text{ign}}$  in the initial section and then determining  $k_{\text{comb}}$  in the section where agglomerated particles underwent active burnout and which entered into a chemical interaction with oxygen in the flame sections  $l_{\text{ign}}$  and  $l_{\text{comb}}$ , the equations of the dynamics of combustion of coal particles proposed by Babiş and collaborators [74] were demonstrated. Estimation of the experimental coefficients  $k_{\text{ign}}$  and  $k_{\text{comb}}$  in the presence of experimental data on the average wall temperature  $T_{\text{mid}}$ , K; the density of CWS  $\rho_{\text{mix}}$ ,  $\text{g}/\text{m}^3$ ; coke residue density  $\rho_{\text{coke}}$ ,  $\text{g}/\text{m}^3$ ; and the oxygen concentration  $O_2$  was carried out according to the equations of connection between the degree of burnout of a polydisperse torch and the heat release of volatile and coke particles.

In the process of calculations, mathematical methods of data processing were used. As a result of solving the coupling equations, mathematical dependencies were obtained:

$$k_{\text{ign}} = k_{\text{ign}}^{\circ} \cdot (1 - W^{\text{daf}}) \cdot \rho_{\text{coke}} / \rho_{\text{mix}} \quad (1)$$

$$k_{\text{comb}} = k_{\text{comb}}^{\circ} \cdot (1 - W^{\text{daf}}) \quad (2)$$

where  $\rho_{\text{coke}}$  is the density of the coal component of the mixture,  $\text{kg}/\text{m}^3$ ;  $k_{\text{ign}}^{\circ} = k_{\text{comb}}^{\circ} = 1.23$ .

Significant progress in the experimental study of the properties of coal dust and processing of the results was obtained for Kazakh and Kyrgyz coals. Comparing the values of these coefficients with similar indicators in the dust of the Karakechi brown coal that are obtained in [74], one can note the discrepancy between the results by almost a factor of two:  $k_{\text{ign}} = k_{\text{comb}} = 0.55\text{--}0.74$  for the CWS, while for the dust of the same coal  $k_{\text{ign}} = k_{\text{comb}} = 1.34$ . The latter is obviously due to the lower relative content of combustible components in droplets with sizes equivalent to similar coal particles. To assess the conditions for the stable combustion of the coal–water mixture of Karakechi brown coal, the balance heat equations were compiled for the  $l_{\text{ign}}$  and  $l_{\text{comb}}$  sections. This made it possible to determine the reduced heat release of volatiles, which, in the first approximation, can be taken as

a criterion for the stability of combustion of high-moisture coals  $Q_{\text{volatile}}^{\text{h.h.c}}$  (kJ/(kg of percent of humidity)):

$$Q_{\text{volatile}}^{\text{h.h.c}} = [Q_{\text{volatile}} \cdot (V^{\text{daf}} - V_{\text{ign}}^{\text{daf}}) - Q_W - Q_A - Q_{\text{reag}}] / W^{\text{daf}}. \quad (3)$$

where  $Q_W = 2500 \cdot W^{\text{daf}} + C_{\text{pw}} \cdot \Delta t \cdot W^{\text{daf}}$  is the amount of heat for evaporation and heating of fuel water, kJ/kg;  $Q_A = C_{\text{pA}} \cdot \Delta t' \cdot A^{\text{dry}}$  is the amount of heat for heating the ash part of the fuel, kJ/kg;  $Q_p = \Delta t' \cdot [V^{\text{daf}} \cdot C_{\text{pv}} + (1 - V^{\text{daf}}) C_{\text{pcoke}} + \alpha V^{\circ} \cdot C_{\text{pair}}]$  is the amount of heat for heating reagents, kJ/kg;  $C_{\text{pw}}$  is the average heat capacity of steam in the temperature range  $\Delta t' = t_{\text{mid}} - t_0$ , kJ/kg K;  $C_{\text{pA}}$  is the average heat capacity of ash in the temperature range  $\Delta t' = t_{\text{mid}} - t_0$ , kJ/kg K;  $C_{\text{pv}}$  and  $C_{\text{pcoke}}$  are the average heat capacities of volatiles and coke in the temperature range  $\Delta t' = t_{\text{mid}} - t_0$ , kJ/kg K;  $C_{\text{pair}}$  is the average heat capacity of air in the temperature range  $\Delta t' = t_{\text{mid}} - t_0$ , kJ/m<sup>3</sup> kg K;  $\alpha$  is the coefficient of excess air in the burner; and  $V^{\circ}$  is theoretical air volume, m<sup>3</sup>/kg.

In addition, the researchers in article [74] compared the data for coals with similar properties. Further, these data were also included in the mathematical models. For the CWS of Karakechi brown coal with  $W^{\text{daf}} = 48\%$ , the value of  $Q_{\text{volatile}}^{\text{h.h.c}}$  is  $\sim 80$  kJ/kg % moisture; for Bashkir coal with  $W^{\text{daf}} = 56\%$   $Q_{\text{volatile}}^{\text{h.h.c}} = 91$  kJ/kg % moisture; and for Chikhez coal with  $W^{\text{P}} = 43.5\%$   $Q_{\text{volatile}}^{\text{h.h.c}} = 144$  kJ/kg % moisture. At the same time, Chikhezian coal burns steadily in flare furnaces, while direct combustion of the coal–water mixture of Bashkir coal without illumination by an additional source of heat release is difficult to organize under these same conditions.

The temperature value that ensures stable combustion of the coal–water mixture of Karakechi brown coal depends on the humidity of the mixture at constant values of the degree of heat supply (removal) by the walls, the fractional composition of the initial dust, and the size distribution of sprayed droplets, in the range  $W^{\text{daf}} = 48 \dots 55\%$ ,  $T_{\text{min}} = 1130 \dots 1150$  K. Temperature data are essential for boundary conditions in combustion reactions.

The results of studies performed on a pilot plant for the preparation and combustion of Karakechi brown coal, that was created in relation to the boiler TP-35 [63,64], in general, confirmed the nature of temperature changes, burnout of volatiles and coke residue, as well as the general dependence of the process on the degree ballasting with moisture and fractional composition of the initial fuel. At the same time, dust combustion is characterized by a shorter section  $l_f$  from the burner cutoff to the zone of maximum temperatures  $T_f$ , which are a higher level of temperatures themselves and therefore the degree of burnout. When switching to combustion of a coal–water mixture, combustion was delayed, the length  $l_f$  increased by 5–6 times, and the degree of burnup at this level decreased to  $a = 0.65 \dots 0.75$ . The degree of burnout of the coal–water slurry in the outlet window of the combustion chamber was  $a = 0.82 \dots 0.85$ . The average temperature level in the furnace was in the range of 1340...1350 K. The maximum size of agglomerates formed in the process of spraying the coal–water slurry in the furnace was 1000...1200  $\mu\text{m}$  with an average value of 350...400  $\mu\text{m}$ . These data later formed the basis of the coal particle model.

The calculation of the degree of fuel burnup for these conditions with a previously determined coefficient  $k_{\text{ign}} = 0.67$  showed an insignificant discrepancy with its experimentally determined value ( $\sim 8 \dots 12\%$ ). Verification of the same method of calculation for dry dust of Karakechi brown coal at  $k_{\text{comb}} = 1.34$  gave a discrepancy, when compared with the experiment, of 5...7%. At the same time, the distributions of dimensionless temperatures and the degree of burnup revealed under the conditions of the stand [64] are typical for the combustion of dust and CWS in the TP-35 boiler. Despite the lower values of the kinetic constants  $k_{\text{comb}}$  for agglomerates when compared to dust, the burnout time of CWSs increases significantly due to a decrease in the flame temperature and an increase in the size of agglomerates compared to the size of dust particles. The obtained values of the combustion constants were included in the standard methods that are used for calculating coals for the Kyrgyz Republic.

Next, we will consider a mathematical model for constructing a pipeline for a coal–water mixture and compare the calculations for this model with data for transportation by road.

The total costs  $K_{c,p}$  for the construction of pipeline transport facilities with a direct-flow water supply system are determined by the formula:

$$K_{c,p} = K_{p,c} + K_z + K_p \cdot L_p + \Sigma K_{a,b} + K_c, \tag{4}$$

where  $K_{p,c}$  is the cost of construction of the pulp preparation complex, USD;

$K_z$ —cost of sump construction, in USD;

$K_p$ —cost of construction of 1 km of the pipeline, in USD;

$K_{a,b}$ —cost of construction of artificial structures along the pipeline route, in USD;

$K_c$ —cost of construction of the CWS storage facility, in USD;

$L_p$ —pipeline length, km.

Formula (4) contains all practically significant capital costs. At the same time, the current costs of operating the pipeline are significant.

Annual operating costs for the maintenance of all hydraulic transport devices are determined by the formula:

$$E_{c,p} = E_{indep} + E_{dep}, \tag{5}$$

where  $E_{indep}$  and  $E_{dep}$  are expenses that do not depend on and that which do depend on the operating time of pipeline transport for a year, respectively, in USD 1000.

The norms of expenses for the maintenance of pipeline transport devices are determined for enterprises located in the central regions of the country. The cost of electricity is taken at the tariff—USD 40 per 1 kVA of installed capacity and USD 0.2 per 10 kWh of power consumption.

Annual costs that do not depend on the operating time of the pipeline transport (with direct-flow water supply) are determined by the formula:

$$E_{indep} = E_{p,c} + E_z + E_{p,st} + E_p \cdot L_p + \Sigma E_{a,b} + E_{pp}, \tag{6}$$

where:

$E_{p,c}$ ,  $E_z$ , and  $E_{p,st}$  are the cost rates, independent of time, for the maintenance of the pulp preparation complex, of the sump; main; and auxiliary pumping stations, respectively, per year, in USD 1000;

$E_p$  is the norm of the expenses for the maintenance of 1 km of pipelines per year, in USD 1000;

$E_{a,b}$  is the expenses for the maintenance of artificial structures along the pipeline route for the year, in USD 1000;

$E_{pp}$  is the rate of expenses for the maintenance of the slurry storage facility at the State District Power Plant, in USD 1000;

$L_p$  is the pipeline length, in km.

Annual costs, independent of the operation of pipeline transport time (and when taking into account the norm), make up:  $E_{indep} = 1604$ , in USD 1000.

Annual costs in USD 1000, depending on the operating time of the pipeline transport system, are determined by the formula:

$$E_{dep} = 0.001 \cdot p \cdot T \cdot (E_{dep,p,c} + E_{dep,z} + E_{dep,p,st}), \tag{7}$$

where:

$p$  is the number of hydraulic transport shifts per day;

$T$  is the number of pipeline transport operation days per year;

$E_{dep.p.c}$ ,  $E_{dep.z}$ , and  $E_{dep.p.st}$  are the cost rates, depending on the operating time, for the maintenance of the complex slurry pumping station; sump and auxiliary slurry pumping station; and head slurry pumping station per shift, respectively, in USD 1000.

Thus, the model takes into account all significant operating costs.

The reduced costs for the Kara-Keche–WPP pipeline transport system were determined by the formula:

$$P_{c,p} = E_{c,p} + Q_{standart} \cdot K_{c,p}. \tag{8}$$

For the fuel and energy complex as a whole, the normative efficiency factor  $Q_{standart}$  is set at the level of 0.12 by the standard methodology. From here:  $P_{c,p} = 3232.866$  in USD 1000.

We present the results of the calculation according to the developed model and obtain the results per 1 ton of the transported coal–water mixture.

The cost of a pressurized hydraulic transportation of Karakechi brown coal from the Kara-Keche deposit to the industrial site of the TPP will be:

$$Pr_{c,p} = E_{c,p}/N, \tag{9}$$

$$Pr_{c,p} = 0.7098 \text{ USD/ton},$$

where  $N$  is the productivity of the pipeline transport system, in tons/year, and equal to 3 million tons/year.

Thus, the value of USD 0.7098/ton should be compared with the same parameter for road construction and vehicle transportation.

Capital investments for the construction of road transport facilities and the acquisition of a rolling stock fleet are determined by the formula:

$$K_{a,t} = K_{eq} + K_{r,s}, \tag{10}$$

where:

$K_{eq}$ —the cost of construction of permanent structures and devices, in USD 1000;

$K_{r,s}$ —the cost of acquiring rolling stock, in USD 1000.

Next, we reveal the meaning of expression (11).

The total costs for the construction of permanent (without cargo and storage) vehicles in transport hubs are found by the formula:

$$K_{eq} = K_{road} \cdot L_{road} + K_{br} \cdot L_{br} + K_{s,p} \cdot F_{s,p} + K_{gar}, \tag{11}$$

where:

$K_{road}$ —the cost of building 1 km of road, in USD 1000;

$K_{br}$ —cost of 1 m of bridge length, in USD 1000;

$K_{s,p}$ —the cost of 1 thousand  $m^2$  of coverage of areas near loading and unloading devices, in USD 1000;

$K_{s,p}$ —the cost of building a garage, in USD 1000;

$L_{road}$ —length of the highway, in km;

$L_{br}$ —bridge length, in m;

$F_{s,p}$ —coverage area, in 1000  $m^2$ .

Capital investments for the purchase of rolling stock are determined by the formula:

$$K_{r,s} = \varphi \cdot \Sigma(K_a \cdot N_a \cdot t/T), \tag{12}$$

where:

$\varphi$  is a coefficient that takes into account the number of cars under repair, stock, etc.;

$K_a$ —the cost of a car of a certain type, in USD 1000;

$N_a \cdot t$  is the number of hours of use per day for a car engaged in transportation;

T—the average duration of car use per day, in h.

As a transport unit, a dump truck with a carrying capacity of m (per 10 tons) is used.

To ensure the cargo flow of S (per 3 million tons) of coal per year with 1.5 shifts of a car for u (per 200 working days) at a distance of 60 km, one car must make n (per 2 trips per day). From here:

$$N_a = S / (n \cdot u \cdot m), \tag{13}$$

$$N_a = 3,000,000 / (2 \cdot 200 \cdot 10) = 750 \text{ autos,}$$

at  $\varphi = 0.2$ ;  $K_a = 16.0$  USD 1000; and  $T = 12$  h.

Capital investments for the purchase of rolling stock are  $K_{r,s} = 2339.61$  in USD 1000.

Thus, calculations according to Formula (10) take into account all significant capital costs.

The indicators of the cost of roads are determined depending on the annual gross freight turnover in gross million tons. Estimated gross freight turnover is determined by the formula:

$$Q_{\text{gross}} = \sum Q_{\text{cargo}} \cdot \eta, \tag{14}$$

where

$Q_{\text{cargo}}$  is the freight turnover handled by the rolling stock of a certain type, mln.t. per year;  
 $\eta$ —transition coefficient from net freight turnover to gross freight turnover, determined for a given type of rolling stock;

$\eta$ —for a dump truck with  $\beta \cdot \gamma = 0.5$  is equal to  $\eta = 3.4$ ,

$\beta$  is the mileage utilization factor;

$\gamma$  is the utilization factor of the vehicle's carrying capacity.

From here:  $Q_{\text{gross}} = 10.2$  million gross tons.

Next, current operating costs are considered.

The total operating costs for road transport for the year is determined by the formula:

$$E_{a,t} = E_{r,s} + E_{eq}, \tag{15}$$

where:

$E_{r,s}$ —expenses depending on the amount of work (for rolling stock) for the year, in USD 1000;

$E_{eq}$  is the cost of maintaining permanent devices for the year, in USD 1000.

Annual operating costs in USD 1000, depending on the volume of work in the transport hub, are generally determined by the formula:

$$E_{r,s} = 0.365 (0.1 \sum E_{\text{load}} \cdot N_{\text{load}} \cdot L + 0.1 \sum E_{\text{emp}} \cdot N_{\text{emp}} \cdot L + \sum E_{\text{stan,h}} \cdot N_{\text{auto}} \cdot T), \tag{16}$$

where:

$E_{\text{load}}$  and  $E_{\text{emp}}$  are the rates of expenses per 10 vehicle km, loaded and empty mileage of certain types of vehicles, in USD;

$E_{\text{stan,h}}$  is the rate of expenses for one hour of idle time on the line of cars of certain types, USD;

$N_{\text{load}} \cdot L$  and  $N_{\text{emp}} \cdot L$  are the average daily mileage of cars of certain types in loaded and empty condition, in vehicle km;

$N_{\text{auto}} \cdot T$ —average daily downtime of cars of the corresponding types on the line, car h.

For dump truck:

$$E_{\text{load}} = 4.20 \text{ USD} \quad N_{\text{load}} \cdot L = 45,000 \text{ vehicle km}$$

$$E_{\text{emp}} = 3.41 \text{ USD} \quad N_{\text{emp}} \cdot L = 45,000 \text{ vehicle km}$$

$$E_{\text{stan,h}} = 2.38 \text{ USD} \quad N_{\text{auto}} \cdot T = 750 \text{ vehicle km}$$

From here:  $E_{r,s} = 13,118.56$  in USD 1000.

Annual operating costs in USD 1000 (for the maintenance of permanent devices), are determined by the formula:

$$E_{eq} = \Sigma E_{road} \cdot L_{road} + 0.001 \Sigma E_{br} \cdot L_{br} + 0.001 \Sigma E_{s,t} \cdot F_{s,t} + E_{gar}, \quad (17)$$

where:

$E_{road}$  is the rate of expenses for the maintenance of 1 km of a certain category of road per year, in USD 1000;

$E_{br}$  is the rate of expenses for the maintenance of 1 m of the bridge length per year, in USD 1000;

$E_{s,t}$  is the rate of expenses for the maintenance of 1000 m<sup>2</sup> of sites near loading and unloading devices per year, in USD 1000;

$E_{gar}$  is the rate of expenses for the maintenance of the garage for the year, in USD 1000;

$L_{road}$  is the road length, in km;

$L_{br}$  is the bridge length, in m;

$F_{s,t}$  is the coverage area of the sites, in 1000 m<sup>2</sup>.

For road transport of Karakechi coal with a cargo flow of 3 million tons per year:

$E_{road} = 8.19$  USD 1000;

$E_{br} = 109.2$  USD;

$E_{s,t} = 837.2$  USD;

$E_{gar} = 2548.0$  USD 1000.

From here:  $E_{eq} = 3053.2$  USD 1000.

Total annual operating costs for road transport:  $E_{a,t} = 16,171.80$  USD 1000.

The reduced costs for road transport of coal to TPPs will be:

$$P_{a,t} = E_{a,t} + Q_{standart} \cdot K_{a,t}, \quad (18)$$

$$P_{a,t} = 19,102.36 \text{ USD 1000.}$$

The cost of transporting coal by road:

$$Pr_{a,t} = E_{a,t} / N, \quad (19)$$

where N is the productivity of the motor transport system, in tons/year, equal to 3 million tons/year.

$$Pr_{a,t} = 5.39 \text{ USD/ton.}$$

Thus, we obtained that the value of 5.39 USD/ton is significantly higher than the analogous parameter during pipeline transportation.

The economic effect from the use of hydraulic transportation of Karakechi brown coal in comparison with road transport, when determined by the difference in the reduced costs, will be:

$$E_{c,p} = P_{a,t} - P_{c,p} = 17,689.49 \text{ USD 1000/year.}$$

An analysis of the technical and economic indicators of the studied technological schemes showed the prospects for using the scheme for burning pipeline transported Karekechi brown coal in boilers equipped with a dust system with fan mills and dust concentrators.

### 3.3. Mathematical Modeling—Artificial Neural Network Approach

Recently, a fairly large number of publications have appeared in which mathematical models are developed to describe the processes associated with coal–water suspensions based on artificial neural networks. For example, we can note article [75]. In this article, the authors describe a mathematical model they developed that allows for the predicting of CWS viscosity value, depending on the system parameters, by using an artificial neural network. The article presents the results of experimental studies for high-ash Indian coal. The Levenberg–Marquardt algorithm was applied to train the artificial neural network;

the multiple correlation coefficient was 0.99. The high value of the correlation coefficient indicates the reliability and adequacy of the developed neural network model.

Additionally, the works of [76–78] can also be mentioned. Vaferi, Samimi, Pakgohar, and Mowla considered the option of constructing an artificial neural network in order to predict the thermal state of a mixture [76]. Chin, Lai, Ibrahim, Jaafar, and El-Shafie built a model that predicts the mixture velocity [77]. Further, Dumitriu T., Dumitriu R., and Manta developed models of gel behavior [78].

The articles of [79,80] present the results of experimental studies of the combustion of pulverized coal. The results obtained are then used to train the neural network. In the articles, the authors solve the problem of burning coal–water suspensions with the help of a new efficient and environmentally friendly technology. The developed technology is based on the use of mathematical models and methods of artificial neural network theory. The technology helps to prevent the occurrence of emergencies during the combustion of fuel in boiler plants. The proposed automated control systems make it possible to reduce the cost of heat generation. Further, the data for training the neural network were obtained via industrial thermal installations. Moreover, the combustion parameters varied over a wide range for different combustion regimes.

Let us note the results of an interesting paper [32], one of the authors of which is the author of this review, K. Osintsev. The article examines the properties of coal–water fuel during its transportation in conditions of negative ambient temperatures, while using combined modeling: physical and computer. The article notes the need to use neural network theory methods and models, which can dramatically reduce the thermal and economic costs of transporting coal–water fuel. In this article, mathematical models for creating a control unit for a transport system for pumping water–carbon fuel was developed. At the same time, neural network algorithms were used, which made it possible to take into account implicit dependencies in the operation of the transport system. Examples of such dependencies are the size of coal particles, fuel consumption, pressure in the pipeline, the temperature difference between the pulp and the surrounding air, and the effect of these parameters on the adhesion of coal particles to welds and valves. Accounting for these dependencies make it possible to reduce the likelihood of an emergency. When carrying out physical modeling, the values of the fluidity of coal–water suspensions were measured, and the costs of electricity for pumping fuel under various modes of operation of the transport system were determined. The optimal structure of the coal–water pipeline transport system and effective methods of its management were determined and recommended for practical use. Based on neural network methods, a highly efficient automatic control system for a pipeline transport complex was developed in the article.

The scientific novelty of the article lies in the development of a fundamentally new design of a coal–water fuel hydro tracking unit, which is designed to study the effect of the thermophysical and rheological properties of the pumped water–carbon fuel in regard to the processes of heat and mass transfer during cooling and heating. The installation is divided into three lines, through which coal–water fuel with different characteristics are pumped. The modeling process involves the use of two experimental sites. It is proposed to use refrigerant at the first site. In the second site, low-boiling liquid is poured into the heat pump. The article reveals the possibilities of automation in technological pipeline transport. On the basis of the conducted studies the scheme of technological process control and control of its main parameters is offered. The proposed scheme includes elements of an automated electric drive and control based on a multi-zone controller. In addition, the implementation of the controller is based on neural network software that allows one to achieve efficiency gains by reducing unnecessary heat losses. The article may be of interest to specialists in the fields of power and information electronics, electric drives, and automation of technological processes.

The results of the conducted research can be used in industrial pipeline transport systems. This will improve the reliability of such systems. The results obtained are especially relevant for regions with difficult climatic conditions and topography.

In coal-mining regions—which are, in various countries, remote from railways and often within an undeveloped automobile network (for example, mountainous regions)—scientists and specialists are developing high-tech technologies for pumping coal–water fuel and burning coal–water suspensions in thermal power plants. One example is China, which is currently the leader in the use of coal–water technologies. In China, a slurry preparation plant has been built and is successfully operating; further, it supplies water–carbon fuel to the largest Maoming thermal power plant in Asia [81]. Similar projects were successfully implemented in the USSR and have continued to be implemented in Russia at the present time [82].

Coal–water suspensions can be prepared not only from high-quality raw materials for metallurgical production, but also from coal enrichment waste. Coal enrichment is carried out for transportation over short distances and direct flaring. At the same time, the costs for the needs of industrial enterprises are reduced. For the sake of comparison, the share of coal generation in the United States is 52%, in Germany 54%, in China 72%, and in Poland 94% [32].

## 4. Discussion and Future Prospects

### 4.1. Discussion

The mathematical models considered in this review are used by researchers to describe the combustion process and the process of transporting coal–water suspension [83,84]. Much attention should be paid to the developments that have proven themselves [85,86].

In Kyrgyzstan, a large amount of coal mining waste is generated annually, which is an excellent raw material for obtaining CWF [87,88]. The CWF currently produced is already competitive today both in relation to the consumed coal and in relation to liquid and gaseous fuels used for combustion in thermal power plants and boiler houses [89,90]. The cost of CWF prepared from coal mining waste, in terms of a ton of standard fuel, is 2–4 times lower than the cost of fuel oil and does not exceed 15–20% of the price of the original coal at the place of its production [91,92]. The creation of new types of coal–water fuels will minimize the cost of re-equipment of boiler units of thermal power plants and make them competitive with fuel oil and diesel fuel when burned in boiler units of thermal power plants and boiler houses.

Currently, coal–water fuel [93,94] is a dispersed composite system consisting of finely divided coal (60–65%), water, and a plasticizing agent (which is prepared from coal, coal-containing waste, and coal sludge) [95,96]. The main mass of coal particles in the developed CWF has a size of 10 . . . 200  $\mu\text{m}$ . Such CWF can be used for combustion in boiler units of thermal power plants [97].

Due to the significant content of large particles in CWF and the presence of an inert aqueous phase (up to 60%), thermal stabilization of the ignition zone of such CWF during ignition is required, which is provided by a fuel oil or gas torch, plasma torch arc, or other methods [98]. In addition, the presence of the mineral part of CWF, when up to 20–25%, necessitates the installation of equipment for ash collection and ash removal, which requires serious capital investments for the conversion of boilers in thermal power plants. These reasons are the main deterrent to the wide spread of CWF in many countries [99,100].

Mathematical models [101,102], created at the turn of the century [103,104], largely determined the direction of development for the composition of suspensions [105,106] and the influence of various factors on plasticity [107,108]. First of all, such factors include temperature, pressure, and the fractional composition of the suspension [109,110].

The use of CWF as an alternative to liquid fuels from oil mainly depends on the successful solution of the following physical and technological problems:

- grinding of the initial coal raw material to the level of 10 microns, and below, at energy costs lower than the existing ones (currently these costs are at 30–35  $\text{kW}/\text{m}^3$ );
- deep demineralization of coal suspension to a salt content of less than 2–3%;
- obtaining, on the basis of demineralized coal dispersion CWF, the necessary technological (thermophysical and rheological) properties.

The solution of the tasks set will make it possible to create fuel for boiler houses that do not require re-equipment.

The use of the cavitation effect in the processing of raw materials, as a result of hydrodynamic loads and shock waves arising in the system, leads to a heating of the substance and an increase in pressure; thus, this is what determines the effectiveness of the method.

Along with the above, it is proposed [111,112] to combine the process of fine grinding with coal demineralization. Intensive hydrodynamic cavitation will allow simultaneous deep demineralization of coal, emulsification of the aqueous phase, and the introduction of plasticizing additives.

The experimental works [113,114] carried out and the literature data indicate that intensive mechanical and hydrodynamic treatment leads to:

- the activation of coals due to the disorder of the structure and thus the formation of defects;
- the transition of coal particles to an ultra-dispersed state, which has a high reactivity, increases the rate of heterogeneous processes, and causes a significant change in the equilibrium parameters characterizing the reactivity of the coal substance.

For developing countries, their own energy independence is in the foreground; this is due to the fact that it is the basis for their economic independence from other sectors of the economy, specifically from the future impact of market changes in fuel prices on the spot world market. The authors of this review explored the possibility of using Kyrgyz brown coal and transporting it through a coal pipeline from a mountainous area to an industrial site for thermal utilization in specialized steam boiler units. As the economic analysis showed, specifically for the conditions of the Republic of Kyrgyzstan, the use of coal–water suspensions and coal pipelines at rising prices for natural gas is economically justified.

According to a review of the works of the authors involved in coal–water suspensions, it is more specifically confirmed that the construction of a coal pipeline is economically justified:

- when it is indispensable for any other modes of transport due to the tendency for spontaneous combustion or the high-water content of the fuel;
- when, due to the conditions of the terrain, it is possible to reduce the length of the pipeline transport main compared to rail or other modes of transport, while hydraulic transport is especially favorable in mountainous or rough terrain if there is an excess of the geodetic height of the supplier in comparison with the consumer;
- with the remoteness of fuel production areas from the places of its consumption and the absence or weak development of highways and railways;
- in the absence of large reserves of labor in pipeline transport, i.e., they do not exceed 30–40% of the cost of rail and road transport.

The results obtained in the process of research allow us to evaluate the modes and speeds of transport. Additionally, we can evaluate the specific pressure losses when moving finely divided Karakechi brown coal in pipelines and, on this same basis, offer graphic and tabular data that can be used in technological calculations at the pre-design and design stages of the development for a pipeline transport system in Kara-Keche—the industrial site of the state district power station.

Karakechi brown coal is satisfactorily wetted when it is fed into water, the non-dehydrated sludge has sufficient fluidity, can be stored in tanks for a long time, the intake from which must be carried out after hydraulic mixing by the suction devices of the pumps.

#### 4.2. Future Prospects

According to the latest works by Yang et al. [94] and Glushkov et al. [49], the combustion of coal–water is increasingly studied in the scientific community, in particular in China and India [94,95]. With the discovery of breakthrough technologies for the combustion of coal–water suspensions, it will be possible to talk about the construction of coal pipelines. In order to issue recommendations on the efficient use of coal pipeline transport, it is

necessary to conduct additional research related to the selection of optimal parameters and modes of transporting these coals through pipelines, including specific head losses, transportation speeds, hydro abrasive wear of pipelines, and grindability of coals during transportation. Separately, it should be noted that studies of the rheological properties of suspensions [87,88] and the construction of their mathematical models are ongoing.

The relevance of the use of coal–water fuel at thermal power plants is due to the emergence of new technologies for its preparation and combustion, which eliminate the previously identified shortcomings. The essence of the new technology for the preparation of CWF is that a mixture of carbonaceous materials with water is subjected to cavitation in special devices, i.e., cavitation dispersers. The result of cavitation treatment, which is characterized by an extremely high level of local dynamic, compression, and temperature effects on the material being processed (up to 2000 °C and 25,000 kgf/cm<sup>2</sup>), is not only the grinding of the solid component of the mixture to a micron degree of dispersion, but also the appearance of properties on the surface of its particles pronounced hydrophilicity. Difficulties associated with attempts to flare CWF in unsuitable existing chamber furnaces are determined by the need to spray the suspension down to micron sizes and increase the residence time of particles in the furnace due to the increased moisture content [111,112]. Therefore, long-flame and gaseous (highly reactive) low-ash coals were recommended for the preparation of CWF, and it is these coals that are quite successfully burned in the form of CWF [113,114] in China.

Taking into account the results of bench combustion of various types of coal–water fuels using various technologies, as the most versatile and especially suitable for combustion of CWF from low-grade fuels, we made a choice in favor of the technology of CWF combustion in a pseudo-boiling layer of an inert material [115,116]. This option, due to the high thermal stability of the mass of fluidized material, allows the ignition and reaction of the fuel at lower temperatures than in chamber combustion. This factor [117] provides a significant reduction in the generation of highly toxic nitrogen oxides, which is also facilitated by an increased content of water vapor in the reaction zone.

**Author Contributions:** Conceptualization, K.O.; methodology, S.A. and K.O.; validation, K.O.; formal Analysis, A.A.; investigation, S.A. and K.O.; resources, S.A. and A.A.; data collection, S.A. and K.O.; writing—original draft preparation, K.O. and S.A.; writing—review and editing, A.A.; visualization, S.A.; supervision, K.O.; project administration, A.A.; funding acquisition, S.A. and A.A. All of the authors contributed significantly to the completion of this review, conceiving and designing the review, and also writing and improving the paper. All authors have read and agreed to the published version of the manuscript.

**Funding:** This research received no external funding.

**Data Availability Statement:** There are no data applicable in this study.

**Acknowledgments:** The authors thank South Ural State University (SUSU) for supporting this research.

**Conflicts of Interest:** The authors declare no conflict of interest.

## References

1. Spalding, D.B. *Some Fundamentals of Combustion*; Butterworth’s Academic Press: London, UK, 1955; 250p.
2. Zeldovich, Y.B. *Collected Works*; Princeton University Press: Princeton, NJ, USA, 1992; Volume 1, 500p.
3. Williams, F.A. *Combustion Theory*, 2nd ed.; Benjamin/Cummings: Menlo Park, CA, USA; Westview Press: Boulder, CA, USA, 1985; 704p.
4. Verwey, E.J.W.; Overbeek, J.T.G. Theory of The Stability of Lyophobic Colloids. *J. Colloid Sci.* **1955**, *10*, 224–225. [CrossRef]
5. Furnas, C.C. *The Relations Between Specific Volume, Voids, and Size Composition in Systems of Broken Solids of Mixed Sizes*; Department of Commerce, Bureau of Mines: Washington, DC, USA, 1928.
6. Krieger, I.M.; Dougherty, T.J. A Mechanism for Non-Newtonian Flow in Suspensions of Rigid Spheres. *Trans. Soc. Rheol.* **1959**, *3*, 137. [CrossRef]
7. Takano, M.; Kambe, H. The Rheological Properties of Concentrated Suspensions. II. Stationary Flow Properties and the Influence of Additives and of Particle Size. *Bull. Chem. Soc. Jpn.* **1963**, *36*, 1424–1431. [CrossRef]

8. Fryling, C.F. The viscosity of small particle, electrolyte- and soap-deficient synthetic latex gels. *J. Colloid Sci.* **1963**, *18*, 713–732. [CrossRef]
9. Rutgers, I.R. Relative viscosity and concentration. *Rheol. Acta* **1962**, *2*, 305–348.
10. Yufin, A.P. *Hydromechanization*; Publication of literature on construction; Nauka: Moscow, Russia, 1965; 496p.
11. Jvarsheishvili, A.G. *Hydrotransport Systems of Mining and Processing Plants*; Nauka: Moscow, Russia, 1973; 351p.
12. Tsarnat, A.A. *Technological Parameters of Earthworks Production by Hydromechanization. Experience in Hydromechanization of Mining Construction, Land Reclamation and Transport Works*; Collection of reports and messages of the seventh intersectoral express conference of hydraulic mechanics specialists; Nauka: Moscow, Russia, 1972.
13. *Temporary Instruction for the Production of Works by the Method of Hydromechanization in Winter*; Gosenergoizdat: Moscow, Russia, 1985.
14. *Recommendations for the Design of Tailing Facilities for Enterprises of the Metallurgical Industry*; VodGEO; Gosstroy of the USSR; Stroyizdat: Moscow, Russia, 1975; 177p.
15. Volkov, G.R.; Gokhman, B.M. Investigation of the thermal regime of surface pipelines of hydraulic mines in winter. *Hydraul. Coal Min.* **1997**, *3*, 203–215.
16. Qin, L.; Lin, S.; Lin, H.; Li, S.; Zhao, P.; Wang, W.; Xue, Z. Unfrozen Water Content and Ice–Water Thawing Mechanism in Cryogenic Frozen Coal. *Nat. Resour. Res.* **2022**, *31*, 2839–2851. [CrossRef]
17. Liu, N.; Sun, L.; Qin, B.; Zhang, S.; Du, W. Evolution of pore and fracture of coal under heating–freezing effects: An experimental study. *Fuel* **2021**, *306*, 121618. [CrossRef]
18. Li, B.; Huang, L.; Lv, X.; Ren, Y. Variation features of unfrozen water content of water-saturated coal under low freezing temperature. *Sci. Rep.* **2021**, *11*, 15398. [CrossRef]
19. Li, B.; Li, L.; Huang, L.; Lv, X. The Temperature Field Evolution and Water Migration Law of Coal under Low-Temperature Freezing Conditions. *Int. J. Environ. Res. Public Health* **2021**, *18*, 13188. [CrossRef]
20. Vitel, M.; Rouabhi, A.; Tijani, M.; Guérin, F. Modeling heat transfer between a freeze pipe and the surrounding ground during artificial ground freezing activities. *Comput. Geotech.* **2015**, *63*, 99–111. [CrossRef]
21. Hou, S.; Yang, Y.; Cai, C.; Chen, Y.; Li, F.; Lei, D. Modeling heat and mass transfer during artificial ground freezing considering the influence of water seepage. *Int. J. Heat Mass Transf.* **2022**, *194*, 123053. [CrossRef]
22. Wang, B.; Rong, C.; Cheng, H.; Cai, H. Experimental investigation on heat transfer law of multiple freezing pipes in permeable stratum with high seepage velocity. *Int. J. Heat Mass Transf.* **2022**, *182*, 121868. [CrossRef]
23. Chen, Y.; Lai, Y.; Li, H.; Pei, W. Finite element analysis of heat and mass transfer in unsaturated freezing soils: Formulation and verification. *Comput. Geotech.* **2022**, *149*, 104848. [CrossRef]
24. Osintsev, V.V.; Dzhundubaev, A.K.; Khidiyatov, A.M.; Kozmin, G.V.; Kostovetsky, S.P. *The Use of Advanced Technologies for the Preparation and Combustion of the Main Energy Coals of Kyrgyzstan*; F. Ilim Publishing House: Bishkek, Kyrgyzstan, 1989; 208p.
25. Zaidenvarg, V.E.; Trubetskoy, K.N.; Murko, V.I. *Production and Use of Coal-Water Fuel*; Publishing House of the Academy of Sciences of Mining Sciences: Moscow, Russia, 2001; 176p.
26. Kashirin, F.T.; Kozmin, G.V.; Dzhundubaev, A.K. On the problem of transporting Karakechi coals with the help of pressure hydraulic transport. *Acad. Sci. Kirghiz SSR* **2021**, *4*, 14. Available online: [https://www.elibrary.ru/ip\\_restricted.asp?rpage=https%3A%2F%2Fwww%2Eelibrary%2Eru%2Fitem%2Easp%3Fid%3D21094198](https://www.elibrary.ru/ip_restricted.asp?rpage=https%3A%2F%2Fwww%2Eelibrary%2Eru%2Fitem%2Easp%3Fid%3D21094198) (accessed on 8 September 2022).
27. Dzhundubaev, A.K.; Khidiyatov, A.M.; Osintsev, V.V. Modeling of technological schemes for burning Kavak brown coal delivered to TPPs by hydrotransport. *Therm. Power Eng.* **1997**, *5*, 59–62.
28. Kuznetsov, G.V.; Piskunov, M.V.; Strizhak, P.A. Evaporation, boiling and explosive breakup of heterogeneous droplet in a high temperature gas. *Int. J. Heat Mass Transf.* **2016**, *92*, 360–369. [CrossRef]
29. Kozmin, G.V.; Dzhundubaev, A.K.; Delyagin, G.N. Experimental combustion of flooded Kavak brown coal in the form of water-coal suspension. *Izv. AN Kirg. SSR.* **1989**, *6*, 65–66.
30. Osintsev, V.V.; Dzhundubaev, A.K.; Toropov, E.V.; Kuznetsov, G.F.; Suleimenov, K.A. *Energy and Environmental Problems of Solid Fuel Combustion in Boiler Plants*; Under the editorship of Prof. Toropov, E.V. Chelyabinsk State Technical University, Chelyabinsk Territorial Scientific Center of the Academy of Engineering Sciences of the Russian Federation; Publishing House of ChGTU: Chelyabinsk, Russia, 1995; 191p.
31. Khidiyatov, A.M.; Osintsev, V.V.; Dubovtsev, L.I. Prospects, main results of research and problems of using water-coal suspensions in the energy sector. *Power Station.* **1988**, *9*, 2–12.
32. Osintsev, K.; Aliukov, S. Experimental and Mathematical Investigation of the Thermophysical Properties of Coal–Water Slurries Based on Lignite. *Energies* **2022**, *15*, 3814. [CrossRef]
33. Osintsev, K.V. Studying flame combustion of coal-water slurries in the furnaces of power-generating boilers. *Therm. Eng.* **2012**, *59*, 439–445. [CrossRef]
34. Mochalov, S.P.; Rybenko, I.A.; Ermakova, L.A. Mechanism and Mathematical Modeling of Coal-Water Slurry Combustion in Swirl Adiabatic Combustion Chamber. *World Appl. Sci. J.* **2012**, *19*, 20–25. [CrossRef]
35. Zhu, L.J.; Gu, B.Q. Computational Modeling of Coal Water Slurry Combustion Processes in Industrial Heating Boiler. In *Computational Methods in Engineering & Science*; Springer: Berlin/Heidelberg, Germany, 2006. [CrossRef]
36. Nunes, L.J.R. Potential of Coal–Water Slurries as an Alternative Fuel Source during the Transition Period for the Decarbonization of Energy Production: A Review. *Appl. Sci.* **2020**, *10*, 2470. [CrossRef]

37. Glód, K.; Lasek, J.; Słowik, K.; Zuwała, J. Combustion of coal water slurry-technology enabling the achievement of a reduced technical minimum of the boiler. *E3S Web Conf.* **2019**, *82*, 01004. [CrossRef]
38. Antonov, D.V.; Vershinina, K.Y.; Kuznetsov, G.V.; Strizhak, P.A. Mathematical Modeling of Ignition of Droplets of Coal-Water Slurry Containing Petrochemicals Using Ansys Fluent. In Proceedings of the 2nd World Congress on Momentum, Heat and Mass Transfer (MHMT'17), Barcelona, Spain, 6–8 April 2017. [CrossRef]
39. Salomatov, V.; Kuznetsov, G.; Syrodoy, S.; Gutareva, N. Mathematical and physical modeling of the coal-water fuel particle ignition with a liquid film on the surface. *Energy Rep.* **2020**, *6*, 628–643. [CrossRef]
40. Kijo-Kleczkowska, A. Analysis of cyclic combustion of the coal-water suspension. *Arch. Thermodyn.* **2011**, *32*, 45–75. [CrossRef]
41. Zeidenberg, V.E.; Trubetskoy, K.N.; Murko, V.I. *Production and Use of Coal-Water Fuel*; Nauka: Moscow, Russia, 2001; 163p.
42. Abdaliev, U.; Tashpolotov, Y.; Yslamidin, A.; Matmusaev, U. Water emulsion fuel: Production conditions, features and properties. *Sci. New Technol.* **2013**, *2*, 11–19.
43. Zhogashatiev, N.; Duisheeva, S.; Sadykov, E.; Tashpolotov, Y. Obtaining nanosized powders from liquid-phase solutions based on the electroionization method. *Bull. South. Branch Natl. Acad. Sci. Kyrg. Repub.* **2011**, *1*, 71–78.
44. Kroyt, G.R. *The Science of Colloids*; Izdatelstvo Inostrannoy Literatury: Moscow, Russia, 1955; Volume 1, 538p.
45. Bukharkina, T.V.; Digurov, N.G. *Chemistry of Natural Energy Carriers and Carbon Materials*; RKHTU im. D.I. Mendeleev: Moscow, Russia, 1999; 195p.
46. Prigogine, I.; Stengers, I. *Order Out of Chaos*; Progress: Moscow, Russia, 1986.
47. Khan, N.; Taqvi, S.; Bin Rafiq, H.; Nafees, A.; Zabiri, H. Selection of Appropriate Model for the Synthesis of Coal Water Slurry (CWS) Using PVA and TEA. *Iran. J. Chem. Chem. Eng.* **2019**, *8*, 253–261. [CrossRef]
48. Messa, G.V.; Yang, Q.; Adedeji, O.E.; Chàra, Z.; Duarte, C.A.R.; Matoušek, V.; Rasteiro, M.G.; Sanders, R.S.; Silva, R.C.; de Souza, F.J. Computational Fluid Dynamics Modelling of Liquid–Solid Slurry Flows in Pipelines: State-of-the-Art and Future Perspectives. *Processes* **2021**, *9*, 1566. [CrossRef]
49. Glushkov, D.O.; Kuznetsov, G.V.; Strizhak, P.A.; Syrodoy, S.V. A Mathematical Model for the Processes in Coal-Water Slurries Containing Petrochemicals under Heating. *Energy Fuels* **2018**, *32*, 8789–8802. [CrossRef]
50. Offengenden, N.E. Prospects for the Development of Pipeline Hydrotransport of Bulk Materials. Long-Distance Pipeline Transport of Bulk Materials (Materials of the All-Union Scientific Conference). 1984. Available online: [https://www.studmed.ru/ofengenden-ne-promyshlenny-truboprovodnyy-transport\\_a04d1f2f47.html](https://www.studmed.ru/ofengenden-ne-promyshlenny-truboprovodnyy-transport_a04d1f2f47.html) (accessed on 13 October 2021).
51. Delyagin, G.N. *Combustion of Water-Coal Suspensions—A Method of Using Watered Solid Fuels: Abstract of the Thesis*; doc. tech. Sciences: 05.283; Moscow Institute of Mountains Fossils: Moscow, Russia, 1971; 48p.
52. Smetannikov, B.N.; Delyagin, G.N. Investigation of ignition and combustion of a water-coal suspension drop. In *Combustion of Solid Fuel*; Nauka: Moscow, Russia, 1969; 556p.
53. Pohl, J.H.; Sepulveda, J.; Rothfield, L.B. Correlation of spray characteristics of coal-water fuels. In *Symposium on Coal Slurry Fuels Preparation and Utilization*; Pittsburgh Energy Technology Centre: Pittsburgh, PA, USA, 2001; pp. 357–376.
54. Khzmalyan, D.M. *Theory of Furnace Processes*; Energoatomizdat: Moscow, Russia, 1990; 351p.
55. Senchurova, Y.A.; Murko, V.I.; Fedyayev, V.I.; Dzyuba, D.A.; Puzyrev, E.M. Results of studies of the atomization of coal-water fuel by pneumo-mechanical nozzles. *Bull. Tomsk. Polytech. Univ.* **2008**, *312*, 37–40.
56. Das, D.; Das, S.K.; Parhi, P.K.; Dan, A.K.; Mishra, S.; Misra, P.K. Green strategies in formulating, stabilizing and pipeline transportation of coal water slurry in the framework of WATER-ENERGY NEXUS: A state of the art review. *Energy Nexus* **2021**, *4*, 100025. [CrossRef]
57. Chen, Z.; Yan, Z.; Jiang, H.; Que, Z.; Gao, G.; Xu, Z. Detecting Coal Pulverizing System Anomaly Using a Gated Recurrent Unit and Clustering. *Sensors* **2020**, *20*, 3271. [CrossRef]
58. Yi, Z.; Zhou, H. Economic comparison of electrical coal pipeline transport and rail transport considering external cost. *J. Wuhan Univ. Technol.* **2012**, *36*, 608–611. [CrossRef]
59. *A Technology Assessment of Coal Slurry Pipelines*; Office of Technology Assessment Publ.: Washington, DC, USA, 1978; 156p.
60. Jianzhong, L.; Ruikun, W.; Jianfei, X.; Junhu, Z.; Kefa, C. Pilot-scale investigation on slurrying, combustion, and slagging characteristics of coal slurry fuel prepared using industrial wasteliquid. *Appl. Energy* **2014**, *115*, 309–319. [CrossRef]
61. Michalik, A.; Hyncar, J.; Kula, H.; Fraś, A. Zakres i Warunki Stosowania Suspensji węGlowo-Wodnych. Conference Zakres i Warunki Stosowania Suspensji węGlowo-Wodnych, Zakopane. 2019. 75p. Available online: <https://se.min-pan.krakow.pl> (accessed on 8 September 2021).
62. Zhao, X.; Zhu, W.; Huang, J.; Li, M.; Gong, M. Emission characteristics of PCDD/Fs, PAHs and PCBs during the combustion of sludge-coal water slurry. *J. Energy Inst.* **2015**, *88*, 105–111. [CrossRef]
63. Osintsev, K.V.; Brylina, O.G.; Prikhodko, Y.S. Modeling and Automation of the Hydro-Transport System of Water–Coal Fuel at Negative Ambient Temperatures. In *Advances in Automation*; Lecture Notes in Electrical Engineering; Springer: Cham, Switzerland, 2020; Volume 641. [CrossRef]
64. Osintsev, K.V.; Dudkin, M.M.; Prikhodko, I.S. Improving Efficiency of Boiler in Case of Coal Hydrotransport. In Proceedings of the 5th International Conference on Industrial Engineering, Sochi, Russia, 25–29 March 2019; Lecture Notes in Mechanical Engineering. Springer: Cham, Switzerland, 2020. [CrossRef]
65. Wan, G.; Yu, J.; Wang, X.; Sun, L. Study on the pyrolysis behavior of coal-water slurry and coal-oil-water slurry. *J. Energy Inst.* **2022**, *100*, 10–21. [CrossRef]

66. Li, D.; Liu, J.; Wang, S.; Cheng, J. Study on coal water slurries prepared from coal chemical wastewater and their industrial application. *Appl. Energy* **2020**, *268*, 114976. [CrossRef]
67. Yao, D.; Zhao, H.; Chen, Z.; Liu, H. Preparation of high concentration coal water slurry with good fluidity based on only modified fine particles under bimodal distribution using the second fluid and the second particle. *Fuel* **2022**, *317*, 123461. [CrossRef]
68. Osintsev, K.V. Prospects for producing activated carbons on the CHP. *Bull. South Ural. State Univ. Ser. Power Eng.* **2013**, *13*, 5–13.
69. Gürses, A.; Açıkıldız, M.; Doğar, Ç.; Karaca, S.; Bayrak, R. An investigation on effects of various parameters on viscosities of coal–water mixture prepared with Erzurum–Aşkale lignite coal. *Fuel Process. Technol.* **2006**, *87*, 821–827. [CrossRef]
70. Boylu, F.; Dinçer, H.; Ateşok, G. Effect of coal particle size distribution, volume fraction and rank on the rheology of coal–water slurries. *Fuel Process. Technol.* **2004**, *85*, 241–250. [CrossRef]
71. Dinçer, H.; Boylu, F.; Sirkeci, A.A.; Ateşok, G. The effect of chemicals on the viscosity and stability of coal water slurries. *Int. J. Miner. Process.* **2003**, *70*, 41–51. [CrossRef]
72. Atesok, G.; Boylu, F.; Sirkeci, A.A.; Dincer, H. The effect of coal properties on the viscosity of coal–water slurries. *Fuel* **2002**, *81*, 1855–1858. [CrossRef]
73. Ziserman, G.N. *Technical and Economic Calculations of the Feasibility of Building a Thermal Power Plant and Developing Brown Coal Deposits in the Kavak Basin in the Kirghiz SSR*; Report, 92169; SAO TEP: Tashkent, Uzbekistan, 1979; 83p, Available online: [https://studbooks.net/1786642/geografiya/ekonomicheskaya\\_chast](https://studbooks.net/1786642/geografiya/ekonomicheskaya_chast) (accessed on 10 May 2021) Report, 92169.
74. Babiy, V.I.; Kuvaev, Y.F. *Combustion of Coal Dust and Calculation of a Pulverized Coal Torch*; Energoatomizdat: Moscow, Russia, 1986; 208p.
75. Sahoo, B.K.; De, S.; Meikap, B.C. Artificial neural network approach for rheological characteristics of coal-water slurry using microwave pre-treatment. *Int. J. Min. Sci. Technol.* **2017**, *27*, 27–379. [CrossRef]
76. Vaferi, B.; Samimi, F.; Pakgohar, E.; Mowla, D. Artificial neural network approach for prediction of thermal behavior of nanofluids flowing through circular tubes. *Powder Technol.* **2014**, *267*, 1–10. [CrossRef]
77. Chin, R.J.; Lai, S.H.; Ibrahim, S.; Jaafar, W.Z.W.; El-Shafie, A. Rheological wall slip velocity prediction model based on artificial neural network. *J. Exp. Theor. Artif. Intell.* **2019**, *31*, 659–676. [CrossRef]
78. Dumitriu, T.; Dumitriu, R.P.; Manta, V.I. Application of Artificial Neural Networks for modeling drug release from a bicomponent hydrogel system. In Proceedings of the 2016 20th International Conference on System Theory, Control and Computing (ICSTCC), Sinaia, Romania, 13–15 October 2016; pp. 675–680.
79. Shadrin, E.Y.; Anufriev, I.S.; Butakov, E.B.; Kopyev, E.P.; Alekseenko, S.V.; Maltsev, L.I.; Sharypov, O.V. Coal-water slurry atomization in a new pneumatic nozzle and combustion in a low-power industrial burner. *Fuel* **2021**, *303*, 121182. [CrossRef]
80. Butakov, E.B.; Pochtar, A.S.; Vinogradov, S.V.; Burdukov, A.P. Experimental studies of the combustion of pulverized coal to form the basis for training a neural network. *J. Phys. Conf. Ser.* **2022**, *2233*, 012016. [CrossRef]
81. Wang, H.; Guo, S.; Yang, L.; Guo, Y.; Jiang, X.; Wu, S. Surface morphology and porosity evolution of CWS spheres from a bench-scale fluidized bed. *Energy Fuels* **2015**, *29*, 3428–3437. [CrossRef]
82. Kijo-Kleczkowska, A. Research on destruction mechanism of drops and evolution of coal-water suspension in combustion process. *Arch. Min. Sci.* **2010**, *55*, 923–946.
83. Khodakov, G.S. Water-coal suspensions. *Energy* **2000**, *2*, 104–119.
84. Tolasov, Y.A.; Khodakov, G.S. Features of obtaining water-coal fuel in drum mills. In *Technology of Preparation and Physical and Chemical Properties of Water-Coal Suspension*; Proceedings of the NPO “Gidrotuboprovod”; Neftegazstroyinform: Moscow, Russia, 1991; pp. 97–110.
85. Redkina, N.I.; Khodakov, G.S. Physico-chemical interpretation of the rheological properties of concentrated suspensions. In *Technology of Preparation and Physico-Chemical Properties of Coal-Water Fuel*; Proceedings of the NPO “Gidrotuboprovod”; Neftegazstroyinform: Moscow, Russia, 1991; pp. 62–77.
86. Khodakov, G.S. *Physics of Grinding*; Nedra: Moscow, Russia, 1972.
87. Khodakov, G.S. Physico-chemical mechanics of technological processes. *Russ. Chem. J.* **2000**, *3*, 93–108.
88. Khrenkova, T.M. *Mechanochemical Activation of Coal*; Nedra: Moscow, Russia, 1993.
89. Rao, A.; Wilson, R.; Macmillan, M.; Kimberly, A. The technology of obtaining and studying fine-dispersed coal-water slurry. *Mod. Eng. Ser. A* **1990**, *1*, 163–173.
90. Tolasov, Y.A.; Zolotukhin, V.S.; Khodakov, G.S. Technological schemes for the preparation of water-coal fuel. In *Technology of Preparation and Physico-Chemical Properties of Water-Coal Suspension*; Proceedings of the NPO “Gidrotuboprovod”; Neftegazstroyinform: Moscow, Russia, 1991; pp. 78–97.
91. Khodakov, G.S. Physical and chemical mechanics of grinding solids. *Colloid J.* **1998**, *5*, 684–697.
92. Khodakov, G.S. Statistical analysis of test results of the Belovo-Novosibirsk coal pipeline. In *Technology of Preparation and Physico-Chemical Properties of Water-Coal Suspension*; Proceedings of the NPO “Gidrotuboprovod”; Neftegazstroyinform: Moscow, Russia, 1991; pp. 110–116.
93. Yang, Z.; Wu, Y.; Zhang, Z.; Li, H.; Li, X.; Egorov, R.I.; Strizhak, P.A.; Gao, X. Recent advances in co-thermochemical conversions of biomass with fossil fuels focusing on the synergistic effects. *Renew. Sustain. Energy Rev.* **2021**, *103*, 384–398. [CrossRef]
94. Xiao, J.; Wang, S.; Duan, X.; Ye, S.; Wen, J.; Zhang, Z. Rheological models for temperature and concentration dependencies of coal water slurry. *Int. J. Coal Prep. Util.* **2022**, *42*, 1185–1203. [CrossRef]

95. Rao, M.A.; Yerriswamy, V.; Kumar, M.V.; Narasaiah, N. A comparative study on the rheological properties of two coal water slurries with sodium tripolyphosphate as dispersant. *Int. J. Coal Prep. Util.* **2022**, *42*, 486–498. [CrossRef]
96. Behera, U.; Das, S.; Mishra, D.; Parhi, P.; Das, D. Enhancing the rheology and leachability of fly ash slurry using natural—Synthetic mixed surfactant system for hydraulic stowing in underground mines. *Int. J. Coal Prep. Util.* **2021**, *3*, 1–21. [CrossRef]
97. Rao, M.A.; Kumar, M.V.; Rao, S.; Narasaiah, N. Rheological behavior of coal-water slurries of Indian coals using carboxymethyl-cellulose as a dispersant—a comparative study. *Int. J. Coal Prep. Util.* **2021**, *41*, 728–738. [CrossRef]
98. Papachristodoulou, G.; Trass, O. Coal slurry fuel technology. *Can. J. Chem. Eng.* **1987**, *65*, 177–201. [CrossRef]
99. Bienstock, D.; Jamgochian, E.M. Coal-oil mixture technology in the US. *Fuel* **1981**, *60*, 851–864. [CrossRef]
100. Trass, O.; Papachristodoulou, G.L.; Gandolfi, E.A.J. Wet Grinding of Coal in the Szego Mill: Limiting Predictions and Experimental Results. *Coal Prep.* **1995**, *16*, 179–201. [CrossRef]
101. Roh, N.-S.; Shin, D.-H.; Kim, D.-C.; Kim, J.-D. Rheological behaviour of coal-water mixtures. 1. Effects of coal type, loading and particle size. *Fuel* **1995**, *74*, 1220–1225. [CrossRef]
102. Laskowski, J.S. Chapter 10 Fine-coal utilization. *Dev. Miner. Process.* **2001**, *14*, 307–351. [CrossRef]
103. Massoudi, M.; Phuoc, T.X. Fully developed flow of a modified second grade fluid with temperature dependent viscosity. *Acta Mech.* **2001**, *150*, 23–37. [CrossRef]
104. Langtangen, H.P.; Munthe, O. Solving systems of partial differential equations using object-oriented programming techniques with coupled heat and fluid flow as example. *ACM Trans. Math. Softw.* **2001**, *27*, 1–26. [CrossRef]
105. Aktaş, Z.; Woodburn, E. Effect of addition of surface active agent on the viscosity of a high concentration slurry of a low-rank British coal in water. *Fuel Process. Technol.* **2000**, *62*, 1–15. [CrossRef]
106. Guo, D.-H.; Jiang, L. Rheological behaviour of a new kind of fuel—Residual oil, coal and water triplex synfuel. *Fuel* **1998**, *77*, 1697–1700. [CrossRef]
107. Atal, A.; Levendis, Y.A. Observations on the combustion behavior of coal water fuels and coal water fuels impregnated with calcium magnesium acetate. *Combust. Flame* **1993**, *93*, 61–89. [CrossRef]
108. Laskowski, J.S.; Pugh, R.J. Dispersions stability and dispersing agents. *Dev. Miner. Process.* **1992**, *12*, 115–171. [CrossRef]
109. Fuerstenau, D.W.; Vazquez-Favela, J. On assessing and enhancing the energy efficiency of comminution processes. *Min. Metall. Explor.* **1997**, *14*, 41–48. [CrossRef]
110. Meffe, S.; Perkson, A.; Trass, O. Coal beneficiation and organic sulfur removal. *Fuel* **1996**, *75*, 25–30. [CrossRef]
111. Singh, M.K.; Kumar, S.; Ratha, D. Computational analysis on disposal of coal slurry at high solid concentrations through slurry pipeline. *Int. J. Coal Prep. Util.* **2020**, *40*, 116–130. [CrossRef]
112. Routray, A.; Das, D.; Parhi, P.; Padhy, M. Characterization, stabilization, and study of mechanism of coal-water slurry using Sapindous Mukorossi as an additive. *Energy Sources Part A Recovery Util. Environ. Eff.* **2018**, *40*, 2502–2509. [CrossRef]
113. Juneja, P.; Kumar, S.; Mohapatra, S.K. Influence of Chemical Leaching on Rheology and Ash Reduction of Indian Coal. *Int. J. Coal Prep. Util.* **2018**, *38*, 260–270. [CrossRef]
114. Xiang, Y.; Wang, R.; Liu, J.; Wu, J.; Zhou, J.; Cen, K. Study on the slurrying and rheological properties of coal–oilfield wastewater-slurry. *Energy Sources Part A Recovery Util. Environ. Eff.* **2016**, *38*, 3687–3693. [CrossRef]
115. Gao, F.; Hu, E.J. Effects of multifactors on rheological properties of bubble petroleum coke water slurry. *Pet. Sci. Technol.* **2016**, *34*, 927–932. [CrossRef]
116. Singh, M.K.; Ratha, D.; Kumar, S.; Kumar, D. Influence of Particle-Size Distribution and Temperature on Rheological Behavior of Coal Slurry. *Int. J. Coal Prep. Util.* **2016**, *36*, 44–54. [CrossRef]
117. Zhou, M.; Wu, S.; Sun, Z.; Qiu, X.; Yang, D. Effect of the Interfacial Agents with Different Types of Hydrophilic Functional Groups on the Rheological Properties of Coal-Water Slurry. *J. Dispers. Sci. Technol.* **2013**, *34*, 1646–1655. [CrossRef]

MDPI  
St. Alban-Anlage 66  
4052 Basel  
Switzerland  
[www.mdpi.com](http://www.mdpi.com)

*Mathematics* Editorial Office  
E-mail: [mathematics@mdpi.com](mailto:mathematics@mdpi.com)  
[www.mdpi.com/journal/mathematics](http://www.mdpi.com/journal/mathematics)



Disclaimer/Publisher's Note: The statements, opinions and data contained in all publications are solely those of the individual author(s) and contributor(s) and not of MDPI and/or the editor(s). MDPI and/or the editor(s) disclaim responsibility for any injury to people or property resulting from any ideas, methods, instructions or products referred to in the content.



Academic Open  
Access Publishing

[mdpi.com](http://mdpi.com)

ISBN 978-3-7258-1196-0